

Implementation of Engine Control and Measurement Strategies for
Biofuel Research in Compression-Ignition Engines

By

Michael Dewaine Mangus

Submitted to the graduate degree program in Mechanical Engineering and the Graduate Faculty of the University of Kansas in partial fulfillment of the requirements for the Degree of Doctor of Philosophy.

Chair: Dr. Christopher Depcik

Dr. Theodore Bergman

Dr. Susan Stagg-Williams

Dr. Edward Peltier

Dr. Terry Faddis

Date Defended: January 27, 2014

UMI Number: 3611282

All rights reserved

INFORMATION TO ALL USERS

The quality of this reproduction is dependent upon the quality of the copy submitted.

In the unlikely event that the author did not send a complete manuscript and there are missing pages, these will be noted. Also, if material had to be removed, a note will indicate the deletion.



UMI 3611282

Published by ProQuest LLC (2014). Copyright in the Dissertation held by the Author.

Microform Edition © ProQuest LLC.

All rights reserved. This work is protected against unauthorized copying under Title 17, United States Code



ProQuest LLC.
789 East Eisenhower Parkway
P.O. Box 1346
Ann Arbor, MI 48106 - 1346

The Dissertation Committee for Michal Mangus certifies that this is the approved version of the
following dissertation:

Implementation of Engine Control and Measurement Strategies for
Biofuel Research in Compression Ignition Engines

Chair: Dr. Christopher Depcik

Date approved: _____

Abstract

The global petroleum fuel supply is a limited resource that is understood to have negative influences on the environment because of its usage. In order address this issue, researchers are investigating sources of sustainable energy to offset this finite energy supply. One promising option for the transportation sector is biodiesel derived from various feedstocks. In order to perform viable research in the area of sustainable biodiesel, a multi-disciplinary effort to study the entire biodiesel spectrum from production to tailpipe emissions is underway at the University of Kansas. A critical aspect of this research includes investigating the effects of biodiesel combustion on engine operation. This includes observing engine power output, fuel consumption, and mechanical wear. In order to detect these characteristics effectively, full instrumentation of a single-cylinder compression-ignition engine is necessary. This engine serves as a test apparatus for experimental fuels and as a student-training tool. Of particular interest is the upgrade of this engine's fuel system to include electronically controlled fuel injection using an engine control unit. To aid in future research and to serve as a training reference, a detailed description of the construction, maintenance, and troubleshooting of the engine, dynamometer, auxiliary systems, and data acquisition equipment is included. Furthermore, this dissertation contains findings from biodiesel studies illustrating how fuel properties, such as fuel viscosity, play a role in injection and combustion behavior. The completed engine testing system provides the opportunity to continue into more sophisticated research venues, such as low temperature combustion and multiple injection events.

Acknowledgements

The work completed within this dissertation would not have been possible if it were not for the support of a number of individuals. This includes the Mechanical Engineering Department at KU for their knowledge and monetary support throughout the graduate process and the Transportation Research Institute for their financial support. Custom parts and machining was completed by Charles Gabel and Ash Shadrick of the Mechanical Engineering Machine Shop. Wes Ellison of the KU Aerospace Engineering Department provided tools necessary to complete the installation of the ECU in the single-cylinder engine test cell. Daniel Tabakh provided measurement of the fuel properties used in Chapters 2 and 3. Additionally, Farshid Kiani provided statistical analysis for the regressions performed in Chapters 2 and 3. The biodiesels used in Chapter 3 were produced by Juan David Castellanos Saganome. Dr. Susan Stagg-Williams of Chemical and Petroleum Engineering and Dr. Edward Peltier of Civil, Environmental, and Architectural Engineering provided technical guidance pertaining to fuel production and characterization and engine emissions behavior, as well as guidance and editing during the publication writing process of Chapters 2 and 3. Dr. Christopher Depcik provided the opportunity to work on this project, including guidance, support, and feedback throughout the entire process. Additional assistance during construction and experimentation was provided by Eric Cecrle, Colter Ragone, Derek Pickett, Chenaniah Langness, and Jonathan Mattson.

Table of Contents

Table of Figures	xi
Table of Tables	xxx
Nomenclature	xxxii
Introduction	1
Emissions	2
Fuel Economy	4
CI Engine Overview	4
NOx-PM Tradeoff	6
Working to Defeat the NOx-PM Tradeoff	7
Injection Systems	8
Influence of Biofuels on CI Engines	12
Research Requirements	13
Dissertation Focus	14

Chapter 1: Installation of Electronically-Controlled High-Pressure Fuel Injection on a Single-Cylinder

Compression-Ignition Engine	18
1.1 Introduction	18
1.2 Equipment	20
1.3 The LabVIEW Programs	25
1.3.1 Engine Signal Simulator for Bench Testing	25
1.3.2 Engine Sensor Signal Converter	31
1.4 Calibration Software	44
1.5 Bench Testing	45

1.5.1	Engine Control Unit Installation for Initial Bench Testing	46
1.5.2	Results of Bench Testing	54
1.5.3	Verifying Injection Timing	55
1.6	Implementation of ECU into Test Cell	57
1.6.1	Installation of the Engine Sensors	58
1.6.2	Bosch Injector Install	61
1.6.3	High-Pressure Fuel System Installation	65
1.6.4	Controlling High-Pressure Fuel Pump Speed and Injection Pressure	70
1.7	System Validation	74
1.7.1	Engine Calibration	76
1.8	Conclusion	85

Chapter 2: Neat and Blended Biodiesel in an Adjusted Single-Cylinder CI engine with Electronically-Controlled Fuel Injection	86	
Study 1: Comparison of Neat Biodiesels and ULSD in a Single-Cylinder Diesel Engine with Electronically-Controlled Fuel Injection	87	
2.1	Abstract	87
2.2	Introduction	87
2.3	Biodiesels Tested	91
2.4	Test Apparatus and Methodology	93
2.5	Results	96
2.6	Regression Analysis	113
2.6.1	Nitrogen Oxides Emissions	115
2.6.2	Partial Combustion Products Emissions	117

2.6.3	Particulate Matter Emissions	120
2.6.4	Fuel Consumption	121
2.7	Conclusion	122
Study 2: Influence of Biodiesel Blends and Fuel Properties in a Single-Cylinder Engine with Electronically-Controlled Fuel Injection		125
2.8	Abstract	125
2.9	Introduction	125
2.10	Test Apparatus and Methodology	128
2.11	Fuel Properties and Blend Percentage Relationships	132
2.12	Engine Testing Results	135
2.12.1	Nitrogen Oxides Emissions	147
2.12.2	Partial Combustion Products Emissions	149
2.12.3	Particulate Matter Emissions	152
2.12.4	Fuel Consumption	155
2.13	Conclusion	157

Chapter 3: Performance and Emissions Characteristics of Hydroprocessed Renewable Jet Fuel Blends in a Single-Cylinder Compression Ignition Engine with Electronically-Controlled Fuel Injection		159
3.1	Abstract	159
3.2	Introduction	159
3.3	Fuels Tested	163
3.4	Test Apparatus and Methodology	167
3.5	Results and Discussion	170
3.5.1	Combustion Behavior	171

3.5.2 Emissions	181
3.5.2.1 Nitrogen Oxides Emissions	182
3.5.2.2 Partial Combustion Products Emissions	185
3.5.2.3 Particulate Matter Emissions	189
3.5.2.4 Fuel Consumption	192
3.6 Conclusion	194

Chapter 4: Operation, Technical Information, and Troubleshooting of the Single-Cylinder Compression-Ignition Engine Test Cell	
	198
4.1 Introduction	198
4.2 Yanmar Single-Cylinder Engine	201
4.2.1 New Engine Preparation and Installation	205
4.2.2 Performing an Engine Oil Change	210
4.3 Turbocharger	211
4.4 Exhaust Gas Recirculation System	218
4.5 Dynamometer	219
4.5.1 Controlling the Dynamometer	220
4.5.2 Calibrating Torque Sensor	222
4.5.3 Tuning the Dynamometer	227
4.6 Data Acquisition and Control	228
4.6.1 Low-Speed System	229
4.6.1.1 Creating Executable for Test Cell Control	237
4.6.2 High-speed Instrumentation	246
4.6.2.1 Intake Reference Pressure Upgrade	247

4.6.2.2 Pressure vs. Volume Plot Upgrade and Net Indicated Parameters	254
4.6.2.3 Increasing Number of Cycles Saved by Program	257
4.6.2.4 Rapid Loading of Reference Files	261
4.6.2.5 Upgrade in Measurement Resolution	264
4.6.2.6 In-Cylinder Pressure System Troubleshooting	269
4.7 Emissions Equipment	270
4.7.1 AVL SESAM FTIR Bench	271
4.7.1.1 AVL SESAM Bench Startup	273
4.7.1.2 The AVL Operating Window	275
4.7.1.3 Calibrating the FID and Oxygen Sensor	277
4.7.1.4 Starting the FTIR	285
4.7.1.5 Recording Emissions Measurements from the FTIR	288
4.7.1.6 SESAM Shutdown Procedure	302
4.7.1.7 Changing PM Filter	303
4.7.2 AVL 415SE Smoke Meter	304
4.7.2.1 Smoke Meter System Maintenance	310
4.8 Post-Processing Engine and Emissions Data	313
4.8.1 Calculation of Brake-Specific Performance and Emissions Parameters	316
4.9 Conclusion	319

Chapter 5: Initial Design and Construction Phases of a Multi-Cylinder, Compression-Ignition Engine

Laboratory	321
5.1 Test Cell Systems	323
5.1.1 Climate Control and Building Integration	326

5.1.2 Safety Systems	332
5.2 Installation of the Duramax Engine	334
5.2.1 Engine Mounts	338
5.2.2 Installation of Torque Dampening Coupler	341
5.2.3 Rear Engine Mount and Scatter Shield	347
5.3 Dynamometer	350
5.3.1 Flow of Electricity Drive Cabinet and Intermediate Cutoff	352
5.3.2 Controller	356
5.3.3 Emergency Stop Integration with Main Test Cell Systems	358
5.3.4 Calibration Procedure	361
5.3.5 Abbreviated Re-calibration Procedure	373
5.3.6 Dynamometer Tuning Procedure	375
Conclusion	385
References	390
Appendices	A1
Supplemental Figures and Tables from Chapter 2 – Study 1	A1
Supplemental Figures and Tables from Chapter 2 – Study 2	A15
Supplemental Figures and Tables from Chapter 3	A53

Table of Figures

Figure 1. Fuel Combustion Process: Injection (left), Diffusion Burn, Light Indicates PM Production (right) [18].	6
Figure 2. Operating Cycle for High-Pressure In-line Fuel Pump [25].	8
Figure 3. In-line Diesel Fuel Pump for a Six-Cylinder CI engine with the Camshaft Input (Blue) and Outlets to the Injectors (Red) [26].	9
Figure 4. Cross Section of In-line Diesel Injector [27].	9
Figure 5. Components of Common-Rail Fuel System. ECU (Blue Arrow), Fuel Pump (Green Arrow), Common-Rail (Red Arrow), and Injectors (Orange Arrow) [32].	10
Figure 6. Electronic High-Pressure Fuel Injector [33].	11
Figure 1-1. Mechanical Fuel Pump (1), High-Pressure Fuel Line (2), and Injector (3) as Installed by Yanmar.	18
Figure 1-2. Cylinder Pressure vs. Crank Angle for ULSD, UCO Biodiesel, and JP-8 From -20° to 30° After TDC at 40% Rated Engine Torque [19].	19
Figure 1-3. Rocker Arms (1), Moved by Upward Motion of Pushrods (2), Used to Actuate Intake and Exhaust Valves (3).	21
Figure 1-4. Depicts Signal Flow from the Intended Cam and Crank Signals (top left) to the ECU (dashed). Instead, Known Encoder and Pressure Signals are Read by a LabVIEW Program that Replicates the Needed Signals Based on Engine Speed and Stroke.	22
Figure 1-5. Crankshaft Signal Diagram as Generated by an Inductive Speed Sensor [34].	22
Figure 1-6. 60-2 Wheel for Inductive Speed Sensor. Gap Serves as TDC Reference [34].	23
Figure 1-7. Diagram Showing the Cam Sensor Timing Wheel with Sync and Phase Marks as Needed to Determine the Engine Cycle [34].	24
Figure 1-8. Output Voltage of the Inductive Cam Sensor as a Timing Tooth Passes [34].	24

Figure 1-9. Front Panel of Engine Simulation Program.	26
Figure 1-10. Block Diagram of Engine Simulation Program, All False Cases.	28
Figure 1-11. True Case Occurring at Piston TDC.	29
Figure 1-12. True Case Occurring at Piston TDC Following the Compression Stroke.	30
Figure 1-13. True Case Occurring At or Between SOI and EOI.	30
Figure 1-14. First Segment of Sensor Conversion Program Block Diagram Showing Initialization of Variables and the High-speed DIO Module.	32
Figure 1-15. Block Diagram Where DIO Module Configuration is Finished and Initialization Counter is Set to One.	34
Figure 1-16. Second Frame Counter to Increase Angle and Pulse Count (False Case). Here, the Encoder Square Wave Signal is Not Changing, so No Action is Required.	35
Figure 1-17. Second Frame Counter to Increase Angle and Pulse Count. Here the Encoder Signal is Changing (Outer True Case), Resulting in Increasing the Pulse and Angle Counters (Not at TDC – Inner Case False).	36
Figure 1-18. Second Frame Counter to Increase Angle and Pulse Counters. Here the Encoder Signal is Changing (Outer True Case) and is at TDC Following Compression, Resulting in Increasing the Pulse Counter and Resetting the Angle Counter (Inner True Case).	37
Figure 1-19. CRK Signal: Leave CRK in its Previous State (High or Low). CAM Signal: Voltage is in Neither High or Low Range, Set to 0 VDC.	38
Figure 1-20. Pulse Count = Six, Flip State of CRK (From True to False, Vice Versa) and Reset Pulse Count.	41
Figure 1-21. Engine in Interval of Timing Gap, but not at 90° after TDC, Set CRK to False.	41
Figure 1-22. Engine is at Exactly 90° After TDC (End of Timing Gap), Set CRK to True, Reset Pulse Count.	42
Figure 1-23. Angle within Range for Front of Cam Wheel Tooth, Set AO0 to 5 VDC.	43

Figure 1-24. Angle Within Range for Zero Crossing and Back of Cam Wheel Tooth, Set A00 to -5 VDC.	44
Figure 1-25. Screenshot of BOSCH Modas Sport ECU Measurement and Calibration Program.	45
Figure 1-26. Depicts Signal Flowchart during 'Bench' Testing.	46
Figure 1-27. Crimping Tool (1), Wire (2), Pins (3), and Blank Connector (4).	46
Figure 1-28. Inserting Stripped 22-Gauge Wire Into Pin.	47
Figure 1-29. Pins Before Crimping (Bottom) and After Crimping (Top).	47
Figure 1-30. Close-Up of the Tines Inside a Connector [41].	48
Figure 1-31. Place Wire into Insertion Tool.	49
Figure 1-32. Press Pin into Desired Pin Slot.	49
Figure 1-33. Press Until a 'Click' is Felt/Heard.	49
Figure 1-34. Remove Insertion Tool.	49
Figure 1-35. Wiring Diagram for CAN-Bus Communication .	50
Figure 1-36. Initial Wiring for Power-up and Communication Showing: ECU with USB Connection (1), Breadboard with CAN Bus Resistance Wiring (2), Preliminary Ignition Switch (3), and 12-Volt Direct-Current Power Supply (4).	50
Figure 1-37. Connection with ECU via USB Connection.	51
Figure 1-38. Configuration of a Voltage Divider to Measure Temperature Using an RTD and a Step-Up Resistor.	52
Figure 1-39. Initial Wiring Needed for Bench Testing of the ECU (1) and Dedicated Test Cell Computer (2).	53
Figure 1-40. Screenshot of Oscilloscope Showing Cam Sensor Signal Voltage Approximating Phase (4) and Sync (1) Marks at Transition from Positive to Negative Voltage.	54
Figure 1-41. Screenshot of BOSCH Modas Sport ECU Measurement and Calibration Program During Initial Bench Tests.	55

Figure 1-42. Injector Voltage Spikes and Start of Injection (12° before TDC) References from LabVIEW.	56
Figure 1-43. Single Injector Voltage Spike and Start of Injection (12° before TDC) Reference from LabVIEW.	56
Figure 1-44. Close-up of ECU Installation.	57
Figure 1-45. ECU Power Switch (red) Next to Dynamometer Controller and High-Speed Computer Screen.	57
Figure 1-46. Bosch Oil Pressure Sensor (red) Installed on the Yanmar and Wired to the ECU. Previous Oil Temperature Location is Shown in Blue.	58
Figure 1-47. Bosch Oil Temperature Sensor (Red) and Auxiliary Oil Drain (Blue).	59
Figure 1-48. Location of Installed Bosch Oil Temperature Sensor Using Thread Adapter.	59
Figure 1-49. Bosch Intake Pressure and Temperature Sensor (Red).	59
Figure 1-50. Original Yanmar Injector (1) and Fuel Pump (2), Bosch Injector (3) with Spacer Gasket from Yanmar Injector (4).	61
Figure 1-51. Yanmar Injector.	62
Figure 1-52. Bosch Injector.	62
Figure 1-53. Stock Yanmar Injector Installation.	62
Figure 1-54. Yanmar Injector, Mounting Plate Removed.	63
Figure 1-55. New Injector Mounting Studs Installed on Yanmar Engine Head.	63
Figure 1-56. Custom-Made Mounting Plate for Bosch Injector (Left). Stock Yanmar Mounting Plate (Right).	64
Figure 1-57. Final Bosch Injector Installation Using New Mounting Studs and Mounting Plate.	64
Figure 1-58. Yanmar Fuel Pump Fed by Rubber Fuel Line, High-Pressure Injection Line Removed.	65
Figure 1-59. Removed Yanmar Fuel Pump.	65

Figure 1-60. Internal Camshaft to Control Injection Timing of Yanmar Pump (1), Fuel Quantity Control Lever (2), Over-Speed Safety Mechanism (3). _____	66
Figure 1-61. Yanmar Fuel Pump Removed with Cover Plate Installed (1). Yanmar Fuel Quantity Control Lever Locked in Place (2). _____	67
Figure 1-62. Electric Motor (1), High-Pressure CP3 Fuel Pump (2), Low-Pressure Fuel Line (3), High-Pressure Fuel Line (4), Fuel Rail (with Sensor and Solenoid) (5), and Injector (6). _____	68
Figure 1-63. Coupler between Drive Motor and Fuel Pump. _____	69
Figure 1-64. DC Motor Controller (1) and DC-controlled AC Relay Activated by Main LabVIEW Program (2). _____	70
Figure 1-65. Control of High-Pressure Pump, ON (Top) OFF (Bottom). _____	70
Figure 1-66. Potentiometer to Control Drive Motor and Pump Speed. _____	71
Figure 1-67. Screenshot of Modas Sport, Adjustment of Rail Pressure. _____	71
Figure 1-68. Screenshot of Modas Sport, Monitoring Rail Pressure Setpoint (1) and Measured Pressure (2). _____	72
Figure 1-69. Adjustment of Beginning of Injection Angle Map in Modas Sport. _____	72
Figure 1-70. Control of Fuel Injection Quantity via LabVIEW Main Program. _____	73
Figure 1-71. Cylinder Pressure and Heat Release Rate at 9 N·m. Injection Timing at -9° After TDC Verified by Heat Release Rate (Red Arrow). Premixed and Diffusion Burn Combustion Phases (Blue and Green Arrows, Respectively). _____	75
Figure 1-72. BSFC vs. Injection Timing at All Loadings. Minimum BSFC at a Given Load Indicates MBT Timing. _____	77
Figure 1-73. Cylinder Pressure vs. Engine Crank Angle for (a) 0.5 N·m, (b) 4.5 N·m, (c) 9.0 N·m, (d) 13.5 N·m, and (e) 18.0 N·m. MBT Timing Traces are Shown in Green. _____	78

Figure 1-74. Cylinder Pressure vs. Engine Crank Angle (a) and Adjusted Heat Release Rate at MBT Timings (b) for All Tested Loads.	79
Figure 1-75. NO _x Emissions (a) and PM Emissions (b) vs. Injection Timing at All Tested Loads. PM Production Expected to Increase at Injection Timings Later than Those Indicated.	80
Figure 1-76. Heat Release Rate vs. Engine Crank Angle for 4.5 N·m Load Injection Timing Sweep.	81
Figure 1-77. Combustion Efficiency (a) and Fuel Conversion Efficiency (b) vs. Injection Timing for All Loads.	83
Figure 1-78. Screenshots of Adjusted Jet-Propellant (Red) and Adjusted ULSD (Yellow) Cylinder Pressure vs. Engine Crank Angle at 13.5 N·m (Left) and 18.0 N·m (Right).	84
Figure 2-1. In-Cylinder Pressure vs. Engine Crank Angle at 0.5 N·m (a, b), 9.0 N·m (c, d), and 18.0 N·m (e, f) at Unadjusted (a, c, e) and Adjusted (b, d, f) Injection Timings.	98
Figure 2-2. Heat Release Rates vs. Engine Crank Angle at 0.5 N·m (a, b), 9.0 N·m (c, d), and 18.0 N·m (e, f) at Unadjusted (a, c, e) and Adjusted (b, d, f) Injection Timings.	102
Figure 2-3. Cylinder Temperature vs. Engine Crank Angle at 0.5 N·m (a, b), 9.0 N·m (c, d), and 18.0 N·m (e, f) at Unadjusted (a, c, e) and Adjusted (b, d, f) Injection Timings.	105
Figure 2-4. Brake-Specific NO _x Emissions vs. Engine Torque for (a) Unadjusted and (b) Adjusted Injection Timings.	107
Figure 2-5. Brake-Specific CO Emissions vs. Engine Torque for (a) Unadjusted and (b) Adjusted Injection Timings.	108
Figure 2-6. Brake-Specific HC Emissions vs. Engine Torque for (a) Unadjusted and (b) Adjusted Injection Timings.	109
Figure 2-7. Brake-Specific PM Emissions vs. Engine Torque for (a) Unadjusted and (b) Adjusted Injection Timings.	110

Figure 2-8. Fuel Conversion Efficiency vs. Engine Torque for (a) Unadjusted and (b) Adjusted Injection Timings.	112
Figure 2-9. Density and Viscosity vs. Biodiesel Blend Percentage.	134
Figure 2-10. Energy Content and Flash Point vs. Biodiesel Blend Percentage.	134
Figure 2-11. In-cylinder Pressure vs. Engine Crank Angle at 9.0 N-m of Torque for Palm (a), Jatropha (b), Soybean (c), and Beef Tallow (d) Biodiesel Blends.	135
Figure 2-12. In-cylinder Pressure vs. Engine Crank Angle at 18.0 N-m of Torque for Palm (a), Jatropha (b), Soybean (c), and Beef Tallow (d) Biodiesel Blends.	136
Figure 2-13. Peak Cylinder Pressure a Function of Biodiesel Blend Percentage for 9.0 N-m (a) and 18.0 N-m (b) Loads.	137
Figure 2-14. Heat Release Rate vs. Engine Crank Angle at 9.0 N-m of Torque for Palm (a), Jatropha (b), Soybean (c), and Beef Tallow (d) Biodiesel Blends.	140
Figure 2-15. Heat Release Rate vs. Engine Crank Angle at 18.0 N-m of Torque for Palm (a), Jatropha (b), Soybean (c), and Beef Tallow (d) Biodiesel Blends.	141
Figure 2-16. Cylinder Temperature vs. Engine Crank Angle at 9.0 N-m of Torque for Palm (a), Jatropha (b), Soybean (c), and Beef Tallow (d) Biodiesel Blends.	144
Figure 2-17. Cylinder Temperature vs. Engine Crank Angle at 18.0 N-m of Torque for Palm (a), Jatropha (b), Soybean (c), and Beef Tallow (d) Biodiesel Blends.	145
Figure 2-18. Brake-Specific NO _x Emissions as a Function of Biodiesel Blend Percentage for 9.0 N-m (a) and 18.0 N-m (b) Loads. Tier 4 Regulation at 7.5 g/kW-hr (Not Displayed).	147
Figure 2-19. Brake-Specific CO Emissions as a Function of Biodiesel Blend Percentage for 9.0 N-m (a) and 18.0 N-m (b) Loads. Tier 4 Regulation at 8.0 g/kW-hr (Not Displayed).	149
Figure 2-20. Brake-Specific HC Emissions as a Function of Biodiesel Blend Percentage for 9.0 N-m (a) and 18.0 N-m (b) Loads.	151

Figure 2-21. Brake-Specific PM Emissions vs. Torque for ULSD and Neat Biodiesel (a), ULSD and Twenty-Percent Biodiesel (b)._____	152
Figure 2-22. Brake-Specific PM Emissions as a Function of Biodiesel Blend Percentage for 9.0 N-m (a) and 18.0 N-m (b) Loads._____	153
Figure 2-23. Brake-Specific Fuel Consumption as a Function of Biodiesel Blend Percentage for 9.0 N-m (a) and 18.0 N-m (b) Loads._____	155
Figure 2-24. Fuel Conversion Efficiency as a Function of Biodiesel Blend Percentage for 9.0 N-m (a) and 18.0 N-m (b) Loading._____	156
Figure 3-1. Measured Fuel Energy Content and Viscosity vs. R-8 Blend Percentage._____	165
Figure 3-2. Measured Fuel Density and Flash Point vs. R-8 Blend Percentage._____	166
Figure 3-3. Cylinder Pressure vs. Engine Crank Angle for Unadjusted (a) and Adjusted (b) Fuel Blends at 9.0 N-m Loading._____	171
Figure 3-4. Cylinder Pressure vs. Engine Crank Angle for Unadjusted (a) and Adjusted (b) Fuel Blends at 18.0 N-m Loading._____	171
Figure 3-5. Peak Cylinder Pressure vs. Blend Percentage for Unadjusted and Adjusted Blends at 9.0 (a) and 18.0 N-m (b) Loading._____	173
Figure 3-6. Heat Release Rate vs. Engine Crank Angle for Unadjusted (a) and Adjusted (b) Fuel Blends at 9.0 N-m Loading._____	176
Figure 3-7. Heat Release Rate vs. Engine Crank Angle for Unadjusted (a) and Adjusted (b) Fuel Blends at 18.0 N-m Loading._____	176
Figure 3-8. Cylinder Temperature vs. Engine Crank Angle for Unadjusted (a) and Adjusted (b) Fuel Blends at 9.0 N-m Loading._____	178
Figure 3-9. Cylinder Temperature vs. Engine Crank Angle for Unadjusted (a) and Adjusted (b) Fuel Blends at 18.0 N-m Loading._____	179

Figure 3-10. Brake-Specific NO _x Emissions vs. Torque for Adjusted R-8, Jet-A, and ULSD.	183
Figure 3-11. Brake-Specific NO _x Emissions vs. Blend Percentage for Unadjusted and Adjusted Blends at 9.0 (a) and 18.0 N-m (b). Loading Tier 4 Regulation at 7.5 g/kW-hr (Not Displayed).	184
Figure 3-12. Brake-Specific CO Emissions vs. Torque for Adjusted R-8, Jet-A, and ULSD.	185
Figure 3-13. Brake-Specific CO Emissions vs. Blend Percentage for Unadjusted and Adjusted Blends at 9.0 (a) and 18.0 N-m (b) Loading. Tier 4 Regulation at 8.0 g/kW-hr (Not Displayed).	185
Figure 3-14. Brake-Specific HC Emissions vs. Torque for Adjusted R-8, Jet-A, and ULSD.	187
Figure 3-15. Brake-Specific HC Emissions vs. Blend Percentage for Unadjusted and Adjusted Blends at 9.0 (a) and 18.0 N-m (b) Loading.	187
Figure 3-16. Brake-Specific PM Emissions vs. Torque for Adjusted R-8, Jet-A, and ULSD.	189
Figure 3-17. Brake-Specific PM Emissions vs. Blend Percentage for Unadjusted and Adjusted Blends at 9.0 (a) and 18.0 N-m (b) Loading. Tier 4 Regulation at 0.4 g/kW-hr (Not Displayed).	190
Figure 3-18. Brake-Specific Fuel Consumption vs. Torque for Adjusted R-8, Jet-A, and ULSD.	192
Figure 3-19. Brake-Specific Fuel Consumption vs. Blend Percentage for Unadjusted and Adjusted Blends at 9.0 (a) and 18.0 N-m (b) Loading.	192
Figure 3-20. Fuel Conversion Efficiency vs. Blend Percentage for Unadjusted and Adjusted Blends at 9.0 N-m (a) and 18.0 N-m (b) Loading.	193
Figure 4-1. Yanmar Single-Cylinder Engine Test Cell. Yanmar (1), Gaseous Mixing Box (2),	198
Figure 4-2. Secondary View of Test Cell with Dynamometer and Emissions Equipment. Dynamometer (1), AVL FTIR Bench (2), AVL Smoke Meter (3), and Engine Control Unit (4).	199
Figure 4-3. Yanmar Engine from the Flywheel End.	202
Figure 4-4. Intake Flow Measurement System. Laminar Flow Element (1), Resonator Barrel (2).	203
Figure 4-5. Yanmar Exhaust System. Yanmar Exhaust Port (1), Muffler (2).	204
Figure 4-6. Stock Yanmar YDG5500 Diesel Generator Containing an L100V Engine. Generator (1),	205

Figure 4-7. Electronic Components of AC Generator.	206
Figure 4-8. Yanmar Generator Rotor and Shaft.	206
Figure 4-9. Generator Rotor Shaft (Top) and Rotor Removal Tool (Bottom).	207
Figure 4-10. Removal tool (with Threads) During Rotor Removal.	207
Figure 4-11. Inner Generator Housing with Four Retaining Bolts (Red).	208
Figure 4-12. Yanmar Engine Ready for Install Into KU Test Cell.	209
Figure 4-13. Draining Oil from Yanmar Engine.	210
Figure 4-14. Filling Yanmar Engine with Oil.	210
Figure 4-15. Aerocharger Turbocharger with Oil Inlet Port (1), Turbine Inlet Transition (2), Compressor, Outlet Boot (3), Boost Controller (4), and Boost Feedback Bleed Valve (5).	211
Figure 4-16. Aerocharger Turbocharger Installed on Yanmar Engine.	213
Figure 4-17. Yanmar Exhaust (1) to Aerocharger Turbocharger (2) Adapter. Also Shown are the EGR Connection (3), and Thermocouple (4) and Pressure Transducer (5) Ports.	214
Figure 4-18. 90-Degree Exhaust Adapter to Match Turbocharger Endpoint Connections.	215
Figure 4-19. Cylinder Pressure vs. Engine Crank Angle for Naturally-Aspirated (N-A) and Turbocharged	216
Figure 4-20. Thermal Efficiency vs. Torque for the Yanmar when Naturally-Aspirated and Turbocharged.	217
Figure 4-21. Intake Throttle Valve.	218
Figure 4-22. Dynamometer Mounting (1) and Driveline with Futek (2) and Yanmar (3).	220
Figure 4-23. Dynamometer Controller Installed in Learned Hall.	220
Figure 4-24. User Controls on Inter-Loc V Controller.	221
Figure 4-25. Following Warm-up Period, Torque Transducer Out of Calibration.	223
Figure 4-26. Calibration Selection Window Displayed By Pressing 'Calibrate'.	223

Figure 4-27. Press ‘Zero’ to Adjust the Offset of The Transducer Signal.	224
Figure 4-28. Signal Offset Adjusted to Zero Torque Measurement.	224
Figure 4-29. Shunt Calibration (+5 VDC) Sent to Transducer to Set Gain Value at Full Torque.	225
Figure 4-30. Signal Gain Adjusted to Span Measurement at Full Torque.	226
Figure 4-31. Torque Transducer Calibrated.	226
Figure 4-32. Dynamometer Speed Response to Ramp Following Calibration.	227
Figure 4-33. Computers for Test Cell. Includes Low-Speed System (1), Second Monitor for Remote-	228
Figure 4-34. Main Operating Window of Low-Speed LabVIEW Program.	230
Figure 4-35. Low-Speed LabVIEW Project.	231
Figure 4-36. Input of Module Seven Signals to Data Cluster.	232
Figure 4-37. Retrieval of Module Seven Data Cluster. Calculation of Fuel Mass Flow Rate.	232
Figure 4-38. Fuel Mass Flow Rate Calculation SubVI.	233
Figure 4-39. Rail Pressure Linear Interpolation SubVI.	234
Figure 4-40. Building Global Data and Global Display Variables in Real-Time Processor.	235
Figure 4-41. Retrieving Inlet Fuel Flow Rate from Global Display Variable.	236
Figure 4-42. Retrieving Data from Global Data Variable for Writing to File with DAQ Write SubVI.	236
Figure 4-43. Creating a New Executable of LabVIEW Program.	237
Figure 4-44. Information Window of Executable Generation.	238
Figure 4-45. Source Files Window of Executable Generation.	238
Figure 4-46. Destinations Window of Executable Generation.	239
Figure 4-47. Source File Settings Window of Executable Generation.	240
Figure 4-48. Icon Window of Executable Generation.	240
Figure 4-49. Version Information Window of Executable Generation.	241
Figure 4-50. Creation of LabVIEW Executable Installer.	242

Figure 4-51. Product Information Window for Executable Installer.	243
Figure 4-52. Destinations Window for Executable Installer.	243
Figure 4-53. Source Files Window for Executable Installer.	244
Figure 4-54. Shortcuts Window for Executable Installer. Browse for Target File.	245
Figure 4-55. Installer for Executable.	246
Figure 4-56. Setting Rack-Mount Computer IP Address and Sending Intake Pressure to In-Cylinder Code.	247
Figure 4-57. High-Speed Measurement Window: Reference Intake Pressure.	248
Figure 4-58. Global Variable in Main Operating Program.	248
Figure 4-59. Main Test Cell Project.	249
Figure 4-60. Sending Inlet Pressure from c-RIO to High-Speed Computer via TCP/IP.	250
Figure 4-61. Startup of c-RIO Communication VI (red), Reading Global Inlet Pressure for Offset.	252
Figure 4-62. Updated In-Cylinder Pressure LabVIEW Project With Communications VI.	252
Figure 4-63. Receive Inlet Pressure From c-RIO Via TCP/IP Communication.	253
Figure 4-64. Pressure vs. Crank Angle (left) and Pressure vs. Volume (right) During Engine Operation.	254
Figure 4-65. Creation of Pressure vs. Volume and Pressure vs. Crank Angle Graphs.	255
Figure 4-66. Calculation of Indicated Net Parameters (IMEP and Indicated Work).	256
Figure 4-67. Storing First Run of FPGA Data to Buffer Text File.	258
Figure 4-68. Storing Second Run of FPGA Data to Buffer Text File.	259
Figure 4-69. Reading Data from Buffer Files to Generate 60-cycle Array.	260
Figure 4-70. Directory for In-Cylinder Pressure LabVIEW Program.	261
Figure 4-71. Example of Pressure vs. Crank Angle Plot with Reference Profile Loaded by Browse for Path Dialog Box.	262
Figure 4-72. Loading Reference Pressure Trace File.	263

Figure 4-73. DIP Switches to Adjust Encoder Resolution [108].	264
Figure 4-74. Kistler Pulse Multiplier.	265
Figure 4-75. Charge Amp: DIP Switches Down for 1° Resolution (left) and 0.2° Resolution (right).	265
Figure 4-76. Lowered Number of Cycles Saved to Memory by FPGA.	266
Figure 4-77. FPGA Code That Waits for Rising Edge of Square Wave.	267
Figure 4-78. Writing FPGA Iterations to Buffer Files.	268
Figure 4-79. Reading of Buffer Files and Building of Single Data Array.	269
Figure 4-80. SESAM 4 Bench (1), FTIR Sampling Hose (2), FTIR Filter Housing (3), Smoke Meter (4), and Smoke Meter Sampling Hose (5).	271
Figure 4-81. Fourier Transformation and Absorption Spectrum Evaluation Method [109].	272
Figure 4-82. Air Supply Piping and Valves in Test Cell.	273
Figure 4-83. Regulator and Filters for Compressed Air.	273
Figure 4-84. Power Switch For Heated Sample Line and Heated Filter.	274
Figure 4-85. Main Operating Window of the AVL Bench Computer.	276
Figure 4-86. Logon Window to Access Other Pages.	277
Figure 4-87. FID Fuel (Hydrogen + Helium), FID Synthetic Air, and FTIR Purge Nitrogen Tanks.	278
Figure 4-88. THC Window. Synthetic Air and FID Fuel Valves Open, Glow Plug Active.	278
Figure 4-89. THC Window. Synthetic Air and FID Fuel Valves Open, Glow Plug Off, FID Lit.	279
Figure 4-90. Main Window with FID Lit.	280
Figure 4-91. Calibration Tubing for FID and Oxygen Sensor Calibration.	281
Figure 4-92. Main Window. Zeroing O ₂ Sensor's Low Range.	281
Figure 4-93. Main Window. Spanning O ₂ Sensor's Low Range.	282
Figure 4-94. Main Window. Zeroing O ₂ Sensor's High Range.	283
Figure 4-95. Main Window. Spanning O ₂ Sensor's High Range.	283

Figure 4-96. Main Window. Zeroing THC Sensor's Low Range.	284
Figure 4-97. Main Window. Spanning THC Sensor's Low Range.	284
Figure 4-98. Main Window. Zeroing THC Sensor's High Range.	284
Figure 4-99. Main Window. Spanning THC Sensor's High Range.	284
Figure 4-100. Pouring Liquid Nitrogen Into FTIR Reservoir.	285
Figure 4-101. Main Window Indicating the Measuring of a New Background.	286
Figure 4-102. Main Window. Ready to Measure, Sampling Room Air.	287
Figure 4-103. Screen Shot of AK Command Window.	289
Figure 4-104. LabVIEW-AVL Communication and Data Collection Window.	290
Figure 4-105. Emissions Recording File Name and Path Dialog Box.	291
Figure 4-106. Initialization of TCP/IP Connection. Transmission of AK Command 'AKON K0'.	292
Figure 4-107. Reading TCP Message From Bench Computer.	293
Figure 4-108. Removing STX and ETX Characters From Received TCP Message.	294
Figure 4-109. Sort Through Species String to Separate Into Individual Species String Array.	295
Figure 4-110. Convert String Array Into Individual Species Variables for Display (and Saving Later).	296
Figure 4-111. Converting Oxygen from PPM to % Concentration.	296
Figure 4-112. Determine File Saving State, Create New File Column Header.	297
Figure 4-113. Creation of File Header, Concatenate With Column Headers, Set File Save Path	299
Figure 4-114. New File Created, Timer Keeps Running Until File Is Closed.	300
Figure 4-115. Write Species and Elapsed Time to File, Reset Time if Needed, Close TCP Connection.	301
Figure 4-116. Example of LabVIEW Output File of Saved Emissions Data.	302
Figure 4-117. Filter Location on Filter Cart.	303
Figure 4-118. Removal of Filter Protective Cover.	303
Figure 4-119. PM Filter Stem.	304

Figure 4-120. Smoke Meter Collection Principle .	304
Figure 4-121. Smoke Meter Sample Probe.	305
Figure 4-122. Orientation of PM Sampling Probe.	305
Figure 4-123. Startup of Smoke Meter, User Level: Monitor.	307
Figure 4-124. Volume Operation Mode, User Level: Operator.	308
Figure 4-125. Time Operation Mode, User Level: Operator.	309
Figure 4-126. Internal Components of AVL Smoke Meter. Reflectometer (1), Downstream PM Filter (2), Paper Supply Roll (3), and Paper Return Roll (4).	310
Figure 4-127. Old Paper Rolls Removed, Reflectometer Jaw Unclamped.	311
Figure 4-128. New Roll Inserted on Carrier. Feed Diagram Indicated At Back of Sensor.	311
Figure 4-129. Old Empty Roll used to Capture Spent Filter Paper using Scotch Tape.	312
Figure 4-130. Sample Clamp and Feed Mechanism Closed, Ready for Sampling.	312
Figure 4-131. Sample Performance Data File.	313
Figure 4-132. Sample In-cylinder Pressure Data File.	314
Figure 4-133. Sample Gaseous Emissions File.	315
Figure 4-134. Sample PM Output File.	315
Figure 5-1. Dyne Systems Dynamometer Installed in Multi-Cylinder Test Cell.	323
Figure 5-2. Inter-Loc V Dynamometer Controller Installation.	324
Figure 5-3. Torque and Power Rating vs. Speed of 351-hp Dyne Systems Dynamometer.	325
Figure 5-4. Test Cell Auxiliary Systems Main Operating Window Reproduced from Bachelor Controls Manual.	326
Figure 5-5. Engine Combustion Air Handling Diagram from Bachelor Controls Manual.	327
Figure 5-6. Test Cell Air Handler Diagram from Bachelor Controls Manual.	328
Figure 5-7. Duramax Coolant Pump.	329

Figure 5-8. Test Cell Glycol System for Engine Jacket Water and Intercooler Loops.	330
Figure 5-9. Test Cell Glycol Cooling System from Bachelor Controls Manual.	331
Figure 5-10. Engine Intercooler. Intercooler Supply (1), Intercooler Return (2), from Turbocharger (3), to Intake (4).	332
Figure 5-11. Gas Sensors and Alarm in Test Cell Control Room.	333
Figure 5-12. Emergency Stop Button Near Control Room Door.	334
Figure 5-13. Emergency-Stop Button, Fire Alarm, Fire Extinguisher Near Test Cell Exit Door.	334
Figure 5-14. Engine Test Cell Pad Prior to Treatment.	335
Figure 5-15. First Half of Pad Treatment, Following Cleaning and Degreasing.	336
Figure 5-16. Drying of Pad After Application of Blackening Fluid (Oxidizer).	337
Figure 5-17. First Half of Pad Treated (Left). Right Side Untreated.	337
Figure 5-18. Engine Pad Following Blackening Treatment.	338
Figure 5-19. Driver Side of Duramax Engine Block Showing Mounting Holes.	339
Figure 5-20. Passenger Side of Duramax Engine Block Showing Mounting Holes.	339
Figure 5-21. Passenger-Side Elephant Foot with Engine Mount Adapter.	340
Figure 5-22. AutoDesk Design of Mount Adapter.	341
Figure 5-23. Installed Mount Adapter.	341
Figure 5-24. Duramax Flywheel with Transmission Flex Plate.	342
Figure 5-25. Flywheel (bottom), Flex Plate (middle), Spacer (top).	343
Figure 5-26. Duramax Flywheel Bolt-Tightening Pattern.	344
Figure 5-27. Bolt Angular Tightening Guide.	344
Figure 5-28. Duramax Flywheel Re-Installed.	345
Figure 5-29. Coupling-Flywheel Adapter.	345
Figure 5-30. Torque-Dampening Coupler Installed.	346

Figure 5-31. Universal-Joint Drive Shaft to Connect Engine and Dynamometer.	346
Figure 5-32. Duramax Transmission Interface, Provided by Gale Banks Engineering, Incorporated.	347
Figure 5-33. Scatter Shield Studs and Structural Tubes.	348
Figure 5-34. Scatter Shield Flange Installed on Duramax. Used as Guide for Outer Structure Construction.	348
	348
Figure 5-35. Water-Jet Scrap as Used for Final Cutting and Welding of Radial Outer Structure.	349
Figure 5-36. Fully Assembled Scatter Shield.	350
Figure 5-37. Dynamometer Mounting Bolts.	351
Figure 5-38. HBM to Universal-Joint Adapter.	351
Figure 5-39. Air Filter and Cooling Blower of Dynamometer.	352
Figure 5-40. Main Dynamometer Circuit Breaker (1NT1) in M2SEC Basement.	353
Figure 5-41. 480VAC Transformer (left) and Dynamometer Drive Cabinet (right).	353
Figure 5-42. Dynamometer Power Lockout Cabinet Closed (left) and Open (right).	354
Figure 5-43. Disconnect Switch in Dynamometer Lockout Cabinet.	355
Figure 5-44. Dynamometer Junction Box Internal Connections.	355
Figure 5-45. Dynamometer Control and Monitoring Interface.	356
Figure 5-46. Dynamometer Controller Emergency-Stop Input.	358
Figure 5-47. Connection of Emergency Stop Input and Output.	359
Figure 5-48. Wiring of Emergency Stop Output from General Purpose I/O Port.	360
Figure 5-49. Emergency Stop Relay, Located Behind the Dynamometer Controller in the Controller Cabinet.	361
	361
Figure 5-50. Locking Mechanism and Safety Proximity Sensor in the Unlocked (left) and Locked (right) Position.	362
Figure 5-51. Calibration Moment Arm and Weight Hanger.	363

Figure 5-52. Dynamometer-Facing Surface of Calibration Arm.	363
Figure 5-53. Torque Induced by Calibration Weight Hanger.	364
Figure 5-54. Inter-Loc V Setup Menu: Modify Display Units.	365
Figure 5-55. Display Units Dialog Box in Inter-Loc V Setup Menu.	366
Figure 5-56. Torque Induced by the Calibration Weight Hanger.	366
Figure 5-57. Calibration Popup Selection Menu.	367
Figure 5-58. Calibration Menu Prior to Calibration.	367
Figure 5-59. Calibration Zeroed for Accurate Gain Determination.	368
Figure 5-60. 100 lb-ft Calibration Torque Application (left) and Displayed Measurement (right).	368
Figure 5-61. 300 lb-ft Calibration Torque Application (left) and Displayed Measurement (right).	369
Figure 5-62. 600 lb-ft Calibration Torque Application (left) and Displayed Measurement (right).	369
Figure 5-63. Span Value Adjustment Input.	370
Figure 5-64. Calibration Window Following Span Calibration.	370
Figure 5-65. Calibration Window Following Calibration Weight Removal.	371
Figure 5-66. Calibration Window Following Offset Zero Calibration.	372
Figure 5-67. Main Operating Screen. Torque Shown in LB-FT (left) and N-m (right).	372
Figure 5-68. Calibration Window: Shunt Active.	373
Figure 5-69. Calibration Window: Storing of New Span Reading.	374
Figure 5-70. Calibration Window: New Gain Value Following Span.	375
Figure 5-71. Main Operating Window: Operating at 1000 RPM Setpoint in Preparation of Tuning.	376
Figure 5-72. Dynamometer Controller Tuning Window.	377
Figure 5-73. Tuning Window: Low P-gain, I- and D-gain set to zero.	378
Figure 5-74. Tuning Window: P-Gain Increased to Near Instability.	378
Figure 5-75. Tuning Window: P-Gain Set, Increasing I-Gain Value.	379

Figure 5-76. Tuning Window: I-Gain Increased To Produce Some Oscillation.	380
Figure 5-77. Tuning Window: I-Gain Value Set for Best Performance.	380
Figure 5-78. Tuning Window: Introducing Derivative Gain to the Controller Response.	381
Figure 5-79. Tuning Window: Derivative Gain Increased.	381
Figure 5-80. Tuning Window: Ramp Response Following PID Tuning.	382
Figure 5-81. Main Operating Window: Ramp Rate Adjustment.	383
Figure 5-82. Ramp Rate Adjustment Dialog Box.	383
Figure 5-83. Main Operating Window: Ramp Rate Changed to 400 RPM/sec.	384
Figure 5-84. Tuning Window: Response to Higher Ramp Rate.	384

Table of Tables

Table 1-1. Location of Beginning, 0 VDC Crossing, and End of Sync and Phase Marks for <i>CAM</i> Signals, Corresponding Values for <i>Angle</i> . _____	40
Table 2-1. Physical Properties and Elemental Composition of the Different Fuels Tested. _____	91
Table 2-2. Biodiesel Fatty Acid Component Mass Fractions. _____	92
Table 2-3. Injection Timings for Common-Rail Fuel Injection System (Degrees Before TDC) as a Function of Engine Torque. ULSD Timings Correspond to Unadjusted Biodiesel Timings. _____	95
Table 2-4. Fuel Property Pearson Correlation Coefficients. _____	114
Table 2-5. NO _x and Fuel Property Pearson Correlation Coefficients. _____	115
Table 2-6. CO and Fuel Property Pearson Correlation Coefficients. _____	117
Table 2-7. HC and Fuel Property Pearson Correlation Coefficients. _____	118
Table 2-8. PM and Fuel Property Pearson Correlation Coefficients. _____	120
Table 2-9. BSFC and Fuel Property Pearson Correlation Coefficients. _____	121
Table 2-10. Anticipated Result of Increasing Independent Fuel Property. _____	123
Table 2-11. Injection Timings (Degrees Before TDC) for ULSD and Biodiesel Blends with ULSD. _____	131
Table 2-12. Fuel Properties of Palm Biodiesel Blends with ULSD. _____	132
Table 2-13. Fuel Properties of Jatropha Biodiesel Blends with ULSD. _____	132
Table 2-14. Fuel Properties of Soybean Biodiesel Blends with ULSD. _____	132
Table 2-15. Fuel Properties of Beef Tallow Biodiesel Blends with ULSD. _____	133
Table 2-16. Neat Biodiesel Fatty Acid Component Mass Fractions. _____	133
Table 2-17. Pearson Correlation Coefficients for Brake-Specific NO _x Emissions as a Function of Increasing Biodiesel Blend Percentage. _____	147
Table 2-18. Pearson Correlation Coefficients for Brake-Specific CO Emissions as a Function of Increasing Biodiesel Blend Percentage. _____	149

Table 2-19. Pearson Correlation Coefficients for Brake-Specific HC Emissions as a Function of Increasing Biodiesel Blend Percentage.	151
Table 2-20. Pearson Correlation Coefficients for Brake-Specific PM Emissions as a Function of Increasing Biodiesel Blend Percentage.	153
Table 2-21. Pearson Correlation Coefficients for Brake-Specific Fuel Consumption Emissions as a Increasing Function of Biodiesel Blend Percentage.	155
Table 3-1. Fuel Properties of ULSD, Jet-A, and R-8.	164
Table 3-2. Pearson Correlation Coefficients of Measured Fuel Properties for Jet-A and R-8 Blends.	165
Table 3-3. Injection Timing for Various Fuel Blend Tests at All Engine Loadings. Unadjusted Blends are Injected at Jet-A Injection Timings at Respective Load (Bold).	169
Table 3-4. Pearson Correlation Coefficients for Brake-Specific NO _x Emissions as a Function of Increasing R-8 Blend Percentage.	184
Table 3-5. Pearson Correlation Coefficients for Brake-Specific CO Emissions as a Function of Increasing R- 8 Blend Percentage.	186
Table 3-6. Pearson Correlation Coefficients for Brake-Specific HC Emissions as a Function of Increasing R- 8 Blend Percentage.	188
Table 3-7. Pearson Correlation Coefficients for Brake-Specific PM Emissions as a Function of Increasing R-8 Blend Percentage.	190
Table 3-8. Pearson Correlation Coefficients for Brake-Specific Fuel Consumption Emissions as a Function of Increasing R-8 Blend Percentage.	193
Table 3-9. Anticipated Result of Increasing Independent Fuel Property.	196
Table 5-1. Duramax Specifications [111].	321
Table 5-2. Dyne Systems Dynamometer Specifications.	325

Nomenclature

Variable	Description	Units
$bsfc$	Brake-Specific Fuel Consumption	(g/kw-hr)
$bsPM$	Brake-Specific PM Emissions	(g/kw-hr)
$\bar{M}_{exhaust}$	Exhaust Molar Mass	(g/mol)
M_i	Exhaust Species Molar Mass	(g/mol)
\dot{m}	Mass Flow Rate	(g/s)
N	Engine Speed	(Rotations per Minute)
P_{engine}	Engine Brake Power	(kW)
p	Instantaneous Cylinder Pressure	(Pa)
Q_{lhv}	Lower Heating Value	(MJ/kg)
PM_{conc}	PM Exhaust Concentration	(mg/m ³)
$P_{exhaust}$	Exhaust Pressure	(Pa)
\bar{R}	Universal Gas Constant	(J/mol-K)
V_d	Engine Displacement Volume	(m ³)
V_{EVO}	Cylinder Volume at Exhaust Valve Closing	(m ³)
V_{IVC}	Cylinder Volume at Intake Valve Closing	(m ³)
$W_{i,g}$	Gross Indicated Work	(kJ/cycle)
x_i	Exhaust Species Molar Fraction	(-)
ρ	Density	(kg/m ³)
τ	Engine Torque	(N-m)
η_c	Combustion Efficiency	(%)
η_f	Fuel Conversion Efficiency	(%)
η_t	Thermal Efficiency	(%)
η_v	Volumetric Efficiency	(%)
Subscripts		
<i>air</i>	Intake Air	
<i>exhaust</i>	Engine Exhaust	
<i>f</i>	Fuel	
<i>j</i>	Exhaust Species	

Introduction

Since the invention of the internal combustion engine, advancements in engine power, efficiency, and exhaust behavior capabilities have been implemented because of various economic and environmental needs. The first internal combustion engines were the coal-gas burning engines of the 1860's developed by J.J.E. Lenoir, which pulled fuel and air into the cylinder during the first half of an intake stroke. Then, a spark ignited the mixture, causing a pressure rise and providing power to the piston. The exhaust subsequently left the cylinder during the return of the piston to repeat the cycle. There were approximately 5,000 engines produced and they operated with up to five percent efficiency[1]. These engines, which operated at atmospheric pressure, were rendered obsolete in 1867 by the work of Nicolaus Otto and Eugen Langen. These two researchers developed an engine that used a moving piston to raise combustion chamber pressure by compressing the fuel-air mixture[1, 2]. The fuel and air mixture was ignited by a gas flame, achieved an efficiency of 11%, and represented a dramatic improvement in engine technology. Otto later developed the four-stroke spark-ignition (SI) engine in 1876, which noticeably raised both engine size and the power to weight ratio. Early versions of this engine were 14% efficient and by 1890, 50,000 spark-ignition engines were sold in Europe and the United States[1]. By this time, it was understood that engine power output is a function of compression ratio, as defined by the ratio of volume from the cylinder's largest capacity to its smallest capacity. In other words, the more that the fuel-air mixture can be compressed before ignition, the more power can be produced[1, 2]. Unfortunately, fuels of that era limited compression ratios of spark-ignition engines to four and less, as a higher compression would cause unwanted engine knock, brought on by pockets of air-fuel mixture exploding before the desired time [1].

Meanwhile, Rudolf Diesel was developing the compression ignition (CI) engine. In his design, fuel is injected into the cylinder following compression of the air, which then ignites due to heat and pressure, rather than by spark. Because the fuel is added at an optimal time, rather than mixed in the air

during compression, much higher compression ratios became possible since the engine is no longer knock limited. This resulted in a doubling of efficiency as compared to other internal combustion engines of the era[1, 2]. Unfortunately, these engines were met with limited acceptance because of technical issues, such as fuel injection and quantity control, along with the wide acceptance and production of spark-ignition vehicles [1].

Development of fuels to power the engines has been as fundamentally important as advances in the engines themselves. Gasoline, and other fractions of crude oil of similar characteristics, became available in the late 1800s and were used in conjunction with carburetors to vaporize the fuel into the air as it was drawn into the engine. A thermal cracking process, developed by Standard Oil of Indiana, provided a means of yielding large quantities of gasoline from heavier oils heated under pressure. However, this type of gasoline was hindered by cold weather starts due to its higher boiling point. This challenge led to the introduction of electric starters, again demonstrating a time when innovation overcame an obstacle to internal combustion engine progress [1]. Anti-knock agents were intensely researched to allow spark-ignition engines to operate with a higher compression ratio, thus providing more power and efficiency[2]. In 1923, General Motors introduced tetraethyl lead as a viable anti-knock agent that gained broad acceptance in the United States. Ongoing fuel research led to improved fuels and, as a result, engines with higher compression ratios, power, and efficiency [1]. However, as more internal combustion engine powered vehicles entered the roads, air quality began to suffer.

Emissions

For people living in the Los Angeles (LA) basin in the 1940's, it was obvious that tailpipe emissions from automobiles were leading to widespread pollution that was being trapped due to the unique geography of the region [3]. Specifically, smog was found to be caused by sunlight promoting the reaction of nitrogen oxides (NO_x) (a combination of nitrogen oxide (NO) and nitrogen dioxide (NO_2)) with hydrocarbon compounds, both of which are known emissions of automobiles [4]. Other hazardous

species including carbon monoxide (CO), sulfur oxides (SO_x), and particulate matter (PM) were subsequently found to influence air quality in the LA basin.

This influence on the environment by internal combustion engines led to the Federal Air Pollution Control Act of 1955, which allotted funds for research on air pollution. Subsequently, federal legislation on pollution control began with the Clean Air Act of 1963, which further promoted research into monitoring and controlling air quality . At this time, the state of California led the charge to reduce vehicle emissions through legislation. This began with the state-level requirement that all new 1966-model-year cars in California implement hydrocarbon (HC) and carbon monoxide (CO) control systems [6]. This legislation led to a 12% reduction in these emissions in the LA basin between 1965 and 1968 [6, 7]. On the federal level, the 1967 Air Quality Act expanded to include monitoring and enforcement following California standards .

During this time, a significant increase in nitrogen oxides (NO_x) was experienced as a result of more automobiles on the road that did not yet contain NO_x reducing technology [7]. Thus, California regulation that began in 1971 required all 1975-year cars to include catalytic converters to reduce NO_x , CO, and HC [6, 7]. This model year also made use of unleaded gasoline, which would not adversely affect the catalyst [6, 7]. Again following California's lead, legislation set by the Environmental Protection Agency (EPA), founded in 1970 [6], indicated nationwide levels of allowable emissions of NO_x , non-methane hydrocarbons, CO, and PM. In the past 30 years, a tiered system has been utilized by EPA with Tier 2 the current levels following earlier implementation of Tier 0 and Tier 1 [8]. Tier 3 is a proposed set of standards for on-road vehicles and fuels beginning in 2017 [9]. To address off-road vehicles, Tier 4 sets standards for CI engines used in equipment such as tractors, and construction, industrial, and airport equipment. This regulation began in 2008 and will be fully phased in by 2014 (2015 for engines larger than 750 horsepower). These tiers place strict limitations on PM and NO_x from CI engines, but do not address fuel economy and greenhouse gas emissions [10].

Fuel Economy

In addition to ever-tightening restrictions on emissions, the necessary fuel economy of vehicles and equipment must continue to improve in order to address the large amount of crude oil consumption occurring in the transportation sector, and to reduce global warming species [11]. This requires an improvement in engine efficiency despite emission controlling techniques, such as Exhaust Gas Recirculation (EGR) discussed later, that diminishes engine performance [12]. Improvements to CI engine fuel economy are of particular interest to the trucking industry, which accounts for roughly 80% of goods transportation in the U.S. [13]. Usage by this sector in the form of box trucks (single vehicle) and combination trucks (truck with trailer(s)) accounts for 10.6 billion and 26.8 billion gallons of fuel per year, respectively [13]. Thus, savings of even a few percent provide the opportunity to conserve large quantities of fuel and money. This need also applies to passenger vehicles in the U.S., where CI engines are beginning to gain market share. For instance, all automotive manufacturers must now produce cars and light-duty trucks with a fuel economy of 54.5 miles per gallon by the year 2025. To meet these lofty goals, automakers will employ more advanced SI and CI engines and transmissions, lower rolling resistance and aerodynamic losses, and improvements to auxiliary systems, such as air conditioning [14]. For these reasons, ongoing engine and fuel research must continue with the focus of this effort on CI engines.

CI Engine Overview

Advancement of the CI engine came about because of both innovations in technology and the opportunity to utilize the inherent advantages of CI engines over SI engines. For instance, CI engines are traditionally un-throttled; their power output is controlled by the amount of fuel added to the cylinder, rather than by throttling the intake of the engine and creating pumping losses [1, 2]. Additionally, CI engines can operate at significantly higher compression ratios (12-24+) since there is no knock limit. Instead, CI engine fuels adhere to specific characteristics that dictate the delay from when the fuel is

injected to when it combusts (cetane number); thus, limiting cylinder pressure below the physical limits of the engine components [1, 2, 15-17]. These benefits lead to increased power density, fuel economy, and efficiency over their SI counterparts. Furthermore, a CI engine's robust construction allows for high-mileage lifespan and is utilized in applications such as marine, trucks, power generation, and agriculture. Further advances in CI engine technology are required due to increasingly stringent fuel mileage and exhaust emissions regulations, as discussed in the previous section [1, 9, 10, 14].

In order to improve CI engines, an understanding of the combustion process is necessary. First, air is compressed during the compression stroke of the piston. Once the piston nears top dead center (TDC) and the pressure and temperature are high enough for combustion, liquid fuel is injected and atomized via a high-pressure (greater than 3000 psi) injector. Injected fuel then vaporizes in the hot environment and, after some mixing with entrained air occurs, the fuel reaches combustible limits[2]. Upon the start of combustion, the flame spreads very quickly throughout the mixture in what is called the premixed combustion phase. This phase results in the highest rate of energy release of the combustion process and, due to its occurrence near TDC, pressures and temperatures rise rapidly promoting the creation of NO_x through the thermal NO mechanism [1, 16].

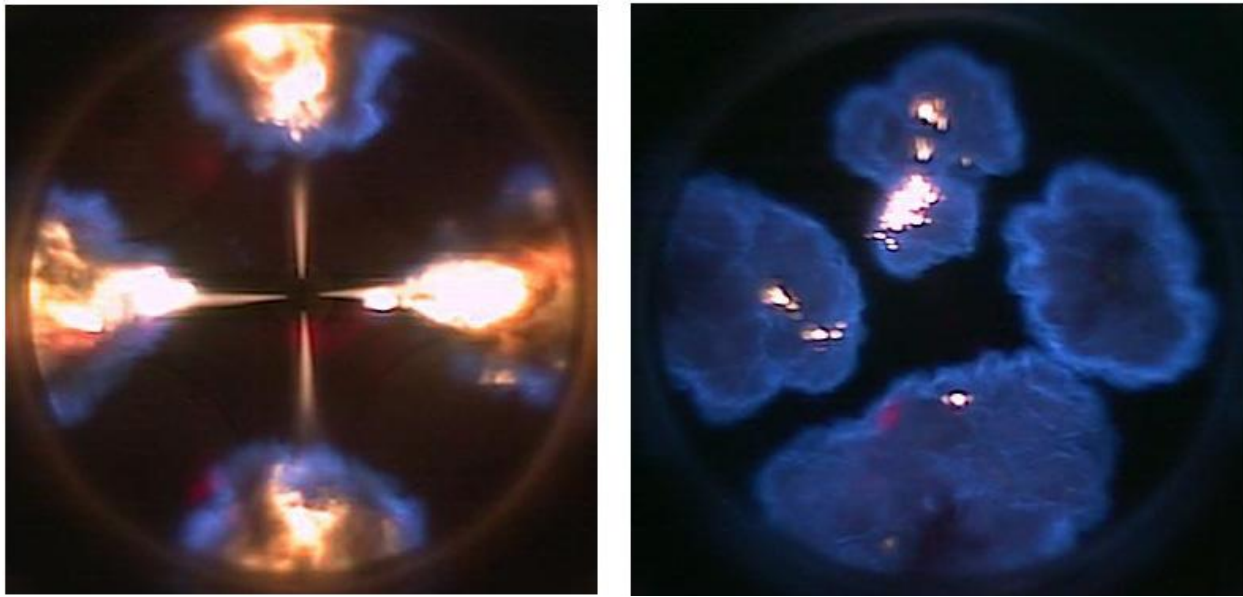


Figure 1. Fuel Combustion Process: Injection (left), Diffusion Burn, Light Indicates PM Production (right) [18].

During the premixed combustion phase, additional fuel continues to be injected into the cylinder. This unburned fuel will mix with remaining air to combust during the second phase of combustion, called the diffusion burn, as shown in Figure 1 [1]. With high fuel quantities and rich mixtures, such as at higher load or near the injector, PM formation is likely, due to a longer-duration diffusion burn that occurs as the cylinder is rapidly expanding. This expansion lowers cylinder pressure and temperature, leading to a cooler combustion environment where fuel does not oxidize as effectively. Heavy hydrocarbons may only partially oxidize and form particulates; this is particularly common at cylinder mixture ratios up to 20% lean of stoichiometry. Following the diffusion burn, the exhaust valve(s) of the cylinder open allowing hot exhaust to exit the cylinder.

NO_x-PM Tradeoff

In order to maximize combustion efficiency while minimizing emissions, engine operation techniques aim to improve fuel-air mixing and fuel atomization. Good mixing reduces rich zones in the cylinder and better atomization results in smaller fuel droplets. The result is less PM, HC, and CO due to improved oxidation. Optimum timing of combustion also improves the efficiency of the engine and

subsequently reduces these species. However, ample mixing and atomization results in a healthy premixed combustion phase (and overall combustion), resulting in high cylinder pressures and temperatures leading to increased NO_x production. To address NO_x production, peak thermodynamic conditions can be limited through later (delayed) injection timing. However, the limiting of the premixed combustion phase results in increased diffusion burn and PM production. This transition between the amounts of pre-mixed and diffusion burn phases of combustion leads to the NO_x-PM tradeoff where the reduced production of one emission species often leads in increased production of the other. This tradeoff between the regulated NO_x and PM emissions is the key issue for CI engines. Therefore, multiple methodologies are in practice to attempt to address this tradeoff through mutual lowering of both emissions.

Working to Defeat the NO_x-PM Tradeoff

Success in defeating the NO_x-PM tradeoff arises when multiple strategies are used in combination. For instance, methods that increase the turbulence and mixing in the cylinder effectively reduce the production of PM and improve the combustion efficiency through better mixing. This strategy promotes healthier combustion but also enhanced NO_x production, so a tactic that lowers cylinder temperatures must be implemented at the same time.

Improving the mixing in the engine cylinder can be accomplished through a variety of methods, such as cylinder inlet geometry, piston geometry, or injection spray. The most common method for CI engines to improve in-cylinder mixing is by using exhaust energy to compress intake air in a process called turbocharging. Turbocharging of the engine results in improved mixing and higher air flow rates, allowing for increased fuel flow and power output. Additionally, combustion is improved due in part to mixing, but also due to higher cylinder pressures and temperatures. This improvement in combustion behavior helps minimize PM emissions and improve fuel economy, but increases NO_x emissions due to the thermal NO mechanism [1, 16, 19, 20].

Therefore, in an effort to minimize NO_x emissions while turbocharging, research into the effectiveness of exhaust gas recirculation (EGR) began in the early 1970's and rapidly grew in acceptance [21-24]. This technology recycles a portion of exhaust gas back into the intake of the engine, thus displacing some of the engine's intake air. This exhaust contains inert combustion products that reduce cylinder temperatures and lowering thermal NO production [1, 21, 22, 24]. However, due to the displacement of intake air by exhaust gas, rich fuel zones are more likely and an increase in partial combustion products occurs. As a result, employing both turbocharging and EGR acts to lower both NO_x and PM emissions simultaneously. More recently, the focus of the industry at defeating the tradeoff has been through improving the spray mixing process using high-pressure fuel injection systems.

Injection Systems

There are two traditional methods for injecting diesel into the cylinder for combustion. The first method is an in-line pump that utilizes plungers and barrels to pressurize the fuel for injection, with one plunger-barrel per cylinder.

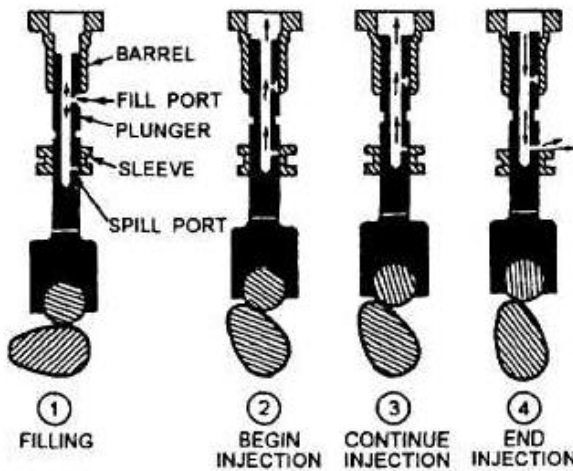


Figure 2. Operating Cycle for High-Pressure In-line Fuel Pump [25].

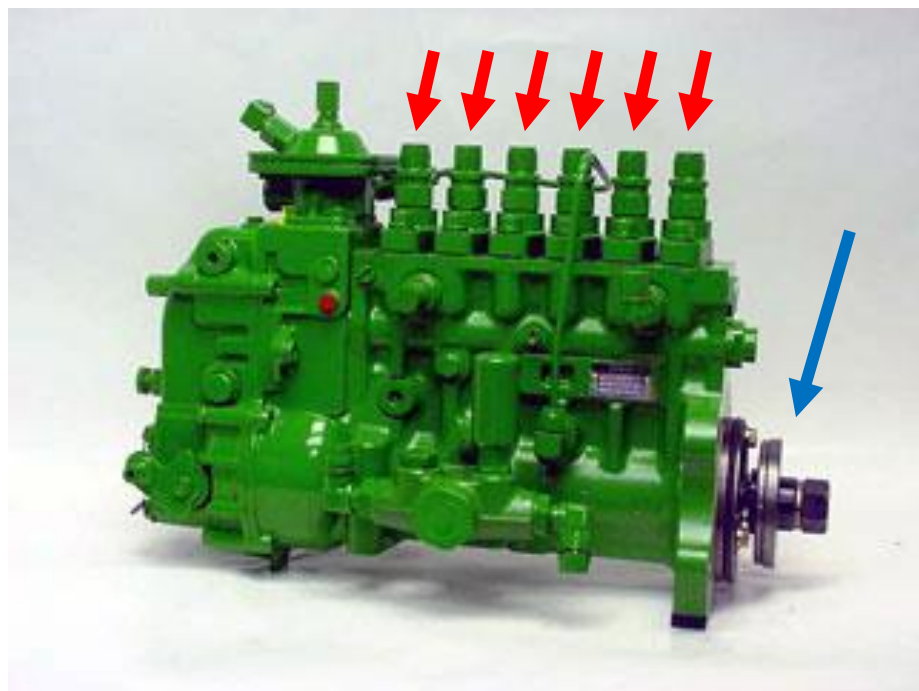


Figure 3. In-line Diesel Fuel Pump for a Six-Cylinder CI engine with the Camshaft Input (Blue) and Outlets to the Injectors (Red) [26].

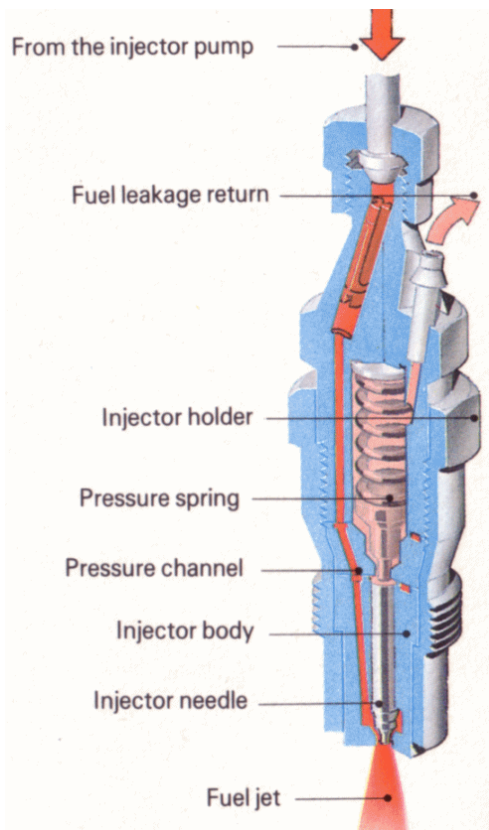


Figure 4. Cross Section of In-line Diesel Injector [27].

A diagram of this combination is shown in Figure 2. The plungers are individually actuated by a rotating cam that forces the plunger up to compress the fuel inside the barrel. The camshaft of the fuel pump (example shown in Figure 3) is driven by the engine and controls injection timing for each cylinder by pressurizing the fuel at the desired point of each piston's thermodynamic cycle. From the barrel, high-pressure fuel travels up the fuel line to an injector, which opens as the high pressure fuel depresses a spring to allow injection, as shown in Figure 4. Excess fuel returns to the fuel tank for subsequent injections. This type of fuel injection system, though simple and robust, has limitations that prevent it from lowering both NO_x and PM emissions. Specifically, precise control and dynamic adjustment of injection is difficult. Additionally, it is limited to a single injection event. Finally, it has been shown that fuels of different density adversely influence the performance of these systems. For instance, fuels such as biodiesel have a higher density and their pressure waves travel more rapidly through the fuel line than petroleum diesel resulting in an advancement of the injection process [15-17, 19, 20, 28-31]. Hence, the use of alternative fuels with this injection system influences the NO_x-PM tradeoff often beyond the user's control

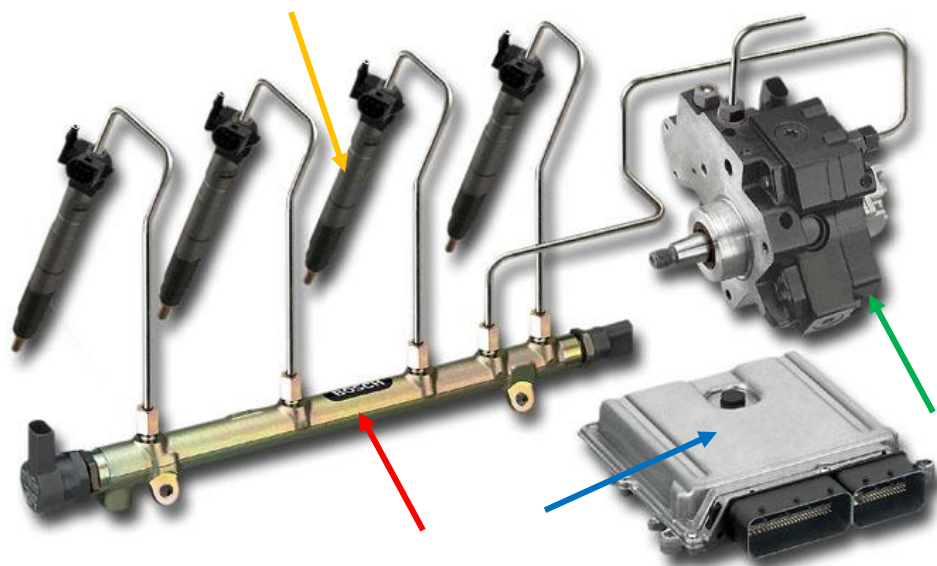


Figure 5. Components of Common-Rail Fuel System. ECU (Blue Arrow), Fuel Pump (Green Arrow), Common-Rail (Red Arrow), and Injectors (Orange Arrow) [32].

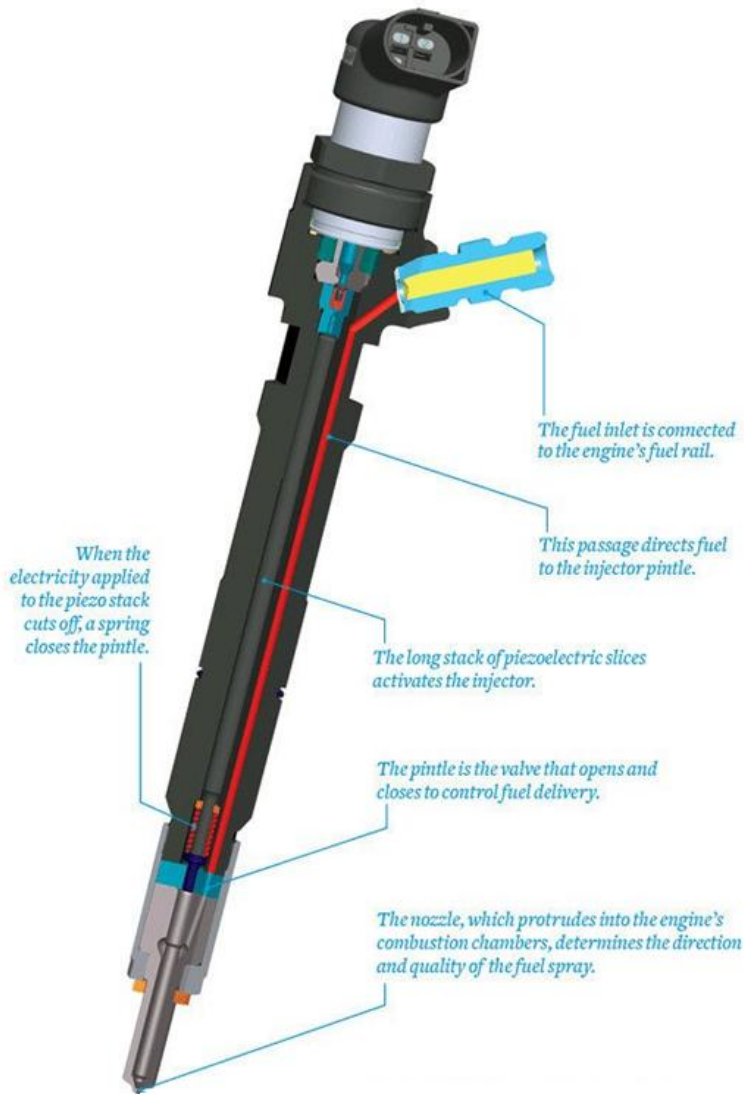


Figure 6. Electronic High-Pressure Fuel Injector [33].

The need for more dynamic injection control leads to the implementation of common rail injection systems. In this configuration, a high-pressure pump feeds a single high-pressure rail that is held at constant pressure. This rail supplies fuel to multiple cylinders as shown in Figure 5. Injection occurs via solenoid injection valves that feed each cylinder, as seen in Figure 6. Rather than being controlled by the pressure of the fuel, which remains constant through the process, injection is initiated by piezoelectric actuators that respond to electrical signals sent by the engine control unit (ECU). As the

electrical signal stops, a spring forces the injector closed in order to await subsequent injections. With the implementation of these systems, engine operators now have the ability to perform multiple injection events per cycle and control the injection timing and pressure dynamically as a function of changing operating conditions [34].

In 1992, the patent for common rail diesel injection was filed [35] signaling the beginning of a gradual shift from mechanical pump-line-nozzle systems to high-pressure electronic injection due to their inherent performance and emissions advantages [35-37]. Today, production engines are utilizing relatively high injection pressures (above 25,000 psi) to improve both fuel atomization and injection control [34]. Precise control of injection pressure and timing allows for combustion normalization and offers the opportunity to address the NO_x-PM tradeoff through advanced injection strategies. However, even with the implementation of turbocharging, EGR, and high-pressure injection, NO_x and PM engine emissions are not low enough to meet EPA regulations without exhaust aftertreatment. Furthermore, effects from biofuel usage are not limited to mechanically-driven fuel systems, but also must be considered when using high-pressure common-rail fuel systems as well.

Influence of Biofuels on CI Engines

Extensive research is underway to find sustainable energy sources to augment petroleum-based fuels [15-17, 19, 20, 28-31]. In particular, biomass-based biodiesel is gaining ground due to its promising production and relative ease of integration into CI engines. This type of fuel has similar characteristics to ultra-low-sulfur diesel (ULSD). In fact, it is miscible in ULSD allowing blending of the two as a means of fueling an engine. However, certain properties of biodiesel influence the operation of the CI engine and its subsystems. For instance, the slightly higher density of the fuel influences the injection process. In mechanical pump-line-nozzle systems, the speed of the high-pressure injection is increased through the fuel line, thus injection occurs earlier in the cycle than for ULSD, resulting in increased combustion temperatures and NO_x emissions [16, 17, 19, 20, 28, 29]. Furthermore, the increase in viscosity of

biodiesel degrades the effectiveness of injector atomization, resulting changes to the combustion process via diminished mixing. This is partially offset by the inherent oxygen quantity of biodiesel that will lead to a generally leaner combustion environment and the opportunity for combustion to begin earlier in the engine cycle.

Because of the changes to combustion caused by fuel property variability, the engine must be recalibrated to ensure effective combustion and emissions reduction. High blends of biodiesel are known to combust poorly during late injection (such as those used for exhaust aftertreatment system control), which may result in fuel droplets coating the cylinder walls. This unburned fuel may make its way into the engine oil, thus diluting the oil and causing engine damage [16]. Due to the influences of biodiesel on engine operation and the importance of sustainable fuel solutions, further research to overcome these challenges is necessary. Furthermore, since some of the effects of biodiesel on engine performance are advantageous (such as reduced PM), the implementation of these fuels can be used in conjunction with engine operation techniques to promote improved fuel economy and help the engine designer work to defeat the NO_x-PM tradeoff.

Research Requirements

History indicates that both engine and fuel technology must be researched at the same time. This is needed to reduce emissions to improve fuel economy and air quality to mitigate harmful environmental effects. However, the NO_x-PM tradeoff is the primary issue of CI engines; hence, research must further explore how to better control the pre-mixed and diffusion burn phases to address both emissions. This includes expansion on previous efforts that investigated EGR. The focus of this dissertation effort will be on improving and exploring a high-pressure injection system of a CI engine. This system addresses the need to better understand the effects of fuels on the injection and combustion events. Furthermore, the implementation of a turbocharger is discussed in order to help facilitate further research on this device and its influence on the NO_x-PM tradeoff. This combination of

systems installed on the engine will provide further research opportunities as CI engine technology moves forward, particularly in areas addressing sustainable fuels and increasingly stringent emissions regulations and fuel economy demands.

Dissertation Focus

The primary focus of this dissertation is to gain an understanding of engine control strategies as a means of performing CI engine research and exploring the NO_x-PM tradeoff, with a focus on sustainable biofuel studies. This knowledge is comprised of efforts that began in the summer of 2009 with initial setup of a single-cylinder CI engine test cell. Upon arriving at the University of Kansas, CI engine research consisted of a single-cylinder Yanmar engine attached to a commercial generator. In its stock configuration, it was a naturally-aspirated engine with an EGR port between the intake and exhaust passages that provided approximately 10% EGR into the intake depending on operating conditions. Speed was controlled using a centrifugal fuel governor and cam lobe to control injection timing, which occurs at approximately 19.8 MPa (~2900 psi) using a mechanical pump-line-nozzle system. For context, improvements to this engine and the author's contribution (in brief) since arrival includes:

- Gas-assisted combustion system [38, 39]: Author assisted with test cell setup for initial experimentation. This included installing the engine, generator, and driveline, as well as the physical instrumentation such as fuel and airflow sensors.
- Ozone-assisted combustion studies: Author helped with equipment setup, data collection during experiments, post processing of data, and writing of publication efforts.
- Cooled EGR [12]: Author assisted in physical EGR component installation, data acquisition, and data post-processing.

- In-cylinder pressure measurement[20]: This system was the primary work of this author's master's thesis. Efforts included engine head and flywheel modification, data acquisition programming, and system validation.
- Heat release modeling [40]: Author provided cylinder pressure data for initial programming and operated test cell for calibration procedure.
- Alternating Current (AC) dynamometer: This author designed and built the driveshaft and base for the dynamometer (with other students' assistance) and oversaw the commissioning of the dynamometer as the primary contact with Dyne Systems, Incorporated.

At the beginning of this dissertation, two major upgrades remained for the single-cylinder engine: electronically-controlled fuel injection and the installation of a turbocharger. In the following chapters, these upgrades are covered in detail. In specific, Chapter 1 presents the installation of an engine control unit, as well as the subsequent bench testing and engine calibration.

Chapter 2 is comprised of two studies performed on various biodiesels. Specifically, a comparison of four biodiesels in both neat and blended form to ULSD in an adjusted and unadjusted manner expands upon previous research. These studies expand on previous research that found direct correlations between emissions and fuel properties of the biodiesels, but was limited by the lack of in-cylinder pressure measurements and un-controlled injection timing [16]. Of specific interest is the influence of viscosity on the start of combustion, as a more viscous fuel will not atomize as effectively, thus larger fuel droplets will enter the cylinder[1, 16]. These droplets delay combustion and result in diminished performance and an increase in partial combustion products, such as hydrocarbons, carbon monoxide, and particulate matter[1, 16]. Additionally, the effect of molecular unsaturation, or the existence of carbon double-bonds in the fatty acid chains of biodiesel, alters the behavior of combustion when these more energetic bonds are broken during oxidization [16, 17]. These tests include four diverse biodiesel feedstocks, soybean, jatropha, beef tallow, and palm oils, which provide a broad

spectrum of fuel properties that can be regressed against measured engine performance and tailpipe emissions. Additionally, the influence of each of these biodiesels with blended ULSD is investigated to ascertain the changes in fuel properties and engine operation as a function of biodiesel/ULSD blend ratio. The tests are performed by optimizing the engine for ULSD fuel economy, then increasing the blending of biodiesel, up to 100% biodiesel. As biodiesel blend increases, the combustion timing advances due to the shorted ignition delay of biodiesel. Performance and emissions data are first taken with constant injection timing to observe changes in combustion due to ignition delay. Then, injection timing is adjusted to normalize blend combustion against pure ULSD to directly investigate the way that biodiesel fuel chemistry alters combustion. This strategy removes the overshadowing effects of combustion phasing, providing the opportunity to understand the chemical aspect of combustion.

In Chapter 3, renewable jet propellant is tested with petrol-based jet-propellant as part of the United States Military's Single Fuel Forward Policy to investigate the effectiveness of renewable jet fuel in a CI engine. This policy dictates that a single fuel (jet-propellant 8) will be used in the battlefield in both land and air vehicles, thus improving logistical advantage [19]. A renewable jet propellant, called R-8, is intended to augment jet fueling, much like biodiesel is used for CI engines. The strategy of this study is to adjust fuel timing using regular jet propellant, then gradually increase the ratio of R-8 to jet-propellant to observe changes of combustion timing and combustion behavior, much as the biodiesel study is performed.

Chapter 4 serves as a manual for the single-cylinder engine test cell. This is necessary due to the custom nature of the test cell and the rapid turnover of graduate student personnel. This includes not only the methods to perform research using the variety of systems available, but also instructions regarding equipment maintenance, troubleshooting, and replacement. The full operation principle and maintenance of the emissions equipment and AC dynamometer is also covered. Finally, the installation of the turbocharger, as well as observed improvements in performance, is discussed.

To facilitate future efforts beyond the single-cylinder test cell, Chapter 5 covers the initial phases of the construction of a multi-cylinder engine test cell. Like the single-cylinder engine test cell, this laboratory will be composed of a variety of complex subsystems that must all work together for accurate experimentation and good engine behavior. Therefore, a description of the process of construction, as well as initial system integration is necessary. This covers the operating principle of the dynamometer, as well as a high-level description of the steps that need to be accomplished in the test cell to reach operational state.

Chapter 1: Installation of Electronically-Controlled High-Pressure Fuel Injection on a Single-Cylinder Compression-Ignition Engine

1.1 Introduction

One of the primary goals for improving the single-cylinder CI engine test cell is to replicate a modern production engine in order to explore methodologies to defeat the NO_x-PM tradeoff. By doing so, experiments performed on this engine will be more applicable to industry. This led to the installation of the cooled EGR system to help control emissions, and an AC dynamometer to simulate engine loading. As mentioned previously, the major remaining limitation of the Yanmar engine was the mechanically-driven fuel injection system.

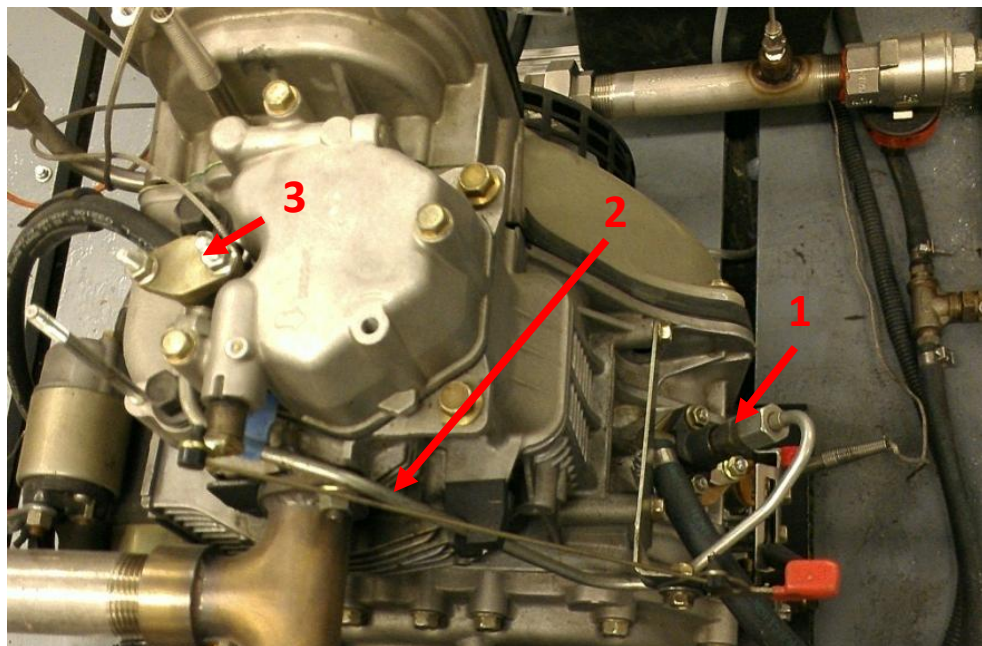


Figure 1-1. Mechanical Fuel Pump (1), High-Pressure Fuel Line (2), and Injector (3) as Installed by Yanmar.

The Yanmar fuel injection system consists of a speed-governed pump that utilizes a plunger to pressurize fuel inside of a cylindrical barrel. This pump is connected via a rigid fuel line to an injector that is actuated by high pressure fuel pulses from the fuel pump itself. These components are labelled in Figure 1-1.

Past efforts at KU [16, 19] determined that the variation in the density of the fuel being tested resulted in dynamic changes to fuel injection timing. This is caused by the fact that the fuel pump, rather than the injector itself, controls the actual injection process. Differences in the bulk modulus of the fuel, which are strongly correlated to density [17, 20], cause the speed of the injection wave to vary, thus resulting in slight injection timing differences. For this reason, it was found that denser fuels, such as biodiesel, are injected earlier than less-dense fuels, such as JP-8. Additionally, the importance of combustion phasing on both engine performance and emissions was also observed. Specifically, combustion that occurs too early results in higher cylinder pressures and temperatures, causing an increase in thermal NO production and combustion efficiency. Conversely, combustion that occurs too late results in lower cylinder pressures, reduced combustion efficiency, and higher hydrocarbon and particulate matter emissions [1, 19, 20]. Furthermore, fuels with a higher cetane number than ULSD (shorter delay in combustion after injection) results in earlier combustion.

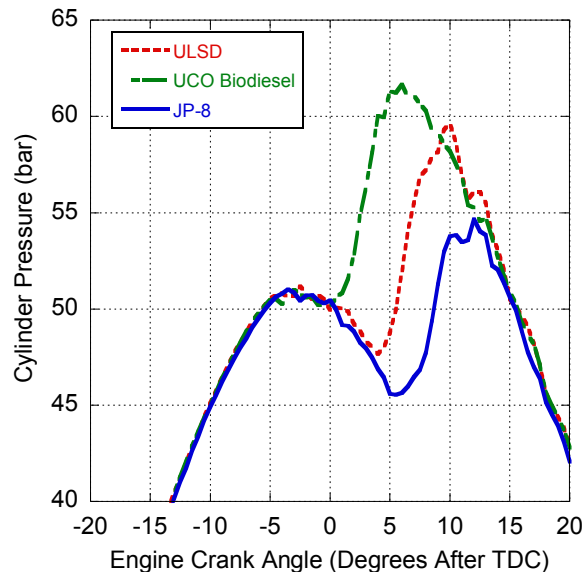


Figure 1-2. Cylinder Pressure vs. Crank Angle for ULSD, UCO Biodiesel, and JP-8 From -20° to 30° After TDC at 40% Rated Engine Torque [19].

This largely explains why biodiesel, with a higher cetane number and density, combusts several crank angle degrees earlier than ULSD and JP-8, as seen in Figure 1-2. Because of the strong influences

on combustion timing, it was not feasible to make direct conclusions about any changes caused by other characteristics of different fuels (e.g., viscosity, energy content, or molecular structure). Therefore, it is vital to be able to control injection timing as a means of adjusting combustion phasing. With the ability to control injection timing, it is possible to delay biodiesel (earlier combustion than ULSD) injection, or advance JP-8 (combustion begins later than ULSD) injection in order to synchronize combustion timing of any fuel tested in this engine. Then, variations in emissions and engine performance during testing of different fuels are caused only by the chemical properties of the fuel, not by variation caused by differences of combustion timing.

Aside from the advantages in fuel combustion research, the upgrade to electronic injection will improve the applicability of said research. Specifically, digital control of injection timing and fuel flow rate will result in the ability to optimize engine performance for fuel consumption or emissions. This will help with investigations into the NO_x-PM tradeoff. Furthermore, the engine is no longer limited to operating at 3600 rotations per minute (RPM), as was previously required to generate 60 Hz electricity. In addition, changes in engine operating characteristics, such as engine intake air temperature, engine oil temperature, or boost pressure can be accounted for with an engine control unit (ECU). Finally, the fuel injection pressure of this system can be up to approximately 200 MPa, which is considerably higher than the injection pressure of the original injection system that injects fuel at 19.8 MPa. This results in much finer fuel spray, and therefore improved fuel economy, fuel and air mixing in the cylinder, and partial combustion products.

1.2 Equipment

The completed common-rail injection system is comprised of the ECU, fuel rail, fuel pump, and certain necessary sensors. These sensors include:

- Intake Air Pressure and Temperature Sensors: Feedback for control based on ambient and turbocharger variability.

- Fuel Rail Pressure: Used to maintain proper fuel injection pressure.
- Oil Temperature: Used to monitor engine temperature.
- Oil Pressure: For monitoring engine oil.
- Inductive Speed Sensor: Used to measure engine speed and determine engine crank angle.
- Cam Sensor: Used to determine which cycle the engine is in as there are two engine revolutions per thermodynamic cycle.

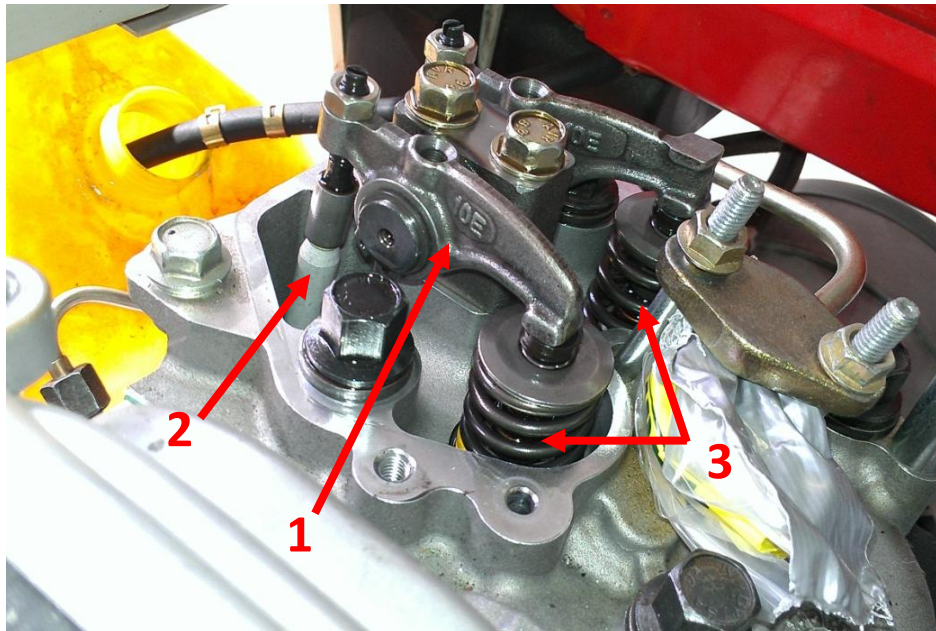


Figure 1-3. Rocker Arms (1), Moved by Upward Motion of Pushrods (2), Used to Actuate Intake and Exhaust Valves (3).

Through extensive discussion with industry professionals, it is known that direct measurement of camshaft rotation is not logically feasible for this single cylinder engine. This is because the Yanmar does not utilize an overhead camshaft, but instead uses an internal camshaft, pushrods, and rocker arms to actuate the valves during operation (see Figure 1-3). As a result, attaching a cam sensor and timing wheel would require either that the sensor be placed inside the engine block, or that the camshaft be extended through the side of the engine block so that the sensor and timing wheel could be installed outside of the engine. This measurement is necessary to determine the engine cycle during its four-

stroke operation (engine spins twice per injection event). In other words, this sensor tells the ECU whether the engine is expelling exhaust gas or compressing intake air while the piston is moving upwards, thus insuring that fuel is injected during the proper cycle (i.e., not during the exhaust stroke).

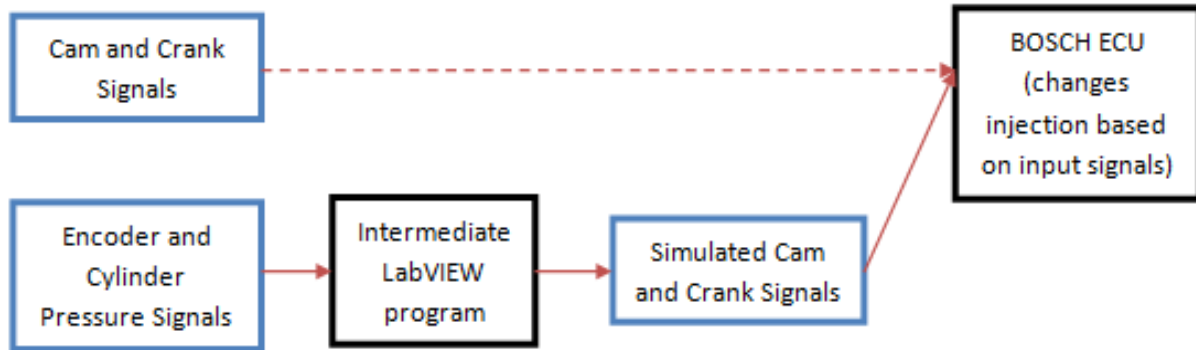


Figure 1-4. Depicts Signal Flow from the Intended Cam and Crank Signals (top left) to the ECU (dashed). Instead, Known Encoder and Pressure Signals are Read by a LabVIEW Program that Replicates the Needed Signals Based on Engine Speed and Stroke.

To circumvent this challenge, a LabVIEW program was constructed to use known signals (engine crank angle and cylinder pressure) to determine the proper engine cycle phasing and crank angle. This program outputs the correct signals to the ECU as if these sensors were in place on the engine. This signal flow is depicted in Figure 1-4. The top path in the diagram shows the intended signal flow to the ECU (directly from sensors); whereas, the bottom path indicates how these signals are created via a high-speed program from other known signals.

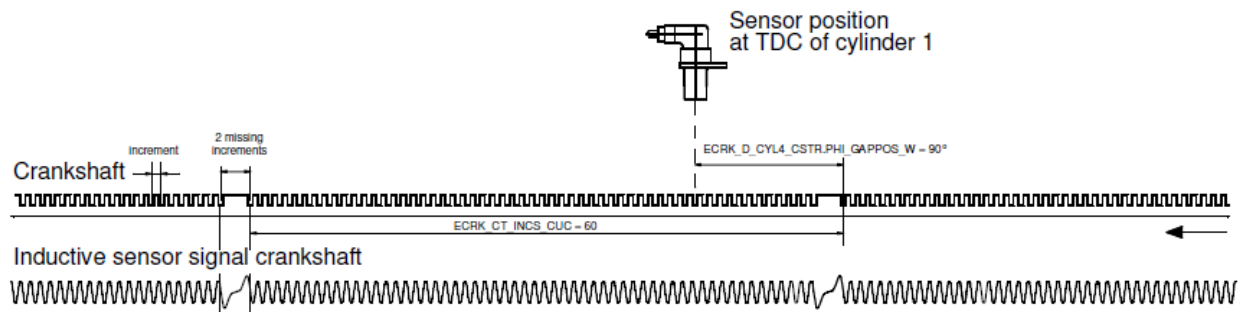


Figure 1-5. Crankshaft Signal Diagram as Generated by an Inductive Speed Sensor [34].

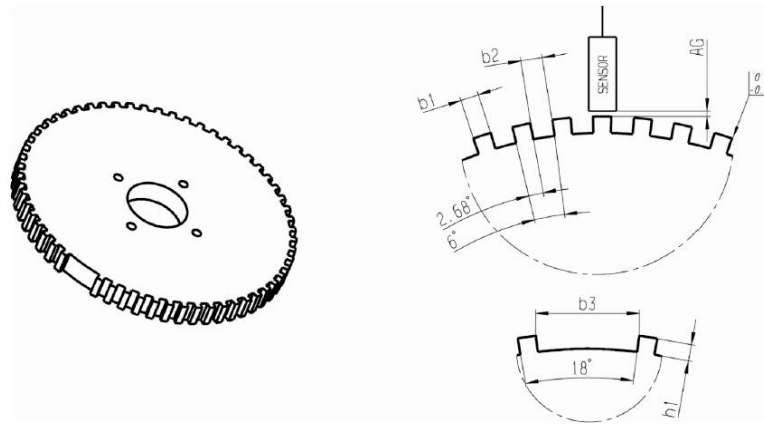


Figure 1-6. 60-2 Wheel for Inductive Speed Sensor. Gap Serves as TDC Reference [34].

The traditional crankshaft signal is a sine wave generated by a crankshaft timing wheel with 60 teeth and an inductive speed sensor, as seen in Figure 1-5. The crank sensor is intended to be installed on a 60-2 wheel. This wheel has space for 60 teeth, but a timing gap where two teeth are missing, as in Figure 1-6, is used to indicate when the piston is at TDC. Simulation of the signal is accomplished using the 360 pulse-per-revolution square wave sent by the Kistler encoder currently used for in-cylinder studies [20]. The rapid response and digital output of this encoder (plus the high number of pulses) makes this an ideal candidate for the job. Conveniently, the needed number of output waves is $1/6^{\text{th}}$ as many as the incoming encoder square waves per revolution. By writing the code to ‘count’ square waves and change its simulated crank output, the code automatically adjusts for changes in engine speed.

The cam sensor also outputs a sine wave, but uses fewer teeth to indicate the engine cycle (note: the cam shaft spins at half the speed of the engine). The most important tooth is called the sync mark as it occurs at a defined time in the engine’s thermodynamic cycle (270° before TDC of the compression stroke).

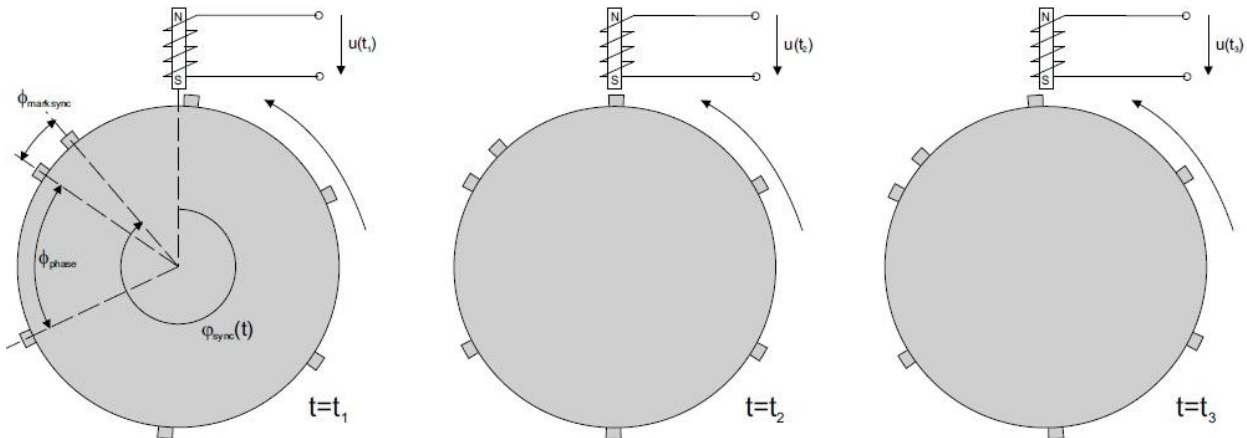


Figure 1-7. Diagram Showing the Cam Sensor Timing Wheel with Sync and Phase Marks as Needed to Determine the Engine Cycle [34].

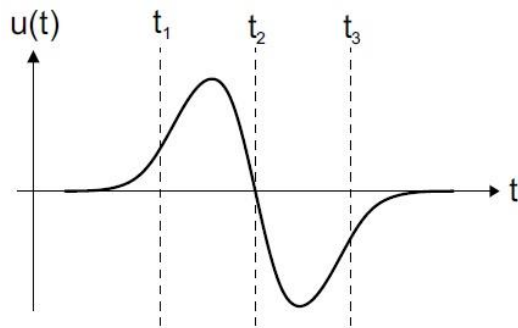


Figure 1-8. Output Voltage of the Inductive Cam Sensor as a Timing Tooth Passes [34].

To improve accuracy, additional phase marks are included and are evenly distributed on the phase wheel. A diagram of the necessary wheel configuration is shown in Figure 1-7 and the cam sensor signal is shown in Figure 1-8. To accurately simulate this sensor's signal, all that is needed is to determine the cycle that the engine is currently in and use this in conjunction with the known engine crank angle. This is determined using the in-cylinder pressure transducer, which outputs a significantly higher pressure signal during compression stroke than during the exhaust stroke (even during starting and motoring). On that basis, both simulated signals for the crankshaft and camshaft sensors can be sent to the ECU.

1.3 The LabVIEW Programs

In total, two LabVIEW programs were used. The first program is an engine simulator that generates the same electronic signature as the Yanmar engine. This aids in initial bench testing because the program can be turned on and off with much less effort than the engine, plus the program can be run indefinitely without worrying about running the engine for long durations. The second program is the code that actually performs signal conversion from the pressure and crank angle signals into useful camshaft and crankshaft signals for the ECU.

1.3.1 Engine Signal Simulator for Bench Testing

Before connecting to actual engine sensor signals, the high-speed rack-mount computer [20], with its NI PCI-7841R card, is used to generate simulated engine signals. The intention is to use clean signals and simplify testing logistics. Using this simulator, the simulated engine speed can be easily changed and run indefinitely, making this program a preferred option for bench testing. In particular, the card is used to generate simulated encoder square waves (both TDC and incremental) and cylinder pressure. The incremental square wave alternates between a *True*, 5 Volts Direct Current (VDC) to a *False* (0 VDC) signal 720 times per engine revolution (every half-degree of crank angle). The TDC square wave is only *True* (5 VDC) at piston TDC. Because piston TDC occurs during every engine cycle, another signal is needed to determine which part of the thermodynamic cycle the engine is in at each piston TDC. To do this, a simulated pressure signal goes from a *False* (0 VDC) to a *True* (5 VDC) signal every other engine rotation, similar to the voltage rise experienced from compression occurring in the actual engine pressure signal.

This program was written to be as streamlined as possible, but does have some user controls that can be used to adjust simulated engine speed and a TDC reference peak (discussed later in the bench test section).

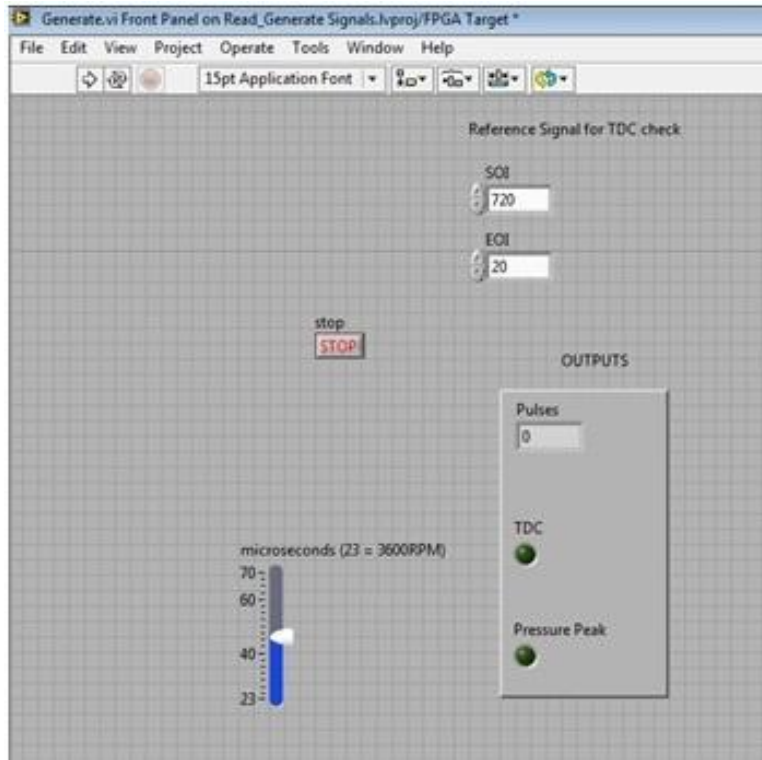


Figure 1-9. Front Panel of Engine Simulation Program.

The main operating window for this program, also known as a Virtual Instrument (VI) is shown in Figure 1-9. In this program, the simulated engine rotates from 0° - 720° of crank angle, with 0° being defined as piston TDC just before combustion occurs. A complete cycle is defined here as occurring over 720° of engine crank angle because the engine is a four-stroke, with two engine revolutions occurring per thermodynamic cycle [1]. At the top of the screen is a pair of numerical controls that allow the operator to output a *True* (5 VDC) reference peak. This is used to verify injection timing as this output signal and the injector signal from the ECU can be compared using an oscilloscope (as discussed later). Any value between 0 and 720 can be entered in these controls, the resulting output voltage changes dynamically to match these values and will remain *True* (5 VDC) from Start of Injection (SOI) to End of Injection (EOI). For instance, if the ECU is injecting 12° before TDC, the SOI value can be changed to 708 to ensure that the ECU and reference signals line up. The EOI value is set to 20 here to be easily

discerned on the oscilloscope, however, it can be used as a measurement tool to determine the ECU injector EOI.

At the bottom-left corner of the screen is a numerical slider that allows the user to control the speed of the simulated engine. The output of the program is a collection of signals driven by an internal counter and the changing simulated square wave of the encoder. The duration of high and low signals (i.e., frequency) of this square wave is adjusted by changing the *microseconds* slider. For example, setting the *microseconds* slider to 23 μ s results in a square wave that is alternatively high and low for 23 μ s, resulting in a simulated engine speed of approximately 3600 RPM as determined using the following:

$$\frac{60 \frac{\text{seconds}}{\text{minute}}}{720 \frac{\text{increments}}{\text{revolution}} \cdot 23 \frac{\text{microseconds}}{\text{increment}}} = 3623.2 \text{ RPM} \quad (1-1)$$

By contrast, increasing the *microseconds* value slows down the frequency of the square wave (and internal pulse counter), thus resulting in a slower simulated engine speed.

Finally, the outputs of the engine simulator are indicated in the *OUTPUTS* box on the right side of the main operating window. The simulated engine's crank angle value (from 0 $^{\circ}$ to 720 $^{\circ}$ crank angle) is indicated in the numerical indicator with Boolean lights for *TDC* and *Pressure Peak* used to indicate *True* outputs being generated by the program.

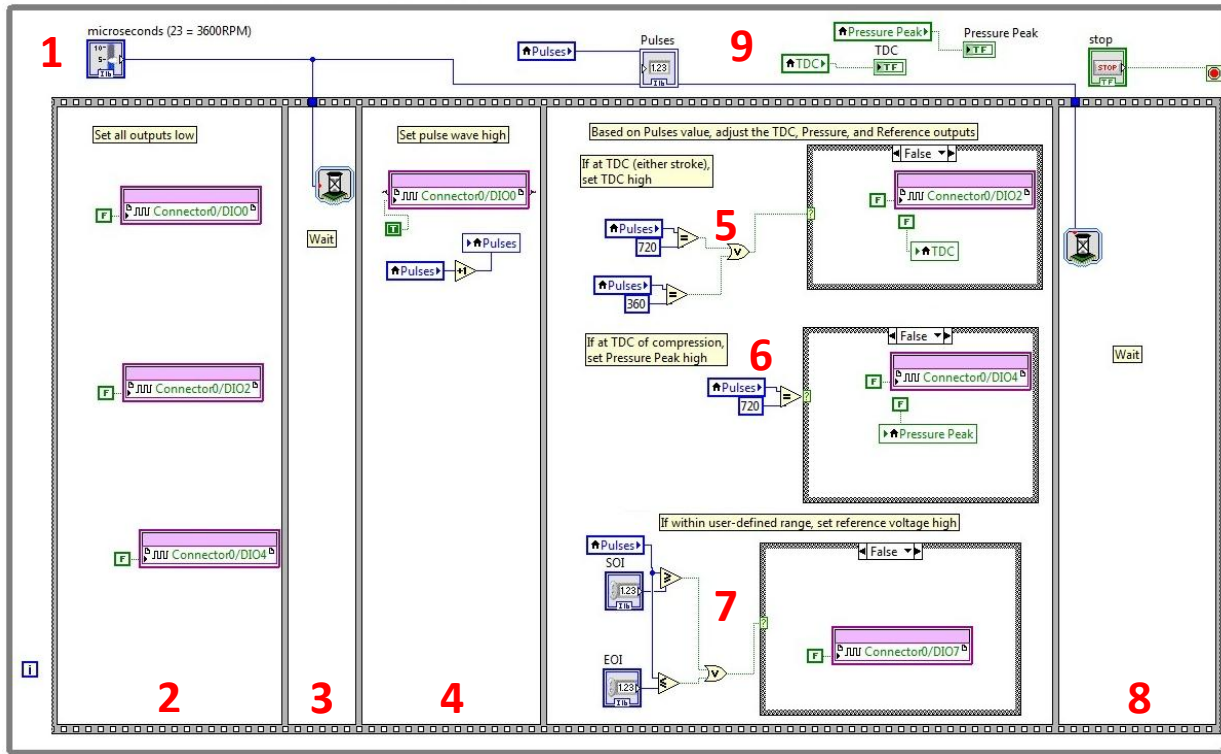


Figure 1-10. Block Diagram of Engine Simulation Program, All False Cases.

In the code shown in Figure 1-10, frames moving from left to right indicate a sequence structure where all actions within a certain frame must finish before the program moves to the next frame in the sequence. As the entire sequence is within a while loop, it repeats until the *STOP* button is pressed. The following actions take place:

1. Input from the user for simulated engine speed, controlled by square wave frequency, (*microseconds*), is read from the main operating window.
2. All Digital Input/Output (DIO) output channels used are set to *False*. Channel DIO0 corresponds to the square wave generated by the encoder. DIO2 is used to output piston TDC. Pressure peak occurrence is output via DIO4. Finally, the SOI and EOI reference signal is output through DIO7. This frame is used to indicate that the engine is not at TDC and the simulated encoder increment is at 0 VDC.

3. This frame uses a wait counter to ensure that the signals being output by the program remain in the *False* state for a certain about of time, as needed to control engine speed via the *microseconds* value.
4. In this frame, the output of the incremental square wave (DIO0) is set to *True* to indicate that the engine has moved forward by one half-degree. The counter, *Pulses*, is used to track simulated engine crank angle from 0° - 720° by one-degree increments. At this point, *Pulses* is increased by one using a local variable.
5. At this point, the value of *Pulses* is checked using a case structure to determine if the engine is at piston TDC, which occurs at either 360° or 720° . In the case shown in Figure 1-10, the value for *Pulses* is not 360 or 720 (i.e., a false condition), so the TDC signal, DIO2, remains *False*. In this case, a false is written to the local variable, *TDC*.

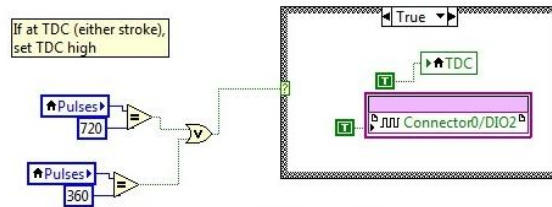


Figure 1-11. True Case Occurring at Piston TDC.

In the true case shown in Figure 1-11, *Pulses* has a value of either 360 or 720 . Because of being at piston TDC, the values for *TDC* and for DIO2 are set to *True*.

6. Similarly, *Pulses* is checked for TDC following the compression stroke. If the simulated engine is at this point, *Pulses* will be equal to 720 . In the false case shown in Figure 1-10, the engine is not at this point of the thermodynamic cycle, so DIO4 remains *False*. A corresponding false value is written to the local variable *Pressure Peak*.

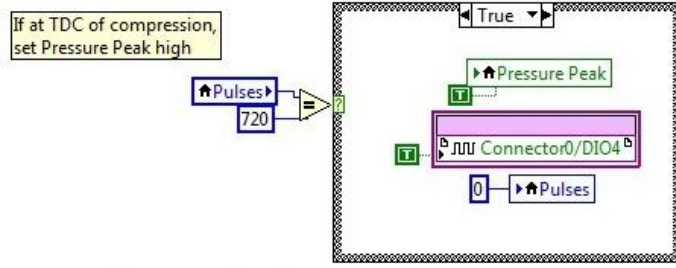


Figure 1-12. True Case Occurring at Piston TDC Following the Compression Stroke.

In the true case, shown in Figure 1-12, the simulated engine is at TDC just following a compression stroke. As a result, the value of *Pressure Peak* and the output of DIO4 are set to *True*. It is important to note that *Pulses* is not initialized at a value of zero because the real engine can be started at any point of its cycle as well. *Pulses* is only set to zero upon first passing TDC during a peak in pressure.

7. In this portion of code, if *Pulses* is found to be outside of the range from SOI to EOI, the output of DIO7 is set to *False*.

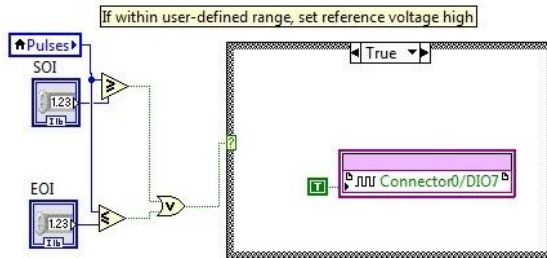


Figure 1-13. True Case Occurring At or Between SOI and EOI.

In Figure 1-13, *Pulses* is found to be greater than (or equal to) the SOI value and less than (or equal to) the EOI values set by the user. As a result, the output of DIO7 will be set to *True* to output 5 VDC.

8. In the last frame of the sequence structure, another user-defined wait occurs in order to pass the amount of time corresponding to the duration of one half-degree of crank angle. The state of encoder increment remains *True* with all other output signals remaining in their states as defined in the previous frame.

9. Local variables for *Pulses*, *TDC*, and *Pressure Peak* are constantly read to be indicated to the user. As *Pulses* is an integer, a numeric indicator is used whereas Boolean indicators show the true/false state of *TDC* and *Pressure Peak*.

1.3.2 *Engine Sensor Signal Converter*

The LabVIEW program needed to convert engine sensor signals (either real or simulated) is installed on the Compact Reconfigurable Input Output (c-RIO) controller located in the test cell instrumentation cabinet. This c-RIO is an NI 9012 with eight chassis modules used to input/output signals analog and digital signals. To read in the digital signals from the Kistler 2614B incremental encoder, a NI 9401 high-speed digital input/output module is installed on the fourth slot of the chassis. To output the analog cam signal to the ECU, a NI 9263 Analog Output (AO) module is installed in the third slot of the chassis and can output the ± 10 VDC signal needed. A NI 9201 module is installed on the sixth slot of the chassis and is used to read in the 0-10 VDC analog pressure signal from the Kistler 5011B. The signals read in by the LabVIEW sensor signal converter program are used to convert these encoder/pressure signals into signals that can be used by the ECU to determine speed and crank angle to control injection. This conversion program is installed on the existing Fully Programmable Gate Array (FPGA) program on the c-RIO. The existing FPGA program is used to pull sensor values in from the low-speed sensors of the test cell and is composed of multiple while loops that run continuously. A separate while loop is used to add the sensor signal conversion program to this FPGA code, thus allowing the loop to run as fast as possible and independent of the speed of other loops. The block diagram for this conversion program is shown in segments from Figure 1-14 to Figure 1-24.

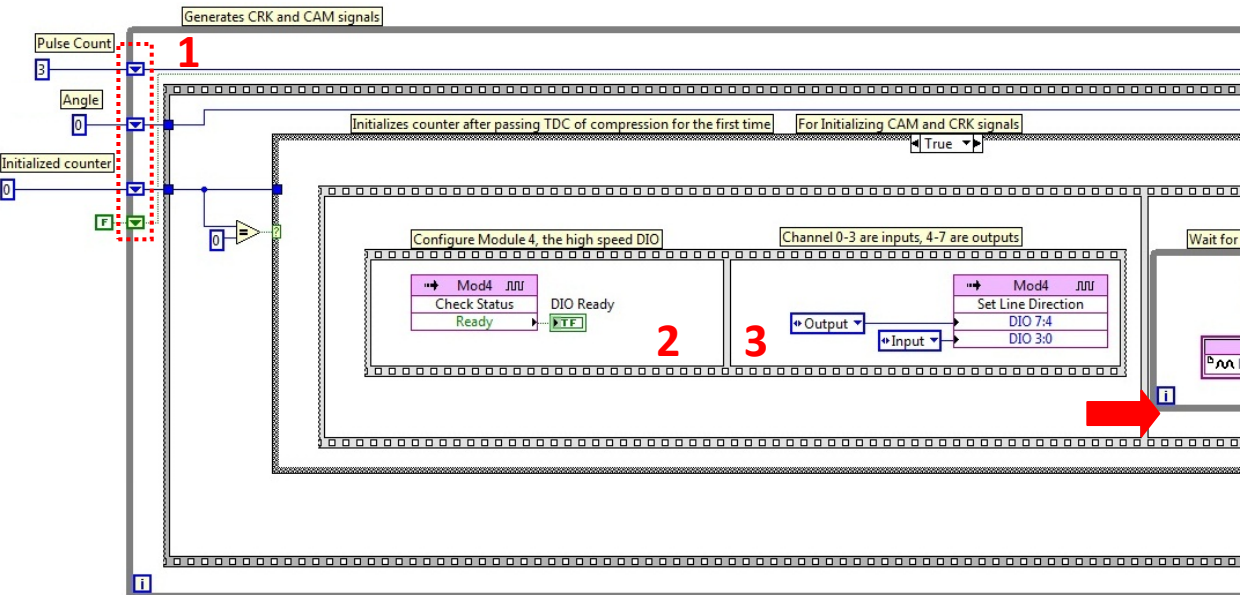


Figure 1-14. First Segment of Sensor Conversion Program Block Diagram Showing Initialization of Variables and the High-speed DIO Module.

In Figure 1-14, the program begins by initializing important program variables and setting up the high-speed DIO module. From there, the program begins using counters and case structures to control needed crank (a.k.a. *CRK*) and cam (a.k.a. *CAM*) signals based on inputs from the Kistler equipment. These steps occur in the following steps.

1. The c-RIO module must be configured at the beginning of program execution. Configuration includes setting the direction of the module's channels for either signal input or output. After initial configuration, the settings of the module are never changed as the program runs. *Initialized Counter* is used to force the configuration segment of the loop one time at program startup.

As the Kistler encoder sends 360 square waves per revolution and the desired *CRK* output signal is a 60 square-wave signal (6:1 ratio), *Pulse Count* is used to repeatedly count Kistler waves from 0-6. According to Figure 1-5, the signal from the speed sensor should be high at TDC as the tooth of the gear is centered on the sensor at this angle. For this reason, *Pulse Count* is initialized at 3.

Angle is used to track the crank angle of the engine from 0-1440 half-degree increments (i.e., an entire 720° thermodynamic cycle where 0° is TDC just after compression). Logic will control the output of both *CRK* and *CAM* signals based on this counter.

Values for all three variables are carried through while loop iterations via shift registers (red rectangle in Figure 1-14). These shift registers correspond to symbols placed at the far right-hand-side (end) of the while loop. As the value changes throughout the program, these signals are wired to the shift register symbols at the end of the while loop. Doing so carries these values back to the beginning of the loop where the new values are used for subsequent iterations of the while loop.

The *False* constant is used to initialize the voltage of *CRK* to 0 VDC.

2. A case structure checks the value of *Initialized Counter*. At startup, the value is zero that results in the true case code to run. In the first frame, the status of module 4 is checked.
3. The second frame in the flat sequence structure, the line direction of module 4 is set. Channels zero through three are set as inputs as the Kistler signals are wired to these channels. Channels four through seven are set as outputs as these channels are used to output the *CRK* signal, as well as other digital signals such as the control for the engine starter relay.
4. After the DIO module is configured upon startup, the next frame in the sequence structure begins.

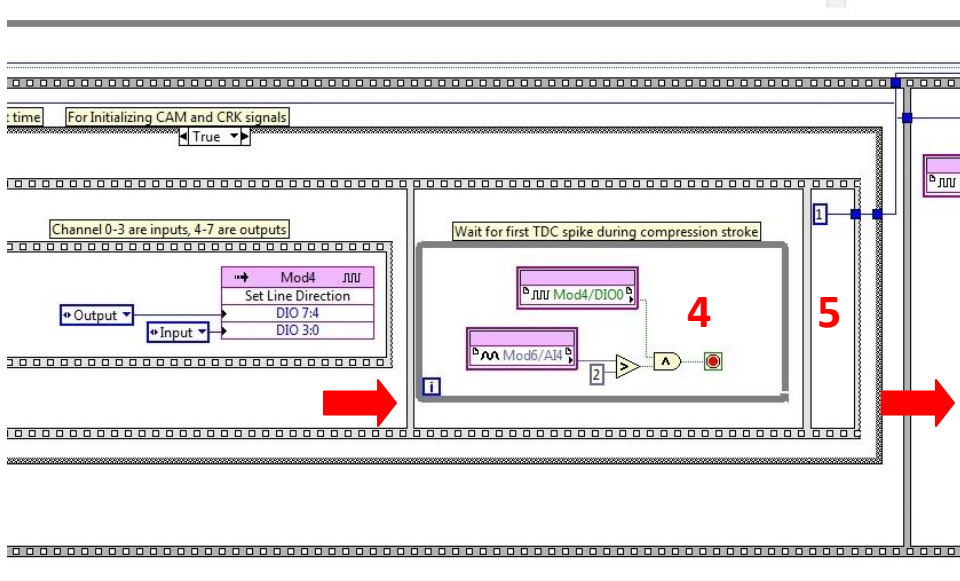


Figure 1-15. Block Diagram Where DIO Module Configuration is Finished and Initialization Counter is Set to One.

Figure 1-15 shows that this frame of the sequence includes a while loop. This while loop runs until the TDC signal from the Kistler encoder (DIO0) is *True* and is accompanied by a rise in pressure indicating TDC following a compression stroke. The value needed for pressure rise is 2 VDC. This is due to scaling of the Kistler charge amplifier, where a voltage of 2 VDC indicates 20 bars of cylinder pressure; much greater than any pressure experienced during the pumping loop, but also about half of the voltage experienced during compression. Once this occurs an And logic gate stops the while loop. This completes the signal conversion program's initialization.

5. Performing the configuration of module four once greatly improves program operation speed when compared to re-configuring at the beginning of each loop iteration. Following the initialization and stopping of the while loop in step four, *Initialized Counter* is set to a value of one. The value is carried throughout the remainder of the operation of the signal conversion program and is unchanged as long as the program runs. In subsequent runs of the main program's loop, the value of one is carried back through via a shift register forcing the

initialization case structure first discussed in Figure 1-14 to run in the false case, which is a ‘do nothing’ case.

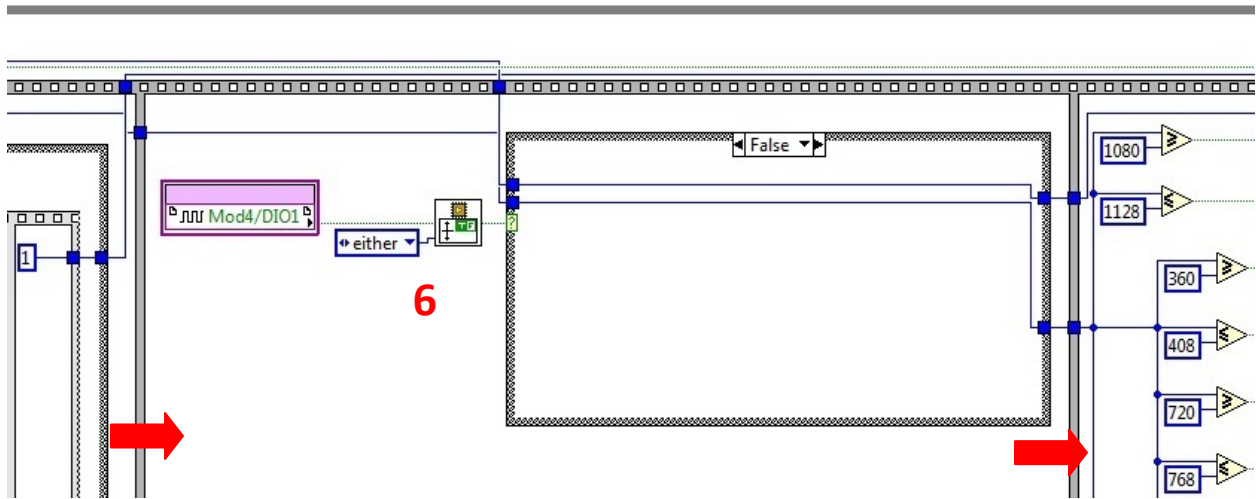


Figure 1-16. Second Frame Counter to Increase Angle and Pulse Count (False Case). Here, the Encoder Square Wave Signal is Not Changing, so No Action is Required.

6. The next section of the engine signal conversion FPGA code (Figure 1-16) begins following the completion of the configuration of module four and the first detection of the beginning of the engine thermodynamic cycle. This segment uses a Boolean logic subVI to wait for a change in the incoming digital square wave from the Kistler encoder. If no change occurs (i.e., false case), the program moves to the next frame in the sequence structure.

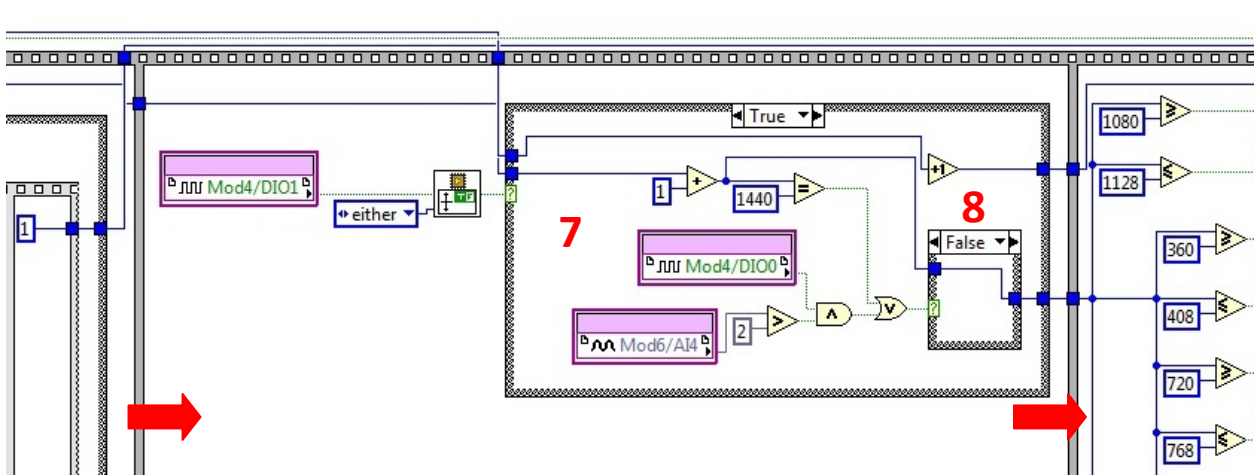


Figure 1-17. Second Frame Counter to Increase *Angle* and *Pulse Count*. Here the Encoder Signal is Changing (Outer True Case), Resulting in Increasing the Pulse and Angle Counters (Not at TDC – Inner Case False).

However, if a change is detected (i.e., true case), indicating that the engine has moved forward by one half-degree, the code shown in Figure 1-17 executes.

7. When the state of the encoder square wave changes (from either *True* to *False* or vice versa) the value of *Angle* and *Pulse Count* are increased by one (half-degree increments). Additionally, a check to determine if the engine is at TDC following compression is performed by checking if the value of *Angle* is 1440 (equal to 720°). As a double check, the program also checks for TDC by determining if the TDC signal and cylinder pressure signals are indicating TDC.
8. In the case of Figure 1-17 (false case), the engine is not at TDC following compression, so the program moves on by carrying the value for *Angle* through to the next frame in the sequence.

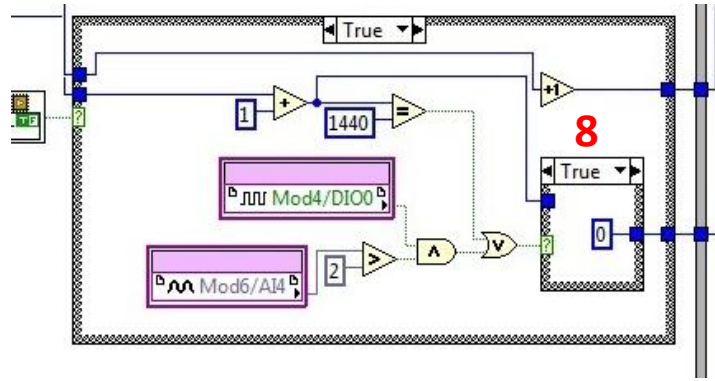


Figure 1-18. Second Frame Counter to Increase Angle and Pulse Counters. Here the Encoder Signal is Changing (Outer True Case) and is at TDC Following Compression, Resulting in Increasing the Pulse Counter and Resetting the Angle Counter (Inner True Case).

Figure 1-18 shows the instance when the engine is found to be at TDC following compression (true case). In the true case, the value for *Angle* is reset to zero. This indicates that the engine is at the beginning of the thermodynamic cycle. The value of zero is now passed into the next frame of the sequence structure.

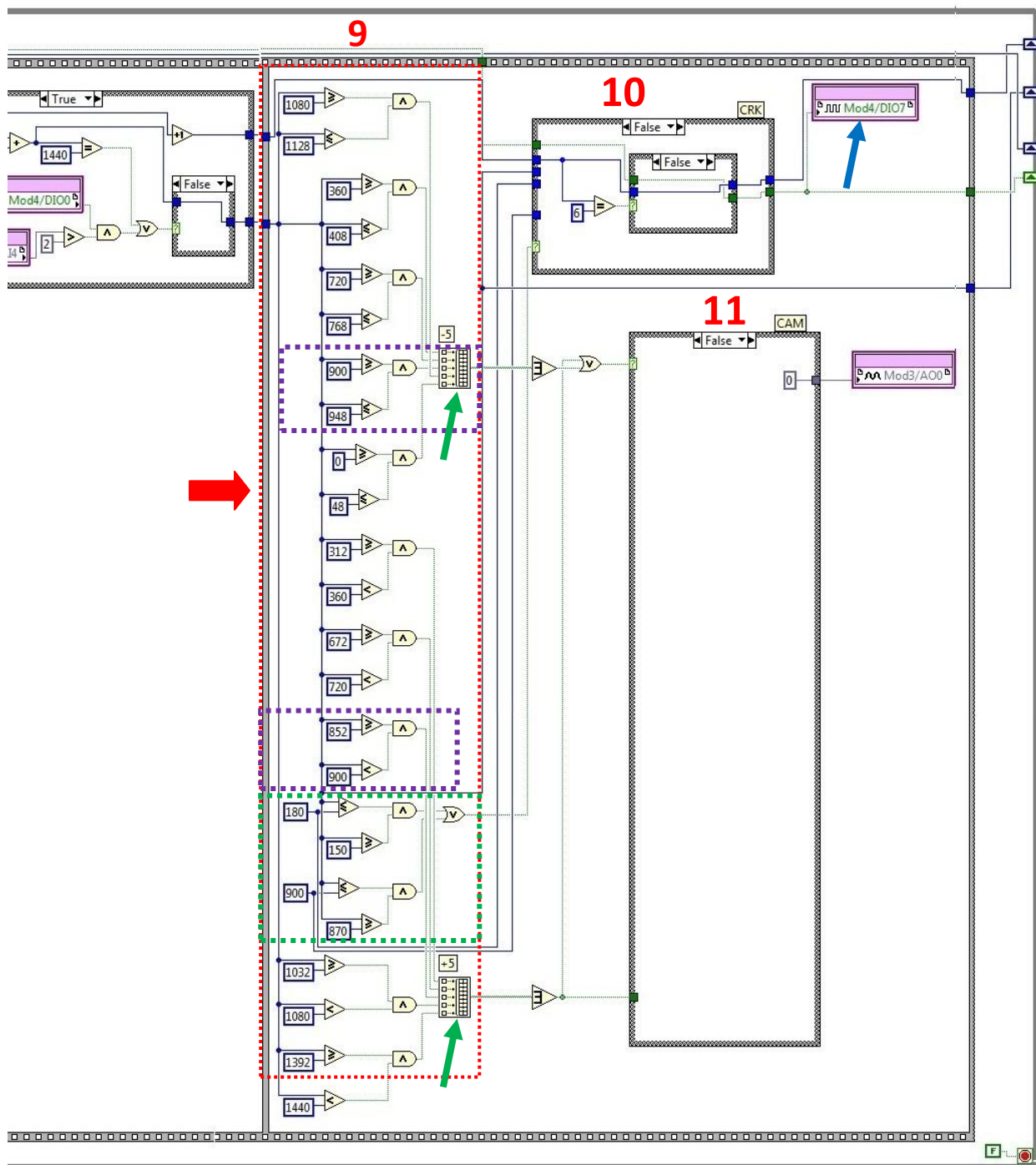


Figure 1-19. CRK Signal: Leave CRK in its Previous State (High or Low). CAM Signal: Voltage is in Neither High or Low Range, Set to 0 VDC.

The next frame in the sequence structure contains the logic needed to create the *CRK* and *CAM* output signals as needed for the ECU. These are intended to replicate the signals in Figure 1-5 and Figure 1-8. The code of this frame is shown in Figure 1-19.

9. In the code enclosed by the red rectangle of Figure 1-19, the value of *Angle* is checked against a series of ranges to determine the condition of the *CRK* and *CAM* signals.

For the *CRK* signal, a square wave is desired, except for during the timing gap that would occur if the speed sensor was installed on the 60-2 timing wheel. This timing gap occurs between 75° and 90° after TDC during each revolution. In the green rectangle of Figure 1-19, *Angle* is checked to see if its value is within this range ($150-180$ or $870-900$ half-degrees) using And logic gates to check ranges and an Or logic gate to account for either of the cases being true. The output of this Or logic gate is sent to the *CRK* case structure.

For the *CAM* signal, a single sync mark and four equally-spaced phase marks are desired, each lasting for 48° of crank angle [34]. As discussed previously, the sensor is inductive and yields a sinusoidal output signal as shown in Figure 1-8. Therefore, the signal must cross 0 VDC at each of the desired marks. The sync mark occurs at 270° before TDC following compression. This crank angle corresponds to a value of 900 for *Angle*. In addition, the four phase marks are set to occur at 0° , 180° , 360° , and 540° . In order to accurately simulate the signal from the cam sensor, *CAM* must go to 5 VDC (equal to the voltage that would have been supplied by the ECU to the actual sensor) 24° before the sync and phase mark crossings are to occur. Following the crossing of 0 VDC at the desired angles, *CAM* must go to -5 VDC for a duration of 24° after.

Table 1-1. Location of Beginning, 0 VDC Crossing, and End of Sync and Phase Marks for CAM Signals, Corresponding Values for Angle.

CAM = 5 VDC		CAM Crossing		CAM = -5 VDC	
Deg. After TDC	Angle	Deg. After TDC	Angle	Deg. After TDC	Angle
696	1392	0	0	24	48
156	312	180	360	204	408
336	672	360	720	384	768
426	852	450 - sync	900	474	948
516	1032	540	1080	564	1128

This is summarized in Table 1-1. Using this table, it can be observed how the logic for CAM works. The code determines if *Angle* is within the ranges where it should be 5 VDC (e.g., greater than (or equal to) 852 and less than 900), or -5 VDC (e.g., greater than (or equal to) 900 and less than (or equal to) 948). The code that checks for the sync mark (example discussed here) is shown in Figure 1-19 in the purple rectangles. If *Angle* is found to be within any of these ranges a *True* is written to the appropriate Boolean array (green arrows). If a *True* is written to any part of either Boolean array then a *True* is sent to the CAM case structure.

10. The state of CRK, which is controlled by the module output DIO 7 (blue arrow in Figure 1-19), is based on the Boolean Or logic gate in the green rectangle of Figure 1-19. During most of the engine revolution, the outer case structure will be false as the engine is outside of the 75°-90° after TDC range most of the time. In the false case, the state of CRK depends only on the value of Pulse Count. If Pulse Count is less than six (from the 6:1 frequency ratio), the state of CRK does not change, as indicated by the inner case structure of the CRK case structure in Figure 1-19.

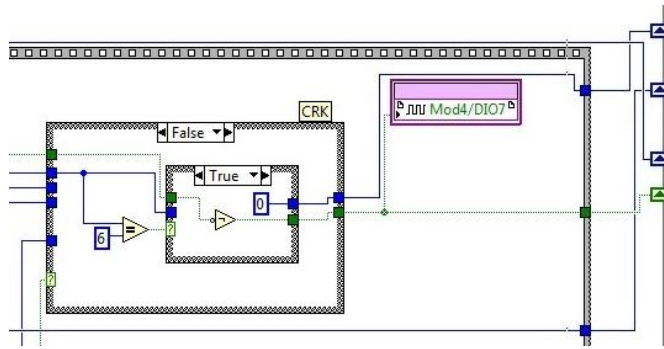


Figure 1-20. Pulse Count = Six, Flip State of CRK (From True to False, Vice Versa) and Reset Pulse Count.

If *Pulse Count* is equal to six, as shown in Figure 1-20, the state of *CRK* is flipped and the value for *Pulse Count* is reset to zero. If the value for *Angle* corresponds to the interval for the timing gap, the outer case structure becomes the true case.

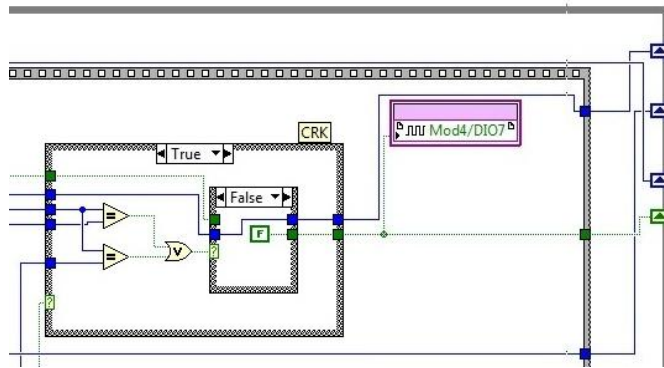


Figure 1-21. Engine in Interval of Timing Gap, but not at 90° after TDC, Set CRK to False.

If the engine is not at exactly 90° after TDC, the inner case structure's false case is executed as shown in Figure 1-21.

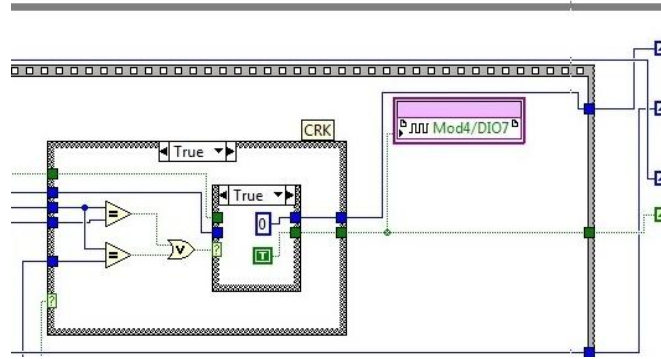


Figure 1-22. Engine is at Exactly 90° After TDC (End of Timing Gap), Set CRK to True, Reset Pulse Count.

If the value for *Angle* corresponds to the engine being at 90° after TDC, the inner case structure is sent a *True* signal from the Or logic gate, resulting in the code in Figure 1-22 to run instead. This code sets *CRK* to *True* and resets *Pulse Count*. From the *CRK* case structure the value of *CRK* is sent to the module four output (DIO7) and shift register while the value for *Pulse Count* is sent to its shift register. Both of these signals will be used in the following iteration of the overall program while loop.

11. In the event that the value stored in *Angle* corresponds to neither a 5 VDC or -5 VDC range, the *CAM* case structure's false case executes. This code is shown in Figure 1-19 and is setting the output of module three AO0 to zero volts. In the case of *Angle* being in the range corresponding to the cam timing teeth, the *CAM* case structure's true case executes.

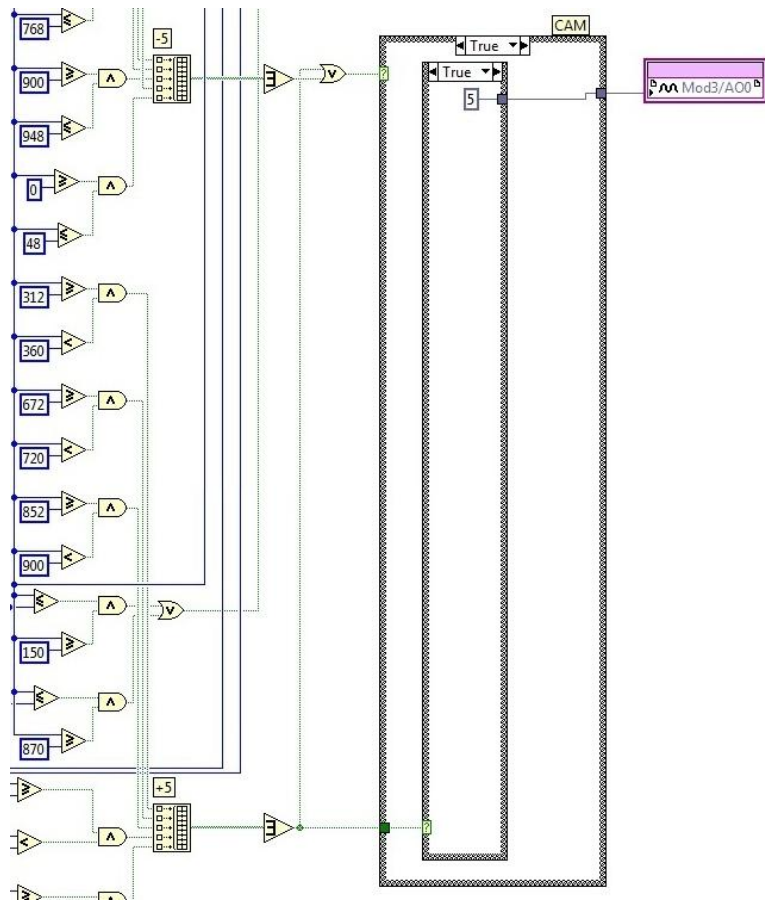


Figure 1-23. Angle within Range for Front of Cam Wheel Tooth, Set AO0 to 5 VDC.

If *Angle* corresponds to a value before the desired zero crossing of the cam signal, an inner case structure executes true case code that sets the analog output signal to 5 VDC, as shown in Figure 1-23.

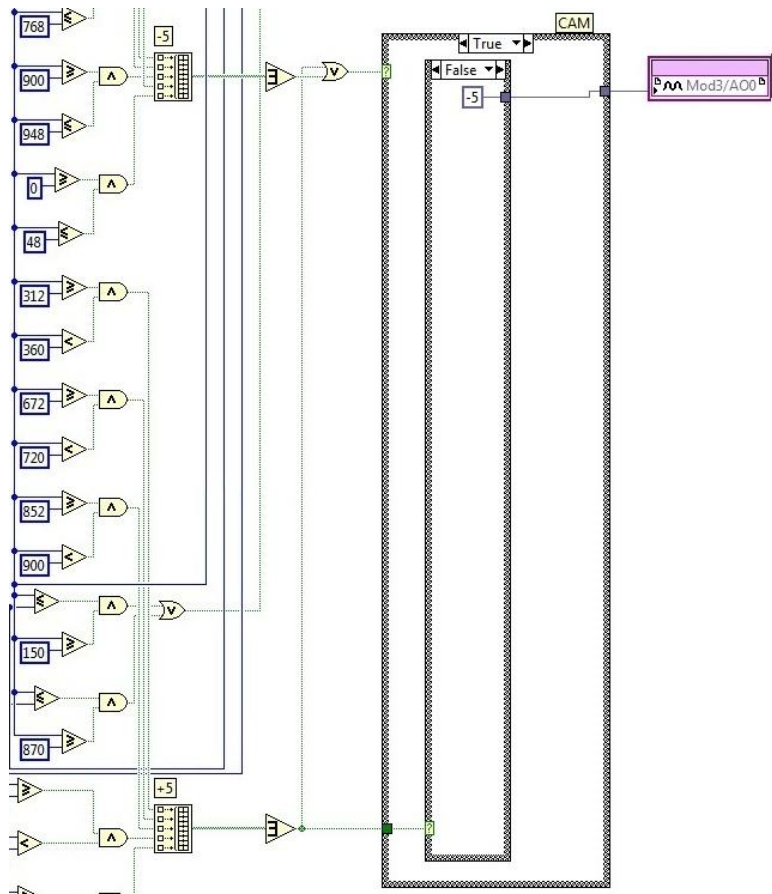


Figure 1-24. Angle Within Range for Zero Crossing and Back of Cam Wheel Tooth, Set AOO to -5 VDC.

Conversely, if the angle is equal to (or greater than) any of the desired zero crossing of the *CAM* signal, the inner case structure's false case will run instead (Figure 1-24), thus setting *CAM* and *AO0* to -5 VDC. Upon the outputs of the *CAM* and *CRK* signals being sent to the ECU, the signal converter program's main while loop repeats using new values for *Angle*, *Pulse Count*, and *CRK*. Like the rest of the FPGA code, this loop will continue iterations until the entire LabVIEW performance monitoring system is stopped.

1.4 Calibration Software

The program used to calibrate and configure the ECU is called BOSCH Modas Sport. This program is used to communicate directly with the ECU and allows the user to define program constants.

Additionally, engine maps can be made and adjusted using this program. Modas Sport can also be used for recording data for later analysis.

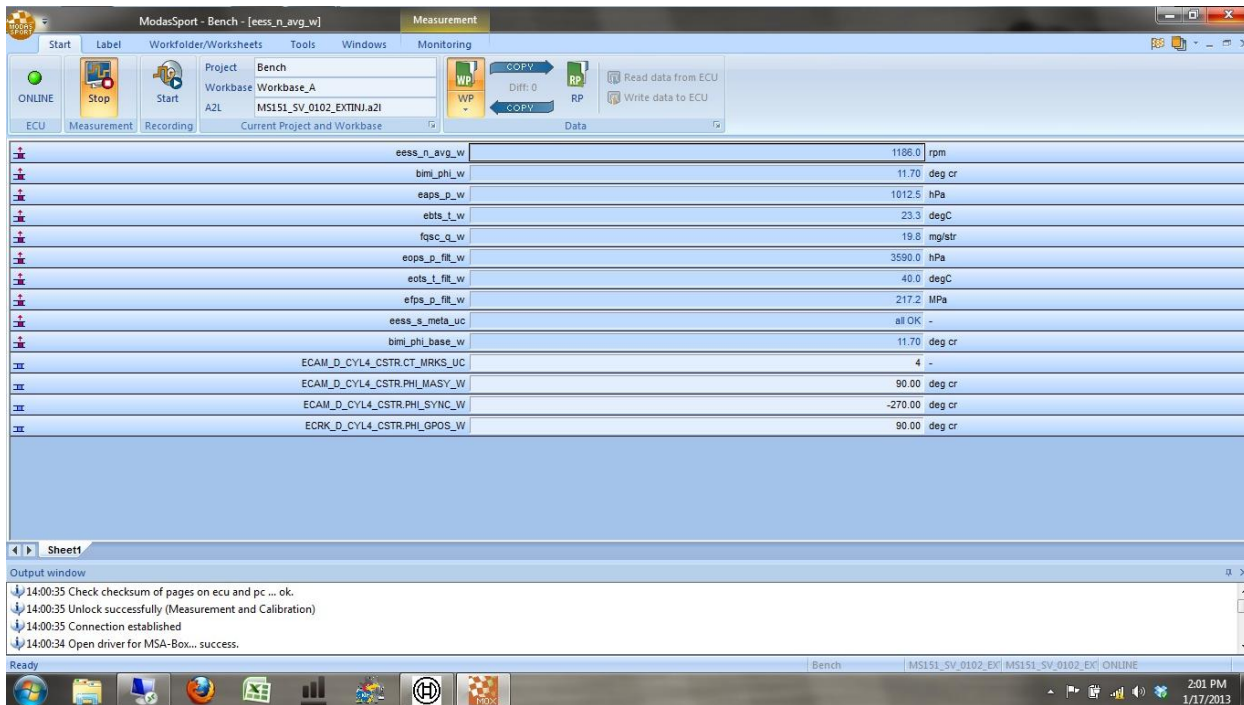


Figure 1-25. Screenshot of BOSCH Modas Sport ECU Measurement and Calibration Program.

A screen shot of the Modas Sport operating window is shown in Figure 1-25. The ECU begins with a default calibration program and calibration of the ECU (via changes to the ECU configuration) can be performed while the engine is running. From this default program, Modas Sport allows the user to save changes under a new name and load them onto the ECU. In essence, separate engine maps and ECU settings are available for the engine depending on the experiment being performed. As a result, separate programs may exist for different fuels or operating strategy, allowing the ECU to be reprogrammed to optimize performance for any configuration (e.g., turbocharged or naturally aspirated) or fuel (e.g., biodiesel or ULSD) operation that was previously calibrated.

1.5 Bench Testing

The first major step in this process is the creation of a ‘bench’ setup to perfect the measurement of sensor signals and injection timing before installing the system on an engine.

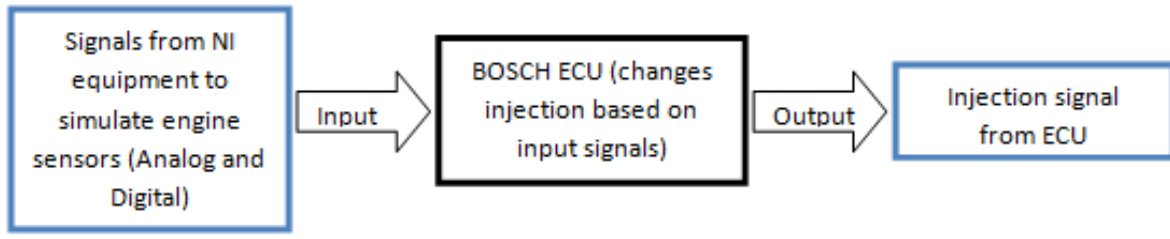


Figure 1-26. Depicts Signal Flowchart during ‘Bench’ Testing.

The bench process involves sending simulated analog and digital sensor signals to the BOSCH ECU while simultaneously reading the output from the ECU to the injector; i.e., sending varying electronic signals to the ECU to calibrate its response. This setup is depicted in Figure 1-26 and is performed because immediate integration of all systems onto an engine makes troubleshooting difficult. By monitoring the electronic output of the ECU, it can be determined if the injection timing and duration will be proper based on the simulated signals.

1.5.1 Engine Control Unit Installation for Initial Bench Testing

Wiring of the ECU and its multi-pin deutsch connectors requires military-specification (M22520/2-01) crimps in order to precisely crimp the wire into the pins of the connector [41]. These crimpers and the crimping process are shown in Figure 1-27 through Figure 1-29.

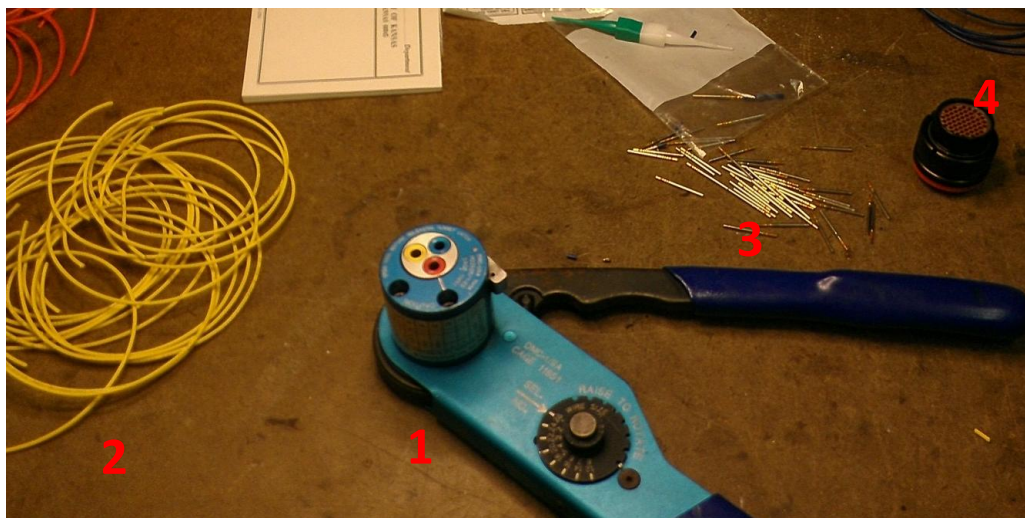


Figure 1-27. Crimping Tool (1), Wire (2), Pins (3), and Blank Connector (4).



Figure 1-28. Inserting Stripped 22-Gauge Wire Into Pin.



Figure 1-29. Pins Before Crimping (Bottom) and After Crimping (Top).

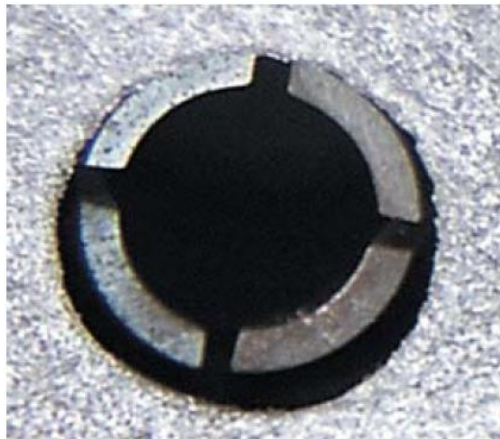


Figure 1-30. Close-Up of the Tines Inside a Connector [41].

Inserting (and removing) the pins into (or out of) the connectors also requires a special tool as small tines (Figure 1-30) snap closed behind the pins to keep them in place. The tool is used to either engage or disengage these tines.

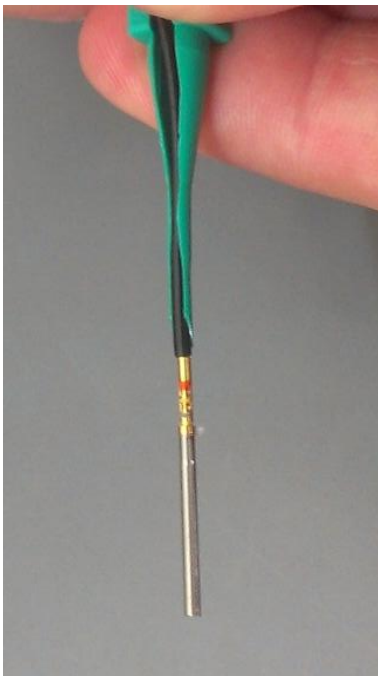


Figure 1-31. Place Wire into Insertion Tool.

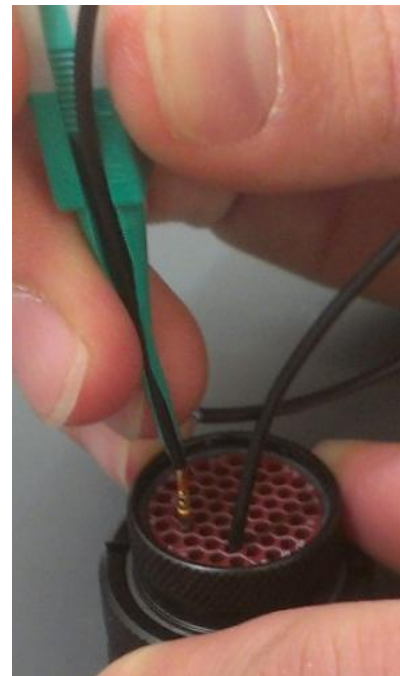


Figure 1-32. Press Pin into Desired Pin Slot.



Figure 1-33. Press Until a 'Click' is Felt/Heard.

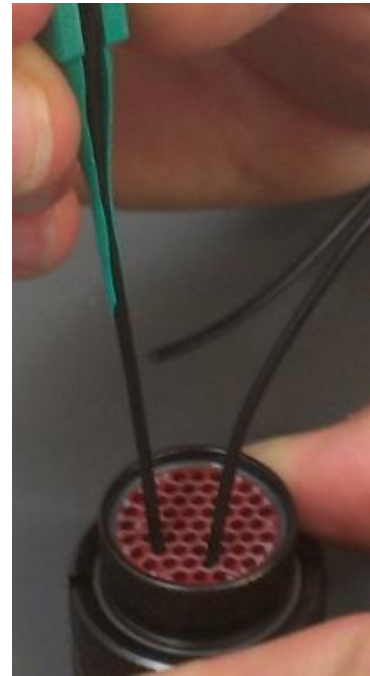


Figure 1-34. Remove Insertion Tool.

Using the special insertion tool and alcohol as lubricant, the pins for the connector are installed in the process shown in Figure 1-31 through Figure 1-34.

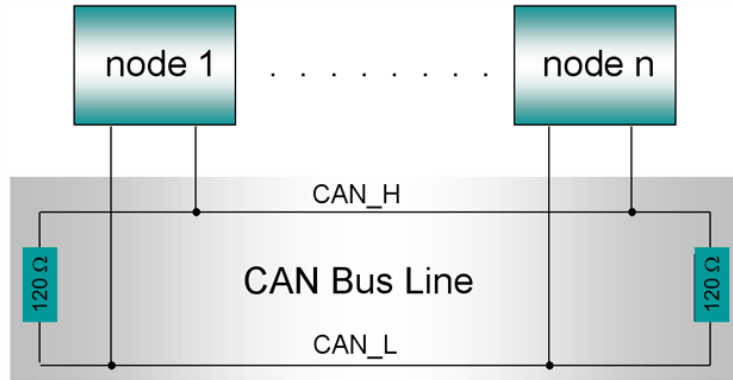


Figure 1-35. Wiring Diagram for CAN-Bus Communication .

Finally, resistance is required to perform Controller Area Network (CAN) communication (Figure 1-35) so 120-Ohm resistors are wired into these circuits [12].

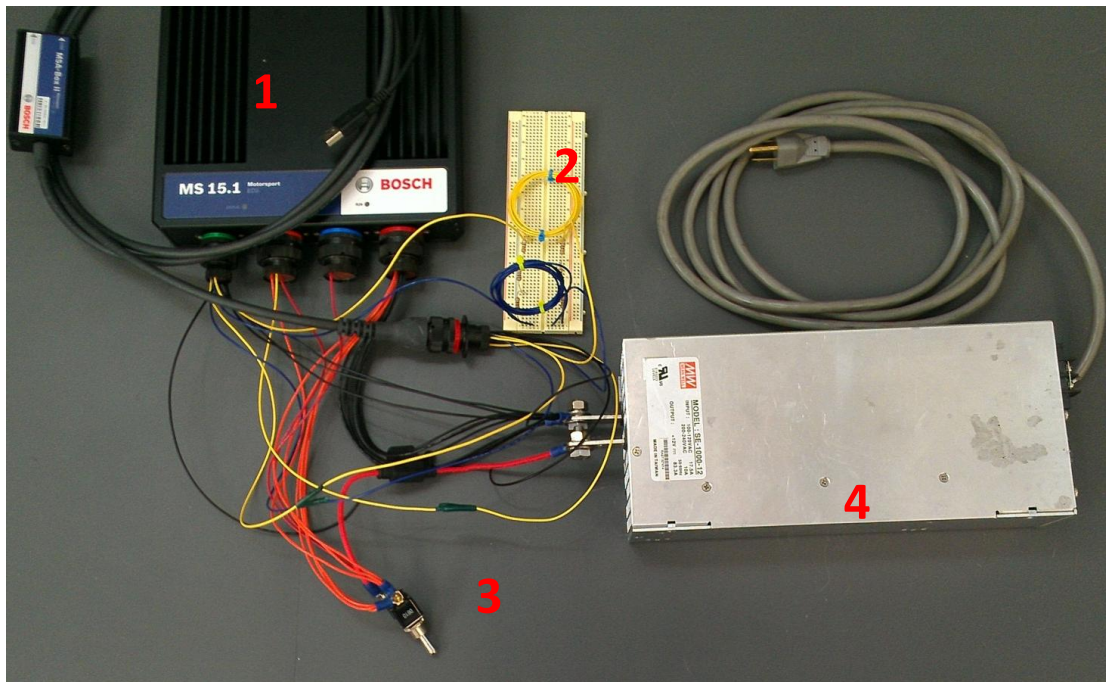


Figure 1-36. Initial Wiring for Power-up and Communication Showing: ECU with USB Connection (1), Breadboard with CAN Bus Resistance Wiring (2), Preliminary Ignition Switch (3), and 12-Volt Direct-Current Power Supply (4).

For preliminary tests, this is accomplished using resistors installed on a breadboard, as shown in Figure 1-36. A more permanent solution is utilized in the test cell following this proof of concept. The CAN communication wiring (with resistors), as well as the initial ECU wiring is also shown in Figure 1-36.

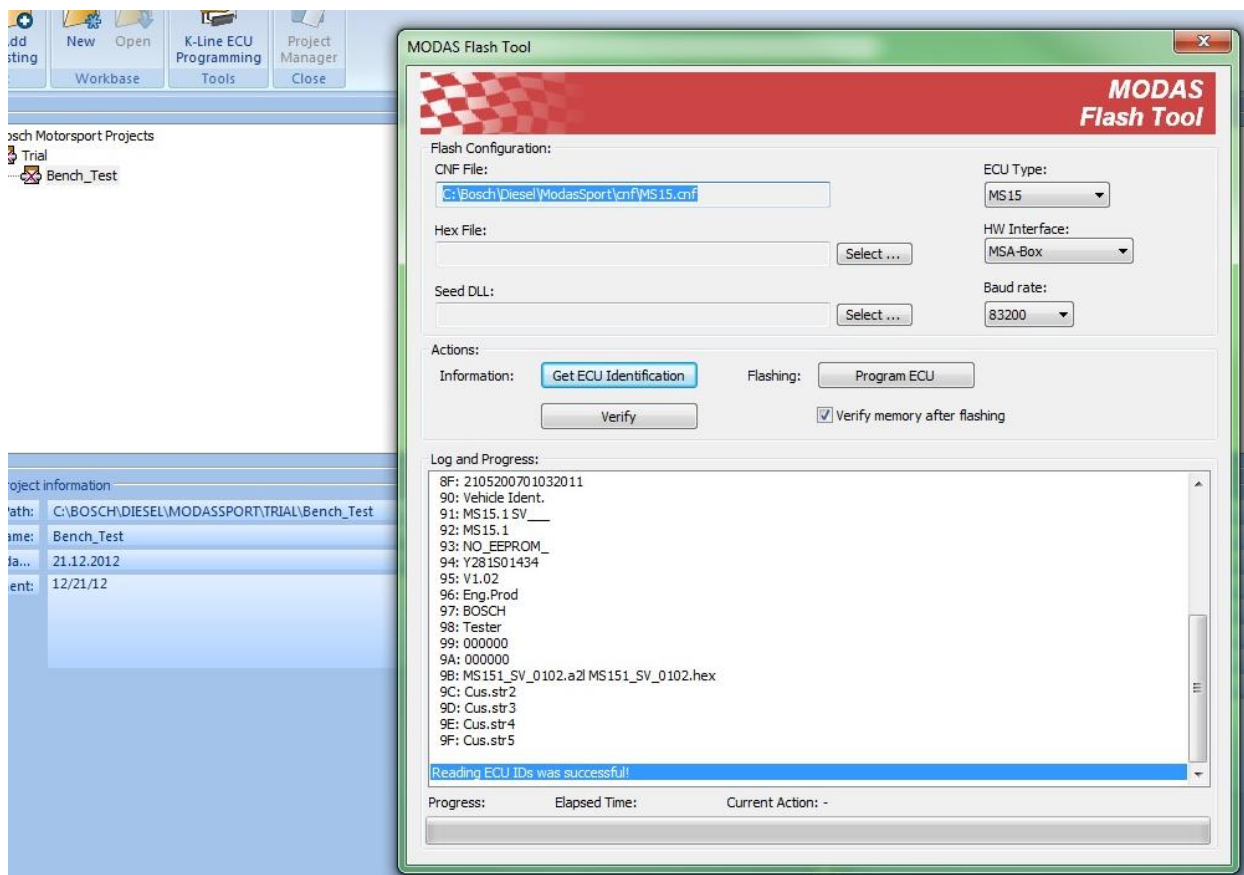


Figure 1-37. Connection with ECU via USB Connection.

Before connection to the computer, Modas Sport and the MSA-Box II drivers must be installed.

Power up is accomplished by first turning on the power supply, then the ignition switch. Finally, connecting to the ECU is accomplished in the screen shot in Figure 1-37. As noted in the screen shot of Figure 1-37, a configuration (CNF), hex, and seed dll file are needed to flash a configuration to the ECU. The configuration file is called MS15.cnf, this file is never changed, but is always used for ECU programming. The .hex file contains the actual engine program changes, therefore multiple versions of this program exist. Finally, the seed .dll “SEED_MSD_DIESEL.dll” is necessary to access and program the ECU.

Sensors wired into the ECU include: intake air temperature and pressure, fuel rail pressure, engine oil pressure, and engine oil temperature. Of these, analog voltages to simulate fuel rail pressure and engine oil pressure are necessary during bench tests in order to ensure that the ECU reads values

for these pressures that are within operating limits. For instance, the ECU can stop the engine due to low oil pressure.

In order to read in boost air temperature and engine oil temperature correctly, the Bosch temperature sensors are of the Resistance Temperature Detectors (RTDs) type. This type of sensor changes resistance with temperature and is necessary because traditional thermocouples output temperature change in millivolts. Therefore, traditional thermocouples would have required an extremely sensitive system in order to determine temperature accurately.

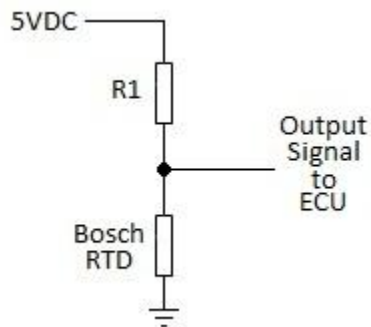


Figure 1-38. Configuration of a Voltage Divider to Measure Temperature Using an RTD and a Step-Up Resistor.

Instead, RTDs are used in order to measure voltage in the zero to five VDC range as needed by the ECU. To actually generate a voltage change as a result of a resistance difference, these RTDs (from $10k\Omega$ to 100Ω with temperature) must be connected in a configuration with a voltage divider including appropriately sized resistors ($1k\Omega$) as shown in Figure 1-38[43, 44].

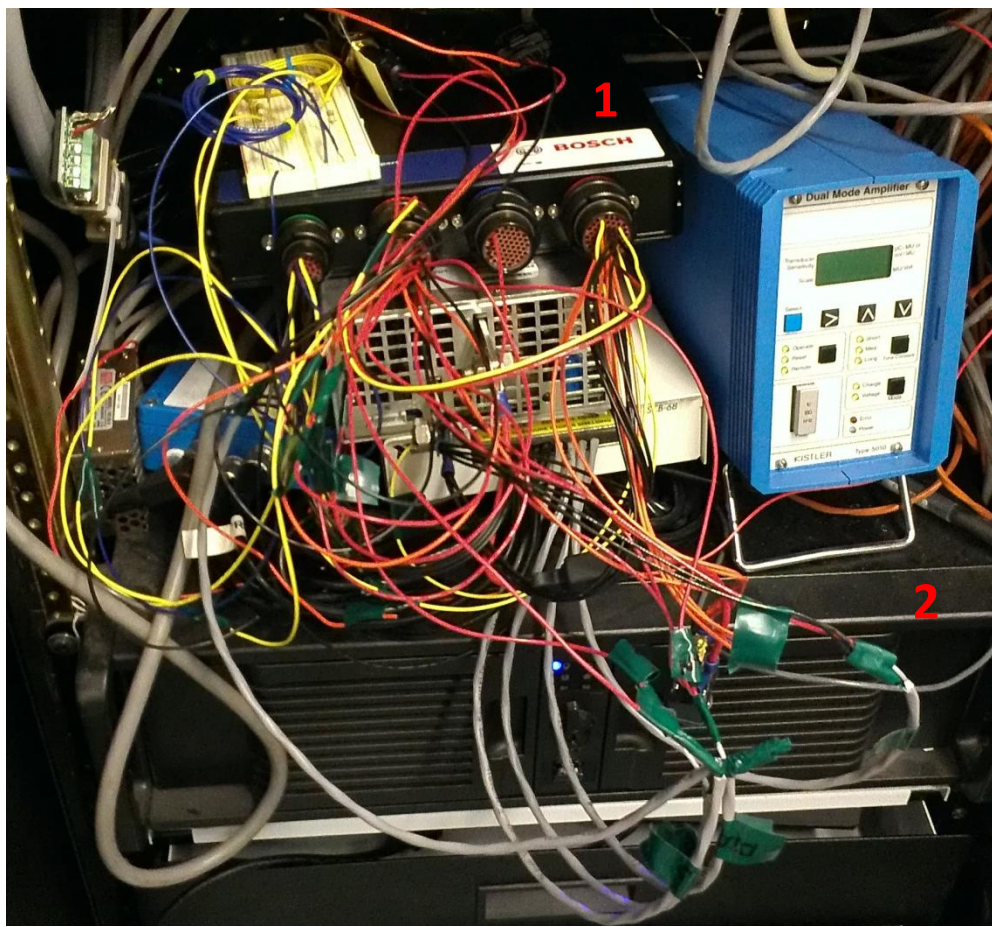


Figure 1-39. Initial Wiring Needed for Bench Testing of the ECU (1) and Dedicated Test Cell Computer (2).

Finally, camshaft and crankshaft signals, created by the custom LabVIEW program, are also connected to the ECU, as shown in initial bench configuration in Figure 1-39. The output signal of the ECU that is of particular interest is the injector signal, which changes based on variations of the above mentioned input sensors. For instance, higher speed sensor frequency indicates faster engine speed and thus, a shorter gap between fuel injections will be observed.

1.5.2 Results of Bench Testing

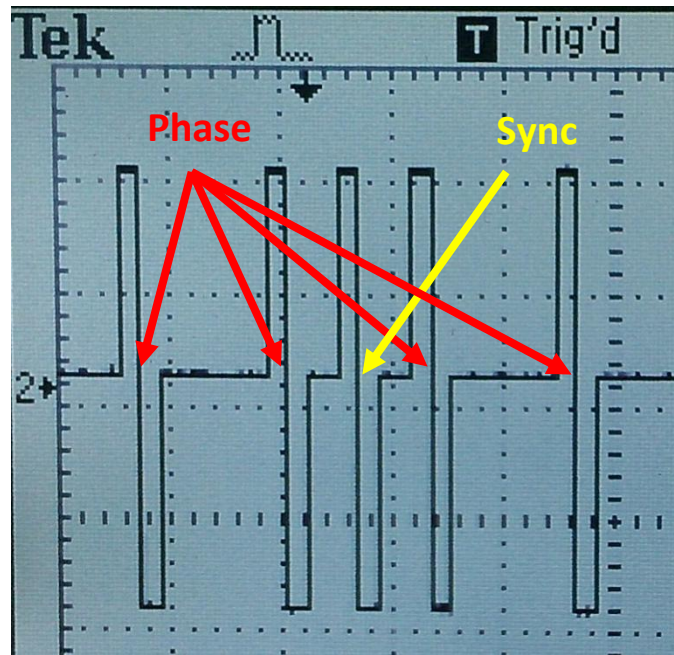


Figure 1-40. Screenshot of Oscilloscope Showing Cam Sensor Signal Voltage Approximating Phase (4) and Sync (1) Marks at Transition from Positive to Negative Voltage.

To verify proper behavior of the cam signal, an oscilloscope was connected in order to observe the output voltage. A screenshot of the cam signal is shown in Figure 1-40. Following the verification of both the cam and crankshaft signals, these signals are wired into the ECU and, using the LabVIEW engine simulation program to vary engine speed and sensor values, the behavior of the ECU is observed.

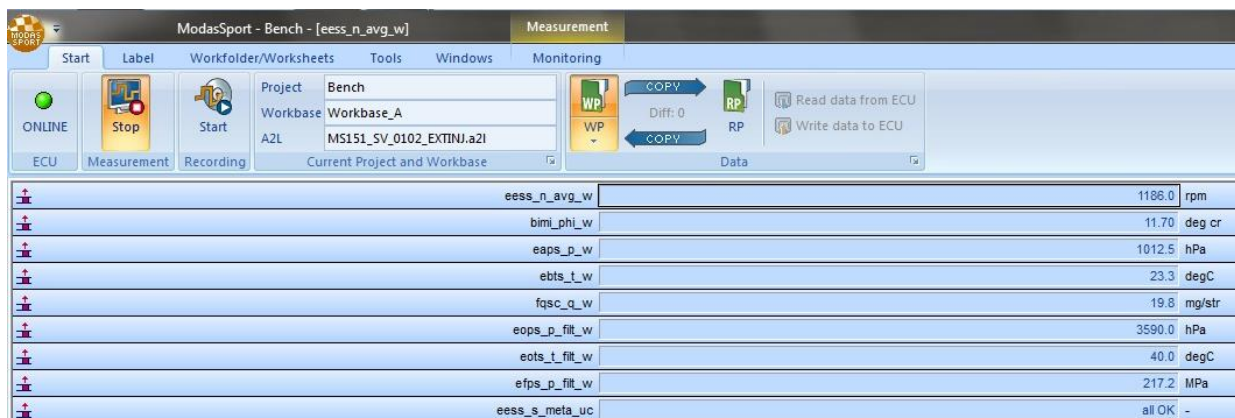


Figure 1-41. Screenshot of BOSCH Modas Sport ECU Measurement and Calibration Program During Initial Bench Tests.

In the Modas Sport screen shot of Figure 1-41, the engine speed, as well as other critical values, is shown during the tests. These values change in real-time allowing the user to observe what is taking place. Specifically, the injection amount (fqsc_q_w: 19.8 mg/str) and crank angle (bimi_phi_w: 11.70 deg cr) change based on speed and fuel needed (via accelerator pedal position). These can be manually changed by adjusting the crank angle map and driver fuel demand maps in the configuration program of the ECU.

1.5.3 Verifying Injection Timing

After verifying that the ECU was reading speed and crank angle correctly (eess_s_meta_uc: all OK in Figure 1-41) and that the ECU was attempting to inject fuel, the next step is to verify that this injection is occurring at the proper engine crank angle. Moreover, that this is happening only during the compression stroke, rather than at each engine revolution, or during the exhaust stroke.

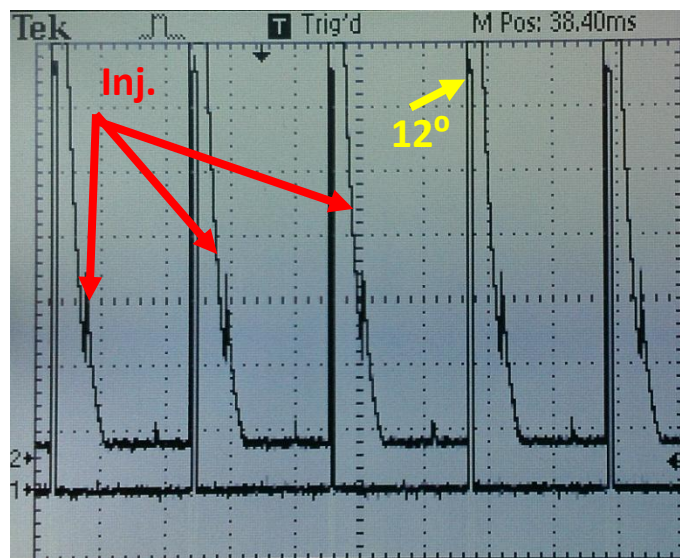


Figure 1-42. Injector Voltage Spikes and Start of Injection (12° before TDC) References from LabVIEW.

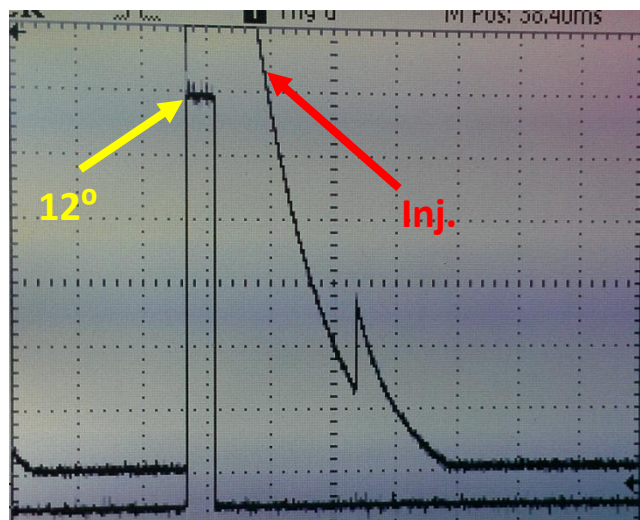


Figure 1-43. Single Injector Voltage Spike and Start of Injection (12° before TDC) Reference from LabVIEW.

Injection timing is validated by again using the oscilloscope, with screenshots shown in Figure 1-42 and Figure 1-43. This time, the injector signal from the ECU and a TDC signal from the LabVIEW program are directly wired to the oscilloscope. Using these signals and the LabVIEW engine simulation program it is possible to verify that injection was both occurring at the desired crank angle and that it changes as a function of simulated engine speed. After the verification of the injection timing, a short test with the injector wired to the ECU demonstrates that the injector was physically attempting to

inject fuel. Additionally, proper connection of the engine oil temperature, engine oil pressure, along with the engine boost temperature and pressure sensors were verified.

1.6 Implementation of ECU into Test Cell

The first step following successful bench testing is to install the ECU in its permanent location in the test cell. The Bosch ECU documentation indicates that the ECU must be within 1.5 meters of the injector. This severely limits the installation locations, as the safety of the ECU is a major concern. The chosen location for the ECU is in an electrical enclosure above the engine.



Figure 1-44. Close-up of ECU Installation.

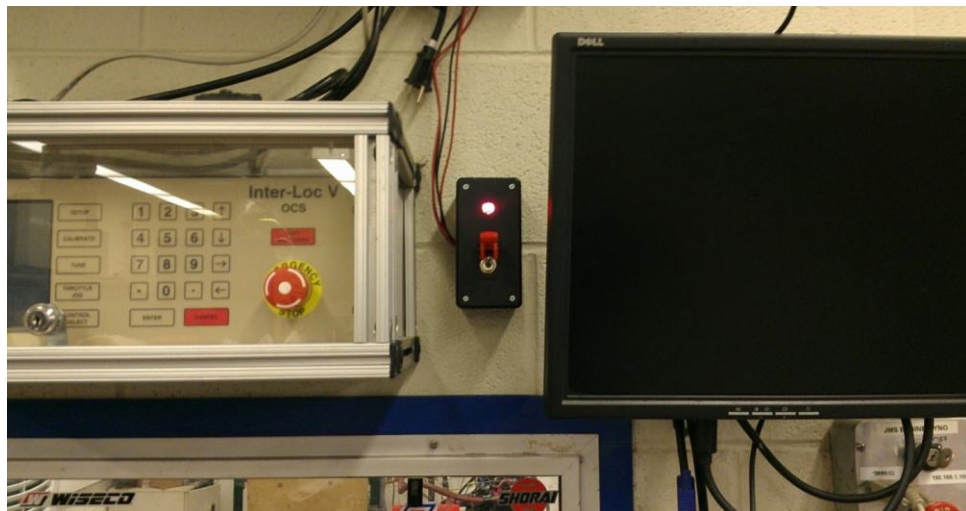


Figure 1-45. ECU Power Switch (red) Next to Dynamometer Controller and High-Speed Computer Screen.

The enclosure chosen has a clear door that provides viewing of the ECU status lights (Figure 1-44). Wiring that connects to the LabVIEW c-RIO (to simulate accelerator pedal, cam and crank signals, etc.) runs above the test cell while the injector and sensor wires run directly down to the engine. Power is supplied via a 12 VDC power supply located in the instrumentation cabinet. This power goes through a switch located outside of the test cell (Figure 1-45), directly above the computer bench. This allows operators to cycle power to the ECU and can be used in an emergency situation to stop fuel injection and shut down the engine.

1.6.1 *Installation of the Engine Sensors*

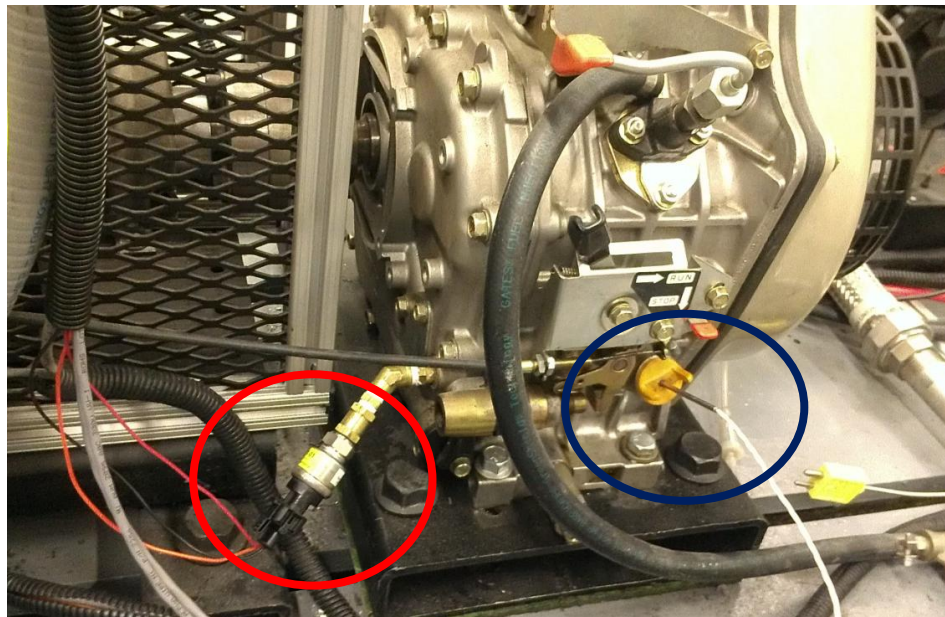


Figure 1-46. Bosch Oil Pressure Sensor (red) Installed on the Yanmar and Wired to the ECU. Previous Oil Temperature Location is Shown in Blue.



Figure 1-47. Bosch Oil Temperature Sensor (Red) and Auxiliary Oil Drain (Blue).



Figure 1-48. Location of Installed Bosch Oil Temperature Sensor Using Thread Adapter.

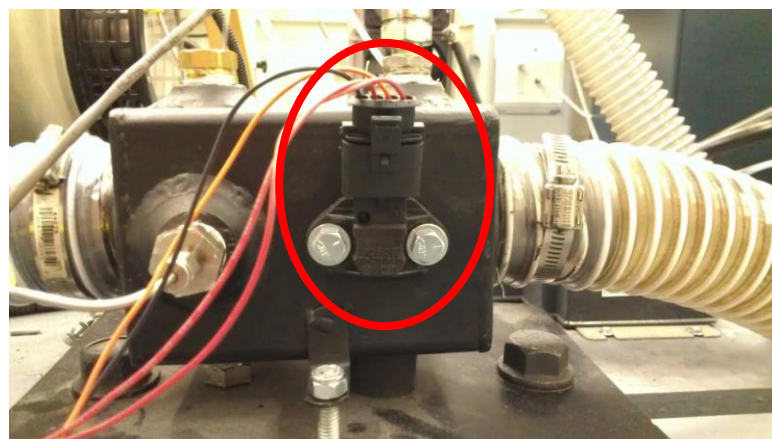


Figure 1-49. Bosch Intake Pressure and Temperature Sensor (Red).

The Bosch oil pressure sensor is installed in the location of the previous oil sensor used by the LabVIEW performance data-recording program (Figure 1-46). This new sensor's readings are sent to both the ECU and to LabVIEW for observation and recording in the same fashion as the Omega pressure transducer used for previous research. It was not feasible to install the new Bosch oil temperature sensor in the location of the previous sensor shown in Figure 1-46. This new sensor, shown in Figure 1-47, has a much shorter probe length that would not be able to reach the oil if installed in the previous location (the previous sensor was six inches long). Instead, an adapter is used to allow the sensor to be installed directly into the auxiliary oil drain plug of the Yanmar (Figure 1-48). Finally, the intake pressure and temperature sensor is installed on the mixing box between the turbocharger and the Yanmar intake. This sensor allows the ECU to compensate for changes in turbocharger settings, intake temperature, EGR, etc. (if so desired). Because these sensors are redundant at this location, the new sensor, shown in Figure 1-49, only communicates with the ECU. Previous sensors for mixing box temperature and pressure are unchanged from their previous configuration.

1.6.2 Bosch Injector Install

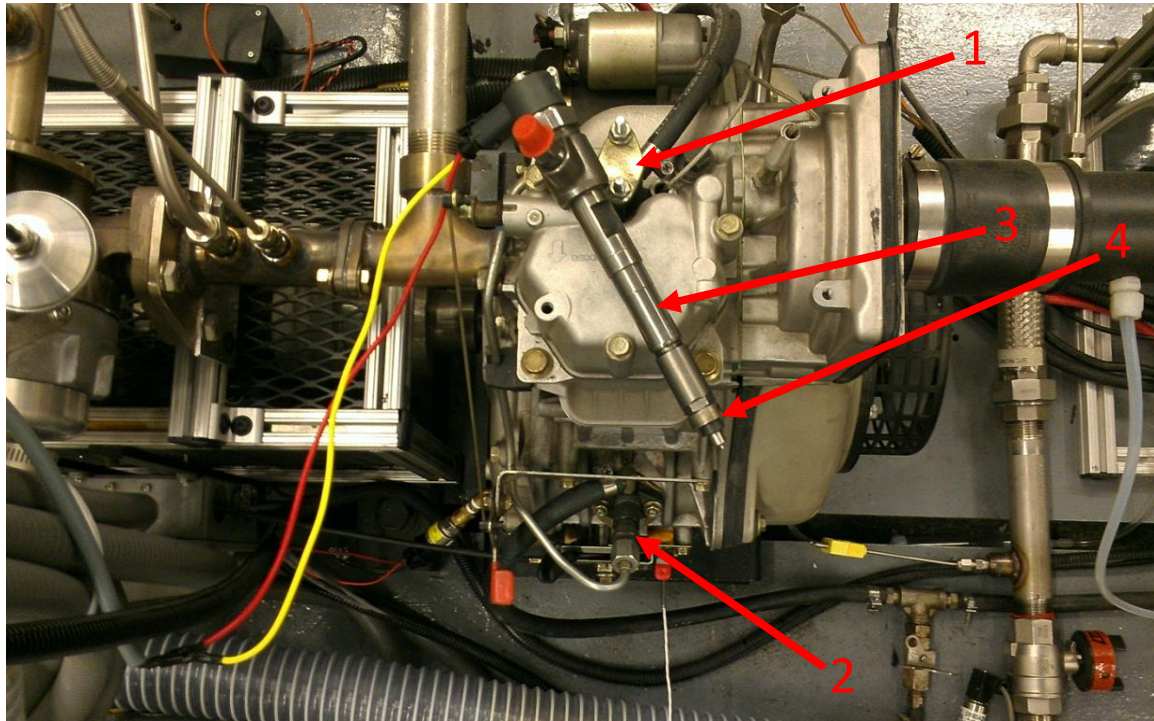


Figure 1-50. Original Yanmar Injector (1) and Fuel Pump (2), Bosch Injector (3) with Spacer Gasket from Yanmar Injector (4).

The new Bosch injector is modified with a spacer gasket to interface with the Yanmar without needing to machine the engine cylinder head. This injector (part # 445110183) was chosen based on the size of the Yanmar cylinder. Though the engine in the Fiat Grande Punto MJTD is larger (1.3L), its individual cylinder dimensions are similar to the Yanmar. Additionally, the diameter and dimensions of this injector allow installation with no engine head machining. A similar engine In Figure 1-50, the stock Yanmar fuel system is shown still installed with the wired-up Bosch injector sitting on the engine head for comparison. By using a shortened spacer gasket from a spare Yanmar injector, the installed Bosch injector protrudes into the cylinder to the same depth as the Yanmar injector.



Figure 1-51. Yanmar Injector.



Figure 1-52. Bosch Injector.

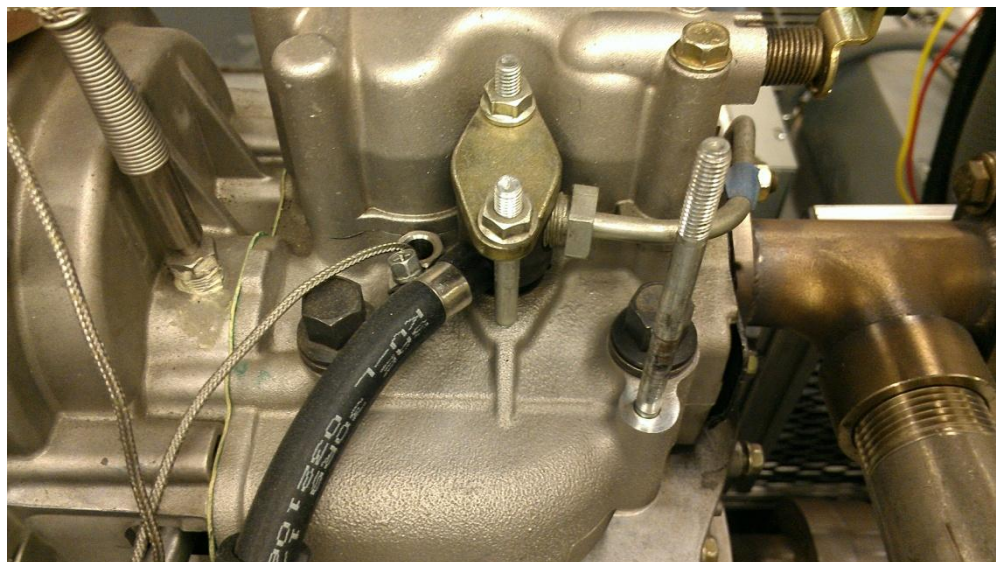


Figure 1-53. Stock Yanmar Injector Installation.

Figure 1-51 and Figure 1-52 show the protrusion of the Yanmar and Bosch injectors through the Yanmar cylinder head, respectively. The installation of the Bosch injector requires the removal of the

Yanmar injector. The stock configuration is shown in Figure 1-53, where two mounting studs hold the injector in using a plate.



Figure 1-54. Yanmar Injector, Mounting Plate Removed.

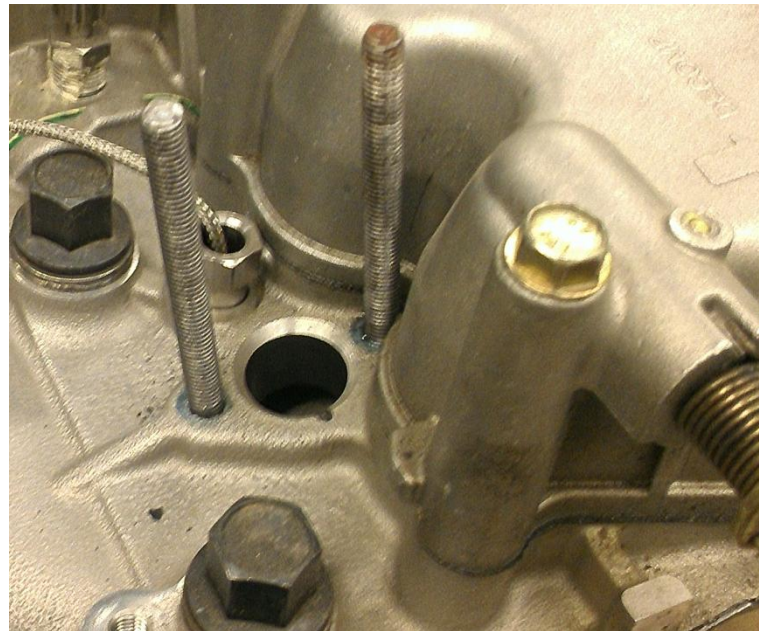


Figure 1-55. New Injector Mounting Studs Installed on Yanmar Engine Head.

The first step is to remove the mounting plate (Figure 1-54). The injector easily pulls out of the injector port on the engine. The previous mounting studs are too short to facilitate the installation of the longer injector. Figure 1-55 shows longer injector studs installed and the empty injector port on the engine head.



Figure 1-56. Custom-Made Mounting Plate for Bosch Injector (Left). Stock Yanmar Mounting Plate (Right).

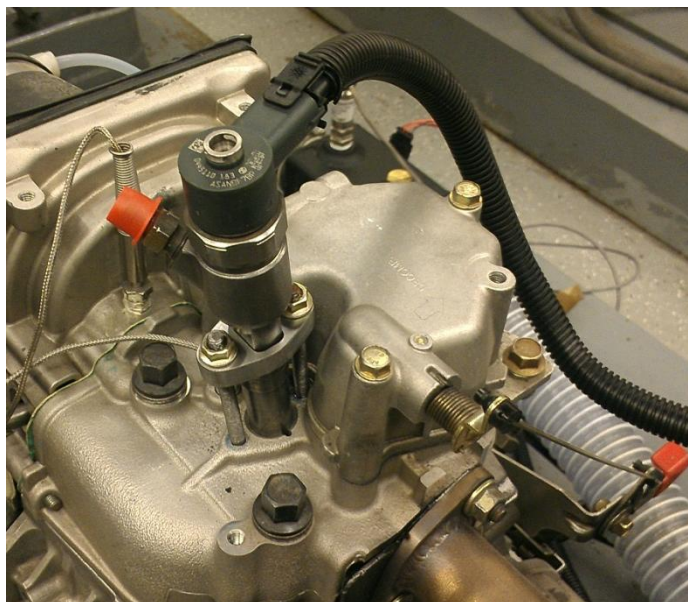


Figure 1-57. Final Bosch Injector Installation Using New Mounting Studs and Mounting Plate.

A custom mounting plate is used to hold the Bosch injector in place. Additionally, this plate keeps the new injector from spinning inside the injector port, insuring that injector orientation does not change. The stock Yanmar injector plate and the new Bosch injector plate are shown in Figure 1-56. Using the new mounting studs and plate, the Bosch injector fits into the engine head and is secure. Final injector installation (and wiring) is complete as shown in Figure 1-57. The next step is the replacement of the Yanmar fuel system with the high-pressure Bosch system.

1.6.3 High-Pressure Fuel System Installation

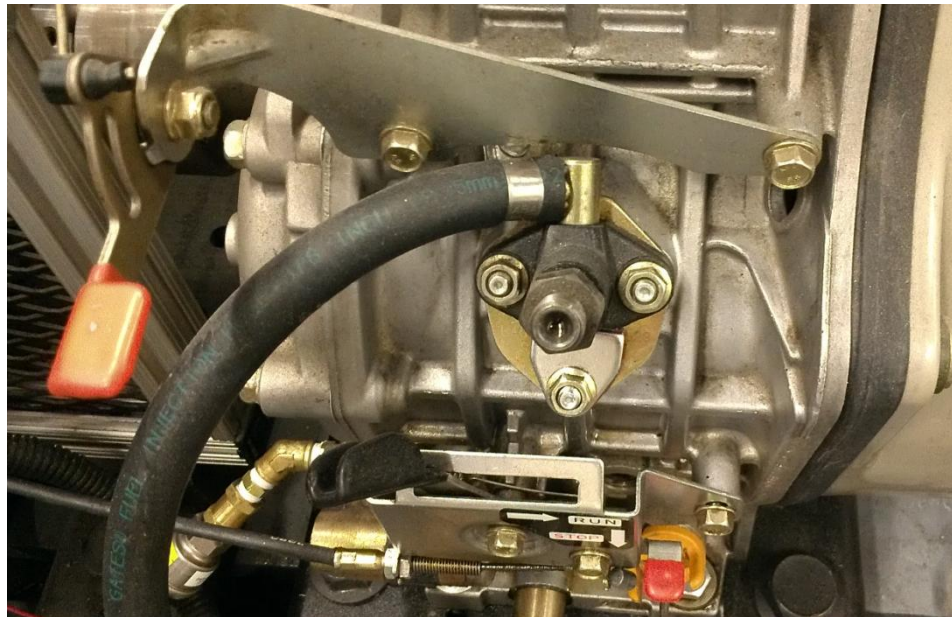


Figure 1-58. Yanmar Fuel Pump Fed by Rubber Fuel Line, High-Pressure Injection Line Removed.



Figure 1-59. Removed Yanmar Fuel Pump.

The first step in the fuel system installation is the removal of the Yanmar fuel pump and fuel system. In Figure 1-58, the injector line is removed from the Yanmar fuel pump. After removal of the fuel lines from the Yanmar fuel pump, removal of the actual pump requires loosening of the pump mounting studs, visible in Figure 1-58. The fuel pump then slides out of the engine block and its internal components can be seen in Figure 1-59.

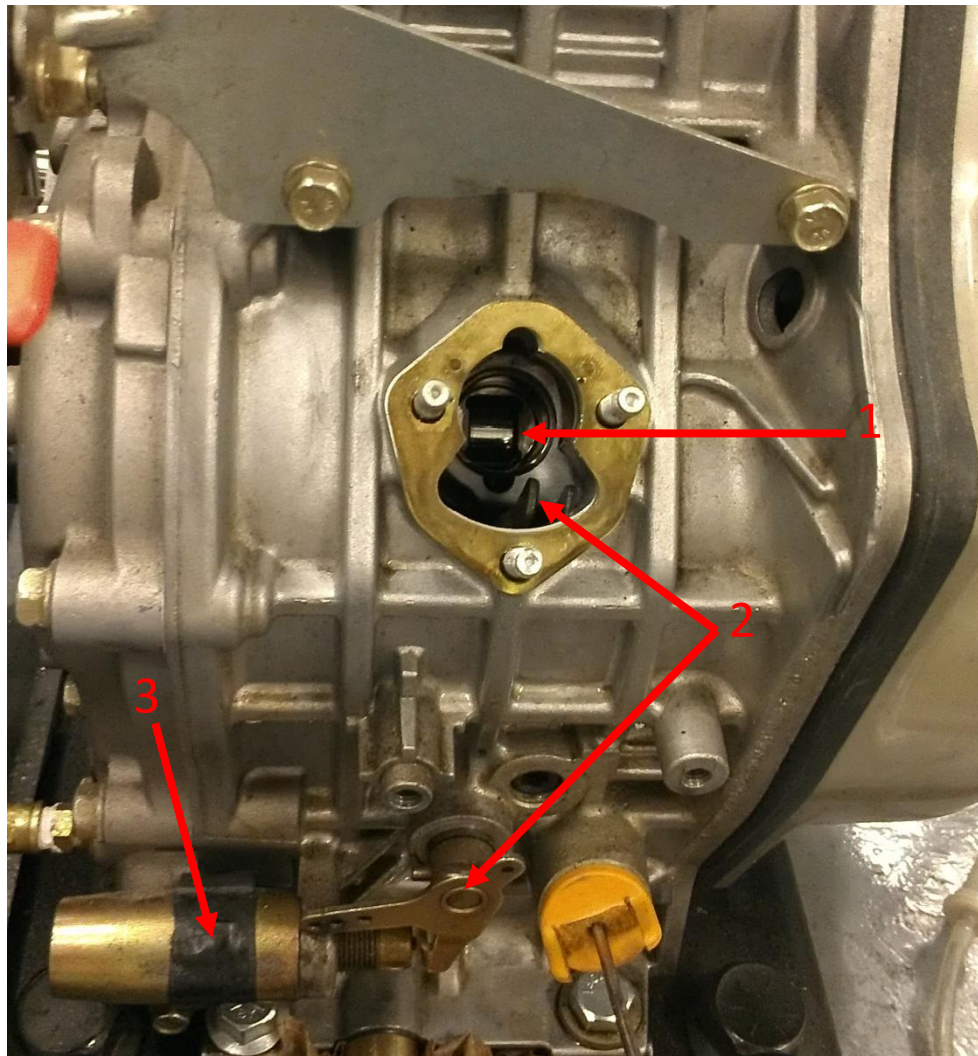


Figure 1-60. Internal Camshaft to Control Injection Timing of Yanmar Pump (1), Fuel Quantity Control Lever (2), Over-Speed Safety Mechanism (3).

Of interest, a camshaft (Figure 1-60), spins inside the engine to provide consistent injection timing. This camshaft presses upwards against the roller and spring of the Yanmar pump, actuating an internal plunger that pressurizes the fuel. Injection amount is controlled via a lever (also shown in Figure 1-60) that moves from side-to-side based on fuel input needs. A safety mechanism prevents engine over-speed.

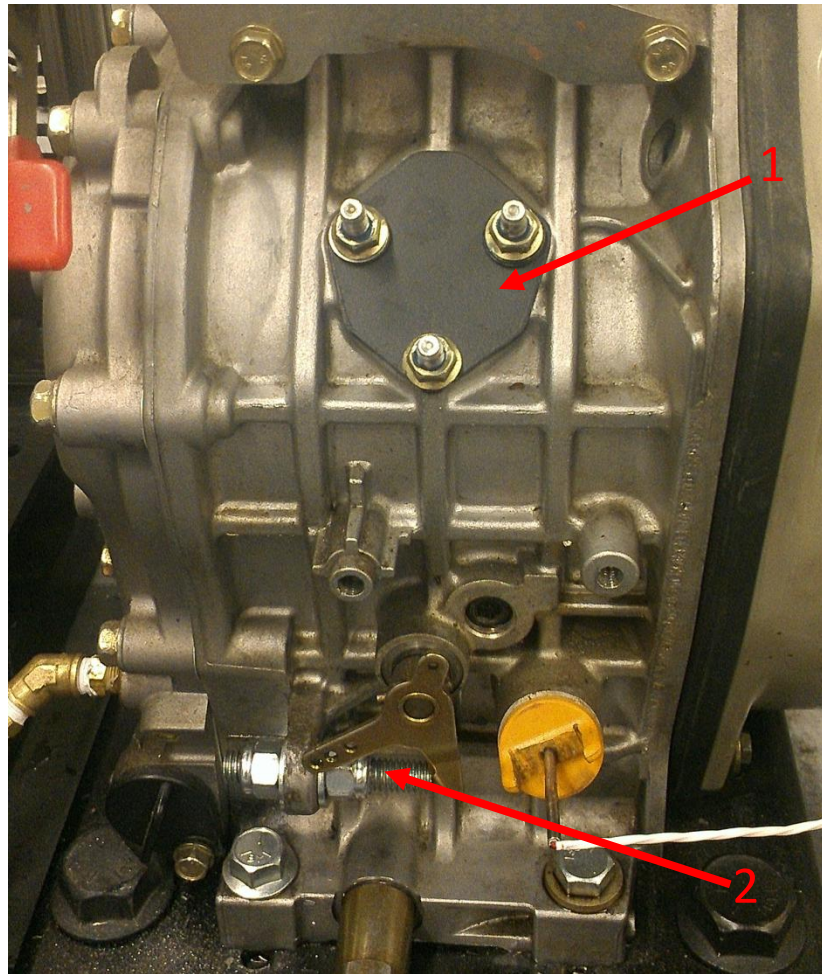


Figure 1-61. Yanmar Fuel Pump Removed with Cover Plate Installed (1). Yanmar Fuel Quantity Control Lever Locked in Place (2).

In its current state (Figure 1-61), the Yanmar fuel pump is removed and a plate is used to seal the engine block. Rather than use the brass gasket utilized by the Yanmar pump, high-temperature gasket sealant is utilized to form a good seal in order to prevent oil contamination and leakage. Additionally, the safety mechanism is no longer needed (over-speed protection now occurs via the dynamometer and ECU programming). Finally, the fuel quantity control lever is held in place via a bolt installed in the boss formerly used to hold the over-speed control mechanism. This prevents the control lever from moving during tests.

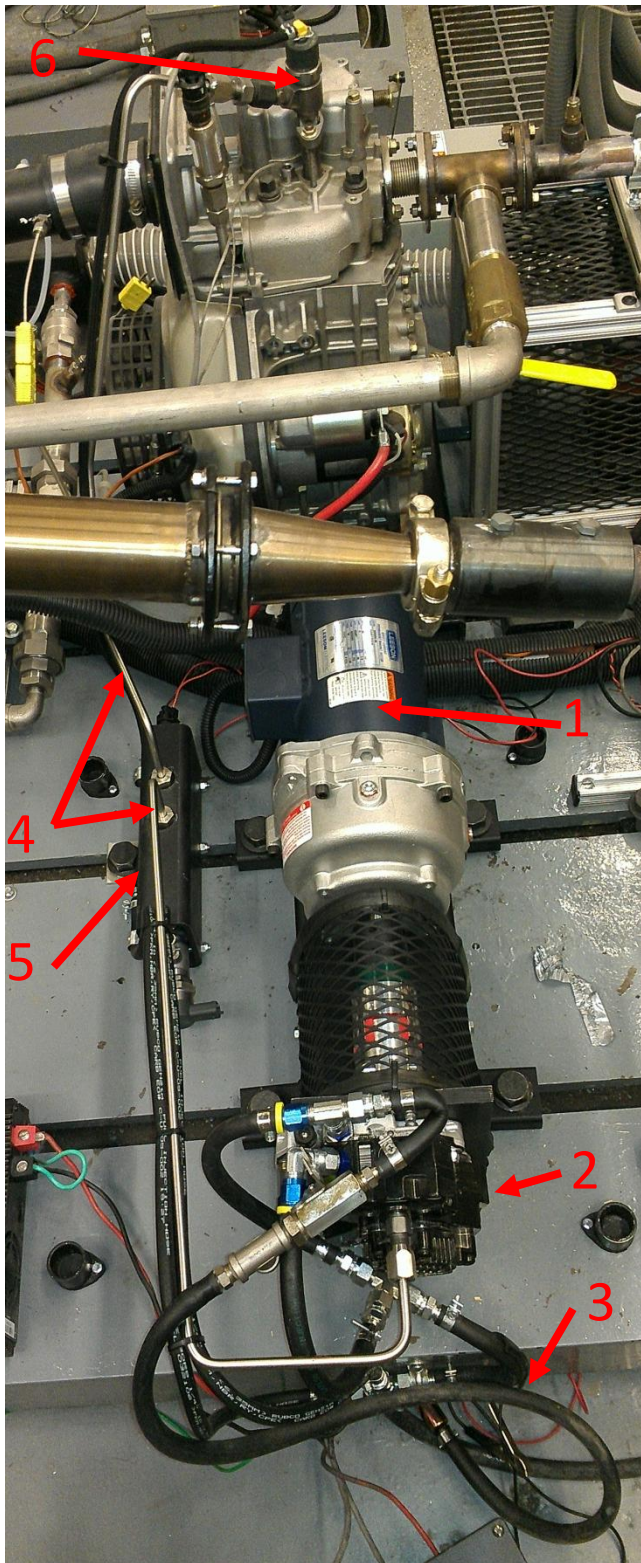


Figure 1-62. Electric Motor (1), High-Pressure CP3 Fuel Pump (2), Low-Pressure Fuel Line (3), High-Pressure Fuel Line (4), Fuel Rail (with Sensor and Solenoid) (5), and Injector (6).

The new fuel system is composed of a high-pressure pump, fuel pressure sensor, fuel pressure control valve, and DC drive motor. The components, including the high-pressure fuel line and injector, are shown installed in Figure 1-62. The necessary shaft output speed was determined by observing bench test videos of the CP3 pump that was rotated at a speed of 150 RPM . The $\frac{1}{2}$ -horsepower motor selected (Leeson model # 108014) does not have the power to spin the pump in a direct-drive configuration; therefore, a speed reducer with a 7.6:1 ratio was used to increase the torque of the motor while maintaining the ability to spin at, or above, 150 RPM. Testing indicates that the pump effectively pressurizes fuel at 100 RPM; hence, this speed setting is used to reduce mechanical wear.

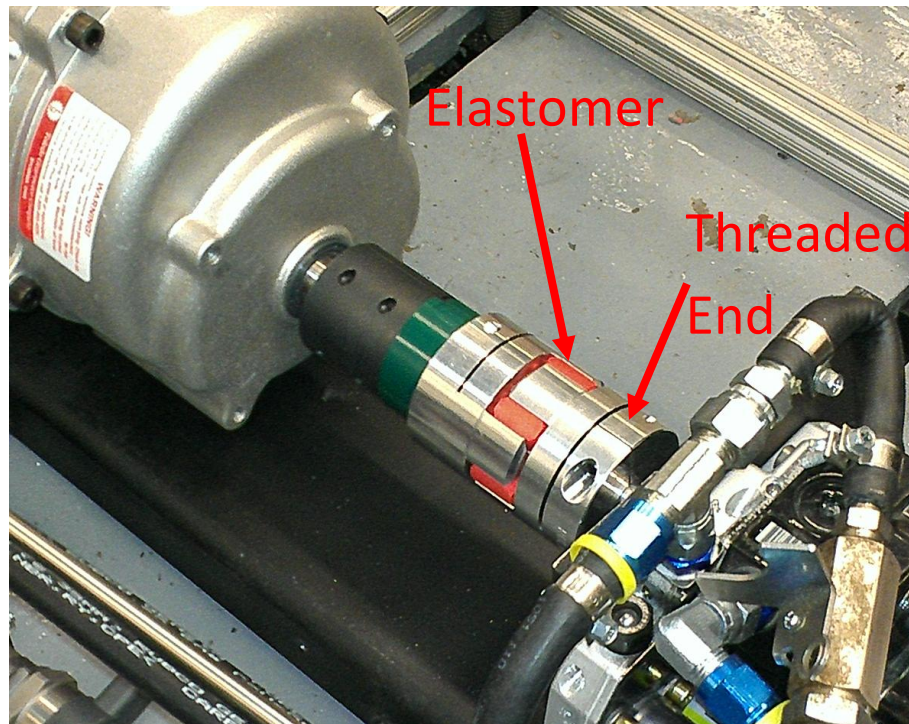


Figure 1-63. Coupler between Drive Motor and Fuel Pump.

A coupler, shown in Figure 1-63, was modified by the KU Machine Shop to screw onto the threaded pump shaft and attaches the electric motor to the high-pressure fuel pump. This coupler utilizes a flexible elastomer insert, allowing for slight misalignment and vibration and is fixed on either end by using clamping jaws.

1.6.4 Controlling High-Pressure Fuel Pump Speed and Injection Pressure

An Alternating-Current (AC) to DC motor controller is used to regulate the amount of electrical power sent to the motor, thus controlling the speed of the motor and fuel pump. This controller receives power directly from a 110 VAC wall outlet, but first travels through an 8-amp fuse and a solid-state AC relay.

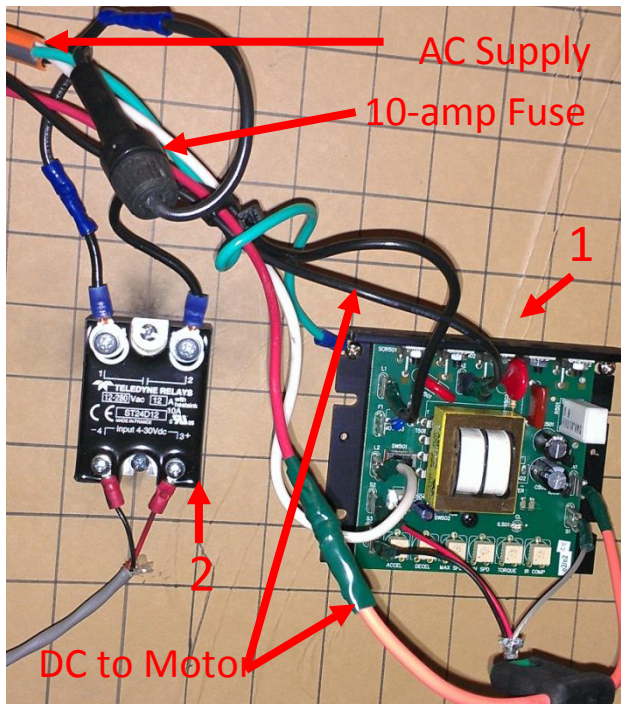


Figure 1-64. DC Motor Controller (1) and DC-controlled AC Relay Activated by Main LabVIEW Program (2).

The relay, shown with the motor controller in Figure 1-64, is activated using a 5 VDC signal from LabVIEW. The control of the motor (via relay) on the main operating window is shown in Figure 1-65.

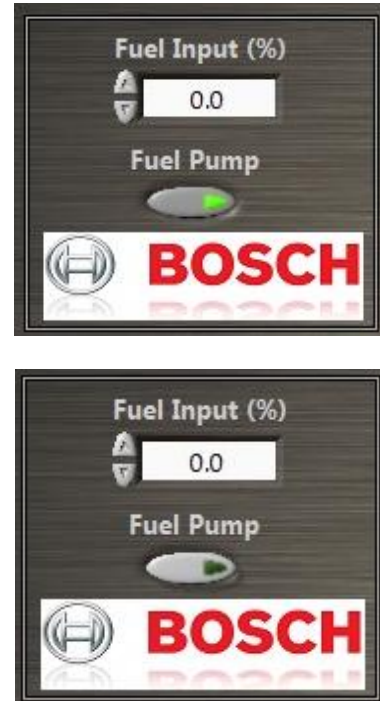


Figure 1-65. Control of High-Pressure Pump, ON (Top) OFF (Bottom).

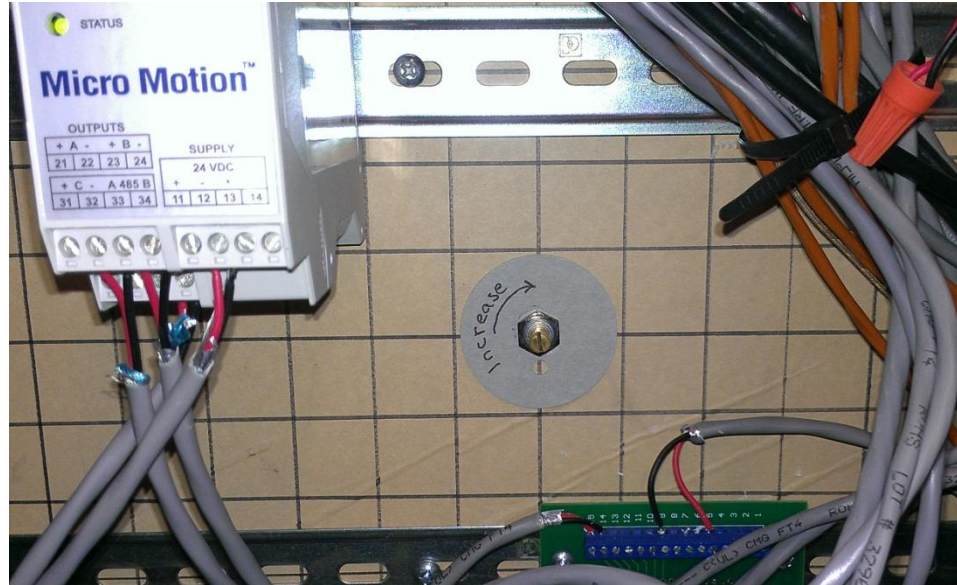


Figure 1-66. Potentiometer to Control Drive Motor and Pump Speed.

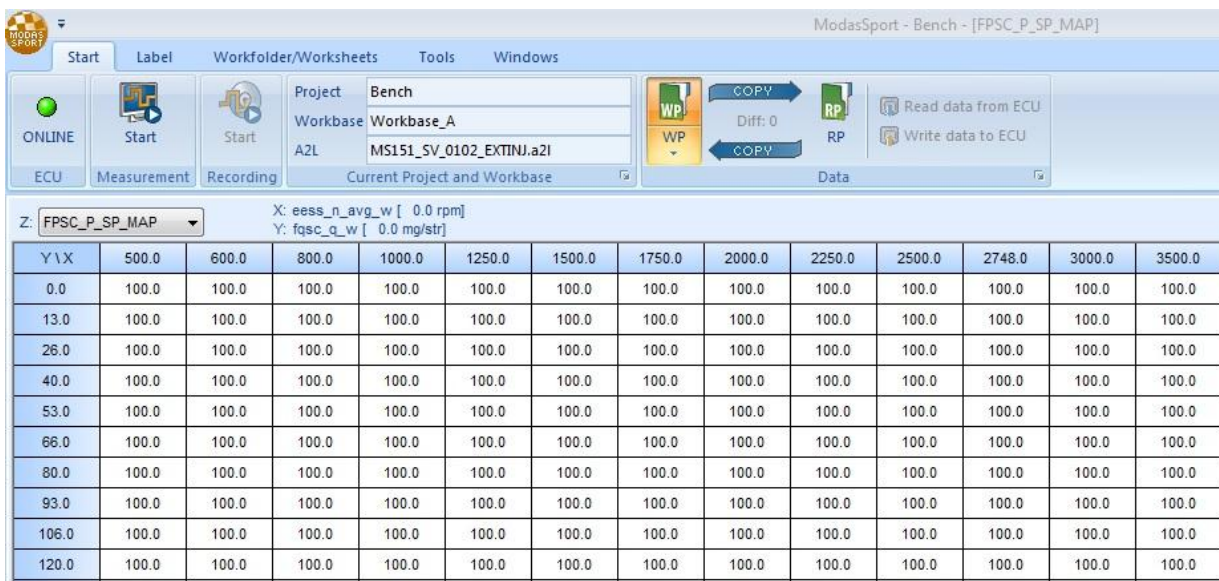


Figure 1-67. Screenshot of Modas Sport, Adjustment of Rail Pressure.

Speed is controlled via a potentiometer mounted in the instrumentation cabinet (Figure 1-66).

Initial speed is set to 100RPM via a laser tachometer, and can be adjusted using this control. Rail pressure is set using Modas Sport by making adjustments to the map named 'FPSC_P_SP_MAP'. The maximum pressure, set via the variable 'FPSC_P_MAX_CUR', is 200 MPa. For testing, it is desired that the fuel rail pressure remain constant, rather than be dictated by engine speed and load. Therefore, the

pressure for the entire map is initially set to 100 MPa, as shown in Figure 1-67. Changes made to the rail pressure map can then be saved to the configuration file and uploaded to the ECU. The pressure is controlled by the ECU using the rail pressure control valve.

eess_n_avg_w	1806.0	rpm
eess_s_meta_uc	all OK	-
fqsc_q_w	0.0	mg/str
dini_dt_mi_w	0	us
eapp_pv_w	0.000	%
bimi_phi_w	12.00	deg cr
efps_u_adc1_w	2977	mV
1 fpss_p_w	100.0	MPa
2 efps_p_w	111.4	MPa
fqsc_q_llim_w	0.0	mg/str
lico_s_preconten_b	1	-
lico_s_preconton_b	0	-
fqsc_q_driver_w	0.0	mg/str
fqsc_q_sp_w	0.0	mg/str
fqsc_s_uc	Driver	-

Figure 1-68. Screenshot of Modas Sport, Monitoring Rail Pressure Setpoint (1) and Measured Pressure (2).

Finally, Figure 1-68 shows the rail pressure setpoint and actual rail pressure being monitored by the variables ‘fpss_p_w’ and ‘efps_p_filt_w’, respectively.

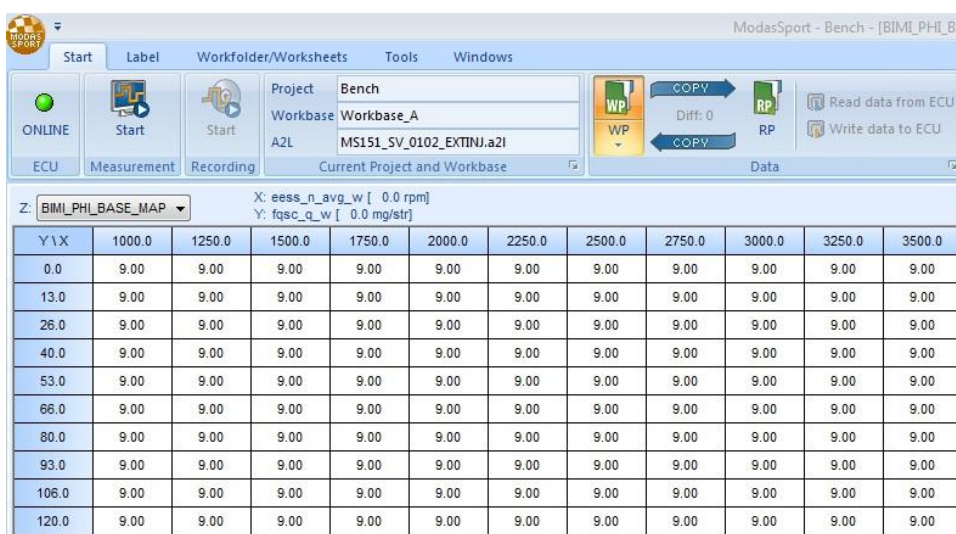


Figure 1-69. Adjustment of Beginning of Injection Angle Map in Modas Sport.

Injection timing can be adjusted via changes to the map ‘BIMI_PHI_BASE_MAP’, as shown in Figure 1-69. This map is dependent on engine speed and injection quantity. Injection amount is changed via the main LabVIEW operating screen that simulated driver demand accelerator pedal position (a.k.a. driver demand). The voltage output (0-5 VDC) is scaled from 0-100% of a preset fuel limit within the ECU configuration file. These fuel limits, called torque limit and smoke limit, are selected based on engine operating conditions. Torque limit is the only limit used in the current application and is intended to prevent mechanical damage to the engine by limiting the amount of fuel that may be injected. The torque limit map (FLIM_Q_TLIM-GMP) can be adjusted to change these limits. Smoke limiting is for certain operating conditions where the air flow rate of the engine creates an opportunity for high production of PM. In the event of low air flow rate, this limit cuts the amount of fuel injected to prevent high PM emissions and is adjusted using the map ‘FLIM_Q_SMOKE_MAP’. For example, if a torque limit of 100 mg/str is applicable at the given conditions, 50% driver demand (sent by LabVIEW) results in 50 mg/str to be injected.

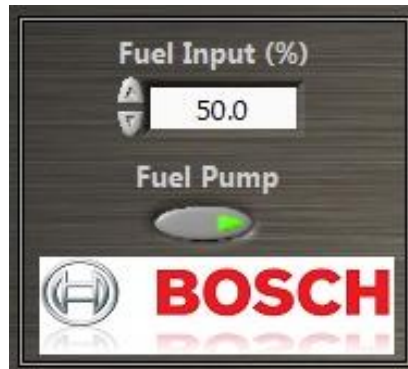


Figure 1-70. Control of Fuel Injection Quantity via LabVIEW Main Program.

Driver demand is modulated using the numerical control box of the main operating window shown in Figure 1-70. This dialog box allows the operator to have control down to 0.1% of engine output power and can dynamically change engine loading. Subsequently, the dynamometer running in speed mode automatically adjusts its voltage in order to maintain the desired test speed.

1.7 System Validation

Initial attempts at running the engine by gradually increasing the injection amount to generate power were hindered by air bubbles in the high-pressure fuel system. Per the suggestion of Bosch engineers, this issue was remedied by setting the rail pressure to 30 MPa (very low for this system), then fuel injection quantity was slowly increased until combustion became apparent via the in-cylinder monitoring system and the dynamometer torque measurement became less negative (i.e., engine starts making power and starts offsetting mechanical friction). Then, the injection pressure was gradually raised to the desired rail pressure of 100 MPa. This value was chosen as it represented half of the full injection pressure of the system. Initial testing was successful and engine loading occurred up to 3 N·m (approximately 20% of rated torque at 1800 RPM).

The next step was to perform an injection-timing sweep at 1800 RPM. The goal of this experiment was to use the in-house cylinder pressure monitoring system and heat release analysis to tune the engine for maximum fuel efficiency at any load based on the timing of peak cylinder pressure and burned fuel quantity. The heat release analysis uses post-processed cylinder pressure to determine ignition delay, start of combustion, heat release (energy release) behavior, and cylinder temperature using the first law of thermodynamics and the ideal gas law [40]. The first part of this process was to verify that the engine can run at its rated torque (18 N·m) at 1800 RPM with combustion timing peak pressures similar to previous conditions (~10° after TDC).

During initial experiments, as the fuel injection quantity was increased and power output grew, the cylinder peak pressure began to exceed the maximum pressure measured during previous tests with the old injection system (approximately 65 bar). As a result, testing was stopped short of the desired 18 N·m of torque. By observing the in-cylinder pressure trace, it was noticed that the rise in pressure was nearly vertical. This is a result of the injection system working exactly as it is designed. The atomization

of the fuel was so effective that more fuel ignites at once (i.e., a high-level of pre-mixed burn) leading to this high-pressure spike.

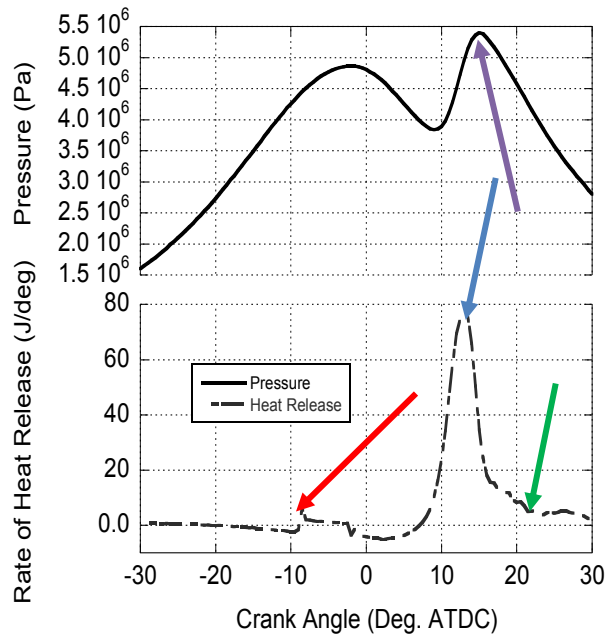


Figure 1-71. Cylinder Pressure and Heat Release Rate at 9 N-m. Injection Timing at -9° After TDC Verified by Heat Release Rate (Red Arrow). Premixed and Diffusion Burn Combustion Phases (Blue and Green Arrows, Respectively).

To reduce the effectiveness of the injector, the rail pressure was reduced to 60 MPa in order to diminish the level of fuel atomization and promote the diffusion burn phase. Figure 1-71 provides the results at half-load (9 N-m of torque) and demonstrates the data recording capabilities of all systems. Peak combustion pressures (purple arrow) at higher loads were still greater than most of the past tests performed with this engine. As a result, injection pressure was further reduced to 45 MPa, this injection pressure was found to be a suitable level for all engine speeds. Finally, injection timing is verified by observing the rise in heat release that occurs at the desired 9° before TDC, as set for this condition using the ECU.

1.7.1 Engine Calibration

Following the successful demonstration of the high-pressure injection system, a complete engine calibration was performed in order to replicate manufacturer's power specifications for the engine. The initial speed chosen for calibration was 1800 RPM. This speed will be used for the majority of future tests due to its central location in the operating speed regime of this engine. At 1800 RPM, a sweep of injection timing is performed while injection amount is changed to maintain constant power output in an effort to find the maximum brake torque (MBT) timing. This timing indicates the required power output with minimal fuel quantity[1, 40].

Due to changes in the combustion process (pre-mixed vs. diffusion burn) at different loads, five torque points are selected to map the MBT timing at 1800 RPM. They are 0.5, 4.5, 9.0, 13.5, and 18.0 N-m. The 0.5 N-m level is defined as the 'unloaded' condition in order to produce more stable results and comparable values for brake-specific fuel consumption (BSFC) and emissions data as found via a previous effort [12]. As mentioned prior, the 18.0 N-m condition corresponds to the rated torque as stated by Yanmar. Intermediate loadings occur at 25%, 50%, and 75% of rated torque at this speed. Injection timing is selected during operation by observing engine fuel flow rates and cylinder pressure behavior as the timing is changed. If the injection timing is ahead of MBT timing, the fuel flow rate increases, just as flow increases if timing is behind MBT timing. At each injection timing, the engine was allowed to reach steady state, as determined by exhaust temperature changing by less than one percent over a minute. Then, performance and emissions data are recorded for two-minutes at rates of 20 Hz and 1 Hz, respectively. Concurrent to the collection of this data, cylinder pressures for 120 engine cycles (60 thermodynamic cycles) are recorded at a resolution of 0.5 degrees of engine crank angle.

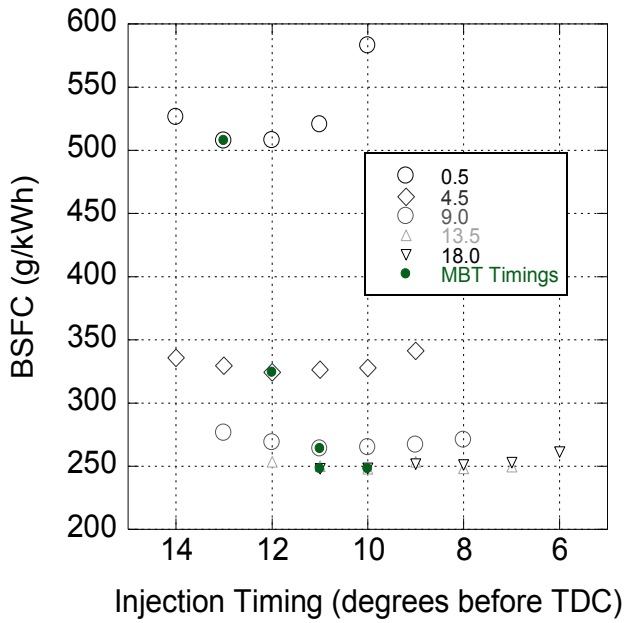
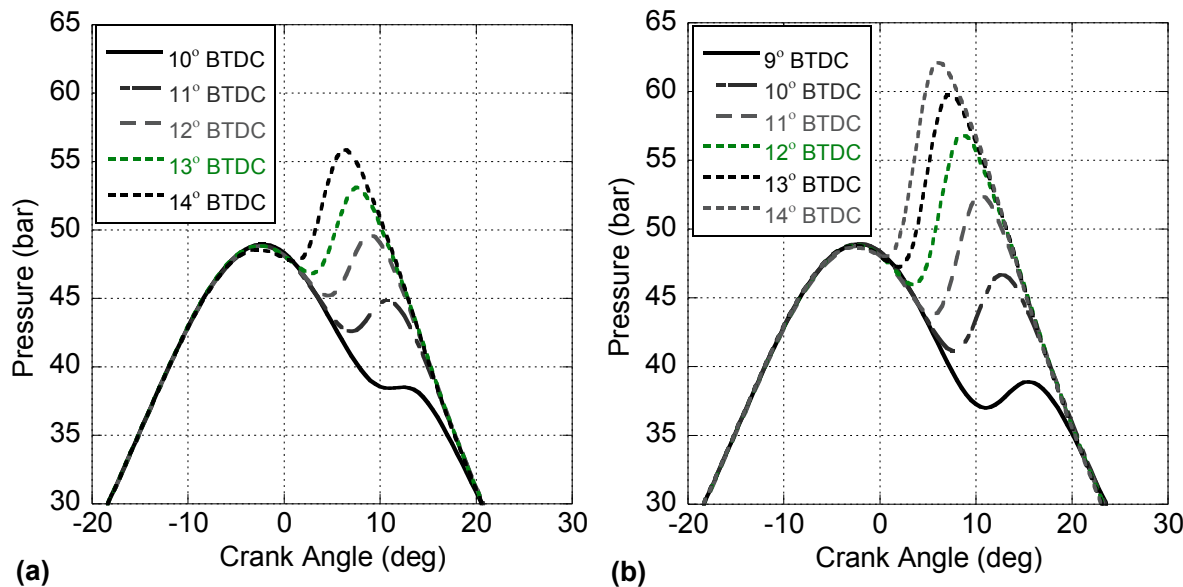


Figure 1-72. BSFC vs. Injection Timing at All Loadings. Minimum BSFC at a Given Load Indicates MBT Timing.

The results for BSFC as a function of engine load and injection timing are shown in Figure 1-72.

These results clearly indicate expected trends in fuel consumption as a function of injection timing. Specifically, a local minimum in consumption exists where the transfer of fuel energy to pressure upon the piston is most effective.



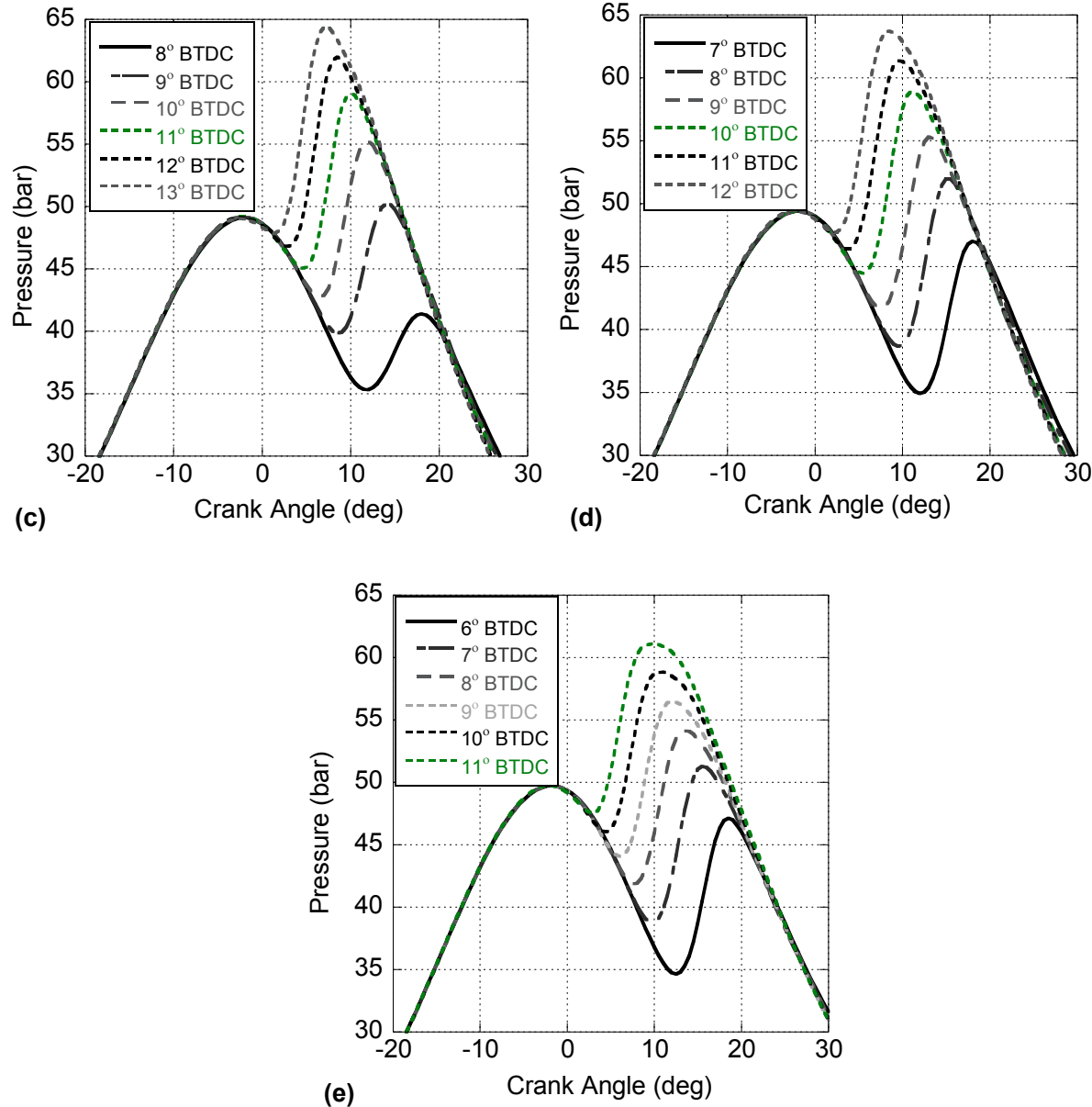


Figure 1-73. Cylinder Pressure vs. Engine Crank Angle for (a) 0.5 N·m, (b) 4.5 N·m, (c) 9.0 N·m, (d) 13.5 N·m, and (e) 18.0 N·m. MBT Timing Traces are Shown in Green.

Cylinder pressure data from the calibration of the engine at 1800 RPM is shown in Figure 1-73 with MBT timing data shown in green (timings in degrees before TDC (BTDC)). Combustion before MBT conditions will reach higher cylinder pressures, but will not produce as effective of a force on the piston due to the nearly vertical orientation of the piston connecting rod (i.e., piston moving slowly and producing little expansion work). Combustion that occurs after MBT timing occurs in a cylinder that is

rapidly expanding, resulting in a relatively cooler combustion process (i.e., lower pressures) and reduced time for expansion work before the exhaust valve opens.

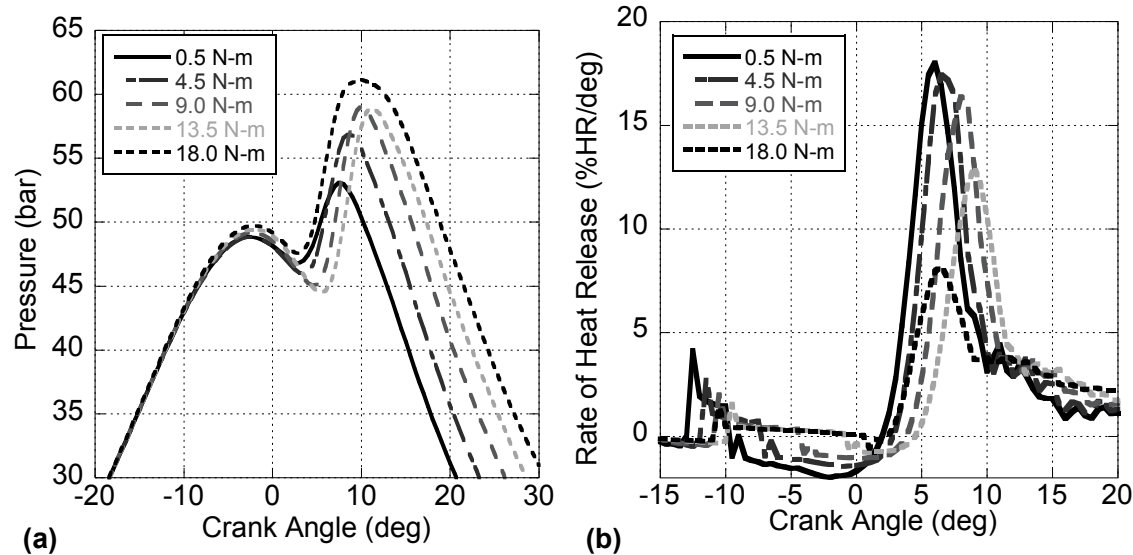


Figure 1-74. Cylinder Pressure vs. Engine Crank Angle (a) and Adjusted Heat Release Rate at MBT Timings (b) for All Tested Loads.

The recorded cylinder pressures and accompanying Adjusted heat release rate analysis for all loads at MBT timing are shown in Figure 1-74. The combined data illustrates the relative behavior of combustion as load increases. For instance, the effects of cylinder conditions (pressure and temperature) on ignition delay (approximately the time from injection to where heat release rate becomes positive) are apparent in the heat release results as the timing from the start of injection to the start of combustion decreases as loading increases. Furthermore, the relative amounts of premixed and diffusion burn phases during each combustion event can be seen. As load increases, the peak rate decreases as higher levels of combustion happens via the diffusion burn phase.

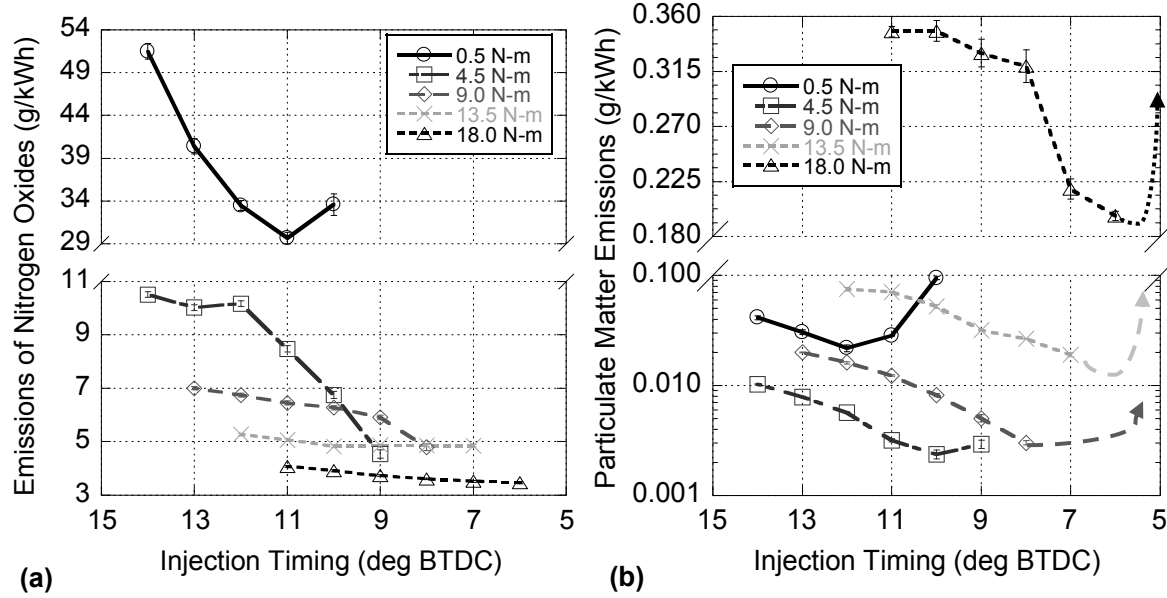


Figure 1-75. NO_x Emissions (a) and PM Emissions (b) vs. Injection Timing at All Tested Loads. PM Production Expected to Increase at Injection Timings Later than Those Indicated.

In addition to BSFC and cylinder pressure measurement, the effect of injection timing on the NO_x-PM tradeoff is investigated via Figure 1-75. It is expected that advancing combustion should lead to more complete oxidation of the fuel (less PM) and the subsequent higher cylinder temperatures leads to increased NO_x as a result of the thermal NO mechanism [1, 16, 19, 20]. However, advancing combustion results in both increased PM and NO_x emissions. To explain, injection at the start of the sweep (11 degrees before TDC or earlier) results in combustion that occurs ahead of optimum timing; thus, more fuel must be added to the cylinder to generate the same amount of output power. Therefore, there is more carbon available to generate PM. As injection timing is delayed, the engine approaches optimum fuel consumption timing. Thus, less fuel enters the cylinder and less PM is created. However, when injection timing is delayed further so that combustion begins later than optimum conditions, the PM results show a continued reduction. As more fuel is being injected (no longer at adjusted timing), an increase in diffusion burn and PM generation should occur due to more fuel, cooler combustion, and a reduced premixed burn phase[1]. However, this behavior does not occur immediately. For this reason, Figure 1-75(b) also indicates the expected PM behavior with even later injection timing using arrows to

show the anticipated increase that should eventually occur. It is postulated that a continued reduction in PM following adjusted timing occurs because the replacement of premixed combustion with diffusion burn does not occur at the same rates.

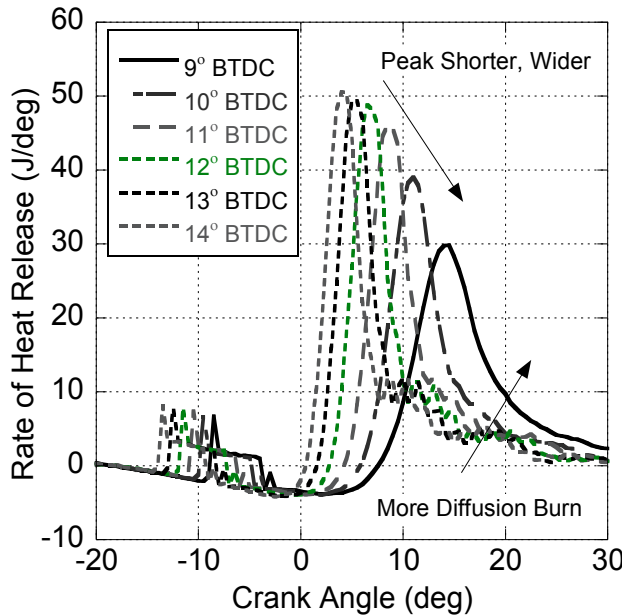


Figure 1-76. Heat Release Rate vs. Engine Crank Angle for 4.5 N·m Load Injection Timing Sweep.

An example of this phenomenon is observed in the heat release rate results for the injection sweep performed at 4.5 N·m, where PM production is just beginning to increase the latest injection timing, as shown in Figure 1-76. These results demonstrate that as injection timing is delayed, the ignition delay becomes longer with the peak heat release rate diminishing. This causes a corresponding reduction in NO_x production due to lower combustion temperatures[40]. This lowering is due, in part, to a decrease in fuel injection as the engine efficiency improves, thus less PM is produced as injection is delayed (before MBT timing)[40]. As timing is delayed further behind MBT timing, the decreasing premixed burn phase and rising diffusion burn produces a less pronounced boundary between these phases of combustion. In this condition, PM formation is reduced due to a hot oxygen-rich (for low loads) combustion environment[40]. Finally, as injection timing becomes even later (e.g. 9 degrees before TDC), engine efficiency drops due to reduced premixed burn and additional diffusion burn. This

combustion event is less efficient and therefore requires more fuel (potential PM) to produce necessary power[40].

Combustion efficiency serves as a means of quantifying how well the combustion process is removing energy from the incoming fuel flow and is found using (1-2) [1]. It is based on the heating value of fuel and the exhaust constituents, such as CO, HC and PM, which contain unused energy. Here, the lower heating values of HC and PM are assumed to be 44,700 kJ/kg and 32,810 kJ/kg, respectively [19, 20, 38, 39]:

$$\eta_c = 1 - \frac{\sum_{j=1}^n \dot{m}_j \cdot Q_{lhv,j}}{\dot{m}_f \cdot Q_{lhv,f}} \quad (1-2)$$

where η_c is combustion efficiency, \dot{m}_j is exhaust constituent mass flow rate, \dot{m}_f is fuel mass flow rate, and $Q_{lhv,j}$ is fuel lower heating value. The quantity of hydrogen is not measureable with the emissions analyzers used (presented in a later chapter); however, due to its considerable lower heating value (120,000 kJ/kg), it must be included for a proper analysis. Therefore, an estimate for hydrogen emissions is made assuming a similar molar ratio of H₂:CO as that of H₂O:CO₂. This assumption is based on the general lean combustion reaction and the typical product species of H₂O and CO₂ [19, 20, 46].

In addition, fuel conversion efficiency (η_f) is a measure of the efficiency of useful work coming from added fuel energy [1, 20, 46]:

$$\eta_f = \frac{P_{engine}}{\dot{m}_f \cdot Q_{lhv,f}} \quad (1-3)$$

Finally, the thermal conversion efficiency (η_t) is an indicator of how effectively fuel is creating actual work and is a combination of the combustion and fuel conversion efficiencies, related by [1, 20, 46]:

$$\eta_t = \frac{\eta_f}{\eta_c} \quad (1-4)$$

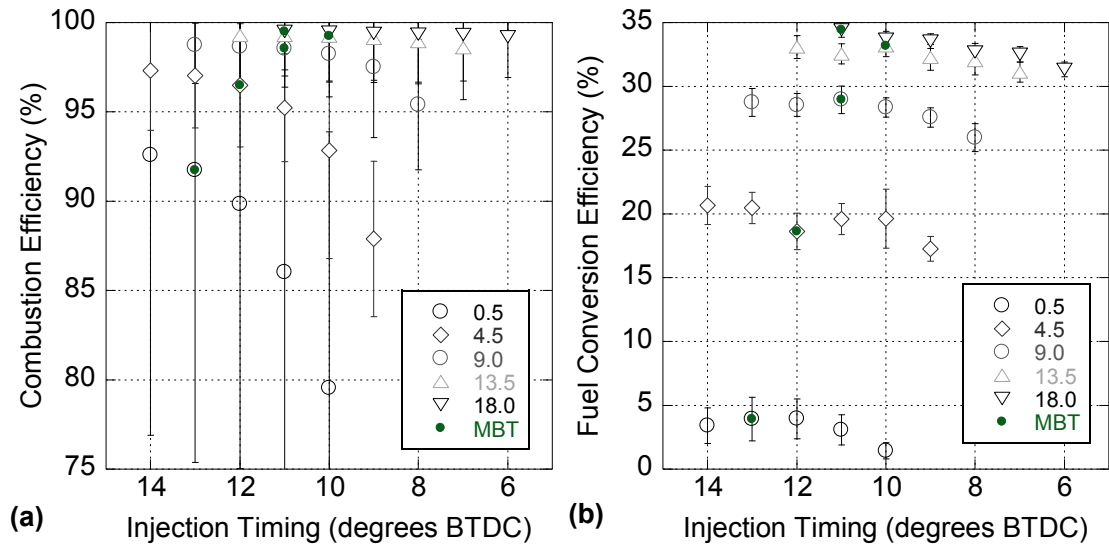


Figure 1-77. Combustion Efficiency (a) and Fuel Conversion Efficiency (b) vs. Injection Timing for All Loads.

The results for combustion efficiency and fuel conversion efficiency for each load's injection sweep are shown in Figure 1-77. These results indicate that as injection timing is advanced, combustion efficiency increases. This is because of a combination of higher cylinder pressures (and temperatures) and longer combustion duration before the exhaust valve opens. It is important to note that the final MBT timings actually correspond to the highest fuel conversion efficiency (with the exception of 4.5 N·m loading). The 4.5 N·m injection sweep represents an anomaly in the observed trends. Final determination of MBT timing was accomplished using post-processed cylinder pressure and heat release results[40], thus this discrepancy is likely caused by uncertainty in fuel measurement or torque at this load. The different efficiency peak location between combustion efficiency and fuel conversion efficiency is due to the geometry of the piston connecting rod. If the piston is too close to TDC when combustion occurs, the energy released does not produce useful work as effectively because the piston is moving slowly and producing little expansion work. Instead this energy is lost through heat transfer to the cylinder walls [40]. At later timings, it is easier for combustion pressure to produce useful piston work as the connecting rod generates rotation through the crankshaft.

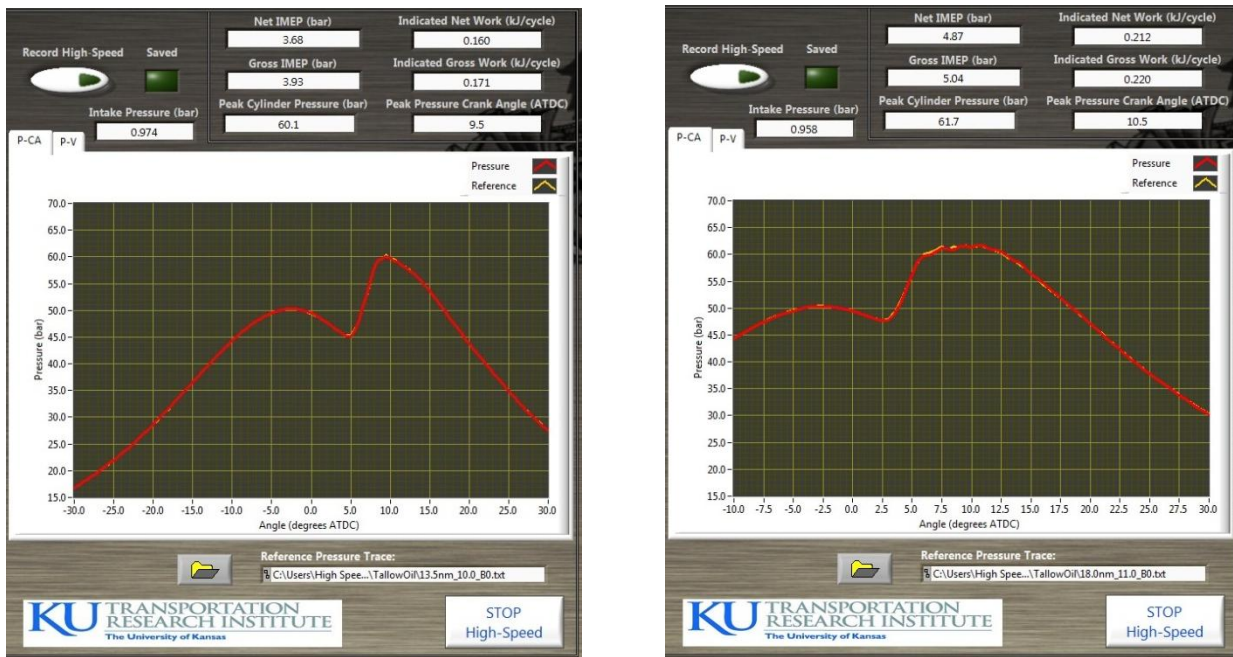


Figure 1-78. Screenshots of Adjusted Jet-Propellant (Red) and Adjusted ULSD (Yellow) Cylinder Pressure vs. Engine Crank Angle at 13.5 N·m (Left) and 18.0 N·m (Right).

The use of the calibrated MBT timings for ULSD can be used to optimize other fuels, such as biodiesel and jet-propellant, by utilizing the real-time in-cylinder pressure measurements to normalize peak cylinder pressures during operation. Figure 1-78 shows the manner in which jet-propellant was adjusted using screen shots of near real-time in-cylinder pressure measurements. The LabVIEW program, written as part of this author's master's work, can be used to load previously saved data files to be used as a 'reference' pressure profile at a later time. In the case of Figure 1-78, ULSD data from the MBT timing study is loaded as a reference profile (shown in yellow). Then, as jet-propellant is being burned in the engine, the timing of the fuel injection is manually changed to align peak pressures. This provides a rapid means of optimizing any fuel during a test. Additionally, the nearly identical behavior of the combustion process, including the small pressure waves observed during the diffusion burn at 18 N·m, demonstrates the repeatability of this system regardless of the fuel used. In this manner, researchers using this system can rapidly and repeatedly perform a variety of experiments without stopping the engine. Furthermore, constant injection timing allows for the opportunity to observe the influences of

the fuel on the start of combustion. Adjusted combustion timing (MBT timing) allows researchers to observe the effects of a fuel's chemistry on combustion without the overshadowing effects of phasing.

1.8 Conclusion

Through the compilation of various engine studies, it was found that the single-cylinder CI research engine at KU required an upgrade from mechanical to common-rail fuel injection. This improvement in fuel control was necessary to ensure comparisons to commercial engine research. Additionally, past research determined that fuel consumption and emissions, such as the NO_x-PM tradeoff, are heavily influenced by combustion phasing. As a result, direct conclusions regarding specific fuel properties and combustion behavior were not possible when using a mechanical fuel injection system. Therefore, a Bosch ECU, fuel pump, fuel rail, and injector were installed on the Yanmar engine.

Successful installation occurred via several steps. First, initial bench testing using a set of simulated engine signals allowed for direct observation of the ECU operation and signals sent to the injector. Next, components were gradually added to the engine and tested individually to ensure that complete control over each component was attained. Finally, the entire electronically-controlled fuel system was tested and validated in the engine.

System capabilities include control over engine operation and fuel injection characteristics. Specifically, the engine may be operated at any speed between 1200 and 3600 RPM. Fuel injection can occur through up to five pulses per combustion event (two pilots, two mains, and one post) and can be controlled down to 0.02° of engine crank angle. The fine adjustment capability provides the opportunity to optimize various fuels for MBT dynamically. Once a new fuel is adjusted, conclusions regarding changes in fuel consumption and exhaust emissions as a function of fuel property are more certain. Furthermore, fuel injection pressure may also be adjusted as a means of adjusting atomization subsequently influencing pre-mixed and diffusion burn behavior.

Chapter 2: Neat and Blended Biodiesel in an Adjusted Single-Cylinder CI engine with Electronically-Controlled Fuel Injection

This chapter is composed of two separate studies derived from a single set of experimentation using four biodiesel fuels, made from palm, jatropha, soybean, and beef tallow oils. These fuels present a diverse set of biodiesels when comparing fuels properties. This set of properties includes both physical properties such as density, viscosity, and energy content and chemical properties, such as molecular unsaturation and oxygen content. In the first study, these fuels are tested with ULSD in neat form. Additionally, two separate injection strategies are implemented in this study. First, the injection timing remains fixed, so that the influence of biodiesel ignition delay can be observed. The second injection strategy modulates injection timing of the biodiesel fuels in order to maintain consistent peak combustion pressure compared to ULSD, which serves as the control for this experiment. This strategy provides the opportunity to investigate the effects of fuel properties on combustion and emissions when the overshadowing effects of combustion phasing are removed.

The second study yielded from the experimental results investigates the blend ratio behavior of biodiesels and is written assuming publication of the first study. This subsequent study blends each biodiesel as a 5, 10, 20, and 50% blend with ULSD (neat values are also included in the analysis). Results are reviewed to observed linear and non-linear effects on engine combustion, performance, and exhaust emissions as a function of biodiesel blend percentage. As with the first study, two injection timing studies are performed in the experiment. However, the first biodiesel study indicated that aligning combustion phasing for all fuels proves a more direct comparison of fuel properties on engine behavior. Therefore, only this data is used for the second study. All data not used explicitly in the two studies are available in the appendix of this dissertation.

Study 1: Comparison of Neat Biodiesels and ULSD in a Single-Cylinder Diesel Engine with Electronically-Controlled Fuel Injection

2.1 Abstract

Biodiesel can be produced from a variety of feedstock oils and, as a result, may have a diverse set of properties based on the oil used to produce it. An understanding of the effects of these properties on engine usage and emissions is needed in order to improve biodiesel production and engine calibration. In this study, four biodiesels, produced from palm, jatropha, soybean, and beef tallow oil, are used to fuel a single-cylinder compression-ignition engine to investigate the effects of individual fuel properties on combustion phasing and behavior and exhaust emissions. This engine uses a common-rail fuel system with electronic control. Electronic control of injection is used to investigate the effects of biodiesel on combustion when combustion phasing is adjusted. Findings indicate that fuel viscosity, energy content, and molecular structure are all critical properties that alter engine combustion behavior.

2.2 Introduction

In an effort to offset the use of petroleum-based diesel fuels, numerous researchers are investigating biodiesel as a renewable fuel for compression-ignition engines [42, 47-56]. This fuel, a combination of mono-alkyl esters of long-chained fatty acids derived from various feedstock oils, is intended to seamlessly integrate into the ultra-low-sulfur diesel (ULSD) infrastructure[50, 56] while maintaining low emissions as required by legislation[10, 57]. In addition to its derivation from sustainable sources, biodiesel carries other intrinsic benefits. Specifically, it has enhanced lubrication properties, a higher cetane number, and is miscible with ULSD for blending applications[51, 53, 56]. However, biodiesel is also an oxygenated fuel, which carries both positive and negative implications for engine operation[42, 56]. For example, while a higher adiabatic flame temperature promotes more complete combustion[1], the reduced energy content of the fuel increases fuel consumption[56].

Furthermore, the typically higher density of biodiesel is found to result in earlier injection for mechanical pump-line-nozzle fuel systems which, when combined with a higher cetane number, promotes advanced combustion timing. This leads to higher cylinder pressures and temperatures and a potential increase of up to ten percent of nitrogen oxides (NO_x) emissions[42, 47, 52, 55, 56, 58]. In addition to thermal NO_x , different compounds and the presence of oxygen in the fuel-rich combustion zones during the injection process alter NO behavior via the Fenimore mechanism (prompt NO) [59] and is of particular importance at equivalence ratios above stoichiometry (near injector) where production of hydrocarbon radicals promote NO production [60]. Specifically, Park et al. found that oxygenated fuel (e.g., biodiesel) reduces prompt NO production because the equivalence ratio is lower [61].

At the same time, the increase in cylinder temperature will typically result in more complete conversion of the fuel and reductions in emissions of carbon monoxide (CO), unburned hydrocarbons (HC) and particulate matter (PM) [1, 56]. This is because the region around the injector nozzle has a leaner mixture that allows the fuel to combust more readily subsequently resulting in fewer rich fuel zones within the cylinder[1]. Complicating this analysis, however, is the increased viscosity of biodiesel fuels, which can adversely affect the injection process through a reduced atomization as compared to ULSD [1, 51, 62, 63].

Multiple previous studies have found that the molecular structure of specific biodiesel fuels also plays a role in combustion performance and emissions [42, 47-50, 56, 64]. In particular, if the biodiesel is composed of predominantly unsaturated (i.e., contain carbon-carbon double bonds) fatty acid methyl esters, the oxidation process releases more energy than a biodiesel with lower unsaturation levels[17, 56]. In previous work by the current authors[56], increased content of unsaturated molecules was associated with both increased NO_x emissions and improved fuel consumption. This association was particularly strong when a greater proportion of poly-unsaturated FAMEs (multiple double or triple bonds) were present. Further conclusions about the reasons behind this relationship could not be

drawn from that study due to a lack of in-cylinder measurements to fully characterize the combustion process. Furthermore, subsequent research with the particular engine tested indicate that its mechanical fuel injection system was subject to injection variability based on fuel density, with biodiesel fuels injected up to two and a half degrees earlier than ULSD[65].

Since the earlier work by Cecrle et al., there has been further research performed in this area. For instance, Fattah et al. published a thorough review of biodiesel that discusses the current state of biodiesel research[66]. They discuss the benefits of biodiesel on agriculture, energy security, and regional economic development. Furthermore, their research on individual feedstocks, specifically, soybean, rapeseed, palm, jatropha, and cottonseed provides insight into not only the biodiesels being tested, but also the testing strategies employed by other researchers[66]. Another review by Atabani et al. discusses the increased global production and area-dependent biodiesel sources, such as jatropha, palm, and soybean, among many others [8]. Their work indicates that a thorough understanding of the influence of fuel properties on compression-ignition combustion behavior is needed due to different biodiesel source oils.

Recently, Westbrook published a review of the current state and direction of biofuel production and research[67]. In particular, Westbrook mentions the positive characteristics of biodiesel, namely, similar molecular size/shape and comparable performance to petroleum-based ULSD. The work by Westbrook also discusses a need to understand the nuances of biodiesel fuel composition and its influence on engine performance, such as the cetane number[67]. This understanding leads to the opportunity to genetically modify crops, such as soybeans, to promote production of feedstock oils with beneficial chemical and physical attributes[67]. Finally, Westbrook discusses the mixing of biodiesel, ULSD, and an alcohol, such as butanol or ethanol, to create a potential fuel for homogenous-charge compression-ignition engines. This type of engine requires specific fuel and control capabilities and represents a new research venue in which biodiesel research may spread[67].

As a result, an understanding of the advantages of injection modulation in engines for a variety of biodiesels is necessary. These engines should minimize fuel consumption while maintaining or reducing critical exhaust emissions, regardless of the biodiesel used. For example, efforts including variable timing are discussed by Ye and Boehman[55]. They used a common-rail fuel injection system in order to perform a study of ULSD and blends of soybean biodiesel (40%) with ULSD by varying injection pressure and injection duration independently. Their findings indicate that neither of these injection strategies are the primary factor for an observed increase in NO_x. Instead, they indicate that the dominant mechanism for NO_x production are higher local temperatures and leaner mixtures due to biodiesel oxygenation[55].

From the efforts of Cecrle et al. and others, it is uncertain if the noted outcomes of biodiesel usage (e.g., higher fuel consumption, NO_x emissions, lower PM) are a result of the effects of higher cetane number and combustion phasing, or the consequence of fuel-specific combustion behavior due to intrinsic fuel properties[56]. Therefore, this study aims to provide further insight by comparing neat biodiesel fuels with distinct physical and chemical characteristics with ULSD in a single-cylinder engine with an electronically-controlled common-rail injection system in order to more thoroughly separate the effects of combustion phasing from the other impacts of biodiesel properties on the combustion process. This is accomplished by first investigating the influence of biodiesel on combustion phasing using in-cylinder pressure measurements. Then, this effort explores combustion behavior through peak pressure timing normalization of both neat biodiesel and ULSD by utilizing a combination of electronic injection control and in-cylinder measurements. While testing, full performance and emissions data are recorded and compared to measured fuel properties through statistical regression analysis of combustion results to obtain a direct understanding of the effects of specific properties on engine behavior when combustion phasing is consistent.

2.3 Biodiesels Tested (Section Contributed to by Daniel Tabakh)

Four biodiesel feedstocks sources (soybean, jatropha, and palm oils and beef tallow) were chosen for this study to present a variety of different fuel properties considered likely to affect engine performance and emissions. All biodiesels used for this test were created in the biodiesel production laboratory at the University of Kansas. The biodiesels were produced through a transesterification process that involved mixing the oil with methanol at a 6:1 ratio for 2 hours at 60°C and 1 atmosphere with continuous stirring. Dissolved potassium hydroxide is used as a reaction catalyst. Following the reaction and gravity separation of glycerin, the biodiesel was washed three times using de-ionized water to remove methanol and impurities and then allowed to sit for 40 minutes to separate the water. Finally, the biodiesel was dried at 105 °C for 50 minutes. This process was followed for all four fuels, although the tallow oil had to be melted prior to addition to the reactor.

Table 2-1. Physical Properties and Elemental Composition of the Different Fuels Tested.

Component	ULSD	Palm	Jatropha	Soybean	Beef Tallow
Cetane Number	40	60	52	45	61
Density @ 20°C (kg/m ³)	837.58	872.63	876.81	881.25	870.98
Energy (kJ/kg)	45636	40479	39809	39798	39933
Kinematic Viscosity (cSt)	2.58	4.51	4.44	4.17	4.70
Flash Point (°C)	55.8	184.8	175.0	164.9	169.0
Oxygen Content (% wt.)	0.0*	10.17±0.29	9.97±0.23	9.92±0.06	10.20±0.31
Carbon Content (% wt.)	86.34±0.20	76.57±0.13	77.00±0.07	77.22±0.04	76.56±0.05
Hydrogen Content (% wt.)	14.27±0.10	13.27±0.16	13.04±0.16	12.87±0.03	13.24±0.35

Following production, each fuel was analyzed to determine significant physical and chemical properties (Table 1). Measurements available in the production laboratory are energy content, viscosity, density, and flash point, the results of which are shown in Table 2-1. Energy content was determined via ASTM standard D240 with a 6200 PAAR calorimeter using 600 mg samples. ASTM D445 was used to determine viscosity via a Koehler KV4000 Series Digital Constant Temperature Kinematic Viscosity Bath (KV4000). For density, ASTM D4052 is used with an Anton Paar Density Meter Analyzer

5000 M model. Flash Point was found using ASTM Standard D93 and a Pensky-Martens closed up FP93 5G2 from ISL by PAC. Since the direct measurement of measure cetane number is not available, published cetane values are used to calculate a cetane number based on weighted averages of known fatty acid constituents [50, 68]; whereas, the cetane number for ULSD is based on the regulated standard [69]. The elemental carbon and hydrogen content of each fuel was directly determined using a Perkin-Elmer 2400 Series II CHNS/O analyzer, with the oxygen content determined by difference from these results.

Table 2-2. Biodiesel Fatty Acid Component Mass Fractions.

Component	Palm	Jatropha	Soybean	Beef Tallow	Chain Length (pm)
C10:0	N/D	N/D	N/D	N/D	1525
C12:0	0.0017	N/D	N/D	N/D	1830
C14:0	0.0049	0.0003	0.0002	0.0288	2135
C15:0	N/D	N/D	N/D	0.0052	2288
C16:0	0.3219	0.1271	0.0904	0.2213	2440
C16:1	0.0013	0.004	N/D	0.0275	2421
C17:0	0.0002	0.0003	0.0003	0.0249	2593
C18:0	0.0396	0.074	0.0481	0.1746	2745
C18:1	0.494	0.4559	0.2542	0.4844	2726
C18:2	0.132	0.3365	0.525	0.0332	2707
C18:3	0.0019	0.001	0.0758	N/D	2687
C20:0	0.0026	0.0009	0.0029	N/D	3050
C22:0	N/D	N/D	0.0026	N/D	3355
C22:1	N/D	N/D	N/D	N/D	3336
C24:0	N/D	N/D	0.0006	N/D	3660
Unsaturation Degree	0.76	1.14	1.53	0.58	-
% Unsat	62.91%	79.74%	85.50%	54.51%	-
% Poly-Unsat	13.39%	33.76%	60.08%	3.32%	-

The fatty acid methyl ester (FAME) content of each biodiesel fuel was determined using an Agilent 6890 gas chromatograph coupled with an Agilent 5973 mass spectrometer. The chromatographic column was an HP-INNOWax Polyethylene Glycol column with a 15m length, 250 µm inner diameter, and 0.5 µm thickness. Each chromatogram was analyzed using HP Chemstation software. Stearic acid ethyl ester was used as a chromatographic internal standard. The resulting component mass fractions

are shown in Table 2-2. The degree of unsaturation for each fuel was calculated by summing all of a biodiesel's fatty acid component fraction weighted by the number of double bonds in each molecule. A lower degree of unsaturation indicates that fuel consists primarily of saturated FAMEs (no double bonds), while higher values indicate the presence of more unsaturated molecules. Calculations also included the percentage of mono- and poly-unsaturated FAMEs (single vs. multiple double-bond molecules) for each fuel. The chain length of each fatty acid component was calculated based on carbon single and double bond lengths of 152.5 and 133.3 pm, respectively [70].

2.4 Test Apparatus and Methodology

The engine utilized is a single-cylinder Yanmar L100V, 0.435L, compression-ignition engine that has been upgraded to utilize a common-rail fuel injection system. This engine is selected because it eliminates non-linearity of heat transfer and fluid dynamics as observed in larger, multi-cylinder engines. Thus, changes observed during testing can be more directly attributed to the fuels. In addition, the lower fuel consumption of this engine means that smaller quantities of fuel are needed for each test. Of interest, this engine originally contained an exhaust gas recirculation (EGR) port between the exhaust and intake runners that provided around ten percent EGR by volume. This port is now blocked in order to utilize an externally cooled EGR system. For this study, this system is disengaged to remove the varying effects of EGR on the combustion process.

The original fuel control for this engine was a mechanical pump-line-nozzle system actuated by an internal camshaft in the engine block[65]. To improve fuel control and provide the ability to vary engine speed, the stock fuel system was replaced with a Bosch common-rail fuel injection system utilizing a Bosch fuel injector (part #0 445 10 183) and controlled by a Bosch Engine Control Unit (ECU) (model # MS15.1). The fuel pump (model # CP3) is powered by an external 0.5-horsepower direct-current electric motor at a constant speed of 100 RPM. The ECU is connected via USB to a computer running the Bosch Modas Sport computer program. This program allows operators to dynamically

control fuel quantity, fuel rail pressure from 40-200 MPa (42.0 ± 0.03 MPa used for this study), and injection timing to a resolution of 0.02 degrees engine crank angle. Although this system is capable of multiple fuel injections per combustion event, a single main injection is used here to minimize combustion variability. Loading is accomplished using a Dyne Systems, Inc. Dymond Series 12-horsepower regenerative Alternating Current dynamometer and Dyne Systems, Inc. Inter-Loc V OCS controller. The dynamometer is connected via driveshaft through a Futek in-line torque transducer (model # TRS-605) that provides torque readings from 0-200 N-m.

Instrumentation for the engine and auxiliary systems include a Micro-Motion Coriolis flow meter (model # CMF010M) to measure fuel flow and a Merriam laminar flow element (model # 50MW20-2) and Omega differential pressure transducer (model # PX277-30D5V) to measure air flow. Also included are thermocouples for ambient air temperature, engine intake temperature, engine oil temperature, exhaust port temperature, and downstream exhaust temperature. Pressures measured include ambient pressure, engine intake pressure, engine oil pressure, fuel rail pressure, and exhaust pressure. Data is recorded using a custom LabVIEW program running on a National Instruments compact-RIO (model # 9014). These parameters are saved at a frequency of ten samples per second for two minutes. Recording occurs concurrently to data collection of cylinder pressure and exhaust emissions.

Pressure measurement in the engine cylinder is accomplished using a Kistler piezoelectric transducer (model # 6052C) and Kistler charge amplifier (model # 5011B). A Kistler incremental encoder (model # 2614B1) and a Kistler pulse multiplier (model # 2614B4) are used to determine the accompanying cylinder volume at each pressure reading at a resolution of 0.5 degrees of engine crank angle. These values are measured and recorded using a custom LabVIEW program installed on a dedicated computer with a National Instruments PCIe card (model # 7841). Each saved set of pressure data includes information from 60 thermodynamic cycles (120 engine revolutions). The pressure profiles presented later in this work represent the averaging of these 60 cycles.

Gaseous engine tailpipe emissions are measured using an AVL SESAM emissions bench. This equipment includes a Fourier Transform Infrared Spectroscope (FTIR) to measure species such as water (H_2O), carbon dioxide (CO_2), oxygen (O_2), CO, nitrogen oxide (NO), nitrous oxide (N_2O), and nitrogen dioxide (NO_2). The FTIR is not capable of measuring diatomic molecules (such as oxygen), so the bench includes a Magnos 106 oxygen sensor. Finally, a Flame Ionization Detector (FID) is used to measure total HC. The entire set of gaseous species is recorded at a frequency of one sample per second over a five-minute period. PM measurement is accomplished using an AVL Smoke Meter (model # 415SE) and a TCP/IP connection with a laptop.

Testing occurs at a single speed of 1800 RPM, which was chosen as a midpoint in the engine's speed envelope and for applicability of the results. At this speed, the Yanmar is rated to 18.0 N-m of torque. Loading occurs at 0.5 N-m (to reduce 'unloaded' variability) and 4.5 N-m, 9.0 N-m, 13.5 N-m, and 18.0 N-m to represent no load, 25%, 50%, 75%, and 100% of rated load, respectively. The dynamometer is operated in speed mode in order to maintain 1800 RPM regardless of fuel input. Engine output power is controlled via the ECU and fuel injection quantity. For this study, steady-state is defined as the condition when the downstream exhaust temperature varies by less than one percent per minute. This parameter is chosen since it is the slowest metric that responds to changes in engine settings.

Table 2-3. Injection Timings for Common-Rail Fuel Injection System (Degrees Before TDC) as a Function of Engine Torque. ULSD Timings Correspond to Unadjusted Biodiesel Timings.

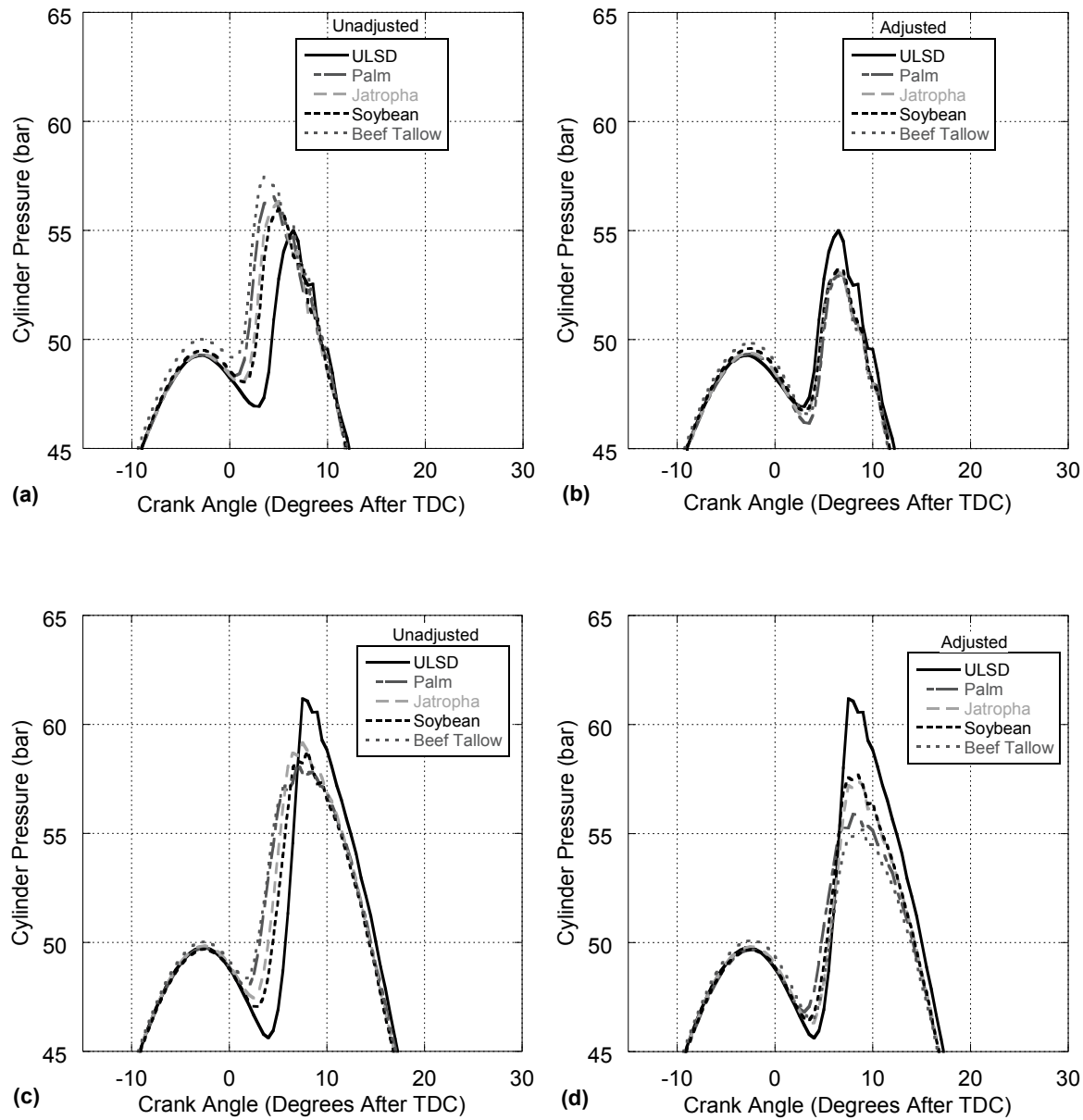
Load\Fuel	ULSD	Soybean Biodiesel	Jatropha Biodiesel	Beef Tallow Biodiesel	Palm Biodiesel
0.5 N-m	12.50	11.30	11.20	10.40	10.50
4.5 N-m	12.50	11.70	11.40	10.60	10.80
9.0 N-m	11.00	10.50	10.10	9.50	10.10
13.5 N-m	10.00	9.25	9.21	8.50	9.21
18.0 N-m	11.00	10.25	10.20	9.60	10.20

This engine is calibrated so that ULSD injection occurs at each tested load at the timing necessary for minimum fuel consumption[40]. During each biodiesel test, a load sweep (from 0.5 N-m to

18.0 N·m) is performed first using ULSD at the prescribed injection timings. The in-cylinder pressure data saved during the ULSD test (at the start of the testing day using pre-determined injection timings) is used to adjust the respective biodiesel based on the measured timing of peak cylinder pressure at that load[40, 71]. Following the testing of ULSD, the fuel system is bled and flushed using the neat biodiesel to be tested. Then, biodiesel testing begins after thirty minutes of run time to insure that no ULSD remains in the system. At each tested load, data is first recorded using the injection timings used for the engine calibrated for ULSD. The data saved from this condition sheds insight on the effects of biodiesel based on ignition delay. Then, data is recorded following the adjustment of injection timing to equilibrate the timing of peak cylinder pressure between biodiesel and ULSD. The respective injection timings used for each biodiesel fuel and ULSD are shown in Table 2-3. The necessary injection timings for biodiesel were delayed compared to ULSD, as expected based on the higher cetane number of biodiesel.

2.5 Results

Measuring the in-cylinder pressure and performing a heat release rate analysis provides significant insight into the combustion process that is occurring within the cylinder[1, 20, 65, 70]. Of interest for this study, this helps determine injection behavior, combustion timing, fuel energy release (aka heat release) behavior, and calculation of cylinder temperature[40].



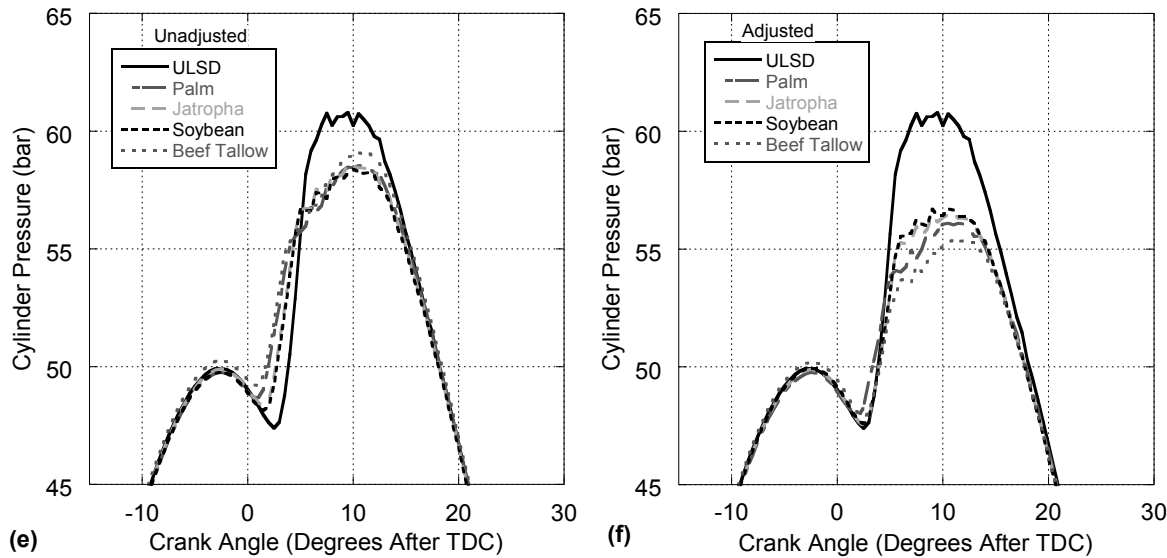


Figure 2-1. In-Cylinder Pressure vs. Engine Crank Angle at 0.5 N·m (a, b), 9.0 N·m (c, d), and 18.0 N·m (e, f) at Unadjusted (a, c, e) and Adjusted (b, d, f) Injection Timings.

The in-cylinder pressure profiles from the tests of 0.5 N·m, 9.0 N·m, and 18.0 N·m are indicated in Figure 2-1 as a function of engine crank angle in degrees after piston top-dead center (TDC) for both the unadjusted and adjusted injection strategies. Only the angles near TDC are shown in order to provide a closer investigation of combustion. The exhaust/air exchange process is relatively unchanged throughout the tests with volumetric efficiency calculations within statistical uncertainty. The figures generated for other loads and for volumetric efficiency (among others), along with the tables used to generate all figures, are available in the supplemental material associated with this work.

Inspection of the unadjusted in-cylinder pressure results in Figure 2-1 indicates that biodiesel combustion is occurring visibly earlier than ULSD. This behavior is especially pronounced at lower loads; for example, the peak pressure of beef tallow biodiesel is occurring up to five degrees earlier than ULSD at the 0.5 N·m loading. It can also be observed that the order of combustion at 0.5 N·m is beef tallow, palm, jatropha, soybean, and finally, ULSD. Previous works incorporating pump-line-nozzle systems show that fuel injection and subsequent combustion timing are advanced for a denser fuel with an associated higher bulk modulus[47, 56, 65]. However, because this engine utilizes electronic common-

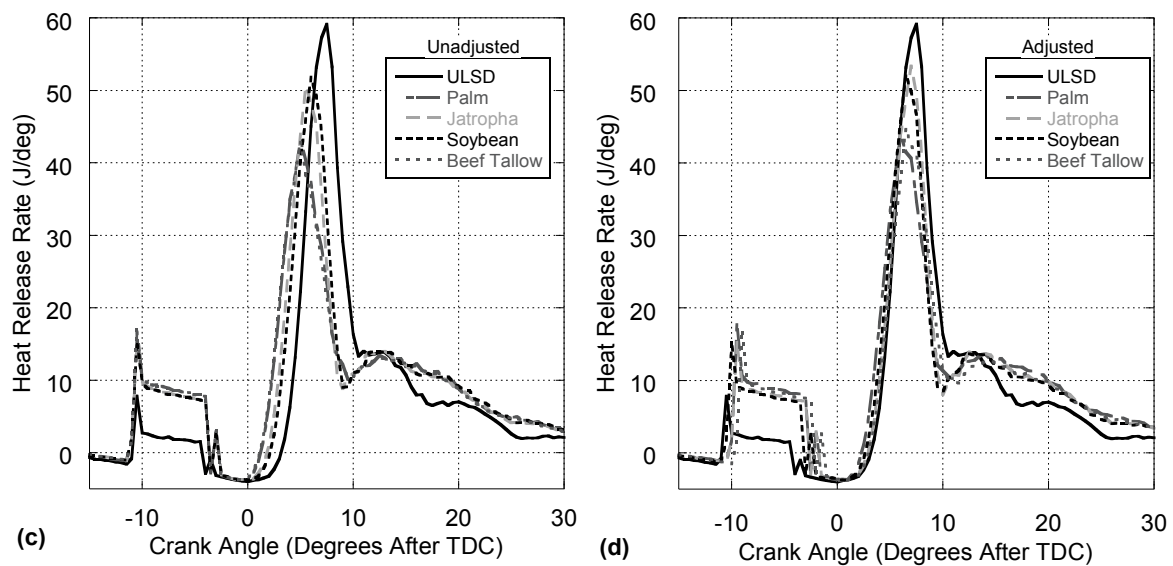
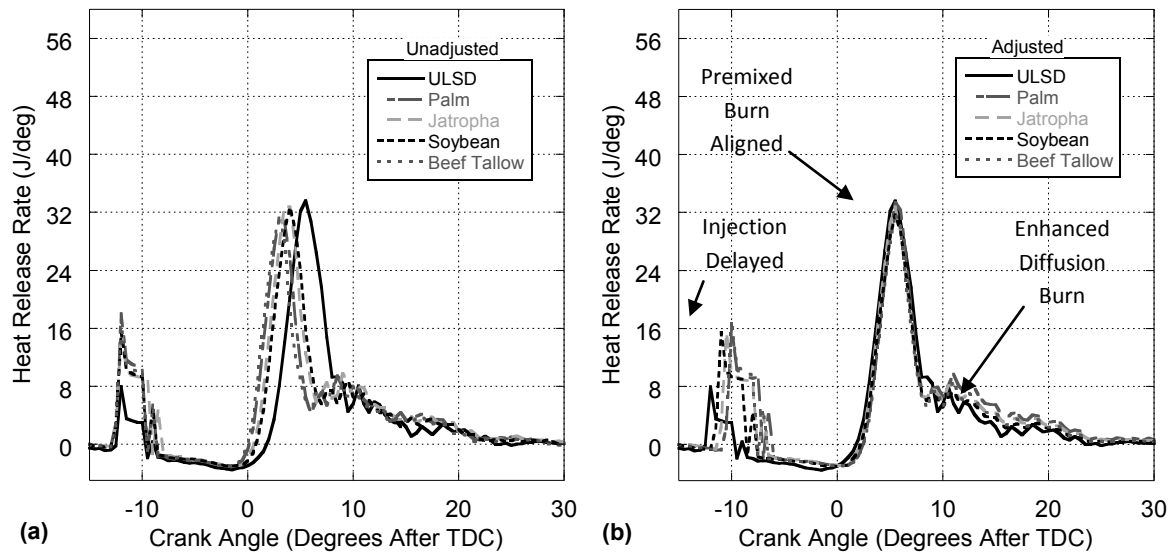
rail injection, the effects of bulk modulus on injection timing are negligible (observable in the unadjusted heat release results presented later). In addition, the injection pressure for the entirety of this study was maintained at 42.0 ± 0.03 MPa to remove adverse changes to injection behavior based on fuel pressure variation. Therefore, this order is largely based on the cetane numbers values for these fuels, which vary as a result of the molecular design of the fuels. Specifically, fuels with longer carbon chains and lower unsaturation (see Table 2-2) are easier to break apart during the combustion process[17, 72]. From Table 2-1 beef tallow has the highest cetane number (via a high concentration of fatty acids of long chain length (Table 2-2)) and thus shortest ignition delay, followed by the other fuels by magnitude of cetane number. Once adjusted, peak pressures for all five fuels occur at virtually the same crank angle; thus, the overshadowing effect of combustion phasing on engine emissions is removed[1, 20, 56, 65].

The adjusted cases show that the biodiesel fuels have a lower peak cylinder pressure than ULSD at all loads. At the 0.5 N-m load, the adjusted pressure profiles for the biodiesel fuels are tightly grouped below ULSD. As load increases, the cylinder pressure during combustion rises until high loadings where pre-mixed combustion diminishes and is replaced by diffusion burn, thus flattening out the combustion pressure peaks of the pressure profile. As load increases, the biodiesel pressure profiles begin to deviate in peak magnitude from each other. Above 0.5 N-m loadings, it can be observed that soybean and jatropha biodiesels have higher combustion pressures than both palm and beef tallow biodiesels.

Variation of combustion pressures with load between biodiesels is due to a variety of physical and chemical factors that all influence combustion in some way. The energy content of the fuel affects the relative amount of premixed and diffusion burn as a more energetic fuel will combust more readily, resulting in an enhanced premixed burn phase, which will increase cylinder pressure[56]. Conversely, viscosity changes the behavior of the injection and atomization process because higher viscosity is associated with larger molecules. A relatively higher viscosity reduces the effectiveness of the injector; thus, larger fuel droplets enter the cylinder and do not mix with air as effectively[1, 56]. As a result, a

diminished premixed burn and reduced cylinder pressures occur for this type of fuel. Density alters how much fuel mass is in a given droplet of fuel as it enters the cylinder. Since the injection process is assumed to be a constant flow process, more mass enters the cylinder for a denser fuel providing for the opportunity for more energy release (and pressure rise) to occur[56]. With respect to chemical properties, a fuel with higher volatility vaporizes more readily in the cylinder, promoting higher cylinder pressures via a more aggressive premixed burn phase[1, 65]. Additionally, fuels with higher average molecular chain length combust more readily (a higher cetane number) which promotes faster combustion and a higher premixed spike[50, 56]. Finally, a fuel that contains oxygen in its molecules reduces the equivalence ratio of the mixture, promoting more rapid combustion[42, 56, 65]. Summarizing, a higher energy content, density, cetane number, oxygen content, lower viscosity, and greater volatility all independently act to increase the premixed burn phase and promote higher pressures.

This is apparent when comparing jatropha vs. palm biodiesels. Jatropha has a higher energy content and density along with a lower viscosity than palm biodiesel. However, jatropha also has slightly lower oxygen content, cetane number, and flash point than palm biodiesel. The higher peak combustion pressure for jatropha suggests that the effects of viscosity, density, and energy content have a larger influence than oxygen content, cetane number, or volatility.



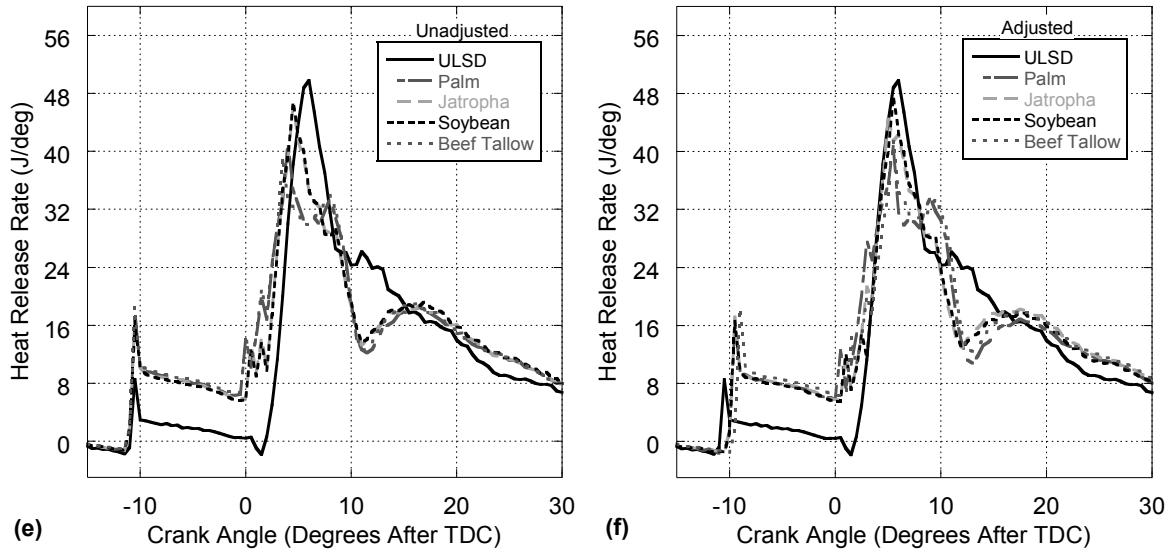


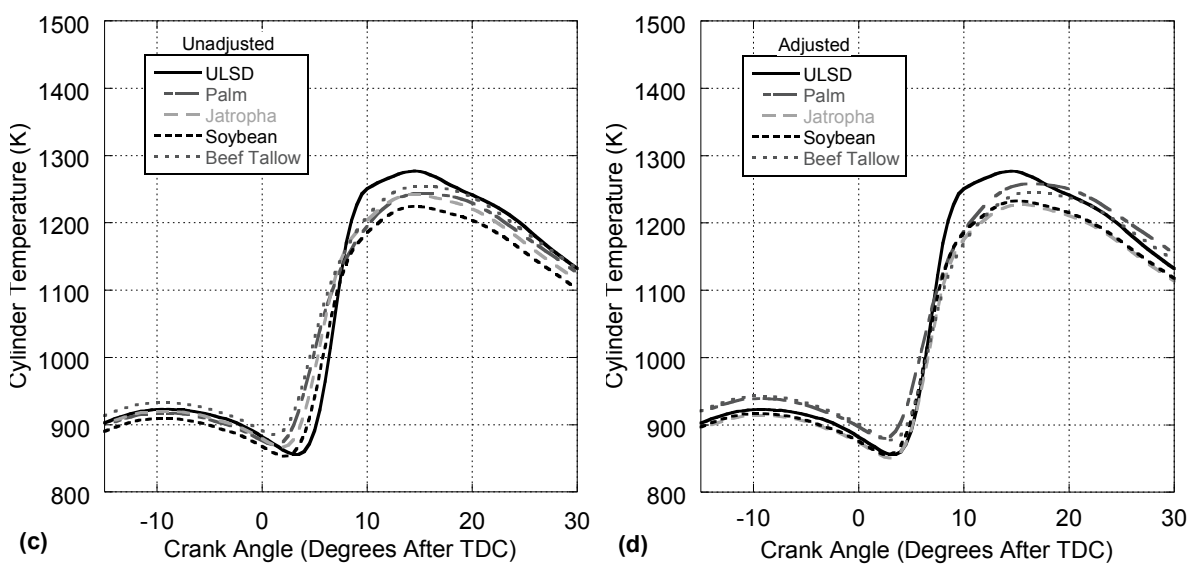
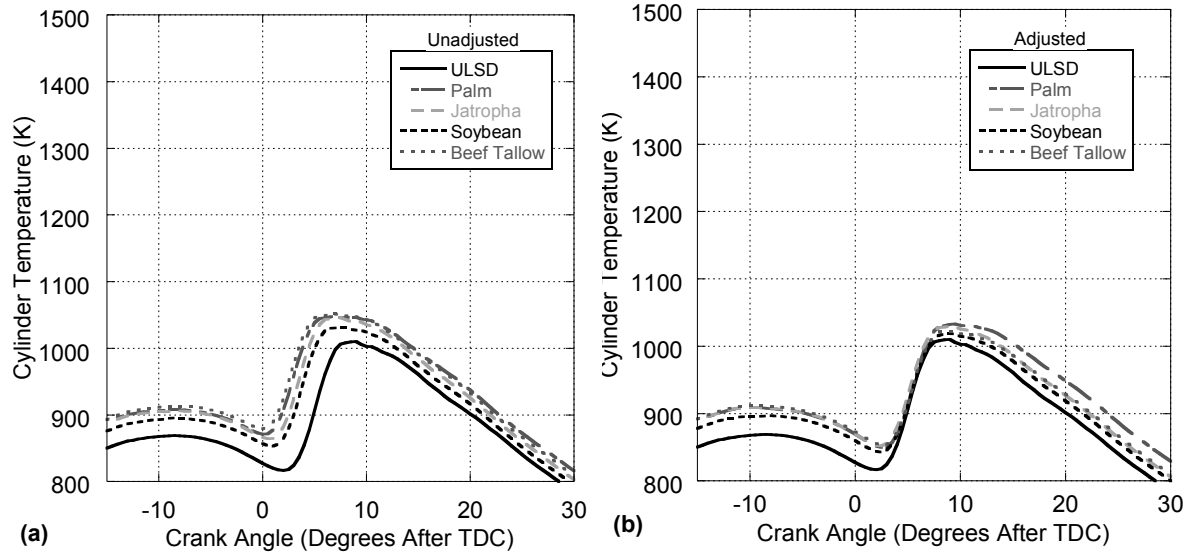
Figure 2-2. Heat Release Rates vs. Engine Crank Angle at 0.5 N·m (a, b), 9.0 N·m (c, d), and 18.0 N·m (e, f) at Unadjusted (a, c, e) and Adjusted (b, d, f) Injection Timings.

The behaviors observed via the in-cylinder pressure results are additionally seen using the heat release rate analysis in Figure 2-2. After normalizing combustion timing, the rate of heat release finds that at the 0.5 N·m load, the peak rate of heat release is similar between all fuels. As load increases, the peak heat release rate of the biodiesel fuels become reduced when compared to ULSD. Palm and beef tallow, appear to have the most diminished premixed combustion spike, with the highest premixed spike among the biodiesels occurring with either jatropha or soybean, depending on load. The reduction in the premixed combustion phase with biodiesel results in a more pronounced diffusion burn phase. In essence, the energy needed to produce the required engine power remains the same; hence, a reduced premixed burn is replaced by additional diffusion burn. This relative duration of heat release will influence cylinder temperatures and associated emissions, as discussed later.

The variation in the heat release rate at injection timing (generally around -10° ATDC, see Figure 2-2) is related directly to the relative densities of the fuels being injected. Within the common rail injection system, fuel flow is on a volumetric basis. For biodiesel fuels, the higher fuel density results in a greater mass flow rate into the system[40]. As a result, the heat release rate in the vicinity of injection

with the biodiesel tests is significantly higher than that for ULSD since there is more mass to take in the latent heat present from the previous cycle[40]. Note that this rate of heat release at injection is indicated as positive. This is due to the assumption¹ in the heat release model that fuel is instantaneously atomized and vaporized after injection; hence, energy is being added to the gas from the liquid fuel immediately converting. This was done in order to simplify the computational effort involved when developing the model. As a result, this positive rate of heat release is an artifact resulting from a net mass addition to the cylinder (the associated energy content of the fuel outweighs the loss in bulk gas energy from vaporization). This artifact proves quite useful in analyzing the results, as it definitively displays the onset and duration of the injection event[40]. After injection, the rate of heat release generally becomes negative, as this vaporization loss in bulk gas energy is also reflected in the governing pressure trace used to generate heat release results. The increased mass flow rate during the biodiesel injection event does not result in an overall shorter injection time. This is because the lower energy content of the biodiesel fuels (in comparison to ULSD) requires more fuel in order to achieve the same engine power output.

¹ Heat release model assumption discussion provided by Jonathan Mattson



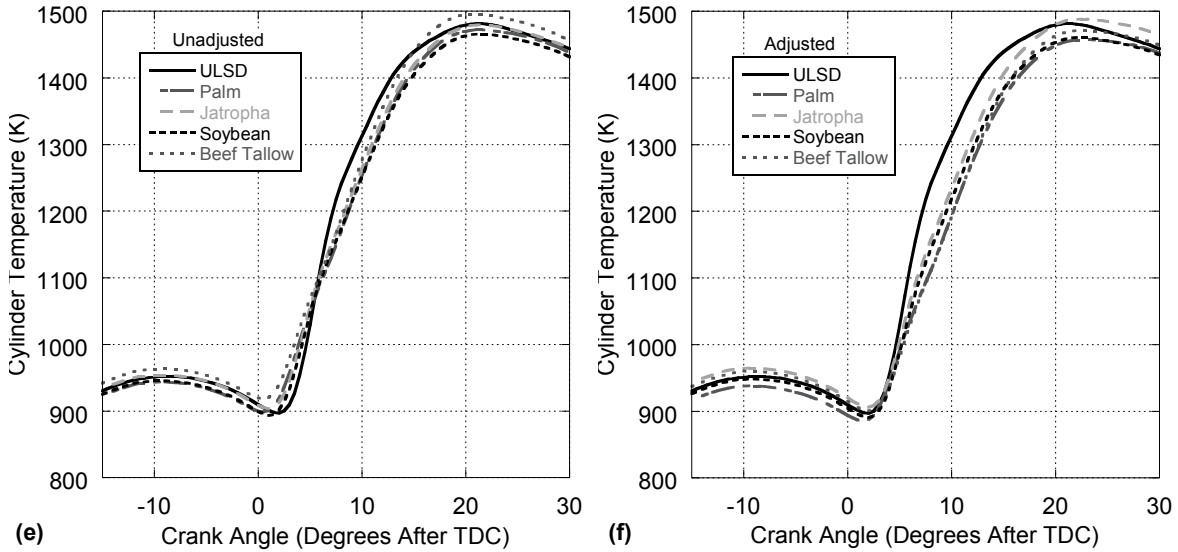


Figure 2-3. Cylinder Temperature vs. Engine Crank Angle at 0.5 N·m (a, b), 9.0 N·m (c, d), and 18.0 N·m (e, f) at Unadjusted (a, c, e) and Adjusted (b, d, f) Injection Timings.

Similar to heat release, the in-cylinder temperature can be calculated using the measured pressure data [40]. This parameter is a helpful indicator for emissions and can further explain the differences between the premixed and diffusion burn behavior between the fuels. Of the fuels tested, the adjusted combustion phasing results indicate that above 0.5 N·m load, ULSD primarily experiences the highest peak cylinder temperatures, which also occur earlier in the combustion event. The exception to this behavior occurs at full load, where jatropha biodiesel has the highest peak temperature. The ranking of temperature for biodiesel appears to depend on load, with palm biodiesel exhibiting highest cylinder temperatures at 0.5 N·m and 9.0 N·m, but the lowest at 18.0 N·m. By contrast, soybean biodiesel has generally lower combustion temperatures than the other biodiesels tested at all loads. Recalling that combustion phasing was adjusted by pressure, the peak temperatures in Figure 2-3 do not necessarily align in the adjusted conditions. This is because fuels, such as beef tallow, that have higher fractions of diffusion burn raise temperatures later in the cycle in comparison to fuels with a lower level of diffusion burn (and more premixed burn), such as ULSD. This effect carries over to subsequent cycles because of a less efficient expansion event (less constant volume-like combustion), as well as a hotter

residual cylinder mixture promoting a greater initial charge temperature. The resulting hotter cylinder walls act to heat the charge air to higher temperatures during compression than those experienced when burning ULSD. From Figure 2-3, it can be seen that at 0.5 N·m, the pre-combustion mixture is heated to higher temperatures for the biodiesels than for ULSD. As load increases and the diffusion burn portion of all fuels increase, the pre-combustion temperatures of each fuel start to group together, with soybean biodiesel's pre-combustion temperatures beginning to match those of ULSD at 4.5 N·m. As load increases to 9.0 N·m, jatropha biodiesel pre-combustion temperatures also align with ULSD, as indicated in Figure 2-3. Because of its relatively high amount of diffusion burn, beef tallow biodiesel does not have its pre-combustion mixture temperatures merge with the other fuels until 18.0 N·m where all fuels have a significant amount of diffusion burn.

The results are analyzed in order to generate brake-specific results for each emission species and fuel consumption at all loads and injection strategies. The brake-specific emissions of NO_x, CO, HC, and PM are shown as a function of engine brake torque with unadjusted injection timing outputs shown to contrast with adjusted injection timing results. Due to the single-cylinder design of this engine and the accompanying torque spikes during operation, there is increased variability at the 0.5 N·m loading. The emissions regression as a function of fuel properties is discussed in the next section.

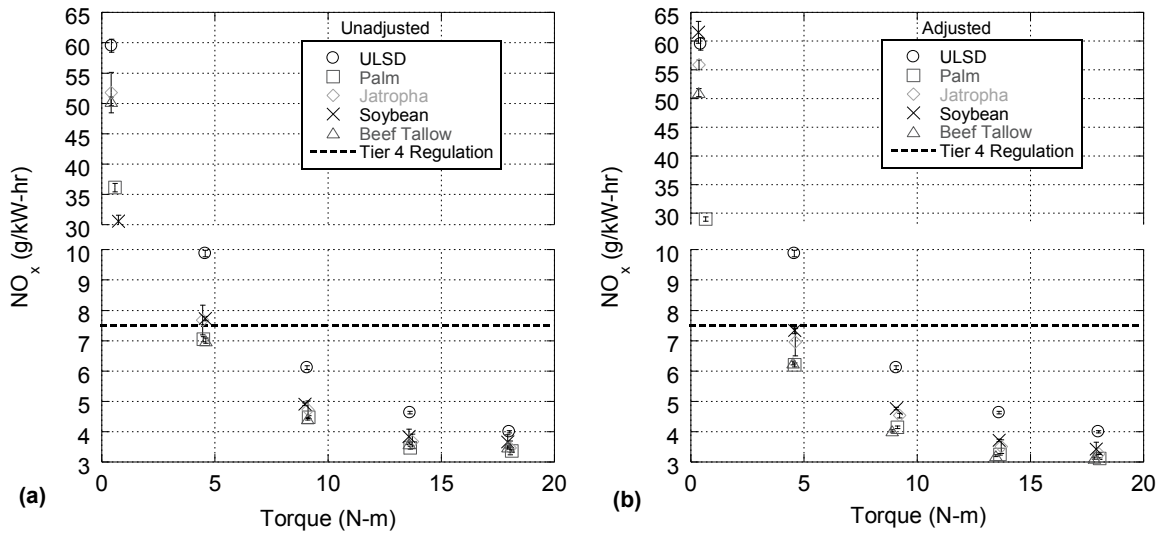


Figure 2-4. Brake-Specific NO_x Emissions vs. Engine Torque for (a) Unadjusted and (b) Adjusted Injection Timings.

The brake-specific NO_x results in Figure 2-4 are comprised of the summation of NO and NO₂ emissions and are plotted alongside the applicable Tier 4 levels for this engine [10]. At the 0.5 N·m load, NO_x is composed of approximately 40% NO, with this fraction increasing to about 98% at full load. Since these individual species display a similar behavior to overall NO_x emissions, the specific figures are not included here. This behavior includes a decrease in brake-specific NO_x emissions as load rises. This is a result of power output increasing more rapidly than the exhaust concentration of NO_x. The NO_x results indicate that ULSD consistently produces the highest levels of NO_x at all loads (other than the no-load condition in Figure 2-4b). From the heat release and temperature results, ULSD has the highest premixed burn phase and often the greatest cylinder temperature. Hence, it has the fastest combustion process at elevated temperatures providing both opportunity and sufficient time for NO_x formation. From there, a general clustering of the biodiesel NO_x emissions occurs with soybean and jatropha biodiesel fuels generally producing the most NO_x. Of note, the equivalence ratio for 18.0 N·m was approximately 0.65 for the biodiesels and 0.59 for ULSD. This higher equivalence ratio for biodiesel provides better global conditions to form NO_x[1]. However, other factors, such as certain fuel properties,

overshadow these enhanced conditions; thus, the formation of NO_x is reduced overall. This behavior will be discussed later using the regression analysis. NO_x emissions for palm and beef tallow biodiesels have similar emission levels throughout loads above 0.5 N-m in both the unadjusted and adjusted cases.

It can be observed that the delaying of injection timing (Table 2-3) for the adjusted case (Figure 2-4) causes a decrease in NO_x for biodiesel at all loads above 0.5 N-m compared to the unadjusted results. This is consistent with the thermal NO_x mechanism where NO_x production exponentially increases with temperature[1]. In particular, the delayed combustion in the adjusted case should result in lower cylinder temperatures and a reduced residence time at the associated combustion temperatures[1].

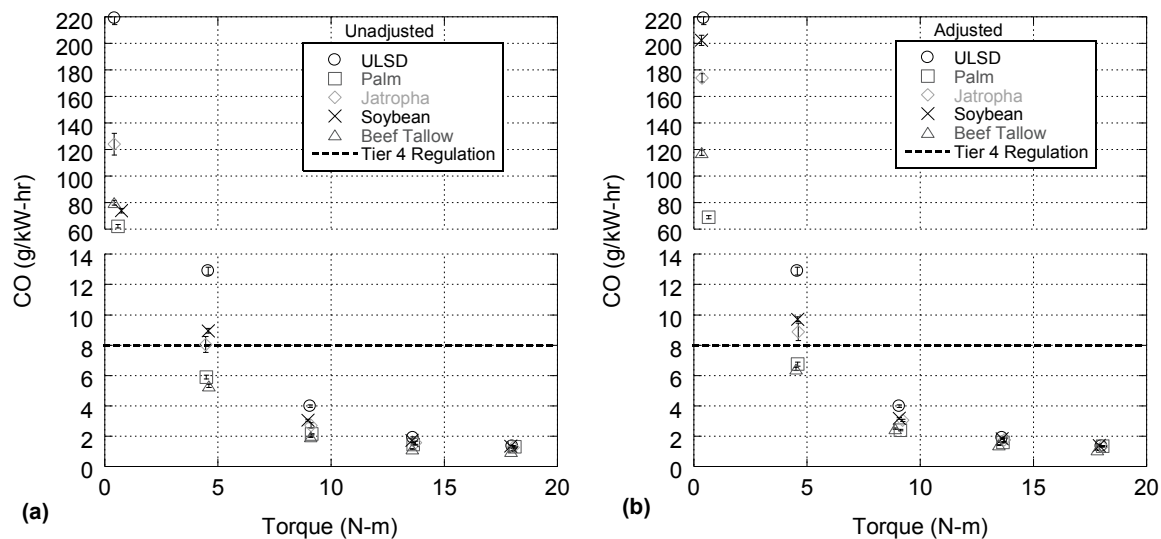


Figure 2-5. Brake-Specific CO Emissions vs. Engine Torque for (a) Unadjusted and (b) Adjusted Injection Timings.

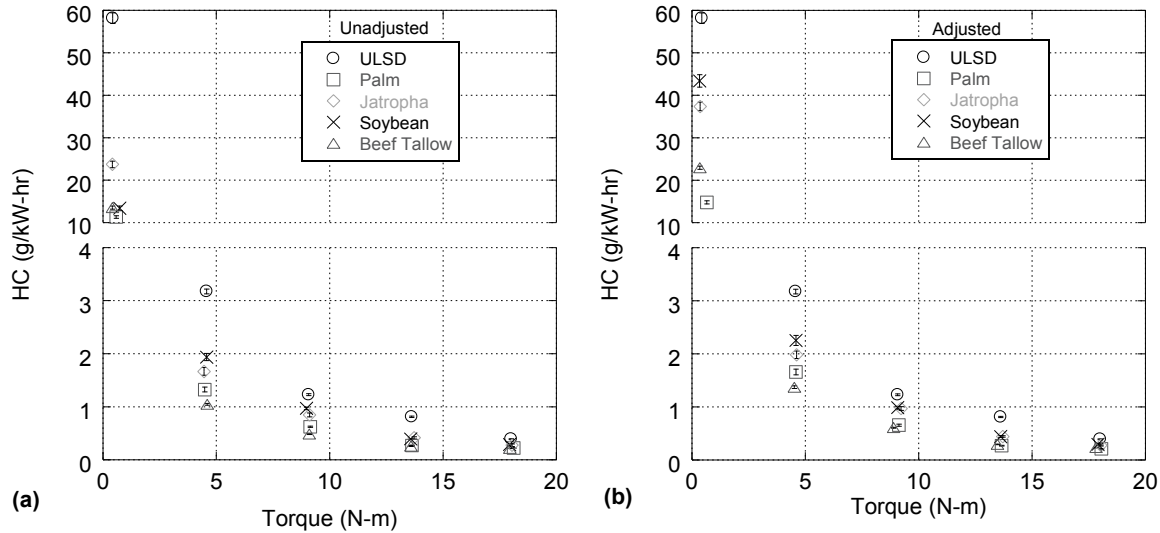


Figure 2-6. Brake-Specific HC Emissions vs. Engine Torque for (a) Unadjusted and (b) Adjusted Injection Timings.

The brake-specific results for CO and HC exhibit similar behavior in regards to load change and fuel ranking at each load, as shown in Figure 2-5 and Figure 2-6, respectively. The corresponding Tier 4 emissions of CO are also indicated in Figure 2-5 [10]. Specifically, as load increases, the brake-specific emissions decrease due to a hotter combustion environment and an increase in engine power output. In other words, combustion efficiency increases (discussed later) promoting lower CO and HC levels at higher engine loadings. Here, ULSD produces the highest amounts of both CO and HC at all loads largely because it does not contain an oxygen component as part of its fuel composition as discussed in the introduction. Of the biodiesels, soybean biodiesel produces the most CO and HC at all loads above 0.5 N-m with the exception of HC at the 13.5 N-m loading in the unadjusted injection timing case (Figure 2-6a). Jatropha biodiesel also produces high HC emissions among the biodiesel group. At loads above 9.0 N-m, these two biodiesel fuels produce relatively similar emissions of CO and HC. The lowest producer of CO and HC is beef tallow biodiesel. At higher loadings, the HC emissions between beef tallow and palm biodiesel become relatively similar. As timing is adjusted to align combustion peak pressures, CO and HC

emissions increase for the biodiesel fuels. This is assumed to be a result of later combustion timing and lower cylinder temperatures causing a slightly diminished combustion environment.

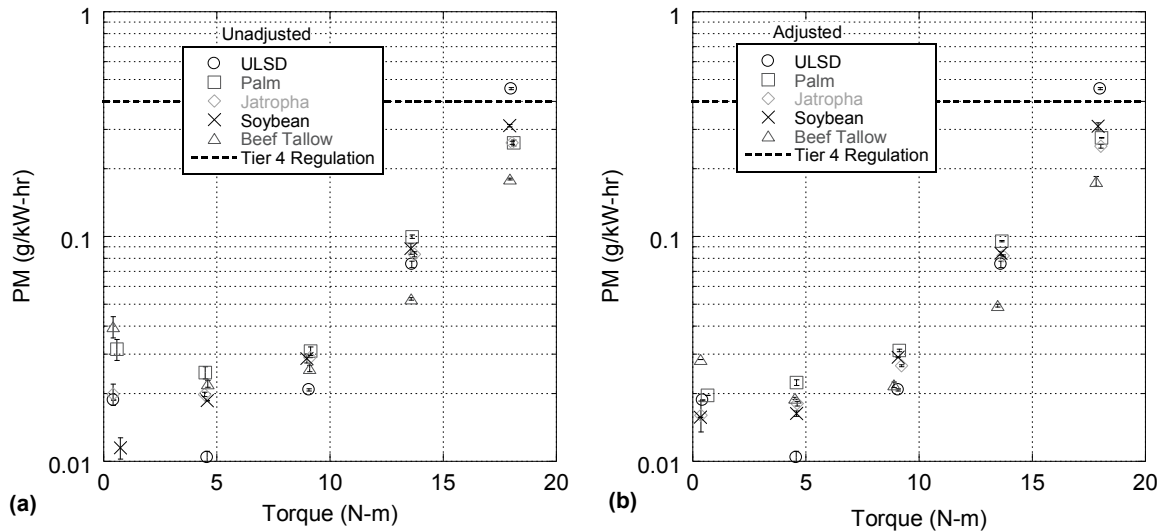


Figure 2-7. Brake-Specific PM Emissions vs. Engine Torque for (a) Unadjusted and (b) Adjusted Injection Timings.

The Particulate Matter emission results and Tier 4 limit shown in Figure 2-7 depict multiple phenomena occurring [10]. At low loads, production of PM is relatively small; however, the brake-specific results are inflated due to low engine output power. As load increases, PM production grows since more fuel is available in the cylinder to form this carbon-based emission species. However, the loading on the engine increases at a faster rate. Thus, a decrease in PM with load occurs initially on a brake-specific basis. Above 4.5 N·m, the increasing amount of fuel needed to produce more engine power yields larger rich zones near the injector and an overall mixture that is closer to being stoichiometric [1]. As a result, there is a decreased oxidation capability and more unburned fuel will eventually coalesce in the form of PM. Furthermore, as load increases, so does the amount of combustion that occurs during the diffusion burn phase. This is the result of combustion occurring when fuel injection and mixing is still happening at higher loads[1]. Thus, as the load approaches rated conditions, the production of PM exponentially rises as the diffusion burn phase becomes more

pronounced (recalling Figure 2-2). When timing is delayed, PM emissions decrease slightly (above the 0.5 N·m case). This occurs because of the shift to optimum combustion timing; thus, it is postulated that slightly less fuel (potential PM) is needed to produce the same amount of power since fuel consumption was within statistical uncertainty. Moreover, additional mixing time is available because the ignition delay is slightly longer at these conditions due to reduced cylinder temperatures (Figure 2-3). Hence, there is an increase in the level of pre-mixed combustion and a reduction in the diffusion burn phase (e.g., Figure 2-2). If injection timing were delayed further, the expectation is that PM production would increase as a result of more diffusion burn at cooler combustion temperatures[1, 40, 71].

Inspection of the PM results shows that ranking of fuels for production depends on load. For the 0.5 N·m load case, the highest producer is beef tallow biodiesel, regardless of the injection strategy used. When combustion phasing is adjusted at this load, ULSD, palm, and jatropha biodiesel all produce similar amounts. As load increases to 4.5 N·m, the adjusted results show a clustering of the biodiesels above the emissions of ULSD. Within this cluster, palm is the highest producer of PM. As load increases further, beef tallow eventually becomes the lowest PM producer (at the rated torque). Furthermore, at full load ULSD becomes the highest producer of PM, as expected from literature[17, 50-52, 56, 58]. These trends will be discussed further in the regression section.

From the adjusted results in Figure 8b, the combustion efficiencies at the 13.5 and 18.0 N·m loadings are tightly grouped approaching 100% because of a significant energy release at lean conditions. At lower loads, soybean consistently has the lowest combustion efficiency of the biodiesel fuels while beef tallow and palm display the highest combustion efficiency. This ordering is consistent with higher premixed burn phase for soybean biodiesel than for jatropha, palm, and beef tallow biodiesels, respectively. This ranking also largely follows the emissions of HC and CO, as discussed in the following section.

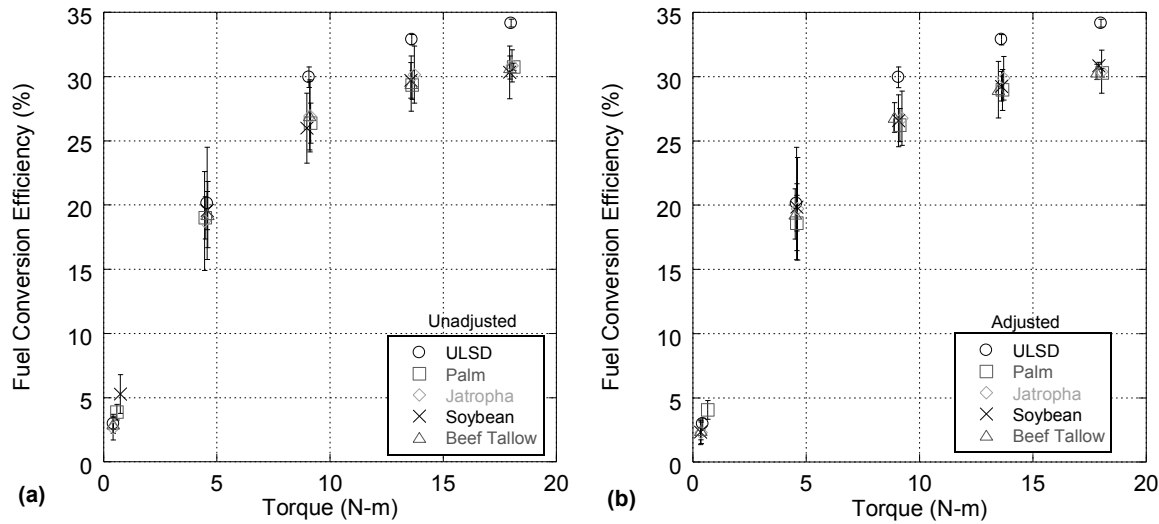


Figure 2-8. Fuel Conversion Efficiency vs. Engine Torque for (a) Unadjusted and (b) Adjusted Injection Timings.

Fuel conversion efficiency is used to gauge the amount of useful work coming from the added fuel energy. Thermal efficiency indicates how effective the fuel is in creating actual work after factoring combustion efficiency[1]. Results indicate that biodiesel fuels achieve greater combustion efficiency for both injection strategies investigated. This is largely because of the reduction in HC and CO in the biodiesel emissions which arises due to the oxygenation of biodiesel[42, 56]. However, due to the relatively similar high combustion efficiencies, fuel and thermal conversion results end up being similar; hence, only the outcomes for fuel conversion efficiency are shown in Figure 2-8 (thermal efficiency is presented in the supplementary material). Comparing the unadjusted and adjusted results indicates a varied amount of improvement or degradation of efficiency based on injection timing. This is due primarily to some uncertainty in the combustion efficiency calculations. However, the effects of delaying combustion resulted in similar fuel consumption behavior for a given fuel, with varied effects based on load and fuel used.

Nevertheless, the fuel conversion efficiency of ULSD is observed to be consistently higher throughout engine loadings (other than 0.5 N-m). This is due to the higher energy content of the fuel

along with the fact that combustion occurs via a greater premixed burn phase, via Figure 2-2 (i.e., more like constant volume combustion instead of a longer, more dragged out combustion process). For the biodiesels, palm biodiesel is generally the least efficient fuel, followed by beef tallow and jatropha biodiesels. Soybean biodiesel has the highest fuel conversion efficiency of the biodiesels tested (above 0.5 N-m). Recalling the heat release results, this appears to be a general result of improved combustion via a higher premixed-to-diffusion burn ratio.

2.6 Regression Analysis (Values Provided by Farshid Kiani)

Using the results presented, a statistical regression analysis of the measured fuel properties in Table 2-1 and Table 2-2 was performed with Matlab using a student-designed code. The resulting Pearson coefficients for both the unadjusted and adjusted injection strategies are shown across all loads. For the upcoming discussion, a strong proportional correlation is defined as a Pearson value equal to or between 0.95 and 1.00. Similarly, a strong inverse relationship is equal to or between -0.95 and -1.00. In some circumstances, correlations with slightly weaker Pearson values are also discussed. The tables indicate an individual outcome, such as NO_x, as a function of the variation of a given fuel property shown in the first column. To assist in visibility, strong regressions are shown in bold; whereas, weaker relationships still with an absolute value greater than 0.90 are italicized. To aid in this analysis, a regression among fuel properties was also performed in order to ascertain the connections between fuel properties, such as the cetane number, unsaturation, and density[17].

Table 2-4. Fuel Property Pearson Correlation Coefficients.

Fuel Property	Cetane Number	Unsat. Degree	Unsaturat ion	Poly-Unsat.	Mono-Unsat.	Density	Energy Content	Viscosity
Cetane Number	1.000							
Unsat. Degree	-0.992	1.000						
Unsaturation	-0.956	0.969	1.000					
Poly-Unsat.	-0.993	0.998	0.950	1.000				
Mono-Unsat.	0.938	-0.944	-0.833	-0.963	1.000			
Density	-0.996	0.999	0.964	0.999	-0.948	1.000		
Energy Content	0.209	-0.327	-0.378	-0.305	0.277	-0.299	1.000	
Viscosity	0.939	-0.970	-0.914	-0.974	0.961	-0.966	0.491	1.000

The fuel characteristics analysis in Table 2-4 indicates that most of the fuel properties are interrelated as expected. For instance, density is strongly proportional to unsaturation degree, percentage unsaturation, and percentage poly-unsaturation. This is similar to the results found by McCormick[17], Lapuerta[73], and Harrington[64]. In addition, density is found to be inversely proportional to the cetane number and viscosity[74]. This connection can be validated via the findings of both Harrington and Knothe who concluded that viscosity and cetane number both increase with chain length[50, 64]. Therefore, if viscosity and cetane number are proportional to chain length[50, 64], and cetane number is inversely proportional to density[17], then density should also be inversely proportional to viscosity[74]. This is because a denser fuel has shorter carbon chains. Of interest, density is also weakly inversely proportional to mono-unsaturation percentage as a result of the longer carbon chains that occur for C18:1 than for C18:2 and C18:3, as indicated in Table 2-2. In particular, Table 2-2 indicates that beef tallow has the highest quantity of mono-unsaturation, with most of it in the form of C18:1 which has longer chain length, and less density, than fuels such as soybean that contain significant quantities of molecular poly-unsaturation. Oxygen content is found to be inversely proportional to energy content as carbon and hydrogen atoms are displaced by oxygen in the molecule, thus making the fuel less energy-dense by mass[56]. Finally, the ratio of hydrogen to carbon in the fuel is indicative of the

amount of unsaturation in the molecules, where carbon double bonds reduce the amount of hydrogen that can be bonded to the molecule[56].

The regressions of engine output versus fuel property show that stronger correlations exist between fuel properties and engine outputs when combustion timing is adjusted to control combustion timing. This allows for independent fuel properties to play a more dominant role in the combustion process rather than being overshadowed by the influence of combustion phasing. For this reason, the upcoming discussion is predominantly weighted towards the results from the adjusted combustion injection strategy.

2.6.1 *Nitrogen Oxides Emissions*

Table 2-5. NO_x and Fuel Property Pearson Correlation Coefficients.

Fuel Property	0.5 N-m		4.5 N-m		9.0 N-m		13.5 N-m		18.0 N-m	
	Unadjusted	Adjusted	Unadjusted	Adjusted	Unadjusted	Adjusted	Unadjusted	Adjusted	Unadjusted	Adjusted
Cetane Number	0.448	-0.727	-0.942	-0.990	-0.999	-0.991	-0.919	-0.999	-0.801	-0.994
Unsat. Degree	-0.515	0.638	0.933	0.969	0.996	0.993	0.865	0.994	0.738	0.976
Unsaturation%	-0.356	0.606	0.979	0.950	0.970	0.986	0.793	0.965	0.598	0.922
Poly-Unsat. %	-0.548	0.645	0.911	0.965	0.993	0.985	0.878	0.992	0.771	0.982
Mono-Unsat. %	0.708	-0.577	-0.771	-0.887	-0.930	-0.902	-0.851	-0.931	-0.825	-0.943
Density	-0.509	0.659	0.932	0.974	0.998	0.992	0.880	0.996	0.759	0.982
Viscosity	0.699	-0.456	-0.830	-0.882	-0.946	-0.938	-0.756	-0.940	-0.660	-0.915
Energy Content	0.606	0.504	-0.200	-0.107	-0.254	-0.288	0.189	-0.228	0.314	-0.118

The observed behavior of regression results for NO, NO₂, and NO_x are similar; hence, only the overall NO_x regressions are discussed here. The regression analysis (Table 2-5) indicates that a direct correlation exists between NO_x and the properties of: unsaturation degree, unsaturation percentage, poly-unsaturation degree, and density at all loads above 0.5 N-m. This behavior suggests that a combination of properties share the overall influence. With respect to molecular unsaturation, NO_x increases may be occurring partially due to more energy being released as a result of the increased

number of double carbon bonds, as discussed by Cecrle et al.[56]. It appears that multiple double bonds in the molecule magnify the behavior, as the unsaturation degree (ratio of poly- to mono-unsaturation) and poly-unsaturation percentage are more closely correlated to NO_x than is the unsaturation percentage. This hypothesis is supported further by the weak inverse correlation of mono-unsaturation with NO_x which indicates that the increase of NO_x with density may also occur as a result of shorter carbon-chained molecules (such as those with poly-unsaturation in Table 2-2) being injected[17, 64]. As a result, fuel is more effectively mixed due to smaller droplet size, contributing to enhanced premixed burn[1]. Therefore, a more dense fuel indicates that more mass is injected per unit volume; thus, enhancing the potential for additional premixed energy release.

The inverse behavior of NO_x and viscosity further echoes the supposed behavior. As a fuel's molecular length becomes longer or kinked via double bonding, the viscosity of the fuel likewise increases[64]. This leads to reduced mixing effects (due to larger fuel droplets) and diminished peak heat release rate during the premixed burn. This can be seen in Figure 2-2 by comparing the peak heat release rates of soybean and beef tallow biodiesels. The viscosity of beef tallow biodiesel is higher, but it yields lower peak heat release rates than that of soybean biodiesel. Furthermore, this leads to a greater diffusion burn in order to generate the same amount of power. The result is a lower combustion temperature and reduced thermal NO_x production while fuel consumption increases. This suggests that injection pressure should be increased when fuel viscosity (and chain length) increases in order to more effectively mix the fuel and air, subsequently promoting premixed combustion and a reduction in fuel consumption.

Finally, an inverse relationship with cetane number likely occurs because of the inherent proportionality to viscosity. Thus, viscosity and its effects of fuel spray and mixing overshadow the influence of cetane number itself (recall that longer molecules have a greater viscosity and cetane number). For example, soybean biodiesel has higher density, unsaturation degree, percent unsaturation,

and percent poly-unsaturation that beef tallow, but also lower viscosity and cetane index (Table 2-1). As a result of these combined factors, the NO_x results in Figure 2-4 show that soybean biodiesel emissions are significantly higher than for beef tallow biodiesel (other than 0.5 N-m load). The higher viscosity and reduced mixing contribute to beef tallow's lower cylinder pressure and reduced premixed burn phase and overshadow a higher cetane index. Conversely, the higher cylinder pressure and premixed heat release observed for soybean biodiesel can be attributed to its higher density, lower viscosity, and poly-unsaturation.

2.6.2 Partial Combustion Products Emissions

Table 2-6. CO and Fuel Property Pearson Correlation Coefficients.

Fuel Property	0.5 N-m		4.5 N-m		9.0 N-m		13.5 N-m		18.0 N-m	
	Unadjusted	Adjusted	Unadjusted	Adjusted	Unadjusted	Adjusted	Unadjusted	Adjusted	Unadjusted	Adjusted
Cetane Number	-0.248	-0.907	-0.982	-0.984	-0.990	-0.958	-0.891	-0.926	-0.663	-0.680
Unsat. Degree	0.205	0.852	0.984	0.979	0.993	0.930	0.938	0.957	0.749	0.764
Unsaturation%	0.403	0.838	0.993	0.987	0.987	0.944	0.957	0.988	0.781	0.781
Poly-Unsat. %	0.153	0.850	0.971	0.968	0.984	0.918	0.921	0.938	0.728	0.748
Mono-Unsat. %	0.102	-0.760	-0.871	-0.867	-0.900	-0.804	-0.837	-0.832	-0.667	-0.700
Density	0.204	0.864	0.982	0.979	0.992	0.935	0.926	0.948	0.728	0.745
Viscosity	0.003	-0.707	-0.920	-0.905	-0.939	-0.813	-0.952	-0.937	-0.839	-0.860
Energy Content	0.216	0.184	-0.291	-0.237	-0.293	-0.050	-0.617	-0.513	-0.869	-0.859

Table 2-7. HC and Fuel Property Pearson Correlation Coefficients.

Fuel Property	0.5 N-m		4.5 N-m		9.0 N-m		13.5 N-m		18.0 N-m	
	Unadjusted	Adjusted	Unadjusted	Adjusted	Unadjusted	Adjusted	Unadjusted	Adjusted	Unadjusted	Adjusted
Cetane Number	-0.287	-0.933	-0.967	-0.964	-0.970	-0.937	-0.875	-0.906	-0.965	-0.940
Unsat. Degree	0.257	0.887	0.989	0.987	0.986	0.933	0.866	0.876	0.955	0.893
Unsaturation%	0.462	0.881	0.987	0.986	0.995	0.984	0.950	0.928	0.983	0.873
Poly-Unsat. %	0.201	0.883	0.978	0.976	0.973	0.910	0.835	0.855	0.939	0.892
Mono-Unsat. %	0.062	-0.786	-0.899	-0.899	-0.881	-0.767	-0.659	-0.704	-0.816	-0.810
Density	0.252	0.897	0.984	0.981	0.981	0.931	0.863	0.879	0.956	0.904
Viscosity	-0.062	-0.753	-0.966	-0.969	-0.949	-0.837	-0.745	-0.737	-0.863	-0.765
Energy Content	0.106	0.102	-0.436	-0.451	-0.403	-0.244	-0.193	-0.034	-0.203	0.110

Due to the relatively similar behavior of both hydrocarbons and carbon monoxide with load and fuel in Figure 2-6 and Figure 2-7, these species are grouped together here as partial combustion products. It is important to remember that the generation of these species is slightly different, with HCs being the result of fuel molecules not fully oxidizing and CO resulting from the in-complete oxidization of carbon[1]. Nevertheless, regression results in Table 2-6 and Table 2-7 indicate strong correlations for both CO and HC that increase with unsaturation degree, unsaturation and poly-unsaturation percentages, and density.

It is believed that, much like NO_x behavior, multiple factors combine to influence the overall partial combustion product emission behavior. For instance, stronger carbon double bonds are more difficult to break, which may cause more HC and CO production during the diffusion burn phase. This is because the combustion environment is not as ideal as during the premixed burn phase. The piston is expanding via the working fluid, subsequently lowering in-cylinder temperatures and combustion rates (seen in Figure 2-3). Therefore, despite a more rapid heat release rate during premixed combustion (where partial combustion products should oxidize), HC and CO emissions may increase overall because of reduced oxidation rates during the diffusion burn phase. This is one reason why soybean biodiesel has

higher CO/HC emissions than beef tallow (Figure 5 & Figure 6) even though it has a smaller diffusion burn phase (Figure 2). The regression results also indicate a direct relationship between density and HC/CO emissions. A denser fuel will carry more energy by mass and, as a result of assumed constant injection volume, more mass is injected and richer mixtures can occur near the injector. As a result, there is more opportunity for HC and CO production to rise with density, despite the presence of oxygen in biodiesel (again, soybean versus beef tallow).

Conversely, CO and HC emissions are found to decrease with higher viscosity, cetane number, and energy content. This appears to be due to longer combustion duration and higher peak temperatures for the more-viscous fuels. Greater levels of diffusion burn cause higher peak cylinder temperatures, especially at higher loads, as observed via cylinder temperature results. Furthermore, with a more energetic fuel, less fuel is needed to generate power resulting in an overall leaner mixture where more oxygen is available to help oxidize both HC and CO before exiting the exhaust. For instance, beef tallow and palm biodiesels have diminished premixed burn phase (Figure 2-2) as a result of higher viscosity (Table 2-1), but their peak cylinder temperatures are higher (Figure 2-3), particularly when compared to soybean, and have lower HC and CO emissions (Figure 2-5 and Figure 2-6).

2.6.3 Particulate Matter Emissions

Table 2-8. PM and Fuel Property Pearson Correlation Coefficients.

Fuel Property	0.5 N-m		4.5 N-m		9.0 N-m		13.5 N-m		18.0 N-m	
	Unadjusted	Adjusted	Unadjusted	Adjusted	Unadjusted	Adjusted	Unadjusted	Adjusted	Unadjusted	Adjusted
Cetane Number	0.972	0.777	0.878	0.816	-0.141	-0.323	-0.342	-0.359	-0.822	-0.716
Unsat. Degree	-0.990	-0.838	-0.815	-0.738	0.260	0.436	0.454	0.469	0.886	0.795
Unsaturation%	-0.990	-0.910	-0.799	-0.686	0.332	0.440	0.499	0.529	0.868	0.768
Poly-Unsat. %	-0.979	-0.807	-0.815	-0.749	0.232	0.424	0.432	0.443	0.878	0.790
Mono-Unsat. %	0.897	0.682	0.727	0.700	-0.187	-0.435	-0.397	-0.389	-0.847	-0.785
Density	-0.985	-0.820	-0.829	-0.758	0.230	0.411	0.427	0.442	0.872	0.779
Viscosity	0.962	0.853	0.661	0.584	-0.417	-0.611	-0.604	-0.605	-0.956	-0.905
Energy Content	0.415	0.715	-0.252	-0.393	-0.994	-0.979	-0.990	-0.985	-0.722	-0.812

The regression analysis in Table 2-8 indicates that there are no strong correlations between fuel properties and PM. This is believed to be a result of competing factors. For example, the higher viscosity of beef tallow biodiesel results in more diffusion burn where PM generation is expected[1] (Figure 2-2). However, this fuel also exhibits higher peak cylinder temperatures (Figure 2-3) during this phase of combustion which acts to reduce PM. Furthermore, beef tallow has greater energy content than fuels such as jatropha and soybean and thus, less fuel is needed in the mixture, promoting leaner mixtures overall. Thus, PM behavior is difficult to discern based on non-linearity and interrelation of combustion behavior.

The unexpected behavior (higher PM for biodiesel than ULSD below 18 N-m) appears to be a result of different fuel properties and the upgraded injection system having varying influences across the load range. At low loads, the high energy content of ULSD means that less fuel is present in the cylinder and, thus, less carbon is available to make PM. Moreover, combustion is largely pre-mixed at these lower loads because of the upgraded injection system promoting finer atomization and better mixing. Therefore, the increased viscosity of biodiesel plays a large role on spray behavior[50]. At higher

loads with an increased diffusion burn phase, ULSD produces more PM than biodiesel because the oxygenation of biodiesel leans out rich fuel cores, such as near the injector, subsequently promoting oxidation in these regions[1, 56]. In the previous pump-line-nozzle system, the difference in mixing performance may not have been as pronounced because of lower injection pressures and larger fuel nozzles on the injector. Future efforts will investigate the effects of biodiesel blending with ULSD, where properties such as oxygen content may exhibit an influence in predominantly-ULSD blends, but be overshadowed by viscosity in blends that are primarily biodiesel.

2.6.4 Fuel Consumption

Table 2-9. BSFC and Fuel Property Pearson Correlation Coefficients.

Fuel Property	0.5 N-m		4.5 N-m		9.0 N-m		13.5 N-m		18.0 N-m	
	Unadjusted	Adjusted								
Cetane Number	0.458	-0.590	0.372	0.779	-0.582	0.106	0.588	0.513	0.458	-0.590
Unsat. Degree	-0.505	0.492	-0.336	-0.702	0.638	0.010	-0.558	-0.497	-0.505	0.492
Unsaturation%	-0.313	0.498	-0.095	-0.700	0.482	-0.025	-0.718	-0.681	-0.313	0.498
Poly-Unsat. %	-0.548	0.490	-0.398	-0.699	0.671	0.013	-0.512	-0.444	-0.548	0.490
Mono-Unsat. %	0.734	-0.390	0.614	0.598	-0.811	-0.108	0.271	0.189	0.734	-0.390
Density	-0.505	0.513	-0.357	-0.718	0.634	-0.013	-0.556	-0.490	-0.505	0.513
Viscosity	0.672	-0.279	0.394	0.517	-0.795	-0.241	0.374	0.326	0.672	-0.279
Energy Content	0.441	0.608	-0.243	-0.396	-0.563	-0.872	-0.026	0.064	0.441	0.608

General correlations with BSFC and measured fuel properties are not found through the biodiesel fuel properties regression in Table 2-9. This is believed to be a result of the offset of viscosity (increases BSFC through reduced premixed burn) with energy content (reduces BSFC through energy release). However, the influence of fuel properties on the combustion process results in variation of the efficiency of combustion at certain loads. Specifically, at loads below 9.0 N-m, combustion efficiency increases with cetane number, viscosity, and energy content due to reduced partial combustion emissions. Due to the inverse nature of the biodiesel properties, combustion efficiency must then

decrease with rising unsaturation degree, poly-unsaturation percentage, and density due to the higher HC and CO emissions for fuels such as soybean biodiesel with the largest values for these properties (Table 2-1 and Table 2-2). Some fuel properties still exhibit strong influence, even as combustion efficiency approaches 100% and diffusion burn becomes more pronounced. Specifically, higher unsaturation yields lower combustion efficiency, likely as a result of fuel double bonds being harder to break apart in the diffusion burn[56], causing a rise in HC and CO emissions at full load. Also, improved energy content yields higher combustion efficiency at all loads other than 13.5 N·m because of leaner mixtures causing improved oxidation.

2.7 Conclusion

In order to offset the use of the finite quantity of petroleum fuel that exists, researchers are turning to sustainable fuel sources, such as biodiesel, which carries many beneficial traits. It can be produced from a wide variety of feedstock oils, is miscible with petroleum-diesel, and can be integrated into operation using current storage, transportation, and engine technologies. However, biodiesel also has inherent differences that must be considered when using this type of fuel. For instance, the type of feedstock used to create the biodiesel will influence the chemical and physical properties of the final product. This, in turn, changes the way that the respective biodiesel burns in the engine. With advanced engine control capabilities currently available, the engine should be adjusted in order to compensate for slight changes in fuel properties, such as those experienced with biodiesel usage. As a result, a complete understanding of the effects of biodiesel properties on engine performance and emissions must be gained in order to determine how to improve both the fuel production process and the proper use of these fuels in an engine.

In this study, four diverse biodiesels are produced from soybean, jatropha, beef tallow, and palm feedstock oils. These biodiesel are then burned in a single-cylinder compression-ignition engine and compared directly with ULSD through engine fuel consumption, emissions, and combustion

behavior measurement and analysis using both non-adjusted and adjusted injection strategies. These results are used in subsequent regressions with measured fuel properties to investigate their connection. Additionally, fuel properties are compared amongst each other to determine interrelationships within the fuel. It is found that fuel density, degree of unsaturation, and oxygen content are positively correlated and are, in turn, inversely proportional to viscosity, energy content, cetane number, and mono-unsaturation. Furthermore, a longer average fatty acid chain length causes increased viscosity and energy content, but a lower fuel density.

Table 2-10. Anticipated Result of Increasing Independent Fuel Property.

Increasing Property	Peak Pressure	Pre-mixed Combustion	Peak Temperature	NO _x	CO	HC	PM	BSFC
Density	↑	↑	↑	↑	↓	↓	↓	↓
Mono-Unsaturation	↓	↓	↓	↑	↓	↓	↓	↓
Poly-Unsaturation	↓	↓	↓	↑	↓	↓	↓	↓
Viscosity	↓	↓	↓	↓	↑	↑	↑	↑
Energy Content	↑	↑	↑	↑	↓	↓	↓	↓
Oxygen Content	↑	↑	↑	↑	↓	↓	↓	↓
Volatility	↑	↑	↑	↑	↓	↓	↓	↓

From the results and regressions, the effects of individual biodiesel properties on NO_x and partial combustion production can be summarized in Table 2-10 where an increase in a given property (first column) results in the respective increase/decrease in performance metric, assuming all other properties stay the same. The strong influence of viscosity on fuel atomization and subsequent combustion behavior and emissions species suggests that injection pressure should be increased as a fuel's viscosity increases as a way of more effectively mixing the longer-chained fuel to promote premixed combustion and improve fuel consumption. Doing so will reduce partial combustion productions, likely at the expense of increased NO_x emissions. Furthermore, a more extensive investigation into PM relationship with fuel properties will help determine any connections between PM and fuel properties. This should include the effects of biodiesel blending, where properties such as oxygen content may exhibit an influence in predominantly-ULSD blends, but be overshadowed by

viscosity in blends that are primarily biodiesel. Furthermore, analyzing the individual hydrocarbon species may help shed more light on the effects of combustion on HC and PM generation.

Study 2: Influence of Biodiesel Blends and Fuel Properties in a Single-Cylinder Engine with Electronically-Controlled Fuel Injection

2.8 Abstract

Researchers across the globe are searching for energy sources to replace the petroleum-based fuels used by the transportation sector. A fuel of particular interest is biodiesel, which can be produced from a diverse variety of feedstock oils. As these feedstock oils vary based on their source, the biodiesels derived from them may have a corresponding variety of fuel properties that can alter the operation and emissions of the engines using them. An advantage to biodiesel is that it may be mixed with petroleum-based diesel, which is a common practice today. Thus, the fuel being used by a diesel engine may vary by both biodiesel blend percentage and biodiesel fuel type. As a result, the influence of biodiesel property as a function of blend is important to understand. In this study, four biodiesels, produced from palm, jatropha, soybean, and beef tallow are tested with blends of ultra-low sulfur diesel at ratios of 5%, 10%, 20%, and 50% biodiesel content. The results are compared with tests of neat diesel and the four biodiesels. Using an electrically-controlled fuel system, injection timing is modulated to normalize combustion phasing for all fuels tested to directly investigate the effects of biodiesel on combustion. The results show that fuel viscosity, energy content, and molecular structure have unique and critical influences on the combustion process that must be considered for successful engine optimization.

2.9 Introduction

Across the globe, researchers are investigating various means of replacing the world's finite fossil fuel supplies with renewable energy sources. One area of particular interest is the transportation sector where traditional fuels, such as diesel and gasoline, are being supplemented with fuels such as biodiesel and ethanol. These bio-fuels are attractive due to their relative ease of production, comparable energy density, and straightforward integration into modern infrastructure [8, 51, 56, 66, 67]. Specifically, biodiesel is intended to replace ultra-low sulfur diesel (ULSD) created from finite crude

oil for use in compression-ignition (CI) engines. Biodiesel carries inherent advantages over ULSD based on its production from renewable sources and specific fuel properties, like higher lubricity, which reduces engine wear. While biodiesel may be used in CI engines in neat form [56], the more common usage is as blends since it is miscible with ULSD [5, 51-53, 75, 76]. This is because the low volatility of neat biodiesel causes issues with the post-injection process required for Diesel Particulate Filter regeneration. In particular, this late fuel spray can accumulate in the crankcase, and dilute the oil causing excessive engine wear that reduces the longevity of the engine [77]. As a result, most engine manufacturers employ a 5-20% biodiesel maximum level [78]. Moreover, current biodiesel feedstock options can only amount to approximately 15% of the total US on-highway diesel fuel usage needs [79]. Therefore, it is currently only feasible to blend biodiesel with diesel to lessen carbon dioxide emissions. To encourage biodiesel use, the United States has passed legislation that allows blends with ULSD up to 5% to be labeled as ULSD to the consumer. This legislation also provides tax incentives and credits to individuals, blenders, and corporations that use biodiesel [81].

Past research shows that fuel properties play a crucial role in the performance and emissions of engines using biodiesel [8, 51, 56, 66, 72]. Since biodiesel is produced from a variety of feedstock oils, these effects need to be understood, both for neat fuels and blends, in order to improve both fuel performance and engine operation [56, 72]. Of particular interest are the effects of the oxygen, viscosity, molecular structure, and energy content that alter the combustion process in unique ways [17, 51, 56]. For example, viscosity increases with molecular carbon chain length. This results in a decreased level of atomization following fuel injection [62] and a longer ignition delay as a result of larger fuel droplets, and diminished initial spray penetration [63] (this assumes comparable cetane number and depends on injection system characteristics as discussed in the next paragraph). As a result, a higher viscosity fuel will have a greater diffusion burn phase at the expense of pre-mixed combustion. Furthermore, the reduced level of vaporization of biodiesel fuels (lower volatility than ULSD) causes

more rich fuel pockets during this diffusion burn phase promoting the emissions of HC, CO, and PM due to incomplete oxidization and soot agglomeration. In addition, the amount of unsaturation, or carbon double bonds, within the fatty acid chain structure of biodiesel results in fuels that are more difficult to break down during the combustion event [56]. This provides an additional opportunity for higher HC, CO, and PM emissions during diffusion burn. However, this is somewhat offset by the oxygen present in the biodiesel molecules that raises the adiabatic flame temperature while creating a leaner mixture near the injector [42, 56].

Due to the bulk modulus of compressibility of biodiesel, injection can potentially occur earlier in the engine cycle for engines that employ a mechanical fuel pump to control injection [47, 56, 65]. This behavior, combined with biodiesel's typically higher cetane number (CN) rating, can advance combustion timing resulting in greater cylinder temperatures [1]. Thus, biodiesel usage typically causes an increase in the engine output of nitrogen oxides (NO_x) [17, 49, 53, 55, 56, 65, 82]. However, recent research performed by the authors with a single-cylinder Yanmar engine upgraded to a high-pressure rail fuel injection system found a decrease in NO_x emissions when using neat biodiesel after normalizing combustion by maintaining consistent peak pressure timing between ULSD and biodiesel. Thus, the strong influence of combustion timing on engine and emissions behavior was removed [1, 65], and the decrease in NO_x was primarily assumed to be an implication of the more viscous biodiesels (seen through a regression analysis) lowering the premixed burn heat release and reducing the thermal NO_x creation mechanism. In addition to thermal NO_x , the influence of different compounds and oxygen in the fuel-rich combustion zones stemming from the injection process will change prompt NO behavior through the Fenimore mechanism [59]. This mechanism becomes particularly important to consider at equivalence ratios above stoichiometry (near injector) where production of hydrocarbon radicals promote NO production [60]. Specifically, experimental work by Park et al. indicates that the presence of oxygen in the fuel (e.g., biodiesel) acts to reduce prompt NO production [61].

The current work aims to determine the behavior of fuel properties as a function of biodiesel blend percentage with ULSD while employing adjusted combustion timing. Specifically, this study investigates the linearity of the changes in emissions and fuel consumption with biodiesel blend percentage. Moreover, this effort determines the properties that are unique to various biodiesels that account for the found behavior via a regression analysis. This is performed using four distinct biodiesels produced from palm, jatropha, soybean, and beef tallow oils via transesterification from feedstock oils. These neat biodiesels each are blended with ULSD in blends of 0% (B0), 5% (B5), 10% (B10), 20% (B20), 50% (B50), and 100% (B100) by volume.

2.10 Test Apparatus and Methodology

The engine used for this study is a naturally-aspirated four-stroke Yanmar L100V single cylinder CI engine with a cylinder displacement of 435 cubic centimeters. This engine was selected due to its small fuel consumption rates, as only ten gallons of each biodiesel fuel was produced. This is enough to perform full tests of 0%, 5%, 10%, 20%, 50%, and 100% biodiesel at five power loadings. Furthermore, the simplicity of this engine design means that multi-cylinder variability due to fluid dynamics and heat transfer was removed. Of note, the biodiesel tests performed here do not use any exhaust gas recirculation as the stock port between the exhaust and intake runners was blocked to facilitate future external cooled exhaust gas recirculation tests. This ensures that similar inlet conditions exist between each fuel tested.

In order to minimize injection variability (and subsequent combustion unevenness) due to fuel property changes, the Yanmar mechanical fuel system was replaced with a common-rail fuel system controlled by a Bosch MS15.1 engine control unit. In this system, a Bosch CP3 fuel pump is powered by a 0.5 hp, direct-current electric motor at a constant speed of 100 RPM. This engine control unit allows communication with a computer via USB connection. Using the program Bosch Modas Sport, the operating parameters of the common rail system can be adjusted per the requirements of the

experiment. For the current study, injection pressure (adjustable from 40-200 MPa) was held constant at 42.0 ± 0.03 MPa as higher injection pressure caused excessive pressure spikes at high loads during combustion at the testing speed of 1800 RPM. Injection timing is dynamically adjustable by 0.02 degrees of engine crank angle resolution. Finally, this system is capable of up to five injections per combustion event; however, only a single main injection event is used here to minimize combustion variability. Engine loading occurs via a Dyne Systems, Inc. Dymond Series 12-horsepower dynamometer. This alternating-current dynamometer is controlled with a Dyne Systems, Inc. Inter-Loc V OCS controller. Torque is measured via an in-line torque transducer (Futek TRS-605) capable of measuring from 0-200 N·m.

Other critical instrumentation includes a Micro-Motion Coriolis flow meter (model # CMF010M) used to measure fuel flow rate. Engine intake flow is determined using a Merriam laminar flow element (model # 50MW20-2) and an Omega differential pressure transducer (model # PX277-30D5V). Thermocouples provide measurement of ambient temperature, intake temperature, engine oil temperature, exhaust port temperature, and downstream exhaust temperature. Pressures are measured using appropriate transducers and include engine oil pressure, ambient air pressure, engine intake pressure fuel rail pressure, and exhaust pressure. Data for these measurements, along with torque, are recorded using an in-house LabVIEW code running on a National Instruments compact-reconfigurable input/output controller (model # 9014). These parameters are saved at a frequency of ten samples per second for two-minute durations. This collection occurs concurrently with the capture of both in-cylinder and emissions data.

Cylinder pressure measurements are gathered using a Kistler piezoelectric transducer (model # 6052C) and charge amplifier (model # 5011B). To determine engine crank angle, a Kistler incremental encoder (model # 2614B1) and a Kistler pulse multiplier (model # 2614B4) are used. This equipment provides data at a resolution of 0.5 degrees of engine crank angle. The pressure and crank angle signals

are analyzed through a custom LabVIEW program installed on a dedicated computer with a National Instruments PCI card (model # 7841). Pressure data presented in the results section comprises an average of 60 thermodynamic cycles (120 engine revolutions) as a means of reducing cycle-to-cycle variability and statistical uncertainty.

To measure gaseous emissions, an AVL SESAM emissions bench is used. This system consists of a Fourier Transform Infrared Spectrometer (FTIR) to measure carbon dioxide (CO_2), oxygen (O_2), CO, nitrogen oxide (NO), nitrous oxide (N_2O), and nitrogen dioxide (NO_2). As the FTIR cannot measure diatomic molecules, and therefore, cannot measure the quantity of oxygen in the exhaust stream, a Magnos 106 oxygen sensor is included in the sampling system. Finally, the total hydrocarbons are measured using a Flame Ionization Detector (FID). These species are recorded at a frequency of one sample per second for five minutes using a dedicated laptop running a custom LabVIEW program and TCP/IP connection. PM measurement is accomplished using an AVL Smoke Meter (model # 415SE) connected to the same emissions laptop as the SESAM system.

Testing occurs at a speed of 1800 RPM in steady-state conditions. This speed is used because it represents a mid-point in the operation range of the Yanmar and because of the applicability of the results. The Yanmar is rated to 18.0 N-m. Testing occurs at loads of 0.5 N-m (to approximate ‘unloaded’ operation while reducing variability) along with 4.5 N-m, 9.0 N-m, 13.5 N-m, and 18.0 N-m to represent 25%, 50 %, 75%, and 100% of rated load, respectively. Using the dynamometer controller in speed mode, the dynamometer will either add or reduce load to maintain 1800 RPM. Engine output power is controlled via fuel input quantity from the engine control unit. Steady state is defined as the condition where the downstream exhaust temperature (slowest variable to equilibrate) varies by less than one percent in a minute.

Table 2-11. Injection Timings (Degrees Before TDC) for ULSD and Biodiesel Blends with ULSD.

Fuel\Load	0.5 N·m	4.5 N·m	9.0 N·m	13.5 N·m	18.0 N·m
ULSD	12.5	12.5	11.0	10.0	11.0
Palm – 5%	12.45	12.21	10.69	9.70	10.71
10%	12.09	12.09	10.59	9.61	10.59
20%	11.70	11.70	10.20	9.20	10.20
50%	10.99	11.11	10.36	9.09	10.29
100%	10.50	10.80	10.10	9.21	10.20
Jatropha – 5%	12.40	12.45	10.90	9.90	10.90
10%	12.09	12.40	10.90	9.75	10.71
20%	12.00	12.25	10.59	9.61	10.59
50%	11.65	11.70	10.41	9.40	10.41
100%	11.20	11.40	10.10	9.21	10.20
Soybean – 5%	12.45	12.40	10.95	9.84	10.95
10%	12.00	12.30	10.75	9.61	10.71
20%	11.80	11.86	10.70	9.40	10.40
50%	11.40	11.80	10.50	9.26	10.25
100%	11.30	11.70	10.50	9.25	10.25
Beef Tallow – 5%	12.14	12.16	10.64	9.75	10.75
10%	11.86	11.86	10.41	10.71	10.59
20%	11.60	11.60	10.20	9.40	10.20
50%	11.95	11.11	9.80	8.90	9.90
100%	10.40	10.60	9.50	8.50	9.60

As stated previously, the combustion timing is adjusted for each blend by adjusting injection timing to maintain constant peak pressure crank angle timings among all fuels tested in this study. In a previous study, injection timing sweeps at these loadings were used to find the minimum ULSD consumption at a given load [40]. The injection timings that correspond to those minimum fuel consumption conditions are used as the injection timings for ULSD in the current work. The in-cylinder pressure data saved during the ULSD test is used to normalize the respective biodiesel based on the measured timing of peak cylinder pressure at that load [40, 71]. After each fuel test, the fuel system is drained and refilled with the next fuel blend to be tested. Between tests, approximately thirty minutes of runtime elapsed before recording data as a means of ensuring that negligible amounts of the previous fuel remained in the system. The injection timings used for ULSD and each biodiesel blend with ULSD are shown in Table 2-11.

2.11 Fuel Properties and Blend Percentage Relationships

Table 2-12. Fuel Properties of Palm Biodiesel Blends with ULSD.

Fuel	Cetane Number	Density @ 20°C (kg/m³)	Energy (kJ/kg)	Kinematic Viscosity (cSt)	Flash Point (°C)	Oxygen Content
ULSD	40.0	837.58	45636	2.578	55.8	0.00±0.00
- Palm -	-	-	-	-	-	-
5%	41.0	839.35	45336	2.608	56.8	0.53±0.02
10%	42.2	841.20	45052	2.714	57.7	1.05±0.03
20%	44.4	844.42	43273	2.849	60.7	2.10±0.06
50%	50.6	854.66	42728	3.395	71.8	5.19±0.15
100%	60.0	872.51	40479	4.605	184.8	10.17±0.29

Table 2-13. Fuel Properties of Jatropha Biodiesel Blends with ULSD.

Fuel	Cetane Number	Density @ 20°C (kg/m³)	Energy (kJ/kg)	Kinematic Viscosity (cSt)	Flash Point (°C)	Oxygen Content
ULSD	40.0	837.58	45636	2.578	55.8	0.00±0.00
- Jatropha -	-	-	-	-	-	-
5%	40.7	840.57	45328	2.426	54.7	0.54±0.01
10%	41.3	841.11	45097	2.623	52.7	1.08±0.02
20%	42.6	844.93	44434	2.650	61.7	2.13±0.05
50%	46.3	856.84	42723	3.446	72.8	5.20±0.12
100%	52.0	876.81	39809	4.440	175.0	9.97±0.23

Table 2-14. Fuel Properties of Soybean Biodiesel Blends with ULSD.

Fuel	Cetane Number	Density @ 20°C (kg/m³)	Energy (kJ/kg)	Kinematic Viscosity (cSt)	Flash Point (°C)	Oxygen Content
ULSD	40.0	837.58	45636	2.578	55.8	0.00±0.00
- Soybean -	-	-	-	-	-	-
5%	40.3	839.86	46395	2.631	42.7	0.56±0.00
10%	40.6	842.04	44958	2.712	65.6	1.12±0.01
20%	41.1	845.94	44376	2.816	64.7	2.21±0.01
50%	42.7	858.89	42635	3.193	82.8	5.30±0.03
100%	45.0	881.25	39798	4.170	164.9	9.92±0.06

Table 2-15. Fuel Properties of Beef Tallow Biodiesel Blends with ULSD.

Fuel	Cetane Number	Density @ 20°C (kg/m³)	Energy (kJ/kg)	Kinematic Viscosity (cSt)	Flash Point (°C)	Oxygen Content
ULSD	40.0	837.58	45636	2.578	55.8	0.00±0.00
- Beef Tallow -	-	-	-	-	-	-
5%	41.2	839.18	45176	2.603	52.7	0.60±0.02
10%	42.5	840.64	44787	2.707	62.7	1.19±0.04
20%	44.8	843.73	44346	2.866	60.7	2.34±0.07
50%	51.4	853.87	42742	3.470	78.8	5.55±0.17
100%	61.0	870.98	39933	4.700	169.0	10.20±0.31

Table 2-16. Neat Biodiesel Fatty Acid Component Mass Fractions.

Component	Palm	Jatropha	Soybean	Beef Tallow	Chain Length (pm)
C10:0	N/D	N/D	N/D	N/D	1525
C12:0	0.0017	N/D	N/D	N/D	1830
C14:0	0.0049	0.0003	0.0002	0.0288	2135
C15:0	N/D	N/D	N/D	0.0052	2288
C16:0	0.3219	0.1271	0.0904	0.2213	2440
C16:1	0.0013	0.004	N/D	0.0275	2421
C17:0	0.0002	0.0003	0.0003	0.0249	2593
C18:0	0.0396	0.074	0.0481	0.1746	2745
C18:1	0.494	0.4559	0.2542	0.4844	2726
C18:2	0.132	0.3365	0.525	0.0332	2707
C18:3	0.0019	0.001	0.0758	N/D	2687
C20:0	0.0026	0.0009	0.0029	N/D	3050
C22:0	N/D	N/D	0.0026	N/D	3355
C22:1	N/D	N/D	N/D	N/D	3336
C24:0	N/D	N/D	0.0006	N/D	3660
Unsaturation Degree	0.76	1.14	1.53	0.58	-
% Unsat	62.91%	79.74%	85.50%	54.51%	-
% Poly-Unsat	13.39%	33.76%	60.08%	3.32%	-

The fuel properties of the biodiesels are determined via appropriate ASTM tests and are shown in Table 2-12 through Table 2-15. The molecular composition of the neat biodiesels is also determined through gas chromatography – mass spectrometry and is shown in Table 2-16. Cetane number for biodiesel is calculated via weighted averaging using published individual fatty acid cetane numbers. With the oxygen content and cetane number of the neat biodiesel and ULSD known, intermediate blend values for these characteristics are estimated using mass-weighted averages [68, 83, 84].

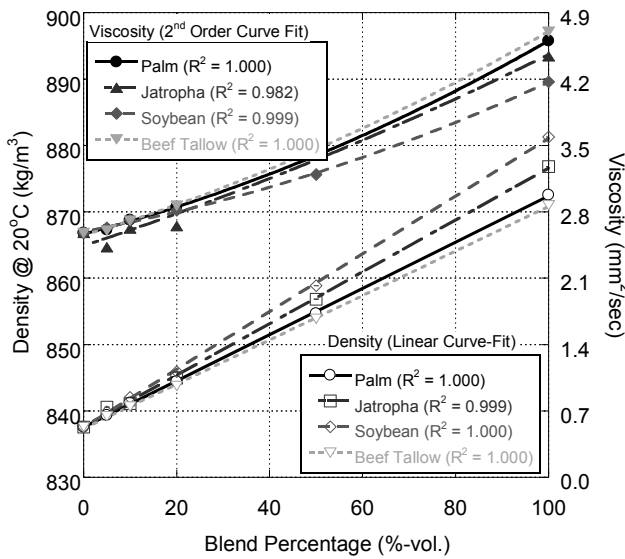


Figure 2-9. Density and Viscosity vs. Biodiesel Blend Percentage.

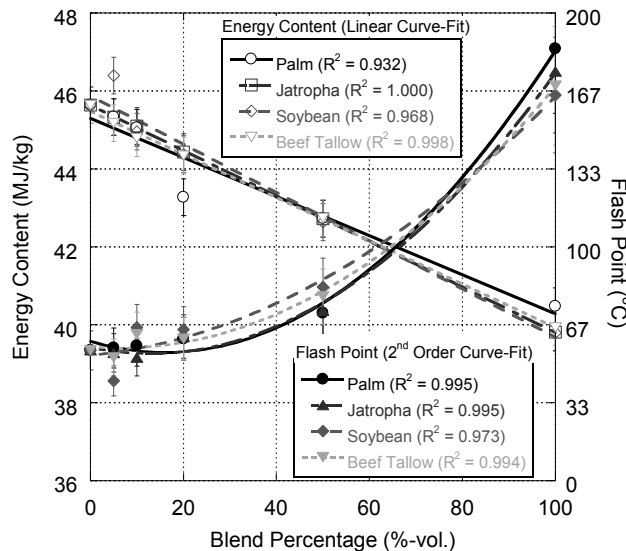


Figure 2-10. Energy Content and Flash Point vs. Biodiesel Blend Percentage.

The measured properties are plotted in Figure 2-9 and Figure 2-10 as a function of volumetric biodiesel blend percentage. Cetane number and oxygen content are not plotted since they are calculated based on an assumed linear relationship. The figures representing fuel properties vs. blend also include curve fits to determine the linear or non-linear behavior of these properties. The curve-fit results indicate linear relationships of energy content and density with blend fraction. However, a

second-order curve-fit is needed to more accurately ($R^2 > 0.95$) fit the measurements of viscosity and flash point as a result of molecular interaction [68, 85]. Of note, there is a strong inverse relationship between biodiesel blend percentage and energy content, as expected due to the increasing oxygen content in the mixture with additional biodiesel [42, 51, 56, 65].

2.12 Engine Testing Results

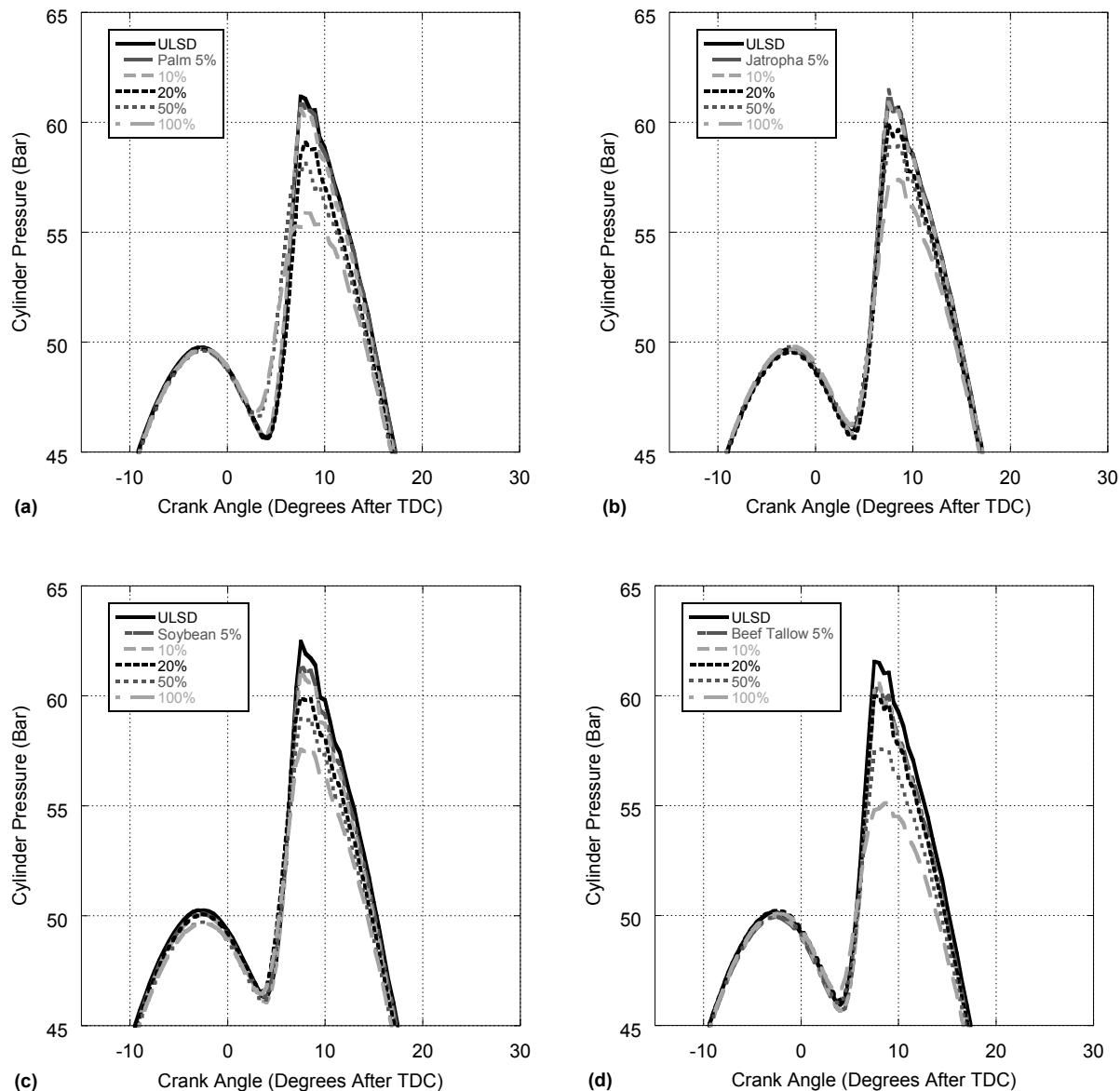


Figure 2-11. In-cylinder Pressure vs. Engine Crank Angle at 9.0 N·m of Torque for Palm (a), Jatropha (b), Soybean (c), and Beef Tallow (d) Biodiesel Blends.

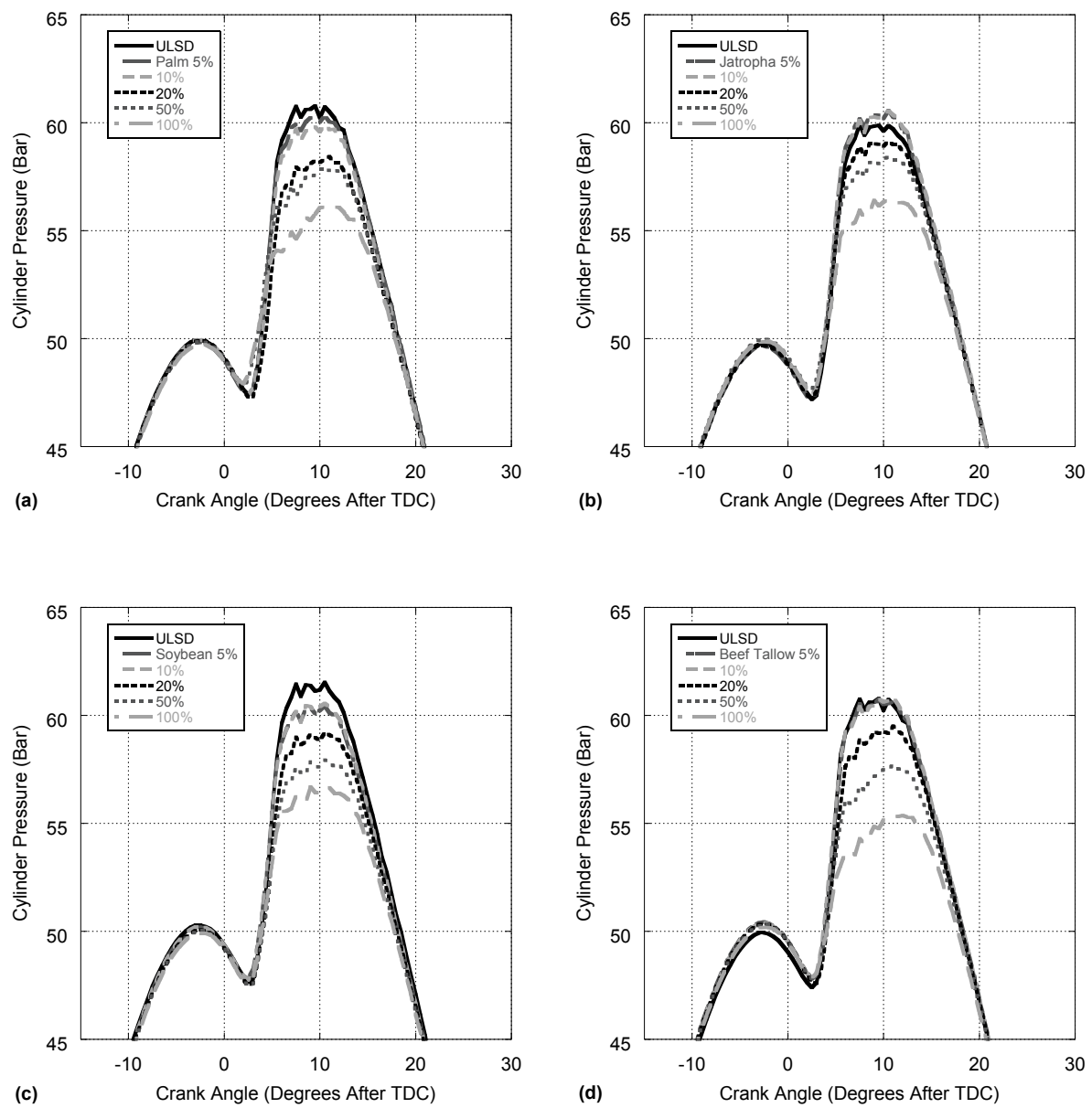


Figure 2-12. In-cylinder Pressure vs. Engine Crank Angle at 18.0 N·m of Torque for Palm (a), Jatropha (b), Soybean (c), and Beef Tallow (d) Biodiesel Blends.

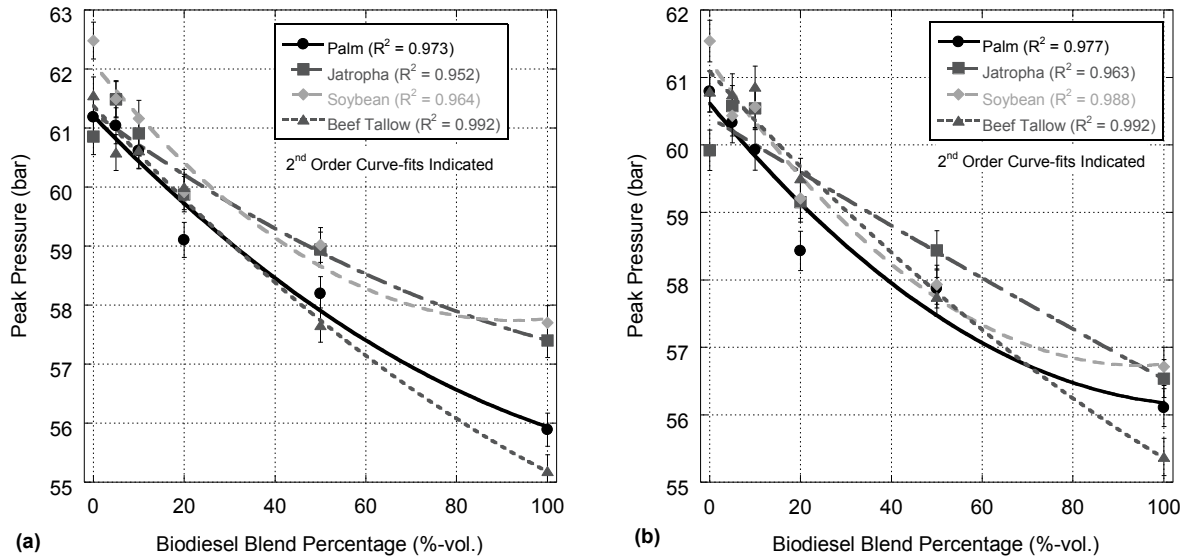


Figure 2-13. Peak Cylinder Pressure a Function of Biodiesel Blend Percentage for 9.0 N·m (a) and 18.0 N·m (b) Loads.

Cylinder pressure results are based on the average of 60 thermodynamic cycles and are shown in Figure 2-11 and Figure 2-12, with peak pressure as a function of blend percentage shown in Figure 2-13. In the interest of brevity, the plots only indicate the data from the 9.0 and 18.0 N·m cases with the results for the other tested loads available in the supplemental material. These cases were chosen because they are indicative of the behavior of other loads and illustrate the difference between a mid-range and high-end loading where the relative amounts of premixed combustion and diffusion burn are dissimilar. Specifically, as load increases, fuel input must also increase and much of the additional fuel entering the cylinder ignites during the diffusion burn phase [1]. This effect is further evident for biodiesel in comparison to ULSD since this more viscous fuel does not atomize as effectively during injection. Thus, less fuel combusts during the premixed burn phase and must instead oxidize during the diffusion burn phase.

The cylinder pressure results shown are separated by biodiesel feedstock and indicate the effects of blending on peak cylinder pressures. At the lower load presented (9 N·m) in Figure 2-11, it is apparent that neat biodiesel fuel exhibits relatively lower combustion pressures than those experienced

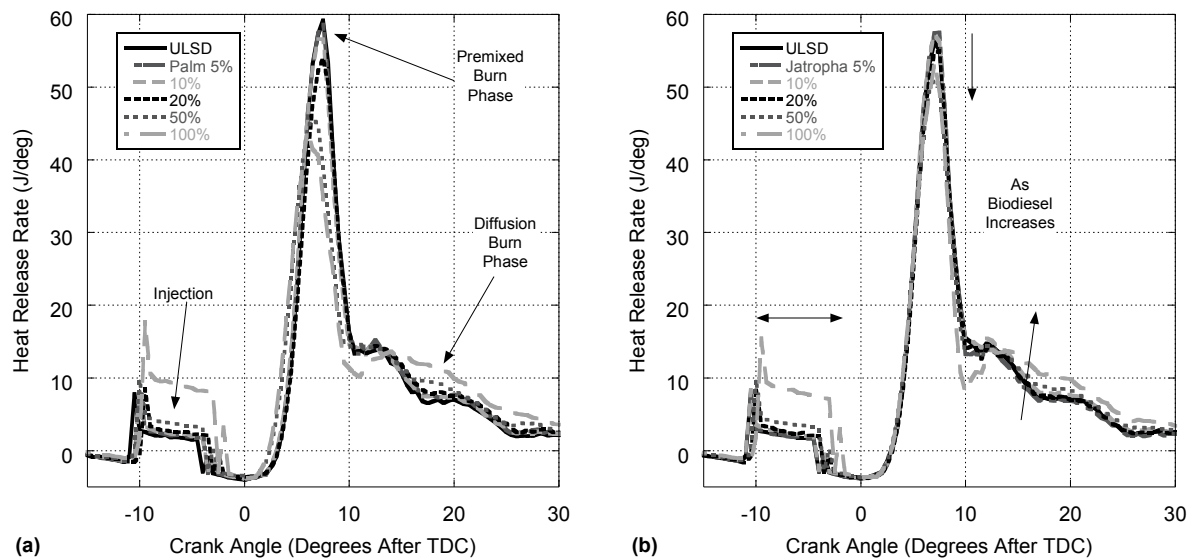
when burning ULSD and predominantly-ULSD blends (i.e., 5% and 10%). Furthermore, the peak pressures of the neat biodiesels differ amongst themselves due to their unique properties, as discussed in the previous study performed by the current authors. Results for rated torque (18 N-m) in Figure 2-12 shows more separation between peak pressures and each respective biodiesel blend. Of particular interest is the behavior of peak pressure as a function of blend percentage, which is displayed in Figure 2-13. In order to achieve an R^2 value greater than 0.95 for all fuels across both engine loads, second-order polynomial curve-fits were needed. When using linear curve-fits, only palm and beef tallow demonstrated an R^2 value greater than 0.95 with beef tallow achieving greater than 0.98 for both loads. Recalling Figure 2-10, density and energy content of the blends was linear in nature; however, viscosity and volatility are non-linear. Since all of these properties play a role in combustion speed, the effects of viscosity and volatility help cause the peak pressure to be non-linear with respect to blend percentage:

- Increased density leads to more fuel injected per unit time and a greater pressure rise.
- Lower energy content results in a reduced flame temperature and lower pressure rise.
- Higher viscosity leads to larger fuel droplets, a lower level of atomization, and reduced pressure rise.
- A lesser flash point is indicative of reduced volatility, and a reduced pressure rise.

The influence of fuel physical properties on combustion is also compounded by the chemical effects of molecular unsaturation and oxygenation on combustion kinetics [17, 42, 59-61]. Specifically, a higher unsaturated percentage fuel contains molecules that are more difficult to break apart during combustion because of carbon double bonds, but release more energy when the bonds are broken [56]. Furthermore, a fuel with a greater oxygen content will lower the equivalence ratio in all zones allowing fuel to combust more readily (more towards stoichiometry), promoting an increase in premixed combustion [42, 56]. Of interest, the peak pressures of 5% and 10% jatropha are actually higher than

ULSD and a similar non-linear behavior is noted for soybean. However, beef tallow and palm exhibit a more representative linear behavior.

Since oxygen content is relatively similar between all biodiesel fuels and associated blends, no direct relationship can be inferred regarding the relative comparison of linearity of trends. However, with respect to unsaturation, soybean and jatropha have the highest levels of poly-unsaturation (C18:2). Therefore, coupling both the physical and chemical influences indicates why soybean and jatropha peak pressures are more non-linear than palm and beef tallow. In other words, soybean and jatropha blends have a greater level of non-linearity with respect to viscosity and volatility while also being more difficult to combust as blend percentage increases due to a larger level of unsaturation.



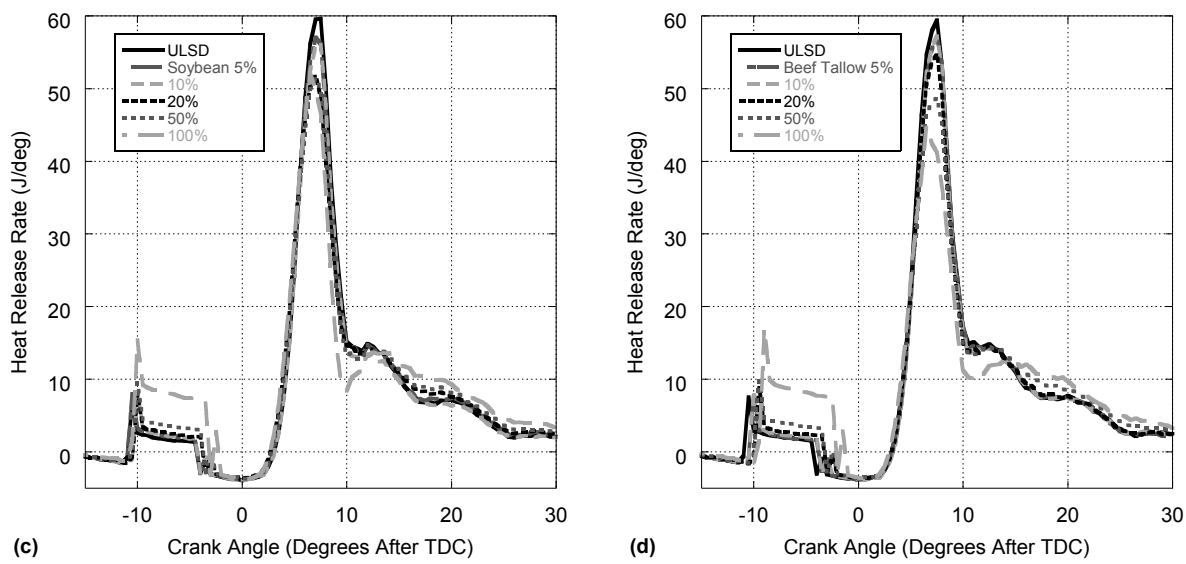
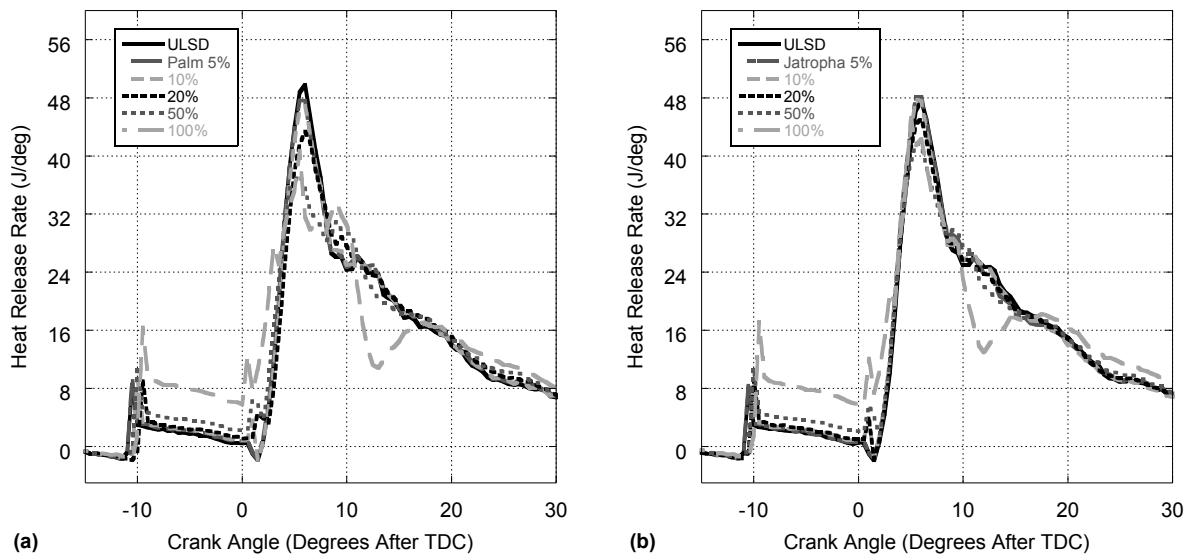


Figure 2-14. Heat Release Rate vs. Engine Crank Angle at 9.0 N-m of Torque for Palm (a), Jatropha (b), Soybean (c), and Beef Tallow (d) Biodiesel Blends.



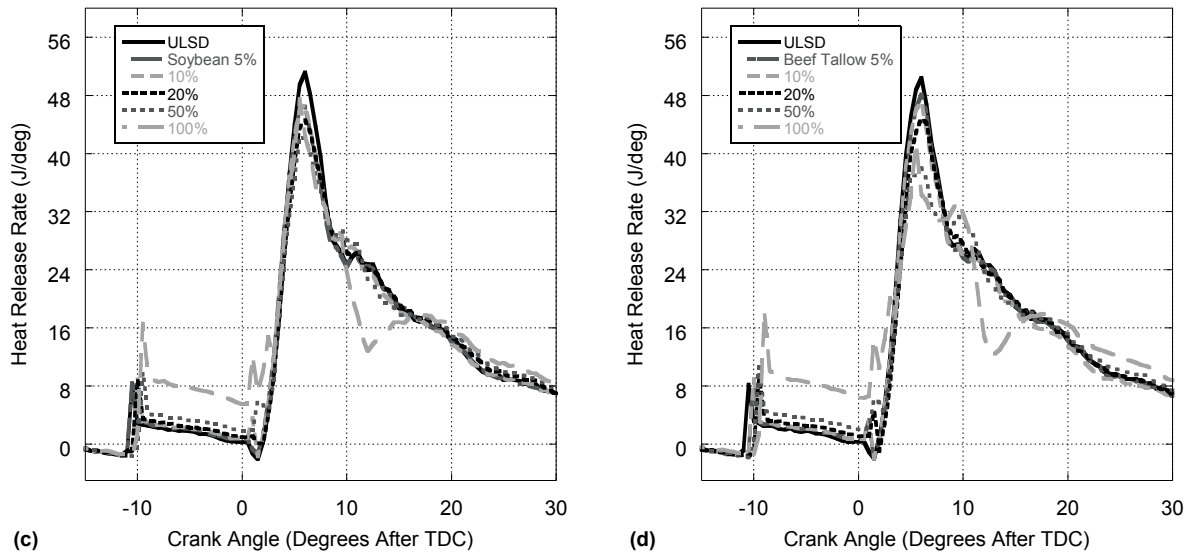


Figure 2-15. Heat Release Rate vs. Engine Crank Angle at 18.0 N-m of Torque for Palm (a), Jatropha (b), Soybean (c), and Beef Tallow (d) Biodiesel Blends.

Based on the non-linear behavior of the pressure results, particularly at low blends, it appears that even small amounts of biodiesel can have a pronounced effect on combustion due to the presence of oxygen, unsaturation, and viscosity. The effects of biodiesel blends on the heat release in the cylinder indicate how biodiesel alters the premixed and diffusion burn phases of combustion. The results shown in Figure 2-14 and Figure 2-15 correspond to the cylinder pressure results discussed at 9.0 and 18.0 N-m of loading, respectively. As blend percentage increases, the peak heat release rate is reduced and the premixed burn phase occurs over a longer duration. This is likely due to higher fuel viscosity and reduced atomization even though more fuel is added per unit time (buffered by a reduced energy content). This reaffirms the earlier presented discussion as to why peak pressures generally decrease for biodiesel blends.

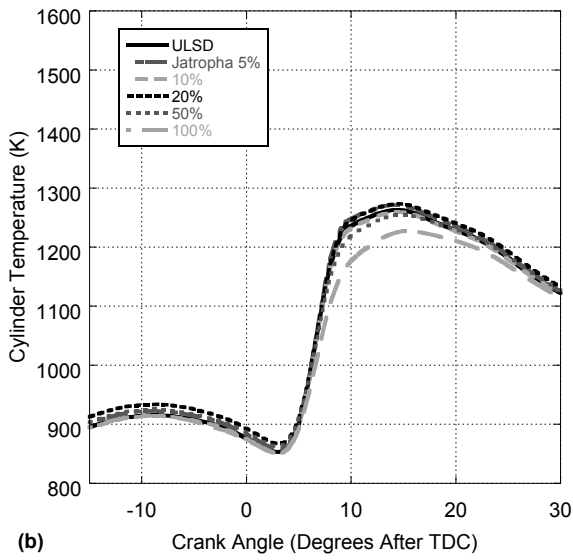
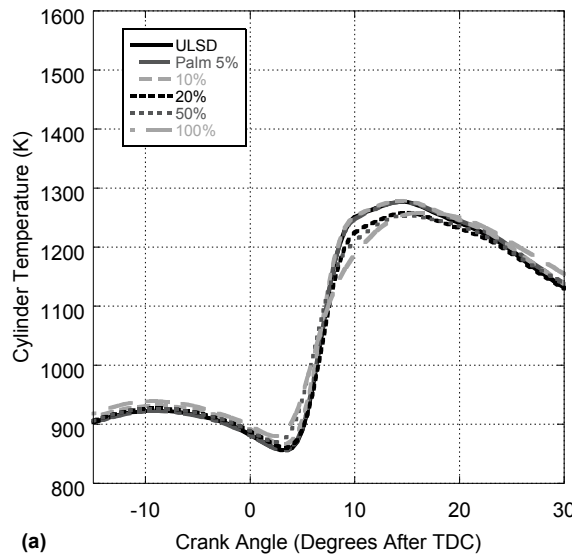
To compensate for this reduction in energy release, additional diffusion burn must occur in order to produce the needed engine shaft work. This phase of combustion, which becomes more prevalent at higher loads, occurs as the cylinder volume is more rapidly increasing. As a result, combustion pressures and associated temperatures are lessened resulting in lower NO_x emissions and

an enhanced opportunity to produce HC, CO, and PM in rich fuel zones near the injector[1]. Furthermore, as this phase of combustion occurs later in the engine cycle, there is less time for these species to oxidize before exiting the cylinder[1]. From the indicated results in Figure 2-14 and Figure 2-15, it can be seen that different biodiesels produce varying amounts of influence on heat release. For instance, the jatropha and soybean biodiesels exhibit smaller changes in combustion behavior compared to ULSD, with only high concentrations of biodiesel showing a reduction in peak heat release. In fact, the jatropha results indicate a slight increase in peak heat release rates for five and ten percent-biodiesel mixtures. On the other hand, palm and beef tallow biodiesel usage results in a greater reduction in peak heat release as biodiesel blend ratio increases, as anticipated based on peak pressure. As a consequence, these blends rely on increased diffusion burn to make the necessary power. All neat biodiesels exhibit a lower heat release rate immediately following the premixed burn, then a higher diffusion burn rate afterwards. This behavior is characterized by the increased physical ignition delay of neat biodiesel, in which fuel entering near the end of injection is not ready to combust immediately following the premixed burn.

It is important to note the variation of the injection event shown in the heat release results (around 10 to 0 degrees before top dead center). The observed increase in heat release with higher biodiesel blend percentage is a combination of a pair of assumptions used to create the heat release profiles². First, it is important to note that the common-rail fuel system allows fuel to flow based on a calculated volume [40]. For a more-dense biodiesel blend, a greater mass of fuel flows into the cylinder which results in more mass to absorb latent heat from the previous engine cycle [40]. Furthermore, the injection event is indicated as positive due to the assumption that the fuel is instantaneously atomized and vaporized after injection. Therefore, energy is being added to the gasses in the cylinder via the

² Heat release assumption discussion contributed by Jonathan Mattson

immediate vaporization of the fuel. Hence, this is not what is physically happening, and is instead an artifact of the model that is useful for further understanding the injection event [40]. For example, the observable duration of the injection event shows that biodiesel-rich blends have longer injection events because more fuel is necessary for biodiesel to achieve the same amount of power due to its reduced energy content.



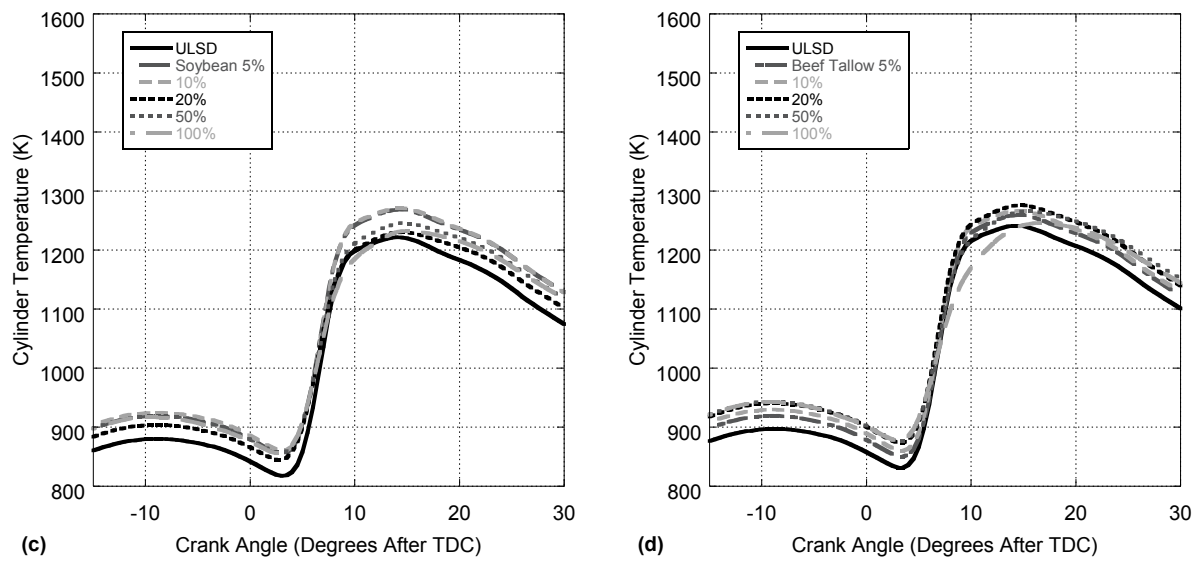
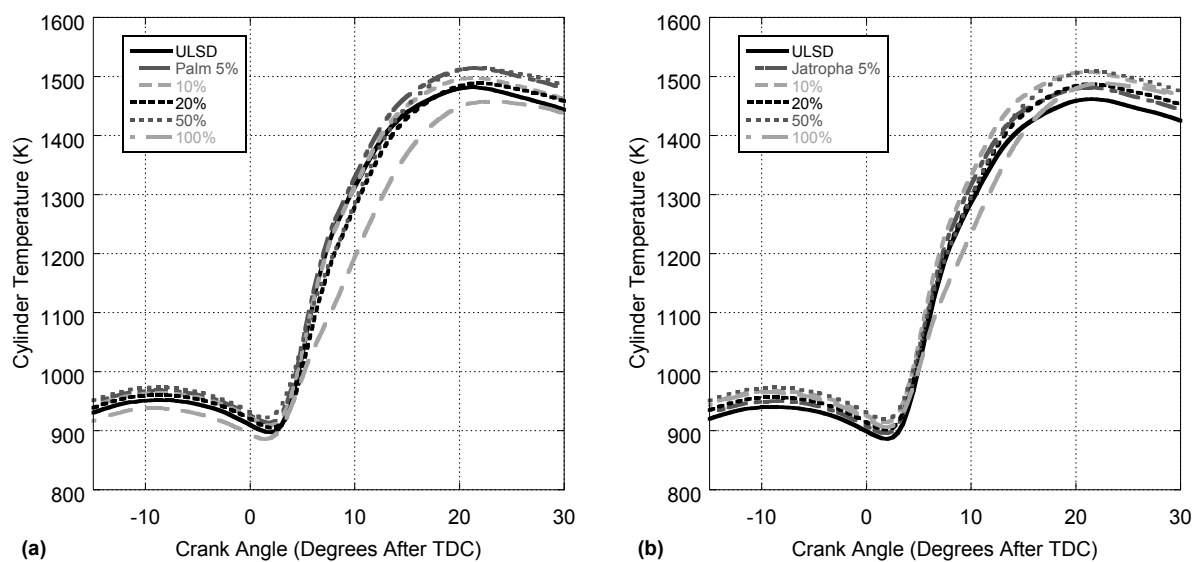


Figure 2-16. Cylinder Temperature vs. Engine Crank Angle at 9.0 N·m of Torque for Palm (a), Jatropha (b), Soybean (c), and Beef Tallow (d) Biodiesel Blends.



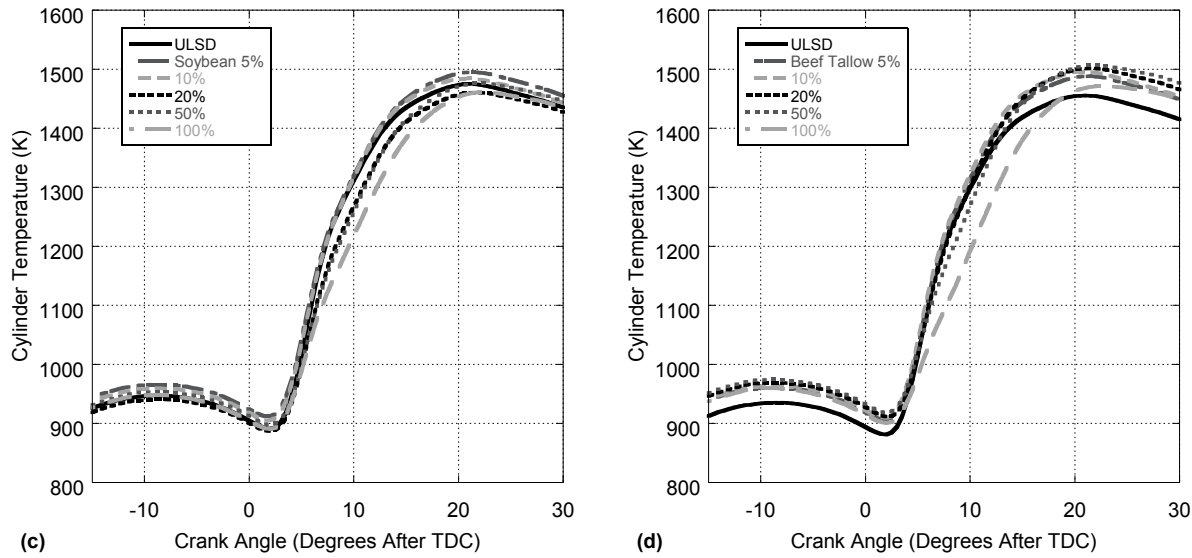


Figure 2-17. Cylinder Temperature vs. Engine Crank Angle at 18.0 N·m of Torque for Palm (a), Jatropha (b), Soybean (c), and Beef Tallow (d) Biodiesel Blends.

To aid in the understanding of the heat release results, cylinder temperature calculations for both the 9 N·m and 18 N·m cases are presented in Figure 2-16 and Figure 2-17, respectively. In the results for Figure 2-16, the peak temperature location of all blends of a specific biodiesel occurs at similar crank angles, with the exception being the neat biodiesel tests. This is because combustion at this load is predominantly pre-mixed, which should occur at approximately the same crank angle via the combustion normalization techniques used in this study. The deviation of neat biodiesel from this trend is because of its relatively larger diffusion burn phase resulting in a later combustion event as indicated in Figure 2-14. Investigating the cylinder temperature results for 18 N·m in Figure 2-17 finds higher cylinder temperatures because of the additional energy release. With respect to peak temperature location, as biodiesel blend percentage increases, the crank angle at which peak temperature occurs is later. This delay in peak combustion temperatures is because of the influence of viscosity on fuel atomization. As a more viscous fuel leaves the injector, the fuel droplets are larger and do not vaporize as effectively. Therefore, more fuel combusts at a later and less ideal part of the combustion cycle; recall, the authors adjusted the combustion timing to minimum ULSD fuel consumption. These factors

cause later peak cylinder temperatures for more viscous fuels, which results in a less efficient expansion event, higher fuel consumption, and the potential for higher HC, CO, and PM emissions [1]. Furthermore, an increase in diffusion burn (and later combustion event) raises the charge air temperature via hotter cylinder walls and a warmer residual fraction following the exhaust event since there is less time for heat transfer during expansion. Hence, there is more charge heating of the incoming mixture resulting in higher temperatures during the compression phase (seen in both Figure 2-16 and Figure 2-17). This behavior is especially noticeable in the results for beef tallow biodiesel as it is the most viscous of the biodiesel fuels tested.

It can be seen that peak cylinder temperature initially increases with biodiesel fraction until a point where additional biodiesel in the fuel causes a reduction. The blend at which the temperature begins to decrease depends on the biodiesel tested. This initial increase in peak temperature is attributed both to the presence of oxygen and to the higher density in the biodiesel/ULSD mixture. Adding a more dense fuel with additional oxygen promotes combustion and a higher adiabatic flame temperature, even in fuel-rich zones of the cylinder, thus creating the potential for enhanced temperatures [1, 42, 51, 56]. Moreover, since the initial temperature of the mixture is higher due to charge heating, the resulting temperature after combustion should be greater. These effects are offset at higher biodiesel blends because of decreased energy content of the mixture along with an increase in fuel mixture viscosity that causes more diffusion burn and later heat release during the expansion process. These cylinder pressure, heat release, and temperature results are helpful to consider as the emission and fuel consumption results are discussed.

2.12.1 Nitrogen Oxides Emissions

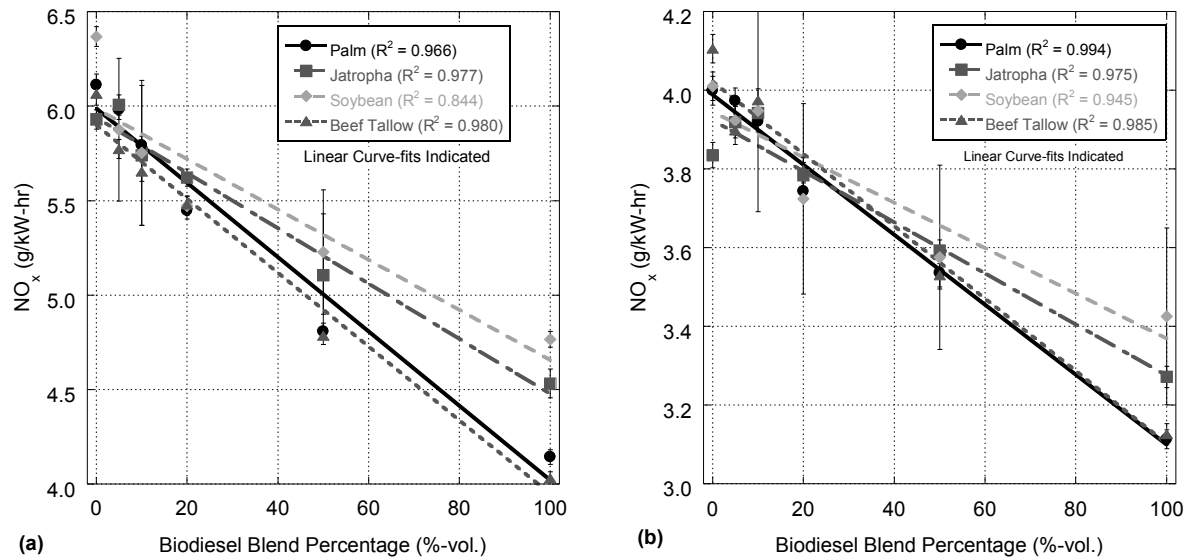


Figure 2-18. Brake-Specific NO_x Emissions as a Function of Biodiesel Blend Percentage for 9.0 N-m (a) and 18.0 N-m (b) Loads. Tier 4 Regulation at 7.5 g/kW-hr (Not Displayed).

Table 2-17. Pearson Correlation Coefficients for Brake-Specific NO_x Emissions as a Function of Increasing Biodiesel Blend Percentage.

Engine Torque (N-m)	Palm	Jatropha	Soybean	Beef Tallow
0.5	-0.622	0.121	0.783	0.146
4.5	-0.984	-0.975	-0.918	-0.991
9.0	-0.983	-0.988	-0.918	-0.990
13.5	-0.986	-0.991	-0.872	-0.971
18.0	-0.995	-0.975	-0.945	-0.985

Brake-specific NO_x emissions for both loads are shown in Figure 2-18. As load increases, the measured concentration of NO and NO₂ in the engine exhaust increases as a result of higher combustion temperatures [1, 56, 65]. However, because power rises at a higher rate than the concentration of NO_x, brake specific NO_x emissions decrease with load. Furthermore, brake-specific NO_x is shown to generally decrease as biodiesel ratio increases, as observed in the regression results presented in Table 2-17. The values indicated are Pearson correlation coefficients computed using Matlab that correspond to an increase in biodiesel blend percentage. A positive number indicates a direct correlation between blend

and a given characteristic. Likewise, a negative number indicates an inverse relationship. A value that is equal to, or greater than, ± 0.95 is considered a strong correlation that is shown in bold. Additional correlations of ± 0.90 or greater are italicized in order to indicate a weak correlation.

The inverse relationship (negative coefficient) is believed to be the cumulative effect of a multitude of different physical and chemical phenomena:

1. Gradual increase in fuel viscosity and lower volatility causing reduced atomization and less premixed burn: $\text{NO}_x \downarrow$
2. Higher cylinder temperatures for the intermediate blends ($\text{NO}_x \uparrow$) with lower cylinder temperatures for the higher blend percentages ($\text{NO}_x \downarrow$)
3. Increase in fuel unsaturation reducing energy release rate during oxidization through stronger bonds ($\text{NO}_x \downarrow$)
4. Prompt NO_x reduction as oxygen present in fuel oxidizes combustion radicals ($\text{NO}_x \downarrow$)

Furthermore, the normalizing of combustion through adjustment of injection timing does not promote a rise in NO_x with blends because of the connection between reduced rapid pressure rise and thermal NO_x when delaying the injection to account for the changing cetane numbers. Of note, the positive correlation with 0.5 N·m load for three of the fuels can be explained by the combination of lower pre-combustion temperatures and small fuel quantities, which provide adequate mixing time for all injected fuel to burn during a premixed combustion phase. This allows the influence of oxygen in the blends to raise combustion pressure and temperature subsequently increasing thermal NO_x levels. The influence of viscosity, volatility, and poly-unsaturation on combustion explains why the NO_x regression results for soybean biodiesel are not as strong as those of other fuels, indicating a non-linear behavior. These physical and chemical properties also provide justification why the 5% and 10% jatropha blends deviate from the linear trends.

2.12.2 Partial Combustion Products Emissions

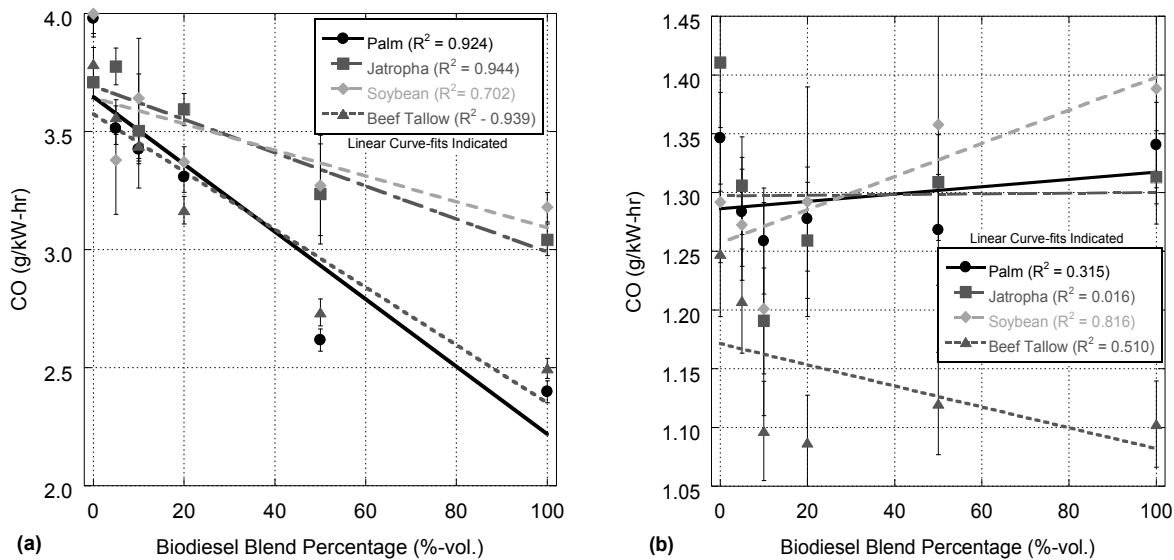


Figure 2-19. Brake-Specific CO Emissions as a Function of Biodiesel Blend Percentage for 9.0 N-m (a) and 18.0 N-m (b) Loads. Tier 4 Regulation at 8.0 g/kW-hr (Not Displayed).

Table 2-18. Pearson Correlation Coefficients for Brake-Specific CO Emissions as a Function of Increasing Biodiesel Blend Percentage.

Engine Torque (N-m)	Palm	Jatropha	Soybean	Beef Tallow
0.5	-0.679	-0.012	0.770	-0.421
4.5	-0.929	-0.701	-0.699	-0.945
9.0	-0.924	-0.944	-0.702	-0.939
13.5	-0.810	-0.701	-0.375	-0.516
18.0	0.315	0.016	0.816	-0.510

The results for brake-specific CO emissions are shown in Figure 2-19 as a function of biodiesel blend percentage for both loads. Overall, the results and the regression analysis of Table 2-18 demonstrate that CO decreases with biodiesel fraction for loads below 18.0 N-m. The behavior of CO emissions can be attributed to:

1. Increased oxygen in biodiesel contributing to a slightly hotter combustion environment and leaner burn during the diffusion phase that helps with complete combustion ($\text{CO} \downarrow$), while also promoting CO_2 dissociation ($\text{CO} \uparrow$) (Figure 2-16)

2. Diminished atomization and vaporization through higher viscosity (via chain length and molecule structure) promote richer combustion zones and an increased diffusion burn phase ($\text{CO}\uparrow$)
3. Fuel consumption also increases with biodiesel blend (indicated later), more carbon (and hydrogen) is present in the cylinder ($\text{CO}\uparrow$)
4. Lower unsaturation (beef tallow and palm) promotes fuel molecule oxidization [56] ($\text{CO}\downarrow$), contributing to more-linear behavior than the fuels with higher unsaturated levels (soybean and jatropha).

For the engine loads below 18.0 N-m, it appears that the influence of the increasing oxygen content in the blends is greater than the growth in diffusion burn and added carbon effects. However, at 18.0 N-m (Figure 2-19b), all of the fuels demonstrate (at different blend percentages) a growth in CO emissions; hence, it is assumed that diffusion burn and added carbon effects dominate. However, within statistical uncertainty, this cannot be stated for certain. Finally, drawing conclusions on CO behavior is compounded by the variety of factors that influence its production.

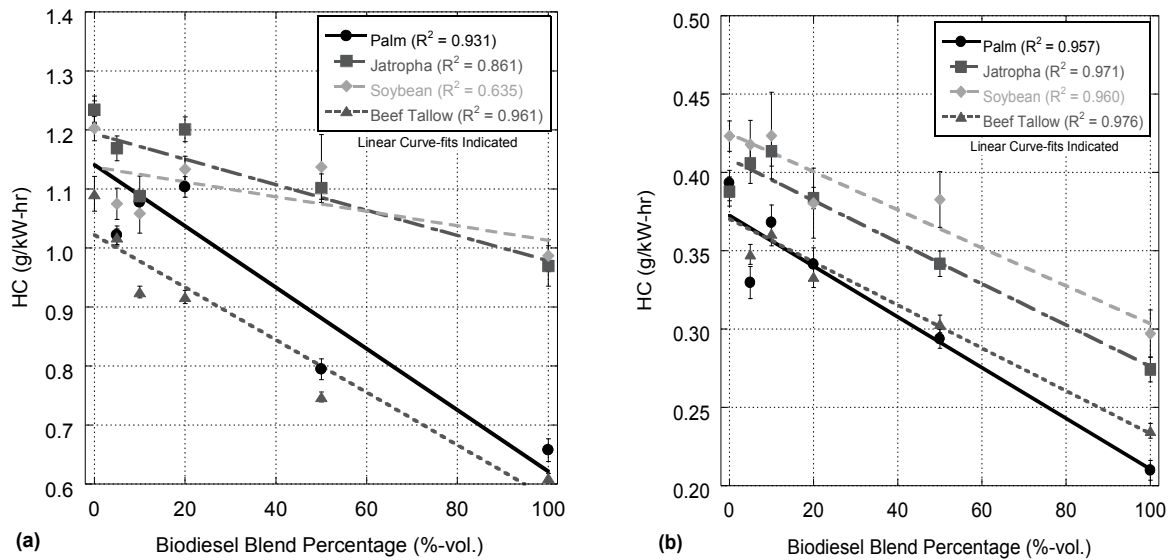


Figure 2-20. Brake-Specific HC Emissions as a Function of Biodiesel Blend Percentage for 9.0 N·m (a) and 18.0 N·m (b) Loads.

Table 2-19. Pearson Correlation Coefficients for Brake-Specific HC Emissions as a Function of Increasing Biodiesel Blend Percentage.

Engine Torque (N·m)	Palm	Jatropha	Soybean	Beef Tallow
0.5	-0.695	-0.125	0.603	-0.656
4.5	-0.928	-0.858	-0.669	-0.954
9.0	-0.931	-0.861	-0.635	-0.961
13.5	-0.972	-0.964	-0.974	-0.921
18.0	-0.957	-0.971	-0.960	-0.976

In general, HC emissions should follow a similar pattern as CO emissions since they are both partial combustion products and indicate the level of complete combustion (Figure 2-20 and Table 2-19) [1]. However, in deference to CO, HC emissions decrease with blend percentage across all loads tested. For this species, there is no influence of dissociation in the production of HC similar to CO forming from CO₂ under high temperatures; hence, one added increasing effect is eliminated. Reviewing the list of attributes, it is assumed that the oxygen influence (hotter and leaner), overwhelms the added level of diffusion burn with an increased amount of hydrogen from the fuel present.

2.12.3 Particulate Matter Emissions

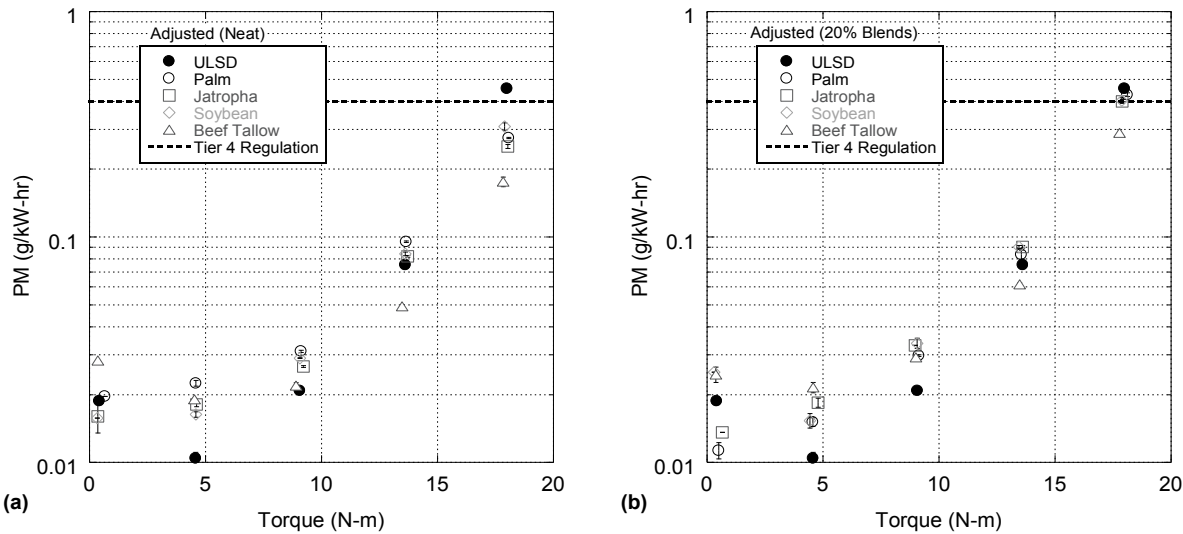


Figure 2-21. Brake-Specific PM Emissions vs. Torque for ULSD and Neat Biodiesel (a), ULSD and Twenty-Percent Biodiesel (b).

The brake-specific PM results as a function of load are shown in Figure 2-21a for ULSD and neat biodiesels along with applicable Tier 4 limits for this engine [10]. The results for 20% blends are shown as compared with ULSD in Figure 2-21b. In general, as load rises the brake-specific PM emissions initially decrease with added load because of higher cylinder temperatures and more stable combustion (presented later via combustion efficiency) that occurs primarily through the premixed burn phase (negligible diffusion burn) [1]. However, when load increases above 4.5 N-m, the increasing level of diffusion burn and abundant fuel present near the injector increases PM emissions for all fuels, despite higher cylinder temperatures and premixed burn heat release [1]. Both neat and 20% blended biodiesels produce more PM than ULSD below 13.5 N-m because of reduced atomization effectiveness due to viscosity. At 13.5 N-m, ULSD production is intermingled with biodiesel results. Finally, at 18.0 N-m, high amounts of diffusion burn, combined with the oxygenation of biodiesel, results in higher PM production for ULSD. The neat results at this load present more separation in emission levels than do the 20% blends due to the influence of increased biodiesel oxygen content that helps to lower production.

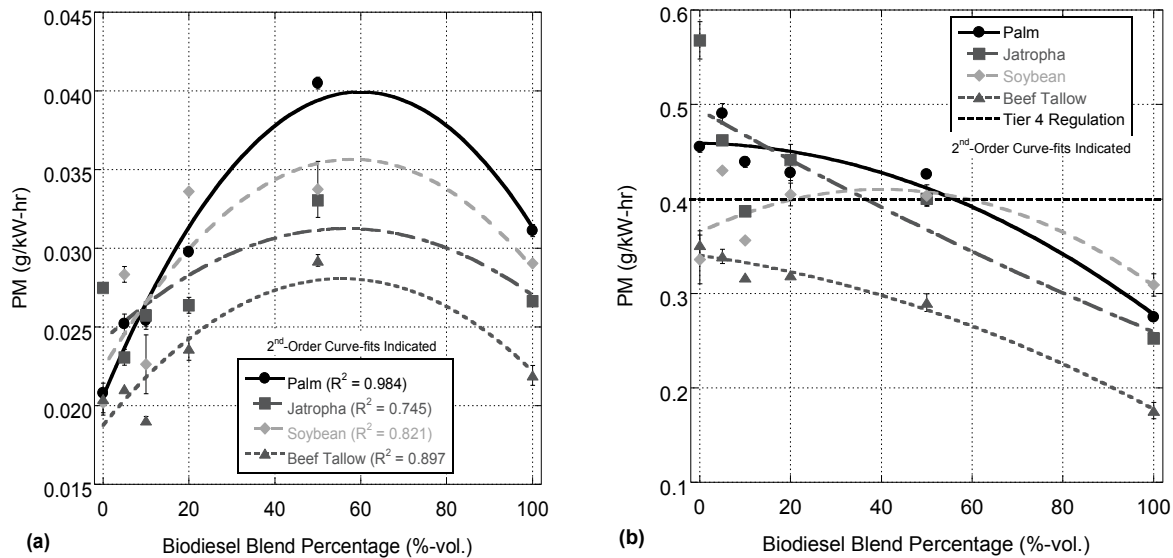


Figure 2-22. Brake-Specific PM Emissions as a Function of Biodiesel Blend Percentage for 9.0 N·m (a) and 18.0 N·m (b) Loads.

Of note, all other results besides PM are linear with increasing load; hence, they have not been included in this paper. Since the brake-specific PM results as a function of blend in Figure 2-22 demonstrate a non-linear profile, the authors thought it was pertinent to revisit the results with load.

Table 2-20. Pearson Correlation Coefficients for Brake-Specific PM Emissions as a Function of Increasing Biodiesel Blend Percentage.

Engine Torque (N·m)	Palm	Jatropha	Soybean	Beef Tallow
0.5	0.033	-0.197	0.012	0.004
4.5	0.833	0.743	0.877	0.835
9.0	0.603	0.333	0.436	0.362
13.5	0.786	0.505	0.552	-0.785
18.0	-0.934	-0.866	-0.464	-0.978

The regression results of Table 2-20 along with Figure 2-22 illustrate that the influence of biodiesel blend on PM is shown to be more variable than the CO and HC emissions. This highly non-linear behavior is observed through a peak in production for all fuels at 50% blends, particularly below 18.0 N·m. This peak in production is attributed to a mixture of competing factors, including the changing PM levels due to load, which promote either the production or reduction of PM as follows:

1. Increased viscosity reduces atomization, reduces premixed burn phase, increases diffusion burn and fuel present ($PM \uparrow$)
2. Oxygen in the fuel (particularly high blends) leans out rich fuel zones and raises combustion temperatures in the diffusion burn phase ($PM \downarrow$), it also helps oxidize soot precursors ($PM \downarrow$)
3. Unsaturated fuel molecules are more difficult to oxidize, providing an opportunity for soot precursors to form ($PM \uparrow$)

The primary exception to this non-linear behavior is beef tallow biodiesel at 18.0 N·m load, whose regression results indicate a strong linear inverse relationship between PM emissions and blend percentage (Table 2-20). Because beef tallow is the most viscous (and least unsaturated) biodiesel, it is again assumed that a major influence on PM production is the viscosity of the fuel blend. Furthermore, the effects of unsaturation, particularly for soybean and jatropha, provide an opportunity to increase in PM production at fifty percent blend before the PM-reducing effects of oxygen outweigh the influence of unsaturation [1, 56, 72].

2.12.4 Fuel Consumption

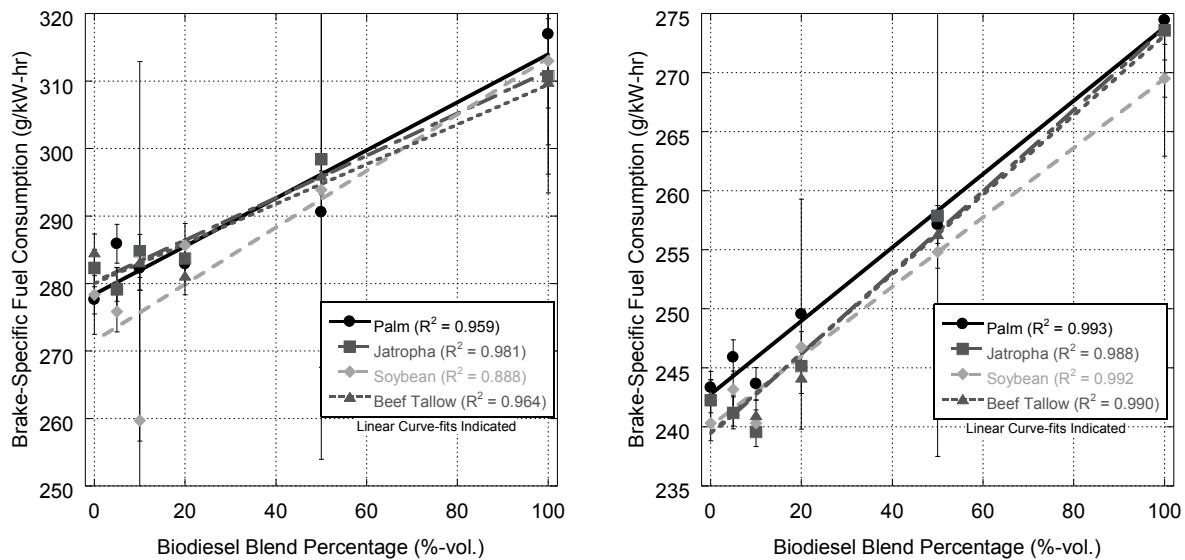


Figure 2-23. Brake-Specific Fuel Consumption as a Function of Biodiesel Blend Percentage for 9.0 N-m (a) and 18.0 N-m (b) Loads.

Table 2-21. Pearson Correlation Coefficients for Brake-Specific Fuel Consumption Emissions as a Increasing Function of Biodiesel Blend Percentage.

Engine Torque (N-m)	Palm	Jatropha	Soybean	Beef Tallow
0.5	-0.286	0.368	0.872	0.502
4.5	0.761	0.879	0.876	0.892
9.0	0.959	0.981	0.888	0.964
13.5	0.976	0.970	0.987	0.985
18.0	0.993	0.988	0.992	0.990

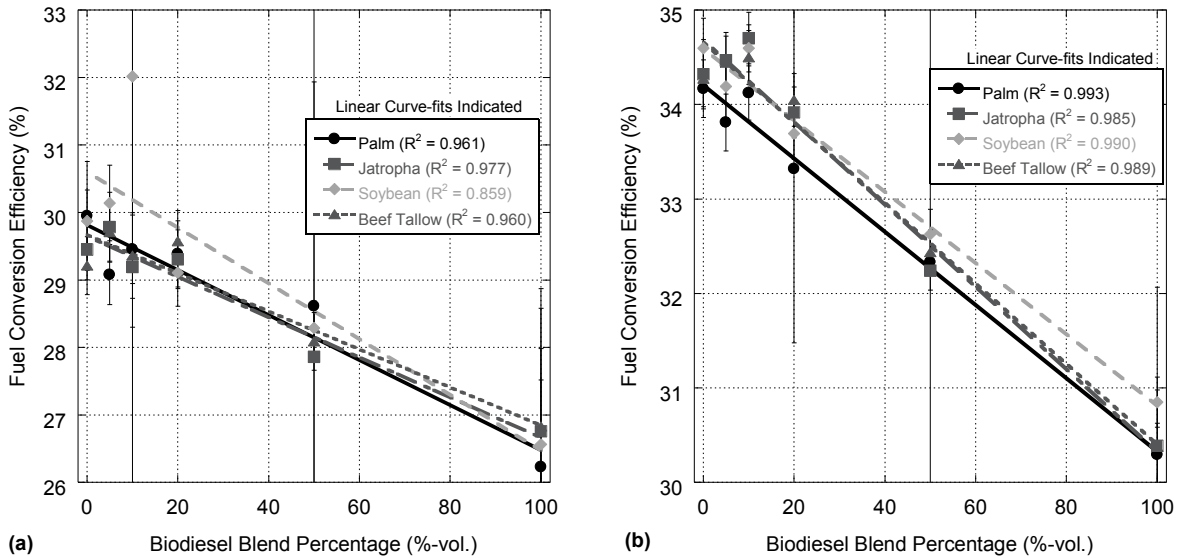


Figure 2-24. Fuel Conversion Efficiency as a Function of Biodiesel Blend Percentage for 9.0 N·m (a) and 18.0 N·m (b) Loading.

Brake-specific fuel consumption decreases with load because of the correlation between engine efficiency and output power. In other words, more useful engine work is being produced at higher loads and represents a more effective use of incoming fuel, rather than just burning fuel to overcome pumping and frictional losses at low loads [1]. The brake-specific fuel consumption results as a function of blend percentage at 9.0 and 18.0 N·m are shown in Figure 2-23. Fuel conversion efficiency at these loads are shown in Figure 2-24. In general, fuel consumption is shown to increase with biodiesel fraction, as also indicated by the regression results of Table 2-21. This rise in consumption is predominantly driven by biodiesel's lower energy content, but is also compounded by higher viscosity diminishing the premixed burn phase resulting in less constant-volume combustion. This behavior is particularly present at loads above 4.5 N·m, where more diffusion burn occurs and strong relationships with blend (and energy content) exist. Thus, the reduction of premixed burn with biodiesel blend leads to a reduction in fuel conversion efficiency. However, due to the beneficial effects of oxygen content on premixed burn, the efficiency of the combustion process is helped somewhat at low biodiesel blends [1]. This acts to improve fuel consumption, as seen through the reduction in fuel flow for low-fraction

biodiesel blends of soybean, jatropha, and palm at 18.0 N·m (Figure 2-23b). The best example of this is jatropha, which exhibits a decrease in fuel consumption from ULSD up to 20% blends because of increased oxygen content and relatively similar viscosity.

2.13 Conclusion

Substantial research is ongoing in an effort to augment current petroleum-based diesel with biodiesel, a sustainable fuel source for the transportation sector. This type of fuel carries inherent advantages, such as miscibility with petrol-based diesel and immediate application with current transportation, storage, and burning technology. Currently, engine manufacturers limit the amount of biodiesel that can be used in production engines due to negative effects on engine performance and aftertreatment systems. In an effort to gain a more thorough understanding of biodiesel blend behavior as a function of fuel properties, four unique biodiesels, made from palm, jatropha, soybean, and beef tallow, are blended with ULSD and tested in a single-cylinder compression-ignition engine. The engine used utilizes an electronically-controlled common-rail fuel system that allows researchers to precisely control injection timing. This provides the opportunity to directly compare the effects of fuel on combustion with the influence of combustion phasing removed. In addition to ULSD serving as a control, mixtures of ULSD with 5%, 10%, 20%, and 50% (vol.) biodiesel occurred. Finally, each biodiesel was tested as a neat fuel. Testing occurred at a speed of 1800 RPM with five loads from approximately unloaded to rated conditions. In addition to a presentation of brake-specific emissions and fuel consumption, regressions of these parameters with biodiesel blend percentage were presented to further aid in discussion.

The results indicate consistent general behavior with rising biodiesel blend fraction. Specifically, a general decrease in NO_x, CO, and HC emissions and an increase in fuel consumption were noted with additional biodiesel in the mixture. Therefore, this behavior would be expected in vehicle emissions when using biodiesel blends. However, at low blend percentages, these effects would be minimal.

Reduction of NO_x emissions are attributed to higher biodiesel viscosity and increased molecular unsaturation which reduce thermal NO_x via diminished premixed burn. Furthermore, the addition of oxygen acts to reduces prompt NO_x formation by oxidizing combustion radicals. Of particular interest are the PM emissions and their relationship to biodiesel blend and fuel characteristic. PM results indicate that a variety of factors are influencing the combustion event because of peak production observed near 50% blends. Specifically, the effects of reduced biodiesel energy content act to increase fuel present in the cylinder for each combustion event, promoting more PM production despite oxygen present. Biodiesel's unsaturation content appears to compound this behavior, as soybean, with high poly-unsaturation, displayed a more prominent peak in PM production at high loads than did more-saturated fuels, such as beef tallow and palm. These effects which raise PM production are overshadowed at higher blend ratios by increased fuel oxygen content that acts to help fuel combust in rich zones near the injector during the diffusion burn phase. As a result, lower PM emissions occur for biodiesel blends above 50%. Future work with a diverse amount of oxygen content in the fuel, perhaps through ULSD additives, may help determine the effects of oxygen content on PM production.

As engines and their control and fuel systems become more advanced, there exists opportunity to dynamically adjust fuel injection strategies to maximize fuel usage while maintaining or reducing harmful exhaust emissions. With respect to biodiesel, understanding the influence of blends on engine performance and emissions presents a particular challenge because of different physical and chemical properties that arise from the diverse feedstocks used in the blends. As shown here and in previous works, these changing properties have a complex influence on combustion and how injection strategy should be changed to adapt to them.

Chapter 3: Performance and Emissions Characteristics of Hydroprocessed Renewable Jet Fuel Blends in a Single-Cylinder Compression Ignition Engine with Electronically-Controlled Fuel Injection

3.1 Abstract

In an effort to offset the usage of petroleum-based jet-propellant, alternative jet fuels made from sustainable sources are being researched for their viability in both commercial and military aircraft applications. As part of the Single Fuel Forward Policy, these jet propellant fuels are also being used as a source by the military for compression ignition engines that were originally designed to burn petroleum diesel. This approach dictates that the effects of both petroleum and renewable jet propellants be tested in compression ignition engines in order to ascertain the effect of fuel properties on engine performance and emissions. In the current study, a single-cylinder compression ignition engine with variable electronically-controlled injection timing is used to compare on-road petroleum diesel fuel (i.e., ultra low sulfur diesel – ULSD) with jet propellant (Jet-A) and hydrotreated renewable jet fuel (R-8). This occurs as neat fuels and in blends of R-8 with Jet-A (5%, 10%, 20%, and 50% R-8 by volume) in order to ascertain the intermediate behavior of these blended fuels. Steady-state results for both Jet-A and R-8 indicate that when timing is normalized to equate peak pressure location (set as the optimum fuel economy for ULSD), engine performance and emissions are similar or improved as compared to ULSD. In particular, the advantageous energy content and lower viscosity of both Jet-A and R-8 reduces fuel consumption as compared to ULSD. Furthermore, nitrogen oxides, carbon monoxide, and hydrocarbon emissions are all lower for both Jet-A and R-8. Finally, particulate matter emissions of these fuels are similar to those of ULSD. As a result, re-calibration of engine injection timing in order to account for the properties of these jet fuels could prove advantageous for military logistics.

3.2 Introduction

In order to improve battlefield logistics and costs, the North Atlantic Treaty Organization and the U.S. Armed Forces have specified that all land-based military vehicles and aircraft should use a single

fuel, Jet-Propellant 8 (JP-8), as part of a Single Fuel Forward Policy (SFFP) [65, 86-89]. Implementation of this policy dictates that engines originally designed to utilize other fuels, such as ultra low sulfur diesel (ULSD), must now utilize JP-8 and associated blends with synthetic/alternative jet fuels [25, 65, 90, 91]. However, these aviation fuels differ in their physical and chemical properties, which results in significant changes to the combustion process.

JP-8 is a liquid fuel designed for military aircraft that utilize turbines for power, including fighter jets, helicopters, and turboprop engines [86, 92, 93]. This kerosene-based fuel is composed of approximately 60% of iso- and n-paraffins, about 20% mono-, di-, and tri-cycloparaffins, and aromatics [65, 94]. Because of a lower distillation curve, JP-8 has higher volatility than other petroleum based fuels, such as ULSD [88]. Additionally, this fuel has a relatively low viscosity that leads to better atomization, vaporization, and spray formation inside the combustion chamber of the turbine. The result is enhanced combustion and lower emissions than that of a more viscous fuel like ULSD [87]. Finally, the higher energy content of JP-8 as compared to other petroleum fuels means that aircraft, with limited fuel weight and volume capacity, have improved range and payload capability than would be possible with these other fuels [94]. Of note, JP-8 is similar in fuel specifications to Jet-A, which is used for commercial aviation. The difference between these fuels is the requirement that JP-8 also have corrosion and icing inhibitors, as well as additives to improve thermal stability and lubricity [25, 26, 86, 95].

The use of jet propellants in compression ignition (CI) engines as part of the SFFP is of concern since no standard exists for their cetane index [26, 95]. This characteristic, which defines a fuel's ignition delay following injection, means that the timing of combustion in a reciprocating engine will vary based on batch-to-batch cetane index variation [1]. Since turbines utilize a continuous combustion process, cetane index is not an issue. However, this is a critical concern for a CI engine, where combustion timing is a primary factor in engine performance and emissions behavior [1, 25, 65]. To compound the potential

issues with cetane index variability, jet propellant fuels also have a lower density than ULSD. This is particularly problematic for older CI engines that utilize mechanically-actuated fuel systems [16, 42, 47, 65]. These fuel systems are composed of a fuel pump containing a plunger for each engine cylinder that is actuated by an internal camshaft. The camshaft moves the plunger to pressurize fuel at the desired engine crank angle preceding injection. The rise in pressure forces fuel to travel from the pump to the injector via a fuel line that then opens to let fuel into the engine cylinder. This entire process is dependent on engine speed and the rate at which fuel pressure waves travel from the mechanical pump to the injector [16, 47, 65]. As a result, jet fuel, with a lower density (and associated bulk modulus of compressibility) than ULSD, acts to delay injection timing and subsequent combustion phasing in the cylinder as a result of slower moving pressure pulses [65]. The delay in combustion timing results in an energy release occurring later in the engine cycle than desired, which results in lower combustion efficiency and an increase in fuel consumption and hydrocarbon (HC), carbon monoxide (CO), and particulate matter (PM) emissions [65]. As a result, injection timing for mechanical fuel systems must be advanced to compensate for this behavior. For more modern CI engines that employ a high-pressure rail injection system, density also influences the injection and combustion event. This occurs because these types of fuel systems inject fuel on a volume-metered basis. Therefore, a more dense fuel will result in more fuel mass being injected into the cylinder. This affects the amount of fuel available for the start of combustion and the premixed burn phase, thus altering the combustion behavior [1, 74].

In addition to a variable cetane rating and lower density, JP-8's higher volatility acts to increase evaporation following injection, leading to changes in mixing and combustion behavior [1, 65]. However, Murphy and Rothamer, in separate works using a single-cylinder compression ignition (CI) engine with both ULSD and jet fuel blends, found that the influence of volatility on combustion, particularly during the premixed burn phase, is negligible [25, 90]. Moreover, jet propellant also has lower fuel viscosity, which will improve the effectiveness of the injector through improved atomization and act to advance

combustion [1, 90]. Therefore, in comparison to ULSD, JP-8 (and Jet-A via its similar nature) can have either a shorter ignition delay due to a higher cetane number and lower viscosity (and possibly owing to a higher volatility), or a longer ignition delay because of the effect of its lower density on the bulk modulus of compressibility.

Since both JP-8 and Jet-A are derived from petroleum crude oil, there has been significant investigation into synthetic jet fuels that can be produced through renewable sources. One synthetic option includes hydrotreated fuels that are produced via a multi-step process in order to generate the desired chemical properties for both long-term storage and combustion [27, 91, 94, 96-100]. First, feedstock oils (e.g., camelina, tallow, jatropha, and other oils and fats) are converted via transesterification [96] leaving fatty acid chains that are then deoxygenated to remove oxygen present in the fatty acid molecule. Removing oxygen facilitates proper thermal stability, characterized by fuel degradation at high temperatures when oxygen is present [101, 102]. The remaining n-paraffin hydrocarbons are hydrocracked to generate alkenes of desired length, resulting in usable aviation fuel that is approximately 10% n-alkanes and 90% iso-alkanes [91, 92]. Limited turbine experimental results using renewable jet fuel produced via this hydroprocessing methodology show a decrease in HC, CO, and PM emissions [91]. This reduction is attributed to a lower aromatic content for this fuel, as compared to petroleum-based fuels [91]. Additionally, experimentation has found that nitrogen oxides (NO_x) emissions vary between renewable and petroleum-based fuels based on engine and operation parameters [91]. Finally, carbon dioxide (CO_2) emissions and fuel consumption are found to improve for the renewable jet fuel because of an enhanced combustion efficiency and higher fuel energy content [91].

As a combined result of the implementation of the SFFP and the gradual increase of renewable jet fuel blends in military applications [25, 26, 65, 89-91, 94, 96], it is critical to investigate the behavior of renewable jet fuels in reciprocating CI engines. Of particular interest is the behavior of modern

common-rail fuel injection systems when using both petroleum and renewable jet fuels. Because of the similar fuel energy content and advantageous fuel viscosity and volatility, it may be possible to use electronically-controlled fuel injection systems to reduce jet fuel consumption to lower than that of the ULSD which the CI engine was designed to employ [65, 88].

In the current study, the viability of both Jet-A and its blends with renewable jet fuel in a CI engine is tested. The single-cylinder engine utilized is typically packaged with a mechanical pump-line-nozzle fuel system, as demonstrated in a previous study with jet propellant [65]. However, it was updated with an electronically controlled common-rail fuel system that uses a higher-quality injector and greater fuel injection pressure, subsequently improving fuel spray atomization as compared to the stock fuel system. Additionally, electronic control, combined with real-time in-cylinder pressure measurements, allows for dynamic adjustment of injection timing and quantity. This ability allows for any fuel burned in this engine to be normalized based on the timing of peak pressure for ULSD [40, 71, 103]. In the current study, Jet-A and renewable blends are tested using two injection timing strategies to determine the effects of these fuels on ignition delay and combustion. In-cylinder pressure data is also used to determine heat release rates and cylinder temperatures in the engine in order to further understand the influence of these fuels on premixed and diffusion burn behavior. Additionally, measurements of fuel flow and exhaust emissions of the jet propellant fuels are compared to those of ULSD. Findings can be used to not only understand the behavior and viability of a CI engine burning blends of various jet fuels, but also how engine operating parameters may be changed as a means of improving engine performance as a function of fuel used.

3.3 Fuels Tested (Properties measured by Daniel Tabakh)

In total, seven experiments composed of three fuels and various blends were performed using the single-cylinder CI engine. Locally purchased, non-winterized ULSD serves as the baseline fuel. Jet-A is used as a surrogate to JP-8 for the SFFP because it is locally available and it has similar properties [25,

26, 86, 95]. In addition, blends of Jet-A with 5%, 10%, 20%, and 50% (by volume) renewable jet fuel were examined. Currently, 50% represents the high end of alternative jet fuel blends that have been investigated in either military or commercial aviation applications and is the highest blending level at which these fuels are certified for aviation use [90, 91]. Finally, a test of neat renewable jet fuel was performed. This synthetic jet fuel, known as R-8, is produced through hydroprocessing using animal fats as the feedstock source [45].

Table 3-1. Fuel Properties of ULSD, Jet-A, and R-8.

Fuel	Cetane Number	Energy Content (kJ/kg) (MJ/m ³)		Viscosity (mm ² /sec)	Density @ 20°C (kg/m ³)	Flash Point (°C)
ULSD	40.0	45636±47	38224±39	2.578±0.008	837.58±0.01	55.8±8.4
Jet-A	43.4	45956±47	36811±38	1.431±0.004	801.02±0.01	49.3±6.4
5% R-8 / 95% Jet-A	44.6	46109±47	36738±38	1.473±0.004	799.03±0.01	43.1±8.4
10% R-8 / 90% Jet-A	45.8	46127±47	36633±38	1.441±0.004	797.10±0.01	45.8±5.8
20% R-8 / 80% Jet-A	48.3	46270±47	36680±38	1.445±0.004	792.74±0.01	46.4±9.3
50% R-8 / 50% Jet-A	55.8	46610±47	36241±37	1.475±0.004	779.82±0.01	44.8±7.2
R-8	68.8	46253±47	35084±36	1.542±0.005	758.54±0.01	48.5±4.6

The fuel properties of interest for this study are cetane number, energy content, kinematic viscosity, density, and flash point, as shown in Table 3-1. Due to laboratory limitations regarding cetane number measurement, the value for ULSD is assumed based on the ASTM minimum specification [104]. In addition, the cetane number for Jet-A is based on an average of the literature; however, a significant variation with this fuel (from 31.8 to 56) has been observed [25]. Finally, the R-8 cetane number was calculated by via ASTM D 976 as indicated by the manufacturer. Cetane number values for intermediate blends of Jet-A and R-8 are based on a mass-weighted average.

Energy content is measured via ASTM standard D240 using a 6200 PAAR calorimeter and 600 mg samples. Viscosity is determined using a Koehler KV4000 Series Digital Constant Temperature Kinematic Viscosity Bath per ASTM D445 specifications. ASTM standard D4052 is used to measure density with an Anton Paar Density Meter Analyzer (model 5000 M). Finally, flash point is found with a Pensky-Martens closed cup ISL by PAC (model FP93 5G2) as specified by ASTM D93. Significant uncertainty exists in the measurement of energy content and flash point as shown in Table 3-1. The energy content measured for ULSD was below all blend and neat measurements of Jet-A and R-8. This is consistent with existing literature, which states that ULSD has a lower volatility than Jet-A and R-8 [25, 65, 90].

Table 3-2. Pearson Correlation Coefficients of Measured Fuel Properties for Jet-A and R-8 Blends.

Property	Blend (%)	Energy (kJ/kg)	Viscosity (mm ² /sec)	Density @ 20 °C (g/cm ³)	Flash Pt (°C)
Blend %	1.000	-	-	-	-
Energy (kJ/kg)	0.521	1.000	-	-	-
Viscosity (mm ² /sec)	0.916	0.353	1.000	-	-
Density @ 20 °C (g/cm ³)	-1.000	-0.520	-0.916	1.000	-
Flash Pt (°C)	0.078	-0.123	0.006	-0.079	1.000

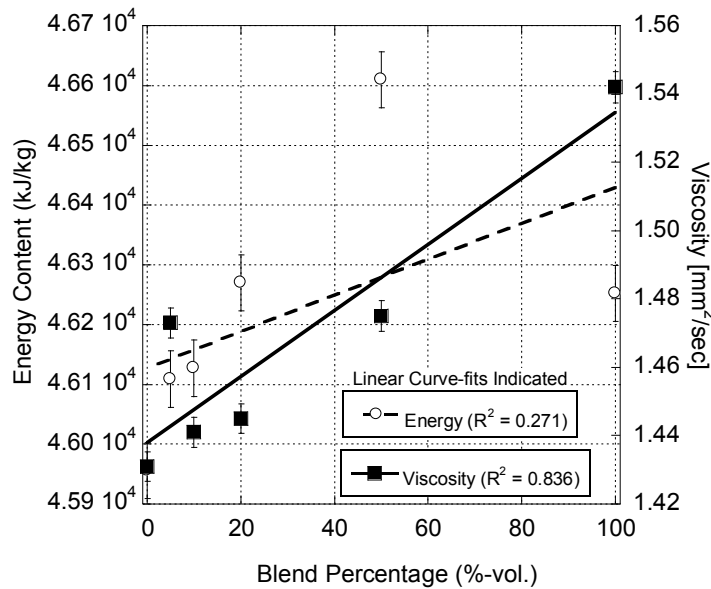


Figure 3-1. Measured Fuel Energy Content and Viscosity vs. R-8 Blend Percentage.

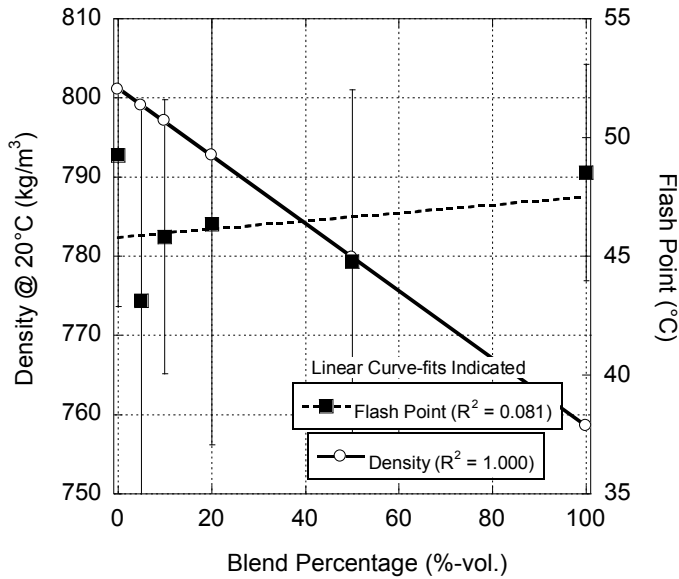


Figure 3-2. Measured Fuel Density and Flash Point vs. R-8 Blend Percentage.

The properties of Jet-A, R-8, and their blends are regressed against each other in order to determine relationships between fuel properties. This series of regressions is performed using MATLAB, the outputs of which are shown in Table 3-2. These values are Pearson coefficients, which indicate not only the strength of a relationship, but also the direct/indirect nature. For the purposes of the current work, a strong correlation is defined as one with a Pearson coefficient of greater than ± 0.95 (shown in bold). Coefficients greater than ± 0.90 are also considered as weaker dependency, and are thus shown in italics. Values for energy content and flash point are based on the original set of measurements taken for this fuel, but shall be updated as new measurements become available. These relationships are also depicted by plotting the fuel properties as a function of R-8 blend percentage as shown in Figure 3-1 and Figure 3-2.

An observed weak correlation exists between blend percentage and viscosity, with a positive coefficient indicating a direct proportionality; i.e., viscosity increases with blend percentage. Additionally, an inverse relationship exists between density and viscosity, indicating that as R-8 blend (and mixture viscosity) increases, fuel density decreases. This is caused by longer fuel molecules, which do not flow past each other as readily as smaller molecules and act to reduce fuel density [64, 74]. No

general trend can be discerned for flash point; whereas, energy content does generally increase with blend percentage although with a low R^2 -value. This information is utilized alongside the measured combustion results later in this work in order to analyze engine output emissions and fuel consumption as a function of blend percentage.

3.4 Test Apparatus and Methodology

The single-cylinder compression ignition engine used for this study is a 0.435-liter Yanmar L100V that is upgraded from the original mechanical fuel system to a common-rail fuel system. This 6.2kW engine is naturally aspirated with a single intake and exhaust port. The engine is beneficial for this type of experiment due to small fuel batches requirements and the elimination of the non-linearity in fluid dynamics and heat transfer experienced with multi-cylinder engines. This engine is manufactured with an exhaust gas recirculation port between the exhaust and intake runners in the engine head used as a means of reducing NO_x emissions. This port has been blocked for other cooled exhaust gas recirculation studies. Therefore, no exhaust gas recirculation is used in the current work. This ensures that exhaust constituents that vary between fuels tested have negligible influence on subsequent engine cycles as a result of external recirculation.

The original mechanical fuel system is replaced with a common-rail fuel system. This fuel system utilizes a Bosch MS 15.1 engine control unit (ECU) to manage fuel pressure and injection timing and quantity through the Bosch fuel injector (part #0 445 10 183). While up to five injections per combustion event are possible with this system, only a single main injection is used for this study. Injection pressure is set at 42.0 (± 0.03) MPa for these experiments. Injection pressure as high as 200 MPa is possible with this system; however, a lower pressure is chosen to protect the engine structure from excessive pressure rise during the initiation of combustion. Fuel is pressurized via a Bosch CP3 pump powered by a 0.5 hp direct-current electric motor at a constant shaft speed of 100 RPM. The ECU is connected via USB

cable to a dedicated computer running Bosch Modas Sport. Among other parameters, this interface allows operators to specify injection timing and pressure.

Engine loading is facilitated by using a Dyne Systems, Inc. Dymond Series 12-horsepower regenerative alternating-current dynamometer controlled by a Dyne Systems, Inc. Inter-Loc V OCS controller. This controller is used to operate the dynamometer in speed mode, meaning that the dynamometer will either add power or load the engine to ensure that a speed setpoint is maintained. Between the engine and dynamometer is a Futek in-line torque transducer (model # TRS-605) which provides measurement of the engine brake torque.

Engine fuel flow is measured using a Micro-Motion Coriolis flow meter (model # CMF010M). Intake air flow is measured using a Merriam laminar flow element (model # 50MW20-2) connected to an Omega differential pressure transducer (model # PX277-30D5V). Measurements of ambient air temperature, intake air temperature, exhaust port temperature, engine oil temperature, and exhaust temperature are collected using appropriate Omega type-K thermocouples. Additionally, ambient pressure, intake pressure, engine oil pressure, and exhaust pressure are collected. The aforementioned parameters are displayed and recorded using a National Instruments compact Reconfigurable Input/Output controller (model # 9014) running a custom LabVIEW program.

In-cylinder pressure measurement is achieved using a Kistler piezoelectric transducer (model # 6052C) and a Kistler charge amplifier (model #5011B). This data is recorded with corresponding engine crank angle measurement as determined by a Kistler incremental encoder (model # 2614B1) and Kistler pulse multiplier (model # 2614B4) at a resolution of 0.5 degrees of engine crank angle. This equipment is connected to a dedicated computer with a National Instruments PCI card (model # 7843). Using a custom LabVIEW program, operators can observe in-cylinder pressure measurements in near real-time for use in injection adjustment. To minimize statistical error through cycle-to-cycle variation, the

program saves 60 thermodynamic cycles (120 engine revolutions) of in-cylinder pressure data. Pressure results presented in the results section are composed of an average of those 60 combustion events.

Gaseous engine exhaust emissions are measured using an AVL SESAM emissions bench. This system used a Fourier Transform Infrared Spectrometer (FTIR) to provide individual gaseous species such as: individual hydrocarbons, nitrogen oxide, nitrogen dioxide, carbon monoxide, and carbon dioxide. Because this system is not capable of measuring diatomic molecules, a Magnos 106 oxygen sensor is included along with a flame ionization detector to measure total hydrocarbons. Data is collected using a laptop and a custom LabVIEW program utilizing TCP-IP connection. PM data is gathered using an AVL 415SE Smoke Meter connected to the same laptop through TCP-IP connection.

Table 3-3. Injection Timing for Various Fuel Blend Tests at All Engine Loadings. Unadjusted Blends are Injected at Jet-A Injection Timings at Respective Load (Bold).

Fuel	0.5 N·m	4.5 N·m	9.0 N·m	13.5 N·m	18.0 N·m
ULSD	12.5	12.5	11.0	10.0	11.0
Jet-A and Unadjusted Blends	12.1	12.1	10.6	9.6	10.7
5% R-8 - Adjusted	12.0	11.9	10.4	9.5	10.6
10% R-8 - Adjusted	11.8	11.8	10.4	9.4	10.6
20% R-8 - Adjusted	11.6	11.6	10.1	9.2	10.5
50% R-8 - Adjusted	11.1	11.1	9.7	8.8	10.4
R-8 - Adjusted	10.5	10.5	9.4	8.6	10.1

Fuel experimentations occur through a series of load sweeps from 0.5 N·m to rated load (18 N·m) by 25% increments for each fuel/blend. The engine speed is set to 1800 RPM because this speed represents a mid-point in the engine's speed envelope. The first test performed is ULSD, chosen to serve as a control for these experiments. Injection timing for ULSD is based on previous calibration efforts used to determine the minimum fuel consumption at each tested load [40]. Pressure trace data recorded at each load for ULSD is used to subsequently normalize Jet-A combustion timing based on the crank angle at which peak cylinder pressure occurs [40, 71]. Following the completion of the Jet-A load sweep, testing of 5%, 10%, 20%, 50%, and 100% R-8 blends are performed. For each subsequent mixture, data is first recorded at the 'unadjusted' injection timings that were used for Jet-A efforts.

Then, the injection timing is changed to normalize combustion timing for each blend based on the measured peak pressure crank angle. This removes the bias of combustion phasing from the analysis where ignition occurs sooner with a higher cetane number fuel [1, 65]. The resulting timings used for this study are shown in Table 3-3.

At each load during a sweep, data recording takes place at steady-state conditions. Steady-state is determined as the condition when exhaust temperature changes by less than one percent over a minute following a change in loading. At steady-state, emissions data collection occurs for a duration of five minutes at a frequency of one sample per second. Concurrently, engine data is recorded for two minutes at a frequency of twenty samples per second (with internal data filtering). During the collection of engine and emissions data, in-cylinder data is also collected for 60 thermodynamic cycles.

3.5 Results and Discussion

The results from steady-state data collection are shown in the figures and tables in this section. First, the behavior of combustion of ULSD, Jet-A, and blends with R-8 is discussed using in-cylinder pressure data along with heat release and cylinder temperature results. Then, brake-specific fuel consumption, emissions, and engine efficiencies are discussed. For each performance parameter, comparison of ULSD to neat Jet-A and R-8 (vs. torque) uses results obtained when all fuels are adjusted to equate peak pressure timing. To demonstrate the importance of injection timing, these parameters as a function of blend are also indicated with both the unadjusted and adjusted combustion timing cases. In the interest of brevity, results for 9.0 N·m and 18.0 N·m are typically presented as examples, though exceptional data is presented as necessary. These conditions are more repeatable than the 0.5 N·m and 4.5 N·m cases where cycle-to cycle-variability increases uncertainty. All data is available in the supplemental data section or upon request.

3.5.1 Combustion Behavior

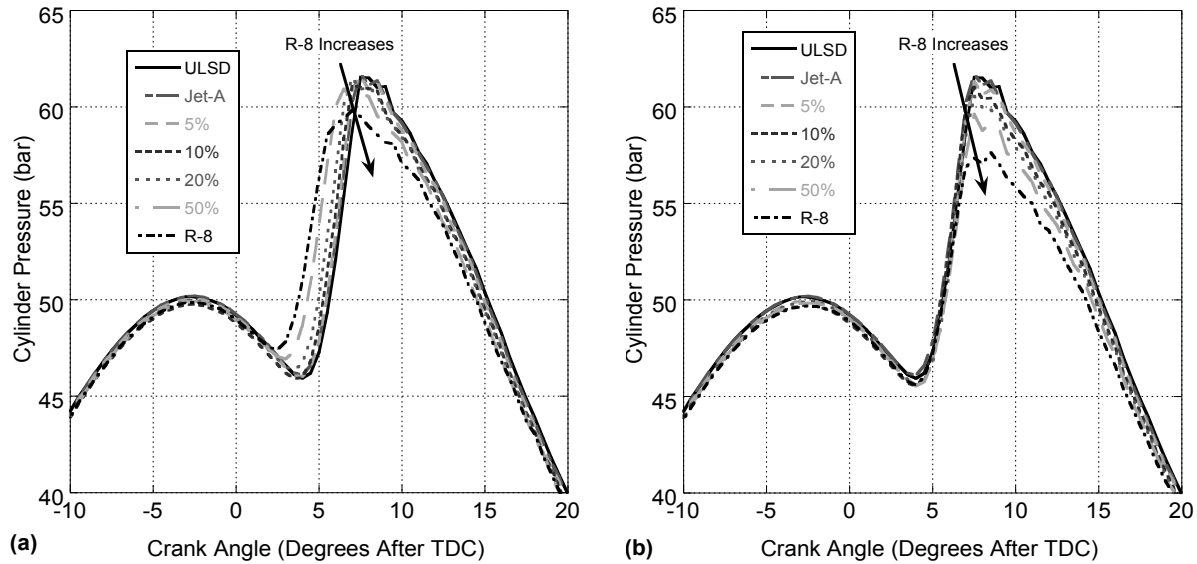


Figure 3-3. Cylinder Pressure vs. Engine Crank Angle for Unadjusted (a) and Adjusted (b) Fuel Blends at 9.0 N·m Loading.

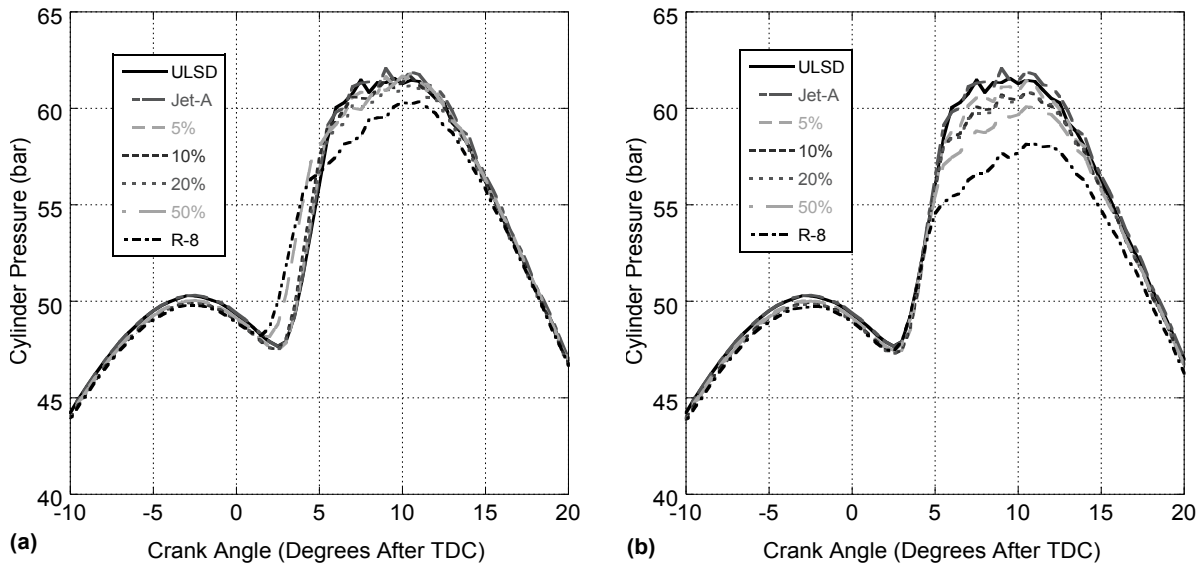


Figure 3-4. Cylinder Pressure vs. Engine Crank Angle for Unadjusted (a) and Adjusted (b) Fuel Blends at 18.0 N·m Loading.

Measurement of cylinder pressure during the compression, injection, and combustion events provides useful insight into the behavior of fuel combustion as a result of changes to fuel properties and

injection strategy. Both the unadjusted and adjusted results for ULSD, Jet-A, R-8, and Jet-A/R-8 blends are shown in Figure 3-3 and Figure 3-4. The shape and phasing of the combustion peak helps determine the relative amount of premixed and diffusion burn that occurs in the engine during the combustion process. Premixed burn is defined as the beginning phase of combustion, where fuel that has been injected, atomized, and vaporized has had ample time to mix with air in the cylinder to reach explosive conditions [1]. This is the primary form of combustion that occurs in Figure 3-3 at 9.0 N·m of load as characterized by a rapid rise in pressure (and temperature) and relatively lower peak crank angle duration in comparison to the full load condition of 18.0 N·m in Figure 3-4 (further illustrated later through the corresponding heat release figures). As long as the premixed burn phase occurs at the optimum time of the engine cycle, the rapid rise in pressure is helpful for engine power and fuel consumption [1, 40]. However, the subsequent increase in temperature influences the creation of NO_x due to its strong exponential dependence on temperature [1, 16, 40, 42, 65]. Therefore, a slight change in the timing or intensity of the premixed burn phase can have pronounced implications on engine efficiency and NO_x output.

As engine load and associated fuel injection amount increases, the diffusion burn phase becomes more prevalent, as indicated by a wider pressure peak in Figure 3-4 at 18.0 N·m. This phase occurs because fuel is still being injected and mixed in the cylinder following the premixed burn phase [1]. This condition is characterized by rich fuel pockets near the injector and by combustion that occurs as the cylinder volume is beginning to expand more rapidly. Thus, richer combustion occurs at lower temperatures providing diminished performance and increased partial combustion products, such as HC, CO, and PM [1, 40]. Similar to the pre-mixed burn discussion, a change to the timing and intensity of the diffusion burn phase can have significant implications to engine efficiency and partial combustion products.

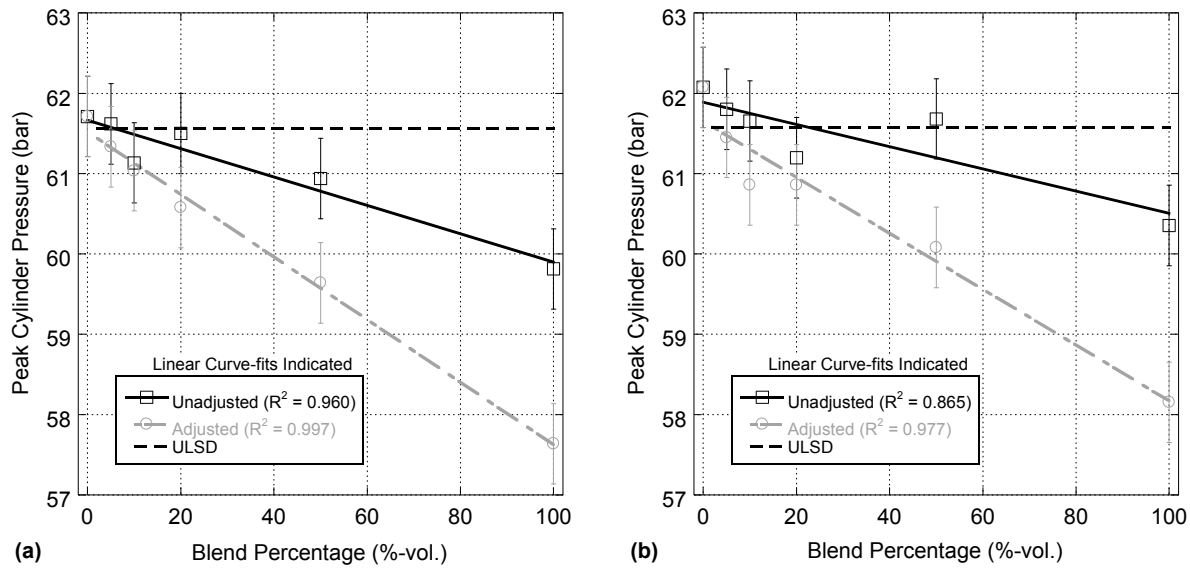


Figure 3-5. Peak Cylinder Pressure vs. Blend Percentage for Unadjusted and Adjusted Blends at 9.0 (a) and 18.0 N·m (b) Loading.

As discussed in the introduction, the combustion of Jet-A is advanced in comparison to that of ULSD for each load tested. This is because of the combined higher cetane number and lower viscosity of Jet-A which acts to alter the injection, mixing, and combustion event. The combination of these factors results in a shorter ignition delay through both the physical and chemical pathways. Specifically, the lower viscosity of the fuel provides the opportunity for better mixing with air in the cylinder. Furthermore, the cetane number reflects chemical properties, such as molecule size and configuration, that influence the readiness of the fuel to combust. Not only will these properties shorten the ignition delay, these combined factors will also enhance the premixed combustion phase for Jet-A as more fuel would be adequately mixed at the start of combustion. Findings by Murphy and Rothamer concluded that volatility does not act to shorten ignition delay, but that other factors, such as air entrainment and cetane number are more influential, particularly at high engine load [25, 90]. Due to similar measurement of fuel flash point and other fuel properties in play (such as density, viscosity, and cetane number) it is difficult to make any additional conclusions regarding volatility. With respect to the lower density of Jet-A compared to ULSD, the influence of the constant-volume injection of the common-rail

fuel system acts to lower the rate of fuel mass entering the combustion chamber, particularly before combustion begins [1, 74, 90]. This acts to reduce the premixed burn phase as less fuel mass has had time to mix before the start of combustion. Finally, since combustion is happening closer towards Top Dead Center (TDC) at a higher compression pressure, this added effect promotes higher cylinder pressures. Overall, while less Jet-A is being combusted, its peak pressure (shown later in Figure 3-5) is higher than that of ULSD because of an enhanced premixed burn and combustion phasing.

Once peak combustion pressure is aligned by delaying the injection timing, the peak cylinder pressure of the tested Jet-A is found to be equivalent to the unadjusted case (also shown later in Figure 3-5). Combustion is now happening later in the engine cycle during the expansion phase when the piston is expanding the working fluid. Hence, lower pressures are seen during fuel injection and mixing, which acts to increase the ignition delay of Jet-A. As a result, more fuel will enter the cylinder prior to the start of the premixed phase. Therefore, while combustion is happening later, more fuel is entering the cylinder prior to the initiation of combustion resulting in an equivalent peak pressure. Similar to the unadjusted case, the enhanced properties of Jet-A promotes a more efficient combustion process over ULSD and a higher pressure.

The unadjusted pressure traces indicate that as R-8 blend increases, combustion advances accordingly because of a significantly higher R-8 cetane number. This advance occurs despite the higher viscosity of R-8, which leads to reduced mixing though diminished atomization by the injector causing larger fuel droplets [62, 63]. Overall, this observed advance in combustion timing with R-8 blend causes combustion to happen more towards TDC. Initially, this advance causes the peak cylinder pressure to be higher for R-8 blends in comparison to ULSD as indicated in Figure 3-5 even though less fuel is combusted. However, the decrease in volumetric fuel energy and increase in viscosity with R-8 blend (Table 3-1) begins to play a more dominant role and starts to reduce the peak pressure below ULSD.

Similar to the prior discussion with JP-8, when adjusting R-8 blends for ignition timing, lower in-cylinder pressures are encountered since combustion is occurring when the cylinder volume is expanding more rapidly. More fuel will be injected before combustion begins; however, inspection of the cylinder pressure results show that as R-8 blend increases, the peak cylinder pressure decreases below ULSD. This is caused largely by the lower volumetric energy content and higher viscosity of R-8, which both act to reduce the premixed burn phase. The reason that R-8 blend peak pressure changes more dramatically with adjustment to injection timing than Jet-A is because of its significantly different properties. Jet-A is relatively similar to ULSD; hence, the adjustment of its injection timing is somewhat minor (see Table 3). However, the large change in cetane number of R-8 promotes a greater combustion phasing effect. Therefore, accounting for this influence demonstrates a much more dramatic change in peak pressure with blend as elucidated in Figure 3-5. Hence, the connection between peak pressure and blend percentage is stronger when combustion phasing is normalized, as indicated by the curve-fits in both Figure 3-5a and Figure 3-5b. This demonstrates why removing combustion phasing promotes a better correlation of results with respect to fuel properties.

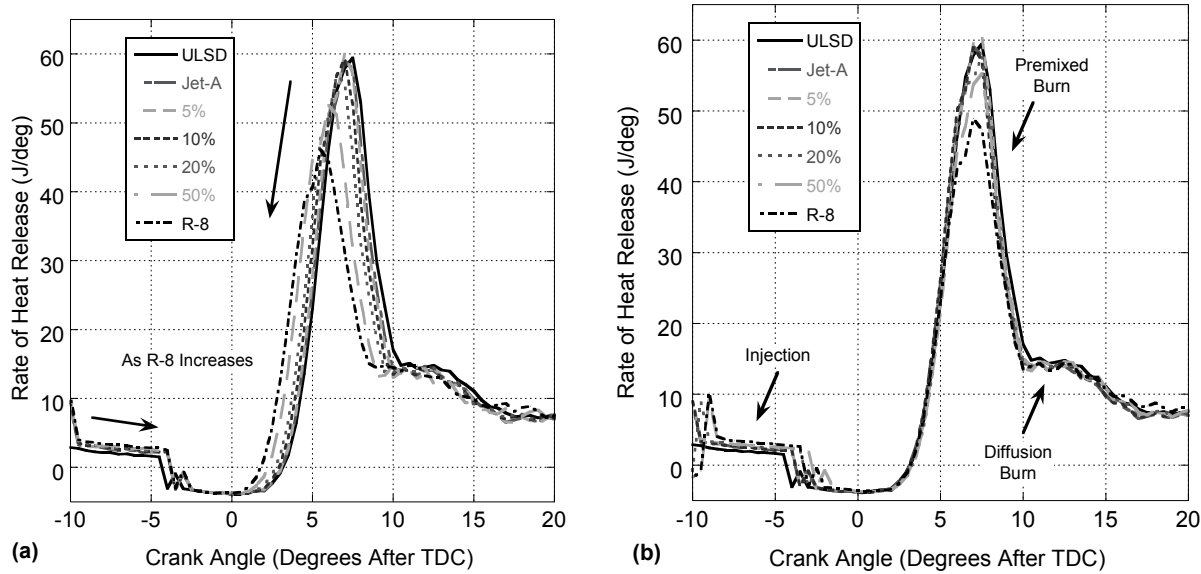


Figure 3-6. Heat Release Rate vs. Engine Crank Angle for Unadjusted (a) and Adjusted (b) Fuel Blends at 9.0 N·m Loading.

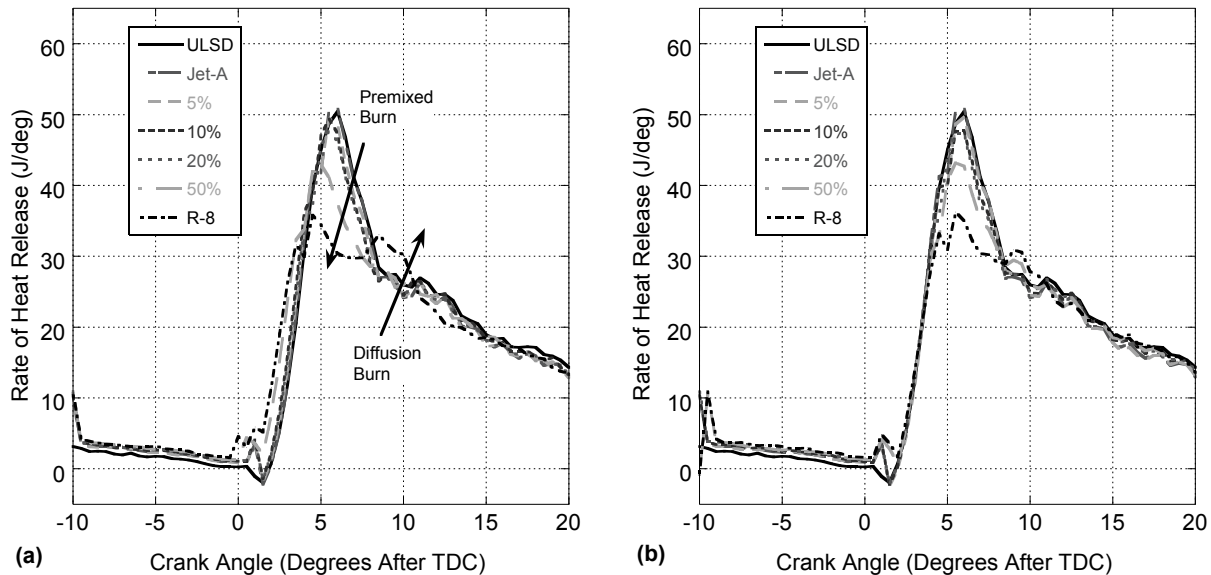


Figure 3-7. Heat Release Rate vs. Engine Crank Angle for Unadjusted (a) and Adjusted (b) Fuel Blends at 18.0 N·m Loading.

In order to visualize the changes in premixed burn and diffusion burn phases, cylinder pressure data is commonly used to perform a heat release analysis. This improves the understanding of individual components of the injection and combustion process as it indicates changes in energy in the cylinder as

a function of engine crank angle, effectively demonstrating each combustion phase [1, 40, 103]. For the purposes of this work, the results (based on 60 thermodynamic cycles) show the changes in injection duration, timing, and magnitude of premixed combustion, and relative reduction/enhancement of diffusion burn phases [103]. The results from both injection strategies at 9.0 N·m and 18.0 N·m are shown in Figure 3-6 and Figure 3-7, respectively. The heat release results clearly show the injection event, beginning around ten degrees before piston TDC (depending on load and injection strategy) and extending towards TDC based on necessary fuel input. Note that the rate of heat release during injection is indicated as a positive rate. This is an artifact of the heat release model used which assumes that fuel is instantaneously vaporized at injection; hence, energy is assumed to be added to the gas via liquid fuel instantly converting to a gas [103]³. This is not physically what is taking place, as a loss occurs in bulk gas energy during vaporization [1], but was assumed in this model to simplify computational burden during development [40]. Nevertheless, this characteristic is useful for analyzing the injection event due to clear indication of the start and end of injection [103]. Notice that the injection event for higher blends of R-8 is longer than those of Jet-A and low-concentration blends. This is best viewed in the 18.0 N·m results in Figure 3-7a. In this case, injection is still taking place for 50% R-8 and neat R-8 in both injection strategies when combustion begins. These results support the findings of the cylinder pressure analysis by indicating that R-8 injection takes longer as a result of decreased volumetric energy content (due to lower density and constant volume injection), which subsequently acts to reduce the premixed burn phase and increase the diffusion burn phase.

The influence of lower density and associated volumetric energy content for R-8 is apparent for all loads, as the premixed burn phase of combustion is proportionally diminished with increasing R-8 fraction, as shown in Figure 3-6. For the unadjusted case, the premixed burn phase for increasing R-8

³ Artifact discussion provided by Jonathan Mattson

blend is also advanced as compared to Jet-A (and ULSD) because of its increased cetane number and lower viscosity causing reduced ignition delay. Of note, Jet-A is also advanced as compared to ULSD for similar reasons. When injection timing is adjusted for R-8 blends (and neat Jet-A), the premixed burn phase increases due to additional mixing time and more fuel added, as expected via the cylinder pressure discussion. This reduction in premixed combustion due to the addition of R-8 becomes more pronounced as load increases. As a result, additional diffusion burn is necessary for R-8 (and neat Jet-A) in order to achieve the proper engine load for both injection timing strategies (Figure 3-7). Of interest, due to the relatively similar energy content of Jet-A and ULSD, the premixed burn heat release rate magnitudes are similar at both loads indicated.

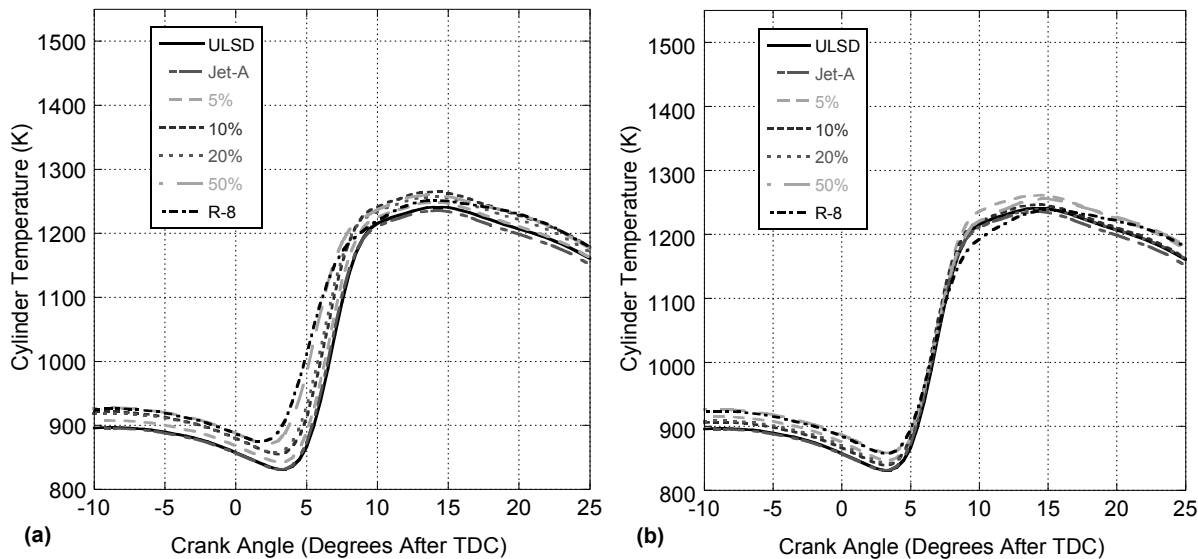


Figure 3-8. Cylinder Temperature vs. Engine Crank Angle for Unadjusted (a) and Adjusted (b) Fuel Blends at 9.0 N·m Loading.

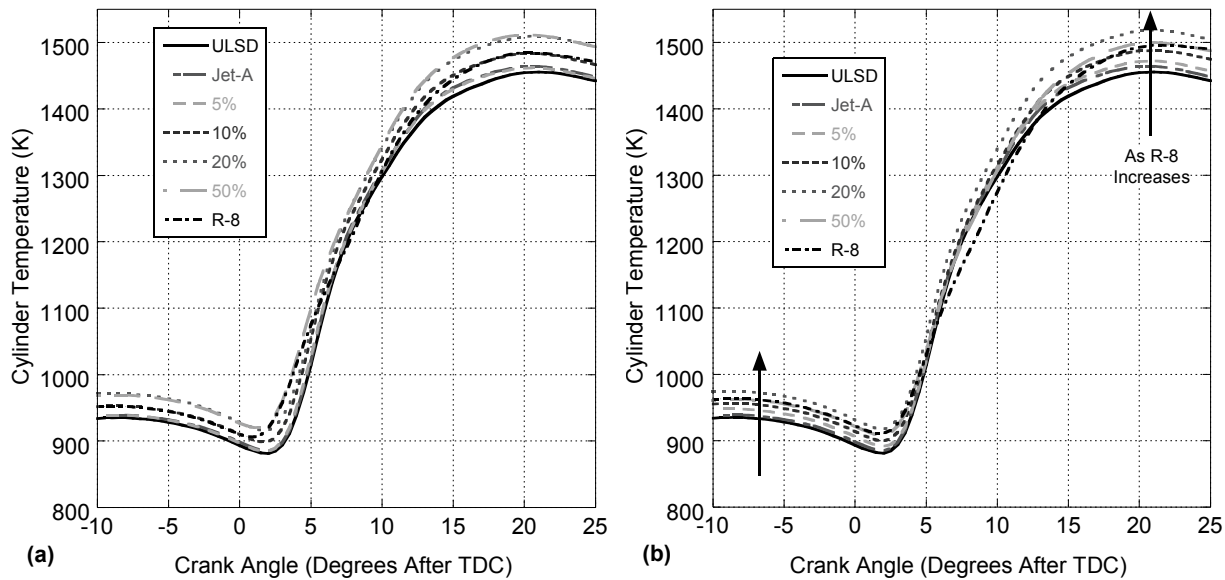


Figure 3-9. Cylinder Temperature vs. Engine Crank Angle for Unadjusted (a) and Adjusted (b) Fuel Blends at 18.0 N·m Loading.

It is important to consider the effects of premixed and diffusion burn on cylinder temperature as this will influence NO_x, CO, HC, and PM emissions [1, 16, 25, 42, 65, 93, 103]. The average cylinder temperatures calculated using the heat release model for 9.0 N·m and 18.0 N·m are shown in Figure 3-8 and Figure 3-9, respectively [103]. In general, cylinder temperatures increase with engine load because of the additional energy release. This effect carries over to subsequent engine cycles through the heating of the cylinder walls during combustion and the hotter residual gas left in the cylinder following the exhaust stroke [1]. These factors lead to hotter mixtures before combustion (e.g., 10 deg before TDC for 18.0 N·m in comparison to 9.0 N·m) reducing ignition delay as evidenced by generally delayed injection timings for all fuels with load in Table 3-3.

With respect to combustion phasing effects, the general expectation is to see higher temperatures as combustion is advanced based on the relationship between pressure and temperature through the ideal gas law. However, not all fuels demonstrate an increased temperature with advanced combustion (e.g., 10% R-8 in Figure 3-8a vs. Figure 3-8b). This is because the later combustion happens

(i.e., less premixed, more diffusion), the less time exists for heat transfer to the cylinder walls, subsequently increasing the gas temperature at exhaust valve opening. This leads to a hotter residual fraction and increased initial mixture temperature. Moreover, there is a relative change in fuel conversion efficiency and less or more fuel will be added to maintain the load (recall: timing was optimized for ULSD). Hence, the trends of maximum cylinder temperature in Figure 3-8 and Figure 3-9 are not necessarily the same because of the shifting energy addition and relative changing magnitude of premixed and diffusion burn phases. Therefore, for brevity only the normalized combustion results will be analyzed to remove the influence of combustion advancement from the discussion.

The results for 9.0 N·m (Figure 3-8) follow largely the trend with premixed burn of Figure 3-6 since combustion at this load is mainly a function of this phase. In particular, ULSD has the lowest peak cylinder temperature because it has the greatest amount of premixed burn (i.e., lowest amount of diffusion burn promoting the coolest residual gas). Correspondingly, the average cylinder temperature of Jet-A exhibits a comparable peak temperature to ULSD because of its similar premixed burn magnitude and crank angle alignment. For Jet-A and R-8 blends, the highest temperature occurs for the lower R-8 blends (e.g., 5% in Figure 3-8b). This is a function of only a slight reduction in the premixed phase and the augmented diffusion burn phase leaving a hotter residual gas (note the cylinder temperatures around TDC) with an energy input relatively similar to Jet-A. As more R-8 is added, the reduced energy content and density of this component plays a significant role in reducing cylinder temperatures. A longer fuel injection process occurs promoting a slower (less constant volume like), and relatively colder burn. Therefore, while combustion is happening closer to the opening of the exhaust valve (which promotes higher residual temperatures), its cycle temperatures are actually reduced as compared to blends such as 5% R-8.

As load increases to rated torque (Figure 3-9), the influence of diffusion burn on peak temperature becomes more visible. Specifically, the lowest peak temperatures for the adjusted case

occurs for ULSD and Jet-A due to their greater level of premixed burn. As R-8 blend increases and more diffusion burn is necessary, the cylinder temperature rises. Prior, in the discussion of the 9.0 N·m results, diffusion burn was increasing with R-8 blend percentage; however, since combustion was largely premixed, this augmented diffusion burn phase caused only a small change in residual gas temperatures. However, now there is a significantly increased level of diffusion burn late into the expansion stroke with growing blend percentage at rated load. This causes a much hotter residual gas as indicated by the wider variation of cylinder temperatures around TDC in Figure 3-9b. Therefore, the significantly longer injection event and combustion process (due to low volumetric energy content) ends up raising the end gas and initial temperatures causing overall higher temperatures for R-8 blends. In order to eliminate combustion duration effects, follow-up work could increase the fuel injection pressure with blend in order to account for the decreased volumetric energy content of R-8.

The combined results of cylinder pressure and the resultant analysis of heat release and cylinder temperature are critical in determining the influence of fuel performance and its effects on engine exhaust emissions and fuel consumption.

3.5.2 *Emissions*

As stated previously, advancement of combustion typically leads to higher cylinder pressures and temperatures during combustion. This promotes increased NO_x production due to its strong relationship with temperature. Furthermore, as combustion advances away from the optimum timing, engine fuel efficiency decreases. Therefore, more fuel (carbon and hydrogen) must enter the combustion chamber in order to produce the necessary power. This provides an additional opportunity for partial combustion products (CO, HC, and PM) to form. However, higher cylinder temperatures and longer combustion residence time prior to exhaust valve opening often overshadow this augmentation. These behaviors, combined with the variability brought about by different fuel spray behavior and chemistry, creates an opportunity for nonlinearities to occur. Therefore, because of the changes to heat

transfer and fuel conversion efficiency with phasing as indicated by the temperature outcomes, only the trends of emissions when combustion is normalized will be discussed in order to understand the direct influence of these fuels on emissions. For purposes of completeness, figures for the unadjusted results as a function of blend percentage are included for the reader's benefit.

3.5.2.1 Nitrogen Oxides Emissions

Emissions of NO_x (primarily NO with a smaller fraction of NO₂), occur due to high combustion temperatures and a relatively long residence time at these conditions. In particular, diatomic oxygen and nitrogen dissociate to collectively form NO, which also leads to the creation of NO₂ [1, 16, 65]. If the mixture temperature remains high, NO₂ will revert to NO and exit the exhaust pipe. NO₂ emissions occur due to interaction of the combustion gas with cooler regions of the cylinder, such as cylinder walls, that halt the reversion back to NO [1]. For this reason, NO₂ emissions are higher at low loads where ample cooler regions exist in the cylinder. As load increases, NO_x emissions become primarily NO [1, 16]. For the sake of brevity and because of the fact that combined NO_x is the regulated emissions species, only NO_x results are discussed here. Furthermore, NO and NO₂, available in the supplemental material, show similar behavior among all fuels discussed.

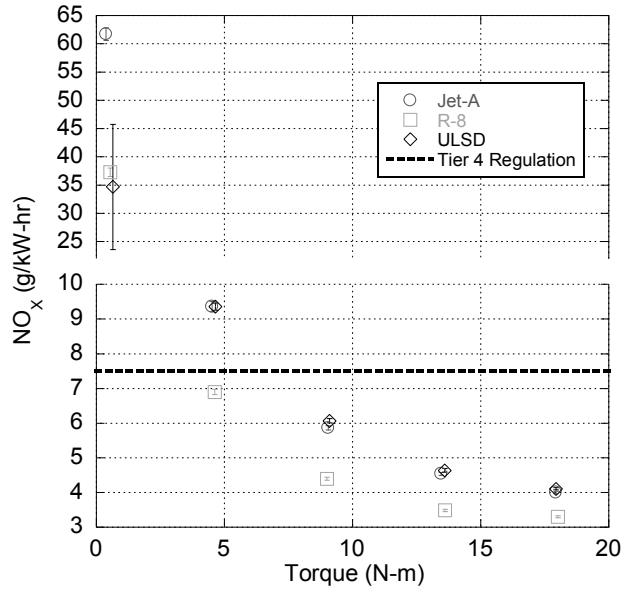


Figure 3-10. Brake-Specific NO_x Emissions vs. Torque for Adjusted R-8, Jet-A, and ULSD.

Experimentation finds an increase in exhaust NO_x concentration with load due to NO_x emissions being strongly driven by combustion temperatures [1]. However, due to the growth in power output, brake-specific NO_x emissions actually decrease with load as indicated in Figure 3-10. This figure shows the relative output of each fuel with adjusted injection compared to applicable Tier 4 levels for this engine [10]. In this figure, comparable values for Jet-A and ULSD (other than at the highly variable condition of 0.5 N-m) are presented. This is to be expected based on the cylinder temperature results and the similarity of Jet-A and ULSD heat release profiles. The small difference between the two fuels could be attributed to fact that combustion timing was optimized for ULSD and not Jet-A. Neat R-8 however, has significantly lower NO_x emissions above 0.5 N-m. While adding R-8 causes the temperature to increase, the large reduction in pre-mixed burn phase (i.e., constant-volume combustion) due to a decreasing volumetric energy content results in a slower and more gradual energy release rate, influencing thermal NO_x emissions. Furthermore, the different chemistry profile of R-8 (as noted by the significantly dissimilar cetane number) may play a role in decreasing the prompt NO_x chemistry pathway.

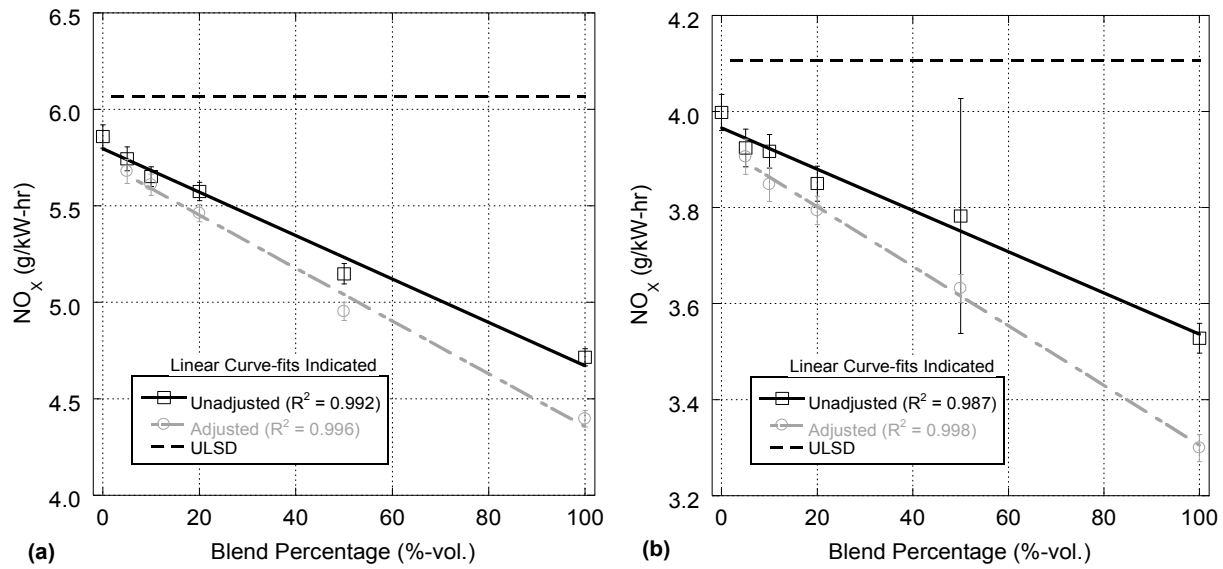


Figure 3-11. Brake-Specific NO_x Emissions vs. Blend Percentage for Unadjusted and Adjusted Blends at 9.0 (a) and 18.0 N·m (b). Loading Tier 4 Regulation at 7.5 g/kW-hr (Not Displayed).

Table 3-4. Pearson Correlation Coefficients for Brake-Specific NO_x Emissions as a Function of Increasing R-8 Blend Percentage.

Engine Torque (N·m)	Unadjusted	Adjusted
0.5	0.670	-0.296
4.5	-0.970	-0.980
9.0	-0.992	-0.993
13.5	-0.986	-0.988
18.0	-0.987	-0.993

The brake-specific results as a function of Jet-A/R-8 blend percentage are shown for 9.0 N·m and 18.0 N·m in Figure 3-11 a and b, respectively with ULSD provided for comparison. As the fraction of R-8 increases, the NO_x emissions decrease linearly. Similar to the discussion involving neat R-8, the more gradual energy release and influence of R-8 chemistry on the prompt NO_x pathway appears to counteract higher global cylinder temperatures. This relationship is strengthened slightly when combustion timing is adjusted and combustion happens later, reducing the residence time at high temperatures. This results in the unadjusted and adjusted NO_x emissions diverging as blend percentage increases, demonstrating the usefulness of injection timing modulation in order to address NO_x levels.

These results are also shown in Table 3-4, which quantifies the regression results for NO_x vs. blend percentage.

3.5.2.2 Partial Combustion Products Emissions

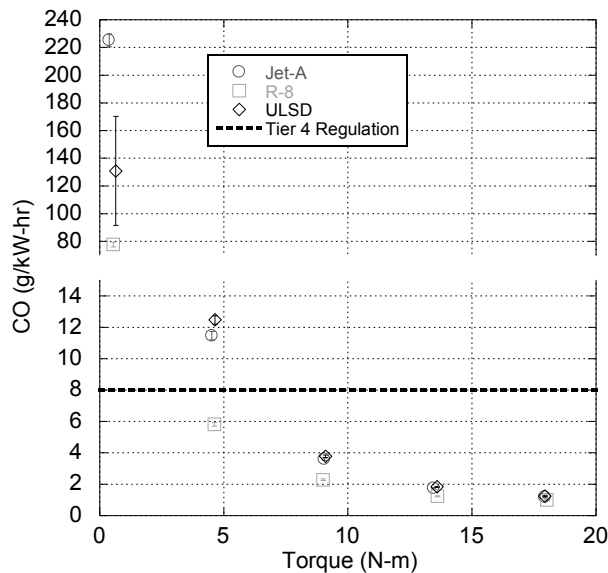


Figure 3-12. Brake-Specific CO Emissions vs. Torque for Adjusted R-8, Jet-A, and ULSD.

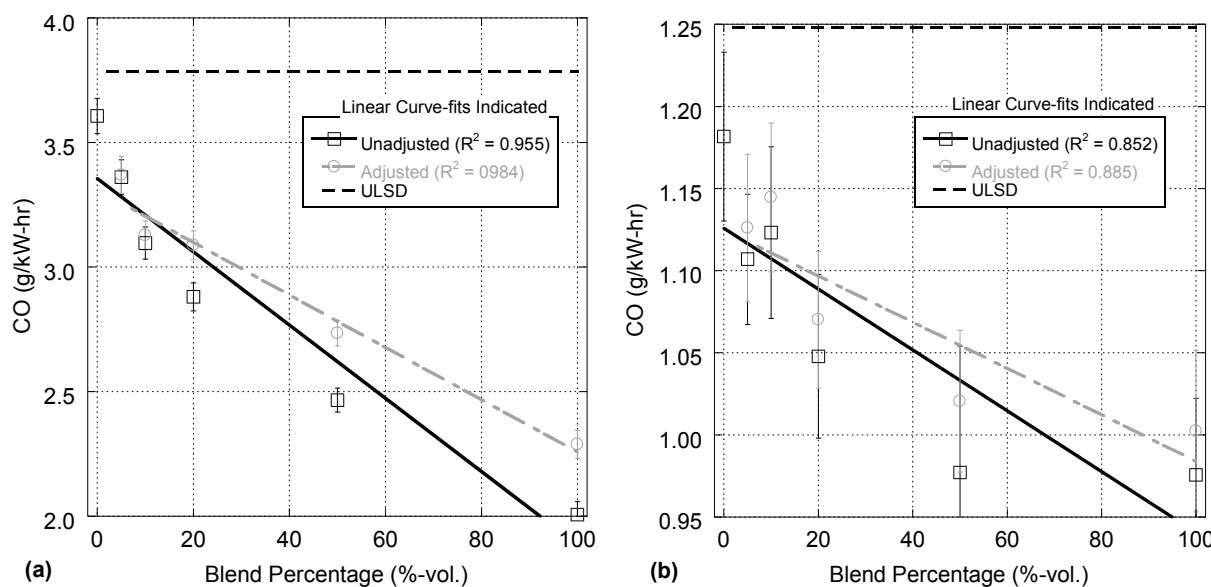


Figure 3-13. Brake-Specific CO Emissions vs. Blend Percentage for Unadjusted and Adjusted Blends at 9.0 (a) and 18.0 N-m (b) Loading. Tier 4 Regulation at 8.0 g/kW-hr (Not Displayed).

Table 3-5. Pearson Correlation Coefficients for Brake-Specific CO Emissions as a Function of Increasing R-8 Blend Percentage.

Engine Torque (N-m)	Unadjusted	Adjusted
0.5	-0.306	-0.546
4.5	-0.944	-0.963
9.0	-0.955	-0.961
13.5	-0.944	-0.965
18.0	-0.852	-0.882

Carbon monoxide is created in fuel-rich zones of the cylinder where carbon molecules do not fully combust to form CO₂ [1]. The cooler the combustion temperature and the shorter the residence time in the cylinder, the lower the likelihood of thermal oxidation of CO. Furthermore, analogous to NO_x, CO can be formed due to the dissociation of CO₂ under high temperatures. Figure 3-12 shows that brake-specific CO emissions decrease with load for all adjusted fuels alongside regulation levels for this engine. This is a result of hotter combustion temperatures experienced with higher load promoting thermal oxidation offset slightly by an increased level of dissociation. In the CO results of Figure 3-12, ULSD and Jet-A exhibit analogous CO emissions again based on the similarity of temperatures and heat release profiles. In contrast, R-8 combustion finds significantly lower CO emissions. From the heat-release discussion, R-8 diffusion burn is more pronounced than ULSD and Jet-A, which would provide the opportunity for CO to form due to additional rich fuel cores. However, the mass-based energy content of R-8 is higher than both Jet-A and ULSD. Therefore, while fuel injection takes longer because of its volumetric energy content, the actual amount needed for power at the desired load is smaller (verified later in the fuel consumption discussion). This provides less carbon in the cylinder to form CO, which subsequently leaves more oxygen available to complete combustion. Furthermore, the lower viscosity of R-8 promotes a finer atomization and a reduction in fuel rich zones. Finally, its higher cetane number and larger global cylinder temperature are indicative of a fuel that is more ready to combust, promoting greater combustion efficiencies. This is further indicated via lower CO emissions with R-8 blend as

shown in Figure 3-13 a and b and regressed via Table 3-5. As a result, the fuel properties of R-8 combine to produce lower CO emissions.

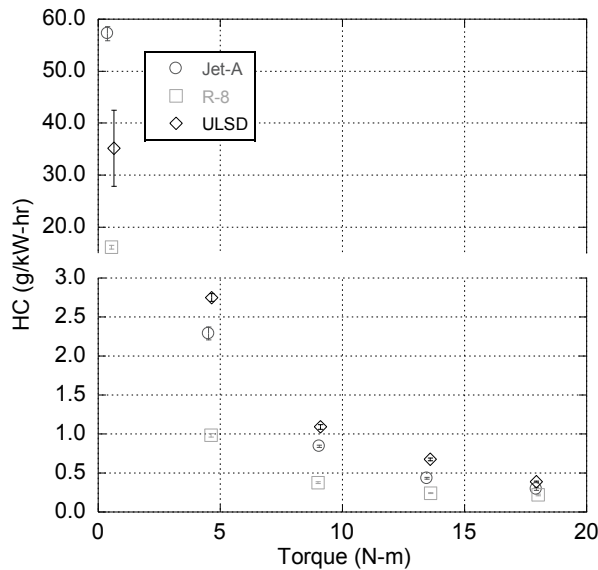


Figure 3-14. Brake-Specific HC Emissions vs. Torque for Adjusted R-8, Jet-A, and ULSD.

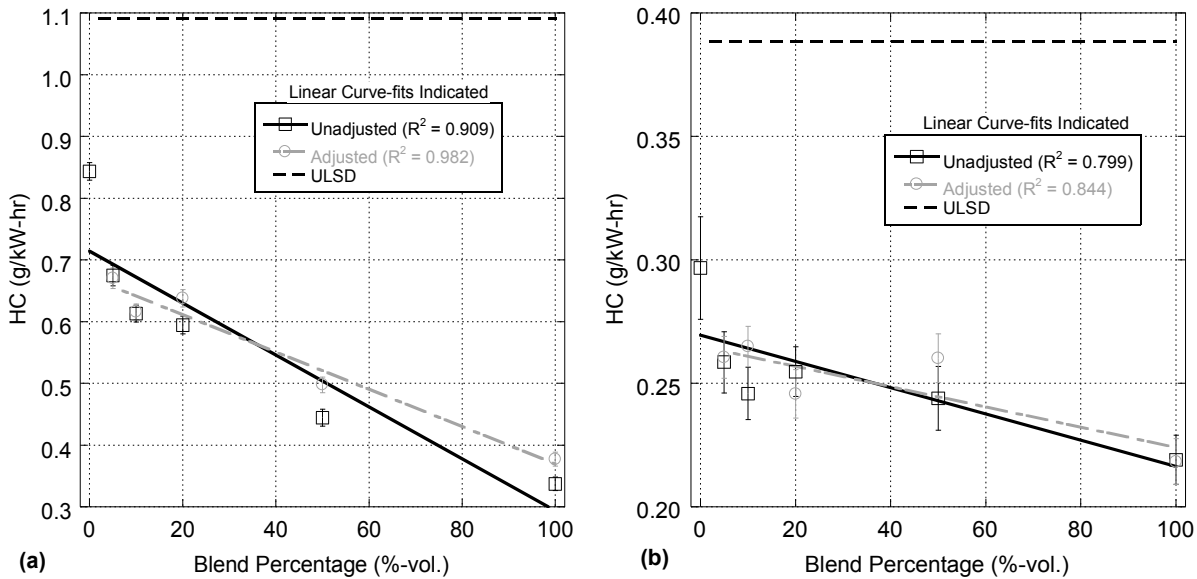


Figure 3-15. Brake-Specific HC Emissions vs. Blend Percentage for Unadjusted and Adjusted Blends at 9.0 (a) and 18.0 N-m (b) Loading.

Table 3-6. Pearson Correlation Coefficients for Brake-Specific HC Emissions as a Function of Increasing R-8 Blend Percentage.

Engine Torque (N-m)	Unadjusted	Adjusted
0.5	-0.519	-0.596
4.5	-0.934	-0.943
9.0	-0.909	-0.904
13.5	-0.906	-0.926
18.0	-0.799	-0.811

Emission of HC species occurs as a result of the hydrocarbon chains of the fuel not fully breaking apart during the combustion process [1, 16, 65]. These emissions are directly influenced by combustion temperature, residence time, level of diffusion burn, and the availability of oxygen [1]. Moreover, unlike the rich combustion product CO, creation of HC emissions due to the dissociation of H₂O and the hydrogen generated is negligible. Despite higher equivalence ratios with load, HC emissions decrease as indicated in the brake-specific results of Figure 3-14 for ULSD and adjusted Jet-A and R-8. This reduction occurs due to an increase in combustion temperatures that promote HC oxidation. Of the three neat fuels, ULSD produces the highest emissions of HCs. This is due to ULSD having the highest viscosity because of longer hydrocarbon chains. Thus, atomization and mixing is reduced prior to the start of combustion. This effect carries into the diffusion burn where large fuel droplets may not fully oxidize in the diffusion burn. Jet-A HC emissions are lower than ULSD because of lower viscosity which promotes mixing and premixed combustion. Furthermore, Jet-A has higher mass-based energy content than ULSD. As a result, less fuel is needed to produce power; thus, reducing the available fuel with which to produce hydrocarbon emissions (verified in fuel consumption discussion). Finally, the emissions of HC for R-8 are the lowest of the three fuels tested at all loads due to a combination of factors that act to reduce total HC emissions. This includes lower viscosity (as compared to ULSD), the highest mass-based energy content (i.e., less potential to produce HC through lower fuel present), and the highest combustion temperatures during the diffusion burn at high loads (Figure 3-9). Therefore, HC emissions decrease with increasing R-8 blend percentage (Figure 3-15 and Figure 3-16). This reduction occurs despite the raising

of fuel mixture viscosity with R-8 blend (Table 3-1) and the reduction of premixed burn with R-8 addition (Figure 3-7). Relatively small effects from adjustment in timing compared to CO may suggest that HC composition could also play a role.

3.5.2.3 Particulate Matter Emissions

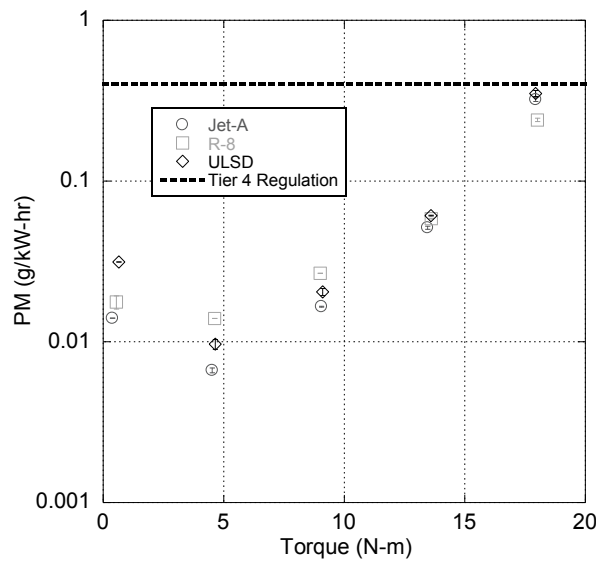


Figure 3-16. Brake-Specific PM Emissions vs. Torque for Adjusted R-8, Jet-A, and ULSD.

Other than NO_x emissions, emissions of PM are of particular concern for CI engines [1, 9, 10, 16, 25, 40, 47, 65]. At low loads, PM is created because of low combustion temperatures and large fuel droplets that do not vaporize and combust [1]. As load and associated cylinder temperature increase, PM production initially drops for all fuels because the combustion environment is more conducive to complete oxidation, as demonstrated in Figure 3-16 [1]. As load increases, diffusion burn becomes prominent and PM production rapidly increases due to an abundance of fuel rich zones near the injector and a shorter residence time in the cylinder [1]. Thus, PM production is highest near full load (Figure 3-16) because the available carbon (through higher equivalence ratio) outweighs higher cylinder temperatures. The PM production levels at this load also approach PM limits set by Tier 4 regulation (also plotted).

Table 3-7. Pearson Correlation Coefficients for Brake-Specific PM Emissions as a Function of Increasing R-8 Blend Percentage.

Engine Torque (N-m)	Unadjusted	Adjusted
0.5	0.906	0.203
4.5	0.997	0.976
9.0	0.978	0.959
13.5	0.810	0.695
18.0	-0.911	-0.961

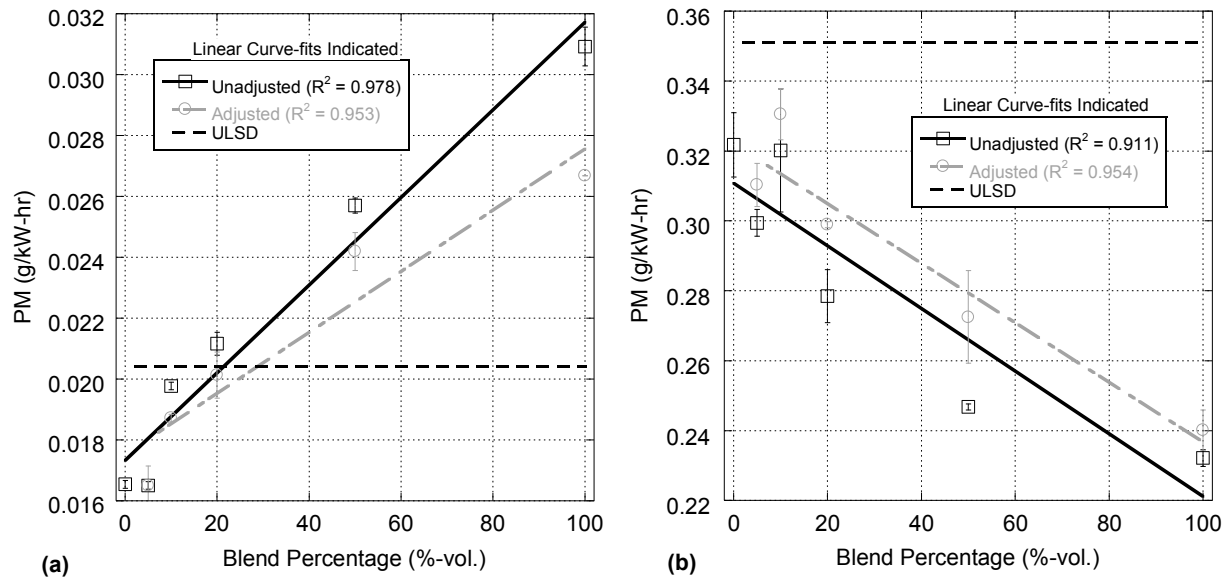


Figure 3-17. Brake-Specific PM Emissions vs. Blend Percentage for Unadjusted and Adjusted Blends at 9.0 (a) and 18.0 N·m (b) Loading. Tier 4 Regulation at 0.4 g/kW-hr (Not Displayed).

With respect to neat fuels, Figure 3-16 indicates that PM production at 0.5 N·m loading is highest for ULSD as its largest viscosity enhances PM production through the injector atomization effectiveness [1]. Jet-A exhibits the lowest PM emissions for all loads below 18.0 N·m. This is a result of Jet-A having the lowest viscosity, leading to advantageous atomization. This promotes greater premixed burn levels, and an accompanying reduction in diffusion burn, where PM is primarily produced. R-8 has higher PM production than Jet-A below 18.0 N·m (and ULSD at 4.5 and 9.0 N·m) as a result of its reduced volumetric energy content which, as discussed previously, leads to more diffusion burn as compared to Jet-A (Figure 3-6b). Furthermore, R-8 is more viscous than Jet-A, so atomization by the injector is less

effective, increasing the possibility of PM production through larger fuel droplets. Table 3-7 indicates the direct proportionality between R-8 blend percentage and PM production below 18.0 N-m. This behavior is further depicted in Figure 3-17a for 9.0 N-m loading.

At full load, ULSD and Jet-A produce similar amounts of PM (Figure 3-16). This is a result of similar amounts of premixed and diffusion burn between these fuels. The potential for higher PM emissions exists for ULSD due to higher fuel viscosity, which may explain why PM is slightly higher than Jet-A. The use of R-8 produces the lowest PM emissions at rated torque, through the highest mass-based energy content and lower viscosity than ULSD. Therefore, the overall equivalence ratio in the cylinder is lowest for this fuel, reducing the carbon available to form PM. Furthermore, the higher cetane number of R-8 and higher average cylinder temperatures at this load may help the fuel combust more readily in the extensive diffusion burn phase than Jet-A and ULSD. The inverse correlation of PM production with R-8 blend fraction (Figure 3-17b) is a result of the increasing mass-based energy content (less fuel present) and higher cylinder temperatures. Interestingly, the combination of lower NO_x and PM for neat R-8 (other than at 9.0 N-m) presents a case where the NO_x-PM tradeoff is reduced through fuel usage as compared to ULSD.

3.5.2.4 Fuel Consumption

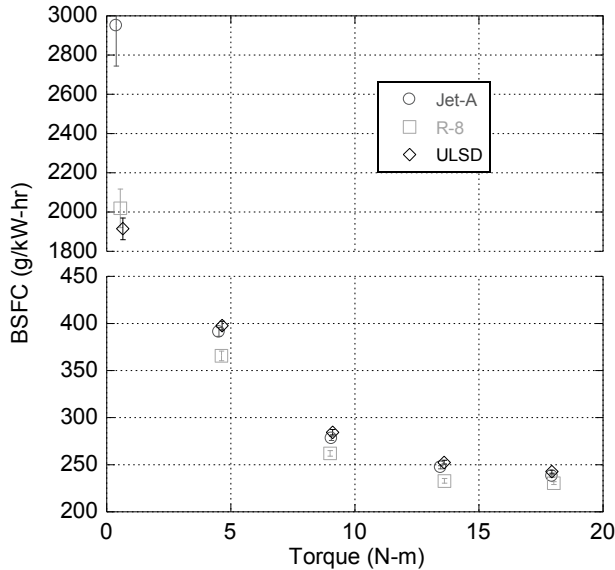


Figure 3-18. Brake-Specific Fuel Consumption vs. Torque for Adjusted R-8, Jet-A, and ULSD.

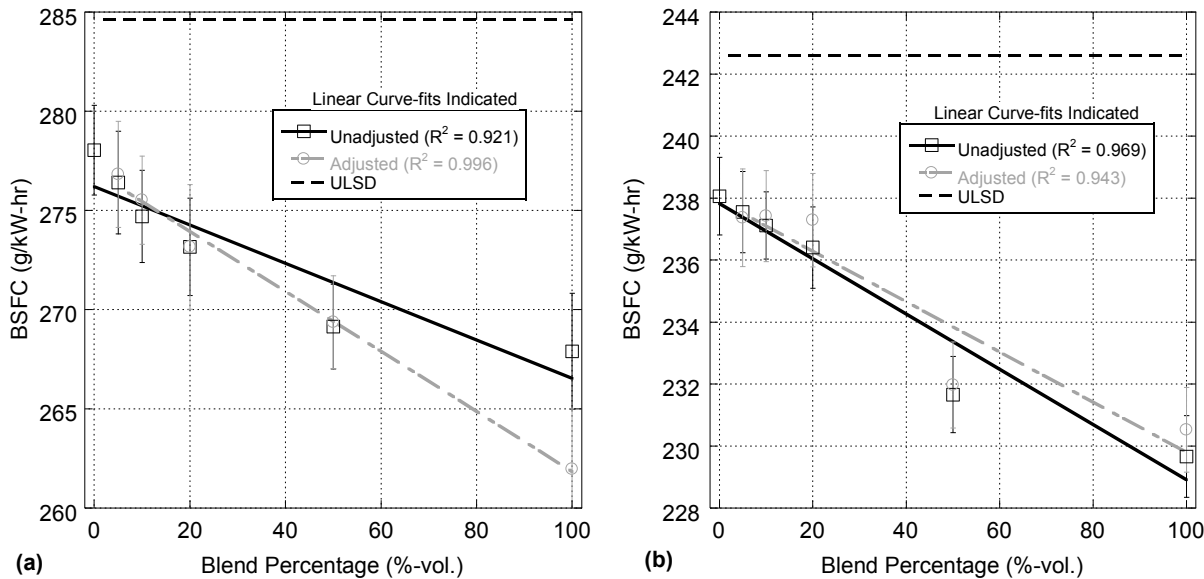


Figure 3-19. Brake-Specific Fuel Consumption vs. Blend Percentage for Unadjusted and Adjusted Blends at 9.0 (a) and 18.0 N-m (b) Loading.

Table 3-8. Pearson Correlation Coefficients for Brake-Specific Fuel Consumption Emissions as a Function of Increasing R-8 Blend Percentage.

Engine Torque (N-m)	Unadjusted	Adjusted
0.5	0.666	-0.230
4.5	-0.861	-0.828
9.0	-0.921	-0.995
13.5	-0.968	-0.989
18.0	-0.969	-0.951

Due to the economic and logistical benefits of operating CI engines on jet fuels, it is important to consider the fuel consumption of CI engines when jet fuels are used. Of particular concern is the possible detrimental effects on combustion phasing due to jet propellant's significant cetane number variability (Table 3-1) [25, 26, 65, 90]. The brake-specific fuel consumption results presented in Figure 3-18 demonstrate the importance of fuel energy content on fuel consumption. As stated previously, the peak pressure timings used in this study correspond to those needed to optimize ULSD. Therefore, these timings may not be optimal for either Jet-A or R-8 due to variable fuel properties.

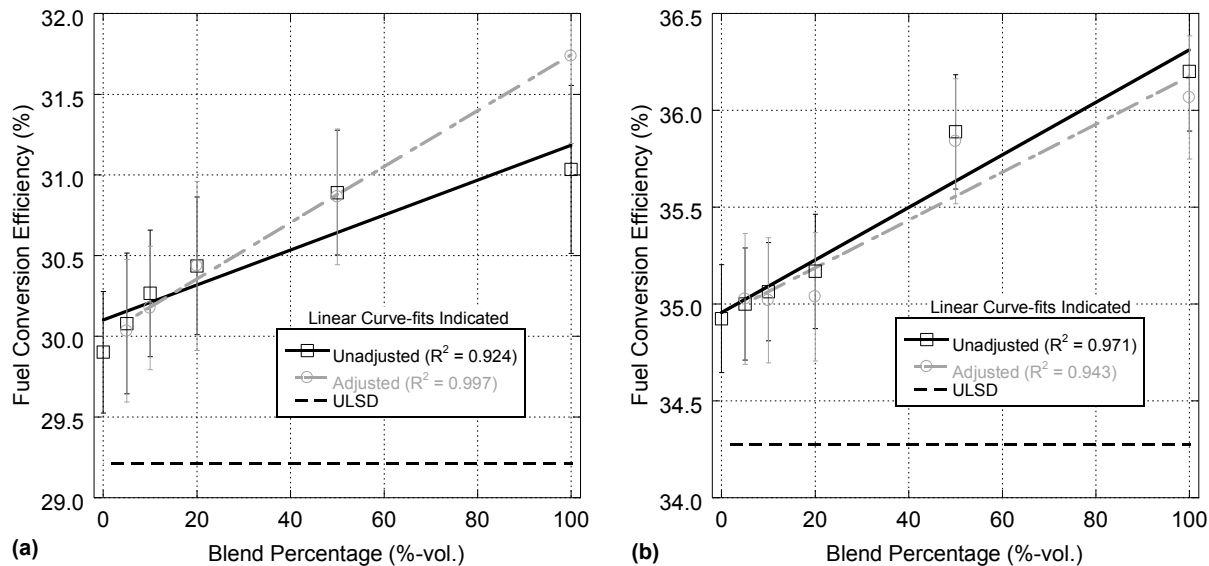


Figure 3-20. Fuel Conversion Efficiency vs. Blend Percentage for Unadjusted and Adjusted Blends at 9.0 N·m (a) and 18.0 N·m (b) Loading.

In general, ULSD has the highest fuel consumption as an effect of ULSD having the lowest mass-based energy content. This characteristic is compounded by the higher viscosity of ULSD, which acts to lower the fuel conversion efficiency, as indicated in Figure 3-20. Because Jet-A has higher mass-based energy content than ULSD it uses less fuel to produce power, thus improving fuel conversion efficiency. Finally, R-8 produces the lowest fuel consumption (and highest efficiency) at loads above 0.5 N·m due to R-8 having the highest mass-based energy content. In blends with Jet-A, fuel consumption and fuel conversion efficiency are improved as R-8 percentage increases, as shown in Figure 3-19, the regression results in Table 3-8, and Figure 3-20. This decrease in fuel consumption occurs despite the reduced premixed burn phase observed and the longer combustion duration. A future study with timing sweeps of Jet-A and R-8 would provide the opportunity to more thoroughly understand the influence of these fuels on fuel consumption optimization and combustion behavior in a CI engine. Furthermore, investigating the behavior of R-8 with variable injection pressure to increase fuel volume injection rate would provide additional opportunity to understand the effects of renewable jet fuel chemistry on the combustion process.

3.6 Conclusion

The Single Fuel Forward Policy set forth by the United States military and the North Atlantic Treaty Organization dictates that military internal combustion engine vehicles use jet fuel. This policy is intended to simplify battlefield logistics and costs through transport of a single fuel. This presents an issue for compression ignition engines because they are not designed to burn this type of fuel. A previous study illustrated that a more antiquated compression ignition fuel system was subject to performance degradation that adversely affected engine performance and emissions potentially influencing durability. Even with modern, adaptive fuel systems, the regulation of jet-propellant fuels does not include cetane number specifications, which are critical fuel parameters needed for good compression ignition operation.

Currently, the commercial and military aviation sectors utilize petroleum-based fuels, such as Jet-A and JP-8, to operate their jet-propelled aircraft in blends up to 50%. A search for sustainable sources of jet fuel is leading researchers to study hydroprocessed fuels created using renewable sources and by-products. This type of fuel is advantageous as it can be tailor-made using a variety of feedstocks, from vegetable oils, including camelina and jatropha, to other sources like animal fat from chicken and cattle production by-products. As a result, the challenge of using jet propellant in a compression ignition engine is further compounded by the addition of renewable jet fuels and variable blends, which have properties that also vary compared to petrol-based jet propellants. Nevertheless, advantageous jet propellant properties, such as a high energy content, present an opportunity to actually improve compression ignition engine performance and emissions when using these fuels over diesel through injection adjustment.

The current work uses a single-cylinder compression ignition engine, outfitted with a common-rail fuel system, to investigate the feasibility of petroleum-based jet propellant and its blends with renewable jet fuels in this type of engine. The common-rail fuel system allows for dynamic adjustment of fuel injection timing. Using this system, Jet-A and blends with a renewable jet fuel produced through hydroprocessing (R-8) were tested to determine the effects of these fuels on combustion behavior and resultant emissions and fuel consumption when the engine is left unadjusted, and when it is changed through dynamic fuel injection control. To serve as a benchmark, these fuels and their respective blends are tested alongside ULSD.

Comparison of Jet-A to ULSD results shows that an improvement in fuel consumption can occur through injection timing calibration of Jet-A. Recalling the injection timing strategy used for this study, the timing used for Jet-A was delayed compared to baseline ULSD timings. This indicates that if R-8 were added directly to an engine with injection timings set for ULSD or Jet-A, combustion timing would be even further advanced. At that point, not only does fuel consumption begin to increase, but engine

durability becomes an issue due to high anticipated combustion pressures [1]. For these reasons, a CI engine should be re-calibrated, or able to adapt injection timing, based on the fuel it will be using.

The results also showed NO_x, CO, HC, and PM levels that were similar to, or lower than, those of ULSD. This is primarily a result of increased energy content and improved fuel mixing via lower viscosity. As a neat fuel, R-8 consistently showed lower fuel consumption and emissions of NO_x, CO, and HC than either ULSD or Jet-A, with PM emissions that were relatively similar to these fuels. This is caused by the unique combination of higher energy content than either ULSD or Jet-A, as well as a lower density that made the injection event longer. These factors act to reduce premixed combustion and associated thermal NO_x production. Of particular interest is the observed possibility of R-8 usage lessening the NO_x-PM tradeoff due to advantageous fuel properties that act to reduce both NO_x and PM.

The effects of blending Jet-A and R-8 produced generally linear progression from the behavior of one fuel to the other with blend. Changing of injection timing throughout the blend study produced improved NO_x and PM emissions along with slightly reduced fuel consumption. The necessary delay in injection timing did cause an increase in CO and HC emissions, which still remained below levels observed for ULSD. Changing fuel injection timing with blend to align peak cylinder pressures as R-8 blend changed provided a better opportunity to investigate the influence of this fuel on combustion without the presence of the strong effects of combustion phasing.

Table 3-9. Anticipated Result of Increasing Independent Fuel Property.

Increasing Property	Peak Pressure	Pre-mixed Combustion	Peak Temperature	NO _x	CO	HC	PM	BSFC
Cetane Number*	↑	↑	↑	↑	↓	↓	↓	↑
Density	↑	↑	↑	↑	↓	↓	↓	↓
Viscosity	↑	↑	↑	↑	↓	↓	↓	↓
Energy Content	↑	↑	↑	↑	↓	↓	↓	↓

To consolidate the previous discussions, Table 3-9 summarizes the independent effects of each fuel property on the combustion process and associated fuel consumption and emissions. Specifically,

this table shows the influence of an increase in a specific fuel property as an increase/decrease (up/down arrow) on measureable performance metrics. This table does not necessarily reflect what occurred through the engine tests in this study due to competing factors, such as density and mass-based energy content, particularly for R-8. Of note, cetane number is a measured index based on other fuel factors, such as fuel chain length and structure. Therefore, its effects noted here are based on what occurs for the unadjusted injection strategy only.

While the long-term effects of renewable jet fuels on a compression ignition engine and modern fuel system are unknown, initial engine behavior shows promising fuel performance because of high energy content and advantageous combustion characteristics, particularly during the diffusion burn phase of combustion. However, these positive results require either the recalibration of the engine or the ability of the engine control system to adapt to the fuel being used.

Chapter 4: Operation, Technical Information, and Troubleshooting of the Single-Cylinder Compression-Ignition Engine Test Cell

4.1 Introduction

The current single-cylinder CI engine test cell uses a diverse variety of equipment in order to fulfill testing requirements. These individual systems, including an engine, dynamometer, exhaust gas recirculation (EGR), in-cylinder pressure measurement, gaseous fuel intake injection, data acquisition, turbocharging, emissions measurement, and high-pressure electronic fuel injection, must all work in unison to perform research successfully in this laboratory.

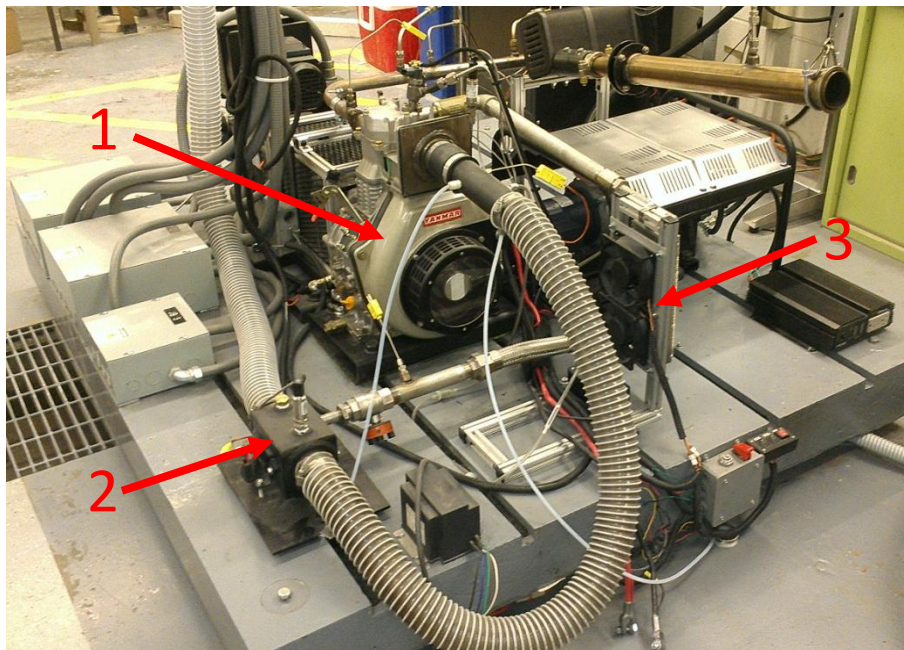


Figure 4-1. Yanmar Single-Cylinder Engine Test Cell. Yanmar (1), Gaseous Mixing Box (2), EGR System Cooler (3).

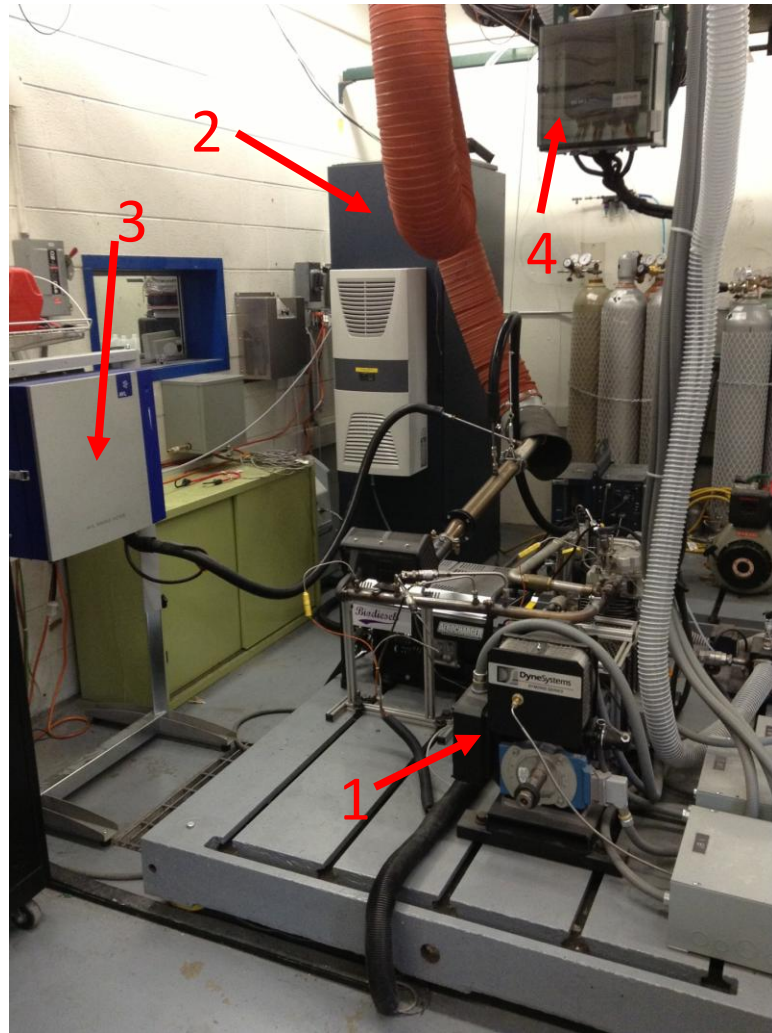


Figure 4-2. Secondary View of Test Cell with Dynamometer and Emissions Equipment. Dynamometer (1), AVL FTIR Bench (2), AVL Smoke Meter (3), and Engine Control Unit (4).

The laboratory, in its current configuration, is shown in Figure 4-1 and Figure 4-2. The single-cylinder Yanmar CI engine is connected to a 12-horsepower alternating-current (AC) dynamometer that provides the ability to load and motor the engine. The gaseous mixing box provides a connection point for both EGR and the assisted gas injection system. This system injects a controlled mass flow rate of gas into this mixing volume prior to flowing into the engine, and has been used for hydrogen-carbon monoxide-assisted biodiesel combustion by Cecrle et al. [39]. In the near future, this system will be used for compressed natural gas-assisted diesel combustion, which is an area of interest for both power generation and transportation due to this abundant domestic energy source. The exhaust gas

recirculation (EGR) system was built by Ragone in order to perform preliminary EGR studies, which serve as a means of reducing NO_x emissions via a reduction of cylinder combustion temperatures [12]. This system is undergoing an upgrade to improve EGR flow control via automated recirculation and intake throttle valves.

In addition to controlling the engine, measuring both gaseous and particulate emissions in an accurate and repeatable fashion is of utmost importance. To serve this need, an AVL SESAM Fourier Transform Infrared (FTIR) bench is connected to the exhaust pipe of the engine to gather a sample stream. The FTIR itself measures individual species, such as NO, NO₂, CO, CO₂, H₂O, and individual hydrocarbons. Total hydrocarbons are measured within this bench using a Flame Ionization Detector (FID) and diatomic oxygen is measured using a Magnos 105 Oxygen Sensor. An AVL smoke meter also collects a sample of exhaust gas in order to measure particulate matter (PM) output. Finally, the exhaust of this engine is designed to be modular, allowing for the removal and reconfiguration for a variety of exhaust systems (e.g., EGR). Of particular interest is the addition of a turbocharger and an exhaust gas energy recovery system. The installation and performance of the turbocharger will be discussed in the following sections. For information regarding the exhaust heat recovery system, see the upcoming dissertation by Charles Sprouse III.

In general, the engine testing systems are in-house designs constructed by graduate students on an as-needed basis over the course of the last five years. As a result of the rapid turnover of these students, and the one-off nature of the apparatus, this chapter is necessary to serve as a teaching manual for students who plan to perform research in this laboratory. The following sections discuss each of these components in detail. Each system's operating principles are discussed to build an initial foundation of knowledge for the reader. From there, the use and maintenance is discussed so that a student can see how to actually utilize, modify, or repair, the equipment. Additionally, the process for performing data analysis following testing is discussed. This process is currently accomplished using a

data post-processing Matlab script; however, it is critical that any user of this system understand the underlying process of the derivation of certain critical engine performance metrics.

4.2 Yanmar Single-Cylinder Engine

The engine used in this laboratory is a single-cylinder CI Yanmar L100V. This engine has a displacement of 0.435 Liters and a compression ratio of 21.2. This engine is air-cooled, meaning that there is no water jacket or radiator. While this may reduce the direct applicability of the results to a modern CI engine (usually liquid cooled), this dramatically simplifies the test cell configuration, saves space on the pad, and improves experimental repeatability. Moreover, this engine is advantageous from a fuel research standpoint as its fuel consumption is much smaller than a multi-cylinder CI engine, such as the Duramax engine discussed in Chapter 5. Research fuel batches are made in lots of approximately four gallons, which is enough to run the Yanmar (with load) for several hours, even as a neat fuel source. In fact, the entire round of biodiesel tests covered in Chapter 2 began with ten gallons of each biodiesel and several gallons were left over.

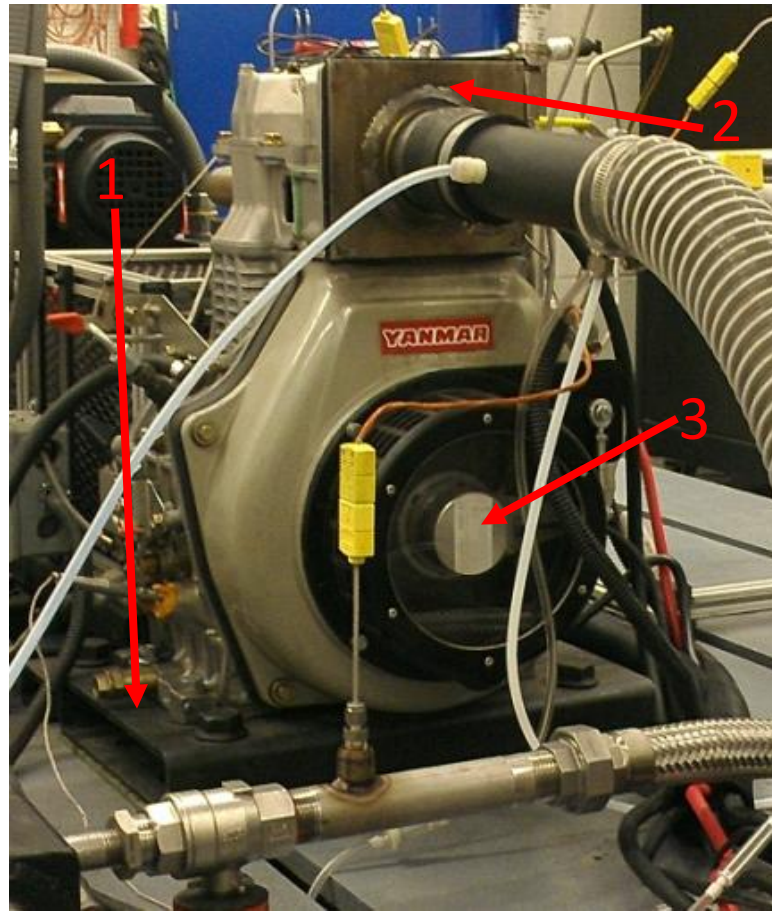


Figure 4-3. Yanmar Engine from the Flywheel End.

The engine is affixed to the skid in the Learned Hall test cell using a custom steel base machined out of square structural steel tubing, shown in Figure 4-3. This adapter is machined to match the four-bolt pattern of the Yanmar. The engine is physically attached by four studs that protrude from the top surface of the adapter. Flange-head nuts hold the engine on the adapter, with a second nut jammed above the first to prohibit loosening over time. The adapter itself is held fast using four $\frac{3}{4}$ "-10 bolts screwed into tee-nuts in the skid channels.

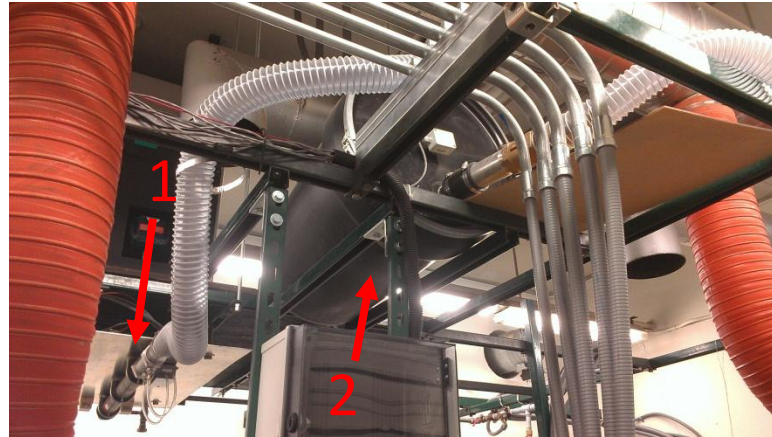


Figure 4-4. Intake Flow Measurement System. Laminar Flow Element (1), Resonator Barrel (2).

The engine intake is custom machined to accept either a straight sampling pipe (Figure 4-3) or direct connection of the flexible intake tube. This tube is connected to a laminar flow element, which measures air flow rate, and a volumetric resonance barrel (Figure 4-4). Original testing of air flow had high statistical uncertainty due to the variable flow caused by the engine because of its four-stroke nature (i.e., pulsations according to valve timing). The barrel is used as a method for dampening the compression and expansion waves that travel up the intake hose when the intake valve of the engine opens. This system, while simple and economic, dramatically improved air mass flow rate measurements by removing fluctuations.

The engine head itself is machined to accept installation of a thermocouple and pressure transducer into the intake runner. In addition, the cylinder head was machined to allow for in-cylinder measurement. The original pull-start cover has also been machined to allow an incremental encoder to be attached to the flywheel [20].

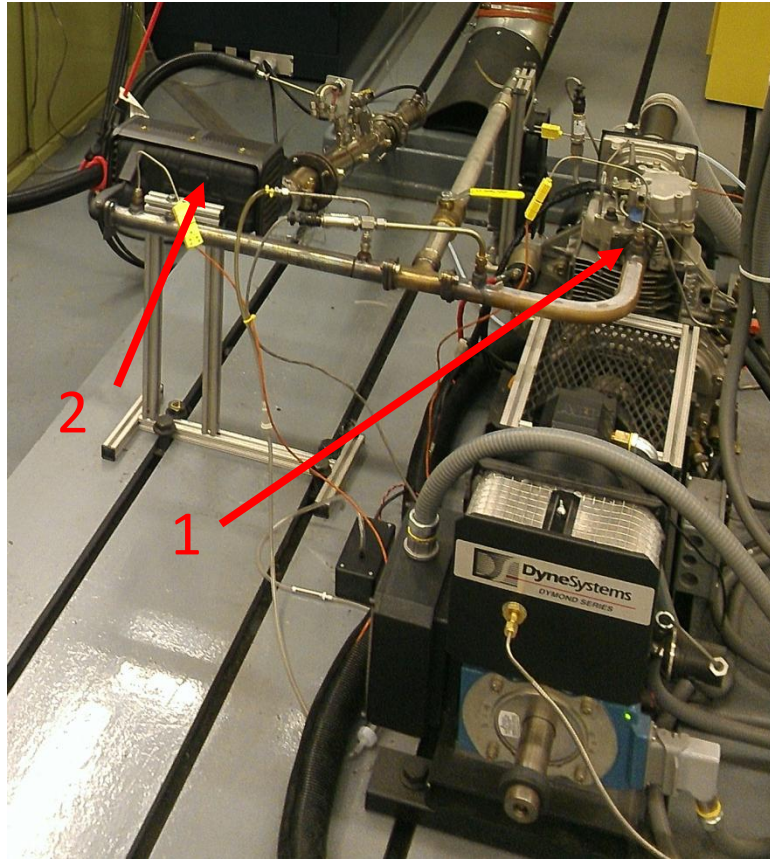


Figure 4-5. Yanmar Exhaust System. Yanmar Exhaust Port (1), Muffler (2).

The custom exhaust (Figure 4-5) is welded to custom-cut two-bolt flanges that mate to the studs on the Yanmar exhaust where the muffler is installed in stock applications. The muffler has been reused via connection further downstream. The end of the muffler is modified to accept either the flow straightener used by the Semtech Mobile Emissions Analyzer [56] or the FTIR and Smoke Meter.

Connection of the engine to the dynamometer (via the torque transducer) is accomplished using a custom-machined flange that adapts the tapered shaft of the Yanmar to a keyed shaft. Elastomer couplers, purchased at IBT in Lawrence, KS, are used to bridge the gaps between the engine, transducer, and dynamometer. Finally, as covered in Chapter 1, the original mechanical fuel system is no longer used. Instead, a common-rail fuel system with electronic control modulates fuel injection.

4.2.1 New Engine Preparation and Installation



Figure 4-6. Stock Yanmar YDG5500 Diesel Generator Containing an L100V Engine. Generator (1), Yanmar Engine (2) [105].

The stock Yanmar engine used at KU is a Yanmar L100V that is sold packaged as a stand-alone generator (model # YDG5500) for commercial and residential use, as shown in Figure 4-6. The engine must be removed from this configuration to be installed in the test cell. First, the heat shields, fuel tank, muffler, and generator rear cover must be removed using standard open-ended wrenches.

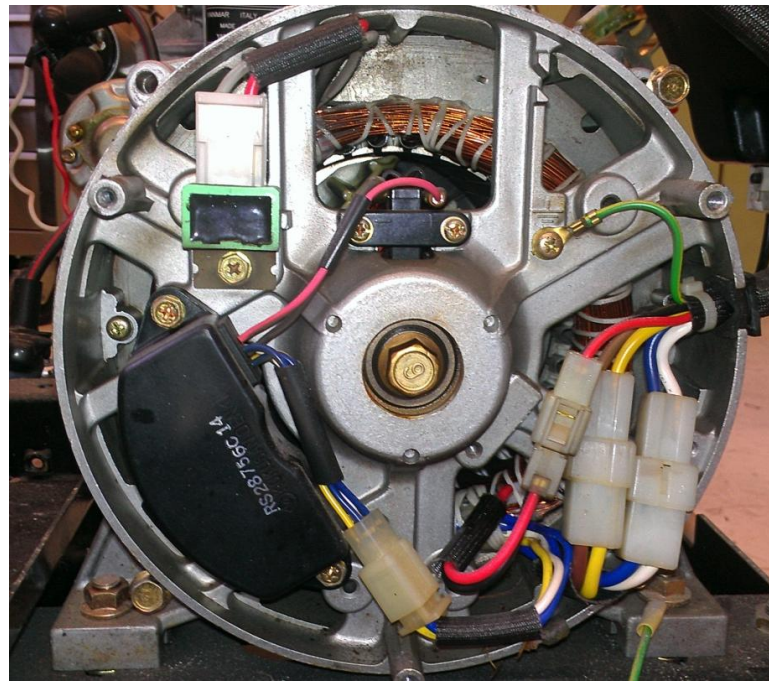


Figure 4-7. Electronic Components of AC Generator.

The next step is to remove the electronics of the generator, shown in Figure 4-7.

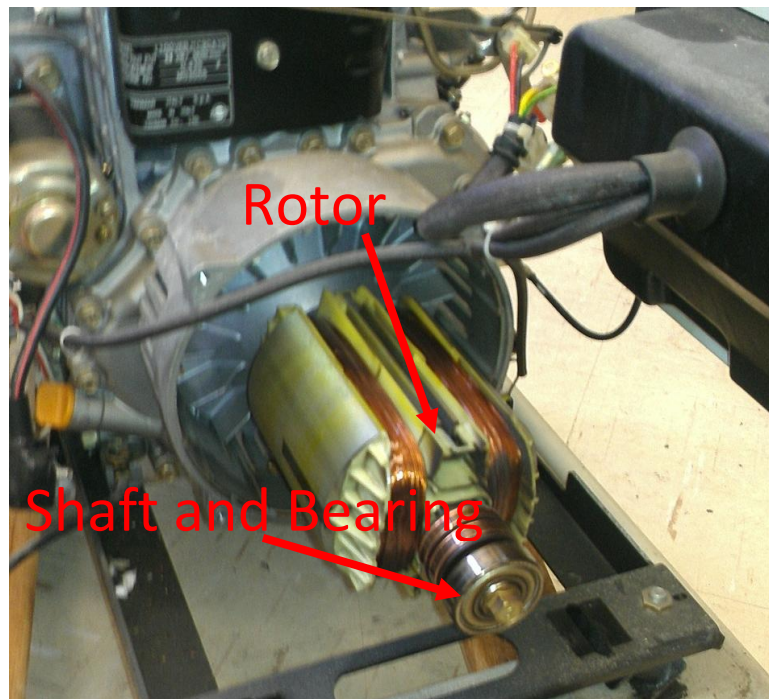


Figure 4-8. Yanmar Generator Rotor and Shaft.

Removing these components allows for the generator stator and rear bearing support to be removed exposing the generator rotor and windings (Figure 4-8).



Figure 4-9. Generator Rotor Shaft (Top) and Rotor Removal Tool (Bottom).

The generator rotor is press-fit onto the tapered output shaft of the Yanmar engine and is held in place by a threaded shaft that screws into the same engine output shaft. Removal of the threaded shaft requires a standard metric wrench, but removing the generator rotor requires a special tool that is used to force the rotor off the engine output shaft. This tool is shown in Figure 4-9.

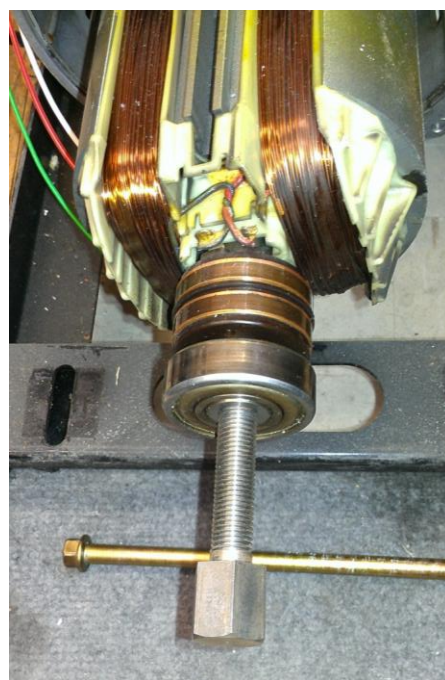


Figure 4-10. Removal tool (with Threads) During Rotor Removal.

The interior of the outboard end of the generator rotor is also internally threaded, thus as the removal tool is tightened, the tool is pressing on the output shaft of the engine while pulling the rotor off (Figure 4-10). To ensure a clean removal of the rotor, it must be hit with a rubber mallet after every few turns of the removal tool.

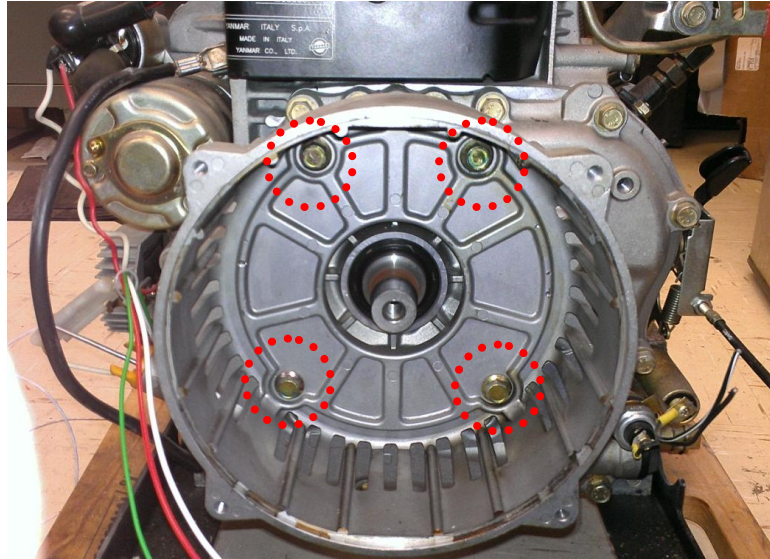


Figure 4-11. Inner Generator Housing with Four Retaining Bolts (Red).

After removing the rotor, the inner housing of the generator is removed by loosening the four retaining bolts in Figure 4-11.



Figure 4-12. Yanmar Engine Ready for Install Into KU Test Cell.

After the removal of the generator, the engine can be removed from the engine/generator frame. This is done by unbolting the four engine mounts located on the bottom of the engine. Doing so will allow the engine to be lifted out of the frame. The engine, shown in Figure 4-12, is ready for install in the test cell.

For the cylinder head exchange process and the installation of the in-cylinder pressure transducer and encoder, see the masters thesis of the author [20]. For the removal of the fuel pump and installation of the injector and sensors, see Chapter 1 of the current work. All other components (intake, exhaust, and driveshaft) are to be installed in a similar manner to the previous engine.

4.2.2 Performing an Engine Oil Change

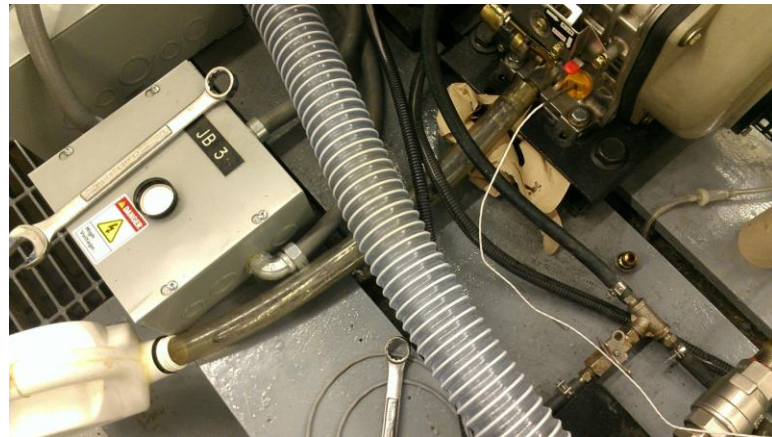


Figure 4-13. Draining Oil from Yanmar Engine.

The engine oil must be changed at least every 100 hours or 6 months. Typically, the oil is also changed before beginning a long-duration fuel analysis study. The oil is drained from the oil pan drain using an open-ended wrench and long piece of clear tubing (Figure 4-13). The tube is necessary because the engine sits very low on the engine pad, thus preventing close access with a waste oil container. The engine cannot be removed from the pad easily; therefore, tilting the engine is not feasible. As a result, the oil will drain slowly.

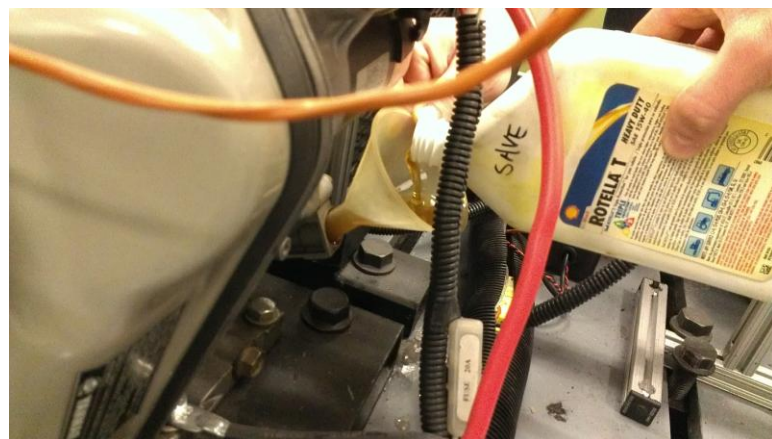


Figure 4-14. Filling Yanmar Engine with Oil.

After draining (and closing the oil drain), oil may be added through the oil dipstick port located on either side of the engine as shown in Figure 4-14. A small container and funnel is recommended due

to limited access to the filling port. The engine uses 3.25 Pints of Shell Rotella T Heavy-Duty Engine Oil (SAE 15W-40). If this brand is not available, other brands may be used as long as the oil weight (SAE 15W-40) is the same.

4.3 Turbocharger

As discussed in the introduction, a popular method of improving CI engine mixing and power output is by coupling to a turbocharger compressor, located upstream of the engine intake. This process increases the amount of air that is drawn into the engine via higher intake pressures that, in-turn, provides more exhaust energy for the turbocharger turbine. The turbocharger used on the single-cylinder Yanmar engine is produced by Aerocharger, LLC of New Century, Kansas. Sizing of the turbocharger was initially based on data from testing at 3600 RPM, which provided Aerocharger engineers with exhaust temperatures, pressures, and mass flow rates to ascertain the proper sizing. However, the size deemed appropriate for this engine was slightly smaller than the smallest turbocharger that Aerocharger produces. Fortunately, their calculations indicated that the turbocharger selected should provide boost to the limited levels desired by KU engineers.

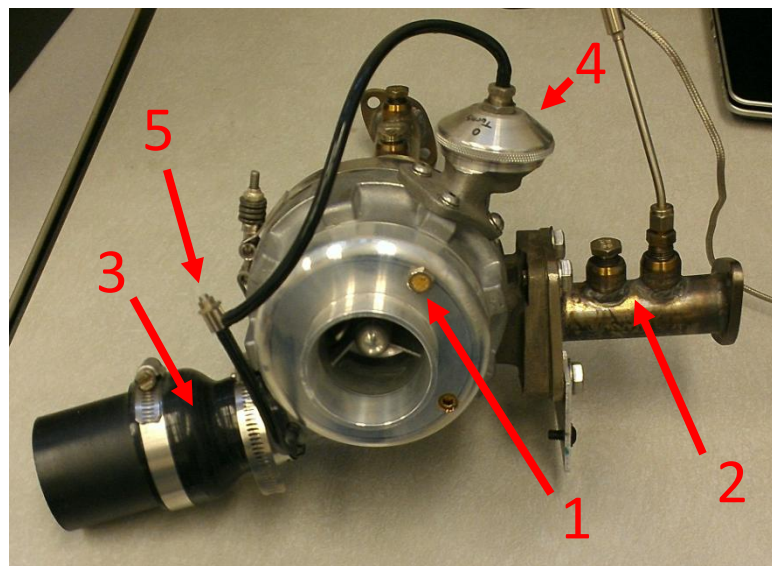


Figure 4-15. Aerocharger Turbocharger with Oil Inlet Port (1), Turbine Inlet Transition (2), Compressor, Outlet Boot (3), Boost Controller (4), and Boost Feedback Bleed Valve (5).

This turbocharger (Figure 4-15) utilizes its own oil system, which it uses to lubricate the bearings located on the compressor (cool) end of the turbocharger shaft. Thus, the turbocharger oil system requires no connection to the Yanmar oil system. This greatly simplifies the turbocharger installation and removal procedure. Filling of the turbocharger oil occurs through the oil port and oil is available directly from Aerocharger.

Controlling turbocharger boost is critically important, as too much boost could lead to excessively high peak cylinder pressures, which could prove more than the engine is mechanically able to withstand (e.g., engine head, piston rod, or crankcase failure). As a result, the pressure the turbocharger produces must be controlled. Typically, this is accomplished via either a waste gate or through variable turbocharger vane geometry. Waste gates are used in the exhaust of the engine to flow the exhaust around the turbocharger turbine, thus removing energy and slowing the turbine. Variable geometry turbochargers modulate vanes inside the turbocharger compressor housing to alter the air flow characteristics into either a more- or less-efficient flow to provide boost control. This is the type of control strategy used for the Aerocharger turbocharger. This vane modulation is self-contained and self-regulating. A diaphragm on the turbocharger is exposed to the outlet (boost) from the turbocharger. This higher pressure exerts a force on a spring. As the force generated by pressure becomes greater than the spring resistance, the diaphragm depresses. The depressing of the diaphragm causes linear actuation of the internal vane mechanism, simultaneously rotating the vanes. The movement of the actuator and subsequent vane variation reduces the flow into the compressor to lower boost pressure. Boost pressure can be set to different pressures by changing the spring used (e.g., a more stiff spring yields higher boost pressure). Boost pressure can be further controlled by using a bleed valve placed on the boost controller input hose. Opening this bleed valve lowers the pressure acting on the diaphragm resulting in higher boost pressure.

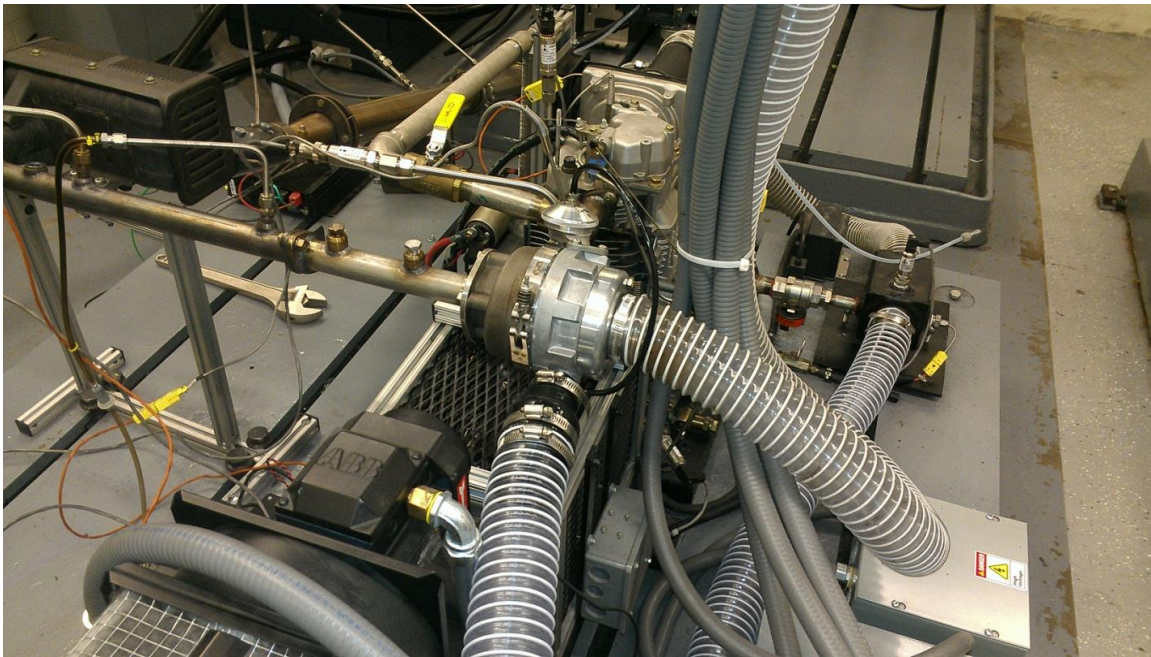


Figure 4-16. Aerocharger Turbocharger Installed on Yanmar Engine.

Due to the self-contained nature of the turbocharger, installation and removal is very straightforward. This is due primarily to the modular design of the exhaust system. When the turbocharger is in place (Figure 4-16), the exhaust makes a 90-degree bend, perpendicular to the driveshaft orientation.

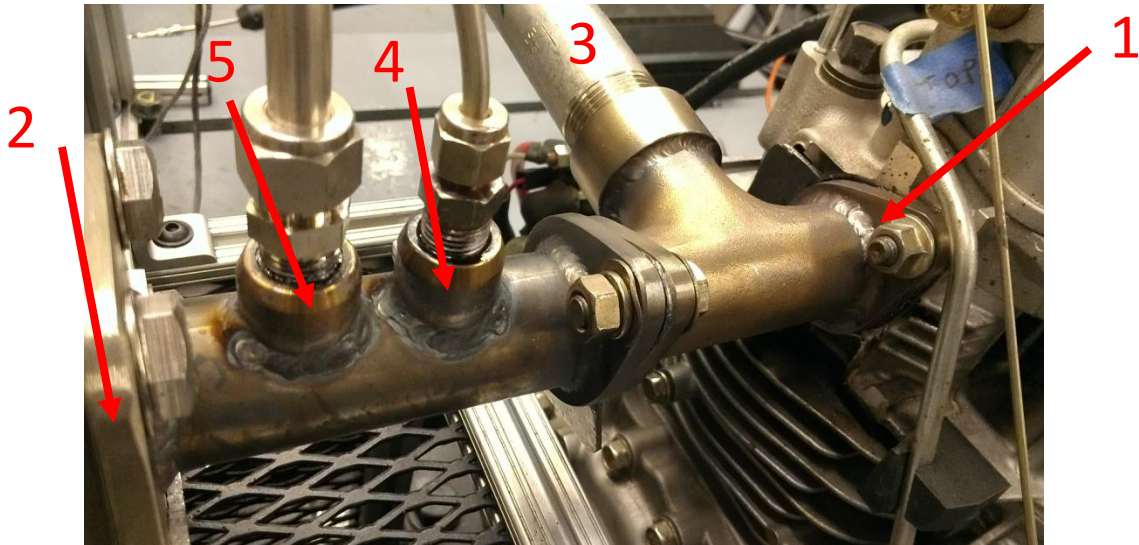


Figure 4-17. Yanmar Exhaust (1) to Aerocharger Turbocharger (2) Adapter. Also Shown are the EGR Connection (3), and Thermocouple (4) and Pressure Transducer (5) Ports.

The adaptation from the Yanmar exhaust to the turbocharger is accomplished using custom-machined flanges and pipes made of stainless steel. These segments have additional sensor ports (1/4" NPT) which allow for additional temperature and pressure sensors. As an example, the connection between the Yanmar and turbocharger is displayed in Figure 4-17. Note, the EGR system receives its exhaust supply from the upstream side of the turbocharger turbine to capitalize on the higher exhaust pressure at this point, which is needed to induce flow to the gaseous mixing box.

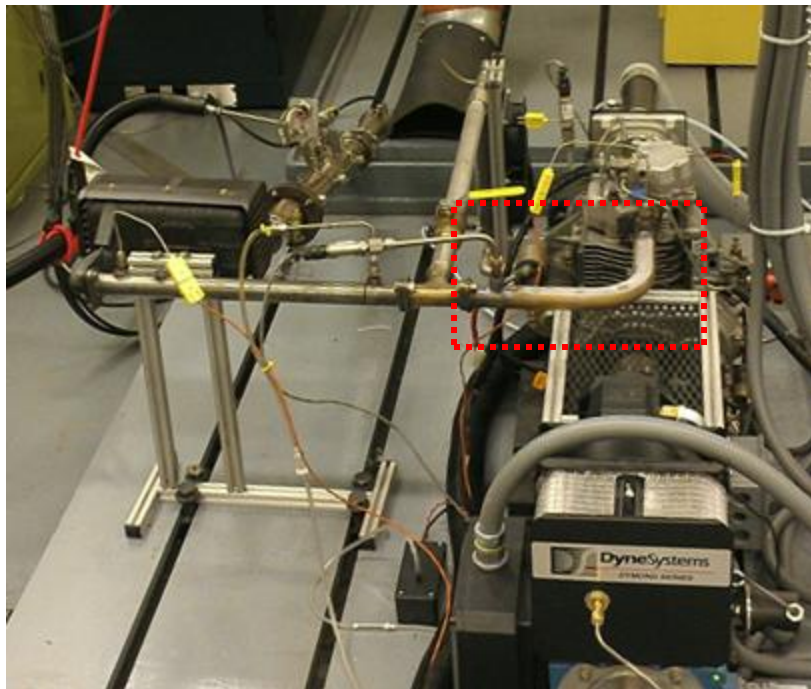


Figure 4-18. 90-Degree Exhaust Adapter to Match Turbocharger Endpoint Connections.

Removal is as simple as installation. This is because of a custom 90-degree stainless steel bend that was designed to replicate the endpoints of the turbocharger, shown installed in Figure 4-18. The exhaust requires little more than the removal of the turbocharger and its two transitional exhaust components because of this modular design. Of note, the EGR is shown here in a different location, due to the flexibility of the system, this section can be located in multiple spots based on experimental requirements. It is important to note that the orientation of the turbocharger is relatively unimportant. However, it should not be placed in a vertical axis as this will reduce bearing lubrication and subsequently damage the turbocharger. Furthermore, the housing of the compressor can be rotated, or re-clocked, to facilitate different exhaust configurations. However, this action should only be done under the direction of Aerocharger engineers as improper re-clocking procedure can jam the boost control mechanism that disables the vanes.

To date, a single speed experiment has been accomplished on the Yanmar with the turbocharger installed. This occurred prior to the fuel system upgrade covered in Chapter 1 and,

therefore, occurred at 3600 RPM with a fixed injection timing of 15.5° before TDC. Emissions were not gathered for this experiment, but data was collected for five steady-state loads of 0.5 N-m, 4.5 N-m, 9.0 N-m, 13.5 N-m, and 18.0 N-m. Of particular interest are the effects of the turbocharger on in-cylinder pressure conditions. The results for cylinder pressure are measured at 0.5-degree crank angle resolution using the system from Chapter 1 through Chapter 3.

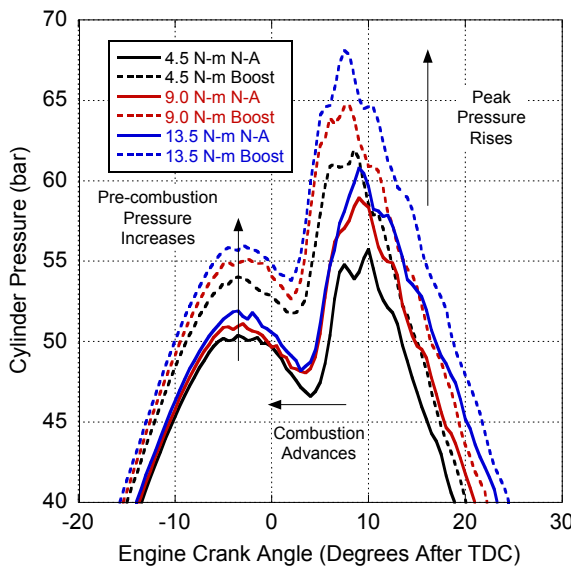


Figure 4-19. Cylinder Pressure vs. Engine Crank Angle for Naturally-Aspirated (N-A) and Turbocharged (Boost) at 4.5, 9.0 and 13.5 N-m of Torque.

The cylinder pressure results for mid-range loads are shown in Figure 4-19 for the Yanmar in both the naturally-aspirated and turbocharged configurations. These results represent what occurs at all loads. Specifically, an increase in cylinder pressure occurs for the turbocharged conditions, as intake pressure was increased by up to 2 psi for higher loads. This increases the pressure following compression because of additional mass in the cylinder [106]. Furthermore, this rise in pressure causes higher pre-combustion temperatures. The additional air promotes enhanced turbulence and mixing during the injection process, which should lead to more pre-mixed combustion. Additionally, because the environment is more conducive to combustion, the ignition delay of the fuel is decreased with a

turbocharger as evidenced by earlier combustion-related pressure rise. This rise in pressure improves combustion efficiency through higher pressures and temperatures and thus, less fuel is required to generate needed power. This behavior, combined with the gains during the pumping loop (inlet pressure is higher than exhaust pressure) further improves the engine's efficiency.

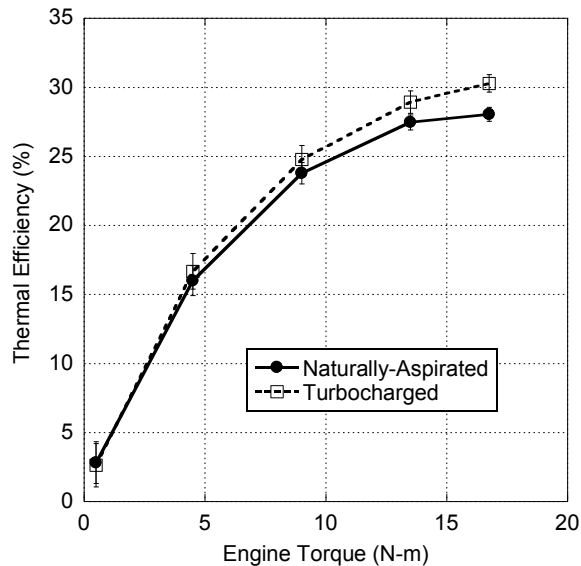


Figure 4-20. Thermal Efficiency vs. Torque for the Yanmar when Naturally-Aspirated and Turbocharged.

This is validated through calculation of engine thermal efficiency based on measurements of fuel flow rate and engine output power with the results shown in Figure 4-20. The thermal efficiency results show that the benefit of the turbocharger increases at high loads because the hotter exhaust that occurs at these temperatures provides the turbocharger with more energy to compress intake air. This is observed through higher boost pressures measured during this experiment. Of note, at low loads the boost controller did not become active (to maintain constant boost pressure) because the turbocharger was not spinning fast enough. Nevertheless, turbocharging improves mixing and the premixed burn phase of combustion that reduces the amount of less-efficient diffusion burn, improving fuel consumption and therefore, thermal efficiency [106].

4.4 Exhaust Gas Recirculation System

The EGR system is currently undergoing significant upgrades that will dramatically improve the system's measurement capabilities and control. In the configuration used by Ragone [12], the exhaust supply to the EGR system is controlled using two valves. The first is a ball valve located upstream of the EGR cooler, this acts primarily as an on/off valve for EGR flow. For better control, a butterfly valve is located downstream of the EGR cooler that provides fine control of EGR flow into the mixing box.



Figure 4-21. Intake Throttle Valve.

Initial experimentation proved that relying only on the positive pressure of the exhaust and vacuum of the intake was not enough to provide desired levels of EGR in the intake. This configuration only produces around 10% EGR by volume. To produce more EGR flow, a butterfly throttle valve is installed on the intake system, below the laminar flow element and resonance barrel, which can be adjusted to lower the intake pressure to induce adequate EGR flow from the exhaust. Figure 4-21 shows this valve in action during EGR testing. Unfortunately, the control of both the EGR and intake valves relies on direct operator hand control, rather than electronic motor control. This system is being upgraded to use a stepper motor to allow finer electronic control of the EGR butterfly valve. Additionally, the single butterfly throttle valve is being replaced by a pair of valves of different sizes to

provide electronic coarse (large valve) and fine (small valve) intake throttling. This is a component of a future master's thesis by Chenaniah Langness.

The EGR system also utilizes CO₂ sensors to determine the amount of EGR entering the engine. This is calculated by measuring the CO₂ concentration in the exhaust and intake independently. Then, the intake EGR concentration is determined by dividing the intake CO₂ concentration by the exhaust CO₂ concentration, as in (4-1). This is assumed based on only small concentrations of CO₂ being present in the ambient air [12].

$$EGR(\%) = \frac{[CO_2]_{in} - [CO_2]_{amb}}{[CO_2]_{ex} - [CO_2]_{amb}} \times 100 \quad (4-1)$$

The CO₂ sensors used are K-33 ICB 30% CO₂ sensors which currently rely on a USB connection and a commercial program for data logging (DAS100). This configuration will also be changed to direct LabVIEW integration through future student efforts.

Finally, control of the EGR cooling fans is currently performed using re-purposed computer fans and DC-based electric power. Thus, the temperature of the EGR can be controlled by varying the cooling capacity of the EGR radiator through convection modulation. Again, this system will be upgraded to interface with LabVIEW for electronic control.

4.5 Dynamometer

The dynamometer is a versatile and effective way to load an engine for performance testing. The dynamometer used at KU is a Dyne Systems, Incorporated 12 hp Dymond series. This dynamometer is capable of fully loading the Yanmar engine and utilizes AC power to either power (motor) or load the engine. Motoring is a useful means to study the effects of engine air pumping and friction. Additionally, pressure traces for engine motoring are useful for heat release analysis. The dynamometer controller, an Inter-Loc V, controls the operation of the dynamometer via measurements of speed and torque. Speed is measured by an encoder located on the outboard end of the dynamometer.

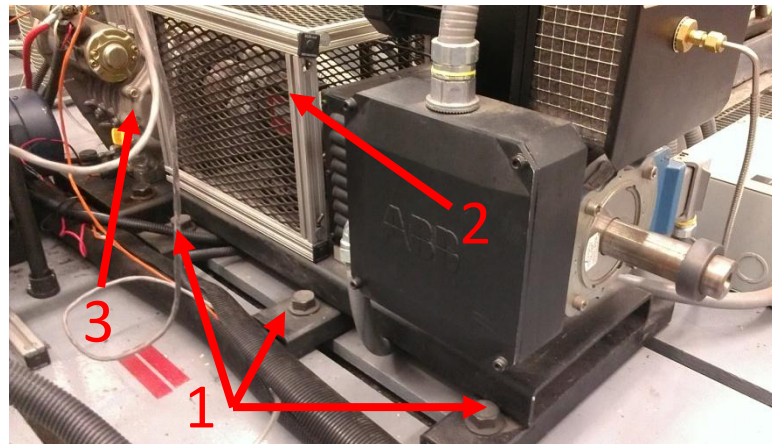


Figure 4-22. Dynamometer Mounting (1) and Driveline with Futek (2) and Yanmar (3).

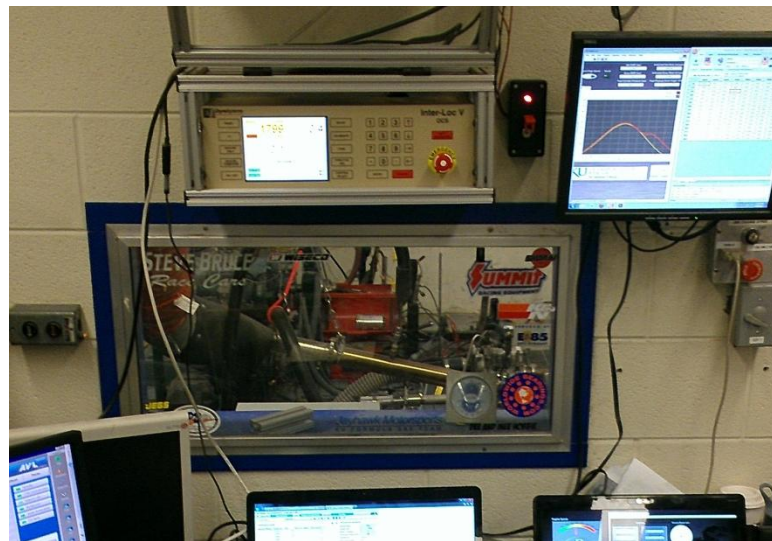


Figure 4-23. Dynamometer Controller Installed in Learned Hall.

Torque is measured using a Futek torque transducer (Model # TRS605) located between the engine and dynamometer shafts, as shown in Figure 4-22.

4.5.1 Controlling the Dynamometer

The dynamometer is controlled via the Inter-Loc V controller interface, shown in Figure 4-23. This controller is mounted outside the test cell, above the computer bench. The Inter-Loc V controller allows the user to specify dynamometer operating mode and desired load or speed. This interface is also used to change setup parameters and perform dynamometer tuning and calibration. These settings are changed using the combination of push-buttons and touch screen.



Figure 4-24. User Controls on Inter-Loc V Controller.

The buttons and their functions are (left to right in Figure 4-24):

- Reset – Clears faults, software shutdowns, and emergency stops. Pressed to restart the dynamometer
- F1 – Configurable per the Inter-Loc V Manual
- Absorb Only – Dynamometer only loads the engine and provides no motoring (power assist)
- Master Computer – Sets a computer to run the dynamometer. This is available through serial communication port and on-hand LabVIEW program (not yet operational)
- ON/OFF – Turns the dynamometer controller on or off
- Setup – Adjust parameters of Inter-Loc V controller. For example, an overspeed limit of 4000 RPM is set to protect engine and dynamometer (max dynamometer speed: 5600 RPM)
- Calibrate – To calibrate the torque transducer
- Tune – used for tuning of motoring and loading – done with proportional-integral-derivative (PID) tuning and ramp rates. Ten tuning sets are available for different engines (retuning necessary for each subsequent engine).

- Throttle Jog – Used to slew throttle towards 100% when Inter-Loc V is used to control engine throttle (not used in KU application)
- Control Select – When the interface is used for multiple dynamometer controllers, this button cycles between controllers (not used in KU application)
- Number Pad – Manual entry of numerical values
- Directional Arrows – Used to move through lists and menus
- Enter – Submits numerical values to the controller
- Cancel – Clears numerical values entered to the controller
- Soft Shutdown – un-powers dynamometer, engine is no longer motored or loaded
- Shutdown ‘Mushroom’ – puts high amount of torque (140% of rated) to rapidly stop the engine

There are two modes of operation for the dynamometer. The first mode is called ‘Torque Mode’ and is used to apply a constant torque to the engine in order to simulate load. This mode is used when another means of controlling engine speed is present. For instance, the original Yanmar engine uses a speed-governed fuel pump to control fuel flow. Thus, torque mode allows for increased loading, while the Yanmar fuel pump regulates speed. The other mode is called ‘Speed Mode’, which is used to maintain a desired speed using the dynamometer to provide either power or loading to the engine to regulate speed. This mode is the mode now used at KU in conjunction with the Bosch ECU. This mode allows the user to specify speed through the dynamometer controller then use the ECU to add fuel to create more engine power. The dynamometer automatically increases loading to counteract the increase in engine power.

4.5.2 Calibrating Torque Sensor

The measurement of torque is one of the most important parameters measured on the Yanmar. This value is used for the calculation of engine power and all brake-specific emissions and fuel

consumption levels. Therefore, the torque transducer must be recalibrated frequently to ensure accurate readings. This is a simple process, but should be repeated prior to each test.



Figure 4-25. Following Warm-up Period, Torque Transducer Out of Calibration.

After turning on the dynamometer power and controllers, the torque transducer undergoes an approximately ten-minute warm up period, where the value of torque indicated on the dynamometer controller screen will start negative and approach 0.0 N·m as the transducer circuits warm up. Once stable the final reading should be near 0.0 N·m, as shown in Figure 4-25.

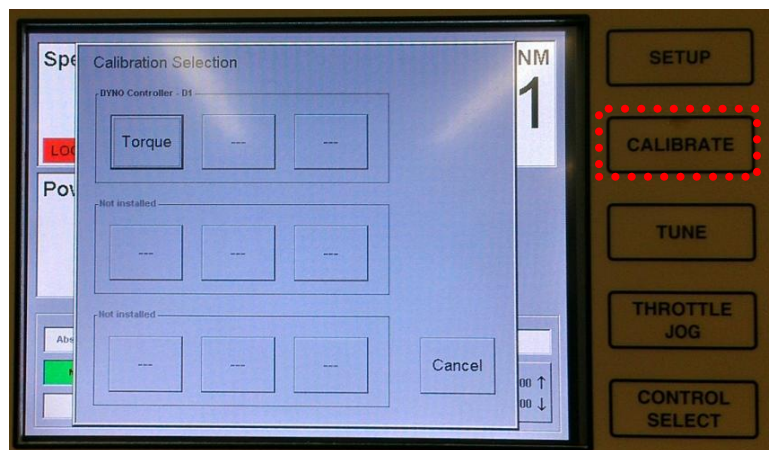


Figure 4-26. Calibration Selection Window Displayed By Pressing 'Calibrate'.

After this warm up period, the torque transducer may be calibrated by pressing the ‘Calibrate’ button on the dynamometer controller and subsequently pressing ‘Torque’ on the touch screen popup menu (Figure 4-26). This brings the user to the calibration menu where the linear offset and gain values are adjusted by zeroing and spanning until desired values are indicated in the measured torque portion of the screen.

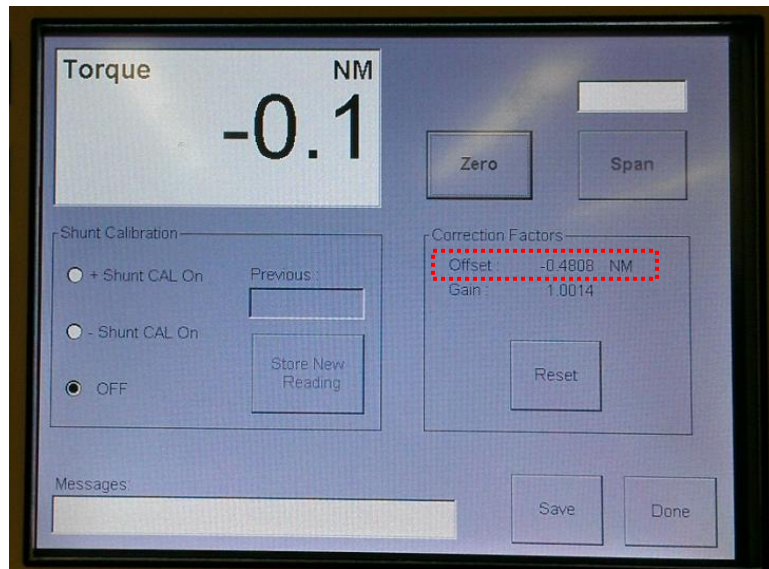


Figure 4-27. Press ‘Zero’ to Adjust the Offset of The Transducer Signal.

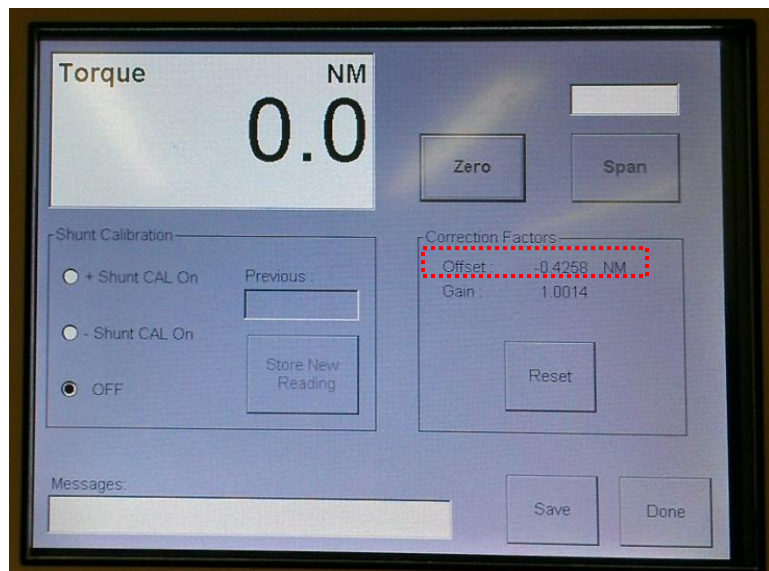


Figure 4-28. Signal Offset Adjusted to Zero Torque Measurement.

Begin by pressing ‘Zero’ on the touch screen. This will adjust the offset correction factor, as shown in the before (Figure 4-27) and after (Figure 4-28) images. With this offset value (-0.4258 N·m), the displayed measured torque value is 0.0 N·m as desired. The gain is adjusted by pressing the ‘+ Shunt CAL On’ button on the touch screen. This sends a 5 VDC signal across the torque transducer shunt circuit to produce a full-scale reading that can be used for gain adjustment.

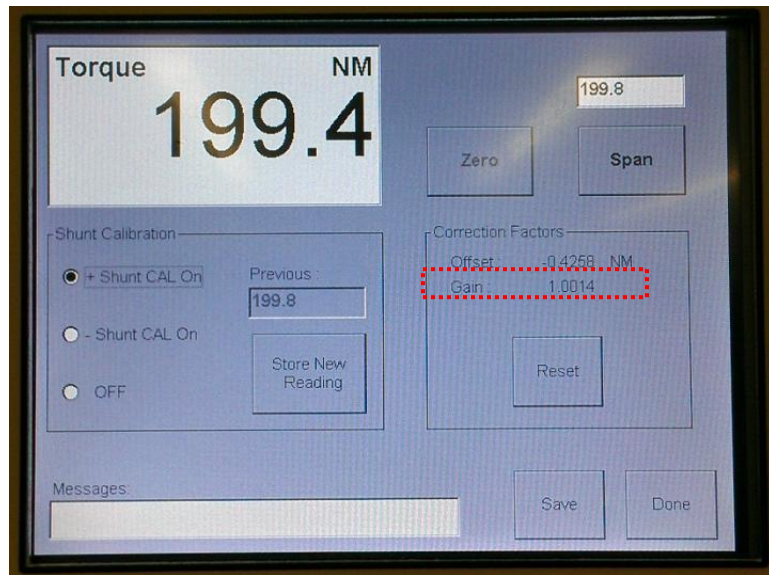


Figure 4-29. Shunt Calibration (+5 VDC) Sent to Transducer to Set Gain Value at Full Torque.

In Figure 4-29, the shunt is active, producing a 199.4 N·m measurement. During initial Dyne Systems, Incorporated commissioning, the full-scale reading was saved as 199.8, which is the value that the sensor is spanned to in subsequent calibrations.

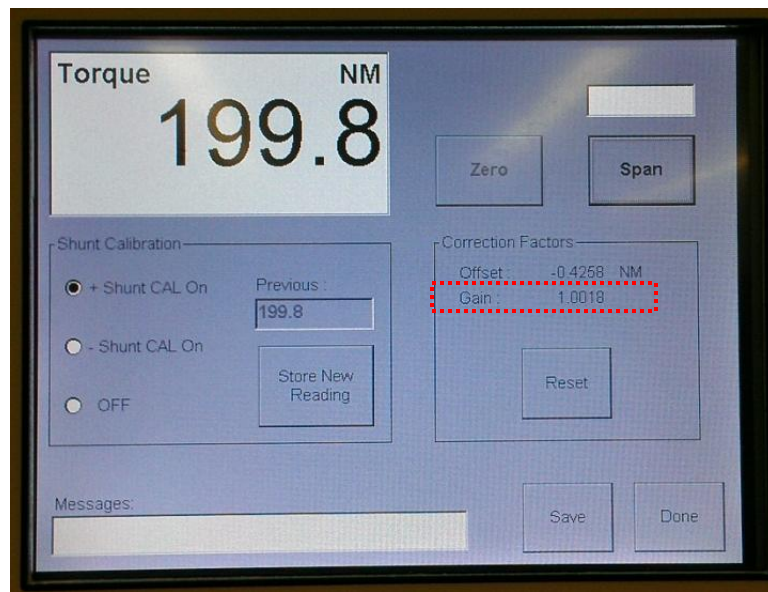


Figure 4-30. Signal Gain Adjusted to Span Measurement at Full Torque.

Pressing ‘Span’ on the touch screen changes the gain so that the measured torque matches the desired output of 199.8 N-m. This is reflected by the new gain correction factor shown in Figure 4-30.



Figure 4-31. Torque Transducer Calibrated.

Finally, the torque transducer shunt circuit is deactivated by pressing ‘OFF’ on the screen. The operator applies the new correction factors by pressing ‘Save’ and ‘Done’ on the calibration window,

which returns the controller to the main control screen. The newly calibrated transducer reflects the desired 0.0 N-m measurement in Figure 4-31.

4.5.3 Tuning the Dynamometer

In addition to the calibration of the torque transducer, the tuning of the dynamometer speed control is vitally important to reduce statistical uncertainty during steady-state tests (particularly at low-load conditions) and ramp rate/overshoot error during ramp experimentation. This process has been already performed on the Yanmar engine, but will have to be done following the connection of the Duramax to the dynamometer in the upcoming multi-cylinder laboratory. Thus, the complete calibration procedure is covered in Chapter 5 of this dissertation.

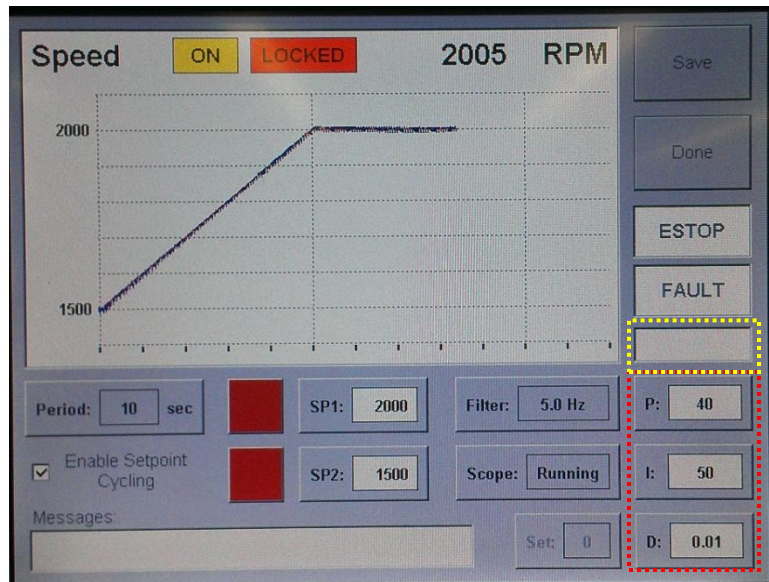


Figure 4-32. Dynamometer Speed Response to Ramp Following Calibration.

The dynamometer uses a proportional, integral, derivative (PID) controller to regulate speed. The gains for these parameters are shown in the calibration window of Figure 4-32. This is accessed by pressing the 'Tune' button on the dynamometer controller. The graph in the tuning window indicates both the setpoint and actual speed measured. Comparison of the speed signal in this figure to those of the unloaded dynamometer in Chapter 5 indicate the implications of a single-cylinder engine on tuning as more speed variation is observed here. Also shown on this screen are the speed setpoints for the

upper and lower setpoints of the ramp cycle (SP1 and SP2). These can be adjusted by entering a new value in the numeric dialog box (yellow) then pressing on the value to be changed. Cycling through upwards and downwards speed ramp can be deactivated by pressing the ‘Enable Setpoint Cycling’ checkbox. Any changes to tuning are saved by pressing ‘Save’. The user is returned to the main operating window by pressing ‘Done’.

4.6 Data Acquisition and Control

A segment of the test cell that is particularly important is the test cell control and data acquisition systems. This series of systems is responsible for managing the engine fuel system, controlling and recording emissions data, and displaying and saving the in-cylinder pressure and engine performance data. Finally, important equipment safety information is relayed to the operator through these interfaces. In total, this requires four computers that all fill a specific need. The computing that takes place can be broken into three categories, low-speed performance data (10-20 Hz sampling), high speed in-cylinder data (42.3 kHz), and emissions.

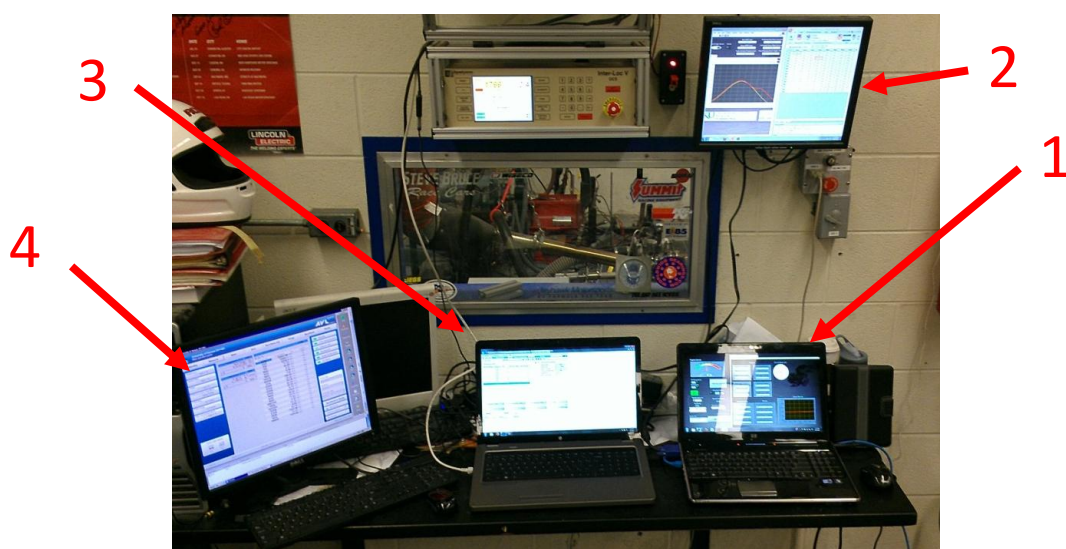


Figure 4-33. Computers for Test Cell. Includes Low-Speed System (1), Second Monitor for Remote-Desktop to High-Speed and ECU Computer (2), and Emissions Laptop (3) and AVL Bench Monitor (4).

The low-speed system (Figure 4-33) uses a compact-Reconfigurable Input/Output (c-RIO) controller to read/send analog and digital signals to the instrumentation and control hardware of the test cell. These signals are predominantly 0-5 or 0-10 VDC analog, mV thermocouple signals, or 4-20mA input/output signals, and serial communication is also available. This c-RIO controller is connected to the School of Engineering network through ethernet cable. This controller communicates with the performance laptop through this engineering network. This connection provides the operator with measurements such as speed, power, torque, fuel consumption, air flow, and intake/exhaust conditions. This is also the interface for the gaseous fuel injection system and will be where the EGR system is controlled. The high-speed computer is a rack-mount computer located inside the test cell instrumentation cabinet that is directly connected to the ECU via USB connection. During testing, this computer is accessed via remote desktop on the low-speed system laptop. The display for this computer is wall-mounted next to the dynamometer controller. The intention is that the main operator will use these two screens to control the entire engine system. The emissions laptop is connected to both the AVL FTIR bench and AVL Smoke Meter via an independent emissions network, which is composed of only the laptop, smoke meter, and FTIR bench. This way, the IP addresses of these components can remain static. Furthermore, the computer located inside the FTIR bench should never be connected to the internet, as instructed by AVL. This computer also has a monitor that is set up on the computer bench for monitoring of errors and other messages on the FTIR screen. These computers are intended to be operated by a second test cell operator, with their primary responsibility being control of the FTIR, smoke meter, and emissions data acquisition.

4.6.1 Low-Speed System

The program that operates the low-speed control/acquisition system is programmed in LabVIEW. This makes the program fully customizable for any specific need of current and future

researchers at KU. Using LabVIEW, an executable for the program can be easily produced following updates to the program.



Figure 4-34. Main Operating Window of Low-Speed LabVIEW Program.

A screen shot of the main window of the low-speed program is shown in Figure 4-34. Data saved with this program is used to determine brake-specific fuel consumption and other important parameters. The program itself is broken down into two main components, a fully-programmable gate array (FPGA) code and a main LabVIEW program. The FPGA code is a separate program that utilizes speed to gather/send data from the eight c-RIO sensor modules. This code also contains the in-cylinder sensor to ECU code discussed in Chapter 1. The main program uses the FGPA signals to perform all calculations that take more computing effort than the FPGA. These calculations can be readily adjusted by entering the program block diagram and making the necessary changes. This program also controls the fuel pump for the common-rail fuel system and sends a simulated accelerator pedal position to the ECU to control.

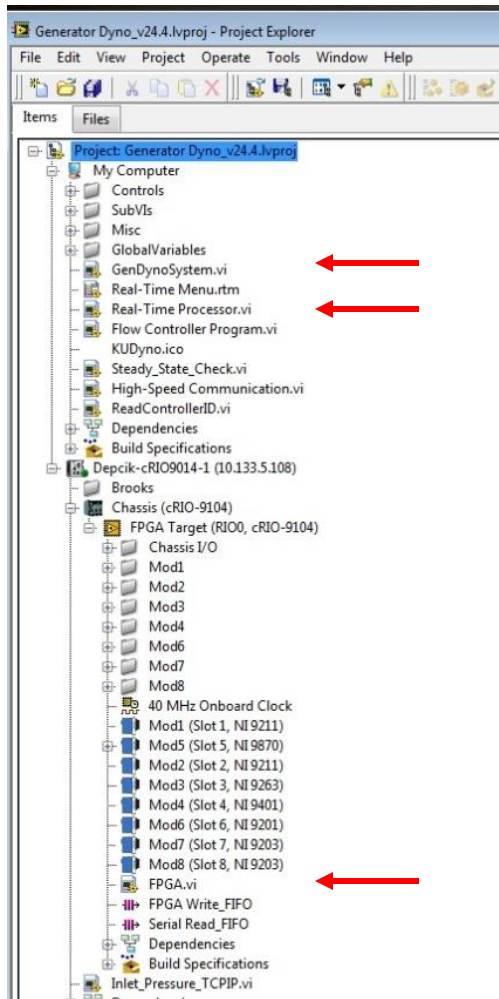


Figure 4-35. Low-Speed LabVIEW Project.

There are many different types of sensors that interface with the c-RIO to perform a variety of measurements and controls. Primarily, the sensors are either an analog voltage (0-5 or 0-10 VDC) or analog current (4-20mA) signal. An example of the calculation of fuel flow rate is used here to elucidate the low-speed control system hierarchy, with the project shown in Figure 4-35. First, all incoming signals from each module on the c-RIO are collected using the 'FPGA' Virtual Instrument (VI) code, indicated by red arrow in Figure 4-35. These signals are then retrieved from memory by the VI called 'Real-Time Processor' for analysis and display on the 'GenDynoSystem' VI, both also indicated by red arrows.

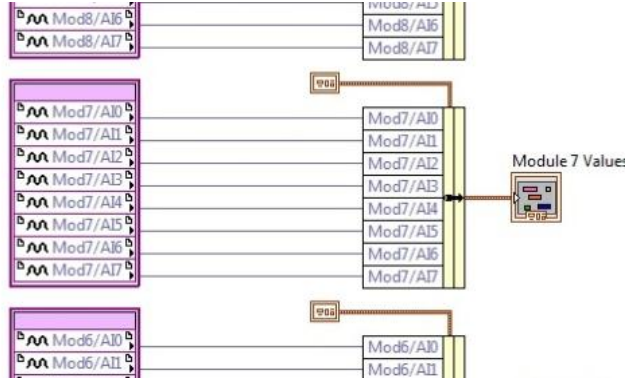


Figure 4-36. Input of Module Seven Signals to Data Cluster.

The FPGA VI section of code pertaining to fuel measurement is shown in Figure 4-36. In this section, all channels of the module (analog input (AI) 0-AI7) are wired from an FPGA I/O Node into a bundle by name function. This consolidates all data into a single set of numbers that are transferred as a unit to the real-time processor for analysis via a data cluster.

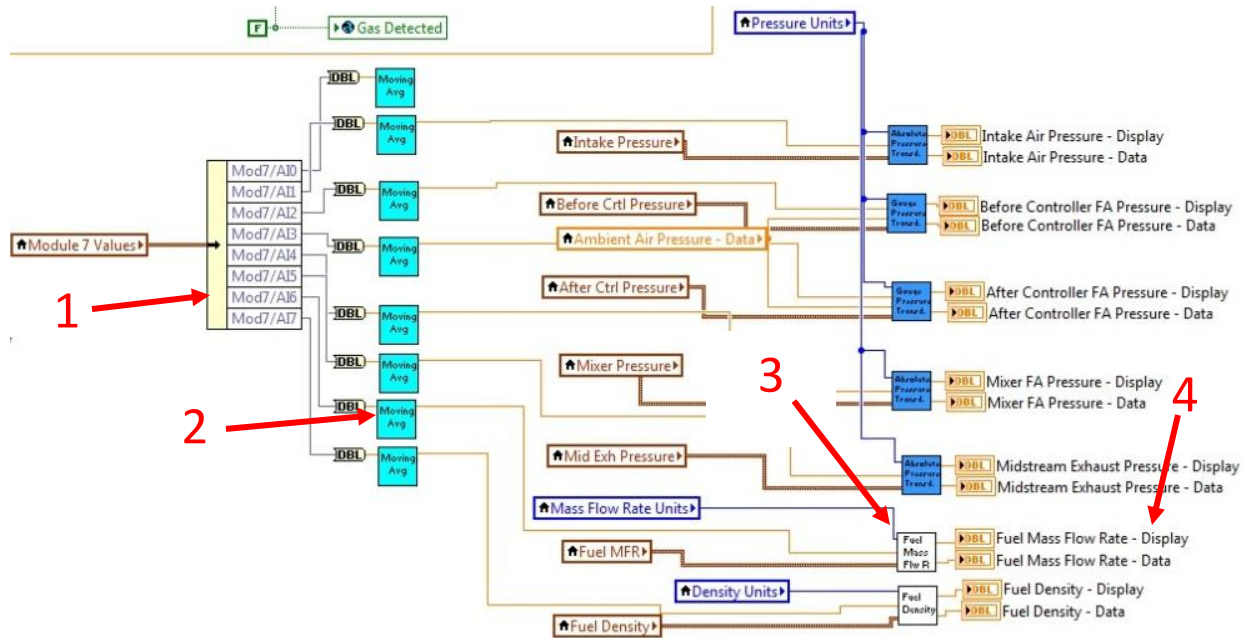


Figure 4-37. Retrieval of Module Seven Data Cluster. Calculation of Fuel Mass Flow Rate.

The real-time code within the ‘Real-Time Processor’ VI that handles fuel flow measurement is shown in Figure 4-37. This section of code proceeds as follows:

1. The data cluster is separated using an unbundle by name function to separate the module into individual channels, which correspond to the sensors wired into it.
2. In the case of the fuel mass flow reading, a 50-value moving average is applied to smooth out signal variation.
3. This average enters a subVI to calculate useful parameters based on the input signal (voltage or current). The subVI shown here calculates fuel mass flow rate, which is described in-depth in the next paragraph.
4. Following the subVI, two values (one each for display and data-saving) are wired to individual local variables. Two types of values are used to so that displayed units may be selectable by the user while data units are set in SI (g/s) for easier post-processing with consistent units.

SubVI's are used to perform smaller tasks within a larger VI. This improves program readability and modularity as oftentimes a subVI may be used in multiple locations to serve the same purpose.

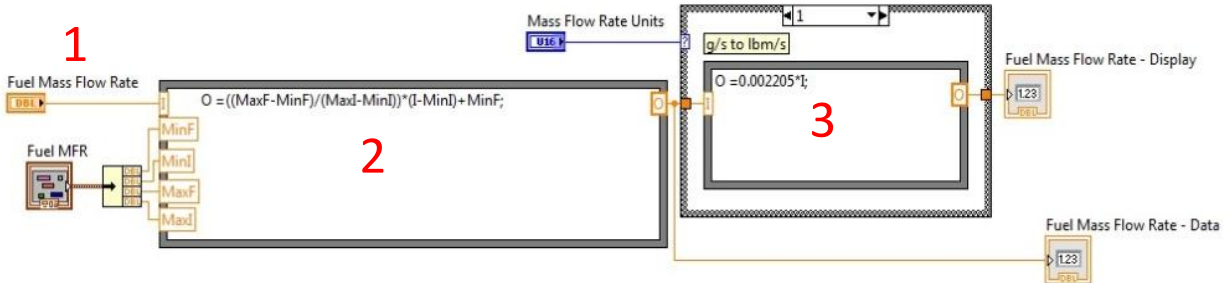


Figure 4-38. Fuel Mass Flow Rate Calculation SubVI.

The subVI that calculates fuel mass flow rate based on input current signal is shown in Figure 4-38:

1. The mass flow sensor signal is wired to a formula node, which allows for mathematical calculations. This particular sensor assumes linear proportionality between flow rate and sensor output signal. Therefore, calculation of the flow rate can be accomplished using linear interpolation. Also needed for interpolation are the mass flow rate limits (zero to span values of 0 to 1.0 g/s for this sensor) and minimum and maximum signal current (4-20mA in this case).

2. Linear interpolation using these inputs yields an output mass flow rate, named 'O' in this example.
3. The output flow rate value is in g/s by default, therefore this signal is wired directly to the data-version of the fuel mass flow rate. Flow units for display are user-defined. In this example, the conversion from g/s to lbm/s is shown. The resulting flow rate in lbm/s is wired to a local variable for display on the operator screen.

In some instances, the calibration of a sensor may be based on a calibration curve or calibration table. A sensor using a calibration curve can be handled in a similar manner to the linear fuel mass flow sensor using a formula node. In the case of a sensor with a calibration table, such as the fuel rail pressure sensor, a different type of approach is needed. For this type of sensor, linear interpolation is used along with a lookup table.

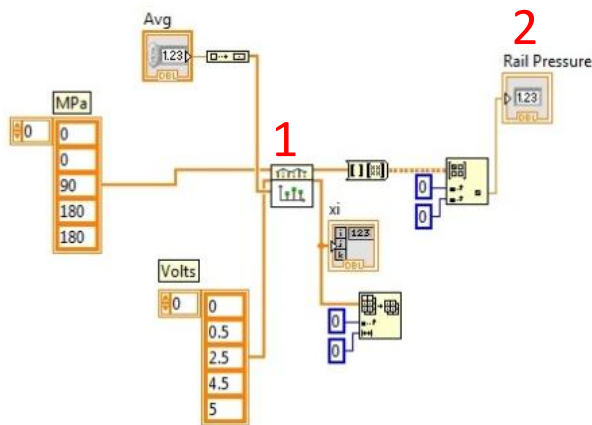


Figure 4-39. Rail Pressure Linear Interpolation SubVI.

The subVI to calculate fuel rail pressure based on input voltage is shown in Figure 4-39. This code functions in two steps:

1. First, an Interpolate 1D subVI calculates the output pressure. This subVI needs two curves to perform linear interpolation based on the input voltage. The curves used are those based on the calibration table for this sensor. In this case, the x-input is the independent input voltage and

the y-input is the dependent pressure. The Interpolate 1D subVI outputs a value called 'xi', which corresponds to the voltage used in the interpolation (used as a check, this results should be the same as the voltage input from the sensor). The subVI also outputs the necessary pressure value as an array.

2. The output is retrieved using a get matrix elements function to yield a single value for rail pressure to be used for both display and data saving. Currently, only MPa is offered for display, lbs/in² is also possible.

After being saved to a local variable following subVI execution, the display and data values are saved to a global variable which can be accessed by other subVI's in the dynamometer project, such as the 'GenDynoSystem' VI.

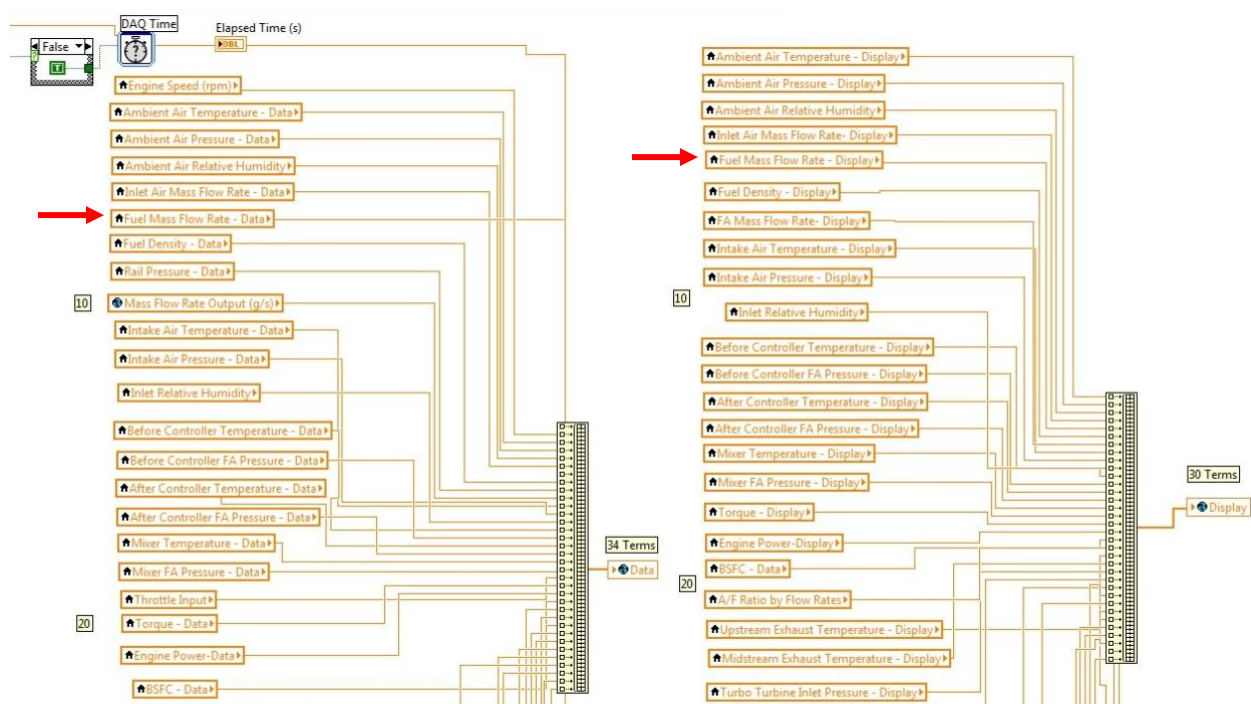


Figure 4-40. Building Global Data and Global Display Variables in Real-Time Processor.

This process is accomplished in Figure 4-40. The left portion of this figure shows the collection of all data values into the Data global variable. Likewise, the right-hand side indicates the filling of the

Display global variable. These variables are individually wired in a specific order using a build array function.

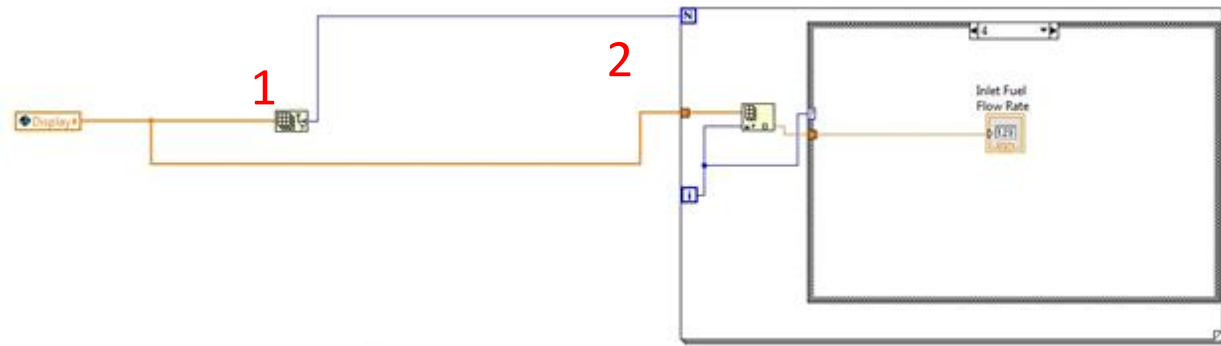


Figure 4-41. Retrieving Inlet Fuel Flow Rate from Global Display Variable.

This order is necessary for retrieval by other VI's in the project, such as by the 'GenDynoSystem' VI example in Figure 4-41. Here, the value for fuel mass flow rate is separated from other values in the global Display variable to be displayed on the main operation screen. This occurs in the following fashion:

1. Using an array size function the number of elements in the global display array is determined.
2. A for-loop runs once for each element in the global display variable. Each iteration retrieves the associated data value in that index. For example, index 4 retrieves the inlet fuel flow rate value for display.

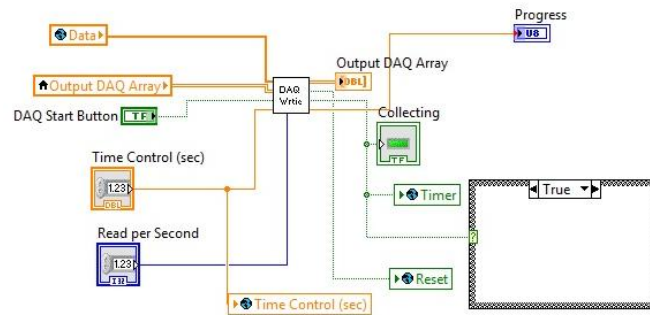


Figure 4-42. Retrieving Data from Global Data Variable for Writing to File with DAQ Write SubVI.

During data collection for saving, the entire Data global variable enters the ‘DAQ Write’ subVI (Figure 4-42). This subVI formats the save file, including column headers, and builds the rows during data collection. As sensors are added, this subVI needs to be changed to reflect the addition of new sensors.

4.6.1.1 Creating Executable for Test Cell Control

After any change is made to the LabVIEW code, a new program executable must be produced in order for those changes to show up upon program opening.

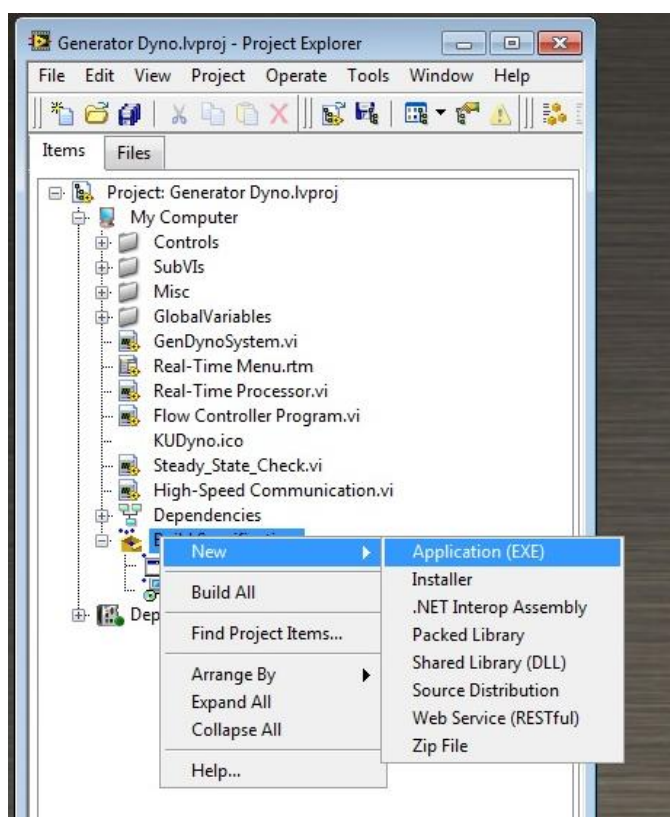


Figure 4-43. Creating a New Executable of LabVIEW Program.

This is done by first saving all changes to the LabVIEW code, then going to the project tree and right-clicking on Build Specification → New → Application, as done in Figure 4-43.

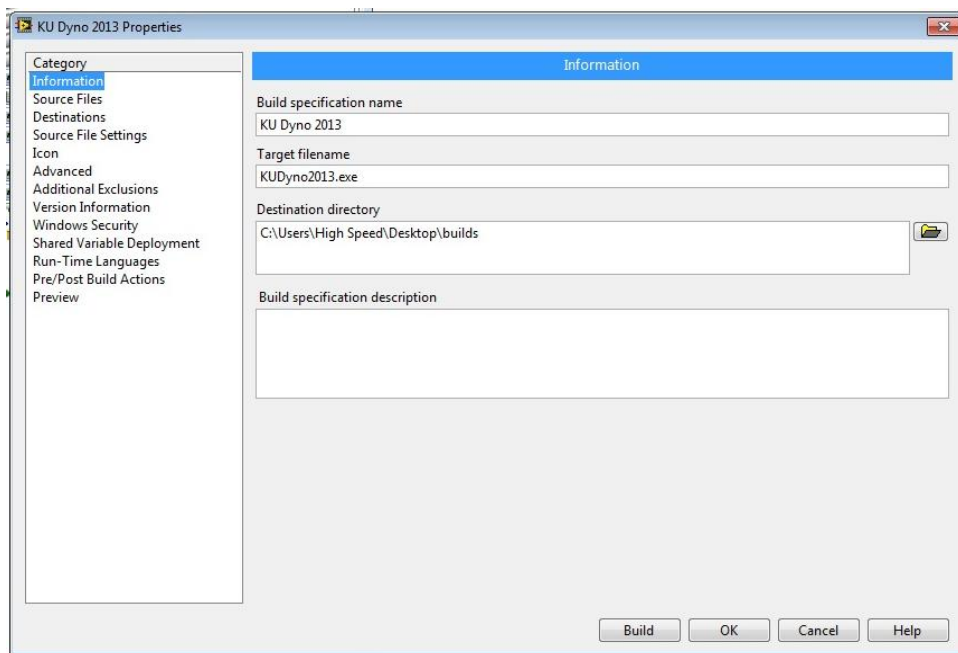


Figure 4-44. Information Window of Executable Generation.

This opens the new executable dialog box, shown in Figure 4-44. Here, the user inputs information such as the executable name (KU Dynamometer 2013) and the destination for the installation files that goes with the program.

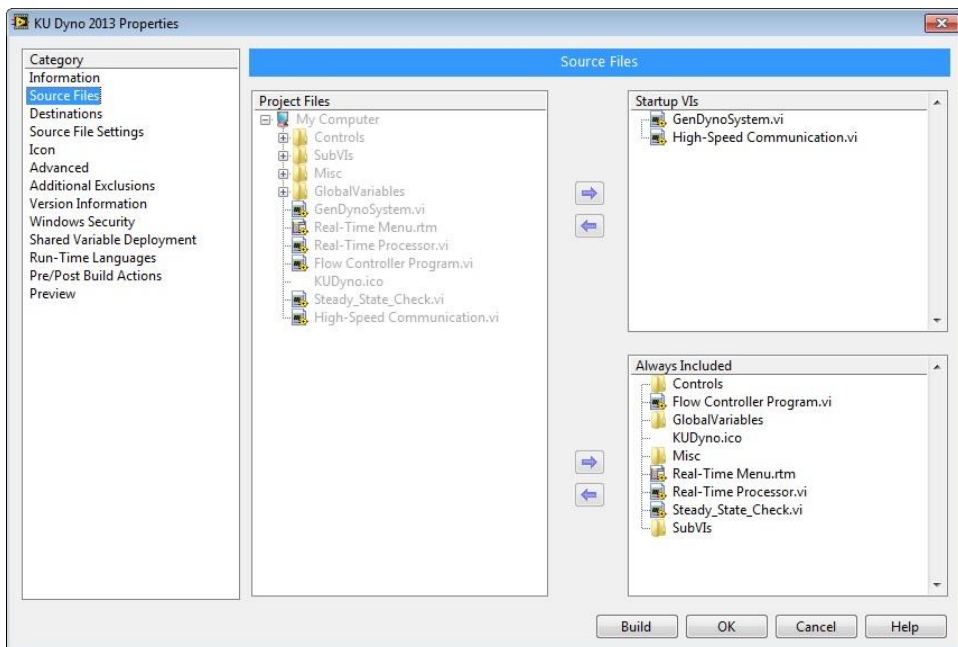


Figure 4-45. Source Files Window of Executable Generation.

From here, the user changes categories (left list in Figure 4-44) to move to the Source Files category (Figure 4-45). This window lets the programmer determine which sections of the project will startup upon executable start, and which programs are also needed for operation. In this case, the ‘GenDynamometerSystem’ and ‘High-Speed Communication’ programs are selected to startup immediately following program initialization. These two code segments call the segments listed in the ‘Always Included’ section.

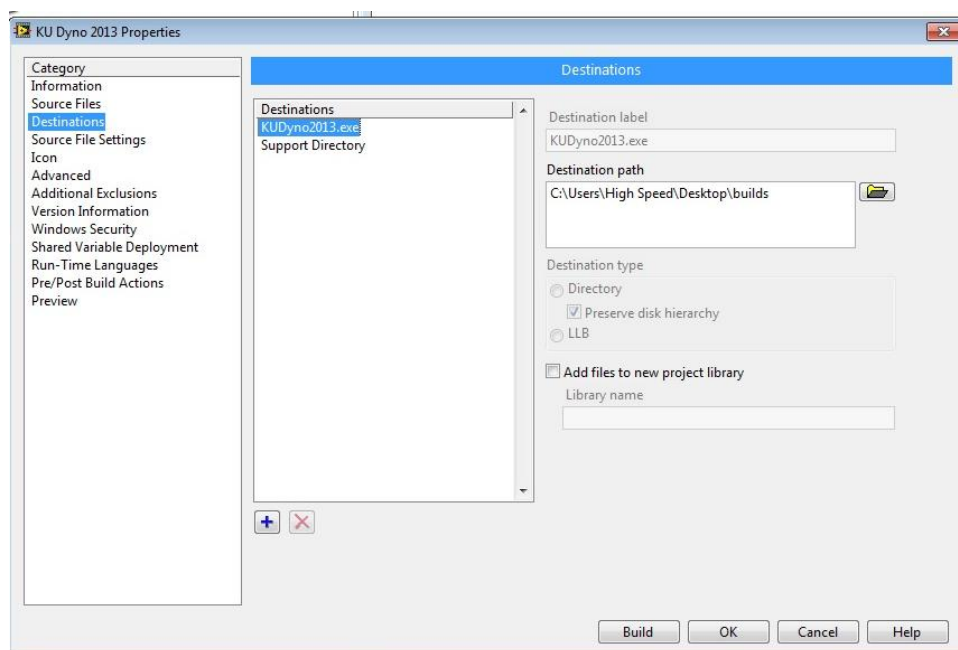


Figure 4-46. Destinations Window of Executable Generation.

The Destinations category (Figure 4-46) sets the final location of the executable, which should be set to the same destination as the destination directory Figure 4-44.

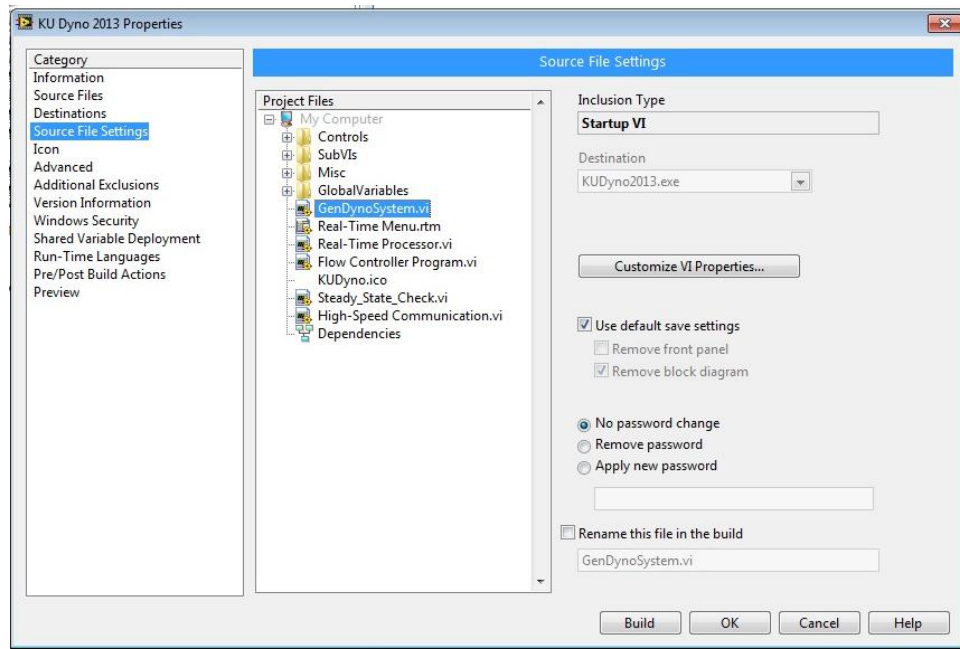


Figure 4-47. Source File Settings Window of Executable Generation.

The ‘Source File Settings’ category window, shown in Figure 4-47, lets the programmer inspect the pre-determined source file settings and set save and password settings. The choices shown here should always be used.

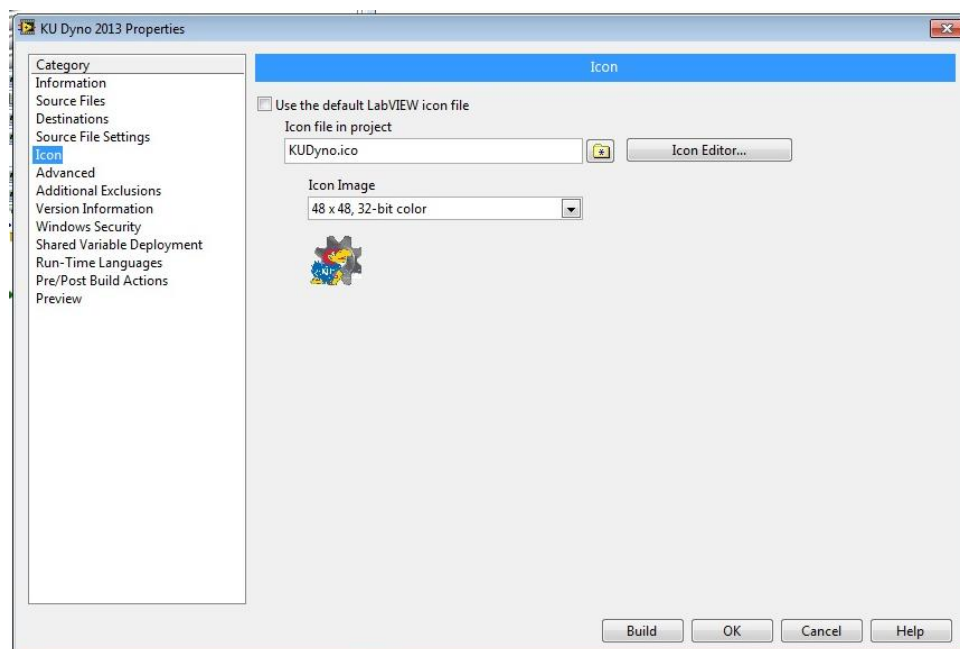


Figure 4-48. Icon Window of Executable Generation.

The creation of an executable allows the programmer to choose an icon. A prior KU Mechanical Engineering logo works well. Other images can be used by browsing in the Icon category window (Figure 4-48).

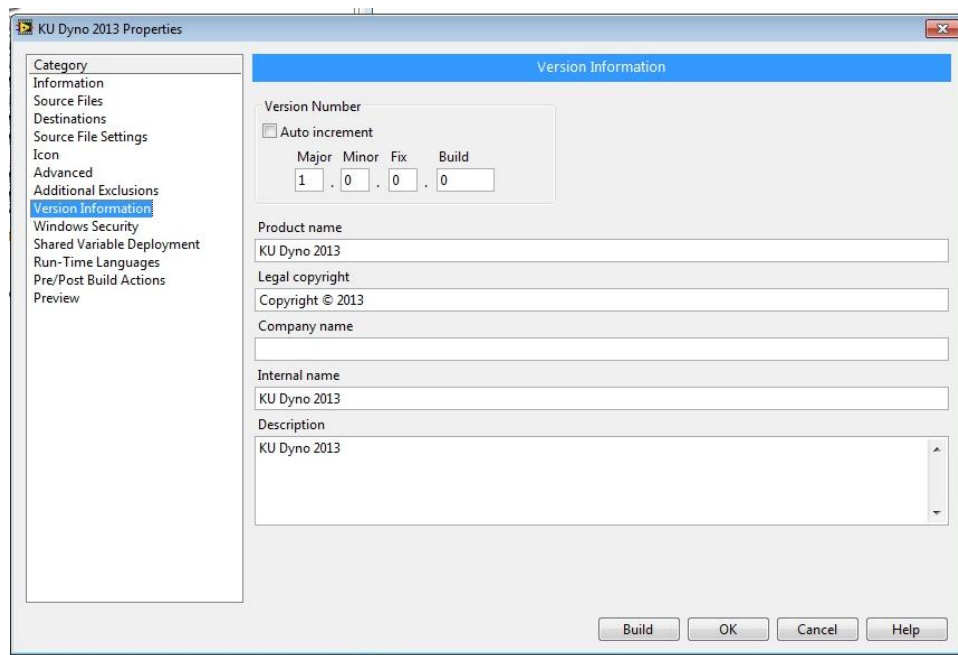


Figure 4-49. Version Information Window of Executable Generation.

Finally, specific version information may be entered (if so desired). This option is available under the Version Information category, shown in Figure 4-49. Other than these settings, the un-mentioned categories should remain in the default settings from prior builds of this project. Now, the executable can be built by pressing the 'Build' button on the executable generation window (Figure 4-49).

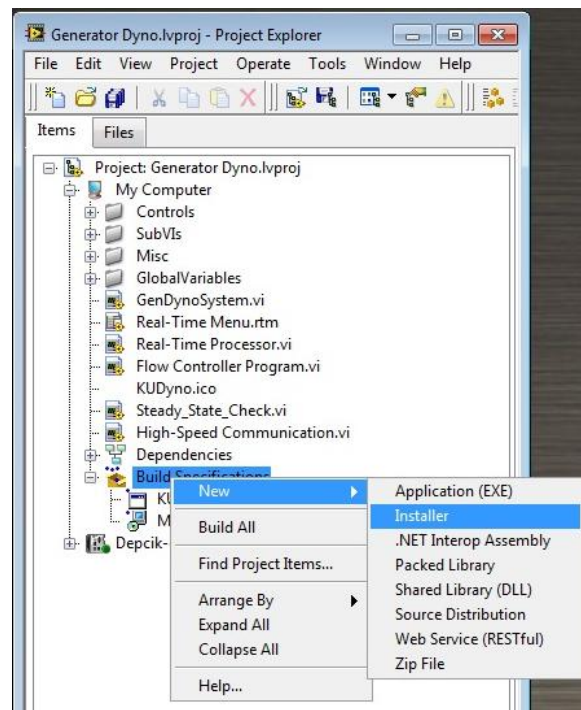


Figure 4-50. Creation of LabVIEW Executable Installer.

Following the building of the executable, the programmer is returned to the project tree, where an installer must also be created for this executable. This is done by right clicking on Build Specifications → New → Installer as indicated by Figure 4-50.

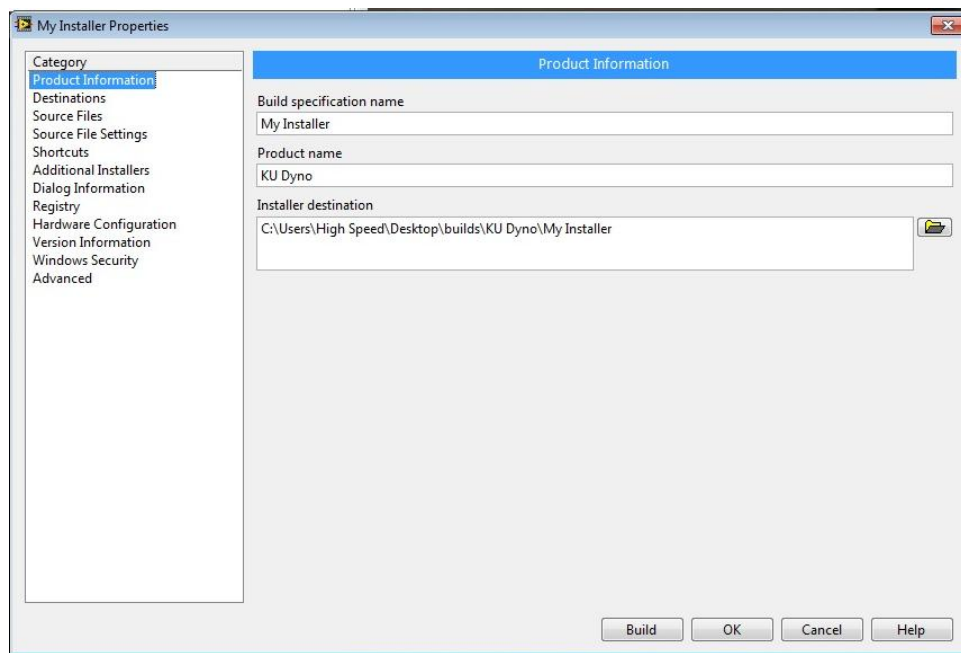


Figure 4-51. Product Information Window for Executable Installer.

Figure 4-51 shows the installer properties window which is similar to the executable properties window. In this window, the installer name and destination are designated. This destination should be the same as that of the executable (...\\Desktop\\builds).

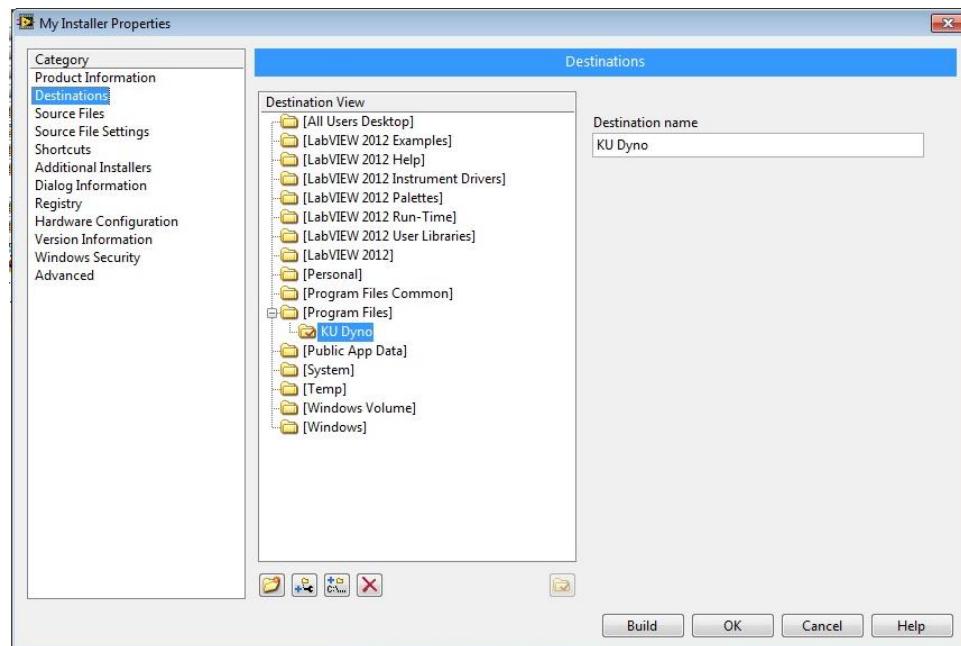


Figure 4-52. Destinations Window for Executable Installer.

The destination of the program following installation is set through the Destinations category of the dialog box in Figure 4-52. The location shown under Program Files is the default location, this means that the actual program files will go in this location following installation.

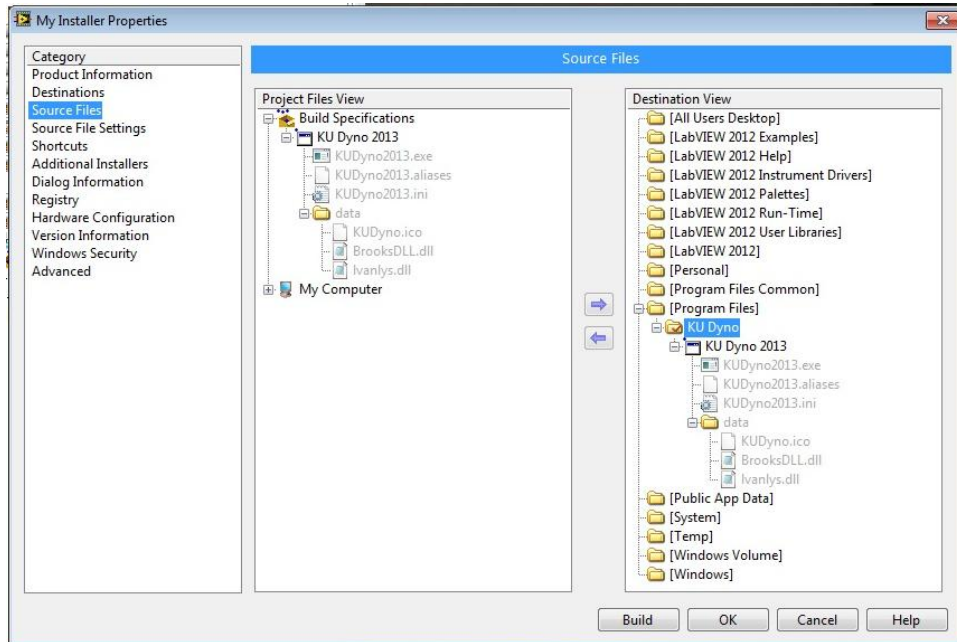


Figure 4-53. Source Files Window for Executable Installer.

The source files used for the installer (linking it to the actual executable) occurs in the Source Files category (Figure 4-53). As shown, the KU Dynamometer 2013 executable and its sub-files (aliases, icon, dll files, etc) are moved from the Project View tree to the Destination View tree using the arrows and by selecting the appropriate destination folder (left-click on KU Dynamometer). This is why the executable must be built first.

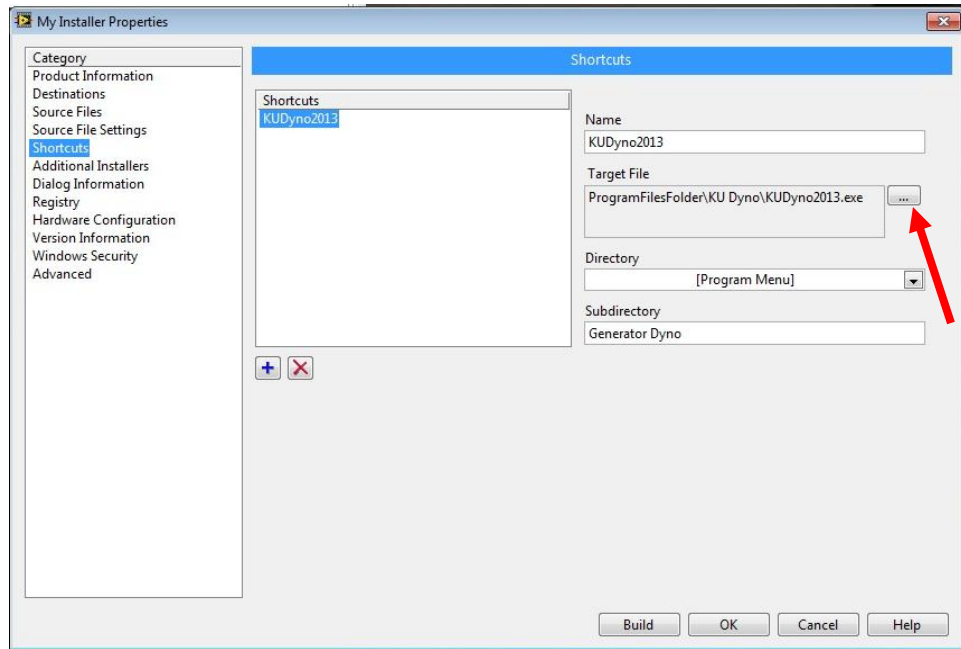


Figure 4-54. Shortcuts Window for Executable Installer. Browse for Target File.

If so desired, a shortcut can be created as well for the taskbar and start menu. This process is shown in the Shortcuts dialog box in Figure 4-54. The shortcut can have a different name from the executable program itself, though in this case it is the same name ('KUDynamometer2013'). The shortcut must be linked to the target executable, which is selected by browsing via clicking of the browse button on this dialog box.

This concludes the steps necessary to create the program installer. The process is completed by clicking 'Build'. Of note, the process to build the installer takes considerably longer than the building of the executable itself. Once the process finishes, the installer is ready to go and available by browsing to the destination chosen during the building process.

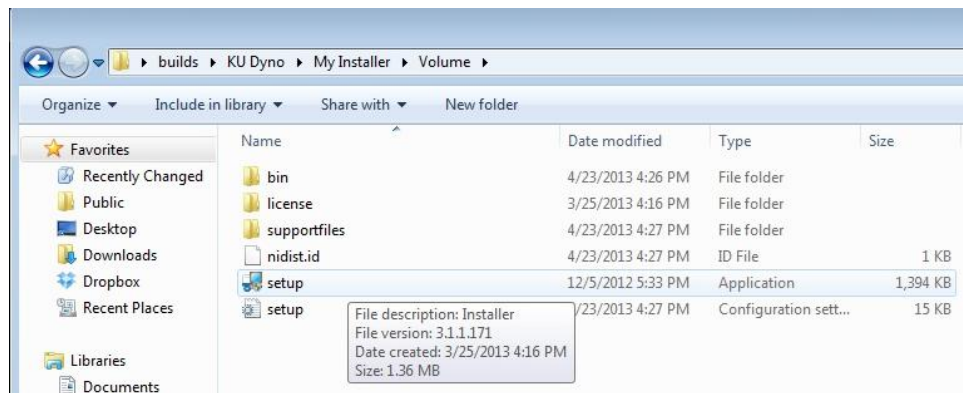


Figure 4-55. Installer for Executable.

The contents of the installer are shown in Figure 4-55. Double-clicking on setup (highlighted in Figure 4-55) will begin the installation process. From there, the shortcut will be available in the Windows startup menu and can be pinned to the taskbar for easy access.

4.6.2 High-speed Instrumentation

The in-cylinder pressure measurement and recording system is discussed at length in this author's master's thesis [20]. This source provides a fundamental understanding of the function of this program, as well as the method in which the pressure transducer and encoder are implemented on the Yanmar engine. However, since that time a series of upgrades have been made to improve the accuracy and usefulness of the system. The first upgrade is the use of measured inlet pressure as a reference pressure. The piezoelectric sensor is useful for detecting changes in pressure, but must have an absolute pressure reading to use as a reference. In this case, the pressure of the intake is assumed to be equal to the pressure in the cylinder at piston bottom dead center prior to the compression stroke [20]. Previously, a static value of 0.95 bars was used because of the relatively constant intake pressure measured [20]. Now that the EGR system and turbocharger are in use, the inlet pressure can be highly variable through changing test configurations. As a result, the absolute pressure measured by the c-RIO system is sent via ethernet connection to the in-cylinder program for pressure referencing.

4.6.2.1 Intake Reference Pressure Upgrade



Figure 4-56. Setting Rack-Mount Computer IP Address and Sending Intake Pressure to In-Cylinder Code.

During operation, the option to send the inlet pressure to the in-cylinder program is determined on the low-speed performance laptop program, this section is shown in Figure 4-56. The user sets the rack-mount computer IP address (can be set as a default value) and activates the switch. Note: the in-cylinder program must be running before pressing the ‘Send to High-Speed’ switch. If it is not running, turn the ‘Send to High-Speed’ switch off and start the in-cylinder program. If this switch is not activated while the in-cylinder code runs, a reference pressure of 0.0 bars is used. This way, if for some reason the intake pressure is not sent to the in-cylinder recording program, offsetting the data with measured inlet pressure during post-processing is very straightforward as data collection for both low-speed and high-speed systems occurs simultaneously.

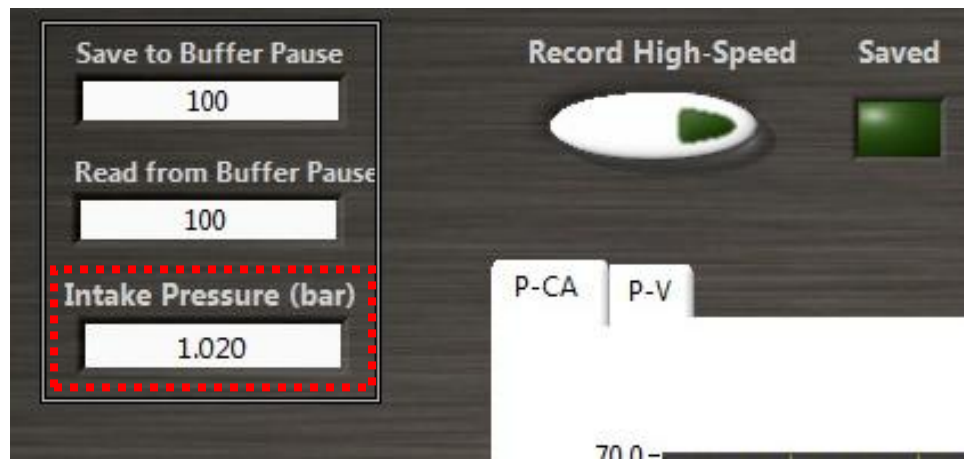


Figure 4-57. High-Speed Measurement Window: Reference Intake Pressure.

As a visual check of performance, the pressure sent from the c-RIO system is displayed on the in-cylinder display, as shown in Figure 4-57. The transfer of the intake pressure from the c-RIO to the rack-mount computer requires two LabVIEW programs that run simultaneously. The first one described here is the High-Speed Communication virtual instrument (VI) that runs in the background of the c-RIO program and is activated by clicking the 'Send to High Speed' button on the main program window of Figure 4-34 and Figure 4-56.



Figure 4-58. Global Variable in Main Operating Program.

Pressing this button sets the global variable 'Communicate' to *True* and sets the rack-mount IP address in the global variable 'High Speed IP Address' as shown in Figure 4-58. This occurs in the main loop of the c-RIO code. As these are global variables, these values are automatically available in the High-Speed Communication.

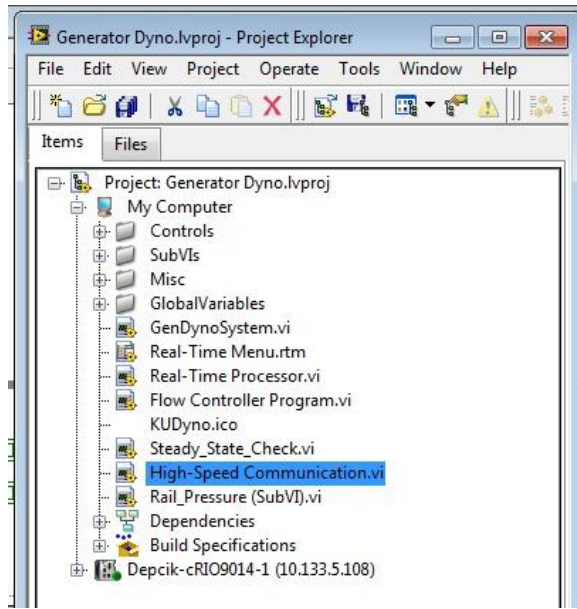


Figure 4-59. Main Test Cell Project.

This program is accessed in the c-RIO project tree by double-clicking on ‘High-Speed Communication.vi’, as done in Figure 4-59. The actual transfer of data over ethernet via Transmission Control Protocol and Internet Protocol (TCP/IP) communication occurs in the separate ‘High-Speed Communication’ program to ensure that if the in-cylinder code were to stop, the rest of the c-RIO operations continue to run without a crash.

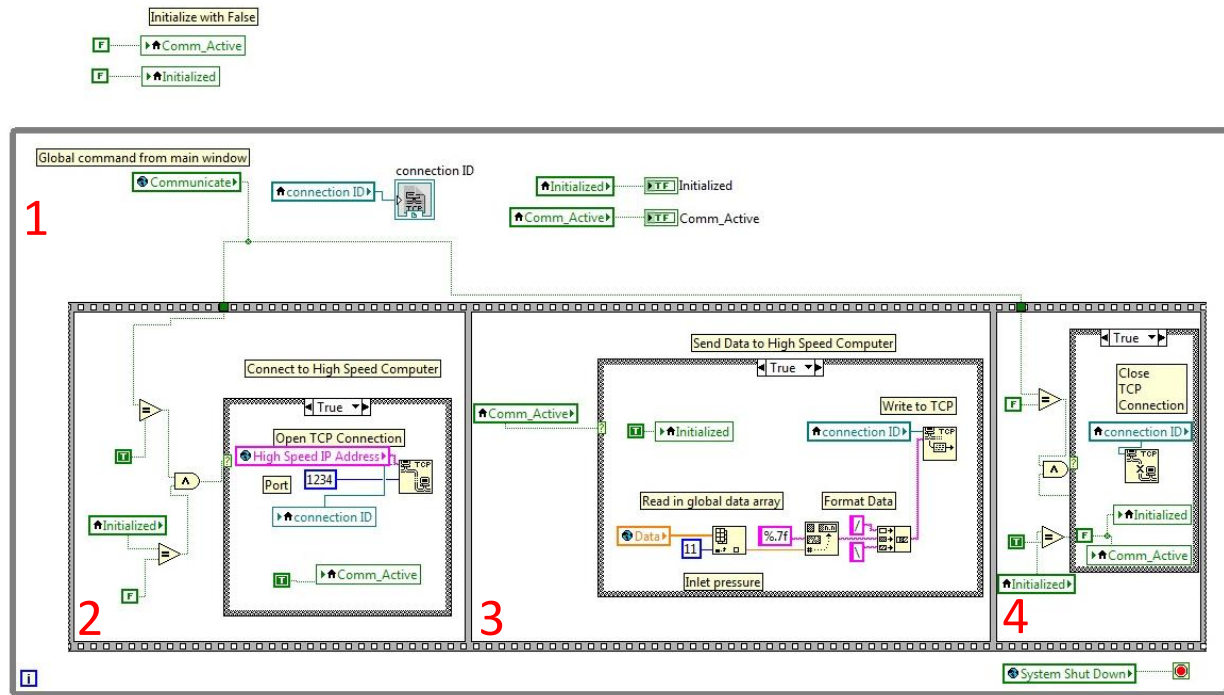


Figure 4-60. Sending Inlet Pressure from c-RIO to High-Speed Computer via TCP/IP.

Other than the two Booleans that indicate initialization and active connection with the rack-mount, there is no useful information on the front panel of this program. The block diagram of the High-Speed Communication VI is shown in Figure 4-60. The code initializes with the starting of the low-speed executable and runs in a while loop for as long as the duration of testing. The Boolean indicators (top of figure) initialize false. The code proceeds as follows:

1. The program flow enters the sequence structure during every iteration of the while loop. The case structure inside the first frame contains a do-nothing false case. Once the Communicate global variable becomes *True* with the pressing of the ‘Send to High Speed’ button, the true case of the case structure runs. This case starts the TCP open connection function to connect to the rack-mount computer based on the user-defined IP address. A remote port is also required by this section of code, which can be thought of as a password, and is set to 1234. Once connected, a connection ID is needed for subsequent TCP data transfer functions. The local variable ‘Comm_Active’ is set to *True* so that the true case structure in the second frame will execute.

2. Now that a connection is established, the local variable ‘Initialized’ is set to *True* to keep the code in the first frame of the sequence from trying to re-establish a new connection. Then, the inlet pressure is sent to the rack-mount LabVIEW program. This is accomplished by retrieving this data from the global variable ‘Data’ and removing the 11th value in the data array. This array carries all values measured by the c-RIO program in a specific order with 11 corresponding to the index for the inlet pressure. This value is formatted into a float with seven digits of precision using the format string function. Then a concatenate strings function is used to place a forward-slash (/) before the pressure value and a back-slash (\) after the value. These are used to determine the start and end of the data string when received in the in-cylinder code on the rack-mount computer. Values are sent using the American Standard Code for Information Interchange (ASCII) protocol [107]. This string is sent to the TCP write function, along with the connection ID, and transmitted to the rack-mount computer.
3. The last frame in the sequence does nothing (in the false case) until the test cell user chooses to deactivate the ‘Send to High Speed’ button on the c-RIO. In this situation, the global variable ‘Communicate’ is *False* and the ‘Initialized’ local variable is *True*. In this case, the TCP close connection function runs, which breaks the connection with the in-cylinder program running on the rack-mount computer. If the in-cylinder program is running, this action will result in the in-cylinder program stopping. Finally, the ‘Initialized’ local variable is set to *False* which prevents the code in the first two frames from running.

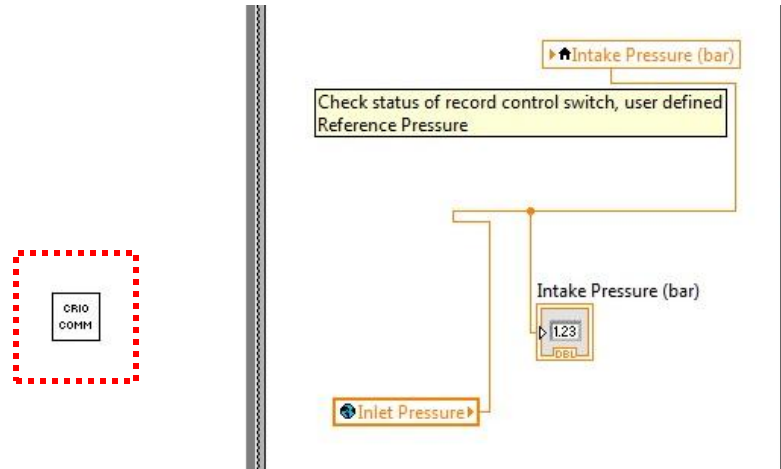


Figure 4-61. Startup of c-RIO Communication VI (red), Reading Global Inlet Pressure for Offset.

The other end of the TCP communication takes place in the in-cylinder program, activated using a VI function, as shown in Figure 4-61. Like the c-RIO performance program, this takes place in a separate VI that also constantly runs in a while loop.

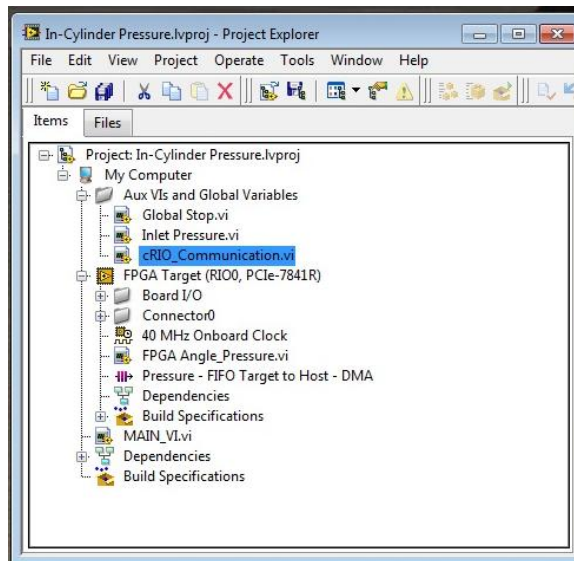


Figure 4-62. Updated In-Cylinder Pressure LabVIEW Project With Communications VI.

The ‘cRIO_Communication’ program is accessed in the in-cylinder project tree by right-click, demonstrated in Figure 4-62.

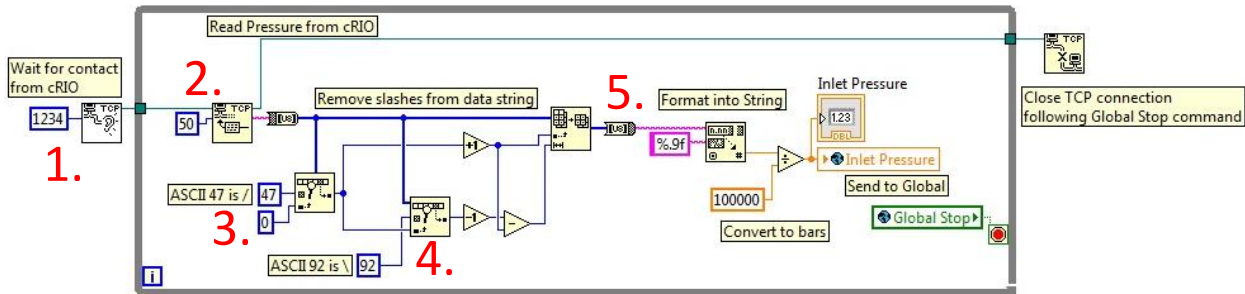


Figure 4-63. Receive Inlet Pressure From c-RIO Via TCP/IP Communication.

This action opens the front panel of 'cRIO_Communication', which leads to the block diagram code as in Figure 4-63:

1. This section of code starts with the main in-cylinder program, and waits for contact from the c-RIO using the TCP listen function. This function only needs a port assignment (1234) to allow connection with the c-RIO.
2. The TCP read function retrieves a given number of bytes from the TCP connection with the c-RIO. This contains the ASCII data that corresponds to the inlet pressure and forward- and back-slashes. This function requires the connection ID from the listen function and the number of bytes to read, fifty bytes corresponds to the size of this message (fixed to seven float digits and two slashes).
3. The pressure value is preceded by a forward-slash, whose ASCII notation is 47. A search 1D array function looks through the bit message to find this value, then returns the index of the message that corresponds to this byte's location.
4. Similarly, another search 1D array looks for 92, which is ASCII notation for a back-slash, which immediately follows the inlet pressure value. This byte's index is also returned.
5. The indexes of the forward- and back-slashes are used in an array subset function to remove the inlet pressure string from the byte string. This function requires the entire string (sent from the TCP read function), a starting index (one more than the index for the forward-slash) and a length

value. The length value is found by subtracting the back-slash index by one, then subtracting this value by the starting index. The array subset function returns a byte string that contains only the inlet pressure data, which can be converted to bars (of 9 float digits) by multiplying the pressure value (Pa) by 100,000 to convert to bars. This value is sent to a global variable called 'Inlet Pressure' for use by the main in-cylinder program. The actual offset of the cylinder pressure data in the main program occurs in a similar fashion to the methodology used in the master's thesis work [20].

4.6.2.2 Pressure vs. Volume Plot Upgrade and Net Indicated Parameters

For the vast majority of operation, the pressure versus engine crank angle plot is the preferred type of pressure profile to use, particularly when adjusting injection timing. However, the inclusion of pressure vs. volume plots requires little effort as instantaneous volume is already calculated by the in-cylinder program and adds a unique teaching and demonstration tool as this type of plot is used in courses such as thermodynamics and internal combustion engines.

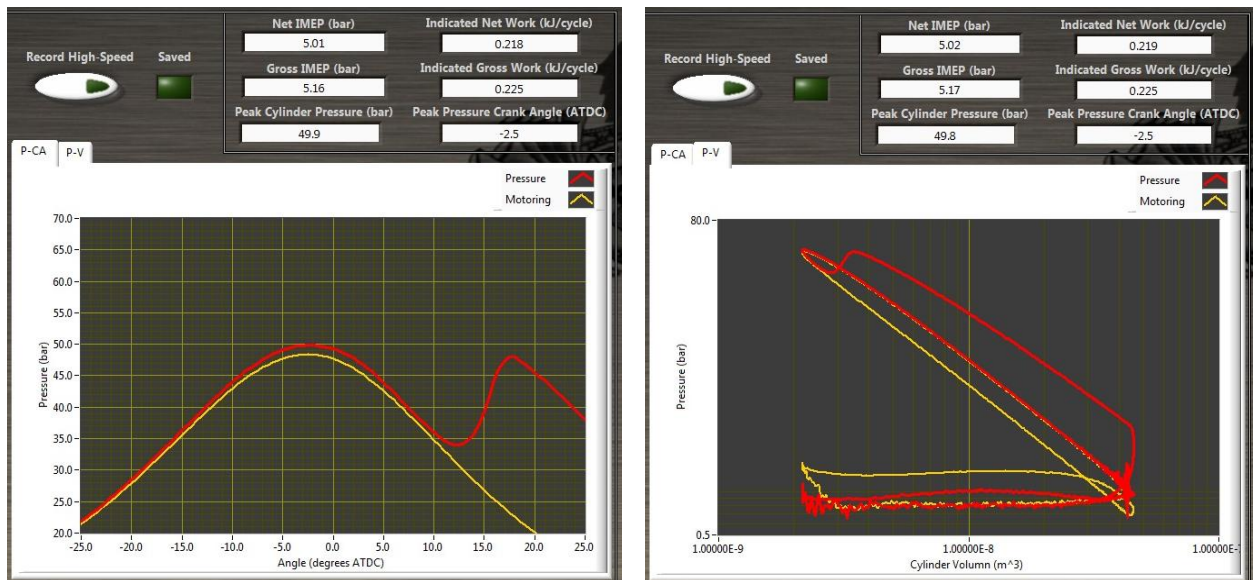


Figure 4-64. Pressure vs. Crank Angle (left) and Pressure vs. Volume (right) During Engine Operation.

The comparison of pressure versus crank angle and pressure versus cylinder volume are shown in Figure 4-64. These screenshots represent the same engine conditions. Again, for the purposes of

injection timing normalization (based on crank angle), using the pressure vs. crank angle plot makes more sense. This plot is also easier to scale as the axes are linear, rather than logarithmic like the pressure versus volume plots. However, the pumping and power loops directly observable in the pressure versus volume plot. Of interest, the combustion timing for these plots is visibly later in the expansion stroke than those used for normalization in Chapter 1. Thus, a loss in efficiency is visually evident in the pressure vs. volume plot.

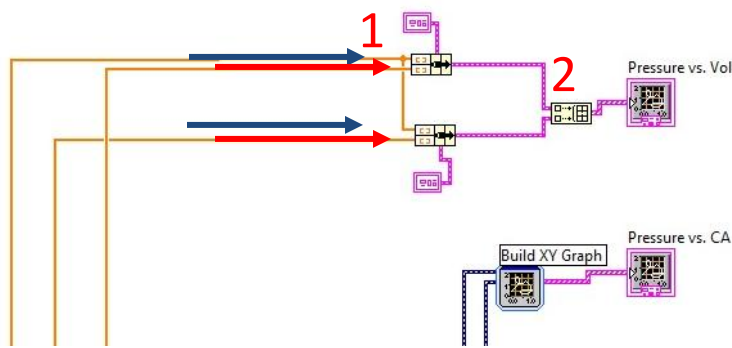


Figure 4-65. Creation of Pressure vs. Volume and Pressure vs. Crank Angle Graphs.

The block diagram to include the pressure vs. volume plot is indicated in Figure 4-65 and works as follows:

1. Arrays for instantaneous cylinder volume (blue arrows) (corresponding to 180° before TDC of compression to 180° after TDC of intake stroke) is wired to bundle cluster functions for the combustion trace (top) and motoring trace (bottom). Pressure data (red arrows) is similarly wired.
2. These clusters are then wired into a concatenate strings function.
3. Finally, the cluster is wired into the ‘Pressure vs. Vol.’ graph for display.

In early versions of the program, only the gross Indicated Mean Effective Pressure (IMEP) was calculated because data is only collected during the power loop (from intake valve close to exhaust valve open) [20]. This does not provide an accurate indication of how much of the piston work is being used to create power and how much is lost to the pumping loop [106]. Additionally, the benefit of the

turbocharger on the efficiency of the engine is reflected through a thermodynamic gain in the pumping loop due to the intake pressure being higher than the exhaust pressure [106]. The net indicated work and net IMEP are calculated via (4-2 and (4-3, respectively:

$$W_{i,n} = \int_{V_{WC}}^{V_{EVO}} p \cdot dV \quad (4-2)$$

$$imep_n = \frac{W_{i,n}}{V_d} \quad (4-3)$$

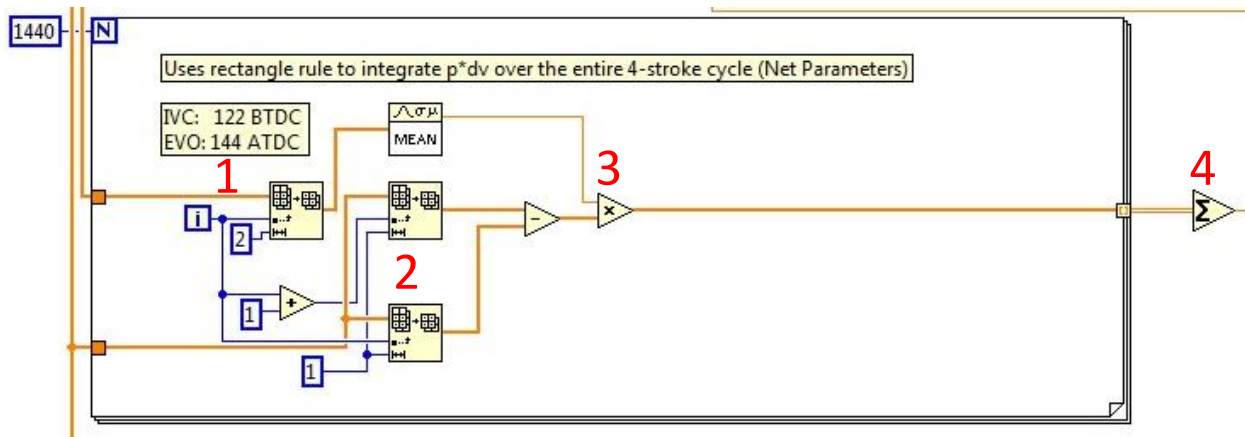


Figure 4-66. Calculation of Indicated Net Parameters (IMEP and Indicated Work).

These parameters are calculated using the rectangular rule programmed into the in-cylinder program in Figure 4-66. The calculation for indicated net work proceeds as follows:

1. A while loop runs this loop once per reading through the entire thermodynamic cycle, in this case 1440 data points exist. Cylinder pressure is wired to an array subset function which returns two pressure values for consecutive pressure values (e.g. at 1.5° and 2.0° after TDC) using the index counter of the while loop.
2. Corresponding instantaneous volume for the pressure data is retrieved from the volume array using array subset functions. The bottom subset function returns the first volume (e.g., at 1.5°) while the upper subset function returns the volume from the next point used in the calculation

(e.g., 2.0°). Then the volume of the second point is subtracted by the volume of the first point as a means of determining the change in volume from one point to the next.

3. The average pressure between two points is multiplied by the difference in volume ($p \cdot dV$).
4. The values from each of the 1440 calculations are added together to produce an integral and corresponding net indicated work. This value is divided by the displacement volume later in the program to calculate net IMEP.

4.6.2.3 Increasing Number of Cycles Saved by Program

Data processing following the initial programming for this author's thesis found that the original 20 thermodynamic cycles used for averaging was not enough to provide satisfactory statistical uncertainty due to cycle-to-cycle variation. This became particularly apparent during a subsequent heat release analysis. Therefore, the number of saved cycles is now set to 60. Additionally, the data for all 60 cycles are saved in the data file following recording (originally, only the average was saved). Unfortunately, this upgrade to the in-cylinder program was not as simple as increasing the number of cycles from 40 to 120 in the FGPA code because of memory storage limitations. The FPGA memory storage is able to handle 42 engine revolutions at 0.5° resolution (or approximately 16 engine revolutions at 0.2° resolution). So, the main LabVIEW code is upgraded to loop the FPGA code multiple times to gather the desired amount of data, with the data from each FPGA execution saved in a buffer file prior to subsequent FPGA runs. For example, if the FPGA file is saving data for 20 thermodynamic cycles and 60 cycles are desired, the FPGA runs once, saves the data to a file, then runs again and saves to a second file, then runs a third time and saves to a third file. These three buffer files then collectively contain data from 60 thermodynamic cycles, which can be read back into LabVIEW to combine the data into a single data matrix for use later in the program code.

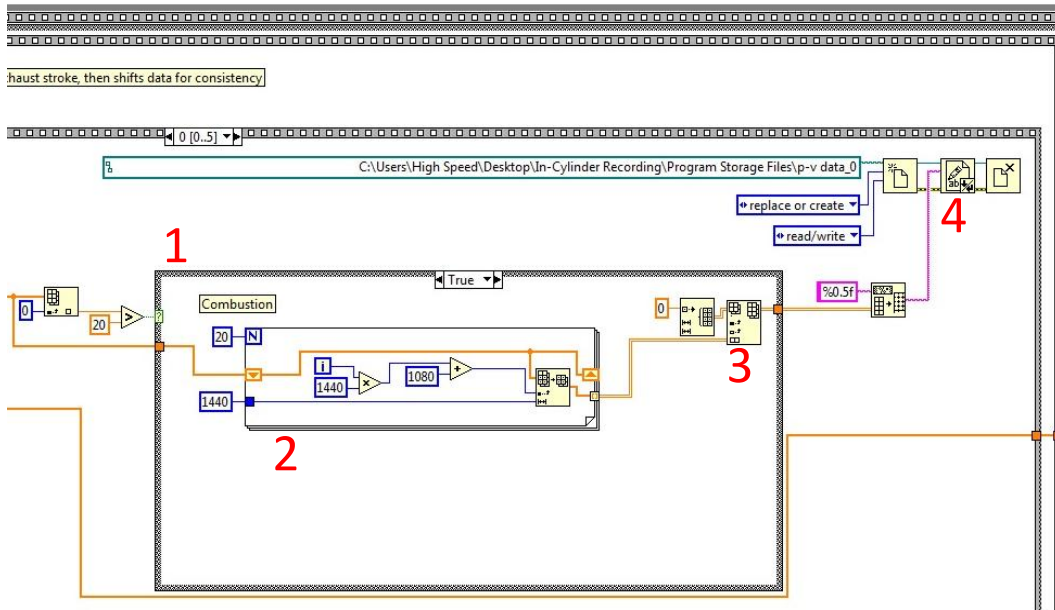


Figure 4-67. Storing First Run of FPGA Data to Buffer Text File.

This process is depicted in the main program block diagram, beginning with Figure 4-67. This segment of code takes incoming FPGA pressure data for 20 thermodynamic cycles and stores it in a text file. The data begins as a single column of pressure data that must be converted into an array of twenty thermodynamic cycle pressure columns, with each row representing a specific engine crank angle. The program proceeds as follows:

1. Data comes from memory beginning at either the TDC before the intake or expansion stroke. In the case shown here (True), the data corresponds to the pressure before the expansion stroke.
2. So, it is shifted by 540 degrees (1080 half-degree steps) so that the first value in the data vector containing 20 cycles corresponds to pressure at 180° before TDC of the compression stroke. A for-loop is used to run twenty times to then build a matrix, with each column representing a thermodynamic cycle and the first row being at 180° before TDC (start of compression).
3. Following each loop iteration, the data matrix builds and is placed into a single 1440 row by 20 column matrix (in this case) using an insert into array function.

4. The data in the matrix is converted to text string and formatted to 5-float precision. Then the matrix is saved to the first buffer file ‘p-v data_0’ using a replace or create file function. Create-file methodology is used so that if the buffer files get deleted, new ones will be made by the program in this directory in a subsequent run. Replace-file methodology prevents multiple files being created as the program runs. This file is closed using the close file function.

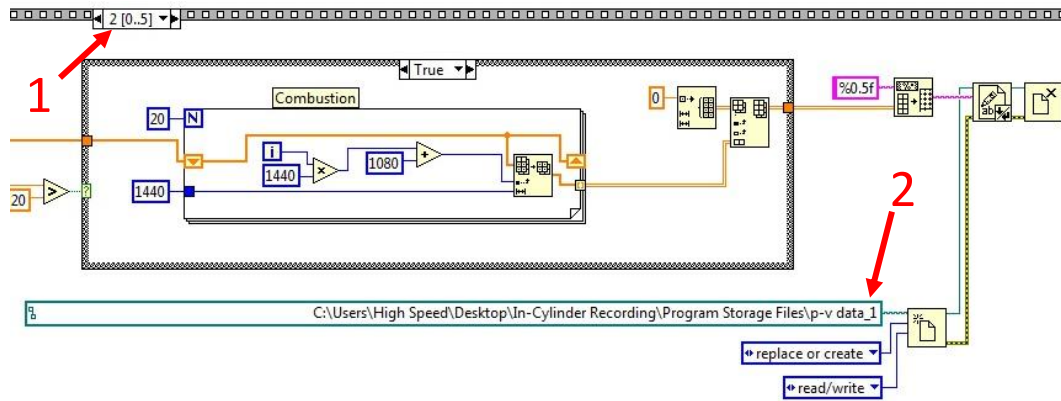


Figure 4-68. Storing Second Run of FPGA Data to Buffer Text File.

Ensuing iterations of the FPGA storage process take place to reach the desired number of cycles. The second run is indicated in the block diagram in Figure 4-68. This section (and similar iterations thereafter) functions in a similar method, with minor differences:

1. While this is the second iteration of the FPGA code, it is the third sequence in this sequence structure (numbered 0, 1, 2, ...). This is because a brief pause is placed in the code following each FPGA run and storage to data file to allow the FPGA system to reset.
2. The path for this data file reflects a new file name ‘p-v data_1’. This prevents the data saved during the first collection from being overwritten by the new data.

This sequence of running FPGA, saving the data matrix, and rerunning can be increased to accommodate any number of cycles.

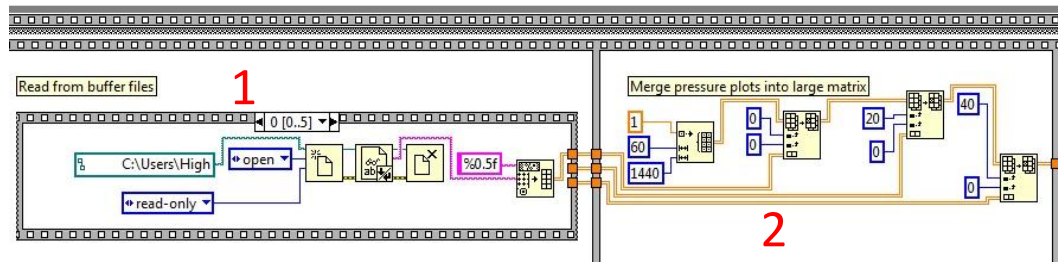


Figure 4-69. Reading Data from Buffer Files to Generate 60-cycle Array.

In a similar manner to data writing, a sequence is needed to retrieve the data from the storage files, as shown in Figure 4-69. Following retrieval, the data is combined into a matrix. This is accomplished by:

1. A sequence structure that opens the file chosen by the path input (green), reads the data, writes it to a matrix using a spreadsheet string to array function, formatted to 5-float digits. Another pause exists between the closing of this file and the reading of the second file (with a corresponding file path input), which occurs in the third frame of this sequence structure.
2. Each outgoing matrix is combined to form a single matrix of all data. In this discussion, each individual matrix is 1440 rows ($720^{\circ} \times 2$ readings/ $^{\circ}$) by 20 columns. The left function is an initialize array function which sets the size of the final array (1440-row, 60-column). Then, each set of 20 cycles are inserted into the final array using sequential insert into array functions.

It is important to note that the path constants for the write and read file functions must be adjusted to reflect any changes in the directory for these files. Otherwise, the program will crash during saving. To mitigate this issue and reduce programming effort, the structure of the program files are arranged so that changes to the program name (version 10 becomes version 11, etc) do not affect the path of the program storage files used for reference pressure traces and buffers.

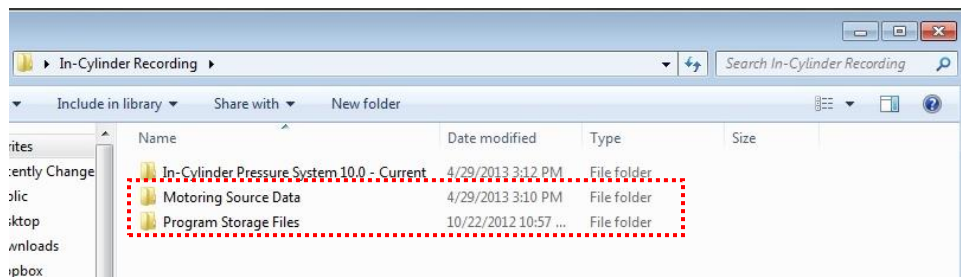


Figure 4-70. Directory for In-Cylinder Pressure LabVIEW Program.

This structure is shown in Figure 4-70. As indicated, the entire program and all auxiliary files are contained in a file called ‘In-Cylinder Recording’. Inside this file, the LabVIEW program itself is saved in a file called ‘In-Cylinder Pressure System 10.0 – Current’. The source files for motoring and program storage are saved in separate files. If the program name were to change to version 11, these files (boxed in red) would still have the same path.

4.6.2.4 Rapid Loading of Reference Files

As indicated in Chapter 1 through Chapter 3, the ability to immediately load saved pressure data to be used as reference pressure profiles helps with engine optimization for different fuels and blends. This feature is made possible using a browse for path dialog box, which uses an open-read-close file sequence to load previously saved data for display.

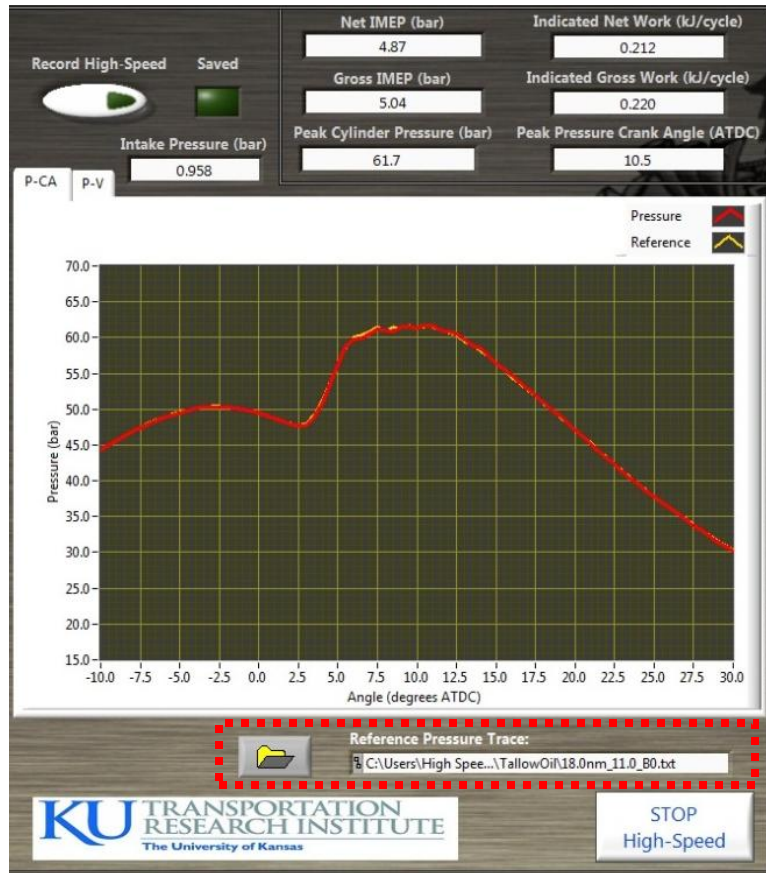


Figure 4-71. Example of Pressure vs. Crank Angle Plot with Reference Profile Loaded by Browse for Path Dialog Box.

An example was shown in Chapter 1 and is repeated in Figure 4-71 for further discussion. To load a reference data file, which is displayed in yellow on the pressure vs. crank angle plot, the user clicks on the browse for path button on the in-cylinder screen. This is shown on the left side of the red box in Figure 4-71. Also indicated is the path of the file currently being used, in this case it is a 0% beef tallow biodiesel blend with ULSD at 18.0 N·m of load with an injection timing of 11.0° before TDC.

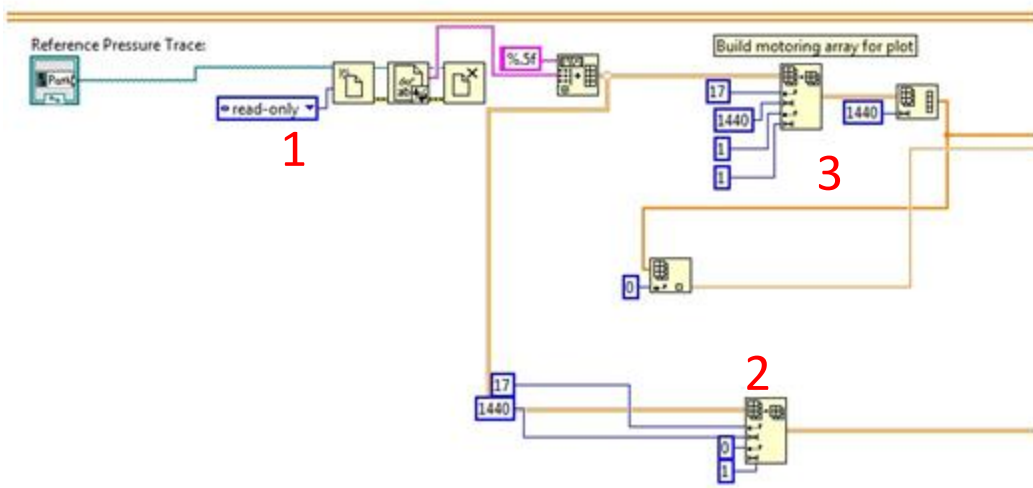


Figure 4-72. Loading Reference Pressure Trace File.

The code to load data from a saved file is very straightforward due to the fixed size and structure of the files created by the program [20], as shown in Figure 4-72. This section of code works in the following manner:

1. After being loaded using the browse-for-path dialog box, the values from the file are changed to an array using a spreadsheet string to array function. This array contains all values of the data file loaded, including the file header, which is a fixed length 16 rows.
2. The crank angle values are retrieved using an array subset function starting at the 17th row. This subset retrieves the crank angle values for the two engine revolutions represented by this profile. In this case, this is 1440 rows of data due to the 0.5° resolution.
3. Similarly, an array subset function is used to remove just the data from the file corresponding to the average pressure profile (raw data is at the bottom). This produces an array that is one-column and 1440 rows long, which is converted to a 1-D array for display. This array, and the array for engine crank angle, are sent to the pressure vs. crank angle plot for display during operation.

4.6.2.5 Upgrade in Measurement Resolution

In an effort to improve the cylinder pressure results and the heat release analysis, the sampling resolution of the system has been upgraded from 0.5° of engine crank angle to 0.2°. Of particular concern for this upgrade is the signal and sampling rates involved for the equipment. For a speed of 1800 RPM, a sampling rate of 0.2 degrees of crank angle resolution generates an encoder square wave with a frequency of 54 kHz. Fortunately, the Kistler encoder (model # 2614B1) is capable of up to 0.1° resolution at 10,000 RPM when a pulse multiplier is used (model # 2614B4). However, triggering of the FPGA counting logic requires polling for state changes in the square-wave encoder signal. Thus, missing a step change becomes a concern as sampling rate approaches the sampling frequency of the FPGA card. However, the analog inputs of the NI 7841r card used in this system sample at up to 200kHz, providing an adequate factor of safety at this speed. For higher speeds, such as 3600 RPM, required sampling rate (108 kHz) could pose future issues.

Number of Pulses per Crankshaft Revolution		DIP Switch #5	DIP Switch #6
3 600 symmetric pulses	7 200 edges	ON	ON
1 800 symmetric pulses	3 600 edges	OFF	ON
720 symmetric pulses	1 440 edges	ON	OFF
360 symmetric pulses	720 edges	OFF	OFF

Figure 4-73. DIP Switches to Adjust Encoder Resolution [108].

The output of the encoder is changed using the pulse multiplier. This component of the encoder system takes in the 360 Hz square wave pulses from the encoder and converts it to other user-defined frequencies. These are adjusted using DIP switches as shown in Figure 4-73.



Figure 4-74. Kistler Pulse Multiplier.

These DIP switches are accessed by removing the switch cover on the pulse multiplier, located in the back of the test cell instrumentation cabinet (Figure 4-74).



Figure 4-75. Charge Amp: DIP Switches Down for 1° Resolution (left) and 0.2° Resolution (right).

This gains access to the switches that can be switched using a small tool, such as a screwdriver.

The conversion from 360 pulses to 1,800 pulses per revolution is demonstrated in Figure 4-75.

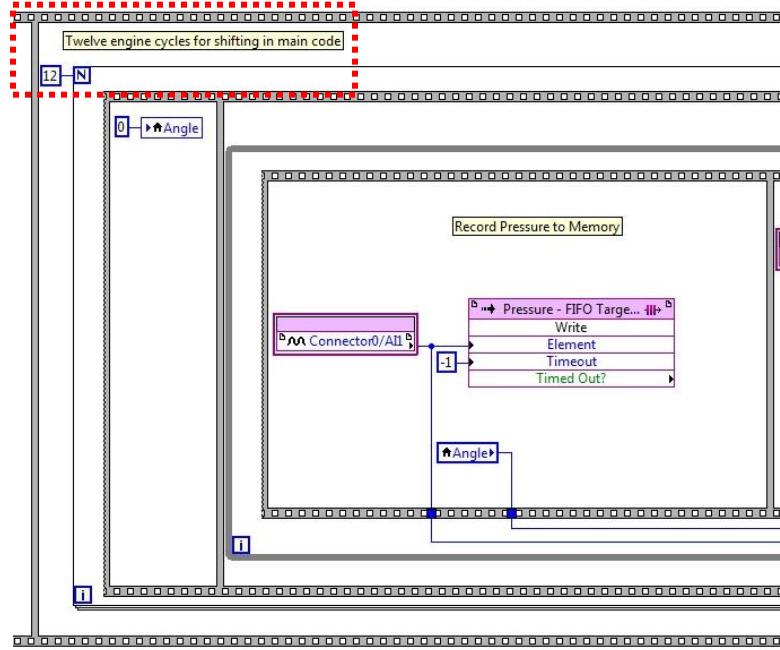


Figure 4-76. Lowered Number of Cycles Saved to Memory by FPGA.

This new configuration requires two changes to the FPGA code. The first is the lowering of the number of engine cycles saved from 42 to 12, highlighted in Figure 4-76. Two extra engine revolutions are saved to ensure that enough data is available when the main program code shifts the data to align the first row of the data matrices at 180° before TDC. The second change is the altering of the counting logic for the program. In the original program version, the 360 pulses-per-revolution square wave is used. To get the desired 0.5° resolution (720 events per revolution), the FPGA looked for both rising and falling edges [20]. Now, there are 1,880 pulses-per-revolution, which is equal to the number of events needed to count by the desired 0.2° resolution.

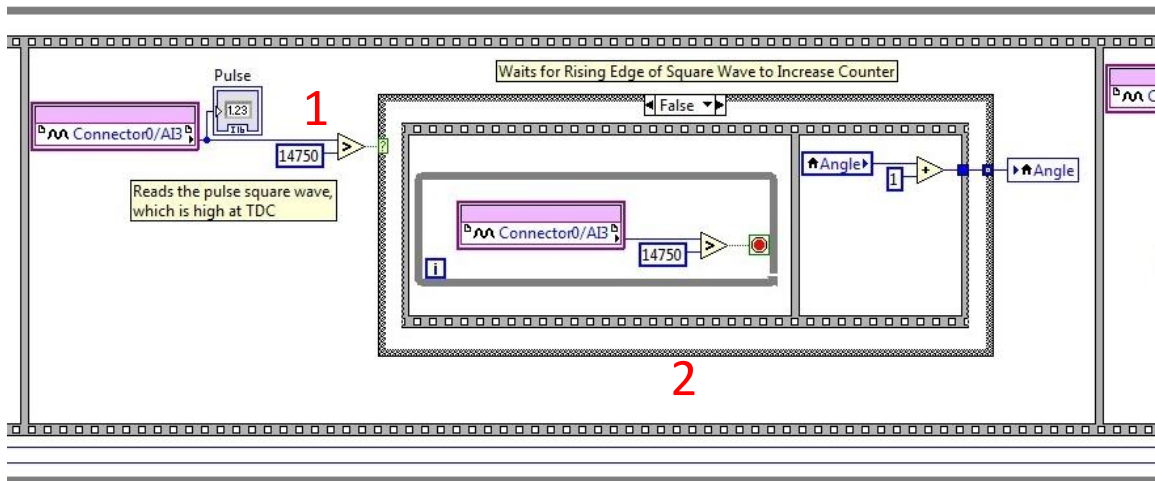


Figure 4-77. FPGA Code That Waits for Rising Edge of Square Wave.

Thus, the code (Figure 4-77) is changed to only count rising edges as the encoder pulse square wave initializes as +0 VDC at TDC [108].

1. This code compares the voltage of the square wave (5 VDC) to a threshold byte value ($14750/32768 \approx 2.2$ VDC).
2. If the voltage is less (0 VDC) then the False case structure starts a while loop that iterates until the square wave voltage goes to 5 VDC and increases the *Angle* counter by 1 and moves on in the code. The true case structure is a 'do-nothing' case.

Another issue with higher sampling resolution is the increase in data storage requirements.

Previously, the FPGA memory could store data from 42 engine revolutions. With a sample rate of 0.2° , the number of engine revolutions is reduced to 12 (five thermodynamic cycles). This poses particular issues for the main in-cylinder code, where the number of storage files must be increased from three to twelve to gather 60 thermodynamic cycles.

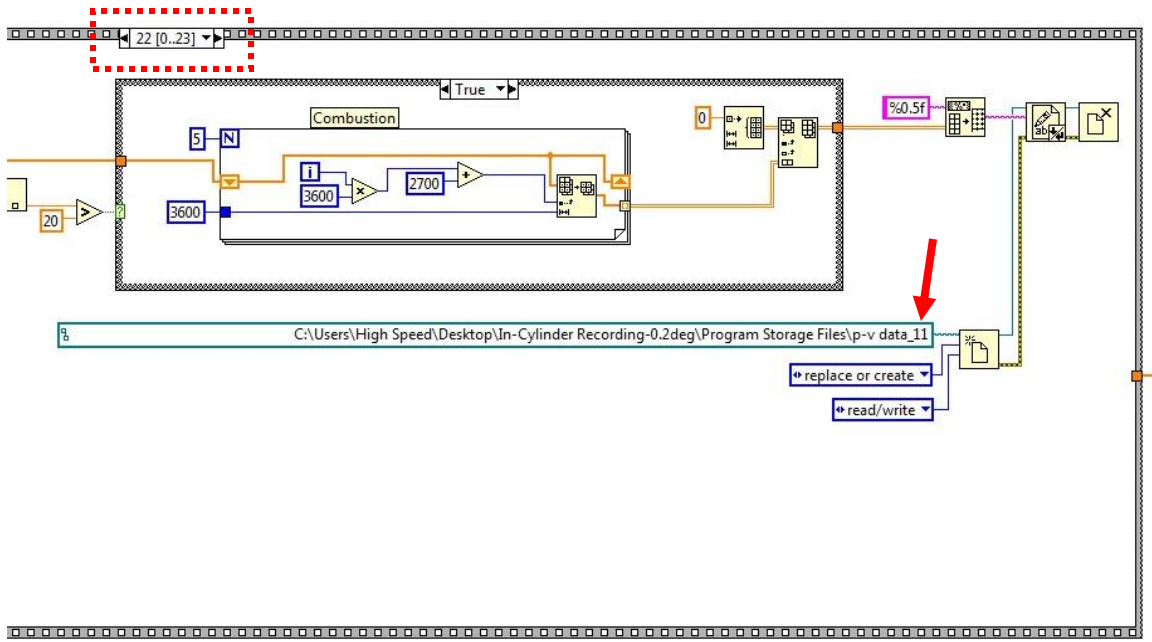


Figure 4-78. Writing FPGA Iterations to Buffer Files.

This change is reflected in the block diagram shown in Figure 4-78. In this diagram, the number of sequences is increased to account for additional file writing (23 in total - red), with timing pauses placed in between. The number of files is accordingly increased to 12 (0, 1, ..., 11) using the replace or create file function (red arrow).

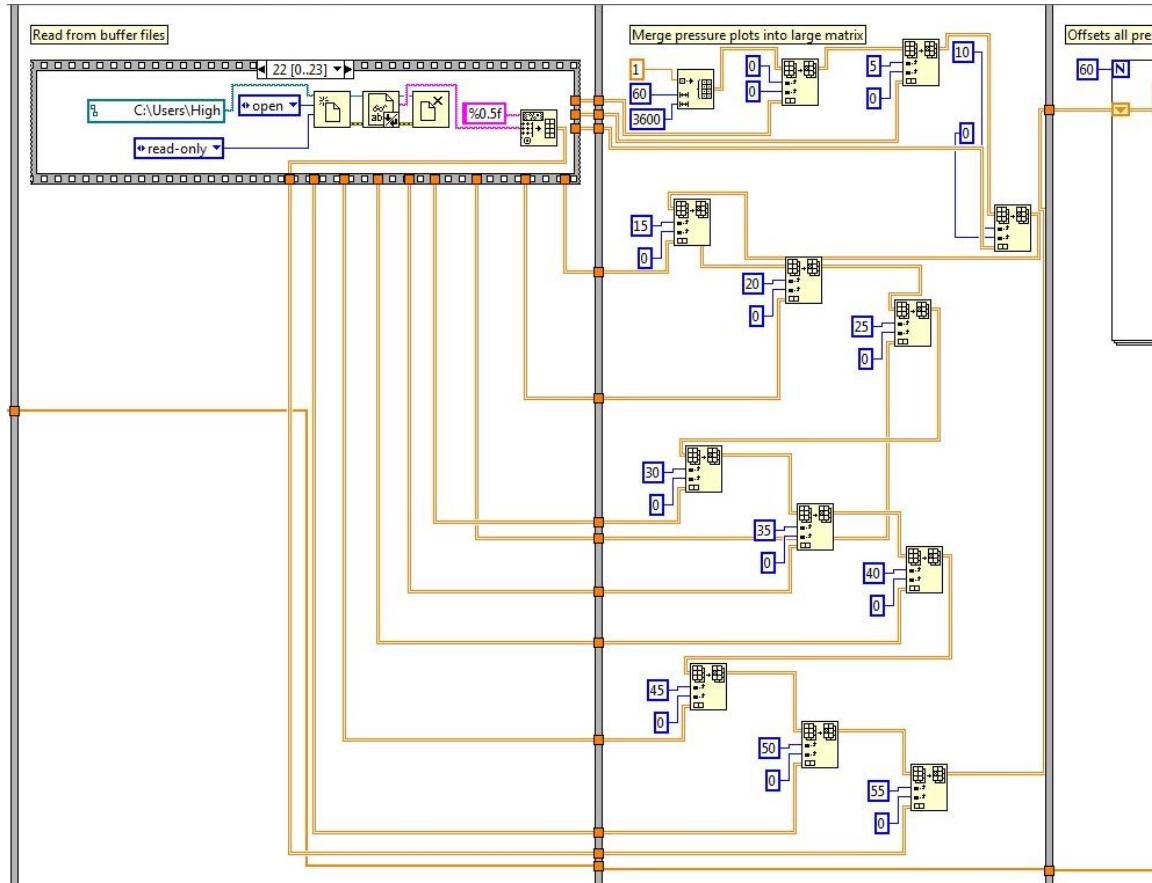


Figure 4-79. Reading of Buffer Files and Building of Single Data Array.

Similarly, the reading of the buffer files and the construction of the single data matrix is shown in Figure 4-79. Now, rather than building a matrix using three insert into array functions, twelve are needed. This code produces a matrix that is 60 columns by 3600 rows ($720^\circ \times 5 \text{ samples}/^\circ$).

Other changes in the main code are straightforward because the only the matrix dimensions are expanded from 1440 to 3600 in these functions and loops. This includes the calculation of gross work (which occurs from 122° before TDC to 144° after TDC) where the number of for loop iterations and starting index (corresponding to intake valve closing) are multiplied by a factor of 5/2.

4.6.2.6 In-Cylinder Pressure System Troubleshooting

There are only two sensors that interface with the in-cylinder pressure measurement program. However, this system is prone to issues with electrical noise and other unforeseen problems.

Fortunately, the wiring and program provide troubleshooting points that can be used to locate issues. The most commonly encountered error occurs because of the charge amplifier experiencing an overload condition. Kistler explained that this occurs when the output of the charge amplifier exceeds 10 VDC. Based on the scaling of the Kistler (20 bar/VDC) this would correspond to a pressure of 200 bars; a pressure never experienced with this engine. The solution to this problem is to stop the engine and reset the charge amplifier. This problem only occurs during startup. Other issues that arise in the signals from the encoder and pressure transducer can be easily observed using an oscilloscope while motoring the engine. The oscilloscope inputs can be connected to the pressure and encoder signals that are wired to the terminal board of the NI PCI 7841r card. These signals can also be checked using the BNC connections on the output of the charge amplifier or pulse multiplier.

If the signals are not the issue, then the problem may lie in the code itself. While the engine is motoring, the values passing through the code (matrices) can be inspected using the probe tool in the block diagram. This will tell the user if the problem is in the code. Sometimes restarting the computer is helpful as this allows the computer to install updates and re-open the program.

4.7 Emissions Equipment

The collective emissions measuring capability of the single-cylinder test cell can be divided into three main components. The AVL SESAM 4 bench, which contains a computer controlling an FTIR, FID, and oxygen sensor, is used to measure gaseous exhaust constituents, such as NO, NO₂, N₂O, CO, CO₂, and other alcohols and hydrocarbons [109]. The AVL 415SE (Smoke Meter) is used to measure the PM output of the engine. This device provides total emissions of PM in either a filter smoke number or concentration (mg/m³). Both systems communicate directly with an emissions laptop through a separate ethernet network devoted to these three devices. Yearly service for both of these emissions systems are recommended by AVL, with smoke meter calibration occurring during that time. SESAM bench calibration is covered later in this section.

4.7.1 AVL SESAM FTIR Bench

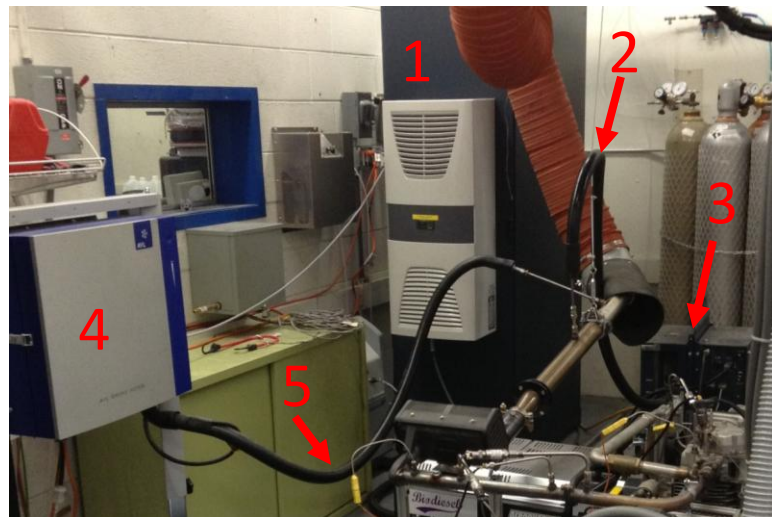


Figure 4-80. SESAM 4 Bench (1), FTIR Sampling Hose (2), FTIR Filter Housing (3), Smoke Meter (4), and Smoke Meter Sampling Hose (5).

This system uses a heated sample line to transfer an exhaust sample into the bench. This first travels through a heated filter to prevent PM from entering the emissions bench, the sample line and filter housing are shown in Figure 4-80. Heated sample lines are used for both the FTIR and Smoke Meter to prevent water that is present in the exhaust from condensing in the sample lines or electronic equipment. After the filter, the sample enters the bench where it is passed through the FTIR, FID, and oxygen sensor for measurement. Bench conditions are kept cool by an air conditioning unit located on the outward facing side of the bench in Figure 4-80. This air conditioning unit has a condensation drain that is fed to the trench floor drain under the engine pad.

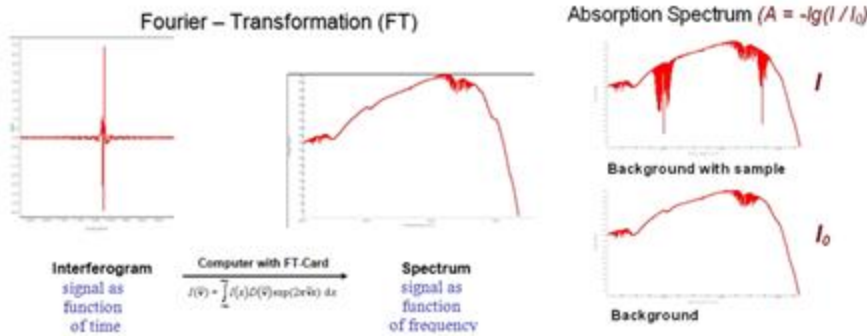


Figure 4-81. Fourier Transformation and Absorption Spectrum Evaluation Method [109].

The FTIR works by calculating a broadband infrared absorption spectrum which comes from Fourier transformation of measured interferograms [109] as shown by the diagram in Figure 4-81. Then, absorption spectrum corresponding to the exhaust sample is compared with the absorption spectrum yielded during calibration (known as the background spectrum). Differences between these spectra indicate the species (based on wavelength) and concentration (based on intensity). As the entire spectrum is measured at once, the analysis provides all species simultaneously.

The FID measures total hydrocarbons in the sample. It does so by burning the sample in a hydrogen flame to measure the ionization of the organic compounds. This is done by measuring the changes in current in an electric field enclosing the hydrogen flame. As the current change increases, more hydrocarbons are present [109].

The FTIR is unable to measure diatomic molecules. Therefore, measurement of diatomic oxygen, which is up to 18% of the Yanmar's exhaust at low loads, is achieved using a separate oxygen sensor. The sensor used is a paramagnetic detector. This type of sensor relies on the magnetic behavior of oxygen in a magnetic field. The sensor contains a pair of cylindrical dumbbell halves that are immersed in an inhomogeneous magnetic field. Oxygen in the exhaust sample is drawn into the magnetic field, which produces a partial pressure increase in the dumbbell to produce a measurable torque. As oxygen content increases, the amount of torque increases which is converted to an electrical signal [109].

4.7.1.1 AVL SESAM Bench Startup



Figure 4-82. Air Supply Piping and Valves in Test Cell.

The SESAM bench uses compressed air for purging of the sample lines. This air is also back-flushed through the heated filter to remove collected PM by sending it back into the main exhaust stream. Air supply comes from the Learned Hall compressed air system, which is supplied at approximately 150 psi, shown in Figure 4-82. This supply is turned on using the main red-handled valve (which supplies both the single-cylinder laboratory and Formula SAE laboratory). The single-cylinder air supply is individually controlled using the yellow-handled valve pointed downwards in Figure 4-82.



Figure 4-83. Regulator and Filters for Compressed Air.

Before entering the SESAM bench, this must be filtered of oil and particles and the pressure must be reduced to 80 psi. This is done using a combination of a regulator and a two-stage filter, depicted in Figure 4-83. The filters are sized to flow the required 6 liters/min at 80 psi, with a first-stage

filtration diameter of 1 micron for particles and 0.5 microns for oil droplets and a second-stage filtration of 0.01 microns for particles and oil droplets. The housings are clear to provide visual inspection of the filter elements. Replacement elements are purchased through McMaster-Carr's website (part number: first stage – 2994K21, second stage – 2994K31).



Figure 4-84. Power Switch For Heated Sample Line and Heated Filter.

With the air supply ready, the next step is to power up the heated filter and sample line using the switch shown in Figure 4-84. Note: these components must reach 190°C before operation, which can take an hour or more. The SESAM computer will not let operation ensue until this temperature is reached. Because of the long warm-up time, this system can be left on indefinitely, or set to lower values for short downtimes. Typically, this is turned on the day before an experiment to expedite the startup process on test day.

The FTIR uses compressed nitrogen to remove air and water vapor from the FTIR measurement chamber. This is accomplished via nitrogen purge at 0.6 liters/min. For day-to-day operation, this purge should be left on constantly. However, since testing in the single-cylinder laboratory occurs on a more occasional basis, the nitrogen purge is typically turned off between tests. This is acceptable as long as the nitrogen purge is reactivated at least six hours prior to testing. Normally, this is turned on the day

before. If any air or water vapor is present in the test chamber during background measurement, the quality of emission data will be diminished. If the background specifications are outside of allowable thresholds, the FTIR will not start. The pressure for this purge should be set to 50 psi and its flow is verified on the main operating screen.

4.7.1.2 The AVL Operating Window

The computer inside the SESAM bench uses specialty AVL programs to operate the FTIR, FID, and O₂ sensors. This is a primarily automated process, but a user window is needed to allow personnel to monitor emissions, view errors, and perform calibration during startup. A duplicate screen and keyboard and mouse are located outside the test cell so that the SESAM bench can be controlled without entering the test cell during operations.



Figure 4-85. Main Operating Window of the AVL Bench Computer.

The main operating window of the SESAM is shown in Figure 4-85. This screen shows the status of major system components including sample line and filters, temperature, chiller temperature, and internal pressures and flow and purge rates during sampling and purge (left side). This screen also indicates concentrations of O₂, THC, and individual species, such as H₂O and NO. Number signs (###) or dashes (---) indicate that a sensor is not currently measuring. Red and green lights indicate the status of critical operational parameters, such as the quality of the background spectrum, FID flame, and FTIR laser cooling. Settings such as sample rate can also be adjusted here. Navigation among individual sensors is possible by clicking on the desired sensor on the right-hand side of the screen. The bottom of the screen shows any past or current errors in the system. These can be manually acknowledged by the

operator by highlighting them and pressing the space bar. This will not actually clear the error from the list until the error condition is remedied. For instance, all errors shown in Figure 4-85 have been confirmed by the user, but are still present because the flame temperature is too low (FID not lit) and the FTIR is too warm (detector cold indicated red). These are normal errors that appear during startup as the FID must be lit and the FTIR liquid nitrogen cooling reservoir must be filled.

4.7.1.3 Calibrating the FID and Oxygen Sensor

First, the FID flame must be lit. This is done by entering the THC sensor window in the SESAM bench program.

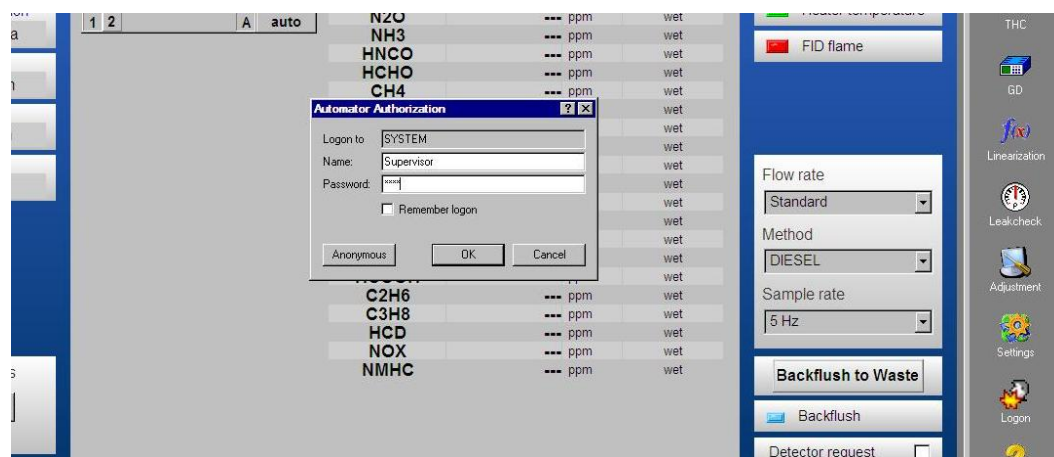


Figure 4-86. Logon Window to Access Other Pages.

Clicking the THC icon on the right requires the operator to logon the first time after startup (Figure 4-86). The username is Supervisor and the password is peus, which is in reverence to PEUS-Systems GmbH subsidiary of AVL.



Figure 4-87. FID Fuel (Hydrogen + Helium), FID Synthetic Air, and FTIR Purge Nitrogen Tanks.

After reaching the THC page, the regulator valves of the FID fuel and FID synthetic air tanks must be opened (Figure 4-87). The pressures for these gasses should both be set to 50 psi.

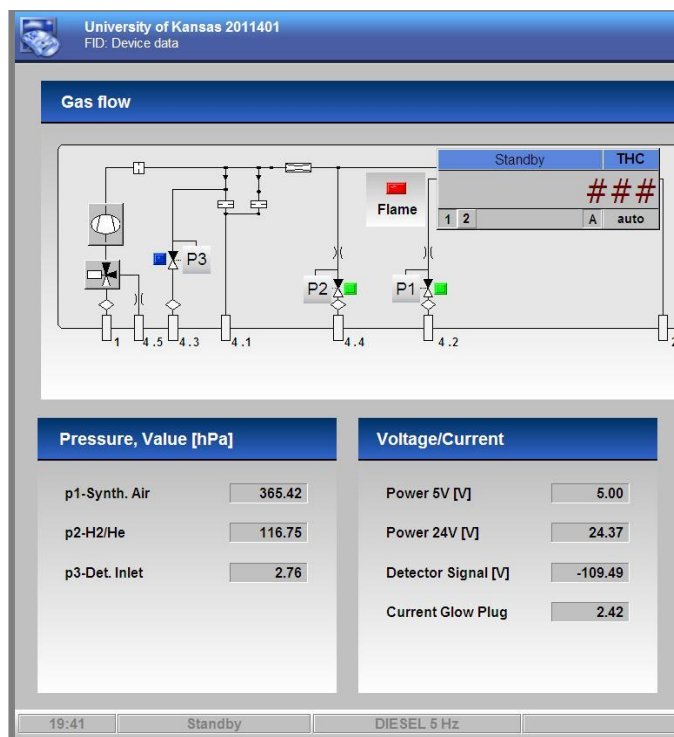


Figure 4-88. THC Window. Synthetic Air and FID Fuel Valves Open, Glow Plug Active.

At this point, the FID sensor will detect synthetic air flow and will attempt to light the FID flame.

This is apparent from the readings on the THC screen, shown in Figure 4-88. In this window, solenoid

valves for the synthetic air (P1) and FID fuel (P2) are open to allow the fuel-air mixture to enter the combustion chamber of the sensor. The glow plug, used to ignite the flame, is registering a current flow of 2.42 amps, indicating that it is attempting to light the flame.

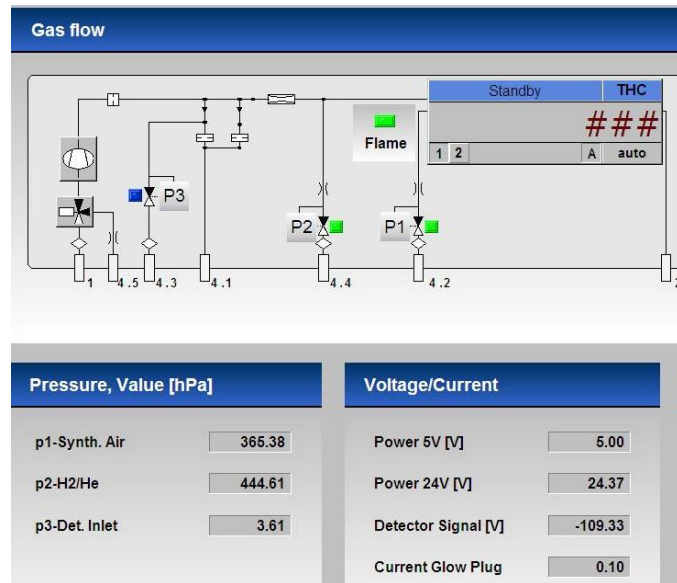


Figure 4-89. THC Window. Synthetic Air and FID Fuel Valves Open, Glow Plug Off, FID Lit.

Successful ignition is reflected by the 'Flame' indicator light, which turns from red in Figure 4-88 to green in Figure 4-89. The low current (0.10 amps) indicates that the glow plug is no longer lighting.



Figure 4-90. Main Window with FID Lit.

Returning to the main operating screen (using right-hand side navigation bar) reflects the change in FID flame status, as indicated in Figure 4-90. The FID is now ready for calibration, as is the oxygen sensor. Zero and span gases are chained to the pad on the North wall of the test cell. There are five bottles used for calibration with the nitrogen gas serving as the zero gas for both sensors. The other four tanks are for spanning the high and low ranges of each sensor.

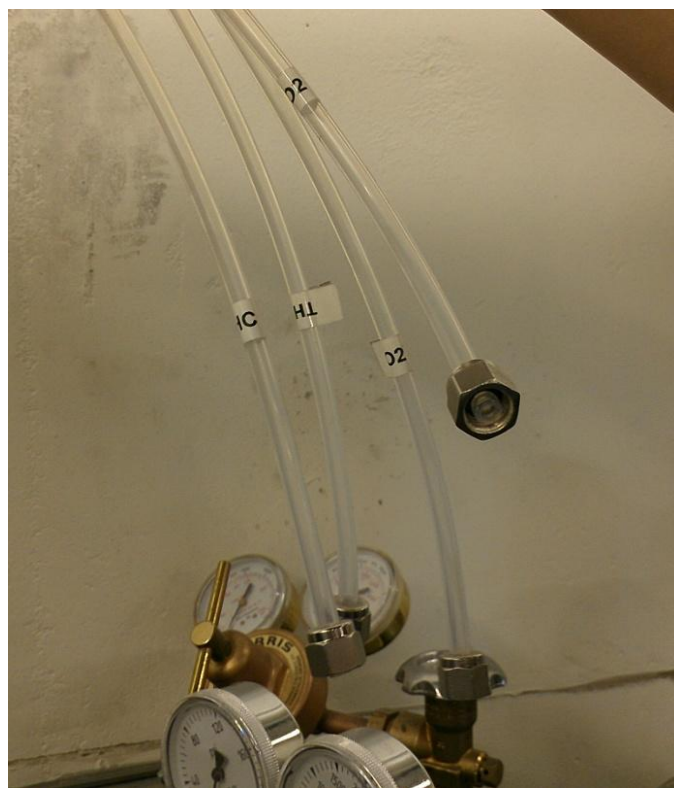


Figure 4-91. Calibration Tubing for FID and Oxygen Sensor Calibration.

Each tank has a corresponding flexible hose that is connected to it during calibration, shown in Figure 4-91. Since there are not enough regulators for all four to be installed at once, some shuffling must take place during calibration. The order that these sensors and ranges are calibrated does not matter.

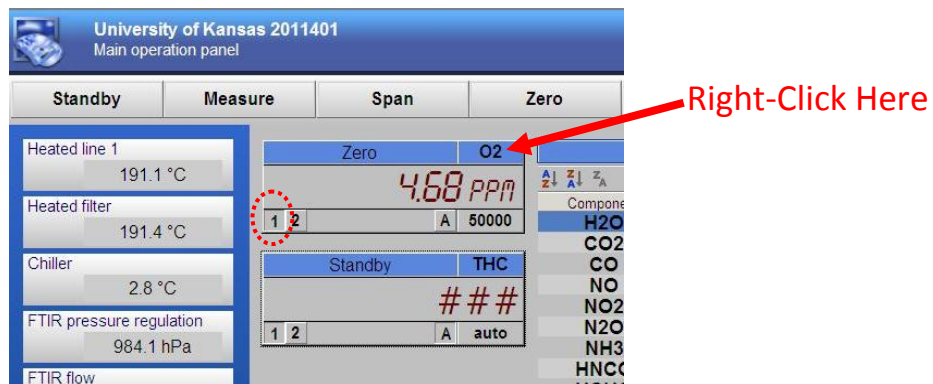


Figure 4-92. Main Window. Zeroing O₂ Sensor's Low Range.

The low-range of the oxygen sensor is calibrated by connecting the tube labeled ‘O2 1’ to the appropriate tank and regulator, which contains a five-percent oxygen mixture with nitrogen. Then, the low-range is calibrated by first clicking on the ‘1’ below the concentration display of the O₂-sensor portion of the main screen, then right-clicking on the O₂ sensor title and clicking zero (Figure 4-92). Clicking ‘1’ tells the O₂ sensor which range is being calibrated. After the measured value settles (indicated 4.68 ppm here) right-click the O₂ title again and select ‘zero calib.’ to calibrate the zero-end of the low range.

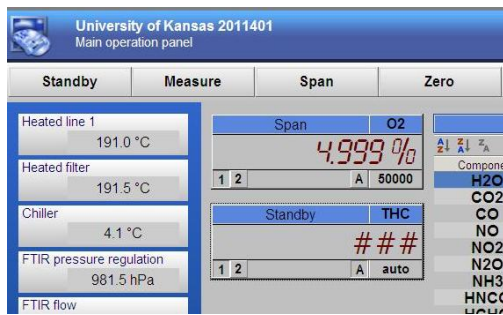


Figure 4-93. Main Window. Spanning O₂ Sensor's Low Range.

Next, right-clicking on the ‘O2’ title and selecting ‘span’ starts the flow of five-percent oxygen calibration gas through the sensor, as in Figure 4-93. After the reading settles near five percent, right clicking on the O₂ title and selecting ‘span calib.’ adjusts the span calibration for the low range of the O₂ sensor. Now, the process should be repeated at least once to ensure repeatable zero and span values for this sensor range. The repeating of zero and span calibrations can be performed as needed. Of note, the oxygen sensor is prone to drifting around over time and may take several calibration attempts to achieve good repeatability.

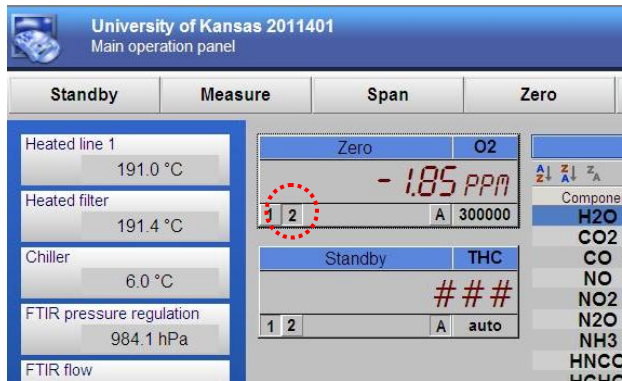


Figure 4-94. Main Window. Zeroing O₂ Sensor's High Range.

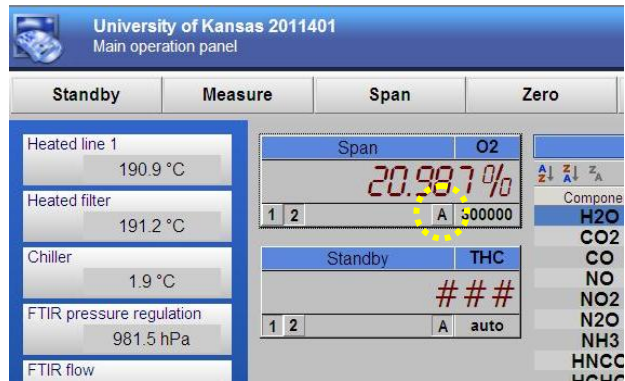


Figure 4-95. Main Window. Spanning O₂ Sensor's High Range.

In a similar manner to the low-range of the O₂ sensor, the high-range can be calibrated after connecting the 'O2 2' hose to the high-range oxygen span bottle, which is 21% oxygen/nitrogen mix. Figure 4-94 and Figure 4-95 indicate this process. Calibration of the high-range can only occur once the '2' is pressed on the oxygen sensor section of the screen (red circle in Figure 4-94). Like the low-range, the calibration process may require several zeroing and spanning steps to ensure good sensor accuracy. This concludes calibration of the oxygen sensor, now the 'A' under the concentration reading (yellow in Figure 4-95) should be pressed. This tells the sensor to automatically shift between low- and high-range based on sample concentration. This improves accuracy at oxygen concentrations below five percent and prevents sensor over-range above five percent oxygen.

The calibration of the FID proceeds in a similar manner to the oxygen sensor. The low range is calibrated after connecting the 'THC 1' hose to the 180 ppm bottle. Note: the bottle is labeled 60 ppm propane (C₃H₈) and air. The hydrocarbon concentration in the FID is three times that amount because of three carbon atoms present in propane. AVL denotes this as C1 calibration.

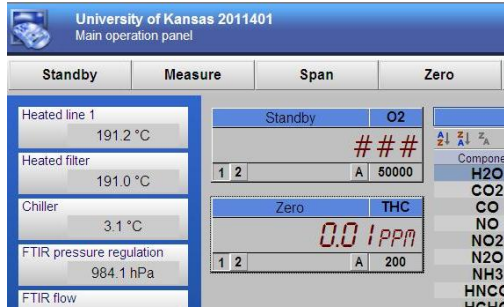


Figure 4-96. Main Window. Zeroing THC Sensor's Low Range.

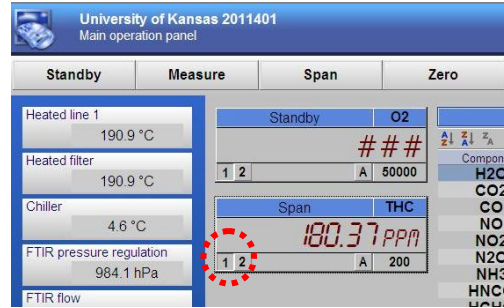


Figure 4-97. Main Window. Spanning THC Sensor's Low Range.

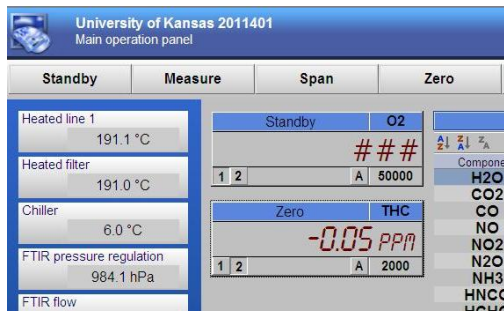


Figure 4-98. Main Window. Zeroing THC Sensor's High Range.

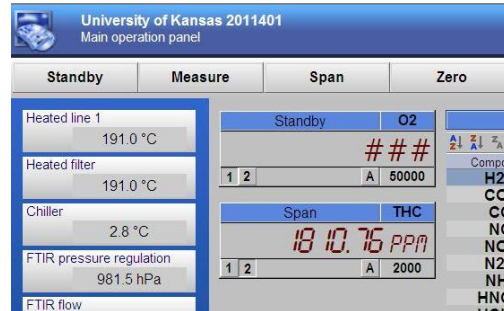


Figure 4-99. Main Window. Spanning THC Sensor's High Range.

The screen images during FID calibration are shown in Figure 4-96 through Figure 4-99. Again, the low-range sensor is selected by clicking '1' on the THC section of the screen (red circle in Figure 4-97). Similarly, the high-range is selected by clicking '2'. The process is repeated with zero and span steps using the 600 ppm propane/air tank (1800 ppm C1 calibration) connected to the 'THC 2' hose. Then, clicking 'A' configures the FID to auto select the proper range based on incoming THC concentration. This concludes the calibration of the oxygen and FID sensors. At this point, the four span calibration bottles can be closed.

4.7.1.4 Starting the FTIR

The FTIR uses liquid nitrogen to cool its laser measuring components. Without this cooling, the system will not operate. The reservoir provides approximately 8-10 hours of operating time before the nitrogen evaporates. Filling of the reservoir occurs during the test-day startup.

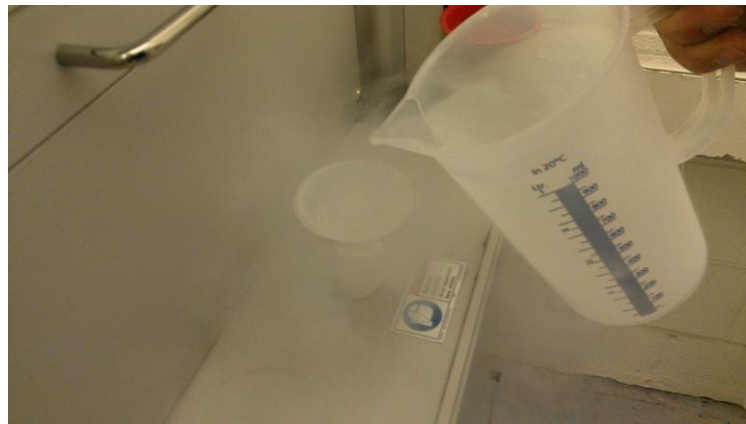


Figure 4-100. Pouring Liquid Nitrogen Into FTIR Reservoir.

The filling of the reservoir is demonstrated in Figure 4-100. The reservoir is located inside the FTIR housing, which slides out for convenient filling and service. The top of the housing contains the nitrogen fill port. This port serves as the evaporation vent, and therefore, has no cap or lid. Liquid nitrogen is slowly poured in using the specialized funnel and a plastic pitcher. The reservoir in the FTIR is approximately 200 mL, but a liter of nitrogen is required to first cool the port and chamber before filling. The reservoir is filled when nitrogen starts to bubble back out of the port. With these extremely cold temperatures, safety equipment should be used when handling liquid nitrogen. This includes safety glasses/face shield and thermal gloves. The operator should be vigilant to droplets falling into shoes.

The main operating window will reflect the filling of the nitrogen reservoir with a green 'Detector cold' light. This means that the background spectrum for FTIR species measurement can be taken. This is accomplished by navigating to the Background screen on the SESAM bench computer.

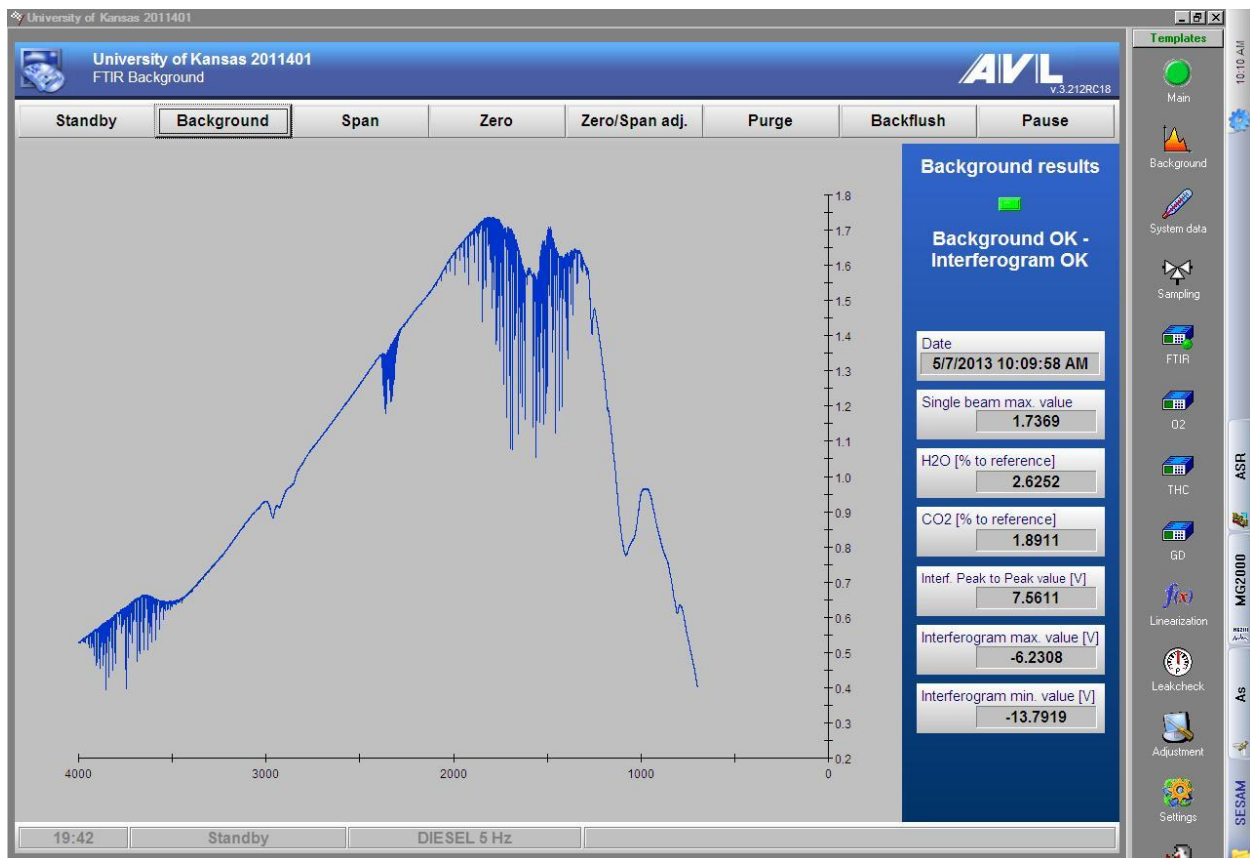


Figure 4-101. Main Window Indicating the Measuring of a New Background.

This main operating window is depicted in Figure 4-101. This panel provides the user with information regarding the background and controls to take a new background (top of screen). The right-hand side of the screen shows information about the last background. Of critical importance is the accuracy of the background compared to the reference spectrum. The reference spectrum is the spectrum taken during calibration. If the amount of water vapor or CO₂ present in the measured background is more than specified thresholds, the FTIR will not run. This is why a nitrogen purge for several hours prior is so important. In this example, the background was taken on May 7th, 2013. Its difference compared to the reference spectrum was 2.6252% H₂O and 1.8911% CO₂. Refer to Figure 4-81 to see the influence of exhaust sample on the spectrum. A new background is taken by clicking 'Background'. This starts the background procedure, which first purges the instrument with nitrogen gas to remove any unwanted species, and then the background reading is taken. This entire process takes

about 45 seconds. To improve the measurement of the background, the ‘Purge’ button can be clicked to run a full one-minute purge through the sensor prior to the initiation of the background procedure. This can also be done if the first attempt at background measurement did not meet background quality requirements due to CO₂ and H₂O being present in the sensor.

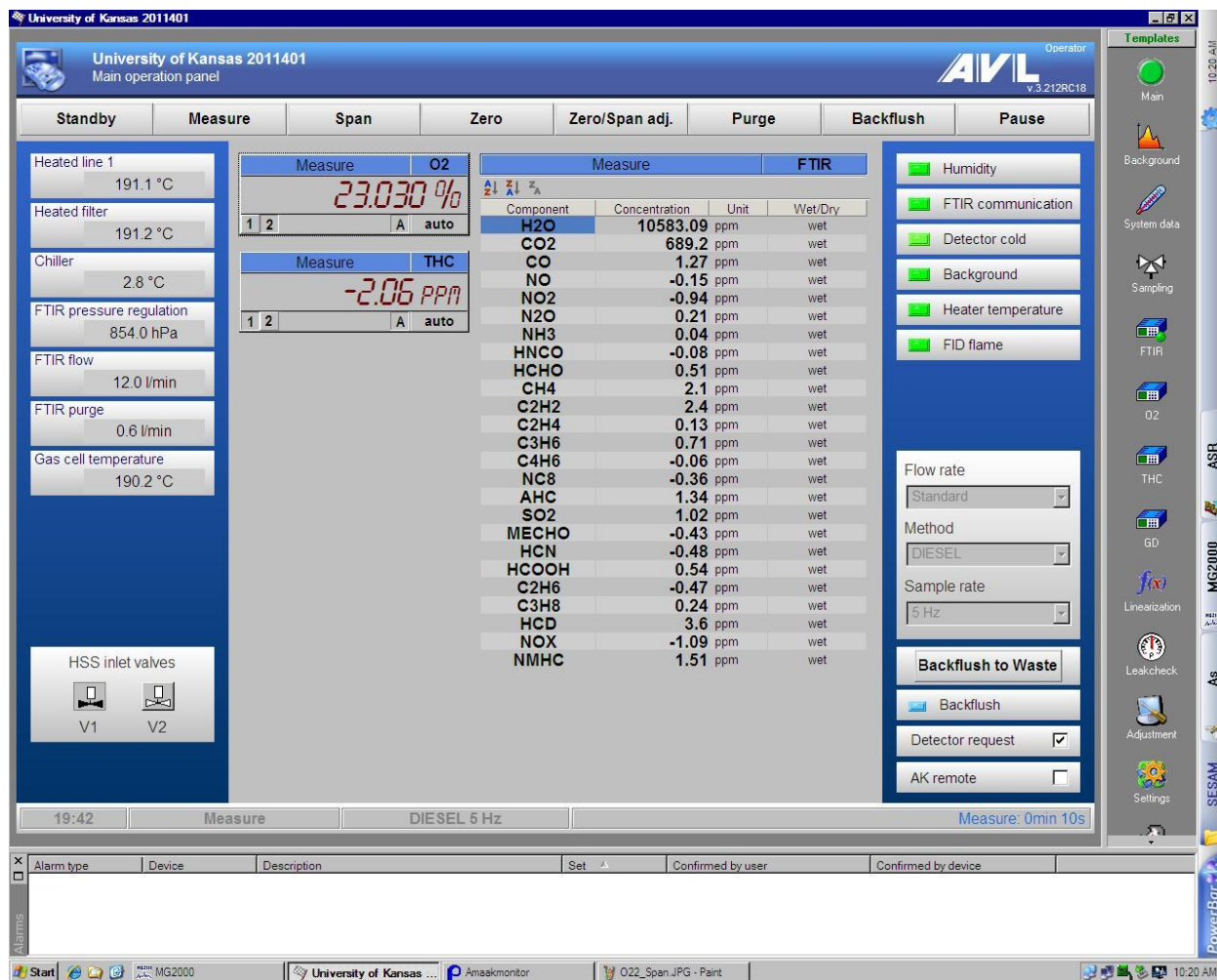


Figure 4-102. Main Window. Ready to Measure, Sampling Room Air.

As this point, all components of the SESAM bench are ready for measurement. This is reflected by all-green indicators in Figure 4-102. Pressing measure begins the flow of sample gas through the sensors and provides measurement readings for observation. In the example shown here, the engine is not running, so the sample stream is essentially room air pulled back through the exhaust. The sample flow rate is 12 l/min and the FTIR pressure regulation maintains an 850 hPa instrument pressure. If the

flow drops below the point that internal flow control can no longer maintain desired pressure, a sensor pressure error will be displayed. The most likely culprit is the PM filter. Its replacement is covered later in this section. Note: the auto ('A') is selected for both the FID and oxygen sensor so that the sensors will automatically change ranges for best accuracy, if this is not done, an over-range error will be displayed. In addition, the measured oxygen content is higher than actual air conditions (should be ~21%). This may be due to the oxygen span bottle being improperly labeled based on its contents.

This screen also provides the user the ability to purge the entire system using nitrogen gas. The user can also perform backflush, which uses compressed air to clean the PM filter by blowing air back through the sample line into the exhaust. This action is executed following every measurement procedure. Of note, running the SESAM bench in measurement during long durations dramatically shortens filter life. Therefore, measurement normally occurs starting just before the recording of engine and emissions data. After data recording is complete, 'Standby' is clicked to purge the system of exhaust gas. Then, the system is backflushed. Backflushing should not be performed while recording engine performance data due to its effects on exhaust pressure.

4.7.1.5 Recording Emissions Measurements from the FTIR

The operating screen of the AVL bench allows the user to perform all necessary functions on the bench (calibration, measurement, backflush, etc.). However, recording the data is not available through this program. Typically, AVL customers write their own datalogging code to facilitate this need. A custom program is indeed how emissions data is recorded at KU. This is accomplished using another program available on the AVL emissions bench computer, called the AK command window. From this window, a user can directly enter any of several commands into the input text box to output messages from the bench (similar to a command prompt in Microsoft Windows).

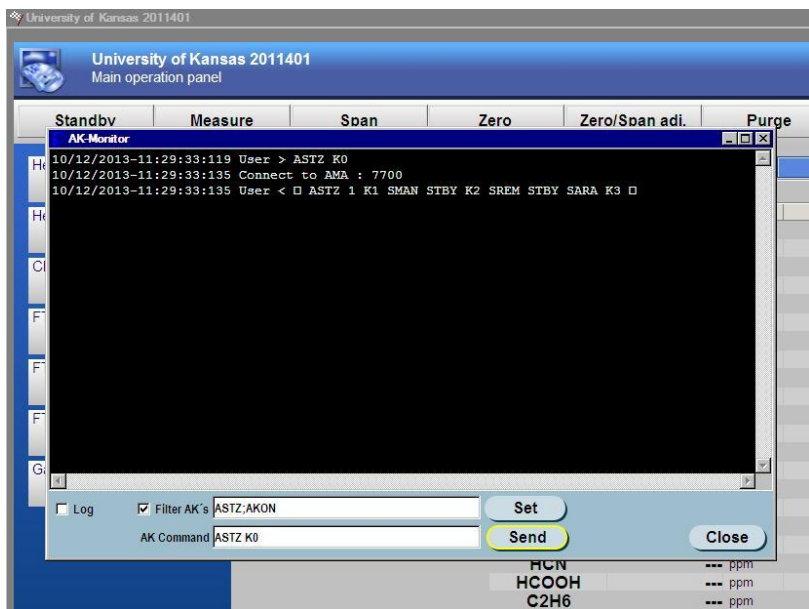


Figure 4-103. Screen Shot of AK Command Window.

A screen shot of the AK command window on the AVL bench computer is shown in Figure 4-103.

This allows the user to enter commands, such as 'ASTZ K0', that returns a message or status. In the example shown, this command is asking for the status of each sensor. The status handle is (ASTZ). Individual sensors could be retrieved by entering K1, K2, or K3, which would return the status of individual FTIR, FID, and O₂ sensors, respectively.

In addition to direct entering of AK commands by a user, this program can also be accessed through TCP/IP communication where transmitting the same codes result in a return of AK window output messages. There are several commands that can be sent through TCP/IP communication to perform different functions, however, the one used here is 'AKON K0' which returns all measured species through the same TCP/IP connection in a specific order. Thus, the species data can be broken down into a usable format using LabVIEW. With the LabVIEW program, the user can both observe and save the emissions data shown on the screen.

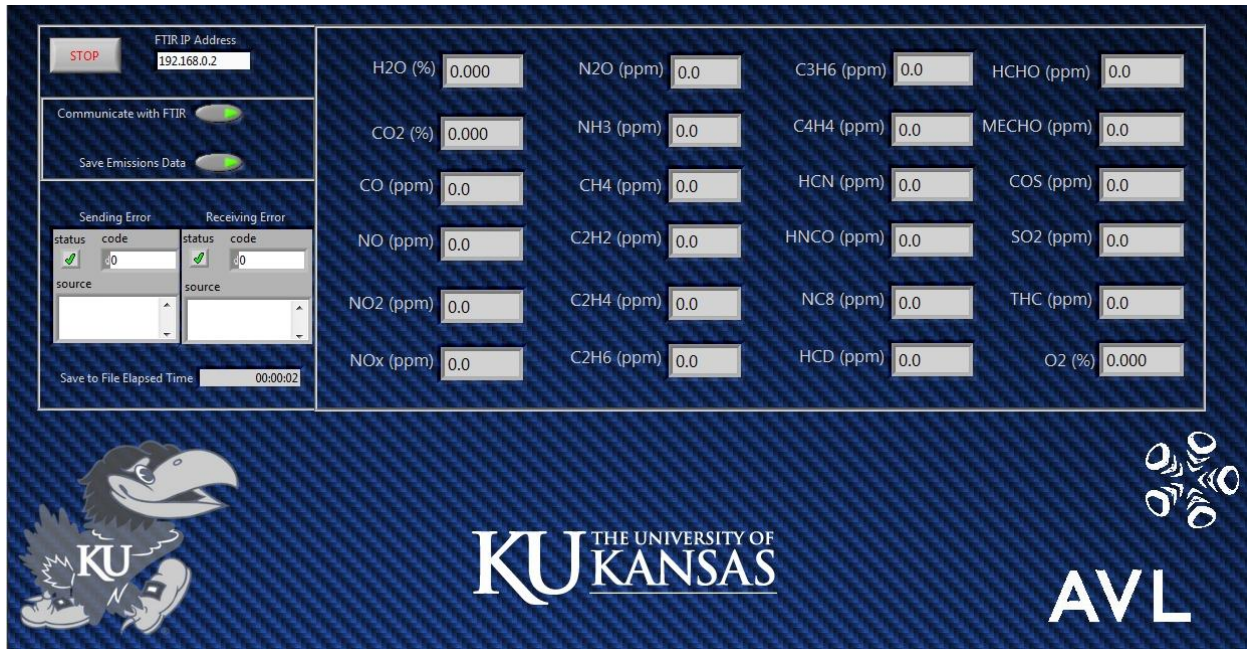


Figure 4-104. LabVIEW-AVL Communication and Data Collection Window.

The main operating window in which LabVIEW communicates with the FTIR for emissions saving is shown in Figure 4-104. In the main window, the user can set the IP address of the bench, which is statically set to 192.168.0.2 as the emissions systems, including the smoke meter, are on their own network. The main controls for the program are to 'Communicate with FTIR' and 'Save Emissions Data'. By turning on the 'Communicate with FTIR' switch, the computer initializes communication with the AVL emissions bench. To aid in troubleshooting, error messages will appear in the 'Sending Error' or 'Receiving Error' text boxes to alert the user of any communications issue. Typical issues include the wrong IP address, un-powered router (located in the instrumentation cabinet), or the AK command window on the FTIR computer being closed. Upon initialization of communication, emissions values should begin to fill the individual species boxes on the main screen.

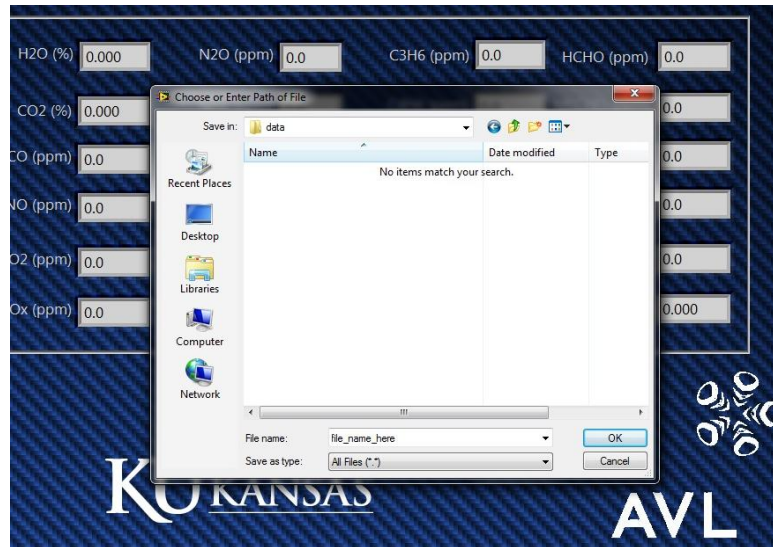


Figure 4-105. Emissions Recording File Name and Path Dialog Box.

Pressing the 'Save Emissions Data' switch will begin recording these species readings to a spreadsheet file. To specify the filename and path, a popup window will ask for user input, as shown in Figure 4-105. As soon as saving commences, a timer called 'Save to File Elapsed Time' begins to count. This timer helps the user track how long the recording has been going. The program will keep recording to file at one sample per second until the 'Save Emissions Data' switch is turned off. Subsequent saving of emissions data will initialize with a reset timer that starts at 00:00:00.

The program works by first initializing a connection with the AVL bench computer, then once a connection is established, the LabVIEW program operates in a while loop that sends the command 'AKON K0' to the bench computer, waits half a second, then receives the species data, displays/saves it, then waits another half a second before repeating the entire loop.

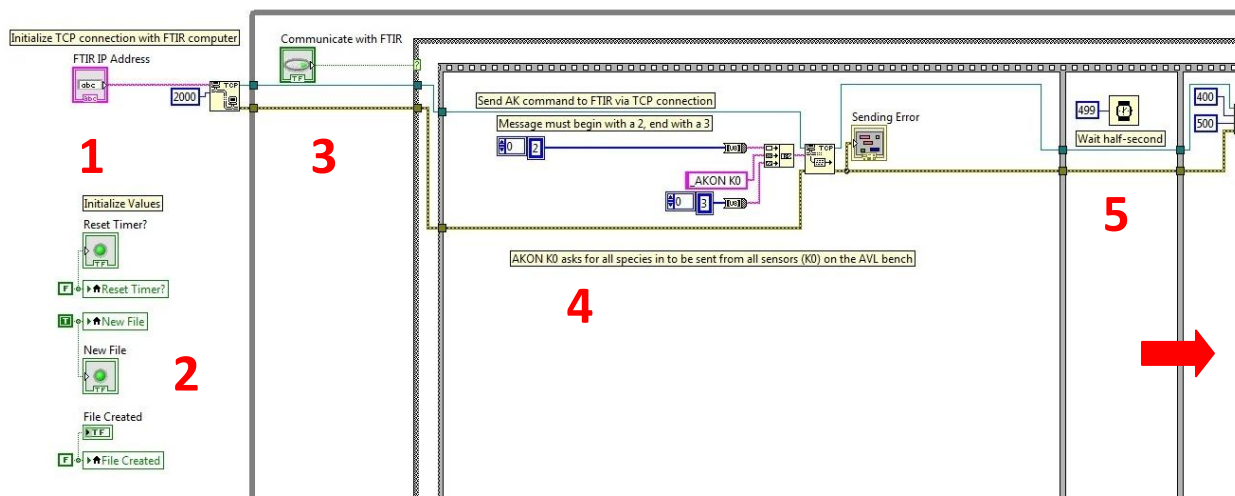


Figure 4-106. Initialization of TCP/IP Connection. Transmission of AK Command ‘AKON K0’.

This process is broken up into several figures, with the first section of block diagram shown in Figure 4-106.

1. In this section, the TCP/IP connection with the AVL bench computer is initialized. The *initialize TCP* node only requires an IP address and a port number to establish a connection. These are specified by the AVL bench computer as 192.168.0.2 and 2000, respectively. A control box is used for the IP address to allow the user to change the address from the front panel of the program, but this should not be necessary unless a change to the emissions network were to occur.
2. Initialization of the program before entering the continuously running while loop includes setting the local variables *Reset Timer*, *New File*, and *File Created* to *False*. These will be changed throughout operation of the program to control the Save to File Elapsed Time timer, user save file dialog box and file header creation, and write to file functions of the program using case structures.
3. Although while the connection between the laptop and bench computer has been established, actual communication will not occur until the ‘Communicate with FTIR’ switch is activated. This is done to prevent a communication error in the event that the laptop tried to communicate

with the bench computer before the bench computer was active. Once the communicate switch is activated, actual program function begins.

4. The message 'AKON K0' is sent to the bench computer via the TCP Write node. AK command structure through TCP, as defined by AVL, must begin with the Start of Text (STX) and End of Text (ETX). Therefore, the actual message sent to the bench computer through TCP communication is 'STX_AKON K0 ETX'. The TCP Write node then sends this message to the bench in ASCII format, which is a byte per character, '2 95 65 75 79 78 32 75 48 32 3' [107].
5. To maintain the one sample per second record rate, a wait function occurs after the sending of the AK command. This wait is for 499 milliseconds. Another wait, also for 499 milliseconds, occurs later in the loop following the reading of species data. The remainder of the loop takes approximately two milliseconds to run, thus ensuring a total loop time of one second.

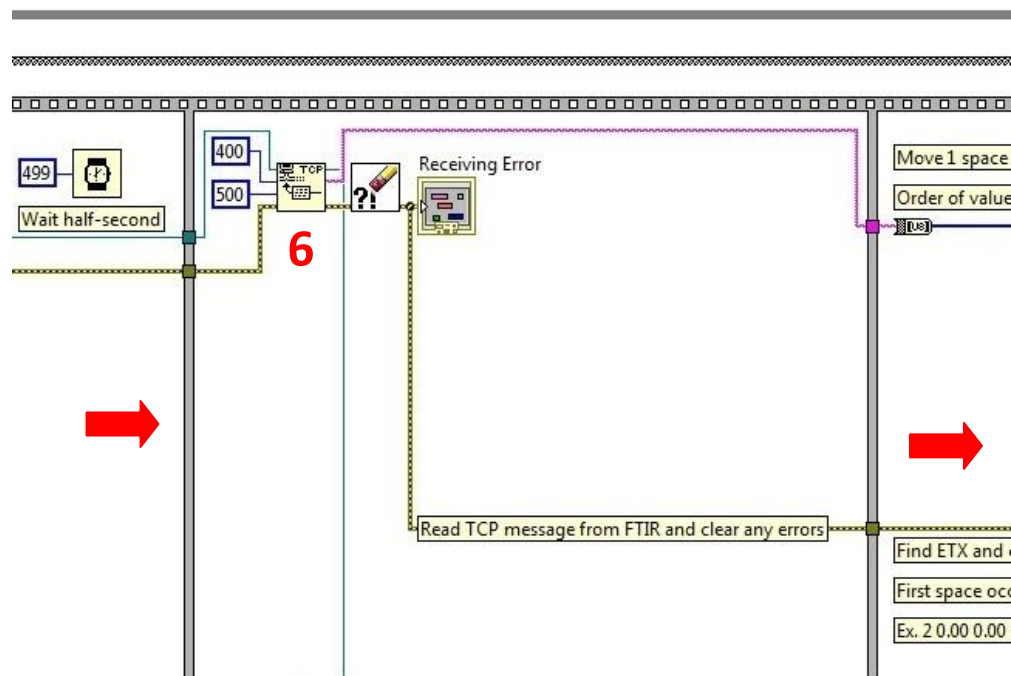


Figure 4-107. Reading TCP Message From Bench Computer.

6. Following this first wait, the reading of the species data from the bench computer is performed (Figure 4-107). The TCP Read node needs the connection ID (send from the TCP Write node), as

well as the number of bytes to read (400), and the timeout wait duration. The number of bytes to read (ASCII characters) is set to 400 to equal the number of characters sent from the bench computer in the species message. The timeout duration is set to 500 milliseconds as an arbitrary time to wait before returning a timeout error. If this occurs, the message is sent to the Receiving Error text box and cleared before moving on in the code. A subsequent attempt at reading species data will occur in the next loop iteration.

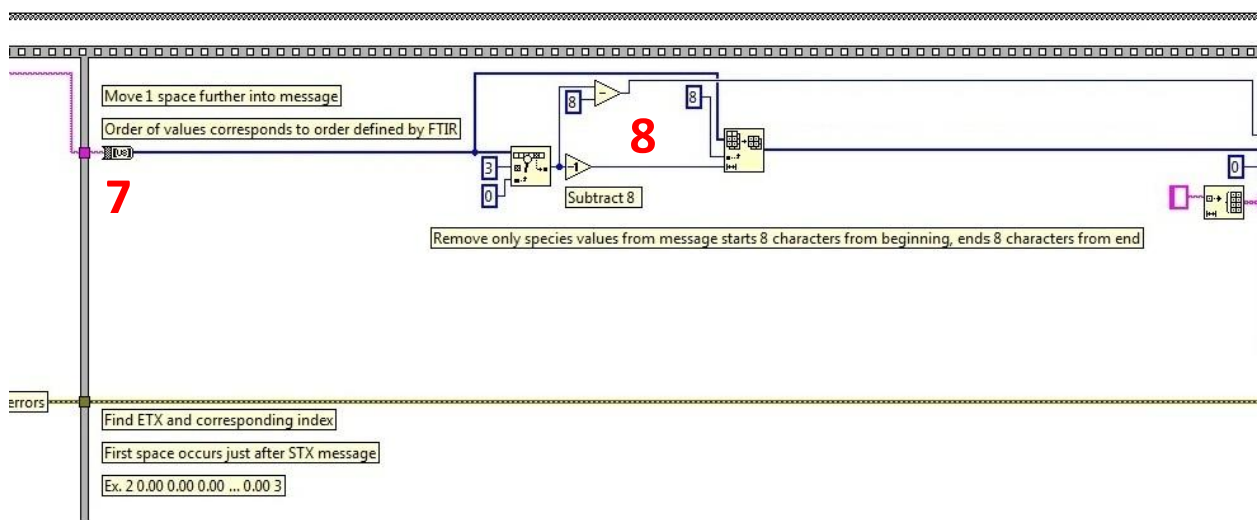


Figure 4-108. Removing STX and ETX Characters From Received TCP Message.

7. The returned message of ASCII characters leave the TCP Read node as a string of characters that are broken into useful information beginning in Figure 4-108. This segment of code removes the STX (2) and ETX (3) from the single string of ASCII characters. It does so by first converting the string to an unsigned byte array (pink to blue wire in Figure 4-108), this array will be searchable by utilizing LabVIEW array functions in step eight.
8. The byte array is first searched using a Search 1D Array node to determine the index in which the ASCII character ‘3’ occurs (ETX). This index is subtracted by one to yield the index corresponding to the end of the species data, which is then wired into an Array Subset node. This node takes in the entire byte array sent from the bench computer and returns an array

composed of a section of the input byte array. To specify the output array, a start index and length input is also required. The start index is eight (just after the byte occupied by the STX character), and the output length is one less than the index where ETX occurs.

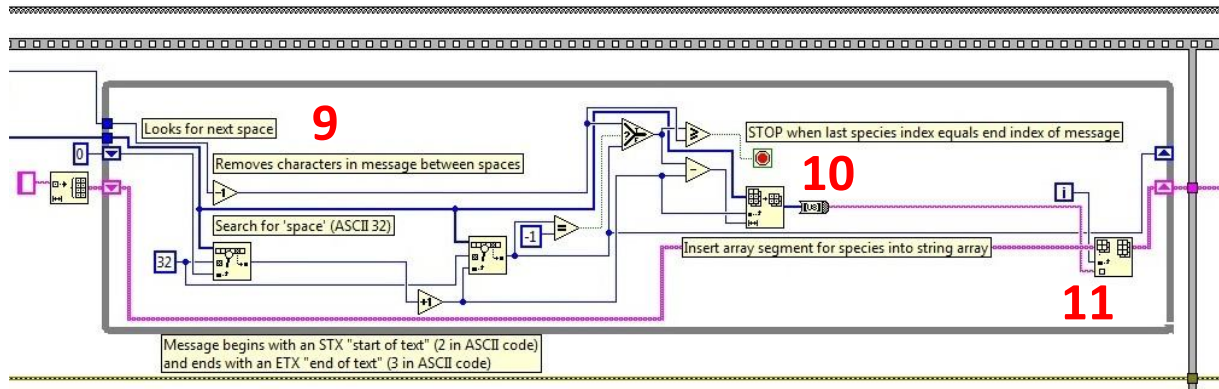


Figure 4-109. Sort Through Species String to Separate Into Individual Species String Array.

9. Finally, the shortened byte array and the index for ETX (minus eight) are passed to the subsequent section in Figure 4-109. A while loop is used to build a string array where each species represents its own string within the array. Each run of the loop removes one species value from the original byte array so that as the loop repeats, the byte array becomes shorter. Eventually, no bytes remain and the loop is stopped.

First, the incoming byte array is searched for the spaces (ASCII 32) that separate each species (e.g. ... 1.23 4.56...) using a Search 1D Array node. The index that returns (indicating the beginning of a species value) is increased by one and passed to a second Search 1D Array node that looks for spaces again. The index yielded by the second Search 1D Array node corresponds to the space immediately following the same species value.

10. Data for a single species can be retrieved by feeding the input byte array (of all species) to an Array Subset node along with the index preceding and following an individual species as found using the Search 1D Array nodes. The index of the space following the retrieved species is used in subsequent runs of the loop and checked to see if this index corresponds to the end of the

long byte array, which indicates that the loop has reached the end of the species array and needs to stop.

11. Each value for a retrieved species is converted to a string and stored in a string array, this array is passed through the loop iterations using a shift register so that all species are built into the string array in the proper order.

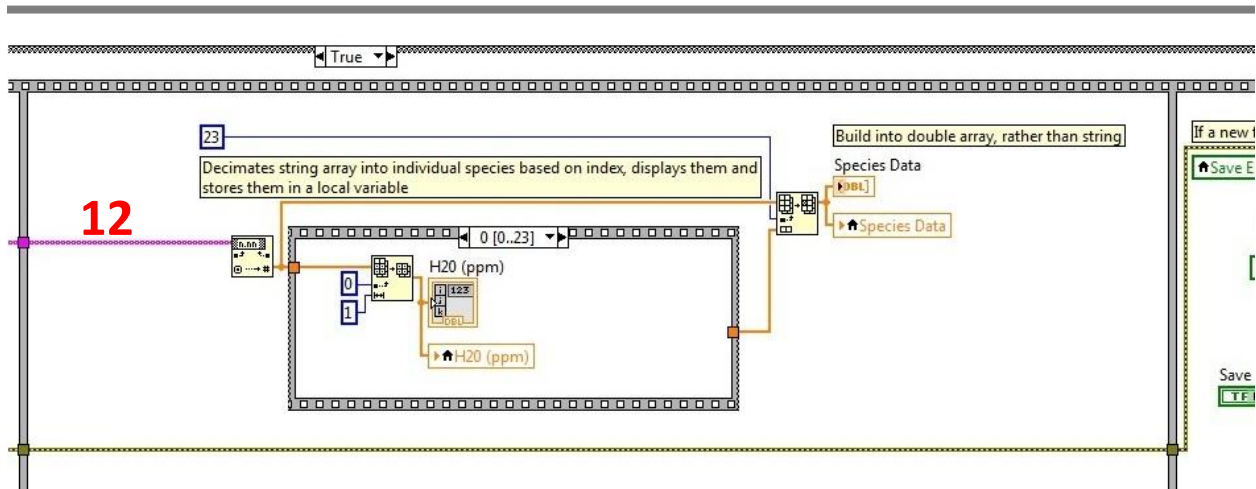


Figure 4-110. Convert String Array Into Individual Species Variables for Display (and Saving Later).

12. In Figure 4-110, the string array is broken into individual numeric values using a String to Number conversion node. Then, this array is sent to a stacked sequence structure where an Array Subset node is used to remove individual species for front panel display and storage to a respective local variable.

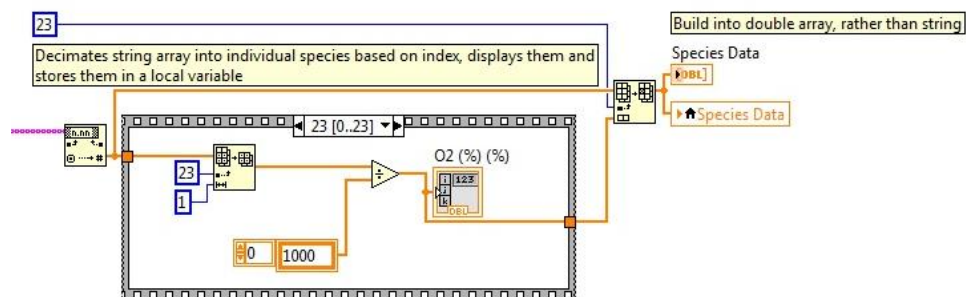


Figure 4-111. Converting Oxygen from PPM to % Concentration.

The high-percentage species O₂ values are divided by 1,000 to convert them from parts per million to percentage and is put into the *Species Data* numeric array using an Insert Into Array node to replace the ppm notation, as in Figure 4-111.

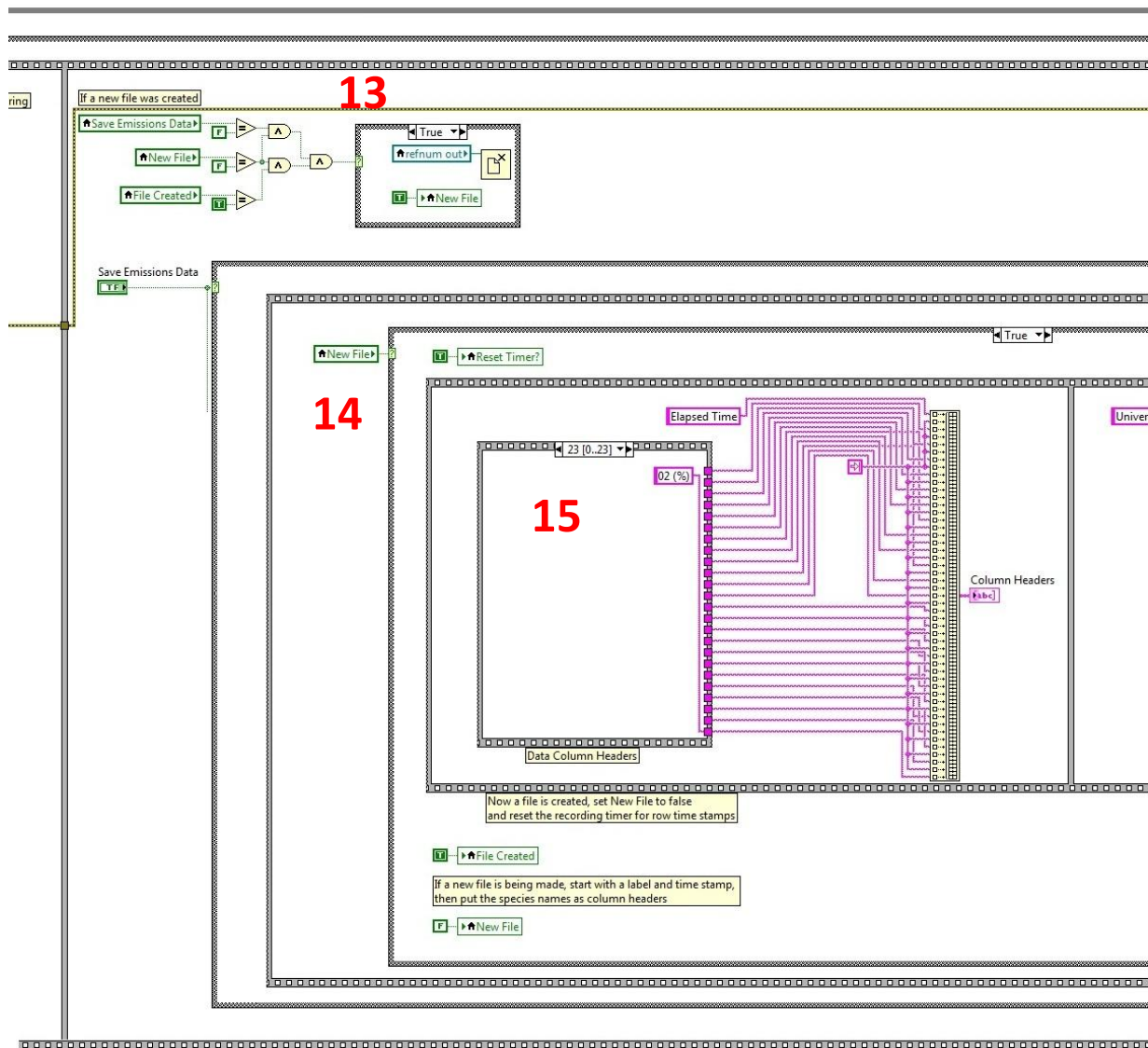


Figure 4-112. Determine File Saving State, Create New File Column Header.

13. This completes the retrieval and display of the chemical species data. Figure 4-112 begins the code used to save the data to file. The action taken by this section of code depends on the Boolean logic shown and is intended to reset the process of creating a new file. A header must first be made with subsequent iterations adding rows of data to a spreadsheet file without

remaking a header each time. During display-only operation, *Save Emissions Data* and *New File* are both *False*. The false case of this structure does nothing. But, if a file has been previously created (*File Created* = *True*) and it is not a new file (there is data in it) and saving has ended (stopped by user), then the true case of the structure closes the text file and resets the *New File* variable to *True*. This variable must be reset so that subsequent save files have a header built onto them, as discussed in step 14.

14. At the beginning of the save process (triggered by *Save Emissions Data* being *True*), a case structure checks to see if this is the first iteration of the save process by checking *New File*. If it is the first iteration (*New File* = *True*), then a header is made, the timer is reset, and *New File* is set to *False* so that later loop iterations will skip the header creation process (step 15) and go directly to the saving of data, discussed beginning with step 20.
15. Inside of the case structure's true case, a stacked sequence structure builds a tab-delimited string array that will serve as column headers, with each species header appearing in a specific order.

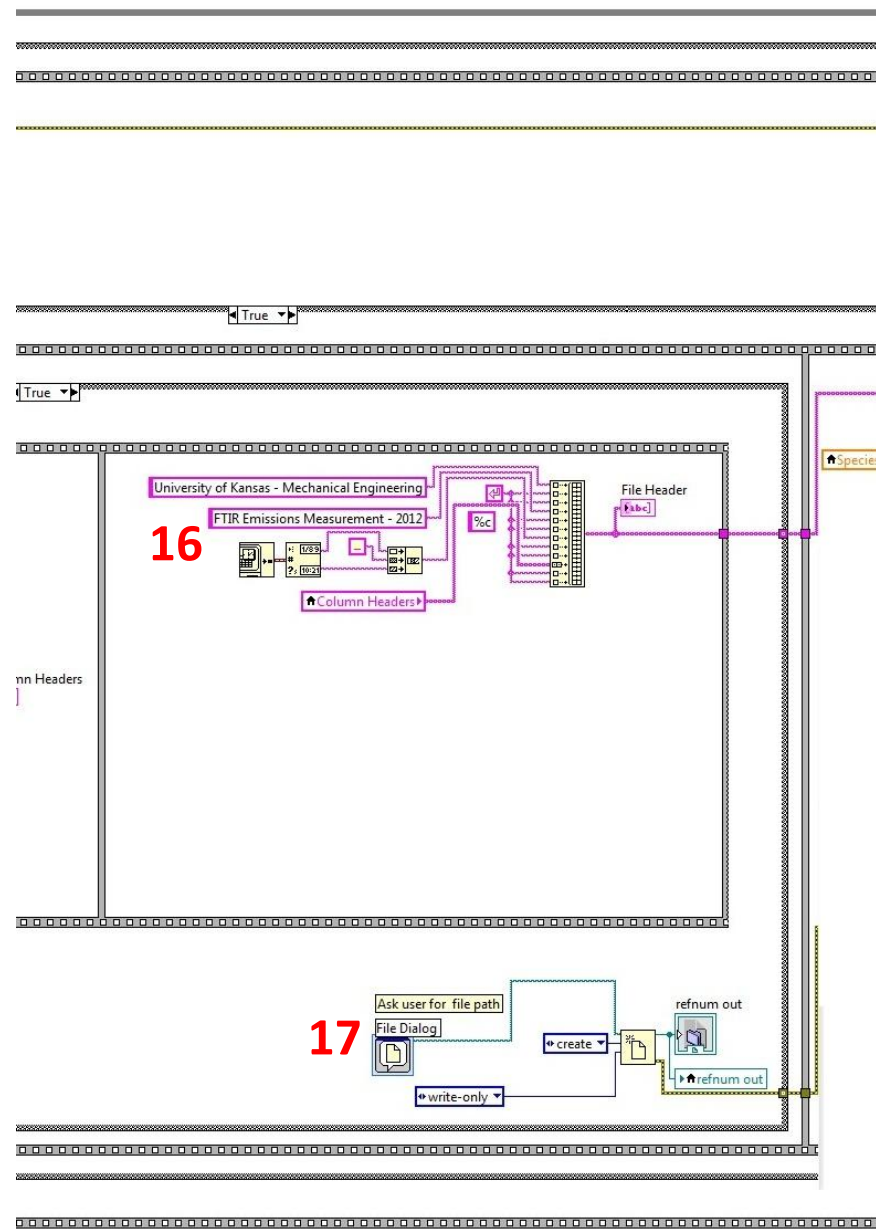


Figure 4-113. Creation of File Header, Concatenate With Column Headers, Set File Save Path

16. This array is saved to the local variable called *Column Headers* to be used in the code shown in Figure 4-113. In this section, the file header is created and separated by carriage return. This includes a date stamp, retrieved from a Get Date/Time In Seconds node and a Get Date/Time String converter node. This header is combined with the previously created column headers array into a single string array that is placed at the beginning of the emissions data file.

17. At this point, the user has just pressed the 'Save Emissions to File' switch and a file header has been made.

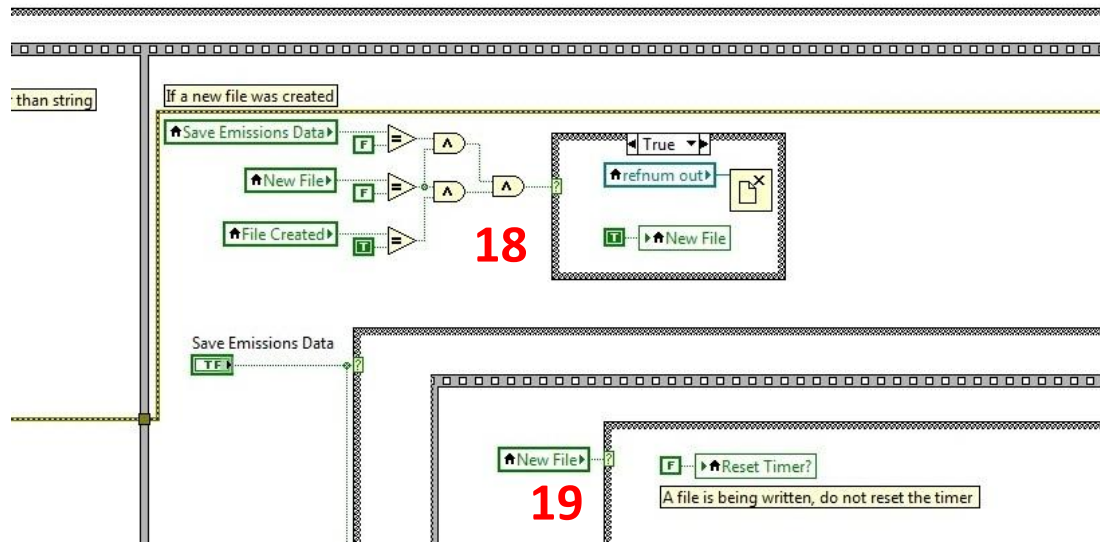


Figure 4-114. New File Created, Timer Keeps Running Until File Is Closed.

18. Now a File Dialog node is used to prompt the user to specify the save location and filename for the new data file, as shown in Figure 4-105. Once, saving is underway (i.e., *Save Emissions Data* and *File Created* are *True*, *New File* is *False*), the false case will run to now start recording data.
19. As *New File* is *False*, the false case structure within the saving structure will run. Which is a 'do-nothing' case. Meaning that no new file header will be made, but that the computer will skip to the next frame in the sequence.

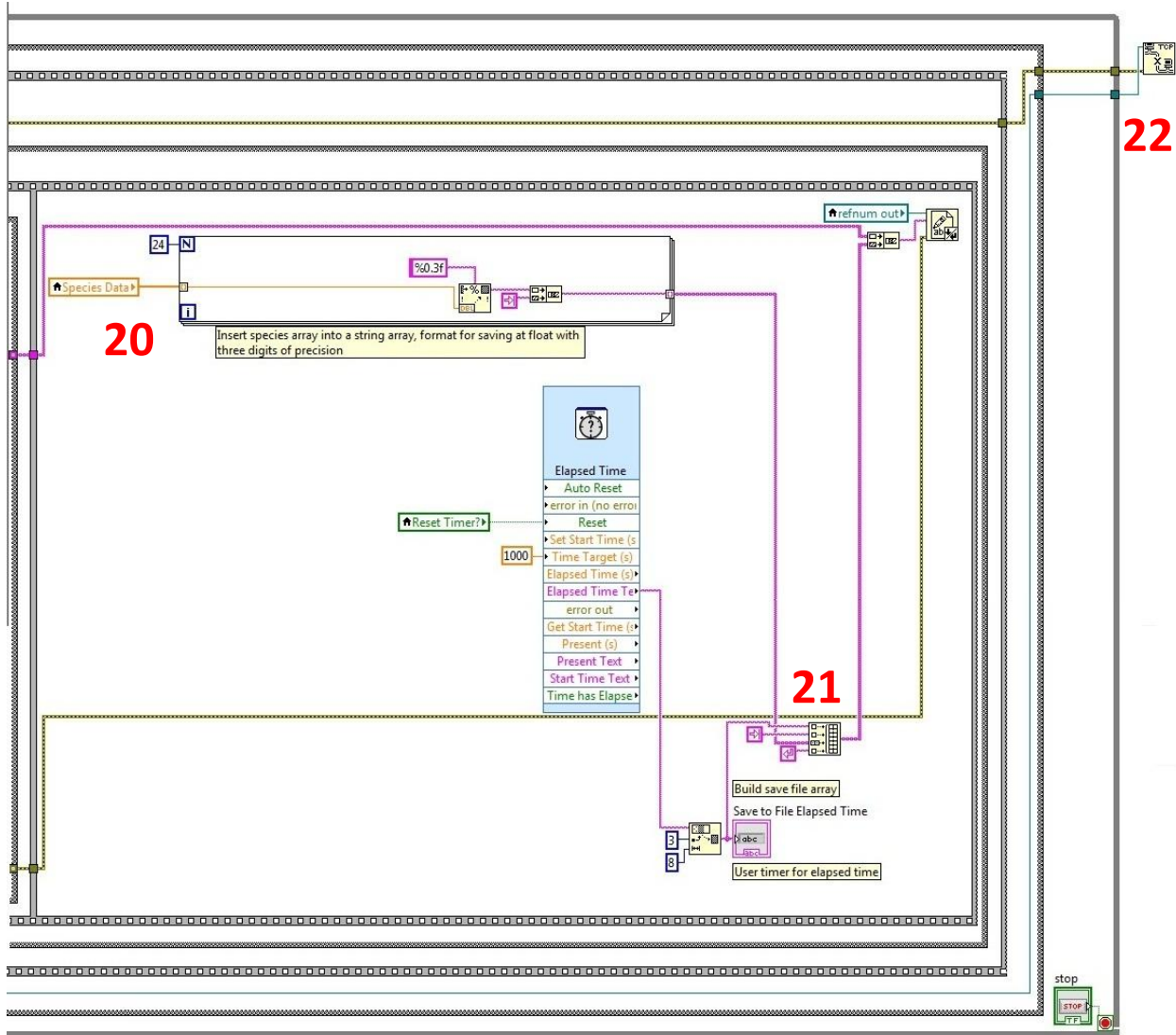


Figure 4-115. Write Species and Elapsed Time to File, Reset Time if Needed, Close TCP Connection.

20. In Figure 4-115, a for-loop is used to extract each species from the *Species Data* numeric array.

Then, each species is converted from a numeric value to a string with three digits of precision.

Finally, a Concatenate String node is used to combine each species with a tab character (for tab delimiting). Upon exiting the for-loop, the individual strings are assembled into a tab-delimited row of emissions values that are ready to be added to the save file.

1	A	B	C	D	E	F	G	H
2	University of Kansas - Mechanical Engineering							
3	FTIR Emissions Measurement - 2012							
4								
5	4/29/2013 15:00							
6								
7	Elapsed Time	H2O (%)	CO2 (%)	CO (ppm)	NO (ppm)	NO2 (ppm)	NOx (ppm)	N2O (ppm)
8								
9	0:00:00	6.101	5.2	711.73	439.4	72.65	512.05	0.95
10	0:00:01	6.317	5.476	593.1	471.08	77.33	548.4	0.71
11	0:00:02	6.326	5.425	589.48	478.04	77.39	555.43	0.65
12	0:00:03	6.318	5.242	587.76	477.76	77.22	554.98	1.15
13	0:00:04	6.355	5.413	570.83	485.3	75.55	560.85	0.86
14	0:00:05	6.342	5.364	574.22	472.78	78.13	550.91	0.42
15	0:00:06	6.452	5.364	569.68	478.83	76.91	5 ⁵ 75	0.97
16	0:00:07	6.348	5.368	563.07	481.25	76.58		1.09
17	0:00:08	6.314	5.534	526.32	495.45	76. ⁸ 2.3		0.71
18	0:00:09	6.406	5.441	567.49	497.17		575.04	0.59
19	0:00:10	6.418	5.619	580.81	488.15		566.92	0.69
20	0:00:11	6.393	5.254	585.43	485.	/9.29	564.38	0.62
21	0:00:12	6.454	5.354	566.25		77.14	558.53	0.78
22	0:00:13	6.343	5.277	596.0 ¹		78.28	548.79	0.95
23	0:00:14	6.316	5.263	609. ⁵ 466.87		79.81	546.68	0.5
24	0:00:15	6.355	5.285	599.26	470.05	79.94	549.99	0.63
25	0:00:16	6.356	5.413	578.76	474.26	79.71	553.97	1.03
26	0:00:17	6.425	5.428	580.68	469.11	78.93	548.04	1.11
27	0:00:18	6.321	5.345	584.55	476.56	80.27	556.82	0.88
28	0:00:19	6.404	5.441	585.57	483.12	79.57	562.69	1.02
29	0:00:20	6.275	5.317	576.12	478.93	78.93	557.86	1.05
30	0:00:21	6.312	5.484	579.39	473.39	79	552.4	0.89
31	0:00:22	6.425	5.348	551.49	481.48	77.81	563.2	0.92
32	0:00:23	6.329	5.516	579.47	469.79	79.05	548.84	1.16
33	0:00:24	6.341	5.32	559.32	486.63	79.07	565.7	1.16

Figure 4-116. Example of LabVIEW Output File of Saved Emissions Data.

21. At this point, *Reset Timer?* is false, so the Elapsed Time node sends a timer signal through a String Subset node to only return the seconds, minutes, and hours from the timer signal. This abbreviated timer value is then displayed for the user (Figure 4-104) and written to file as the first value in the row of emissions data saved during this iteration of the saving loop. An example of the output file is shown in Figure 4-116 as opened in Microsoft Excel.
22. Finally, upon the event of the user pressing the *Stop* button, the main while loop stops and the TCP connection is closed.

4.7.1.6 SESAM Shutdown Procedure

Compared to the startup procedure, the SESAM bench shutdown process is very short. The compressed bottles of FID fuel (hydrogen/helium) and synthetic air should be closed. This automatically shuts off the FID. If the calibration bottles are still open, they should be closed as well. If the nitrogen purge is not to remain on for future tests, this can be shut off too. Finally, the power to the heated

sample line and heated PM filter can be turned off. For a longer downtime, the computer itself can be powered down.

4.7.1.7 *Changing PM Filter*

Generally speaking, maintenance of the SESAM bench is limited. Yearly on-site calibration and upkeep are provided by AVL.



Figure 4-117. Filter Location on Filter Cart.

However, the heated PM filter requires occasional replacement. This filter is located on a heated stem, which can be removed through an access port on the back of the filter housing, as in Figure 4-117.



Figure 4-118. Removal of Filter Protective Cover.

The guard for the filter stem is easily rotated upwards, as the right-hand side fastening screw is not fully tightened (Figure 4-119).



Figure 4-119. PM Filter Stem.

The stem itself is removed by turning the black handle counter-clockwise and gently pulling straight outwards. The removed stem is shown in Figure 4-119. The front of the stem (right side of figure) is removed by turning with a wrench on the flattened portion of the round stem at the highlighted (red arrow) location. Then, the filter can be removed by hand and a new filter put in place. Used up filters are very black, to a need for replacement should be visually apparent.

4.7.2 AVL 415SE Smoke Meter

The AVL smoke meter performs the vital function of PM measurement.

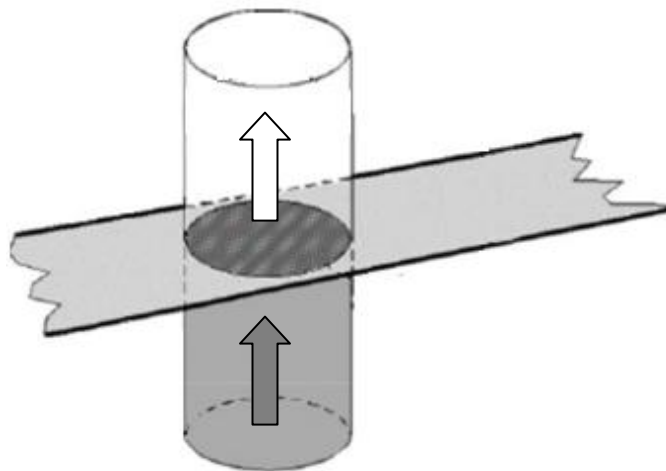


Figure 4-120. Smoke Meter Collection Principle .

This system functions by passing a pre-determined volume of exhaust sample (heated by sample line) over a section of clean filter paper, as shown by the diagram in Figure 4-120 . The collection of PM on this paper darkens the previously white paper. This darkening is measured by a photoelectric ‘reflectometer’ that is analyzed to produce a filter smoke number. Based on the volume of exhaust in the sample, a concentration (mg/m^3) value is produced .



Figure 4-121. Smoke Meter Sample Probe.

Exhaust gas enters the heated sample line using a stainless steel probe threaded into a welded pipe bung on the exhaust, as shown in Figure 4-121. This probe extends into the center of the exhaust stream and is designed to be installed facing upstream. This alignment is important for consistent results between tests.

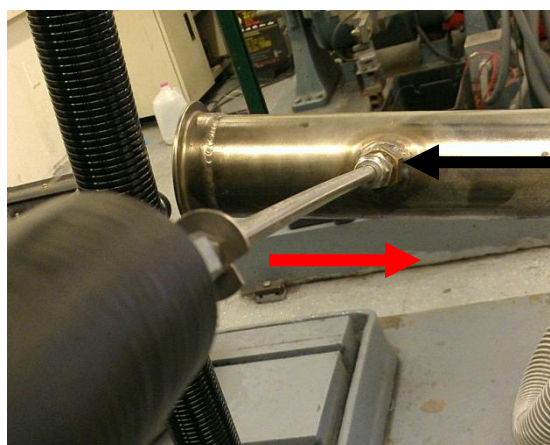


Figure 4-122. Orientation of PM Sampling Probe.

The direction of the sample probe can be verified after installation by inspecting the probe directional indicator in Figure 4-122. This flat piece of stainless steel at the end of the rigid stainless steel probe has a notch cut out of it that indicates the probe sampling direction (red arrow), which is shown in Figure 4-122 to be in the opposite direction of exhaust flow (black arrow). Testing with the system oriented in this direction during the summer of 2012 found substantial variability in the measured concentrations. AVL technicians suggested that this is caused by single-cylinder pressure pulsation. The solution recommended by AVL is to turn the probe 180° to face downstream instead. This approach produces much more consistent results and is the method used currently. Experimentation with the new fuel system (Chapter 1 through Chapter 3) finds extremely low production of PM at low loads, suggesting that the original upstream orientation may be worth reconsidering.

The smoke meter interfaces with a computer using an ethernet connection that plugs into the side of the meter housing. This ethernet cable is connected to the same off-grid router used by the emissions laptop and SESAM bench computer. Any computer can be connected to this meter to take measurements. This is accomplished by opening a web browser on the laptop and entering the smoke meter IP address into the browser web address bar. The IP address is indicated directly above the ethernet port on the smoke meter.

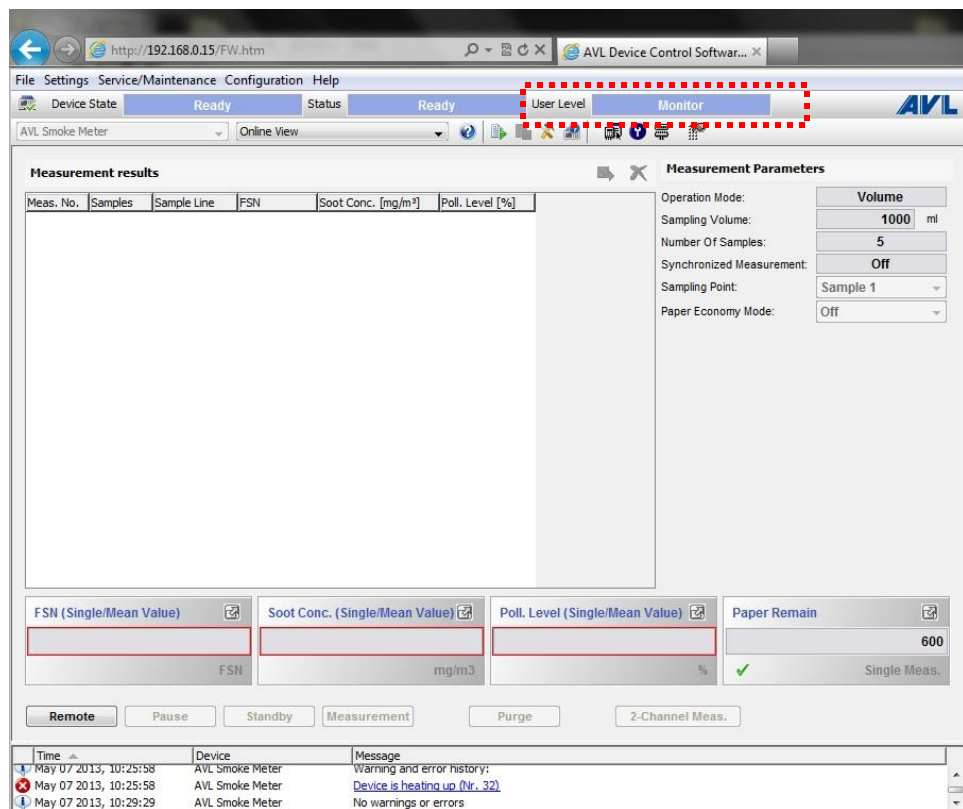


Figure 4-123. Startup of Smoke Meter, User Level: Monitor.

The operating screen that loads is shown in Figure 4-123. The first screen that opens is meant for monitoring of the system only, as indicated by the user level being set to monitor. Clicking the 'Remote' button at the bottom of the screen (red arrow in Figure 4-123) changes the user level to operator.

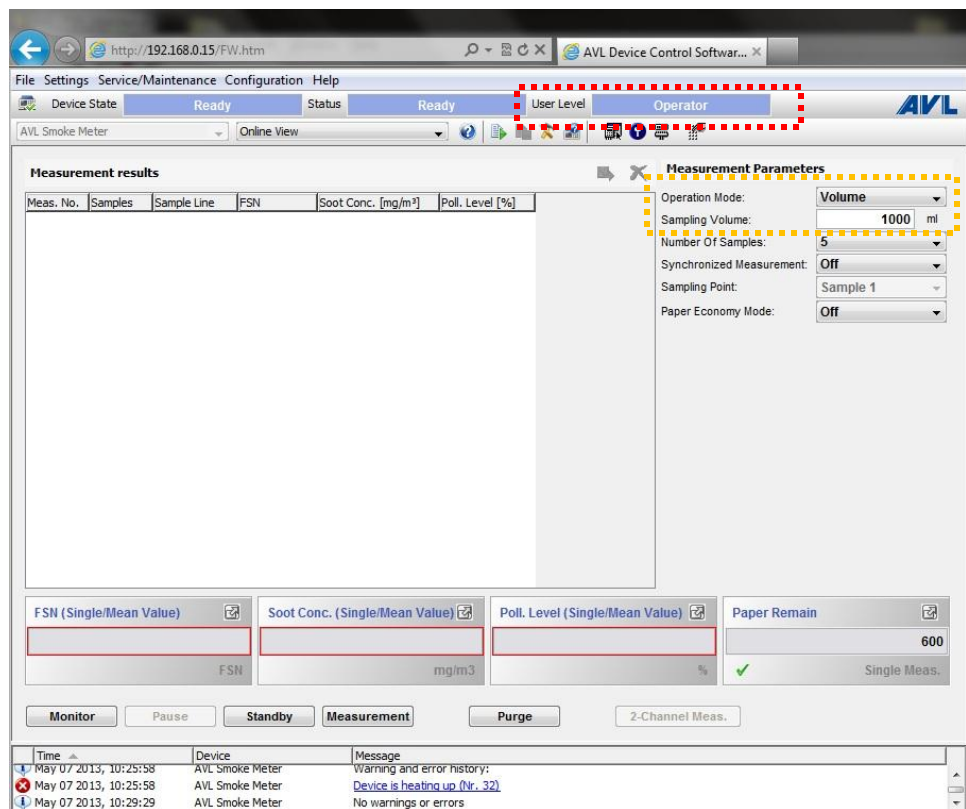


Figure 4-124. Volume Operation Mode, User Level: Operator.

Figure 4-124 reflects the shift to operator mode. Now, the operator can make changes to the measurement volume, number of samples, and perform measurements. The default sample method is volumetric sampling (orange box in Figure 4-124), which pulls a user-defined amount of volume through the filter paper. The preferred method used in the laboratory is to set the sampling time, changed using the operation mode drop-down menu.

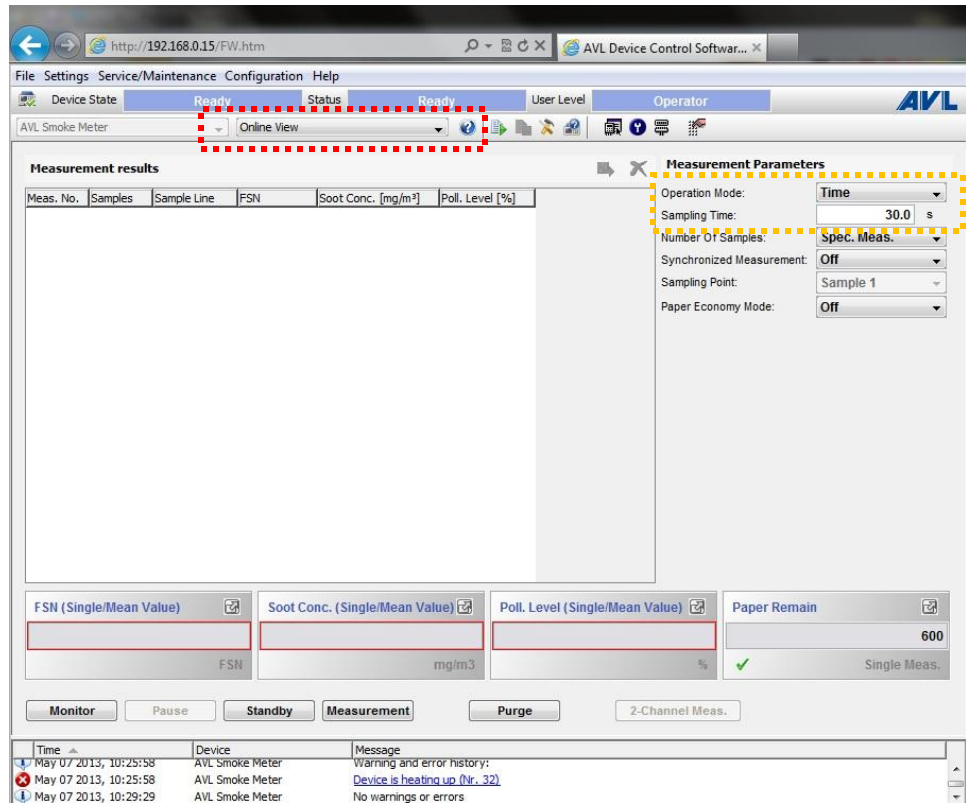


Figure 4-125. Time Operation Mode, User Level: Operator.

In this mode (Figure 4-125), the operator sets how long to sample the exhaust. Internal calculations in the meter make the instrument operation consistent between operating modes, so this is purely user preference. Of more importance is the choice of sample volume/time needed to produce good results. AVL states that the filter blackening number should be maintained between one and six, with three to four being an optimal value. This is important because too short of a sample time will not darken the paper much, diminishing accuracy. Likewise, too long (or high of a blackening number) reduces accuracy, as well. This value is checked by clicking the 'Online View' drop-down menu (red in Figure 4-125) and selecting 'Service View Numerical'. The paper blackening number is displayed. During a test, once a proper sampling volume/time is found for a particular load to produce a blackening number around three to four, this same volume/time should be used consistent throughout samples at this condition. For example, if 30-seconds of sampling produce a blackening number of 3.5 at 4.5 N·m of load, this is the sampling time that should be used at all tests at this load to ensure consistent

measurement. This will reduce sample numbers later in the test and improve experimental efficiency through time saving.

4.7.2.1 Smoke Meter System Maintenance

Like the SESAM bench, there is little to do in the form of maintenance on this equipment. In fact, only two tasks exist.

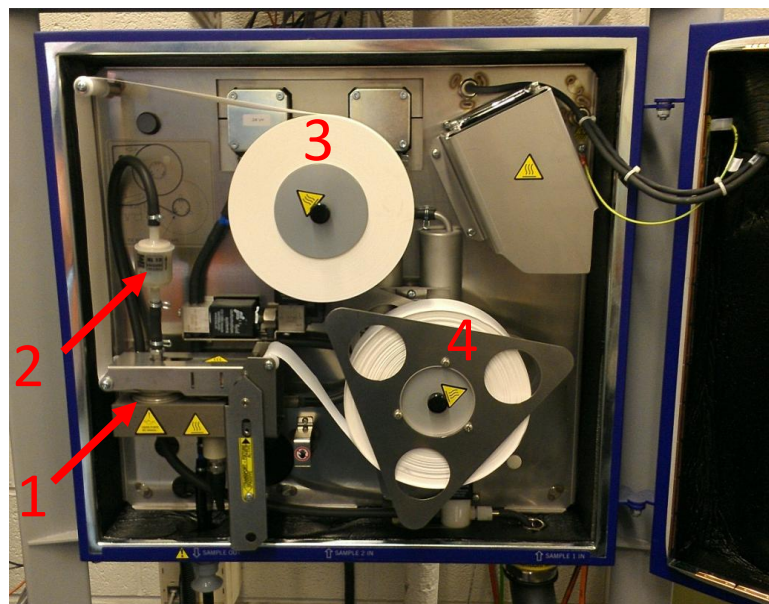


Figure 4-126. Internal Components of AVL Smoke Meter. Reflectometer (1), Downstream PM Filter (2), Paper Supply Roll (3), and Paper Return Roll (4).

First is the PM filter, located downstream of the filter paper section, shown in Figure 4-126. These filters have a clear housing and, therefore, should be changed when the filter element becomes visibly black. An error will also be indicated on the operator screen of the laptop if the sample volume drops too low, indicating a new filter is needed. These are available through AVL.

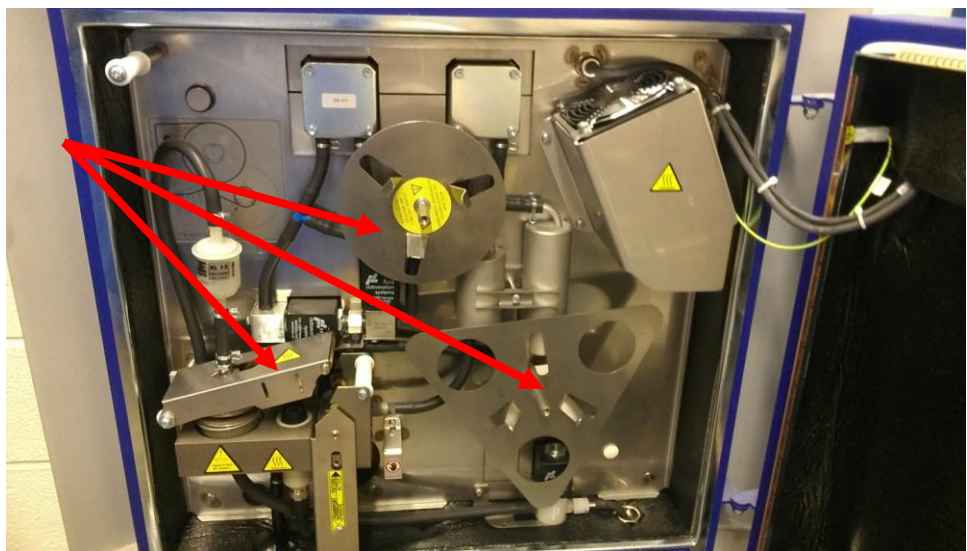


Figure 4-127. Old Paper Rolls Removed, Reflectometer Jaw Unclamped.

The other, more regular, maintenance task is the replacement of the filter roll. As shown in Figure 4-126, filter paper is fed through the sample stream then loaded onto a used paper roll. The front of the smoke meter (LED's), and the operator screen indicate how much paper is left, reducing the possibility of running out of paper during a test. The paper rolls are removed by unscrewing the outer roll retainers and unclamping the reflectometer jaw mechanism, as shown in Figure 4-127.

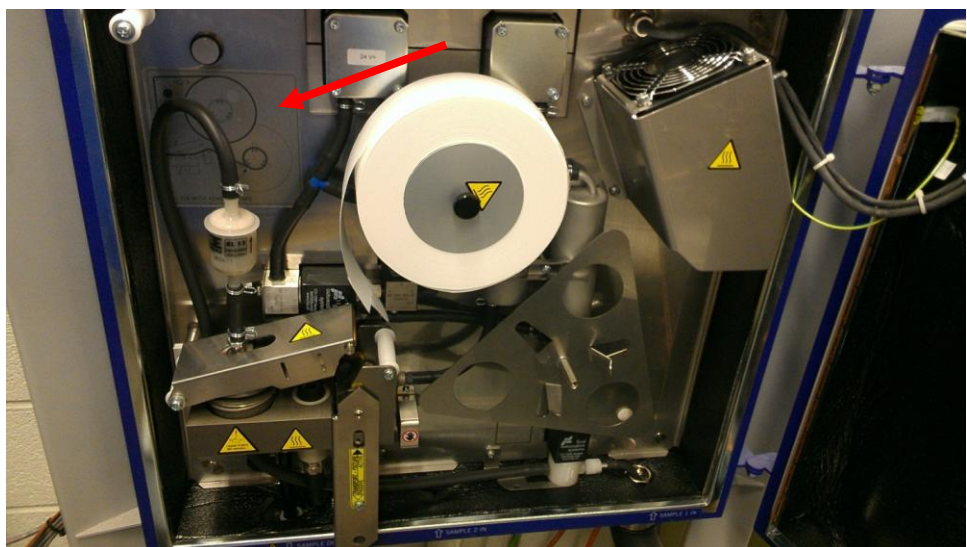


Figure 4-128. New Roll Inserted on Carrier. Feed Diagram Indicated At Back of Sensor.

Then, a clean roll is placed on the feeder wheel of the smoke meter, depicted in Figure 4-128. Once the wheel is in place, the roll retainer is screwed into place. For reference, proper paper feed pattern is shown on a diagram on the back of the smoke meter interior.

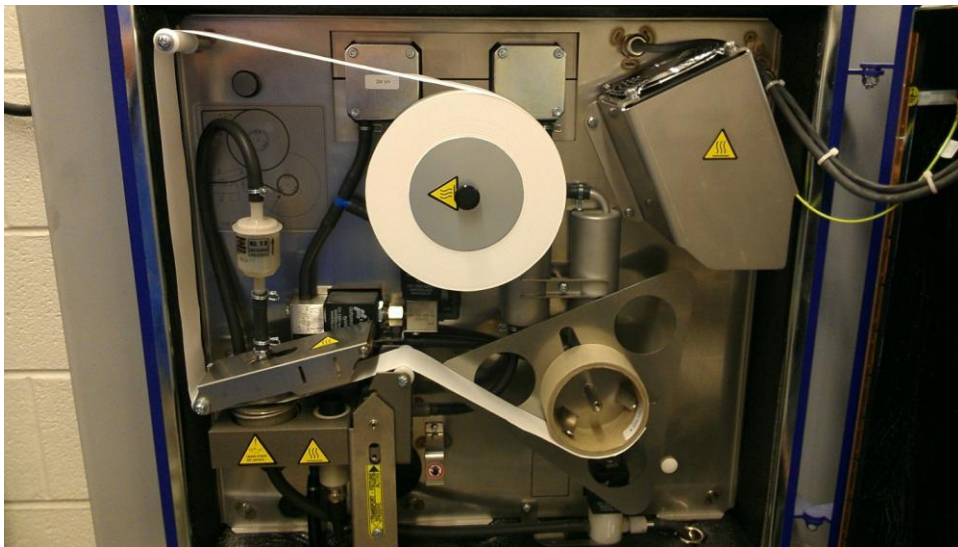


Figure 4-129. Old Empty Roll used to Capture Spent Filter Paper using Scotch Tape.

Then, the empty roll previously removed is used to collect the used paper, as shown in Figure 4-129. The clean paper is fed through the sampling mechanism and taped to the empty used-paper roll using tape.



Figure 4-130. Sample Clamp and Feed Mechanism Closed, Ready for Sampling.

Finally, the sensor clamp is pressed back into locked position and is ready to operate (Figure 4-130). This concludes the discussion on the emissions measurement systems, for more in-depth reference pertaining to maintenance, operation, and troubleshooting, consult the SESAM and Smoke Meter manuals or contact AVL technicians.

4.8 Post-Processing Engine and Emissions Data

	A	B	C	D	E	F	G	H	I
1	Time	Speed (rpm)	Ambient F	Ambient F	Ambient F	Inlet Air M	Fuel Mass	Densi Fuel f	f
2									
3	0	1795.55779	303.694	97186.9	72.1826	5.47488	0.17814	825.175	40.3
4	0	1795.34288	303.694	97218.3	72.188	5.45157	0.17812	825.238	40.3
5	0.057	1801.32578	303.695	97265.4	72.196	5.41655	0.17809	825.333	40.3
6	0.09901	1795.63302	303.696	97294.8	72.2376	5.44163	0.17809	825.343	40
7	0.16201	1796.05228	303.696	97338.8	72.2998	5.47931	0.17808	825.358	39.5
8	0.20101	1796.59007	303.697	97368.2	72.3413	5.50444	0.17808	825.367	39.7
9	0.25901	1802.66795	303.697	97412.2	72.4036	5.54217	0.17808	825.382	39.5
10	0.30202	1803.25307	303.697	97441.6	72.4451	5.56733	0.17808	825.392	39.4
11	0.34202	1797.64508	303.668	97453.3	72.471	5.60995	0.17808	825.355	39.2
12	0.40202	1797.65586	303.669	97444.4	72.4863	5.69716	0.17811	825.228	39.1
13	0.44403	1803.27475	303.67	97438.4	72.4966	5.75527	0.17813	825.143	39.0
14	0.50203	1802.64628	303.67	97410	72.4912	5.84264	0.17819	825.018	39.0
15	0.53803	1796.60083	303.671	97365	72.46	5.90117	0.17827	824.938	39.1
16	0.60303	1796.59007	303.671	97297.5	72.4131	5.98882	0.17839	824.817	39.4
17	0.64104	1802.59213	303.671	97252.6	72.3818	6.04716	0.17848	824.737	39.6
18	0.68104	1796.94519	303.672	97207.6	72.3506	6.10542	0.17856	824.656	39.7
19	0.74104	1797.5266	303.691	97145.1	72.332	6.18884	0.17866	824.534	40.0
20	0.78304	1803.53493	303.691	97109.9	72.3574	6.24061	0.17868	824.449	40.1
21	0.84405	1803.7518	303.69	97057.3	72.3955	6.31816	0.17873	824.322	40.3
22	0.88105	1797.93597	303.69	97022.1	72.4209	6.3698	0.17875	824.238	40.4

Figure 4-131. Sample Performance Data File.

Use of the three LabVIEW systems produces three files per data collection event. The first is the low-speed engine performance file, organized by column with descending rows with time. A sample is shown in Figure 4-131. This data file includes all sensors brought into the c-RIO, as well as some calculations, such as engine power and brake-specific fuel consumption. This type of data file can be used for transient and steady-state tests. For steady-state tests (the vast majority of tests so far), the average and standard deviation of each data column provide values that can be used for other calculations, such as brake-specific emissions.

The screenshot shows a Microsoft Excel spreadsheet titled 'M38'. The data is structured as follows:

- Header:**
 - Row 1: University of Kansas - Mechanical Engineering
 - Row 2: In-Cylinder Pressure System - 2012
 - Row 3: (empty)
 - Row 4: Net Indicated Work (kJ/cycle)
 - Row 5: 0.04718
 - Row 6: (empty)
 - Row 7: Gross Indicated Work (kJ/cycle)
 - Row 8: 0.06144
 - Row 9: (empty)
 - Row 10: Net Indicated Mean Effective Pressure (bar)
 - Row 11: 1.08292
 - Row 12: (empty)
 - Row 13: Gross Indicated Mean Effective Pressure (bar)
 - Row 14: 1.41034
 - Row 15: (empty)
- Cycle Data:**

	Angle (degrees ATDC)	Pressure (bar)	Volume (m ³)
18	-180	0.96275	4.57E-04
19	-179.5	0.95197	4.57E-04
20	-179	0.95401	4.57E-04
21	-178.5	0.95553	4.57E-04
22	-178	0.94902	4.57E-04
23	-177.5	0.95421	4.57E-04
24	-177	0.9535	4.57E-04
25	-176.5	0.94984	4.57E-04
26	176	0.94051	4.57E-04

Figure 4-132. Sample In-cylinder Pressure Data File.

In-cylinder data files already contain the average of sixty cycles, which is saved below the header and indicated performance parameters, as shown in the example file in Figure 4-132. This data file can be used for plotting for analysis (as in Chapter 1 through Chapter 3). This file can also be loaded to perform heat release analysis using the custom Matlab code created by Jonathan Mattson as part of his Master's degree [40, 103]. This process is also used in the previous chapters of this dissertation.

	A	B	C	D	E	F	G	H
1	University of Kansas - Mechanical Engineering							
2								
3	FTIR Emissions Measurement - 2012							
4								
5	6/12/2013 11:53							
6								
7	Elapsed Time	H2O (ppm)	CO2 (ppm)	CO (ppm)	NO (ppm)	NO2 (ppm)	NOx (ppm)	N2O (ppm)
8								
9	0:00:00	31796	18228	628.91	123.17	27.4	150.56	0.4
10	0:00:01	32391	18450	648.23	105.61	47.59	153.2	0.5
11	0:00:02	31832	17864	669.36	103.73	48.01	151.74	0.2
12	0:00:03	31817	18279	662.5	100.83	49.51	150.34	0.5
13	0:00:04	31697	17167	659.21	100.97	49.99	150.96	1.5
14	0:00:05	32231	17810	654.2	100.03	51.42	151.45	0.6
15	0:00:06	32390	17602	659.63	99.23	52.43	151.66	0.5
16	0:00:07	32105	17265	663.73	96.8	52.35	149.15	0.8
17	0:00:08	32389	18615	671.69	96.95	54.17	151.12	0.5
18	0:00:09	32479	17174	667.53	97.99	54.92	152.91	1.1
19	0:00:10	31990	18669	669.65	96.78	55.46	152.24	0.7
20	0:00:11	32272	18496	664.79	97.42	55.78	153.2	0.5
21	0:00:12	32143	19571	669.08	98.32	56.27	154.59	0.5
22	0:00:13	31868	17293	680.76	95.94	57.34	153.28	0.6
23	0:00:14	32098	17838	658.15	95.73	56.22	151.96	0.8
24	0:00:15	31951	17513	651.53	95.09	56.8	151.89	1.5
25	0:00:16	31717	17862	670.32	93.7	57.71	151.4	0.5
26	0:00:17	32329	18586	655.19	96.76	58.28	155.04	0.4
27	0:00:18	32143	17807	647.33	98.07	58.71	156.78	0.7

Figure 4-133. Sample Gaseous Emissions File.

An example of the output file from the SESAM data-saving LabVIEW program is shown in Figure 4-133. This file is formatted much like the performance data file, with headers (and units) indicated per column, descending with time.

	A	B	C	D	E	F	G
1	Meas. No.	Samples	Sample Line	FSN	Soot Conc. [mg/m ³]	Prtl. Level [%]	
2	1	1	Sample 1	0.01	0.1	-3.43	
3	2	1	Sample 1	0.01	0.1	-3.43	
4	3	1	Sample 1	0.04	0.46	-3.16	
5	4	1	Sample 1	0.04	0.49	-3.14	
6	5	1	Sample 1	0.01	1.53	-2.41	
7	6	1	Sample 1	0.01	1.53	-2.4	
8	7	1	Sample 1	0.04	5.91	0.4	
9	8	1	Sample 1	0.04	6.01	0.45	
10	9	1	Sample 1	0.02	48.28	16.34	
11	10	1	Sample 1	2.01	48.77	16.47	
12	11	1	Sample 1	2.08	51.47	17.15	
13	12	1	Sample 1	0.01	0.07	-3.45	
14	13	1	Sample 1	0.01	0.07	-3.45	
15	14	1	Sample 1	0.01	0.07	-3.45	
16	15	1	Sample 1	0.01	0.07	-3.45	
17	16	1	Sample 1	0.02	0.29	-3.29	
18	17	1	Sample 1	0.02	0.3	-3.28	
19	18	1	Sample 1	0.02	0.3	-3.28	
20	19	1	Sample 1	0.02	0.28	-3.29	
21	20	1	Sample 1	0.1	1.34	-2.54	
22	21	1	Sample 1	0.1	1.28	-2.58	
23	22	1	Sample 1	0.32	1.32	-2.55	

Figure 4-134. Sample PM Output File.

Currently, PM measurement takes place in a different fashion, with all PM measurements being saved in the same data file. Therefore, great care must go into keeping track of which samples correspond to which fuel/engine operation condition. An example of this file is shown in Figure 4-134. The column of interest in this file is the soot concentration, which yields the mg/m^3 value that can be converted to $\text{g}/\text{kW}\cdot\text{hr}$.

4.8.1 Calculation of Brake-Specific Performance and Emissions Parameters

During the early stages of research in this laboratory, all calculations for brake-specific engine performance were performed manually using Microsoft Excel. As the testing capability and amount of data increased, this rapidly became cumbersome and prone to typographic errors. Therefore, Chenaniah Langness was tasked with creating a Matlab post-processing code to automatically output the desired engine parameters. This program saves countless hours of post-processing work because of the large amounts of data now being collected. That being said, it is important to understand the underlying calculations that are taking place to yield metrics such as engine power, brake-specific fuel consumption, brake-specific emissions, and efficiencies, such as combustion, fuel conversion and thermal efficiency.

Engine power and brake-specific fuel consumption are calculated directly inside the LabVIEW code using (4-4) and (4-5).

$$P_{\text{engine}} = 2\pi \cdot N \cdot \tau \quad (4-4)$$

$$\text{bsfc} = \frac{\dot{m}_{\text{fuel}}}{P_{\text{engine}}} \quad (4-5)$$

where N is engine speed, τ is engine torque, and \dot{m}_{fuel} is fuel mass flow rate.

These calculations are performed inside the code to reduce the round-off error that occurs during manual calculation, as digits of precision are lost during saving to file.

Brake-specific emissions calculation requires the use of some assumptions. First, the mass flow rate of exhaust is assumed to be equal to the sum of the mass flow rate of the intake air and fuel injected due to no crankcase ventilation [106]:

$$\dot{m}_{exhaust} = \dot{m}_{air} + \dot{m}_{fuel} \quad (4-6)$$

where $\dot{m}_{exhaust}$ is exhaust mass flow rate and \dot{m}_{fuel} is fuel mass flow rate.

The emissions are based on a molar ratio, this must be converted to a mass ratio to calculate an emissions flow rate in g/s. This is accomplished by first determining the molar mass of the exhaust mixture:

$$\begin{aligned} \bar{M}_{exhaust} &= \sum x_j \cdot M_j = x_{H_2O} \cdot M_{H_2O} + x_{CO_2} \cdot M_{CO_2} + x_{O_2} \cdot M_{O_2} + x_{CO} \cdot M_{CO} + \dots \\ &\dots + x_{NO} \cdot M_{NO} + x_{NO_2} \cdot M_{NO_2} + x_{THC} \cdot M_{THC} + x_{H_2} \cdot M_{H_2} + x_{N_2} \cdot M_{N_2} \end{aligned} \quad (4-7)$$

where $\bar{M}_{exhaust}$ is the exhaust molar mass, x_i is the molar fraction of each constituent, and M_i is the molar mass of each constituent. Of note, the concentration of NO_x is not included because NO and NO_2 are used to form a total NO_x level. The concentrations of H_2 , N_2 , and argon are not directly measured. The amount of H_2 emitted is estimated by assuming that the $H_2:CO$ ratio is the same as the $H_2O:CO_2$ ratio via a general lean combustion reaction [56, 65]. Because argon is an inert gas and only a small concentration of the atmosphere, its value is lumped with N_2 . Conveniently, the measured species are denoted in a parts-per-million basis. Thus, it is assumed that the addition of molar concentrations of H_2 , N_2 , and argon round out to an even million moles of exhaust. The mass for THC is assumed to be 16 g/mol based on the C1-calibration of the FID. Using the exhaust molar mass, exhaust mass flow rate, and engine power, the brake-specific emissions are produced as follows:

$$bs_{emissions} = \frac{x_i \cdot M_j \cdot \dot{m}_{exhaust}}{\bar{M}_{exhaust} \cdot P_{engine}} \quad (4-8)$$

Brake-Specific PM emissions require a slightly different calculation due to the concentration basis of its measurement. This requires the density of the exhaust, which is calculated based on measured temperature, pressure and the ideal gas law:

$$\rho_{exhaust} = \frac{P_{exhaust}}{\left(\frac{\bar{R}}{M_{exhaust}}\right) \cdot T_{exhaust}} \quad (4-9)$$

where $\rho_{exhaust}$ is the exhaust density, \bar{R} is the universal gas constant, and $T_{exhaust}$ is the exhaust temperature. With this density, brake-specific PM emissions are calculated as:

$$bsPM = \frac{PM_{conc} \cdot \dot{m}_{exhaust}}{\rho_{exhaust} \cdot P_{engine}} \quad (4-10)$$

where PM_{conc} is the measured concentration of PM in the exhaust (g/m^3).

Volumetric efficiency, η_v , is a parameter used to determine the effectiveness of the air exchange process in the engine [106]:

$$\eta_v = \frac{\dot{m}_{air}}{2 \cdot \rho_{air} \cdot N \cdot V_d} \quad (4-11)$$

where \dot{m}_{air} is air mass flow rate, ρ_{air} is intake air density, and V_d is engine displacement volume.

Combustion efficiency indicates the effectiveness of the combustion process at removing energy from the fuel by considering the amount of chemical energy left in exhaust constituents, such as H₂, CO, HC, and PM [106]:

$$\eta_c = 1 - \frac{\sum \dot{m}_j \cdot Q_{lhv,j}}{\dot{m}_{fuel} \cdot Q_{lhv,fuel}} = 1 - \frac{\dot{m}_{CO} \cdot Q_{lhv,CO} + \dot{m}_{H_2} \cdot Q_{lhv,H_2} + \dot{m}_{HC} \cdot Q_{lhv,HC} + \dot{m}_{PM} \cdot Q_{lhv,PM}}{\dot{m}_{fuel} \cdot Q_{lhv,fuel}} \quad (4-12)$$

where \dot{m}_i is the mass flow rate of the exhaust constituent, $Q_{lhv,i}$ is the lower heating value of the exhaust constituent, and $Q_{lhv,fuel}$ is the lower heating value of the fuel. Of note, as HC and PM are a mixture of several species with unique energy contents, composite lower heating values for HC and PM are assumed to be 44.7 MJ/kg and 32.8 MJ/kg, respectively [12, 39, 65].

Fuel conversion efficiency indicates the efficiency of useful power exiting the engine compared to the amount of fuel energy added [106]:

$$\eta_f = \frac{P_{\text{engine}}}{\dot{m}_{\text{fuel}} \cdot Q_{\text{lhv,fuel}}} \quad (4-13)$$

Finally, thermal efficiency is used to characterize the effectiveness of the engine and combustion process when converting potential thermal energy (from fuel) into power. This takes into account both fuel conversion efficiency and combustion efficiency:

$$\eta_t = \frac{\eta_f}{\eta_c} \quad (4-14)$$

This concludes the primary calculations that are performed using the Matlab-based post-processing program. Due to the high amount of data taken using a variety of sensors, other methods of engine characterization are possible and should be used as appropriate to improve experimental analysis.

4.9 Conclusion

The University of Kansas is currently involved in research pertaining to sustainable fuel sources for the transportation sector. In particular, biodiesel and its byproducts are being investigated due to advantageous production and fuel properties. In order to perform this research, an engine laboratory is necessary as a means of characterizing fuel end-use performance and emissions behavior. A single-cylinder engine was chosen to serve this purpose. This engine is ideal for the need because of its simple, yet robust, design. It is easy for graduate students to modify and requires very small fuel batches when compared to larger multi-cylinder engines. Moreover, this engine is air-cooled which reduces the complexity of the system.

Since the installation of this engine, several modifications and system integrations have occurred. This includes an externally-cooled EGR system, in-cylinder pressure measurement, a turbocharger, an AC dynamometer for loading, modified intake and exhaust, emissions measurement,

and high-pressure common-rail fuel injection. Additionally, the generation of usable engine performance and emissions data required the creation of three LabVIEW programs to display readings, control engine systems, and record data. These physical and electronic systems are unique in that they are student-designed and constructed. However, this presents a particular issue for an academic research laboratory due to high personnel turnover. As a result, this chapter was written to provide a high-level description of each system to serve as a primer and reference for future students using this laboratory. This includes a description of the engine and its subsystems, as well as, the process for engine replacement, the dynamometer and its control system, the data acquisition system, and the emissions equipment. In closing, years of effort have been devoted to this system, particularly on the part of this author. It is expected that future users of this laboratory will treat this system with the same sense of pride and ownership as those who came before them. It is a unique engine that provides a wealth of knowledge and research opportunities to those who use it.

Chapter 5: Initial Design and Construction Phases of a Multi-Cylinder, Compression-Ignition Engine Laboratory

With continuing biofuel research, including the ongoing efforts at the University of Kansas (KU), a method of characterizing fuel performance for end-use is important. In other words, the biofuels produced for research should eventually be tested in a production engine as a means of determining how well these fuels work in a real-world situation [52, 66, 75]. This is best accomplished using a modern production engine, such as the one being installed in the Measurement, Materials and Sustainable Environment Center (M2SEC) at KU. This approach ensures that biofuel research findings are applicable to large-scale use by consumers. The engine selected for this purpose is a Duramax eight-cylinder CI engine.

Table 5-1. Duramax Specifications [111].

Manufacturer	DMAX
Model	LBZ
Year Equivalent	2006-2007
No. of Cylinders	8 (90-degree V configuration)
Displacement	6.6 Liters
Bore	103.12 mm
Stroke	99.1 mm
Compression Ratio	16.8:1
Injection	Bosch CP3 Common Rail (179.3 MPa)
Valvetrain	Over-Head Valve (Four Valves per Cylinder)
Inertia (including flywheel)	1.055316 kg·m ²
Speed Range	650-3200 RPM
Maximum Torque	880 N·m (@1600 RPM)
Peak Horsepower	268.5 kW (@3200 RPM)
Cooling	Liquid
Aspiration	Garrett Variable-Geometry Turbocharger and Intercooler
Block	Cast Iron
Oil Capacity	10 quarts (w/ Filter)
Cylinder Heads	Aluminum
Aftertreatment	Diesel Oxidation Catalyst and Diesel Particulate Filter

The specifications of the Duramax are shown in Table 5-1. This engine was used to power the 2006 and 2007 model year Chevrolet Silverado HD, GMC Sierra HD, Chevrolet Kodiak, and GMC Topkick [111]. Of particular value is the common-rail fuel system, which, when coupled to an advanced engine

control unit (ECU), will allow researchers to perform advanced injection strategies including: multiple injections per combustion event, low-temperature combustion, and gaseous-assisted combustion.

This engine laboratory fits well in the hierarchy of biofuel and engine test cell capabilities at the University of Kansas. It is intended to complement and enhance the research currently being performed using the single-cylinder CI Yanmar engine. The single-cylinder test cell possesses many advantages for initial research. In particular, it has a simple, rugged construction that allows student researchers, many with little to no engine experience, to learn how to perform experiments. Furthermore, the Yanmar engine is air-cooled, meaning that the logistical challenges of liquid cooling are removed, freeing up space and resources for other systems, such as an exhaust energy recovery system. In addition, initial batches of biodiesel are produced in a research reactor at an amount less than five gallons. This quantity of fuel is not practical for large-scale research, but is appropriate for the Yanmar, which can operate for several hours on five gallons of biodiesel [16, 65]. As a particular biodiesel reaches advanced stages of research through single-cylinder research, larger batches (e.g., fifty gallons) can be produced for use in the multi-cylinder. Finally, the single-cylinder laboratory is intended to act as a training tool for students. The systems in the single-cylinder laboratory, including the data acquisition system (low-speed and in-cylinder), emissions equipment, and dynamometer, will operate in the same fashion as the systems in the new multi-cylinder laboratory. Therefore, as students prove their knowledge and testing experience, they can transition to the multi-cylinder engine for more advanced research. Of additional interest, electricity generated through engine loading, as well as excess heat from the engine cooling system, are tied into the building electrical and heated/chilled beam systems. Engine exhaust is also plumbed to a laboratory on the second floor of M2SEC for analysis and experimentation. This integration provides the opportunity to study waste heat recovery, integration of electrical generation into the grid, and catalyst aftertreatment studies.

5.1 Test Cell Systems

In addition to the engine, many separate subsystems are necessary to control engine load, room conditions, intake and exhaust handling, engine cooling, and data acquisition. Each of these systems must work in unison to ensure safe and repeatable operation of the test cell.

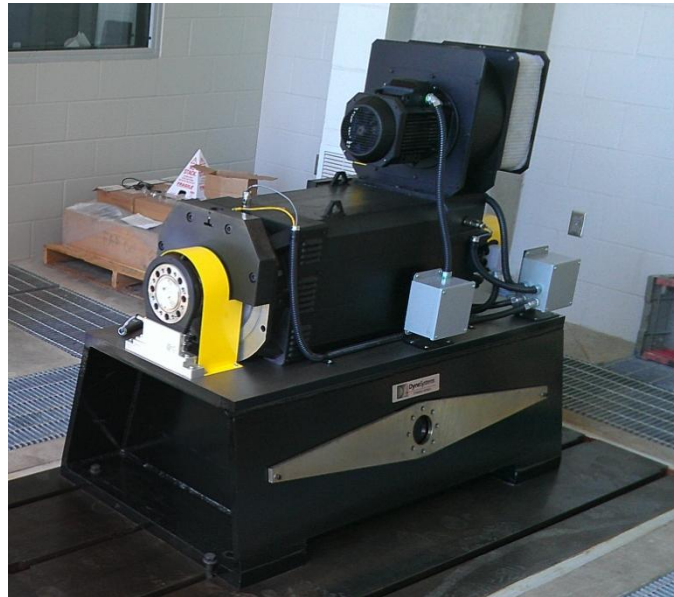


Figure 5-1. Dyne Systems Dynamometer Installed in Multi-Cylinder Test Cell.

A Dyne Systems, Incorporated regenerative alternating-current (AC) dynamometer is used to simulate engine loading, shown installed in Figure 5-1. This AC dynamometer has a low inertia, so that its speed can be changed rapidly during transient testing. In addition, this AC dynamometer can provide power to spin the engine, which is particularly useful for fuel injection and frictional studies.



Figure 5-2. Inter-Loc V Dynamometer Controller Installation.

The dynamometer is a Dymond Series 351-hp model controlled via a Dyne Systems Inter-Loc V dynamometer controller, shown in Figure 5-2. Conveniently, this is the same model of controller currently used in the single-cylinder CI test cell in Learned Hall. This controller permits the dynamometer to be operated in either ‘torque’ or ‘speed’ mode. Torque mode places a given amount of resistive load on the engine and is not dependent on speed. Thus, the actual engine speed can increase or decrease based on fuel input to the engine. Speed mode is preferred for engine research, particularly injection studies, as this mode permits the dynamometer to either assist or load the engine as necessary to maintain a desired speed setpoint. This ensures that the engine does not over-speed due to the engine generating more torque than the dynamometer.

Table 5-2. Dyne Systems Dynamometer Specifications.

Manufacturer	Dyne Systems, Incorporated
Model	Dymond Series 351
Type	3-Phase Alternating Current
Maximum Speed	5600 RPM
Maximum Continuous Power	261.7 kW (2000-3600 RPM)
Maximum Continuous Torque	1249 N-m (0-2000 RPM)
Over-rating	140% for 60 seconds
Torque Measurement	HBM Inline Torque Flange (2kN-m)
Cooling	Air-Cooled
Control	Inter-Loc V

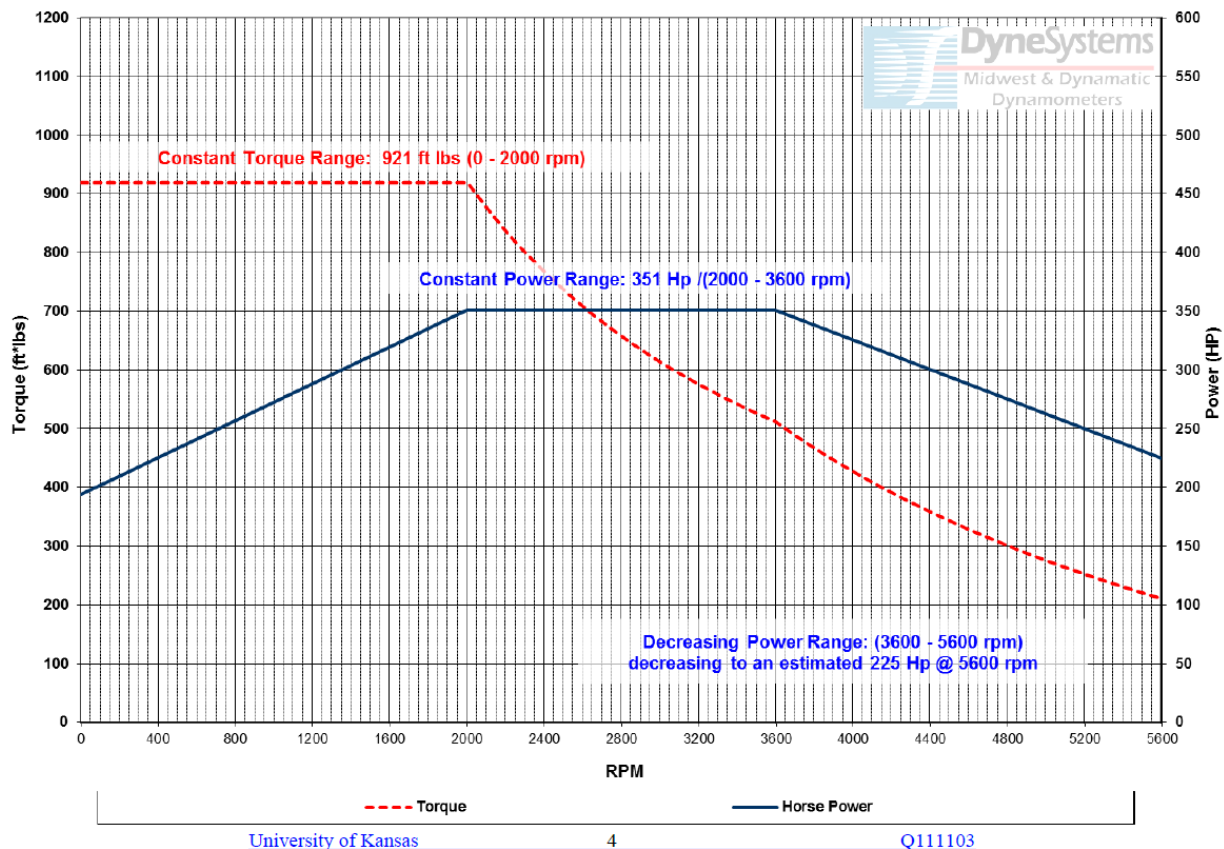


Figure 5-3. Torque and Power Rating vs. Speed of 351-hp Dyne Systems Dynamometer.

The specifications of the dynamometer are shown in Table 5-2. The torque and power ratings of the dynamometer change with speed (shown in Figure 5-3), which must be considered when planning tests at various speeds.

5.1.1 Climate Control and Building Integration

A critical aspect to engine testing repeatability is the method in which the air, coolant, and exhaust are modulated. These systems are controlled by a stand-alone National Instruments compact-Reprogrammable Input/Output (c-RIO) controller. This controller was programmed by Bachelor Controls and allows the user to change setpoints for engine intake air pressure, temperature, and relative humidity, test cell pressure and temperature, along with water jacket and intercooler temperatures.

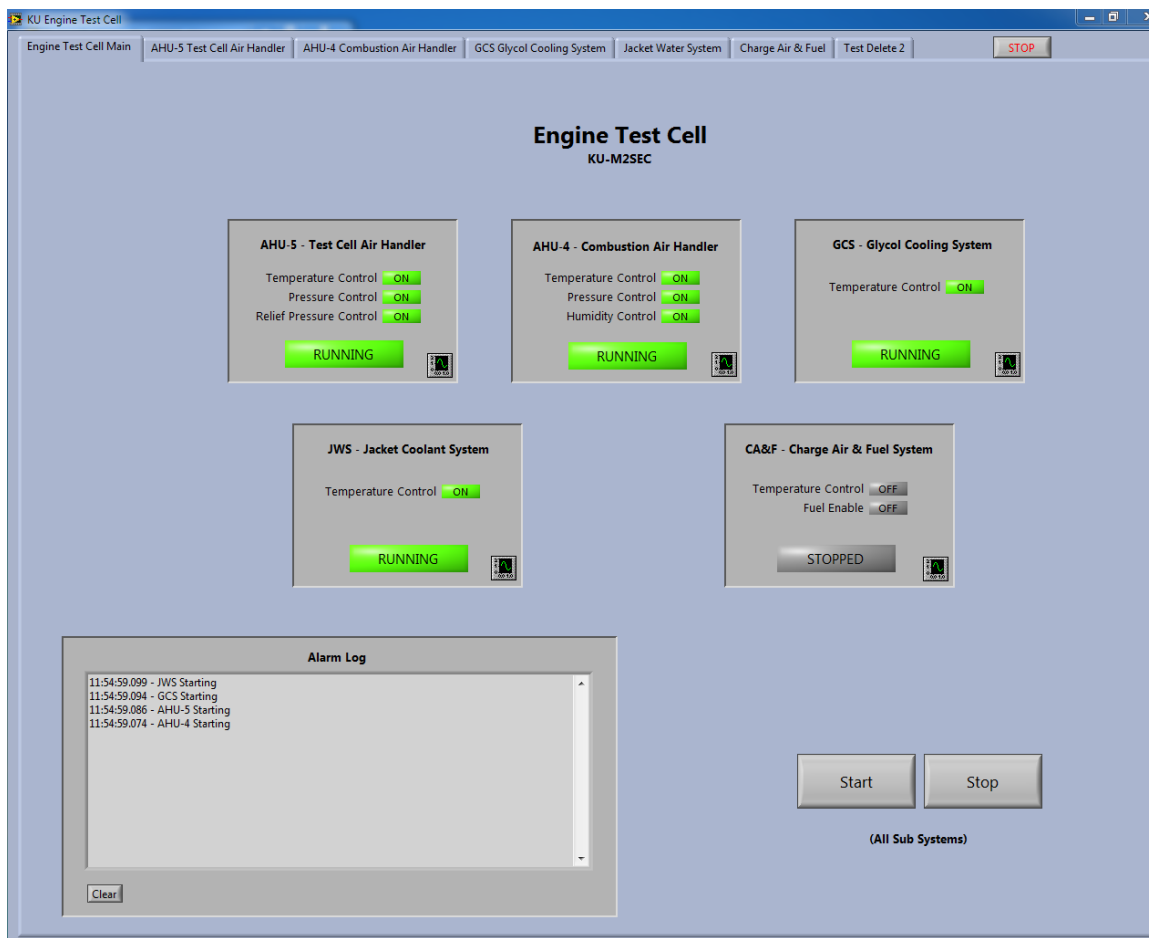


Figure 5-4. Test Cell Auxiliary Systems Main Operating Window Reproduced from Bachelor Controls Manual.

This system is controlled using a dedicated computer, to be located in the test cell control room. The main operating window is shown in Figure 5-4. To start the auxiliary systems startup sequence, the user clicks the 'Start' button. Direct correspondence with the c-RIO programmer indicates that startup

requires approximately ten minutes. Pressing ‘Stop’ initiates the shutdown procedure. A complete listing of controls and functions are available through the user manual provided by Bachelor Controls.

Engine intake air conditions must remain as consistent as possible between tests to ensure that changes in the results are a function of different engine operating parameters or fuel and are not a result of different intake pressure, temperature, or relative humidity [112]. Changes in pressure and temperature alter the intake and compression process, which will affect later stages of the engine cycle [1]. Water vapor in the air acts as a heat sink, thus more vapor present can act to delay combustion phasing [1]. This proved to be problematic in past testing with the Yanmar single cylinder engine due to the sensitivity of in-cylinder measurement equipment [12].

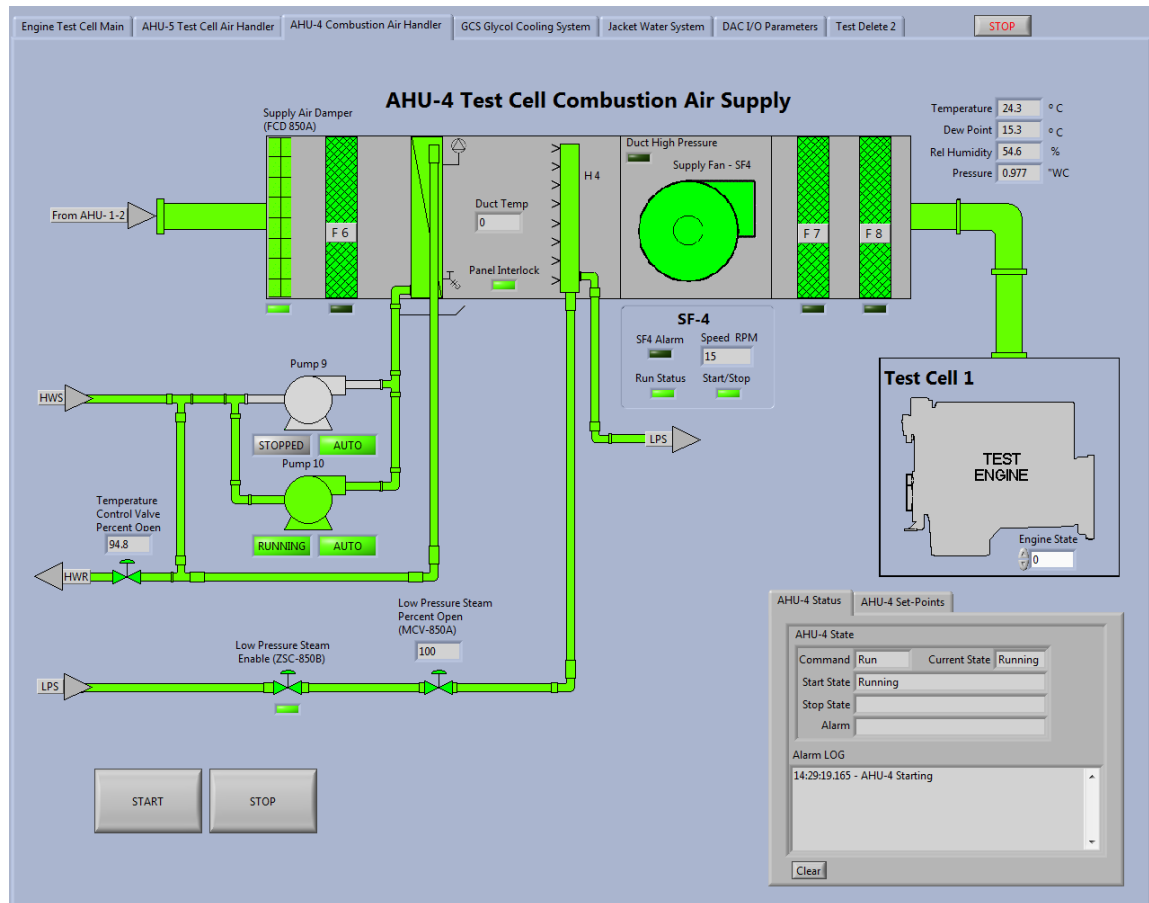


Figure 5-5. Engine Combustion Air Handling Diagram from Bachelor Controls Manual.

To circumvent this issue in the multi-cylinder test cell, a combustion air handler is located in the mechanical rooms above the engine test cell, a diagram of which is shown in Figure 5-5. In addition to fans and dampers which control pressure, this system uses heating elements and building steam to control temperature and humidity based on desired setpoints.

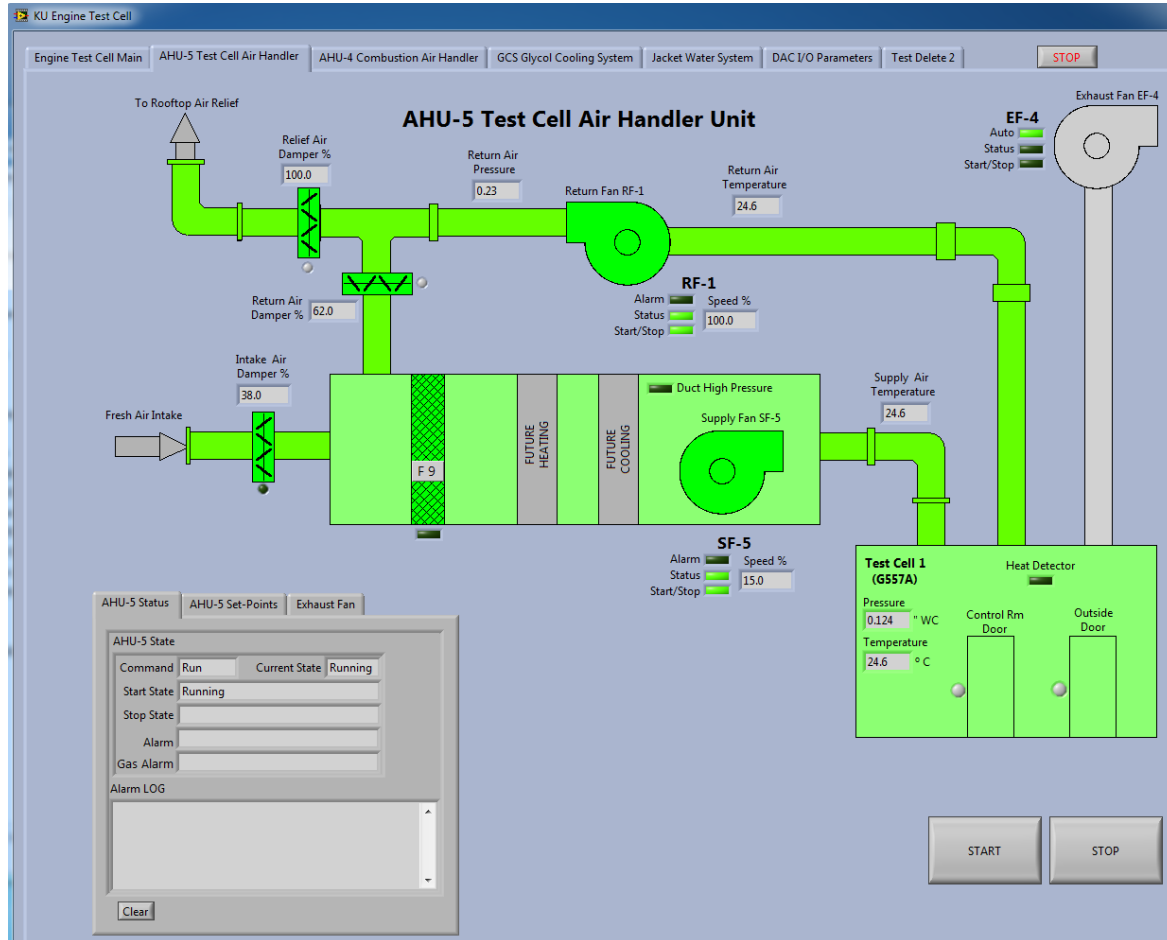


Figure 5-6. Test Cell Air Handler Diagram from Bachelor Controls Manual.

A similar system is utilized to control room conditions, particularly pressure and temperature, which are important to maintain due to their effects on engine and coolant heat transfer effects. This system is depicted in Figure 5-6. A slight negative pressure is maintained to keep any exhaust leaks from entering the test cell control room or adjacent corridor. Temperature is increased or decreased based on room and outdoor conditions. Ducted fans and a set of dampers either recirculate room air or draw outside air to change temperature. For example, if the ambient conditions are cooler than the test cell

setpoint, more outside air is brought in to regulate room temperature. However, if the test cell is below desired temperature, room air is recirculated to allow the engine to warm up the room.

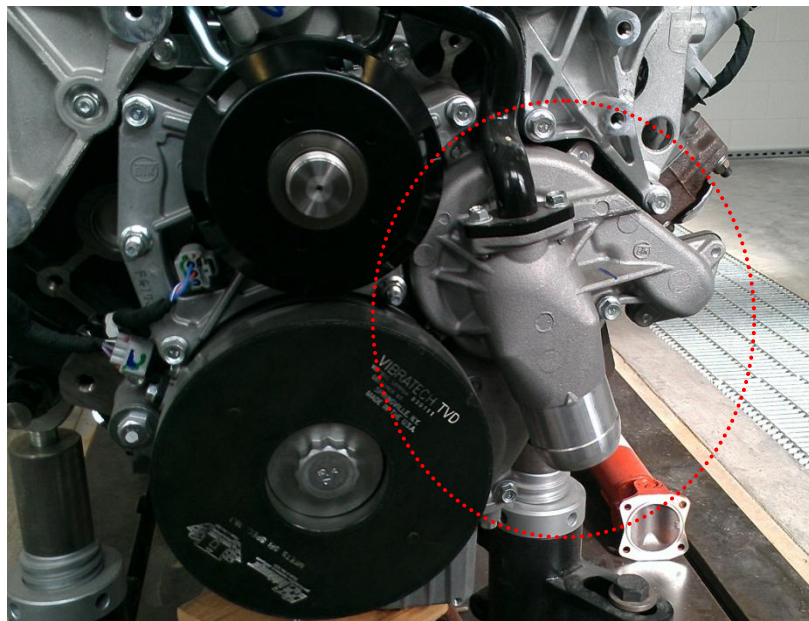


Figure 5-7. Duramax Coolant Pump.

Engine coolant temperature is regulated using a series of glycol coolant loops and heat exchangers that are located in both the engine test cell and the mechanical room upstairs. In the test cell, engine coolant is circulated in the jacket water coolant loop using the water pump installed on the Duramax engine (Figure 5-7). This pump moves coolant back through the heat exchanger.

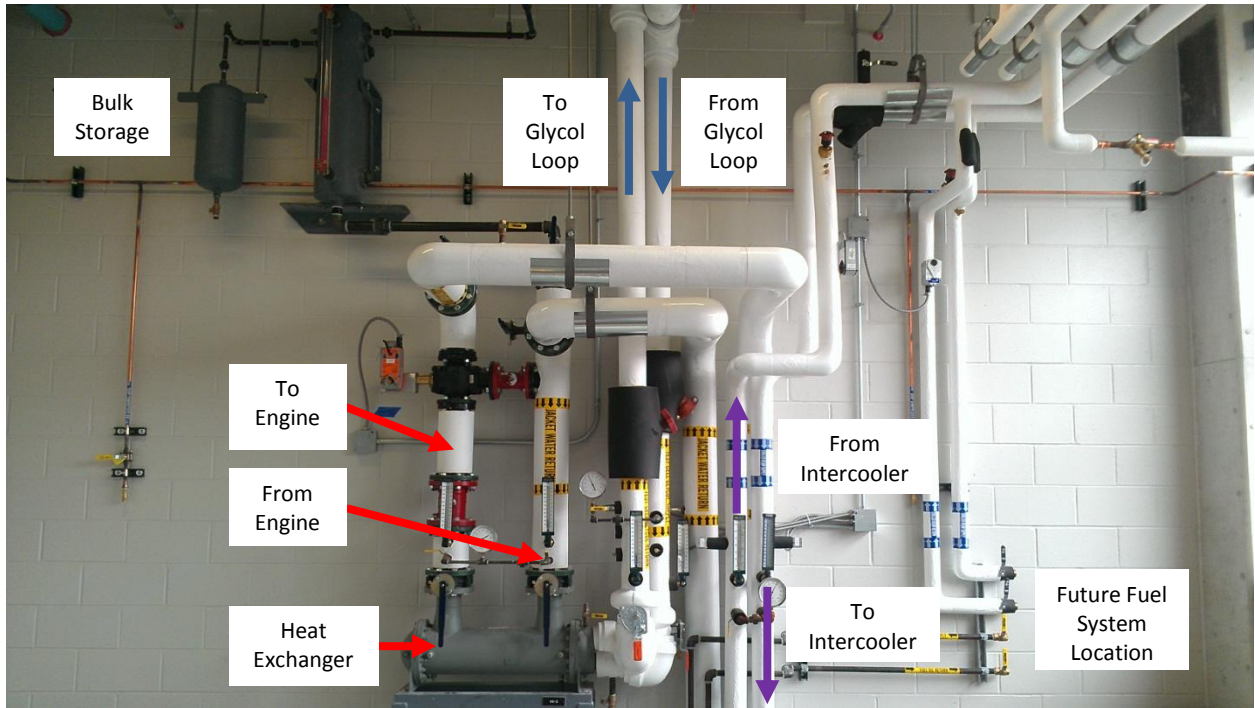


Figure 5-8. Test Cell Glycol System for Engine Jacket Water and Intercooler Loops.

Excess coolant, used to cool EGR system is pumped into the bulk storage coolant reservoir to re-enter the main jacket water loop. The piping of the test cell, including the jacket water to glycol cooling loop heat exchanger, is shown in Figure 5-8. This heat exchanger removes heat from the jacket water system to be either transferred to the building glycol system on the second floor (via another heat exchanger) or removed via a rooftop radiator. This equipment was installed by P1 Group of Lawrence, Kansas.

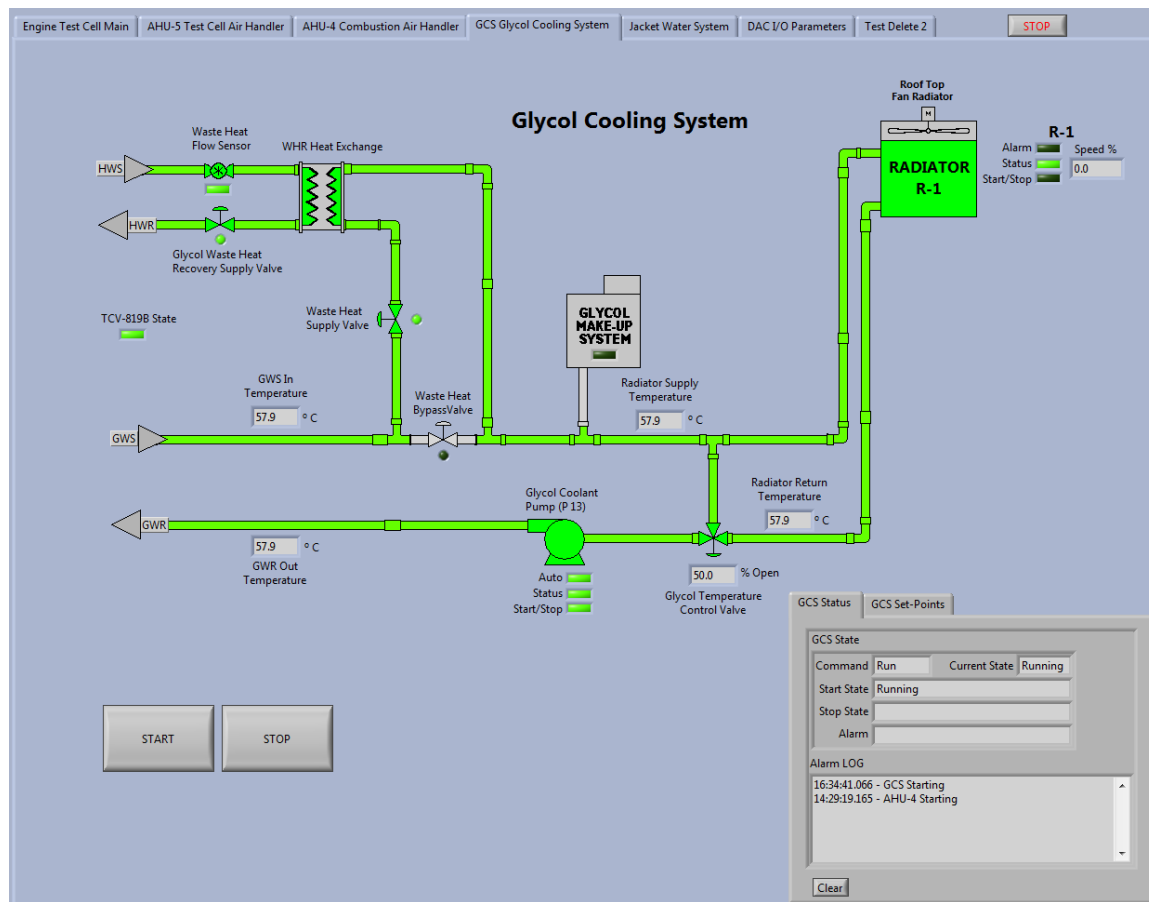


Figure 5-9. Test Cell Glycol Cooling System from Bachelor Controls Manual.

The diagram of the glycol cooling system, as indicated on the test cell c-RIO, is shown in Figure 5-9. This diagram indicates the glycol water supply (GWS) which is either sent through the waste heat recovery heat exchanger or the rooftop radiator. Cooled glycol returns downstairs via the glycol water return (GWR).

Intercooling is the process of cooling engine intake air following compression in the turbocharger. This practice is done as a means of improving engine volumetric efficiency [1]. As cooler air is more dense, lowering the temperature of the intake air following compression (and warming up) from the turbocharger improves the efficiency of the intake process [1].

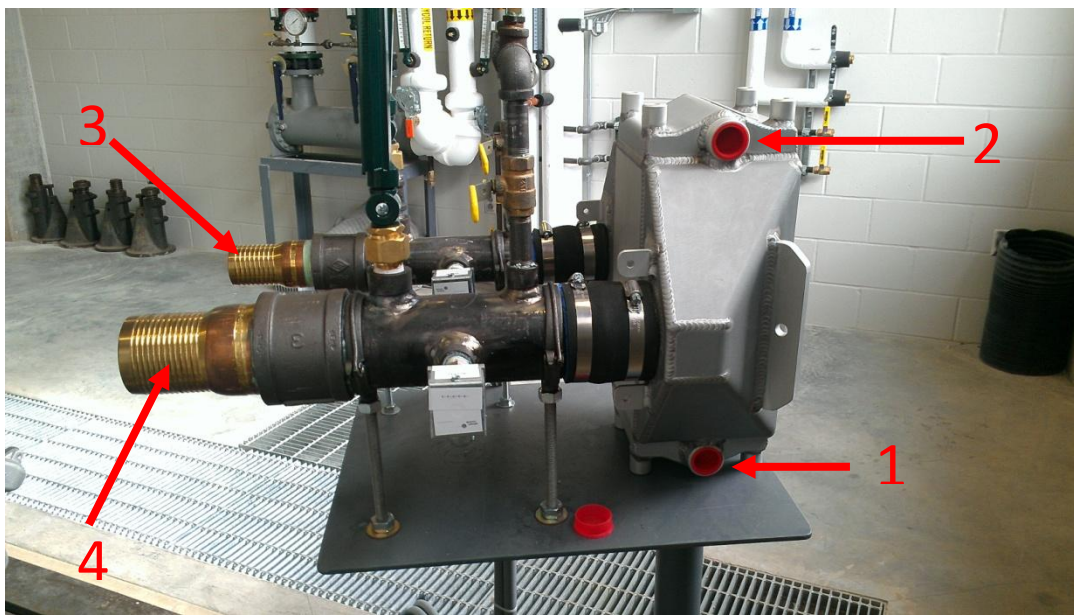


Figure 5-10. Engine Intercooler. Intercooler Supply (1), Intercooler Return (2), from Turbocharger (3), to Intake (4).

Much like the jacket water system, the intercooler uses a glycol loop that exchanges heat with the main glycol-cooling loop (Figure 5-8). The engine intercooler is shown in Figure 5-10. Through modulation of glycol flow rate, it will be possible to regulate the intake temperature based on test and repeatability requirements.

5.1.2 Safety Systems

With equipment this powerful and high-voltage circuits in place, safety is a primary concern. There are currently software emergency shutdown conditions programmed into the test cell air handling and glycol systems that will initiate a shutdown procedure.



Figure 5-11. Gas Sensors and Alarm in Test Cell Control Room.

One such safety criteria is the detection of dangerous levels of explosive gas, which trips a sequence to evacuate the room by drawing in fresh outside air. These sensors are shown in Figure 5-11.



Figure 5-12. Emergency Stop Button Near Control Room Door.



Figure 5-13. Emergency-Stop Button, Fire Alarm, Fire Extinguisher Near Test Cell Exit Door.

In the event of a manual emergency stop, there are red emergency stop buttons located throughout the test cell (Figure 5-12 and Figure 5-13). These mushroom buttons initiate the software shutdown procedure in the air handling system and direct the dynamometer controller to perform a hard shutdown as a means of stopping the engine. Once the ECU is in place, tripping of these buttons will also turn off power to the ECU, which will also stop the engine.

5.2 Installation of the Duramax Engine

Vibrational dampening and mechanically sturdy mounting of the engine are a critical consideration when installing an engine [112]. For this reason, a steel tee-slot base was special ordered and installed in the concrete floor of the engine test cell. This base is isolated from the concrete floor by grout layers in order to dampen vibration from reaching the rest of the building. Additionally, the slots,

which run the length of the skid, provide ample flexibility in mounting location but remain strong enough to hold down an engine or dynamometer. This pad was installed during building construction and left untreated for several months.



Figure 5-14. Engine Test Cell Pad Prior to Treatment.

As a result, a layer of rust formed on the surface as shown in Figure 5-14, requiring removal using wire-wheels and wire brushed before treatment by mechanical engineering graduate students. After some deliberation and contacting of various epoxy and paint suppliers, it was decided that tool-blackening treatment would be used to seal the pad from further rust. This method was chosen over paint and epoxy for a couple of reasons. First, poly-urethane paint, such as what is used in the single-cylinder test cell and the mechanical engineering machine shop, is prone to scratching and chipping from heavy objects. Epoxy would have taken much longer to cure, and adds a layer of thickness to the machined surface.

The method of tool blackening used on the pad is a three-part process using chemicals produced by Precision Brand. The process of treating the pad took two days due to the size of the pad and the dynamometer occupying half of the space.



Figure 5-15. First Half of Pad Treatment, Following Cleaning and Degreasing.

Following the removal of rust, the first step was to apply a cleaning and degreasing chemical, followed by a wash with water. This process is completed in Figure 5-15. Following treatment with the degreaser, the tool blackening chemical was applied using foam brushes. The surface of the pad turned black within a couple of seconds from rapid oxidization. Per the instructions, water was used to rinse the surface after one minute of set time. The area was left to dry overnight.

The next day, a layer of rust had formed on the surface as anticipated based on product instructions. Again, wire brushing of the pad removed the rust layer, requiring much less effort than removal of the original rust.



Figure 5-16. Drying of Pad After Application of Blackening Fluid (Oxidizer).

The sanding process is shown in Figure 5-16 mid-way through completion.



Figure 5-17. First Half of Pad Treated (Left). Right Side Untreated.

Finally, the third step in the process was to coat the treated surface with an oil-based spray. This film acts to seal the surface from water. Excess oil was wiped off, thus completing the treatment process. Figure 5-17 shows the first half of the pad following completion, with the second half still rusted prior to treatment.



Figure 5-18. Engine Pad Following Blackening Treatment.

In the second treatment phase, the dynamometer was moved to its permanent location using two heavy-duty pallet jacks and large pry bars. It was decided that this effort would have already damaged a paint coating and required repainting. Following a similar process, the second half of the pad was completed, as shown in Figure 5-18. Maintenance of the treated surface is minimal. In the event of a deep scratch that exposes untreated metal; retreat the area with the same chemicals used for blackening.

5.2.1 Engine Mounts

Mounting of the engine presents a unique challenge due to the combination of non-symmetric, complex engine geometry and vibrational dampening requirements. Through correspondence with engineers at Dyne Systems, Incorporated, it was decided that the best method would be to fabricate parts to adapt from stock engine mounts typically used to connect the Duramax engine to the frame of a production vehicle.



Figure 5-19. Driver Side of Duramax Engine Block Showing Mounting Holes.



Figure 5-20. Passenger Side of Duramax Engine Block Showing Mounting Holes.

The mounting holes for the Duramax are shown in Figure 5-19 and Figure 5-20. The engine mounts, purchased from a local Chevrolet dealership, are intended for a 2007 Silverado HD pickup. Custom adapters were made to adapt from these mounts to the 'elephant feet' bases that attach to the tee-slot pad in the test cell. These adapters are made from steel stock, bored and tapped to adapt from the elephant feet to heavy-duty steel rod ends. These rod ends allow the engine height and tilt to be

adjusted and are rated to 48,617 kg of static radial load or approximately 150 times the amount of force generated by the engine at this location.



Figure 5-21. Passenger-Side Elephant Foot with Engine Mount Adapter.

The rod end and steel adapter are shown installed on the passenger-side elephant foot in Figure 5-21. Final connection between the rod end and factor engine mount is accomplished using a solid steel rod, machined and tapped to bolt to the engine mounts. Fore and aft motion is arrested using locking shaft collars.

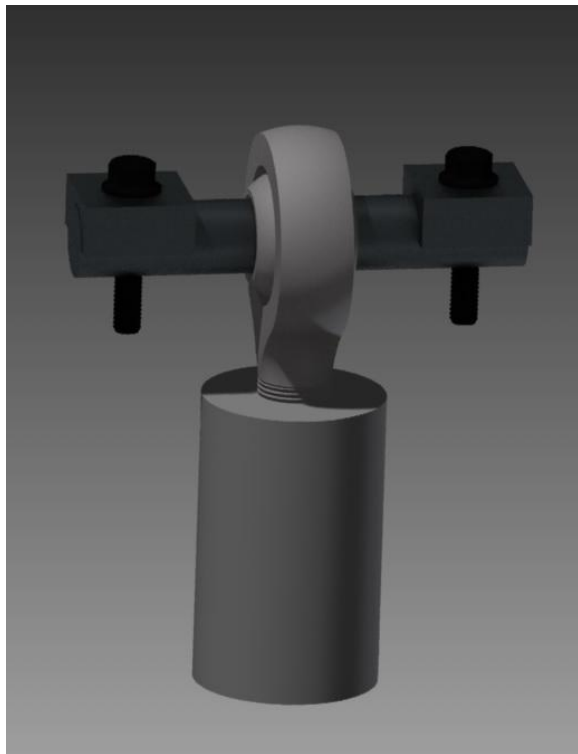


Figure 5-22. AutoDesk Design of Mount Adapter.



Figure 5-23. Installed Mount Adapter.

The driver and passenger-side mounting adapters are interchangeable, as constructed by the KU mechanical engineering machine shop per the assembly shown in Figure 5-22. The assembled mounts are shown installed on the engine in Figure 5-23. Currently, the rear engine mounting adapter is still in the design phase, but will include similar rubber components to dampen engine vibration. A possible candidate is the flexible transmission mount used in stock Silverado applications.

5.2.2 Installation of Torque Dampening Coupler

Designing a custom driveline to connect the single-cylinder Yanmar to the dynamometer presented a unique challenge because of large torque spikes. From a torque standpoint, the output power of the Duramax should be much smoother as an internal balance between cylinders exists. Specifically, as one cylinder is expanding due to combustion, another is compression air and requiring opposing torque. Nevertheless, the amount of torque involved in this application is approximately 45

times higher than that of the Yanmar, so collaboration with engineers at Dyne Systems occurred to ensure proper driveline design and dampening considerations.

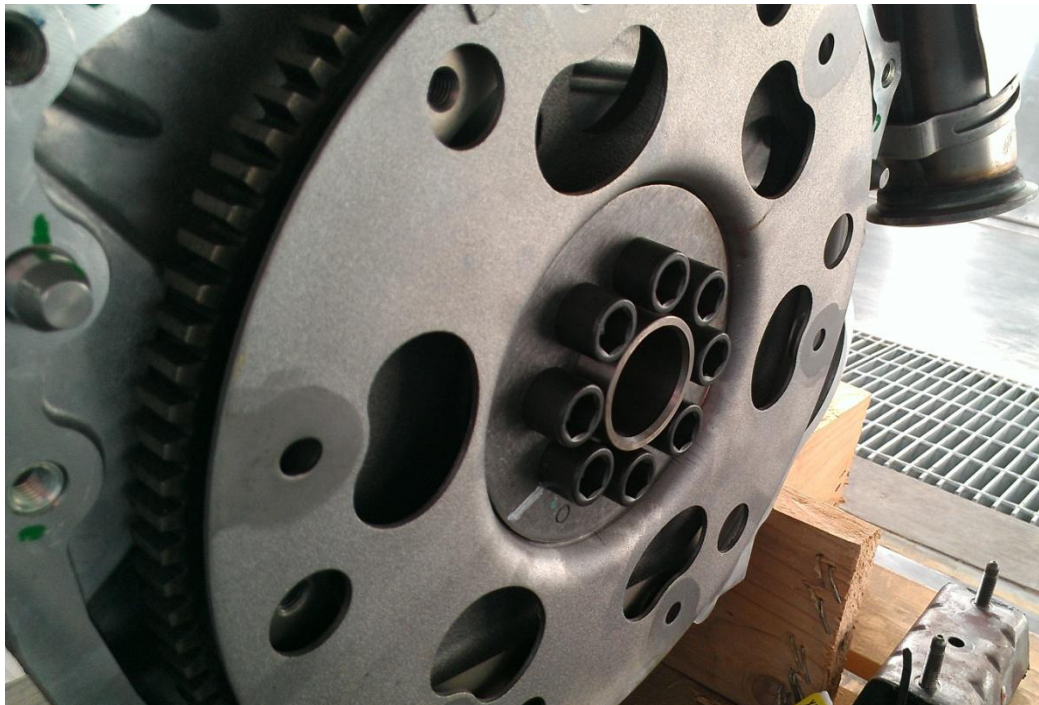


Figure 5-24. Duramax Flywheel with Transmission Flex Plate.

This culminated in the design of a torque-dampening coupler to join the Duramax flywheel to a universal-joint driveshaft which, in-turn, connects to the dynamometer via a custom adapter plate. A final decision had to be made regarding the inclusion or removal of the flywheel flex plate (Figure 5-24) used to connect the engine to the transmission. Per discussions with contacts at Gale Banks Engineering, Incorporated, it was determined that this component be removed to eliminate the degree of freedom in this component. Subsequent design considerations with Dyne Systems, Incorporated reflected this decision.



Figure 5-25. Flywheel (bottom), Flex Plate (middle), Spacer (top).

The flywheel flex plate was cut off following flywheel removal from the Duramax (the center section of the flex plate was kept). The bolts used to attach the flywheel to the engine are one-time-use as they are torque-to-yield upon installation. Subsequent use of these bolts would cause the flywheel to come loose. The flywheel, flex plate, and bolt spacer are shown in Figure 5-25.

The flywheel was reattached following the removal of the flex plate. The spacer and center of the flex plate are still necessary to ensure proper bolt thread engagement in the output shaft of the

Duramax. Documentation for the flywheel installation process was provided by the local Chevrolet dealership. First, the flywheel is fastened using new bolts, pre-lubricated with molybdenum disulfide coating.

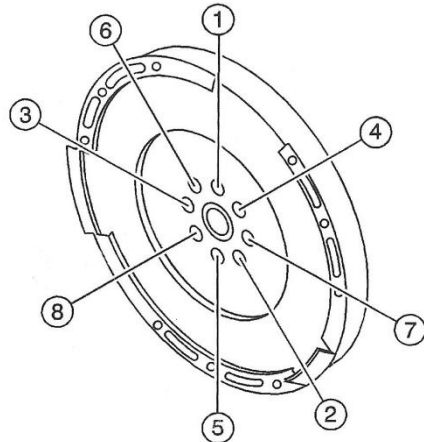


Figure 5-26. Duramax Flywheel Bolt-Tightening Pattern.

The bolts are then tightened in the sequence shown in Figure 5-26. The tightening process requires the use of a torque wrench to first tighten the bolts to 79 N·m of torque. Then, a second pass is made requiring all bolts to be tightened by 60 degrees. A final pass through the pattern requires the bolts to be tightened 60 degrees more.

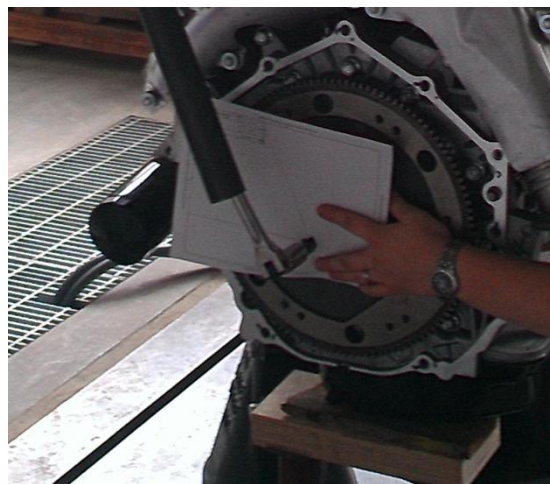


Figure 5-27. Bolt Angular Tightening Guide.

Measurement of turn angle was accomplished by printing out a reference guide using Autodesk Inventor and cutting a bolt hole through the paper (Figure 5-27).



Figure 5-28. Duramax Flywheel Re-Installed.

Completed installation is shown in Figure 5-28. The process required three people. One held the reference guide and prevented the engine from turning (using a wrench leveraged against the flywheel). Another tightened the bolts while a third monitored the angle of the wrench from a direct vantage point during tightening.

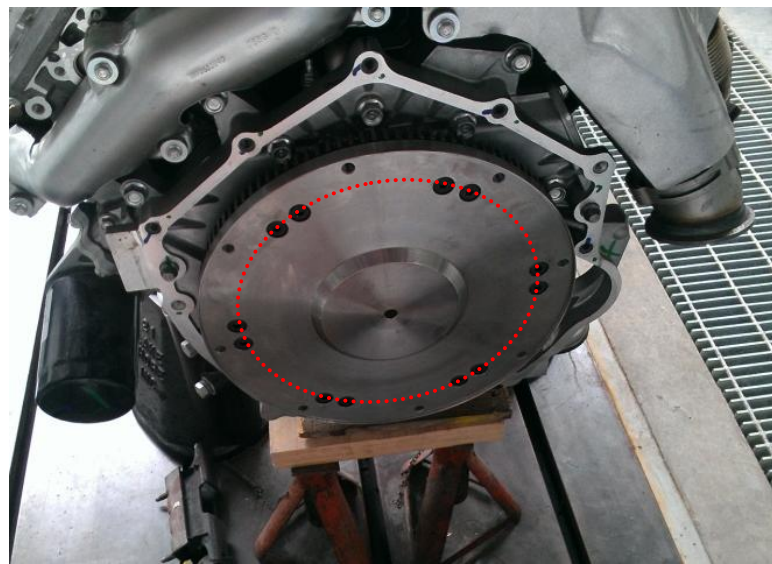


Figure 5-29. Coupling-Flywheel Adapter.

The installation of the Arcusaflex coupling, shown installed in Figure 5-29, required first installing the adapter plate; custom machined to bolt directly to the flywheel. Instructions specify to use grade 8.8, M10 bolts (supplied), tightened to 50 N-m. Tightening sequence was not specified for the coupler, so a star pattern was used with the first pass tightened the bolts to half of specified torque (25 N-m).

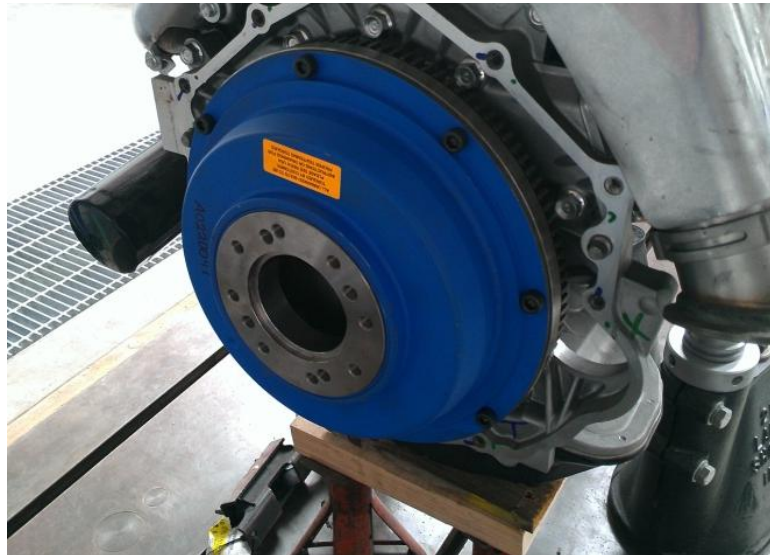


Figure 5-30. Torque-Dampening Coupler Installed.

Next, the actual torque dampening coupler is installed using supplied grade 8.8, M10 bolts. These were also tightened to 50 N-m using a similar tightening method to that of the flywheel adapter. The installed coupler is shown in Figure 5-30.



Figure 5-31. Universal-Joint Drive Shaft to Connect Engine and Dynamometer.

Following completion of the rear-end engine supports, the engine will be connected to the dynamometer in preparation for motoring using the driveshaft selected by Dyne Systems based on expected engine performance, shown in Figure 5-31.

5.2.3 Rear Engine Mount and Scatter Shield

With the torque dampening coupler installed, a scatter shield was designed to fulfill multiple purposes. First, the scatter shield is primarily intended to protect equipment and lab personnel in the event of a catastrophic driveshaft failure by keeping all components contained inside this enclosure. A secondary purpose of this shield is to provide support for the outboard end of the engine using the two remaining elephant feet.

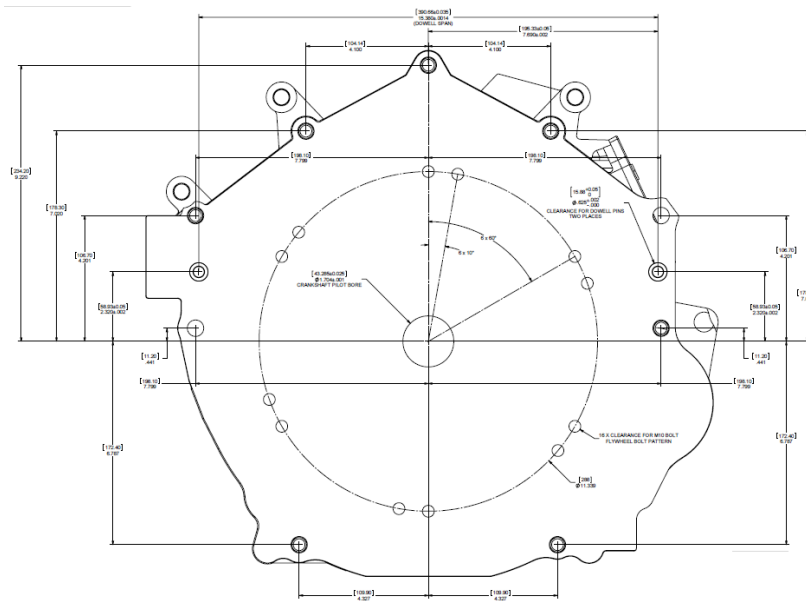


Figure 5-32. Duramax Transmission Interface, Provided by Gale Banks Engineering, Incorporated.

This shield uses the bolt pattern typically used by the transmission bell housing. Gale Banks Engineering, Incorporated provided dimensioned drawings of this interface, shown in Figure 5-32.

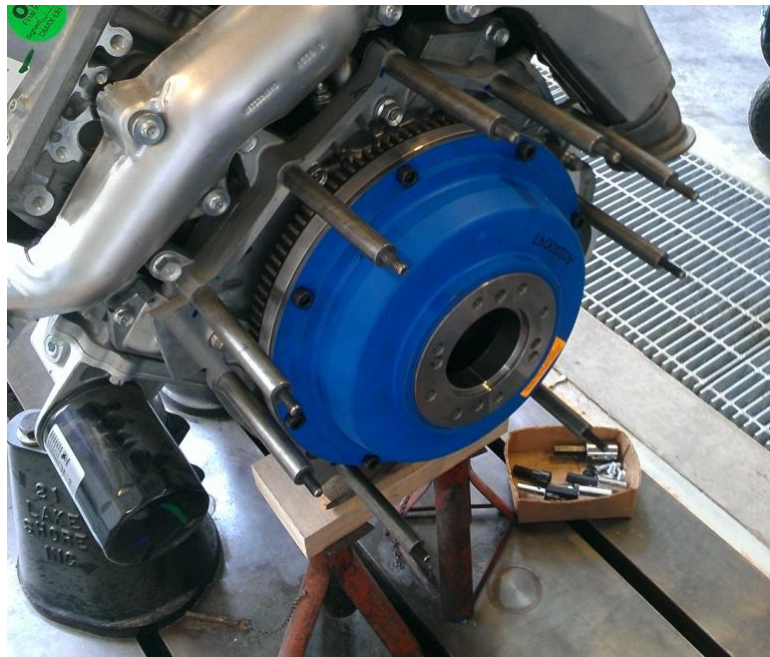


Figure 5-33. Scatter Shield Studs and Structural Tubes.

The scatter shield is held in place by nine threaded studs (3/8"-16 thread). The studs are inserted into steel tubes, as shown in Figure 5-33.

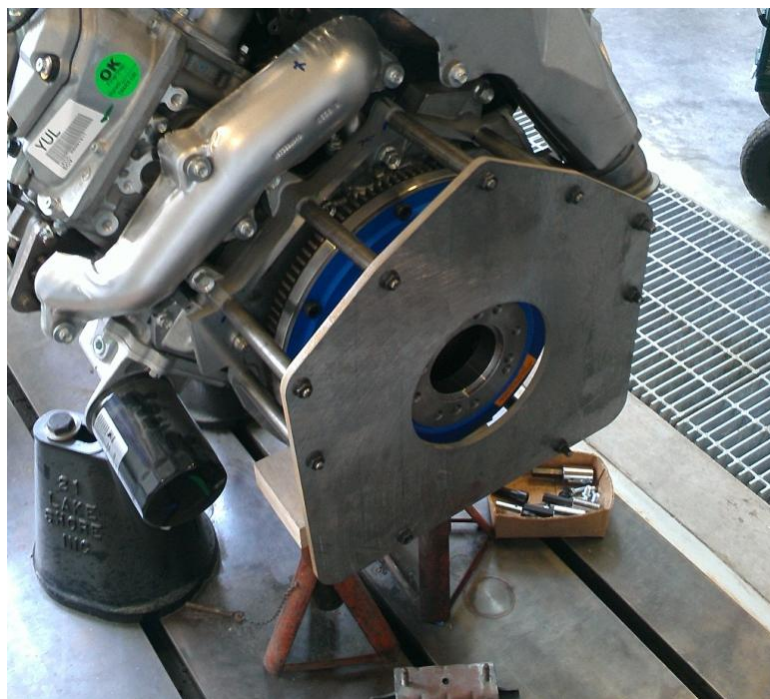


Figure 5-34. Scatter Shield Flange Installed on Duramax. Used as Guide for Outer Structure Construction.

The bolt-pattern from the Duramax transmission interface was used to design the cover flange for the scatter shield, shown in Figure 5-34. This shield is held in place on the end of the studs by 3/8"-16 vibration-resistant flange nuts that are additionally filled with loctite to resist loosening from vibration. The flange was water-jet cut by C & R Manufacturing of Kansas City, KS. To facilitate the construction of the outer structure of the scatter shield, the flange was installed on the studs. Then, initial outer pieces were cut using this assembly as a guide.

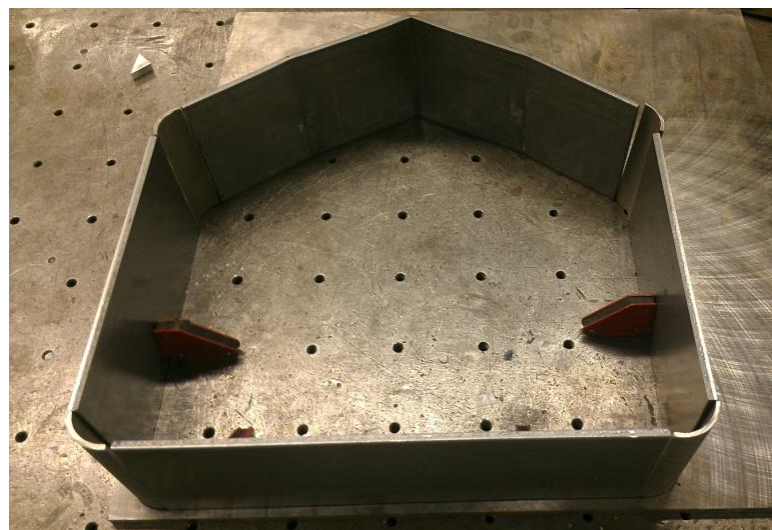


Figure 5-35. Water-Jet Scrap as Used for Final Cutting and Welding of Radial Outer Structure.

Then, the remaining steel from the water-jet cut was used as a jig for the final trimming and welding of the radial sections of the shield, shown in Figure 5-35.

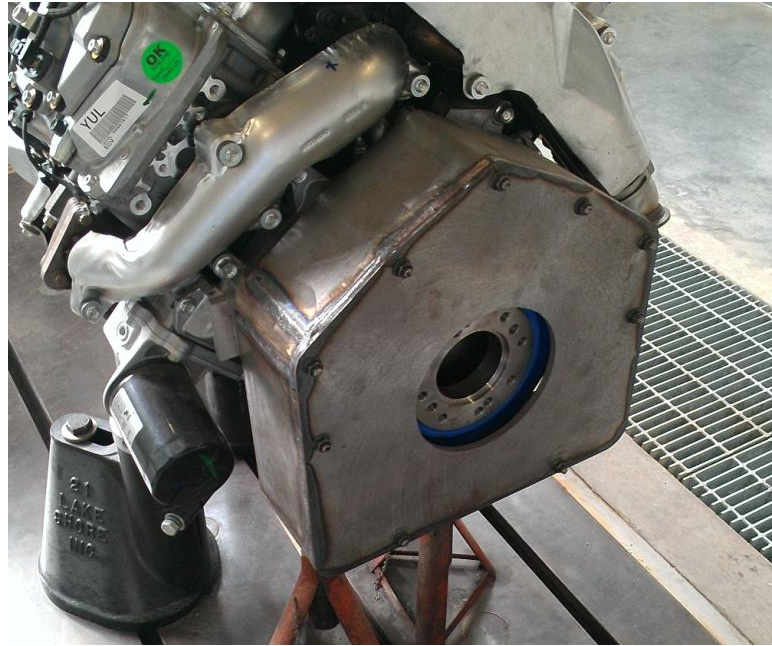


Figure 5-36. Fully Assembled Scatter Shield.

Now that the outer segments of the scatter shield were a single piece, the outboard flange was removed from the studs and the outer shield was slid into place. Then, the flange was tack-welded to the outer shield for removal and subsequent full welding in the machine shop. Figure 5-36 shows the completed and installed shield. The shield has not been treated to prevent rust. This is because the connection of the shield to the elephant feet (via vibrational dampening) has not yet occurred. This will likely involve welding to this assembly. The scatter shield will be powder-coated following complete adaptation to support the rear end of the engine.

5.3 Dynamometer

Following the completion of the pad preparation, the dynamometer was placed in its final location at approximately one foot from the end of the pad farthest from the loading dock door.



Figure 5-37. Dynamometer Mounting Bolts.

It is affixed using eight $\frac{3}{4}$ "-10 bolts threaded into sliding tee-slot nuts, as shown in Figure 5-37.

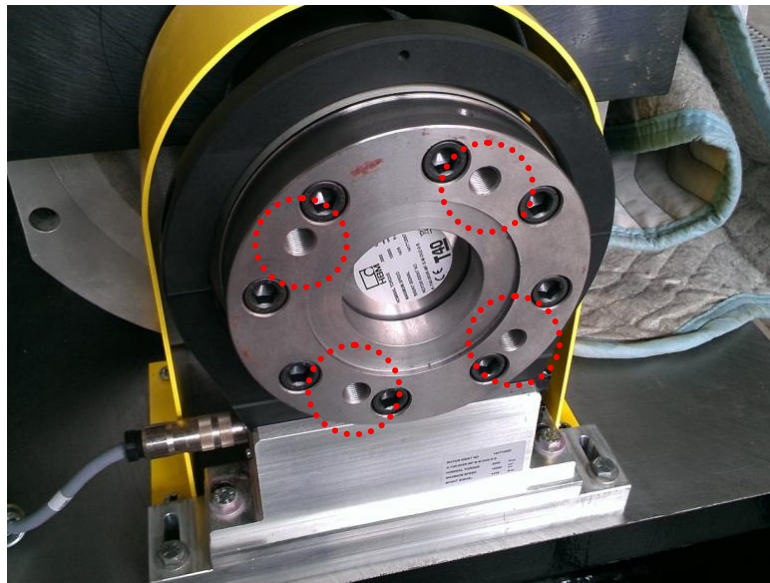


Figure 5-38. HBM to Universal-Joint Adapter.

An adapter is needed to connect the HBM torque transducer to the Spicer-type yoke of the universal-joint driveshaft. This was purchased through Dyne Systems, Incorporated along with the driveshaft and torque dampening coupler. This adapter (Figure 5-38) uses eight 12.9-grade M12 bolts to connect to the HBM. These are tightened to 92 ft-lb of torque using two star-pattern passes, with the first tightening to half-torque. Four bolts are used to tighten the universal joint driveshaft to the

adapter, (red bolt circle in Figure 5-38). Similarly, four bolts are also required to fasten the driveshaft to the torque dampener.

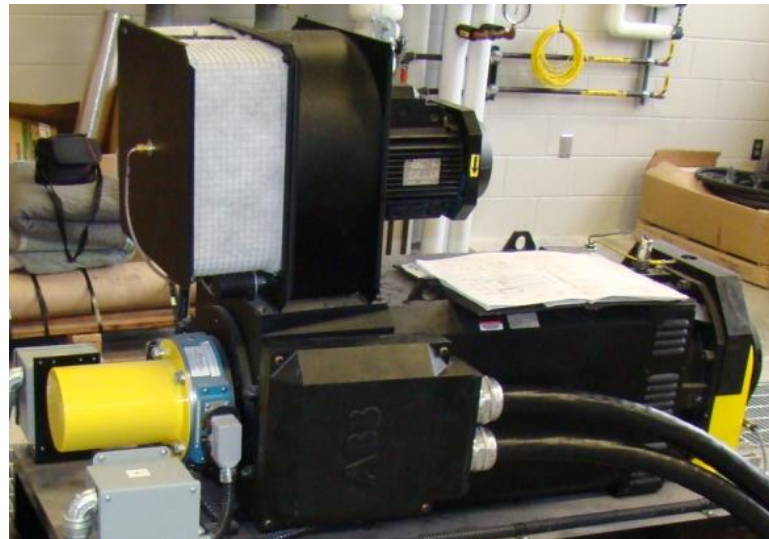


Figure 5-39. Air Filter and Cooling Blower of Dynamometer.

Finally, maintenance of the dynamometer is straightforward. Forced air cooling is accomplished through the use of a separate blower motor which flows air through the bearings and windings. The air filter (Figure 5-39) for the cooling system should be removed and blown out (using compressed air) twice a year. Replacement filter material is available through online hardware distributors, such as McMaster-Carr. At the same time, attachment bolts of the dynamometer base and driveline connections should be checked for loosening.

5.3.1 Flow of Electricity Drive Cabinet and Intermediate Cutoff

The dynamometer is connected to a three-phase 480VAC building circuit. When the dynamometer is motoring, this circuit provides electrical power. When loading the engine, the regenerated electricity is sent from the dynamometer back to this circuit.



Figure 5-40. Main Dynamometer Circuit Breaker (1NT1) in M2SEC Basement.

The breaker for the dynamometer is located in the basement of M2SEC. This breaker (Figure 5-40) can only be de-activated by electricians of KU Facilities and Services.



Figure 5-41. 480VAC Transformer (left) and Dynamometer Drive Cabinet (right).

From the basement breaker, the three-phase power is directly connected to a 480VAC-480VAC transformer. This transformer is used to remove electrical noise from the primary circuit to provide high-quality power. From the transformer, AC power is sent to the dynamometer drive cabinet, next to the transformer in the mechanical service room above the test cell, shown in Figure 5-41. The drive cabinet communicates directly with the dynamometer controller to modulate motor power flow.

Additionally, dynamometer speed (via encoder) and torque signals are sent to the drive cabinet for remote control (from the cabinet interface) and for hardware over-speed and over-torque protection.

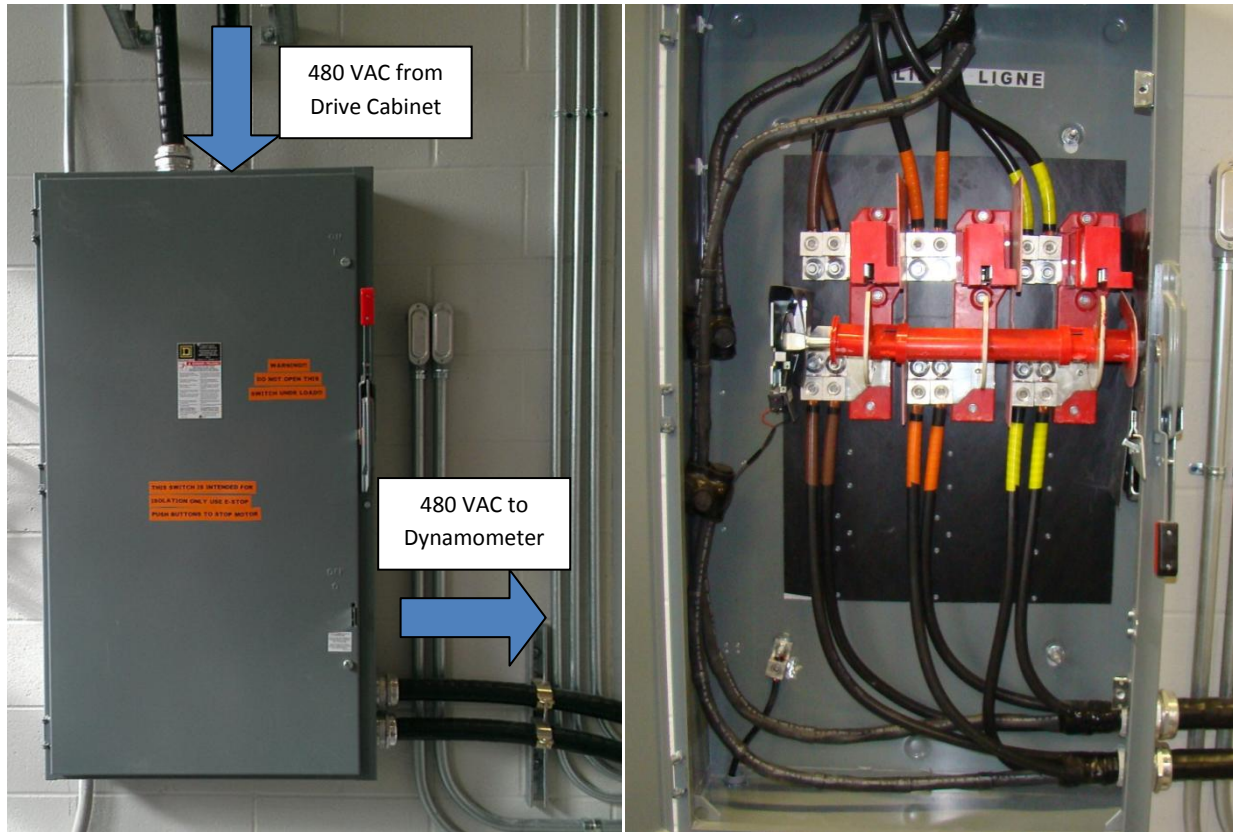


Figure 5-42. Dynamometer Power Lockout Cabinet Closed (left) and Open (right).

Typically, this mechanical room is not accessible by test cell personnel. For safety, a lockout system was implemented for use during engine down time. This lockout cabinet physically disconnects the three-phase AC power between the drive cabinet and dynamometer. This cabinet is located on the test cell wall, as seen in Figure 5-42. When this cabinet is opened, the three AC disconnects can be inspected and serviced (by Quality Electric). Warning, this lockout is intended to only be used to protect personnel during service. This *is not* an emergency stop. Throwing this disconnect while the dynamometer is loaded will cause an over-voltage in the windings of the dynamometer (nowhere for the power to go), causing catastrophic failure.

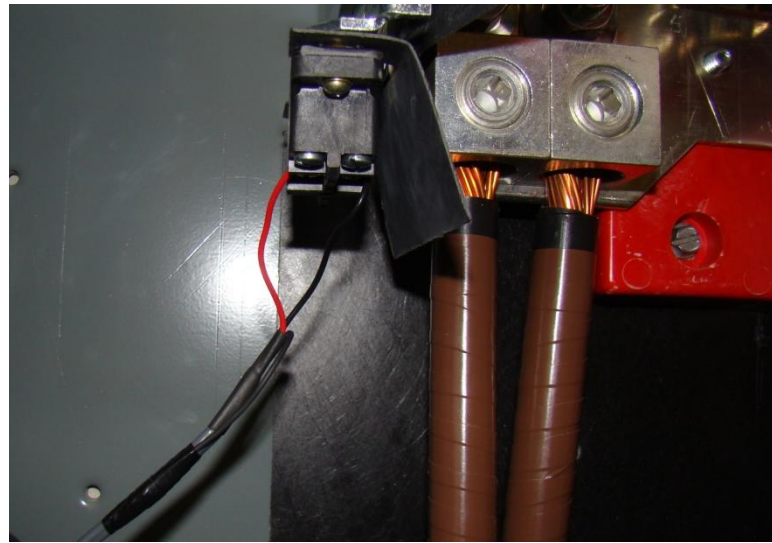


Figure 5-43. Disconnect Switch in Dynamometer Lockout Cabinet.

A safety switch (Figure 5-43) was installed to help protect the dynamometer from trying to run with the power disconnected. This switch is connected to the drive cabinet and serves as a binary go or no-go switch that will direct the drive cabinet to disable AC power.



Figure 5-44. Dynamometer Junction Box Internal Connections.

The terminals for AC power and bearing, winding, and blower temperature are shown in the opened dynamometer terminal box in Figure 5-44. The installation of the electrical components for the dynamometer was performed by Quality Electric, Incorporated of Lawrence, KS. This includes the drive cabinet, lockout cabinet, heavy-duty VFD cable from the drive cabinet to the dynamometer, and the

dynamometer controller itself. High-voltage connections, including the drive cabinet, lockout cabinet, and terminal box should only be serviced by Quality Electric, Incorporated.

5.3.2 Controller



Figure 5-45. Dynamometer Control and Monitoring Interface.

Multiple user interfaces provide dynamometer and monitoring capability to the user. These interfaces are located at the bottom of the dynamometer control cabinet in the test cell control room, as in Figure 5-45. The other two modules are for actual dynamometer control and torque interface box, which perform functions based on input commands from the human interface modules. The upper module provides measurement of the dynamometer windings, bearings, and ambient temperatures in Fahrenheit. These readings serve as protection for the dynamometer and will cause the controller to perform an immediate shutdown in the event of overheating. The drive-end (DE) and opposite drive-end (ODE) bearing temperature limits are 180°F. The three windings, which correspond to the three phases of AC power, are limited to 302°F. Finally, ambient temperature is limited to 105°F. Above this ambient

temperature, the air cooling system cannot provide adequate cooling capacity. If these temperatures are exceeded prior to dynamometer starting (particularly ambient) the dynamometer will not operate.

The bottom module is the Inter-Loc V controller interface that allows the user to specify dynamometer operating mode and desired load or speed. This interface is also used to change setup parameters and perform dynamometer tuning and calibration. These settings are changed using the combination of push-buttons and touch screen. The buttons and their functions are (left to right in Figure 5-45):

- Reset – Clears faults, software shutdowns, and emergency stops. Pressed to restart the dynamometer
- F1 – Configurable per the Inter-Loc V Manual
- Absorb Only – Dynamometer only loads the engine and provides no motoring (power assist)
- Master Computer – Sets a computer to run the dynamometer. This is available through serial communication port and on-hand LabVIEW program (not yet operational)
- ON/OFF – Turns the dynamometer controller on or off
- Setup – Adjust parameters of Inter-Loc V controller. For example, an overspeed limit of 4000 RPM is set to protect engine and dynamometer (max dynamometer speed: 5600 RPM)
- Calibrate – To calibrate the torque transducer
- Tune – used for tuning of motoring and loading – done with proportional-integral-derivative (PID) tuning and ramp rates. Ten tuning sets are available for different engines (retuning necessary for each subsequent engine).
- Throttle Jog – Used to slew throttle towards 100% when Inter-Loc V is used to control engine throttle (not used in KU application)
- Control Select – When the interface is used for multiple dynamometer controllers, this button cycles between controllers (not used in KU application)

- Number Pad – Manual entry of numerical values
- Directional Arrows – Used to move through lists and menus
- Enter – Submits numerical values to the controller
- Cancel – Clears numerical values entered to the controller
- Soft Shutdown – un-powers dynamometer, engine is no longer motored or loaded
- Shutdown ‘Mushroom’ – puts high amount of torque (140% of rated) to rapidly stop the engine

5.3.3 Emergency Stop Integration with Main Test Cell Systems

The dynamometer controller must be integrated into the test cell to communicate with other auxiliary systems, particularly for emergency stop conditions. As mentioned previously, the test cell has a series of emergency-stop buttons located throughout the room. These buttons are wired in a series configuration so that as soon as one button is pressed, the entire e-stop button circuit is broken. The loss of continuity triggers the e-stop procedure in the auxiliary systems controller (in the mechanical room). The actuation of these emergency stop buttons must also stop the dynamometer and, likewise, the emergency stop ‘mushroom’ button on the dynamometer controller must also trigger the same auxiliary system shutdown.



Figure 5-46. Dynamometer Controller Emergency-Stop Input.

An emergency signal from the room buttons relies on the auxiliary test cell controller. This signal is connected to the Inter-Loc V controller through the OCS 3 connector, as in Figure 5-46. In this figure, the input to OCS 3 is shown with a wire jumper. This is how the dynamometer was initially commissioned, with this input checking continuity at these pins to determine e-stop state, with a broken circuit indicating emergency-stop. When the continuity of the test cell e-stop circuit is broken by 'mushroom' button actuation, a relay in the auxiliary systems control cabinet (upstairs mechanical room) trips. This relay contains both normally-open and normally-closed outputs. To complete the e-stop circuit input to the dynamometer, a pair of wires connected to normally-closed terminals, is connected to the dynamometer through the OCS 3 input connection.

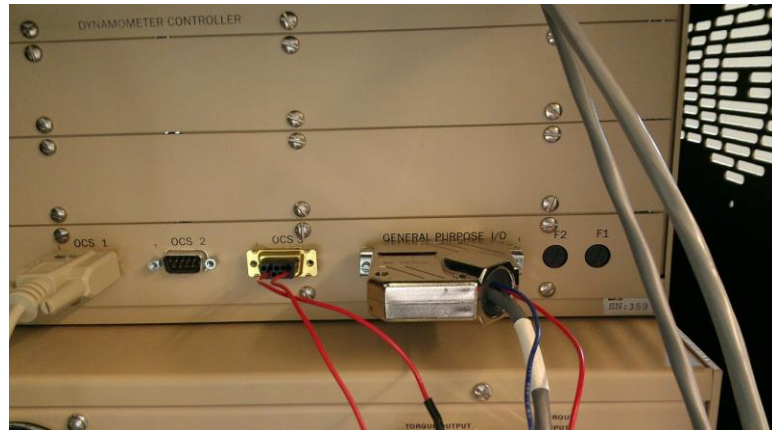


Figure 5-47. Connection of Emergency Stop Input and Output.

Figure 5-47 shows the connection of the test-cell emergency-stop buttons into the dynamometer controller. This figure also shows the output configuration of the dynamometer controller e-stop 'mushroom' button to the test cell controller (red and blue pair). The signal from the Inter-Loc V controller is a 24 VDC signal on the General Purpose I/O connection that is active during normal operation. When the e-stop 'mushroom' button on the controller is pressed, the voltage drops to zero VDC. This signal is used in conjunction with a relay with a 24 VDC input coil. This wiring had to be performed following commissioning. The output of the 24 VDC signal occurs from pin 20 (red wire) of the I/O port, with pin 15 being used as the common pin (blue wire).

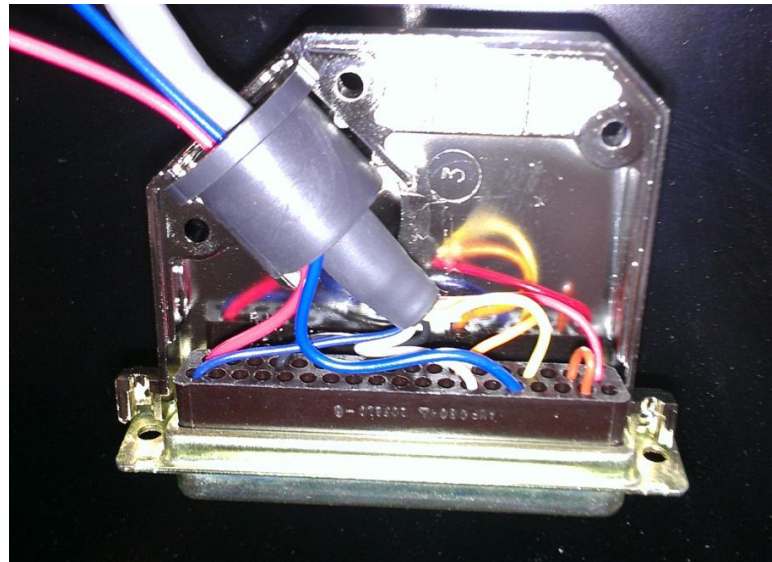


Figure 5-48. Wiring of Emergency Stop Output from General Purpose I/O Port.

This wiring was performed using crimp-style pins, purchased at the local Radio Shack, inserted into the corresponding pins, as in Figure 5-48. The 24 VDC signal is wired to the relay coil using twisted pair wire soldered to the General Purpose I/O wiring of Figure 5-48 with black being soldered to blue (common) and red soldered to red (24 VDC). This relay is connected in series with the test cell ‘mushroom’ buttons. Thus, the dynamometer now acts in a similar manner to any other test cell e-stop button.

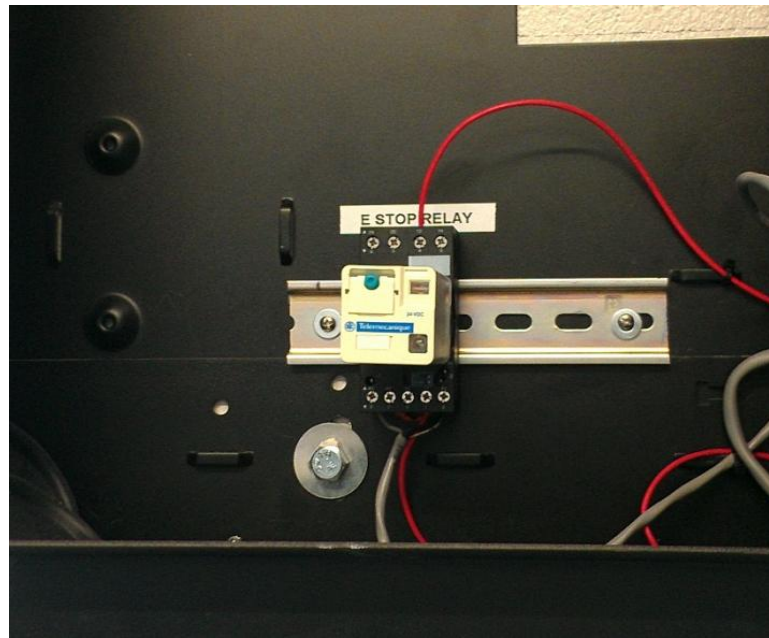


Figure 5-49. Emergency Stop Relay, Located Behind the Dynamometer Controller in the Controller Cabinet.

The relay, and the red pair of wire connecting its normally-closed terminals to the test cell auxiliary controller, is shown in Figure 5-49.

5.3.4 Calibration Procedure

The torque transducer used to measure engine torque outputs a linear signal analog signal that is scaled using a voltage offset and gain value. The voltage offset defines the voltage that corresponds to zero torque. Voltage gain provides scaling, for example, the number of N-m per volts that is set based on full scale output of the torque transducer (2 kN-m). Over the duration of successive testing, the accuracy of these offsets and gains can deteriorate, resulting in a need for periodic recalibration of the torque transducer. This is accomplished using either a full recalibration, which requires disconnecting the driveshaft from the dynamometer, or an abbreviated calibration, which can be done using only the dynamometer controller.

A full calibration is accomplished by removing the driveshaft and adapter from the input flange of the dynamometer. Then, a calibration torque must be applied to the torque transducer, which can be

performed by locking the dynamometer rotor in place and applying a known torque to the input flange of the torque transducer.

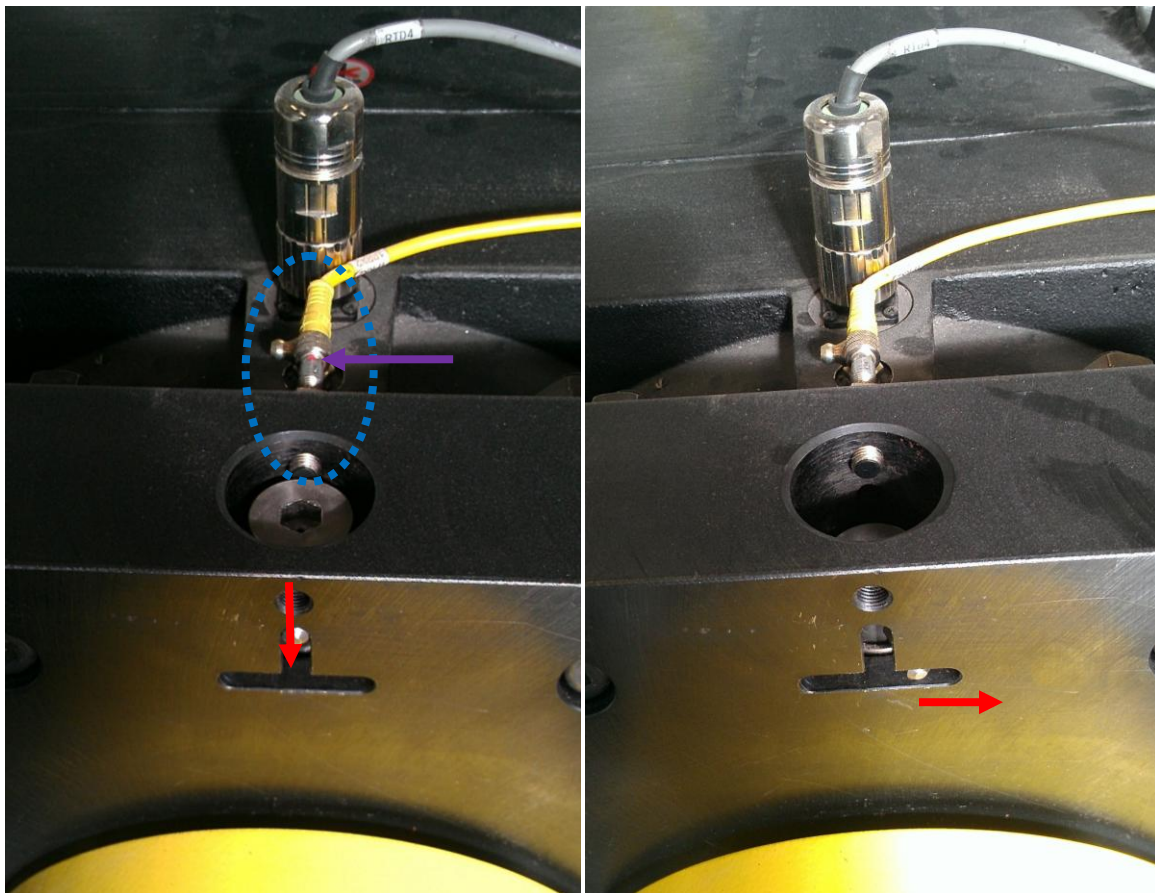


Figure 5-50. Locking Mechanism and Safety Proximity Sensor in the Unlocked (left) and Locked (right) Position.

The dynamometer internals are locked using the shaft lock, located near the drive-end of the dynamometer. The dynamometer is locked by pressing the shaft lock downwards, then turning the shaft lock so that it remains in the locked position. The shaft lock is shown in Figure 5-50 in both the unlocked and locked position. A proximity sensor is used to prevent the dynamometer from being started with the shaft lock engaged. This sensor is outlined in blue in Figure 5-50. It lights up to indicate that the shaft is unlocked (purple arrow) when the sensor detects nearby metal objects.

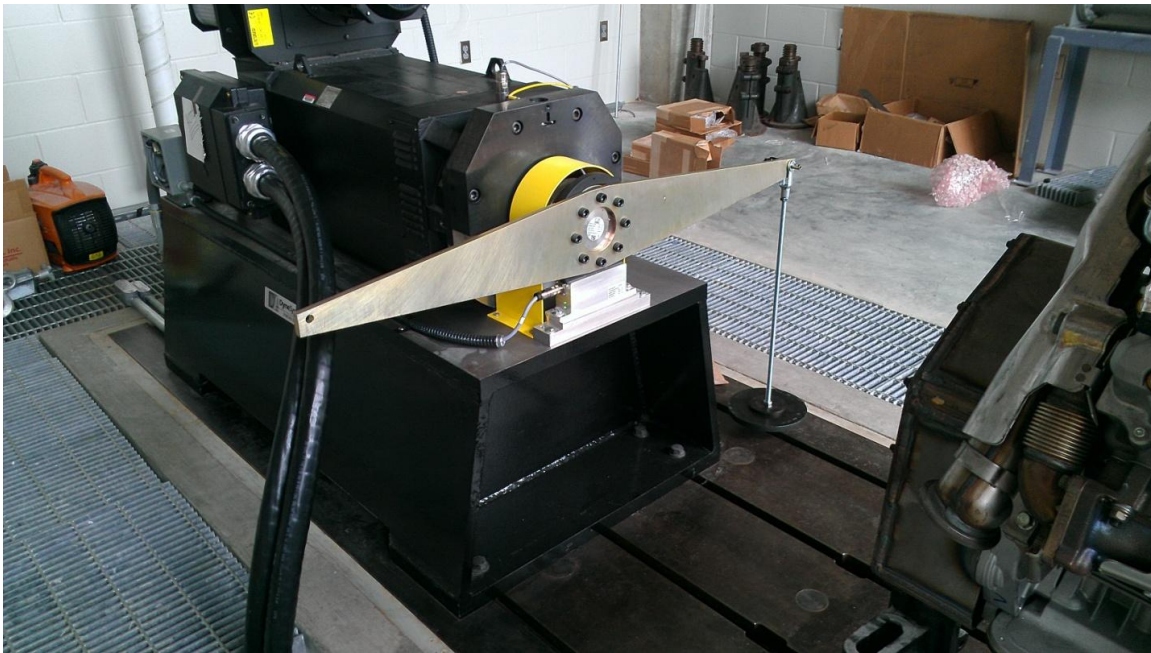


Figure 5-51. Calibration Moment Arm and Weight Hanger.

Torque is applied using calibrated weights and a moment arm horizontally attached to the torque transducer input flange using the M12 bolts from the driveshaft adapter flange. The moment arm and calibration weight hanger are shown in Figure 5-51. The distance from the center of the dynamometer input shaft to the calibration weight hanger pin is two feet, thus a calibration weight of 50 pounds produces a torque of 100 lb-ft. The calibration arm is symmetrical to prevent artificial torque from imbalance.



Figure 5-52. Dynamometer-Facing Surface of Calibration Arm.

The arm must be installed with the smooth surface of the arm facing towards the engine, the other side of the moment arm is machined so that it does not impinge upon the front face of the dynamometer, as in Figure 5-52.



Figure 5-53. Torque Induced by Calibration Weight Hanger.

Once the hanger is installed, a torque is being applied to the transducer. This is reflected by the torque reading observed on the screen of the dynamometer controller, as in Figure 5-53. This torque is indicated by an N-m reading, rather than a lb-ft value. The dynamometer can be calibrated while using N-m values using a unit conversion during spanning. The units displayed on the screen are changed in the Inter-Loc V setup menu. This is accessed by pressing the 'setup' button, then pressing 'Inter-Loc V' on the touch-screen popup menu.

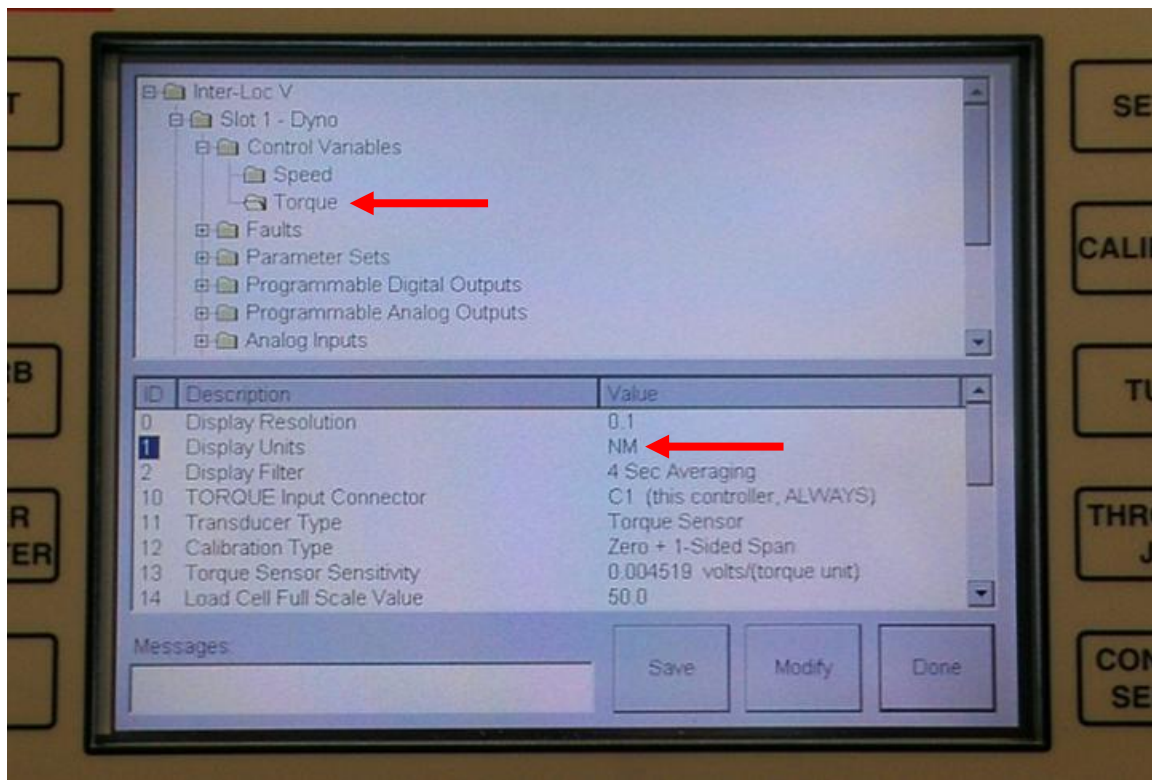


Figure 5-54. Inter-Loc V Setup Menu: Modify Display Units.

This brings the user to the Inter-Loc V setup menu shown in Figure 5-54. The cursor begins in the upper section of the screen. The directional arrow buttons expand the menu. At the desired parameter (torque) pressing the 'enter' button moves the cursor to the lower half of the screen, where directional arrows move up or down.

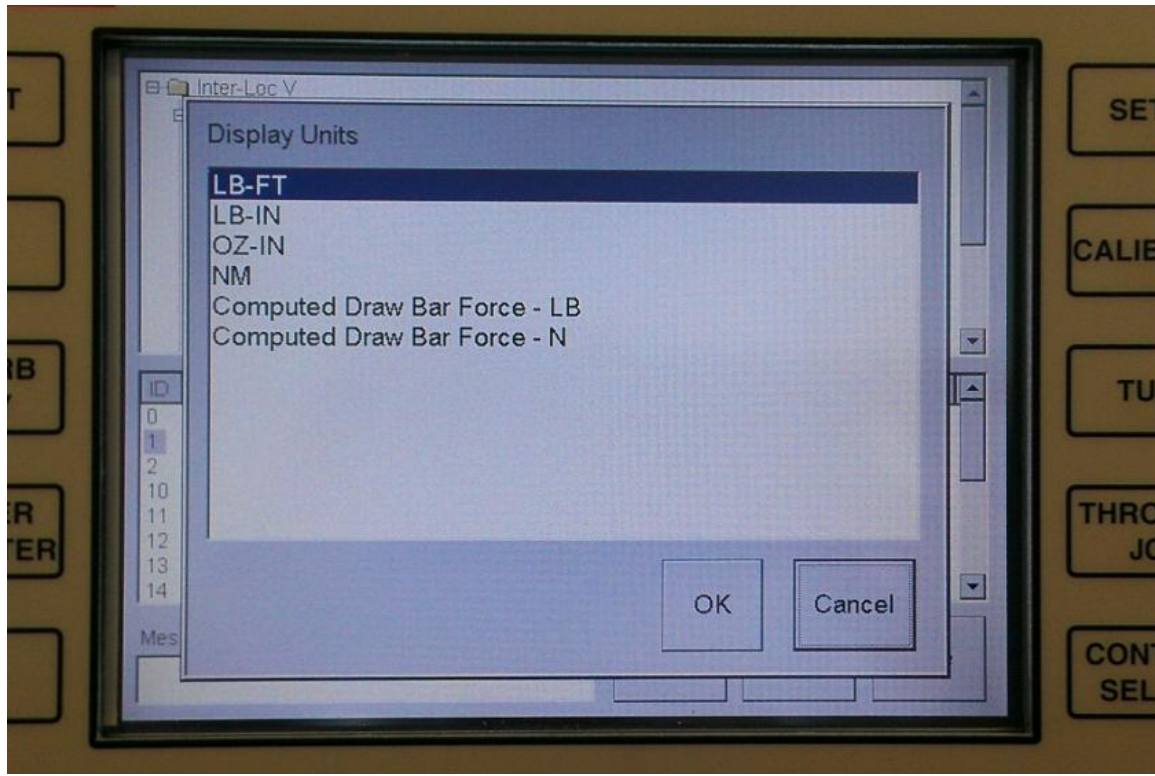


Figure 5-55. Display Units Dialog Box in Inter-Loc V Setup Menu.

At 'Display Units' pressing 'Modify' on the touch screen opens the Display Units dialog box in Figure 5-55. The directional arrows navigate to the desired units (lb-ft highlighted). Pressing 'OK' on the touch screen modifies the display units.



Figure 5-56. Torque Induced by the Calibration Weight Hanger.

Pressing save and done in the setup menu (Figure 5-54) returns to the main screen. The screen now indicates 23.8 lb-ft of torque, as in Figure 5-56.

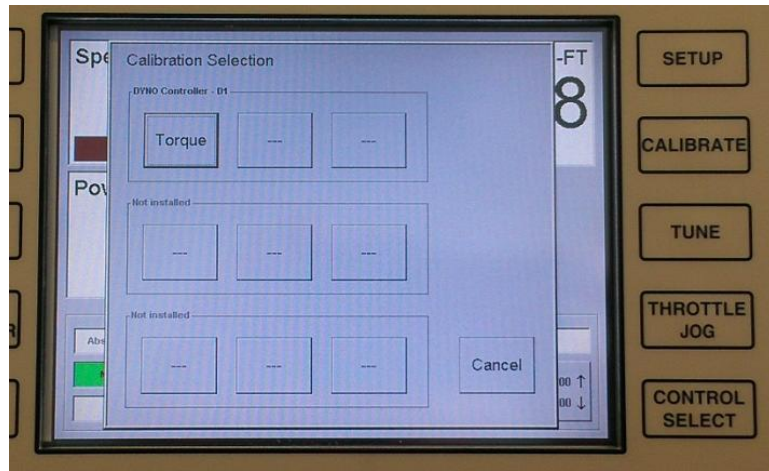


Figure 5-57. Calibration Popup Selection Menu.

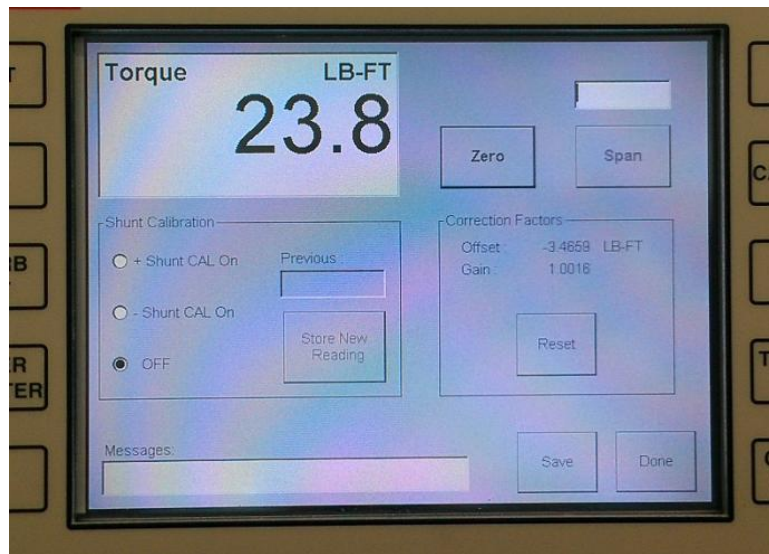


Figure 5-58. Calibration Menu Prior to Calibration.

Pressing the 'Calibrate' button and selecting 'Torque' on the calibrate popup menu (Figure 5-57) brings the user to the calibration menu (Figure 5-58). This screen shows the offset and gain factors used for calibration.

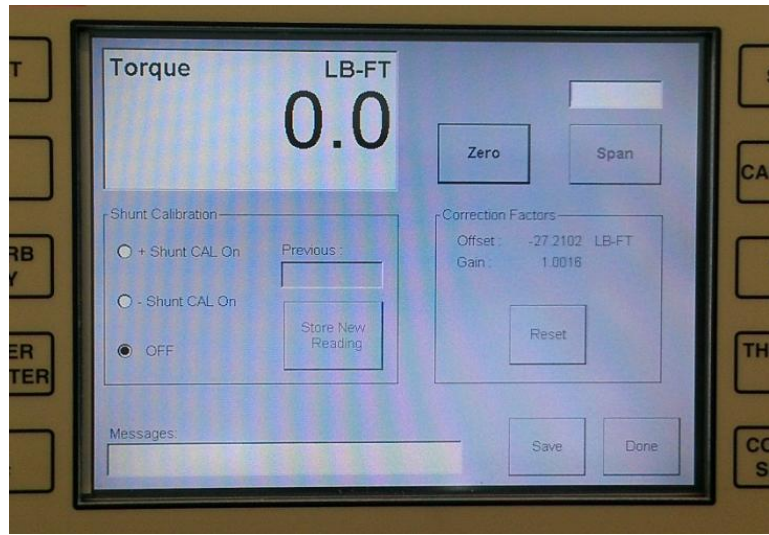


Figure 5-59. Calibration Zeroed for Accurate Gain Determination.

First, the gain is calibrated, which is performed by first pressing ‘Zero’ on the calibration menu. This changes the measured torque to 0.0 lb-ft, as shown in Figure 5-59. This make the offset voltage value change and, because a torque is being applied, incorrect. However, this must be done so that when the calibration weights are added, the appropriate value will be shown on the screen for obtaining the gain.

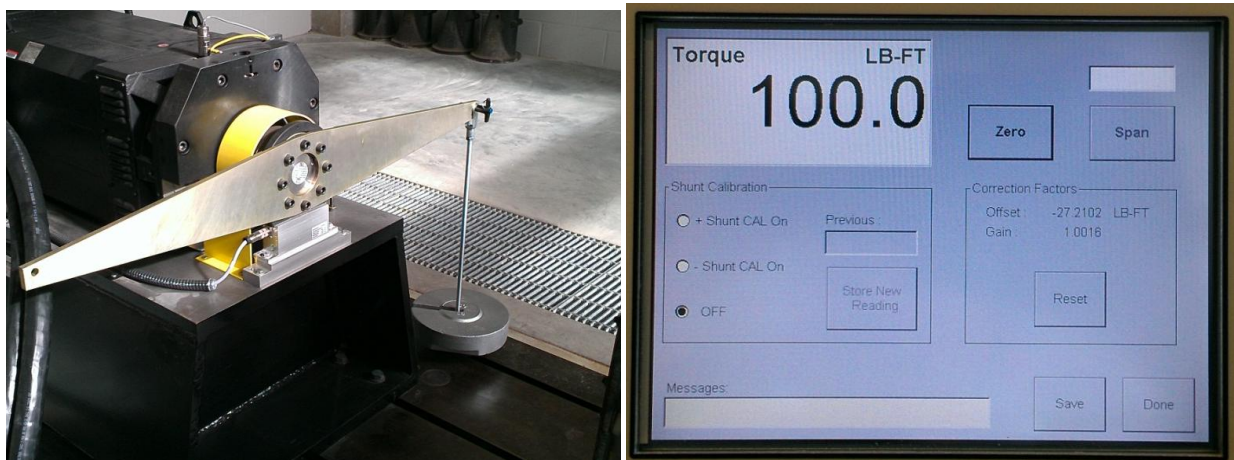


Figure 5-60. 100 lb-ft Calibration Torque Application (left) and Displayed Measurement (right).

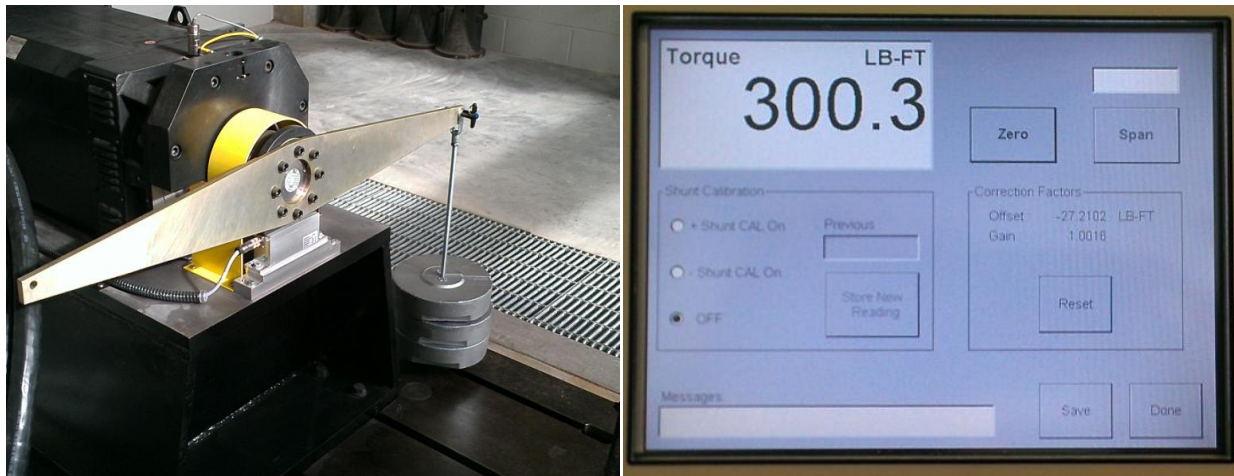


Figure 5-61. 300 lb-ft Calibration Torque Application (left) and Displayed Measurement (right).

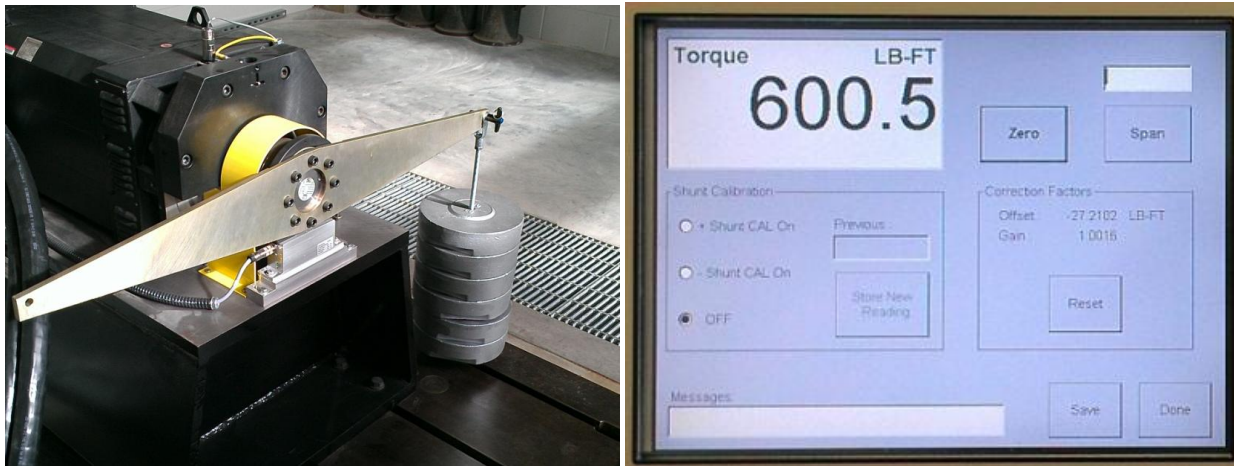


Figure 5-62. 600 lb-ft Calibration Torque Application (left) and Displayed Measurement (right).

Now, the calibration weights are added to the hanger. As weight is added, the torque measured increases accordingly. Each weight is precision machined to 50 lbs. Thus, as each one is added, torque increases by 100 lb-ft. This is a good opportunity to monitor the linearity of the torque transducer (this cannot be adjusted). Figure 5-60 through Figure 5-62 show the linearity of the sensor as weight is added.

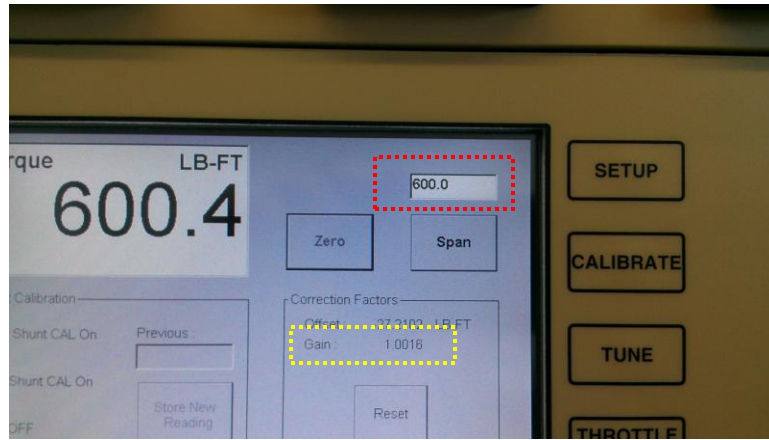


Figure 5-63. Span Value Adjustment Input.

With the full weight in place, a torque of 600.0 lb-ft should be measured. To adjust the gain to display this measurement, manually enter 600 as span value by touching the span value input value box (red outline in Figure 5-63) and entering '600.0' using the numerical buttons and pressing the 'enter' button.

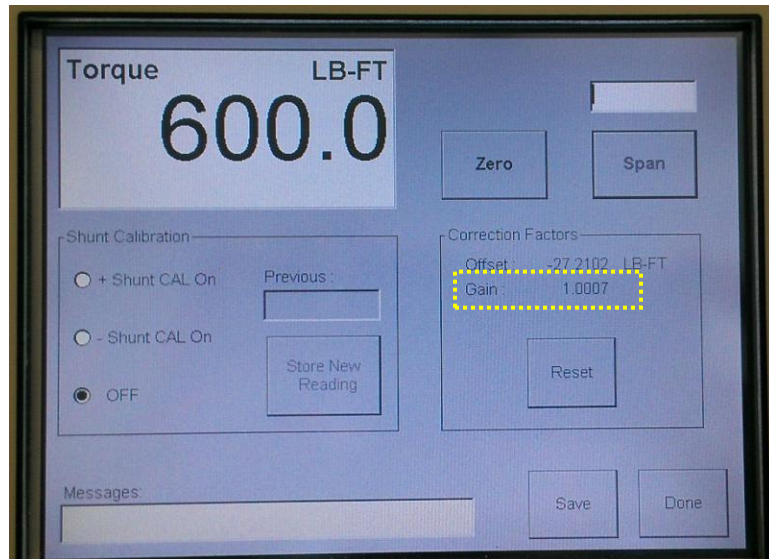


Figure 5-64. Calibration Window Following Span Calibration.

Pressing 'Span' on the touch screen makes the dynamometer control adjust the gain value so that the measured torque is equal to the desired span value (600 lb-ft). The change of gain value is observed by comparing the gain value of Figure 5-63 and Figure 5-64 where the yellow-outlined gain has changed from 1.0016 to 1.0007. This point marks the successful calibration of the gain factor. The next

step of the process is to remove the weights from the hanger in order to calibrate the zero of the torque transducer.

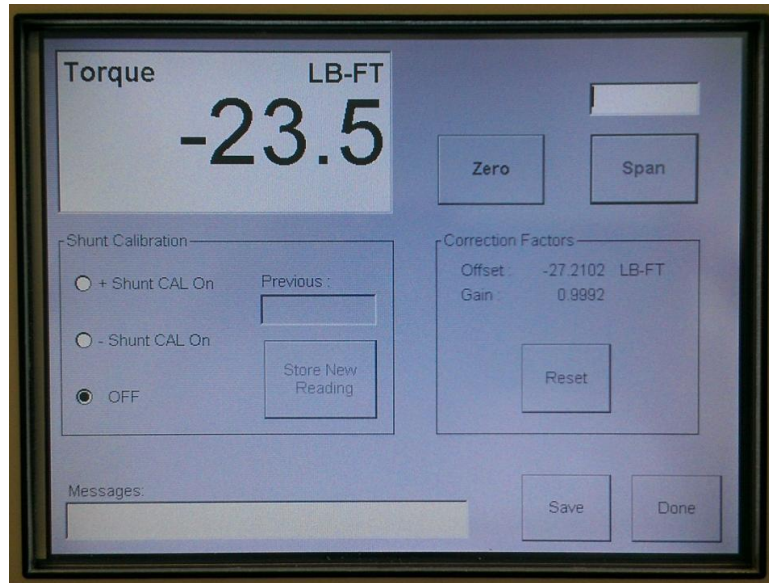


Figure 5-65. Calibration Window Following Calibration Weight Removal.

Following the removal of the weight hanger and calibration lever arm, the screen shows a negative 23.5 lb-ft (Figure 5-65) due to the negative offset of the hanger weight that is no longer inducing a torque. Now that no torque is being exerted on the torque transducer, the offset factor is calibrated by pressing 'Zero' on the touch screen.

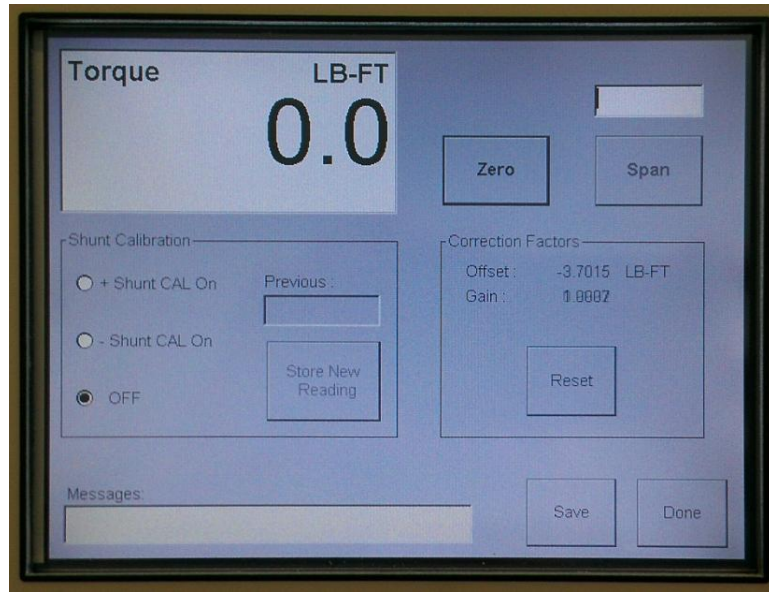


Figure 5-66. Calibration Window Following Offset Zero Calibration.

Figure 5-66 shows the change in offset factor following zero calibration. Note: the gain value is a value between 1.0007 and 0.9992, thus the displayed value changes intermittently as reflected through these figures.



Figure 5-67. Main Operating Screen. Torque Shown in LB-FT (left) and N-m (right).

Calibration is completed, the next step is to press 'Save' and 'Done' on the calibration menu screen, which brings the user back to the main operation screen (Figure 5-67). The units of torque are still in lb-ft at this point, which can be changed back to N-m through the Inter-Loc V setup menu, as

performed previously in the procedure covered here. The dynamometer is calibrated and ready to measure torque. The universal joint adapter plate and driveshaft can be reattached.

5.3.5 Abbreviated Re-calibration Procedure

Between full calibrations, an abbreviated calibration may be performed that removes the need for the removal of the driveshaft and shaft adapter flange from the dynamometer. This type of calibration activates a shunt located inside the torque transducer that causes it to output a torque signal corresponding to a value near the upper end of the transducer torque range which can be used to adjust the gain correction factor in the dynamometer controller. This procedure should be performed following a full calibration to set the correct span reading for subsequent abbreviated calibrations.

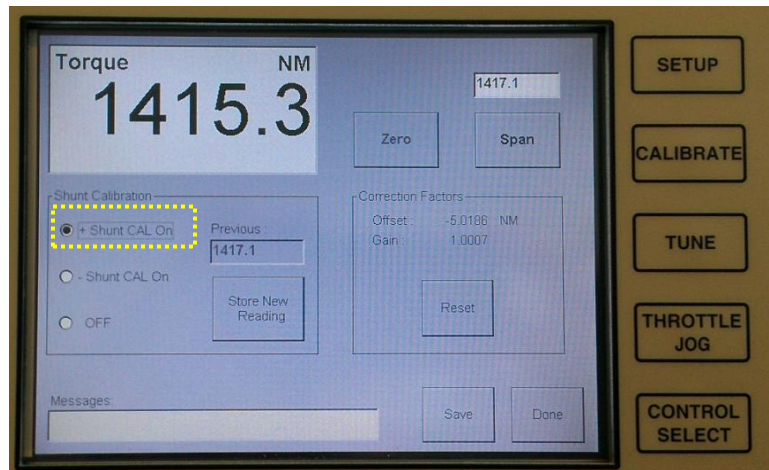


Figure 5-68. Calibration Window: Shunt Active.

First, the calibration window is accessed by pressing the 'Calibrate' button on the Inter-Loc V controller. Then, the offset factor is adjusted by pressing 'Zero' in the calibration window. Then, '+ Shunt CAL On' is pressed on the touch screen (yellow in Figure 5-68) to activate the torque transducer calibration shunt.

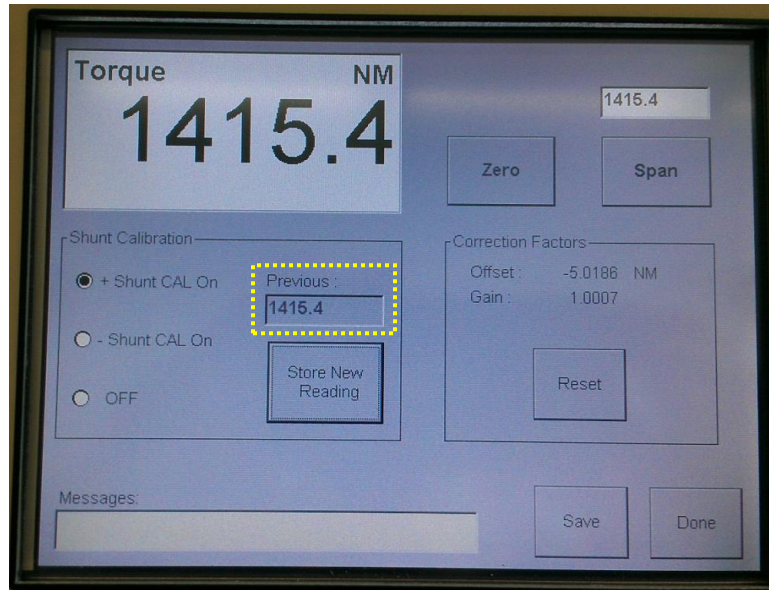


Figure 5-69. Calibration Window: Storing of New Span Reading.

When this procedure is performed following a full calibration, press the 'Store New Reading' button on the touch screen. This will save the span value for future abbreviated calibrations, highlighted in yellow in Figure 5-69 and place this value in the span dialog box. The value of 1415.4 replaces the value 1417.1 from a previous calibration. In the event of an abbreviated calibration not immediately following full calibration, the user should not press 'Store New Reading' but should instead manually enter the span value that was used for previous calibrations. In this case, the user would have entered 1417.1.

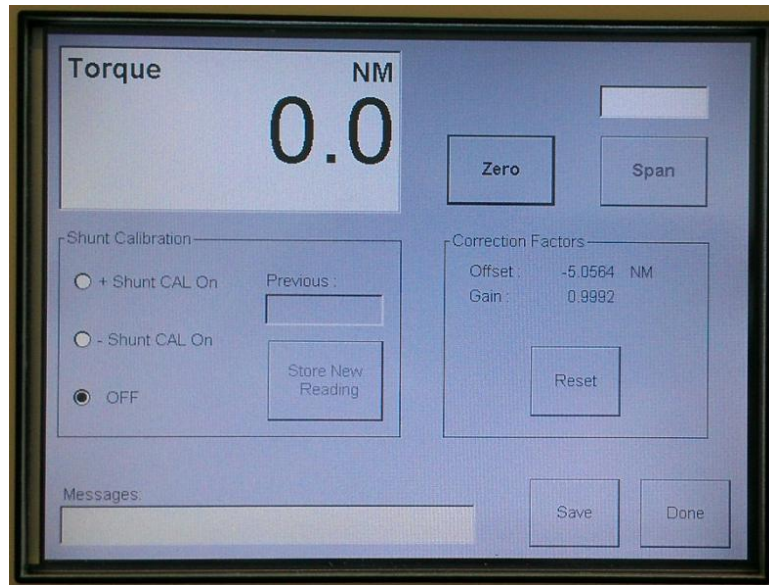


Figure 5-70. Calibration Window: New Gain Value Following Span.

Following the storing of the new span reading, the gain can be adjusted by pressing ‘Span’ on the calibration window, which changed the gain from 1.0007 to 0.9992 (Figure 5-70). Pressing ‘Save’ and ‘Done’ on the touch screen completes calibration and returns the user to the main operating window.

5.3.6 *Dynamometer Tuning Procedure*

When performing both steady-state and transient experiments, it is important to have the dynamometer well-tuned to provide accurate loading on the engine. For steady-state tests, this is particularly helpful at removing statistical uncertainty in the torque readings, which influence brake-specific results. For transient tests, tuning improves the control during speed and load ramping. In the case of the Inter-Loc V controller, a proportional integral derivative (PID) controller architecture is used, with gains for each adjusted during the tuning process. For manual tuning, the P-term depicts the present error between the desired condition and the actual condition; thus, apply named proportional gain. Raising the proportional gain will reduce the error between the actual and desired speed/torque (demonstrated later). The integral gain is based on both error magnitude and the amount of time that the error between actual and desired points has existed. Increasing the integral term reduces the overshoot experienced during step changes in the dynamometer tuning process (demonstrated later).

However, if the integral term is too high, instability can occur. Finally, the derivative gain is based on the slope (rate of change) of the error between desired and actual value. This gain will reduce response time following a step change, however too much derivative gain will cause overshoot.



Figure 5-71. Main Operating Window: Operating at 1000 RPM Setpoint in Preparation of Tuning.

To begin, the dynamometer must be spinning. For this demonstration, slower speeds produced better results. With an engine attached, higher speeds may be necessary. The dynamometer is brought up to speed by pressing the ‘Speed’ section of the touch screen, then entering a setpoint to the dialog box (yellow in Figure 5-71) using the numerical pad and ‘enter’ button. This indicates the dynamometer is running in speed mode. Of note, the torque mode is activated by pressing inside the ‘Torque’ portion of the touch screen then entering a torque value.

Once operating, the current speed of the dynamometer is shown in the ‘Speed’ section of the operating window, with the current setpoint indicated in parenthesis. A similar display occurs for torque mode. The dynamometer tuning window can be accessed by pressing the ‘Tune’ button on the controller interface, indicated by the red box in Figure 5-71.



Figure 5-72. Dynamometer Controller Tuning Window.

The tuning screen opens, as shown in Figure 5-72. In the tuning window, the current speed is indicated at top of the plot. The plot itself shows both the measured speed (feedback) and the speed setpoint being sent to the dynamometer by the controller. Values on this screen are adjusted by manually entering the desired number into the input dialog box (red box in Figure 5-72) using the numerical pad and ‘Enter’ button followed by touching the number that needs changing. For instance, scaling of the plot can be accomplished by entering range values, then pressing the number at the upper or lower bound of the speed axis (1000 or 1500 in Figure 5-72). Due to the small sections on this screen, a stylus is recommended. Shown elsewhere on the tuning window of Figure 5-72 are the PID gains (black box), upper and lower speeds for ramp tuning (yellow box), and ramp period and activation (orange box). Touching the ramp period value opens a popup menu to allow adjustment of the period length. Up to ten tuning sets are available in the event of different engines being connected to the dynamometer (purple box), removing the need to retune an engine that was previously connected. The PID gains shown represent the values chosen by tuning by Dyne Systems, Incorporated personnel during initial commissioning.

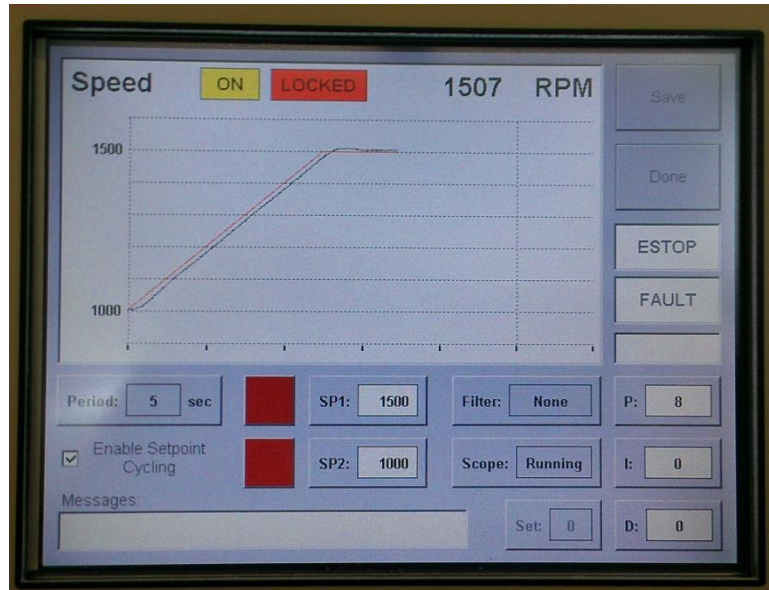


Figure 5-73. Tuning Window: Low P-gain, I- and D-gain set to zero.

To begin tuning, the I- and D-terms should be set to zero first then, the P-value should be set to a relatively low value (~10), as in Figure 5-73. Gain this low causes visible error during ramp, with the actual speed (red) being lower than the input speed (black). Additionally, overshoot is evident once the dynamometer reaches 1500 RPM.

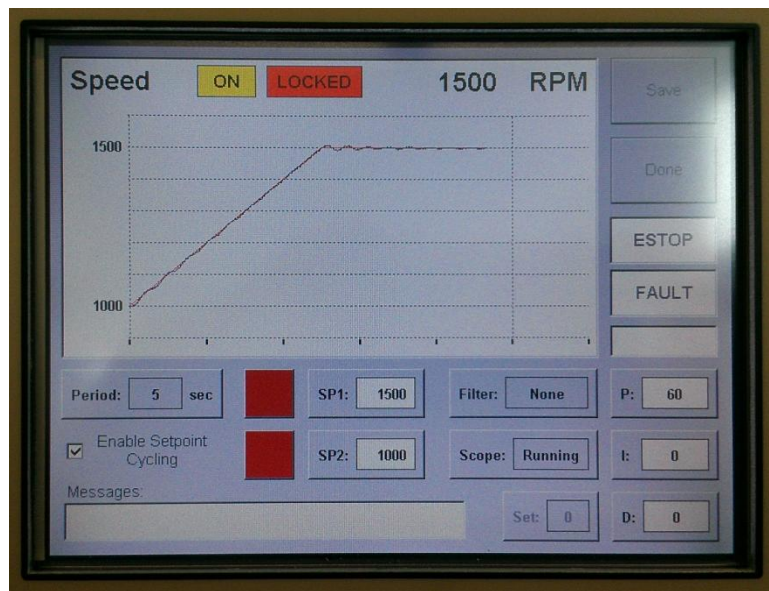


Figure 5-74. Tuning Window: P-Gain Increased to Near Instability.

The P-gain is increased to the point of instability. In the case of Figure 5-74, the continuous second-order oscillation at 1500 RPM is shown, but the error between the two speeds during ramping is dramatically reduced. At this point, the P-gain term is reduced by half and the I-gain value is increased to reduce the overshoot.

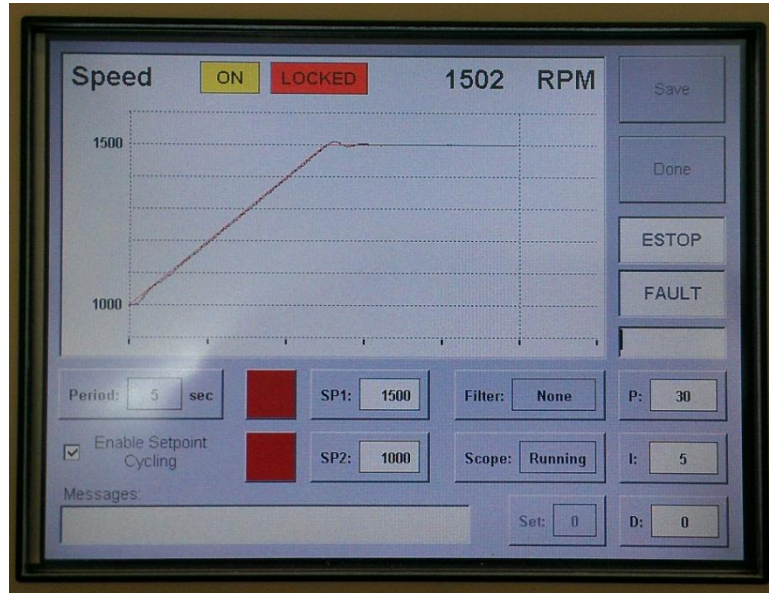


Figure 5-75. Tuning Window: P-Gain Set, Increasing I-Gain Value.

In Figure 5-75, the overshoot and oscillation are reduced as a combined function of the halved P-gain and the addition of integral gain.

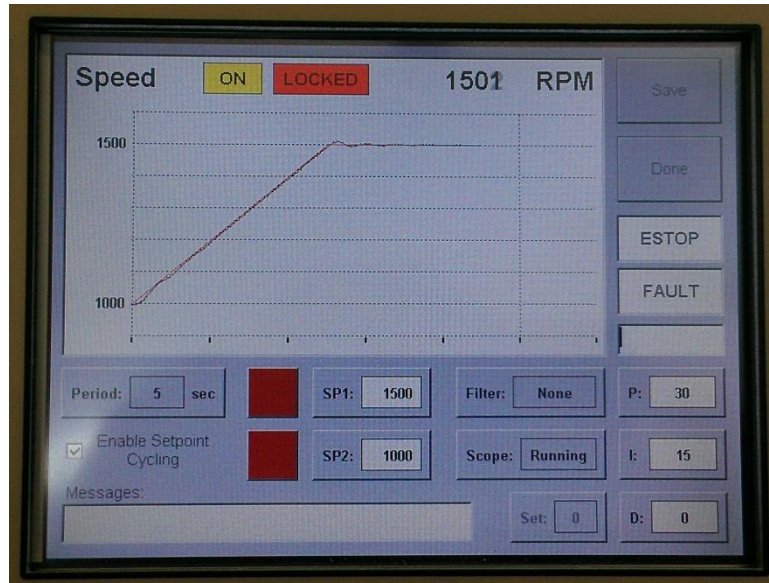


Figure 5-76. Tuning Window: I-Gain Increased To Produce Some Oscillation.

The addition of too much integral gain produces instability too, characterized by oscillations following a step change, as shown in Figure 5-76.

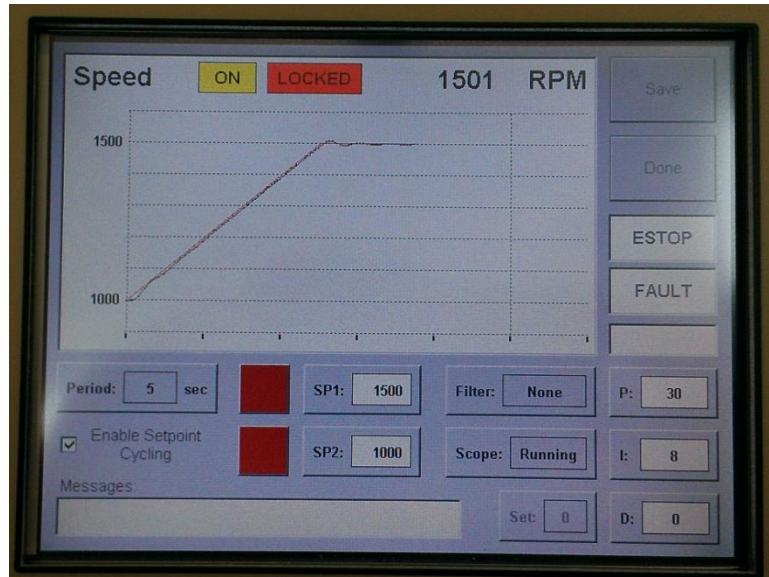


Figure 5-77. Tuning Window: I-Gain Value Set for Best Performance.

An integral gain between 5 and 15 produces the best overshoot dampening, as indicated in by a gain of 8, shown in Figure 5-77. Finally, adjustment of the derivative gain requires a much smaller value

as too much D-gain produces overshoot through excessive response to error. The goal is to dampen oscillation to the desired setpoint quickly, but without excessive D-gain.

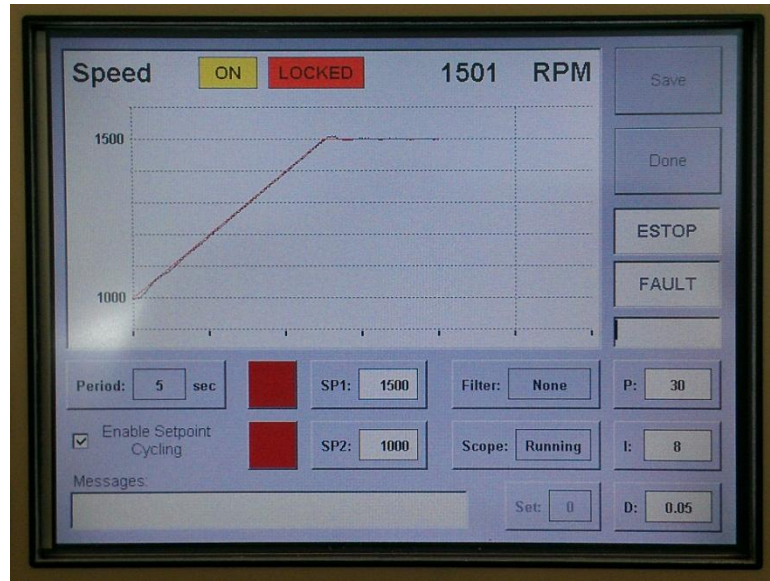


Figure 5-78. Tuning Window: Introducing Derivative Gain to the Controller Response.

A small amount of gain is being used in the ramp of Figure 5-78. In comparing the results with and without D-gain, perhaps a slight reduction in overshoot exists.

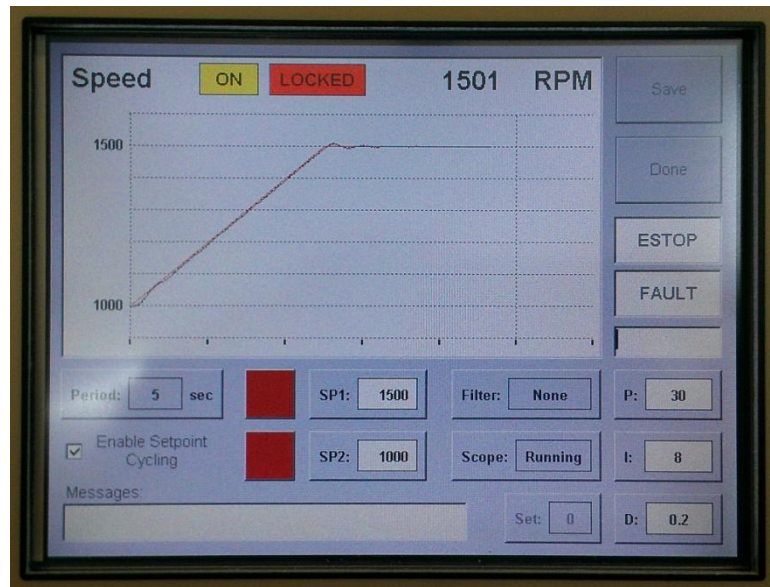


Figure 5-79. Tuning Window: Derivative Gain Increased.

The derivative gain is increased again in Figure 5-79. This plot indicates a slightly higher amount of overshoot than when the gain is set to 0.05.

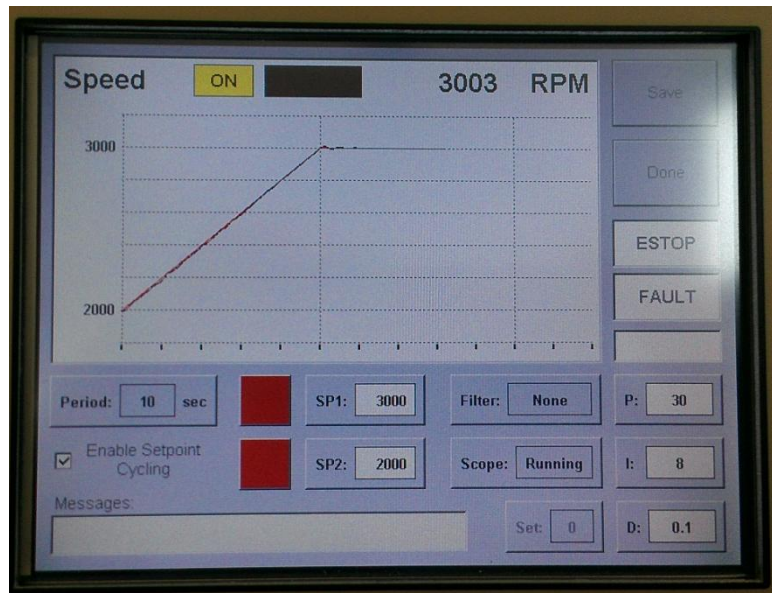


Figure 5-80. Tuning Window: Ramp Response Following PID Tuning.

Thus, the derivative gain is reduced to 0.1, producing the best results, as shown in Figure 5-80. These gains are saved to the controller by pressing 'Save' and 'Done' on the touch screen. Finally, the P, I, and D gains for the unloaded dynamometer are set to 30, 8, and 0.1, respectively. This is in agreement with the tuning performed during dynamometer commissioning by the personnel of Dyne Systems, Incorporated. Following the connection of the engine, the dynamometer control gains will need further tuning for optimum performance.

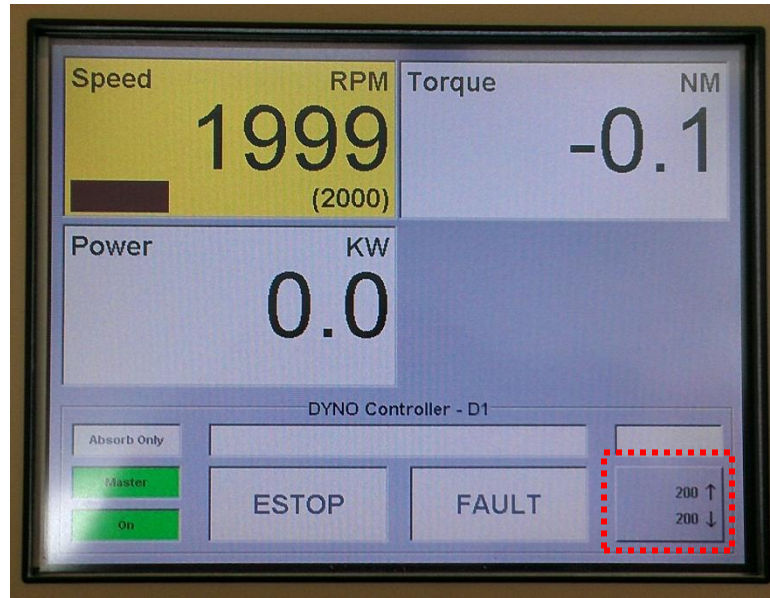


Figure 5-81. Main Operating Window: Ramp Rate Adjustment.

The ramp rate used during tuning (and for transient tests) can be changed during operation from the main operating screen by pressing the ramp rate button on the touch screen (red in Figure 5-81).

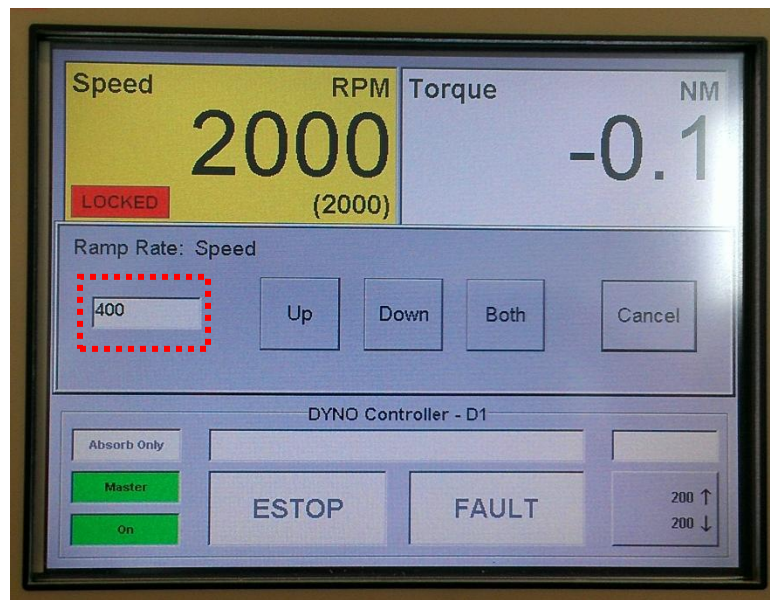


Figure 5-82. Ramp Rate Adjustment Dialog Box.

Pressing this portion of the screen opens the ramp rate adjustment dialog box, shown in Figure 5-82. The operator may use this box to input new ramp rates that correspond to ramps up in speed,

down in speed, or both up and down. This is done by entering a number value into the input box (red box) and pressing the desired ramp direction to apply the value to (Up, Down, Both).

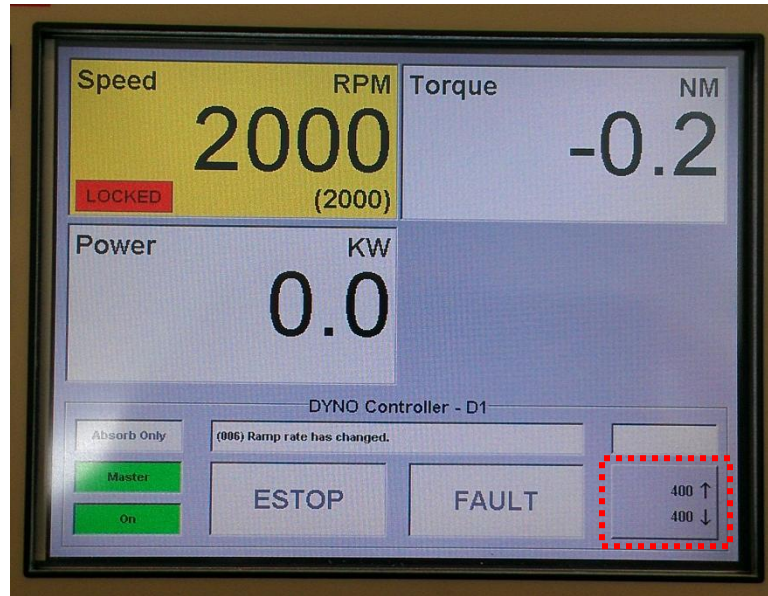


Figure 5-83. Main Operating Window: Ramp Rate Changed to 400 RPM/sec.

This closes the window, but changes are reflected on the main operating window, as indicated by the red box in Figure 5-83.

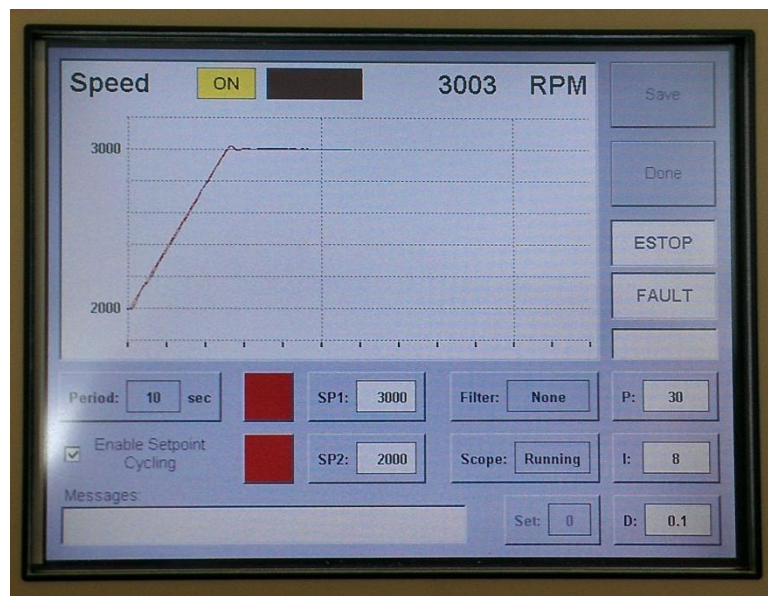


Figure 5-84. Tuning Window: Response to Higher Ramp Rate.

The effects of ramp on the dynamometer response is shown by re-entering the tuning window and initiating a cyclic setpoint, the slope of the ramp is steeper, but good response is evident in Figure 5-84. If additional tuning at this ramp rate is necessary, this can be done at this point. If no tuning is needed, pressing ‘Done’ on the touch screen returns the operator to the main operating window.

Conclusion

The University of Kansas is devoting significant effort into biofuel research in order to determine the feasibility of providing sustainable energy sources for the transportation industry. Specifically, engineers are working to understand not only the growth and production process, but also the way in which these potential fuels can be burned using existing engine technologies. At KU, this is currently accomplished using a single-cylinder CI engine. Through years of graduate student development, this engine presents many experimental opportunities due to its variety of systems. This includes the work from Chapter 1 of this dissertation that covers the replacement of the mechanical fuel injection system with a modern, electronically-controlled, common-rail fuel system. This system gives researchers precise control of the fuel injection process and allows not only dynamic adjustment of injection timing and pressure, along with the opportunity to perform up to five injection events per combustion event. This ability opens the doors to low-temperature combustion research and natural gas-assisted combustion.

This working system was used to perform two studies on biodiesel, which were covered in Chapter 2 of this dissertation. The first study investigated the effects of biodiesel fuel properties, such as viscosity, unsaturation, and energy content on engine combustion and emissions. This experiment also utilized the dynamic injection control (and in-cylinder pressure measurement) to perform combustion phasing normalization. This strategy removed the overshadowing effects of combustion timing on combustion heat release and resultant exhaust emissions, allowing for direct comparison between the results of each fuel. The results indicated that relationships between fuel property and in-cylinder behavior and emissions were more strongly correlated when combustion phasing was adjusted.

Furthermore, the observed reduction in NO_x emissions for biodiesel was concluded to be a result of higher biodiesel viscosity, which reduced the premixed combustion phase. This reduction, however, led to higher PM production at low engine loadings due to reduced injector effectiveness. The second study of Chapter 2 used the same four feedstock biodiesels burned as blends with ULSD in 5%, 10%, 20%, 50%, and neat biodiesel mixtures. The results supported the findings of the first, neat-biodiesel study and expanded upon it by investigating the linear/non-linear behavior of combustion and emissions as a function of biodiesel blend percentage. Results indicated that the non-linear behavior of viscosity and flash point with blend percentage, combined with the strong influence of viscosity on combustion, produces a non-linear cylinder peak pressure correlation through a reduced premixed burn phase. This non-linear behavior affects engine fuel economy and emissions in a similar non-linear fashion. Of particular interest was the output of PM with respect to biodiesel blend, with a peak in PM production occurring at 50% biodiesel for all biodiesel feedstocks below rated torque. This was attributed to the increase in viscosity with blend, which reduces atomization, eventually being offset by the increasing oxygen content with biodiesel blend, which acts to lean out rich fuel cores through fuel oxygenation. The effect of molecular structure, particularly poly-unsaturation, was evident through a more non-linear PM behavior with blend as fuel unsaturation increased. This is an artifact of this fuel being more difficult to fully oxidize. Eventually, this too was overshadowed by viscosity at higher biodiesel blends.

Much like the search for viable renewable fuels for ground-based engines, research is ongoing in the field of renewable jet fuels for turbine engines. Because of the US Military's single fuel forward policy and approval of renewable fuels in turbine engines, it is important to study and understand the viability of burning both renewable and petroleum-based jet propellant in a CI engine. Renewable jet fuels, such as the hydrotreated fuel tested in Chapter 3 (R-8), are produced in a similar method to biodiesel, but carry little oxygenation in the fuel molecules. As a result, R-8 carries higher energy content and lower viscosity than ULSD, for which the engine and fuel system are designed. In this study,

potential performance of petroleum and renewable jet propellants are tested against ULSD through adjustment of injection timing for minimum fuel consumption. The results indicated that the renewable jet fuel tested consistently has lower fuel consumption and NO_x, CO, and HC emissions than either petroleum-based jet propellant (Jet-A) or ULSD. PM production was similar between all three adjusted fuels. The high performance of R-8 was attributed to its higher energy content and lower viscosity and density, which extended the injection timing event and reduced premixed combustion and associated thermal NO_x emissions. In addition to experimentation with neat fuels, blends of Jet-A and R-8 found a generally linear progression in the behavior of combustion and emissions with R-8/Jet-A blend ratio. Adjustment of injection timing through the blend experiment showed a reduction in NO_x and PM emissions and slightly reduced fuel consumption. As a result of injection timing delay with R-8 blend, an increase in CO and HC are observed due to lower combustion temperatures.

Chapter 4 covers the operation, maintenance, and upgrading procedure of the single-cylinder engine. This is necessary due to the highly customized nature of this engine and the rapid turnover of graduate personnel. With the material covered, new students will have a good primer for conducting research, as well as, a foundation for how to upgrade the laboratory to perform their own experiments. While the single-cylinder engine is capable of performing a variety of research endeavors, it is highly customized and is therefore, only a representation of a modern production engine. In order to obtain a full understanding of the effects of different biodiesels on a production engine, a new laboratory is being built around a multi-cylinder Duramax CI engine. This engine uses current production technology, including cooled EGR, turbocharging, and common-rail fuel injection. Like the single-cylinder engine laboratory, completion of the new multi-cylinder laboratory will take considerable time and effort. This is primarily due to the expansive amount of auxiliary systems needed to test an engine. Major systems include engine control, loading, cooling, fuel integration, instrumentation, and emissions measurement.

In its current state, the Duramax engine sits in its final location, supported by two of the four anticipated engine supports. A driveline system has been partially installed, which includes a torque-dampening coupler to remove torque spikes from the engine. This coupler is housed in a steel scatter shield to protect equipment and personnel in the event of a failure. The three-phase AC dynamometer is installed with power available and commissioning complete. Power generated by the engine is sent onto the grid through the regenerative capabilities of the dynamometer. Test cell environmental control is largely in place and ready for operation. This system is composed of several auxiliary systems. The engine intake air handling systems allows researchers to specify intake air pressure, temperature, and relative humidity. Additionally, the test cell air handling system maintains constant room pressure and temperature, though temperature is dependent on outside temperature as cooling capabilities are not yet in place. Hot engine coolant is chilled via a glycol loop that transfers generated heat to the building glycol system for heating. A similar system is used to lower the temperature of engine intake air following compression by the turbocharger.

Currently, several major milestones remain before the engine can be actually motored and begin to burn fuel. These tasks will be completed as time and resources allow. They are:

- Connection of the engine to building auxiliary systems (coolant, intercooler, fuel system, intake air, and exhaust)
- Completion of the engine mounting supports
- Coupling of the engine to the dynamometer
- Retuning of the dynamometer to account for the added inertia of the engine
- Installation and configuration of engine control unit to manage fuel, turbocharger, and EGR systems
- Purchase and installation of instrumentation to measure engine performance (particularly air flow, fuel flow, intake conditions, engine torque, exhaust conditions, in-cylinder pressure, etc.)

- Setup of data acquisition system to display and record measurements and communicate with auxiliary test cell controller and dynamometer
- Emissions equipment will also be necessary in order to perform research, but is not immediately necessary to get the engine running

Following the completion of these objectives, the engine will be ready for initial testing. Many of the systems in place will be operated in a similar, albeit more complicated, fashion than the single-cylinder test cell. Nevertheless, students that are trained on the single cylinder engine will be able to immediately contribute to the research in the multi-cylinder laboratory. In closing, it is the hope of this author that the knowledge shared here will prove to be a useful foundation for future students who perform their own engine research at the University of Kansas.

References

- [1] J. B. Heywood, "Internal combustion engine fundamentals," 1988.
- [2] R. Ferguson Colin and T. Kirkpatrick Allan, "Internal Combustion Engines: Applied Thermo sciences," *John Wiley & Sons, Inc*, 2001.
- [3] W. D. Van Vorst, "Impact of the California clean air act," *International Journal of Hydrogen Energy*, vol. 22, pp. 31-38, 1997.
- [4] A. Haagen-Smit, "Chemistry and physiology of Los Angeles smog," *Industrial & Engineering Chemistry*, vol. 44, pp. 1342-1346, 1952.
- [5] W. A. Eckerle, E. J. Lyford-Pike, D. W. Stanton, L. A. LaPointe, S. Whitacre, and J. C. Wall, "Effects of methyl ester biodiesel blends on NOx emissions," *SAE SP*, vol. 2169, p. 53, 2008.
- [6] (1994). *Milestones in Auto Emissions Control*. Available: <http://www.epa.gov/otaq/consumer/12-miles.pdf>
- [7] M. V. Melosi. (December 17, 2013). *The Automobile and the Environment in American History - Auto Emissions and Air Pollution*. Available: http://www.autolife.umd.umich.edu/Environment/E_Overview/E_Overview4.htm
- [8] A. Atabani, A. Silitonga, I. A. Badruddin, T. Mahlia, H. Masjuki, and S. Mekhilef, "A comprehensive review on biodiesel as an alternative energy resource and its characteristics," *Renewable and Sustainable Energy Reviews*, vol. 16, pp. 2070-2093, 2012.
- [9] U.S.E.P.A. (2013, June 15, 2013). *Tier 3 Vehicle Emissions and Fuel Standards Program*. Available: <http://www.epa.gov/otaq/tier3.htm>
- [10] U.S.E.P.A. (2004, June 15, 2013). *Regulatory Announcement - Clean Air Nonroad Diesel Rule*. Available: <http://www.epa.gov/otaq/documents/nonroad-diesel/420f04032.pdf>
- [11] B. Bradley, T. Ridge, and D. Walker, "Road To Recovery: Transforming America's Transportation," 2011.
- [12] C. Ragone, "Emission Reduction and Assisted Combustion Strategies for Compression Ignition Engines with Subsequent Testing on a Single-Cylinder Engine," KU ScholarWorks, 2012.
- [13] (2007, December 17, 2013). *U.S. Department of Energy 21st Century Truck Partnerships: Roadmap and Technical White Papers*. Available: http://www1.eere.energy.gov/vehiclesandfuels/pdfs/program/21ctp_roadmap_2007.pdf
- [14] N. H. T. S. Administration. (2012, June 16, 2013). *Obama Administrations Finalizes Historic 54.5 mpg Fuel Efficiency Standards*. Available: <http://www.nhtsa.gov/About+NHTSA/Press+Releases/2012/Obama+Administration+Finalizes+Historic+54.5+mpg+Fuel+Efficiency+Standards>
- [15] G. Knothe, J. H. Van Gerpen, and J. Krahl, *The biodiesel handbook* vol. 1: AOCS press Champaign, IL, 2005.
- [16] E. Cecrle, C. Depcik, A. Duncan, J. Guo, M. Mangus, E. Peltier, S. Stagg-Williams, and Y. Zhong, "Investigation of the Effects of Biodiesel Feedstock on the Performance and Emissions of a Single-Cylinder Diesel Engine," *Energy & Fuels*, vol. 26, pp. 2331-2341, 2012.
- [17] R. McCormick, M. Graboski, T. Alleman, A. Herring, and K. Tyson, "Impact of biodiesel source material and chemical structure on emissions of criteria pollutants from a heavy-duty engine," *Environ. Sci. Technol*, vol. 35, pp. 1742-1747, 2001.
- [18] U. Azimov, E. Tomita, and N. Kawahara, "Combustion and Exhaust Emission Characteristics of Diesel Micro-Pilot Ignited Dual-Fuel Engine," 2013.
- [19] M. Mangus and C. Depcik, "Comparison of ULSD, Used Cooking Oil Biodiesel, and JP-8 Performance and Emissions in a Single-Cylinder Compression-Ignition Engine," 2012.
- [20] M. D. Mangus, "Design, Construction, and Validation of an In-Cylinder Pressure Recording System for Internal Combustion Engine Analysis," KU ScholarWorks, 2012.

- [21] K. Komiyama, "Predicting NoDx Emissions and Effects of Exhaust Gas Recirculation in Spark-Ignition Engines," 1973.
- [22] G. A. Lavoie, J. B. Heywood, and J. C. Keck, "Experimental and theoretical study of nitric oxide formation in internal combustion engines," *Combustion Science and Technology*, vol. 1, pp. 313-326, 1970.
- [23] R. C. Yu and S. Shahed, "Effects of injection timing and exhaust gas recirculation on emissions from a DI diesel engine," *SAE Prepr.;(United States)*, vol. 811234, 1981.
- [24] D. Kawano, H. Ishii, Y. Goto, A. Noda, and Y. Aoyagi, "Effect of Exhaust Gas Recirculation on Exhaust Emissions from Diesel Engines Fuelled with Biodiesel," *SAE Technical Paper*, pp. 24-0128, 2007.
- [25] L. Murphy and D. Rothamer, "Effects of Cetane Number on Jet Fuel Combustion in a Heavy-Duty Compression Ignition Engine at High Load," *Internal Combustion Engines*, vol. 2013, pp. 04-08.
- [26] D. S. T. Fuel and K. T. Aviation, "JP-8 (NATO F-34), NATO F-35, and JP-8+ 100 (NATO F-37)," MIL-DTL-83133F2008.
- [27] X. Hui, K. Kumar, C.-J. Sung, T. Edwards, and D. Gardner, "Experimental studies on the combustion characteristics of alternative jet fuels," *Fuel*, vol. 98, pp. 176-182, 2012.
- [28] A. L. Boehman, D. Morris, J. Szybist, and E. Esen, "The impact of the bulk modulus of diesel fuels on fuel injection timing," *Energy & Fuels*, vol. 18, pp. 1877-1882, 2004.
- [29] C. J. Mueller, A. L. Boehman, and G. C. Martin, "An experimental investigation of the origin of increased NO_x emissions when fueling a heavy-duty compression-ignition engine with soy biodiesel," *SAE Int. J. Fuels Lubr*, vol. 2, pp. 789-816, 2009.
- [30] M. Tat and J. Van Gerpen, "Measurement of biodiesel speed of sound and its impact on injection timing," *National Renewable Energy Laboratory, NREL/SR-510-31462*, 2003.
- [31] M. E. Tat, J. H. Van Gerpen, S. Soylu, M. Canakci, A. Monyem, and S. Wormley, "The speed of sound and isentropic bulk modulus of biodiesel at 21 C from atmospheric pressure to 35 MPa," *Journal of the American Oil Chemists' Society*, vol. 77, pp. 285-289, 2000.
- [32] (September 1, 2013). Available: <http://www.alexldiesel.com/upload/image/25517981.jpg>
- [33] C. Csere. (2011, Piezo Fuel Injectors Explained. (January 2011). Available: <http://www.caranddriver.com/features/tech-department-piezo-fuel-injectors-explained>
- [34] T. Zobel. (2010, Function Sheet MS15.1 - Solenoid Valve.
- [35] T. M. Martin, "High pressure electronic common-rail fuel injection system for diesel engines," ed: Google Patents, 1992.
- [36] N. Guerrassi, "A common rail injection system for high-speed, direct-injection diesel engines," 1998.
- [37] G. Stumpp and M. Ricco, "Common rail: an attractive fuel injection system for passenger car DI diesel engines," *SAE paper*, vol. 960870, p. 996, 1996.
- [38] E. D. Cecrle, "Controls and measurements of KU engine test cells for biodiesel, SynGas, and assisted biodiesel combustion," *KU ScholarWorks*, 2011.
- [39] E. Cecrle, C. Depcik, J. Guo, and E. Peltier, "Analysis of the effects of reformatte (hydrogen/carbon monoxide) as an assistive fuel on the performance and emissions of used canola-oil biodiesel," *International Journal of Hydrogen Energy*, 2011.
- [40] J. Mattson, "Power, Efficiency, and Emissions Optimization of a Single Cylinder Direct-Injected Diesel Engine for Testing of Alternative Fuels Through Heat Release Modelling," *KU ScholarWorks*, 2013.
- [41] "Meeting the aspirations of a Global Market Technical Manual for Autosport," D. A. LTD, Ed., ed, 2005.

- [42] C. Mueller, A. Boehman, and G. Martin, "An Experimental Investigation of the Origin of Increased NOx Emissions When Fueling a Heavy-Duty Compression-Ignition Engine with Soy Biodiesel," *SAE International Journal of Fuels and Lubricants*, vol. 2, p. 789, 2009.
- [43] "Temperature Sensor NTC M12-H Datasheet," B. Motorsport, Ed., ed, 2012.
- [44] "Pressure Sensor Air PST Datasheet," B. Motorsport, Ed., ed, 2012.
- [45] Syntroleum. (November 8, 2013). *Bio-Synfining -Dynamic Fuels Plant*. Available: <http://www.b2i.us/profiles/investor/fullpage.asp?BzID=2029&to=cp&Nav=0&LangID=1&s=0&ID=11923>
- [46] E. D. Cecrle, "Controls and Measurements of KU Engine Test Cells for Biodiesel, SynGas, and Assisted Biodiesel Combustion," Master of Science, Mechanical Engineering, University of Kansas, Lawrence, Kansas, 2011.
- [47] A. Boehman, D. Morris, J. Szybist, and E. Esen, "The impact of the bulk modulus of diesel fuels on fuel injection timing," *Energy Fuels*, vol. 18, pp. 1877-1882, 2004.
- [48] A. Duncan, A. Ahosseini, R. McHenry, C. Depcik, S. Stagg-Williams, and A. Scurto, "High-Pressure Viscosity of Biodiesel from Soybean, Canola, and Coconut Oils," *Energy & Fuels*, pp. 125-164.
- [49] M. S. Graboski and R. L. McCormick, "Combustion of fat and vegetable oil derived fuels in diesel engines," *Progress in Energy and Combustion Science*, vol. 24, pp. 125-164, 1998.
- [50] G. Knothe, "Dependence of biodiesel fuel properties on the structure of fatty acid alkyl esters," *Fuel Processing Technology*, vol. 86, pp. 1059-1070, 2005.
- [51] G. Knothe, J. Van Gerpen, J. Krahl, and C. Press, *The biodiesel handbook*: AOCS press Champaign, IL, 2005.
- [52] R. McCormick, A. Williams, J. Ireland, M. Brimhall, and R. Hayes, "Effects of biodiesel blends on vehicle emissions," *Milestone Report. National Renewable Energy Laboratory, NREL/MP-540-40554*, 2006.
- [53] R. L. McCormick, J. R. Alvarez, M. S. Graboski, K. Tyson, and K. Vertin, "Fuel additive and blending approaches to reducing NOx emissions from biodiesel," *SAE Tech. Pap*, p. 1658, 2002.
- [54] A. Pinto, L. Guarieiro, M. Rezende, N. Ribeiro, E. Torres, W. Lopes, P. Pereira, and J. Andrade, "Biodiesel: an overview," *Journal of the Brazilian Chemical Society*, vol. 16, pp. 1313-1330, 2005.
- [55] P. Ye and A. L. Boehman, "Investigation of the Impact of Engine Injection Strategy on the Biodiesel NOx Effect with a Common-Rail Turbocharged Direct Injection Diesel Engine," *Energy & Fuels*, vol. 24, pp. 4215-4225, 2010.
- [56] E. Cecrle, C. Depcik, A. Duncan, J. Guo, M. D. Mangus, E. Peltier, S. M. Stagg-Williams, and Y. Zhong, "An Investigation of the Effects of Biodiesel Feedstock on the Performance and Emissions of a Single-Cylinder Diesel Engine," *Energy & Fuels*.
- [57] U. S. E. P. Agency, "Summary of Current and Historical Light-Duty Vehicle Emission Standards."
- [58] United States Environmental Protection Agency, "A Comprehensive Analysis of Biodiesel Impacts on Exhaust Emissions," Assessment and Standard Division, Office of Transportation and Air Quality, USEPA, Washington, DC EPA 420-P-02-001, 2002.
- [59] R. N. P. Diego Romero, Subramanyam R. Gollahalli, "LAMINAR FLAME CHARACTERISTICS OF PARTIALLY PREMIXED PALM METHYL ESTER GAS FLAMES," in *ASME 2013 International Mechanical Engineering Congress and Exposition*, San Diego, California, 2013.
- [60] C. Fenimore, "Formation of nitric oxide in premixed hydrocarbon flames," in *Symposium (International) on Combustion*, 1971, pp. 373-380.
- [61] J. Park, J. S. Park, H. P. Kim, J. S. Kim, S. C. Kim, J. G. Choi, H. C. Cho, K. W. Cho, and H. S. Park, "NO emission behavior in oxy-fuel combustion recirculated with carbon dioxide," *Energy & Fuels*, vol. 21, pp. 121-129, 2007.
- [62] C. S. Lee, S. W. Park, and S. I. Kwon, "An experimental study on the atomization and combustion characteristics of biodiesel-blended fuels," *Energy & Fuels*, vol. 19, pp. 2201-2208, 2005.

- [63] C. He, Y. Ge, J. Tan, and X. Han, "Spray properties of alternative fuels: A comparative analysis of biodiesel and diesel," *International Journal of Energy Research*, vol. 32, pp. 1329-1338, 2008.
- [64] K. Harrington, "Chemical and physical properties of vegetable oil esters and their effect on diesel fuel performance," *Biomass*, vol. 9, pp. 1-17, 1986.
- [65] M. Mangus and C. Depcik, "Comparison of ULSD, Used Cooking Oil Biodiesel, and JP-8 Performance and Emissions in a Single-Cylinder Compression-Ignition Engine," *SAE International Journal of Fuels and Lubricants*, vol. 5, pp. 1382-1394, 2012.
- [66] I. Rizwanul Fattah, H. Masjuki, A. Liaquat, R. Ramli, M. Kalam, and V. Riazuddin, "Impact of various biodiesel fuels obtained from edible and non-edible oils on engine exhaust gas and noise emissions," *Renewable and Sustainable Energy Reviews*, vol. 18, pp. 552-567, 2013.
- [67] C. K. Westbrook, "Biofuels Combustion*," *Annual review of physical chemistry*, vol. 64, pp. 201-219, 2013.
- [68] M. García, A. Gonzalo, J. L. Sánchez, J. Arauzo, and J. Á. Peña, "Prediction of normalized biodiesel properties by simulation of multiple feedstock blends," *Bioresource technology*, vol. 101, pp. 4431-4439, 2010.
- [69] "Standard Specification for Diesel Fuel Oils," *ASTM International Specification: ASTM D975-10c*, 2010.
- [70] D. R. Lide Jr, "A survey of carbon-carbon bond lengths," *Tetrahedron*, vol. 17, pp. 125-134, 1962.
- [71] G. G. Zhu, C. F. Daniels, and J. Winkelman, "MBT Timing Detection and its Closed-LoopControl Using In-Cylinder Pressure Signal," *SAE Technical Paper*, 2003.
- [72] G. Knothe, ""Designer" Biodiesel: Optimizing Fatty Ester Composition to Improve Fuel Properties†," *Energy & Fuels*, vol. 22, pp. 1358-1364, 2008.
- [73] M. Lapuerta, J. Rodríguez-Fernández, and O. Armas, "Correlation for the estimation of the density of fatty acid esters fuels and its implications. A proposed Biodiesel Cetane Index," *Chemistry and physics of lipids*, vol. 163, pp. 720-727, 2010.
- [74] A. Demirbas, "Relationships derived from physical properties of vegetable oil and biodiesel fuels," *Fuel*, vol. 87, pp. 1743-1748, 2008.
- [75] R. L. McCormick, A. Williams, J. Ireland, and R. Hayes, "Effects of Biodiesel Blends on Vehicle Emissions: Fiscal Year 2006 Annual Operating Plan Milestone 10.4," National Renewable Energy Laboratory (NREL), Golden, CO.2006.
- [76] M. Kousoulidou, G. Fontaras, L. Ntziachristos, and Z. Samaras, "Biodiesel blend effects on common-rail diesel combustion and emissions," *Fuel*, vol. 89, pp. 3442-3449, 2010.
- [77] R. Kotrba. (November 24, 2013). *Understanding the Post-Injection Problem*. Available: <http://www.biodieselmagazine.com/articles/2290/understanding-the-post-injection-problem/>
- [78] (2013, October 15, 2013). *OEM Statement Summary Chart - National Biodiesel Board*. Available: <http://www.biodiesel.org/using-biodiesel/oem-information/oem-statement-summary-chart>
- [79] J. Van Gerpen, "Business management for biodiesel producers," *Report from Iowa State University for the National Renewable Energy Laboratory, NREL/SR-510-36242*, 2004.
- [80] *Energy Information Administration Sales of Distillate Fuel Oil by End Use*. Available: http://www.eia.gov/dnav/pet/pet_cons_821dst_a_EPD2D_VHN_Mgal_a.htm
- [81] (2012, October 15, 2013). *Federal Laws and Incentives for Biodiesel - U.S. Department of Energy*. Available: <http://www.afdc.energy.gov/fuels/laws/3251/US>
- [82] R. L. McCormick, M. S. Graboski, T. L. Alleman, A. M. Herring, and K. S. Tyson, "Impact of biodiesel source material and chemical structure on emissions of criteria pollutants from a heavy-duty engine," *Environmental Science & Technology*, vol. 35, pp. 1742-1747, 2001.
- [83] J. Guo, E. Peltier, R. E. Carter, A. J. Krejci, S. M. Stagg-Williams, and C. Depcik, "Waste Cooking Oil Biodiesel Use in Two Off-Road Diesel Engines," *ISRN Renewable Energy*, vol. 2012, 2012.

- [84] M. J. Ramos, C. M. Fernandez, A. Casas, L. Rodriguez, and A. Perez, "Influence of fatty acid composition of raw materials on biodiesel properties," *Bioresource technology*, vol. 100, pp. 261-268, 2009.
- [85] K. Krisnangkura, T. Yimsuwan, and R. Pairintra, "An empirical approach in predicting biodiesel viscosity at various temperatures," *Fuel*, vol. 85, pp. 107-113, 2006.
- [86] M. H. Topal, J. Wang, Y. A. Levendis, J. B. Carlson, and J. Jordan, "PAH and other emissions from burning of JP-8 and diesel fuels in diffusion flames," *Fuel*, vol. 83, pp. 2357-2368, 2004.
- [87] G. Fernandes, J. Fuschetto, Z. Filipi, D. Assanis, and H. McKee, "Impact of military JP-8 fuel on heavy-duty diesel engine performance and emissions," *Proceedings of the Institution of Mechanical Engineers, Part D: Journal of Automobile Engineering*, vol. 221, pp. 957-970, 2007.
- [88] K. Wadumesthrige, N. Johnson, M. Winston-Galant, and E. Sattler, "Performance, Durability, and Stability of a Power Generator Fueled with ULSD, S-8, JP-8, and Biodiesel," *Training*, vol. 2013, pp. 11-04, 2010.
- [89] T. Moran, "The Logistics Battle: US wages a one-fuel war," *Automotive news*, 2003.
- [90] D. A. Rothamer and L. Murphy, "Systematic study of ignition delay for jet fuels and diesel fuel in a heavy-duty diesel engine," *Proceedings of the combustion institute*, 2012.
- [91] S. Blakey, L. Rye, and C. W. Wilson, "Aviation gas turbine alternative fuels: A review," *Proceedings of the combustion institute*, vol. 33, pp. 2863-2885, 2011.
- [92] E. Corporan, T. Edwards, L. Shafer, M. J. DeWitt, C. Klingshirn, S. Zabarnick, Z. West, R. Striebich, J. Graham, and J. Klein, "Chemical, thermal stability, seal swell, and emissions studies of alternative jet fuels," *Energy & Fuels*, vol. 25, pp. 955-966, 2011.
- [93] E. Corporan, M. J. DeWitt, V. Belovich, R. Pawlik, A. C. Lynch, J. R. Gord, and T. R. Meyer, "Emissions characteristics of a turbine engine and research combustor burning a Fischer-Tropsch jet fuel," *Energy & Fuels*, vol. 21, pp. 2615-2626, 2007.
- [94] J. I. Hileman, P. E. Donohoo, and R. W. Stratton, "Energy content and alternative jet fuel viability," *Journal of propulsion and power*, vol. 26, pp. 1184-1196, 2010.
- [95] A. International, "Standard Specification for Aviation Turbine Fuels," ed.
- [96] P. Kallio, A. Pásztor, M. K. Akhtar, and P. R. Jones, "Renewable jet fuel," *Current Opinion in Biotechnology*, vol. 26, pp. 50-55, 2014.
- [97] D. R. Shonnard, L. Williams, and T. N. Kalnes, "Camelina-derived jet fuel and diesel: Sustainable advanced biofuels," *Environmental Progress & Sustainable Energy*, vol. 29, pp. 382-392, 2010.
- [98] D. Daggett, O. Hadaller, L. Maurice, and M. Rumizen, "The Commercial Aviation Alternative Fuels Initiative," *Training*, vol. 2007, pp. 08-21.
- [99] T. Edwards, C. Moses, and F. Dryer, "Evaluation of combustion performance of alternative aviation fuels," *AIAA/ASME/SAE/ASEE Joint Propulsion Conference and Exhibit*, 2010.
- [100] C. Allen, D. Valco, E. Toulson, T. Edwards, and T. Lee, "Ignition behavior and surrogate modeling of JP-8 and of camelina and tallow hydrotreated renewable jet fuels at low temperatures," *Combustion and Flame*, 2012.
- [101] S. Darrah, "Jet Fuel Deoxygenation," DTIC Document1988.
- [102] R. N. Hazlett, *Thermal Oxidation Stability of Aviation Turbine Fuels: Monograph 1* vol. 1: Astm International, 1991.
- [103] J. Mattson and C. Depcik, "Emissions-calibrated equilibrium heat release model for direct injection compression ignition engines," *Fuel*, 2013.
- [104] "Standard Specification for Diesel Fuel Oils," *ASTM International Specification: ASTM D975-13*, 2013.
- [105] (2012, December 4, 2013). Yanmar YDG5500E Diesel Generator. Available: <http://www.riequip.co.nz/shop/Generators/Yanmar+YDG5500E+Diesel+Generators/Yanmar+YDG5500E+Diesel+Generator.html>

- [106] J. B. Heywood, *Internal Combustion Engine Fundamentals*. New York: McGraw-Hill, Inc., 1988.
- [107] (2010, December 8, 2013). *ASCII Table and Description*. Available: www.AsciiTable.com
- [108] "Kistler Instruction Manual Crank Angle Encoder 2614B," Winterthur, Switzerland2011.
- [109] (2013, December 9, 2013). *SESAM i60 FT Multi Component Exhaust Measureing System*. Available: <https://www.avl.com/sesam-i60-ft>
- [110] (December 10, 2013). *ALV Smoke Meter 415SE*. Available: https://www.avl.com/c/document_library/get_file?uuid=27a3547f-6f90-4a0a-bc4c-c570f2c08129&groupId=10138
- [111] (2013, November 22, 2013). *Duramax LBZ Specs*. Available: <http://www.duramaxdieselspecs.com/lbz.html>
- [112] A. J. Martyr and M. A. Plint, *Engine Testing: The Design, Building, Modification and Use of Powertrain Test Facilities*: Butterworth-Heinemann, 2012.

Chapter 6: Appendices

The following sections comprise the supplemental material produced during the biodiesel studies of Chapter 2 and the renewable jet fuel study of Chapter 3.

A.1 Supplemental Figures and Tables from Chapter 2 – Study 1

Normalized Heat Release Rate is calculated by the division of instantaneous heat release rate (as a function of crank angle) by the total heat release that occurs in that combustion event. Normalized heat release rate serves as a means of determining the relative amount of energy released during the premixed and diffusion burn phases[40].

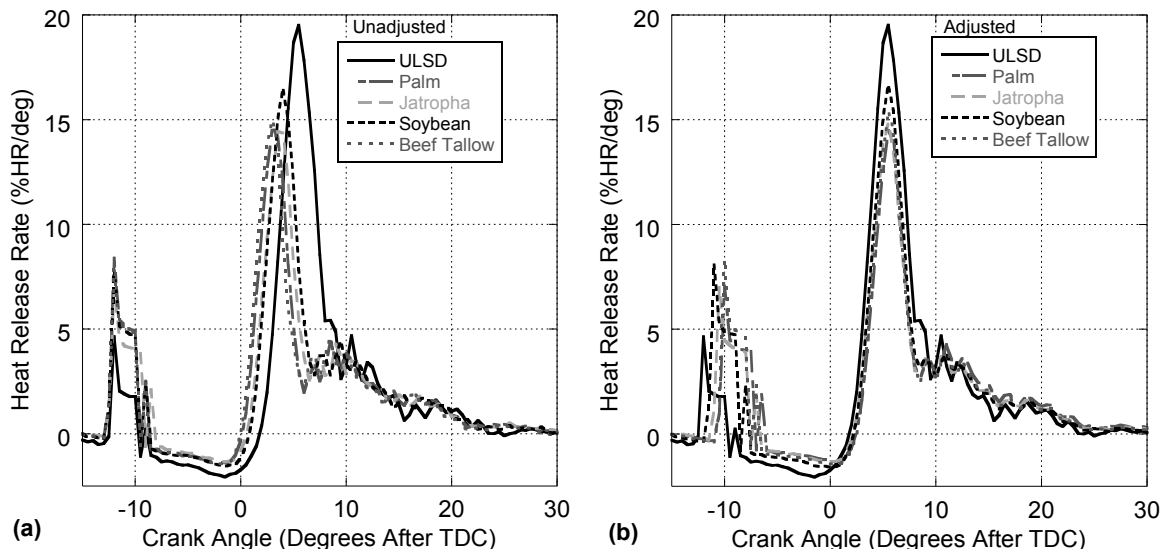


Figure A-1. Normalized Heat Release Rate vs. Engine Crank Angle at 0.5 N·m Load for Unadjusted (a) and Adjusted (b) Injection Timing.

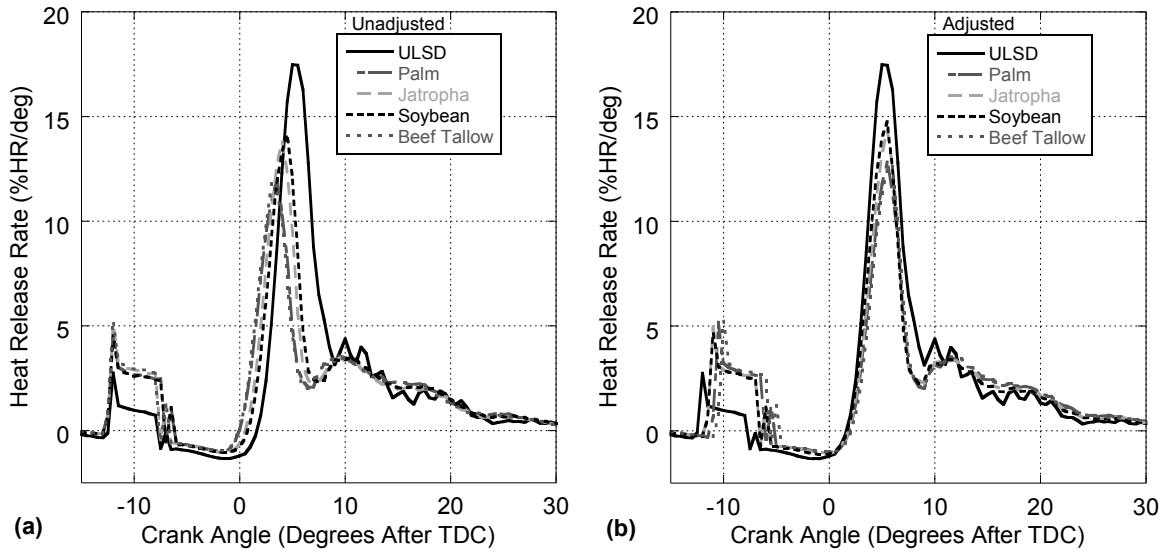


Figure A-2. Normalized Heat Release Rate vs. Engine Crank Angle at 4.5 N·m Load for Unadjusted (a) and Adjusted (b) Injection Timing.

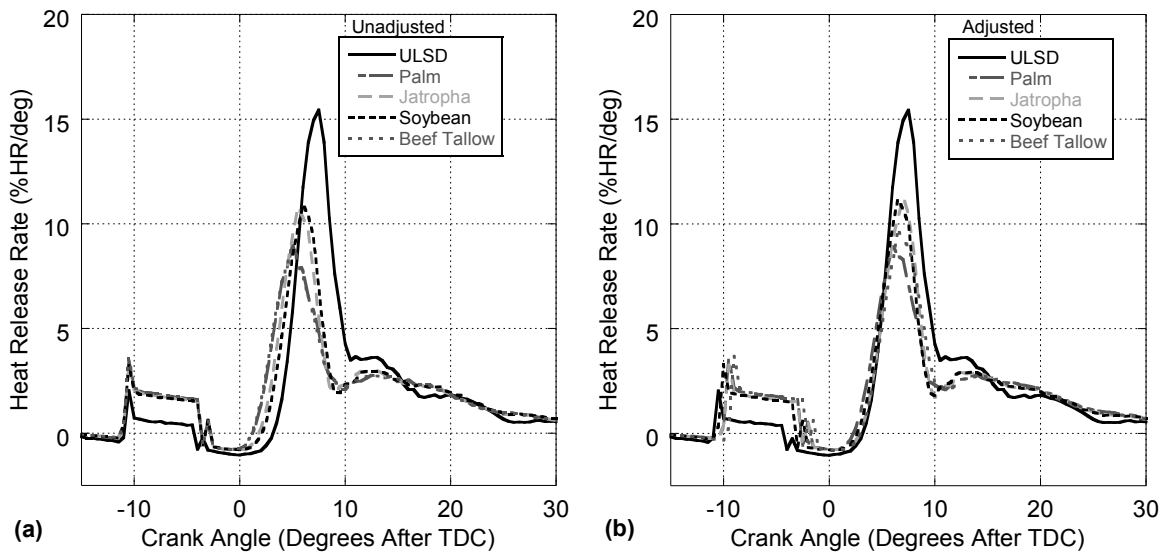


Figure A-3. Normalized Heat Release Rate vs. Engine Crank Angle at 9.0 N·m Load for Unadjusted (a) and Adjusted (b) Injection Timing.

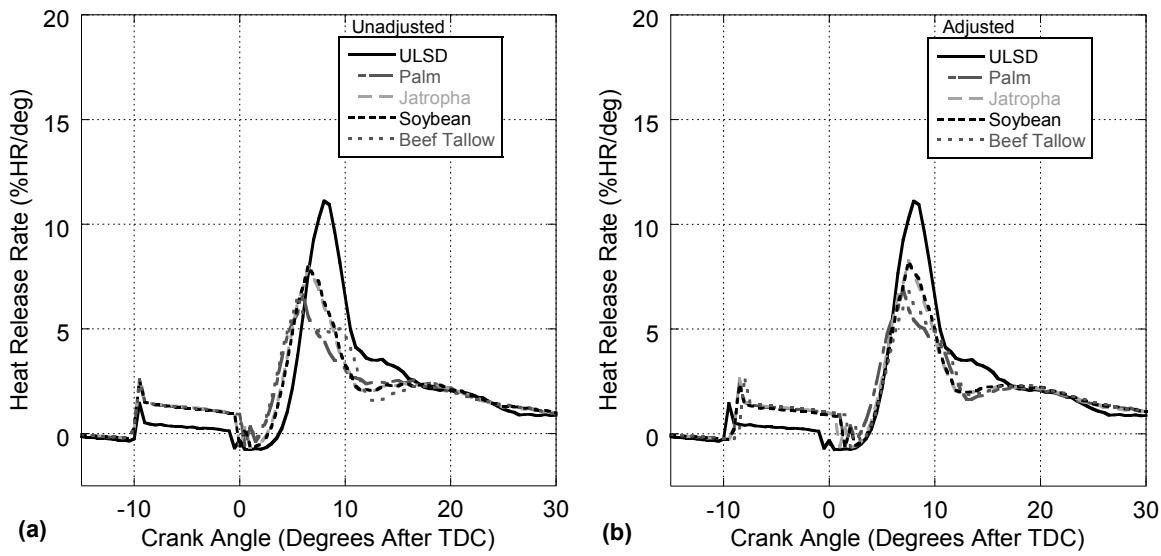


Figure A-4. Normalized Heat Release Rate vs. Engine Crank Angle at 13.5 N·m Load for Unadjusted (a) and Adjusted (b) Injection Timing.

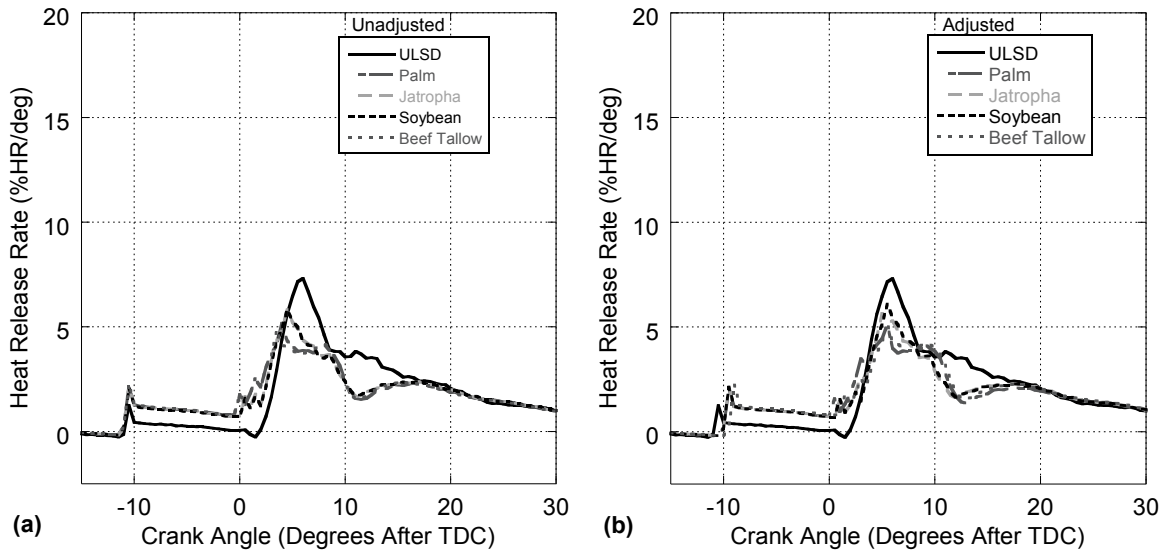


Figure A-5. Normalized Heat Release Rate vs. Engine Crank Angle at 18.0 N·m Load for Unadjusted (a) and Adjusted (b) Injection Timing.

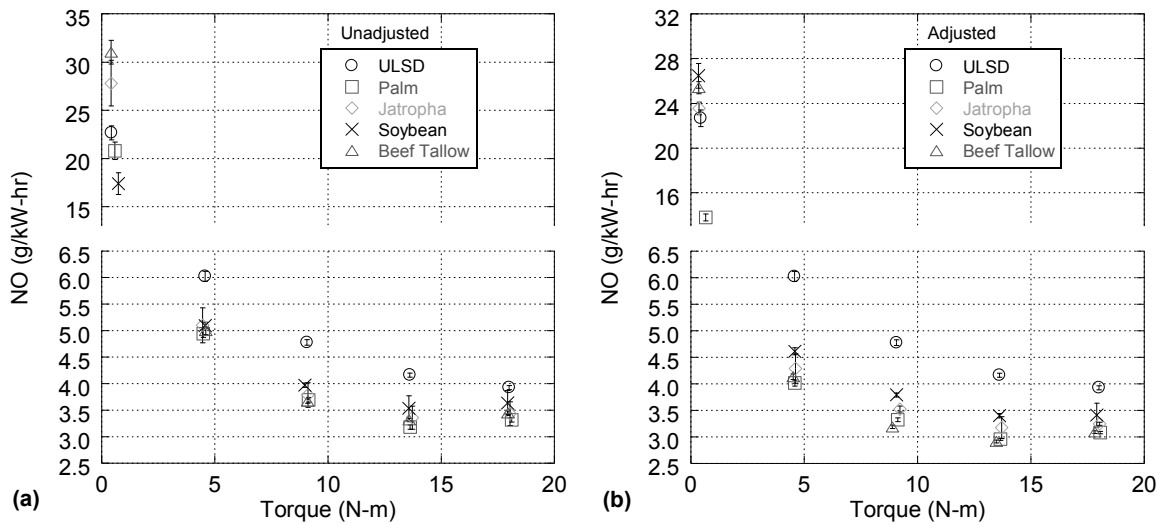


Figure A-6. Brake-Specific NO Emissions vs. Engine Torque for Unadjusted (a) and Adjusted (b) Injection Timing.

Table A-1. Brake-Specific NO Emission (g/kW-hr) vs. Engine Torque for Unadjusted Injection Timing.

Torque (N-m)	ULSD	Palm Biodiesel	Jatropha Biodiesel	Soybean Biodiesel	Beef Tallow Biodiesel
0.5	22.67±0.74	20.81±0.89	27.81±2.36	17.42±1.13	31.02±1.23
4.5	6.02±0.09	4.94±0.07	5.10±0.33	5.10±0.06	5.00±0.08
9.0	4.78±0.05	3.70±0.04	3.79±0.23	3.97±0.04	3.67±0.04
13.5	4.17±0.04	3.18±0.04	3.36±0.22	3.54±0.23	3.32±0.03
18.0	3.93±0.04	3.32±0.04	3.44±0.22	3.64±0.24	3.45±0.03

Table A-2. Brake-Specific NO Emission (g/kW-hr) vs. Engine Torque for Adjusted Injection Timing.

Torque (N-m)	ULSD	Palm Biodiesel	Jatropha Biodiesel	Soybean Biodiesel	Beef Tallow Biodiesel
0.5	22.67±0.74	13.79±0.31	23.55±0.56	26.46±1.11	25.41±0.55
4.5	6.02±0.09	4.02±0.06	4.29±0.28	4.62±0.07	4.13±0.05
9.0	4.78±0.05	3.33±0.04	3.53±0.06	3.80±0.04	3.19±0.03
13.5	4.12±0.04	2.96±0.02	3.18±0.21	3.40±0.04	2.92±0.03
18.0	3.93±0.04	3.08±0.03	3.25±0.03	3.41±0.22	3.09±0.03

Table A-3. Pearson Correlation Coefficients for Brake-Specific NO Emissions (g/kW-hr) as a Function of Fuel Property.

Fuel Property	0.5 N-m		4.5 N-m		9.0 N-m		13.5 N-m		18.0 N-m	
	Unadjusted	Adjusted	Unadjusted	Adjusted	Unadjusted	Adjusted	Unadjusted	Adjusted	Unadjusted	Adjusted
Cetane Number	0.577	-0.530	-0.854	-0.958	-0.980	-0.987	-0.896	-0.999	-0.833	-0.995
Unsat. Degree	-0.654	0.423	0.801	0.923	0.977	0.999	0.839	0.995	0.774	0.977
Unsaturation%	-0.546	0.358	0.839	0.836	0.895	0.960	0.744	0.952	0.640	0.922
Poly-Unsat. %	-0.672	0.441	0.785	0.939	0.989	0.998	0.859	0.996	0.805	0.983
Mono-Unsat. %	0.767	-0.420	-0.644	-0.932	-0.988	-0.954	-0.858	-0.950	-0.852	-0.944
Density	-0.642	0.449	0.810	0.935	0.982	0.998	0.856	0.997	0.794	0.983
Viscosity	0.818	-0.239	-0.632	-0.854	-0.960	-0.981	-0.741	-0.950	-0.699	-0.917
Energy Content	0.739	0.718	0.170	0.033	-0.228	-0.359	0.220	-0.230	0.267	-0.123

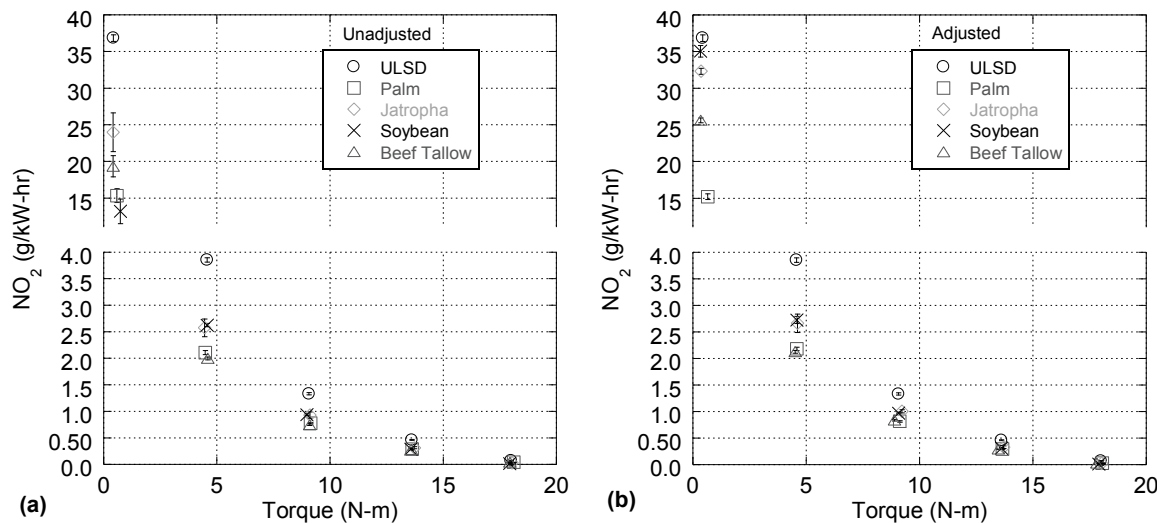


Figure A-7. Brake-Specific NO₂ Emissions vs. Engine Torque for Unadjusted (a) and Adjusted (b) Injection Timing.

Table A-4. Brake-Specific NO₂ Emission (g/kW-hr) vs. Engine Torque for Unadjusted Injection Timing.

Torque (N-m)	ULSD	Palm Biodiesel	Jatropha Biodiesel	Soybean Biodiesel	Beef Tallow Biodiesel
0.5	36.84±0.45	15.31±0.95	23.97±2.65	13.16±1.68	19.32±1.46
4.5	3.85±0.04	2.11±0.04	2.58±0.17	2.63±0.03	2.00±0.03
9.0	1.33±0.02	0.78±0.01	0.93±0.06	0.94±0.02	0.75±0.01
13.5	0.46±0.01	0.29±0.01	0.32±0.02	0.29±0.02	0.28±0.01
18.0	0.07±0.01	0.04±0.00	0.03±0.00	0.02±0.00	0.04±0.01

Table A-5. Brake-Specific NO₂ Emission (g/kW-hr) vs. Engine Torque for Adjusted Injection Timing.

Torque (N-m)	ULSD	Palm Biodiesel	Jatropha Biodiesel	Soybean Biodiesel	Beef Tallow Biodiesel
0.5	36.84±0.45	15.20±0.37	32.32±0.41	35.05±0.78	25.61±0.32
4.5	3.85±0.04	2.18±0.03	2.66±0.17	2.73±0.07	2.13±0.03
9.0	1.33±0.02	0.82±0.01	1.01±0.03	0.97±0.01	0.84±0.01
13.5	0.46±0.01	0.29±0.01	0.33±0.02	0.31±0.01	0.29±0.01
18.0	0.07±0.01	0.03±0.00	0.02±0.00	0.01±0.00	0.03±0.00

Table A-6. Pearson Correlation Coefficients for Brake-Specific NO₂ Emissions (g/kW-hr) as a Function of Fuel Property.

Fuel Property	0.5 N-m		4.5 N-m		9.0 N-m		13.5 N-m		18.0 N-m	
	Unadjusted	Adjusted	Unadjusted	Adjusted	Unadjusted	Adjusted	Unadjusted	Adjusted	Unadjusted	Adjusted
Cetane Number	0.231	-0.823	-0.944	-0.953	-0.938	-0.849	-0.477	-0.656	0.991	0.995
Unsat. Degree	-0.277	0.750	0.945	0.945	0.937	0.822	0.484	0.643	-1.000	-0.989
Unsaturation%	-0.067	0.741	0.992	0.984	0.988	0.905	0.683	0.799	-0.968	-0.929
Poly-Unsat. %	-0.327	0.749	0.923	0.926	0.914	0.793	0.426	0.596	-0.998	-0.995
Mono-Unsat. %	0.553	-0.654	-0.786	-0.793	-0.772	-0.614	-0.168	-0.360	0.945	0.968
Density	-0.278	0.766	0.942	0.944	0.934	0.823	0.472	0.637	-0.999	-0.993
Viscosity	0.467	-0.578	-0.861	-0.850	-0.847	-0.672	-0.349	-0.487	0.973	0.953
Energy Content	0.365	0.341	-0.287	-0.216	-0.267	-0.045	-0.246	-0.124	0.338	0.215

Table A-7. Brake-Specific NO_x Emission (g/kW-hr) vs. Engine Torque for Unadjusted Injection Timing.

Torque (N-m)	ULSD	Palm Biodiesel	Jatropha Biodiesel	Soybean Biodiesel	Beef Tallow Biodiesel
0.5	59.51±1.08	36.12±0.70	51.78±3.34	30.58±0.97	50.34±0.70
4.5	9.88±0.11	7.05±0.08	7.68±0.49	7.72±0.07	7.00±0.09
9.0	6.11±0.06	4.48±0.04	4.71±0.29	4.91±0.04	4.42±0.04
13.5	4.63±0.04	3.47±0.04	3.68±0.24	3.83±0.25	3.60±0.03
18.0	4.00±0.04	3.36±0.04	3.47±0.22	3.66±0.24	3.49±0.03

Table A-8. Brake-Specific NO_x Emission (g/kW-hr) vs. Engine Torque for Adjusted Injection Timing.

Torque (N-m)	ULSD	Palm Biodiesel	Jatropha Biodiesel	Soybean Biodiesel	Beef Tallow Biodiesel
0.5	59.51±1.08	28.99±0.40	55.87±0.81	61.51±1.89	51.02±0.71
4.5	9.88±0.11	6.20±0.07	6.95±0.44	7.34±0.11	6.26±0.06
9.0	6.11±0.06	4.14±0.04	4.53±0.08	4.77±0.04	4.03±0.04
13.5	4.63±0.04	3.25±0.02	3.51±0.23	3.71±0.04	3.21±0.03
18.0	4.00±0.04	3.11±0.02	3.27±0.03	3.43±0.22	3.13±0.03

Table A-9. Brake-Specific CO Emission (g/kW-hr) vs. Engine Torque for Unadjusted Injection Timing.

Torque (N-m)	ULSD	Palm Biodiesel	Jatropha Biodiesel	Soybean Biodiesel	Beef Tallow Biodiesel
0.5	219.18±4.96	62.22±1.30	123.99±8.25	73.99±1.66	79.94±1.87
4.5	12.89±0.25	5.90±0.13	8.03±0.52	8.94±0.16	5.31±0.10
9.0	3.98±0.08	2.13±0.04	2.71±0.17	3.05±0.06	1.96±0.04
13.5	1.91±0.04	1.44±0.04	1.57±0.11	1.70±0.12	1.16±0.03
18.0	1.35±0.04	1.29±0.05	1.27±0.09	1.34±0.10	0.99±0.04

Table A-10. Brake-Specific CO Emission (g/kW-hr) vs. Engine Torque for Adjusted Injection Timing.

Torque (N-m)	ULSD	Palm Biodiesel	Jatropha Biodiesel	Soybean Biodiesel	Beef Tallow Biodiesel
0.5	219.18±4.96	69.06±1.16	174.02±3.21	202.32±3.89	117.65±2.01
4.5	12.89±0.25	6.75±0.13	8.87±0.58	9.71±0.16	6.43±0.11
9.0	3.98±0.08	2.40±0.05	3.04±0.07	3.18±0.06	2.50±0.04
13.5	1.91±0.04	1.59±0.04	1.75±0.12	1.83±0.04	1.42±0.03
18.0	1.35±0.04	1.34±0.04	1.31±0.04	1.39±0.10	1.10±0.040

Table A-11. Brake-Specific HC Emission (g/kW-hr) vs. Engine Torque for Unadjusted Injection Timing.

Torque (N-m)	ULSD	Palm Biodiesel	Jatropha Biodiesel	Soybean Biodiesel	Beef Tallow Biodiesel
0.5	58.18±1.27	11.34±0.28	23.72±0.80	13.38±0.54	13.54±0.37
4.5	3.17±0.04	1.33±0.04	1.67±0.07	1.94±0.07	1.05±0.02
9.0	1.23±0.02	0.63±0.01	0.85±0.04	0.97±0.02	0.49±0.01
13.5	0.81±0.01	0.27±0.00	0.42±0.02	0.39±0.01	0.26±0.01
18.0	0.39±0.01	0.22±0.01	0.28±0.02	0.29±0.02	0.22±0.01

Table A-12. Brake-Specific HC Emission (g/kW-hr) vs. Engine Torque for Adjusted Injection Timing.

Torque (N-m)	ULSD	Palm Biodiesel	Jatropha Biodiesel	Soybean Biodiesel	Beef Tallow Biodiesel
0.5	58.18±1.27	14.80±0.37	37.40±1.01	43.40±1.48	22.96±0.41
4.5	3.17±0.04	1.66±0.05	1.98±0.07	2.25±0.09	1.37±0.03
9.0	1.23±0.02	0.66±0.02	0.97±0.03	0.99±0.03	0.61±0.01
13.5	0.81±0.01	0.27±0.00	0.44±0.02	0.44±0.02	0.30±0.00
18.0	0.39±0.01	0.21±0.00	0.27±0.01	0.30±0.01	0.23±0.00

Table A-13. Brake-Specific PM Emission (g/kW-hr) vs. Engine Torque for Unadjusted Injection Timing.

Torque (N-m)	ULSD	Palm Biodiesel	Jatropha Biodiesel	Soybean Biodiesel	Beef Tallow Biodiesel
0.5	0.019±0.000	0.032±0.003	0.020±0.002	0.011±0.001	0.040±0.004
4.5	0.010±0.001	0.025±0.002	0.020±0.000	0.019±0.000	0.022±0.001
9.0	0.021±0.000	0.031±0.001	0.029±0.000	0.029±0.001	0.026±0.001
13.5	0.075±0.003	0.100±0.002	0.083±0.002	0.088±0.005	0.053±0.001
18.0	0.455±0.006	0.261±0.008	0.261±0.004	0.311±0.004	0.180±0.002

Table A-14. Brake-Specific PM Emission (g/kW-hr) vs. Engine Torque for Adjusted Injection Timing.

Torque (N-m)	ULSD	Palm Biodiesel	Jatropha Biodiesel	Soybean Biodiesel	Beef Tallow Biodiesel
0.5	0.019±0.000	0.020±0.000	0.016±0.003	0.016±0.000	0.028±0.000
4.5	0.010±0.001	0.022±0.001	0.018±0.000	0.016±0.000	0.019±0.000
9.0	0.021±0.000	0.031±0.000	0.027±0.000	0.029±0.000	0.022±0.001
13.5	0.075±0.003	0.095±0.001	0.082±0.001	0.084±0.002	0.049±0.001
18.0	0.455±0.006	0.275±0.001	0.252±0.005	0.309±0.012	0.176±0.009

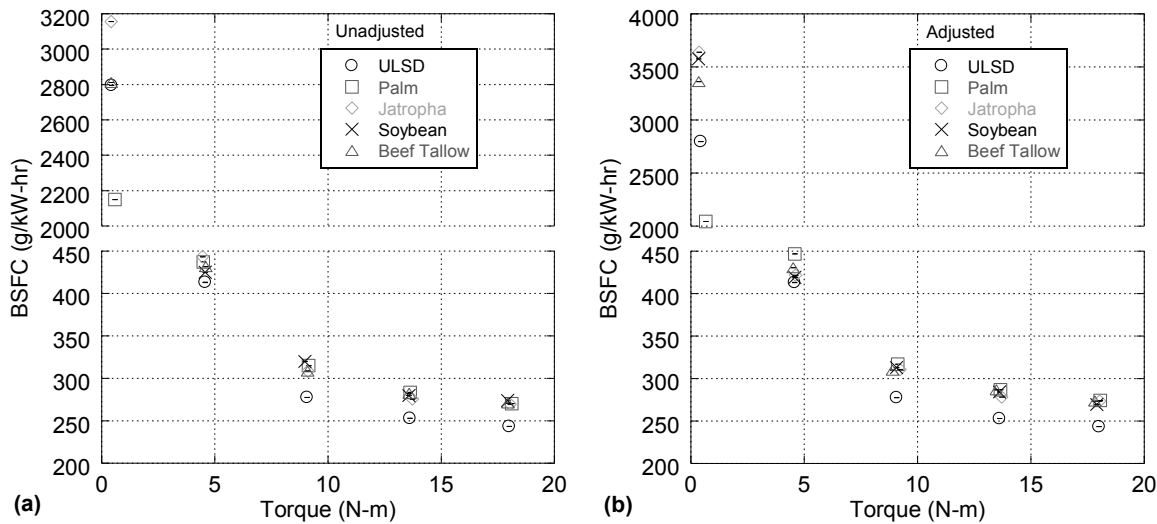


Figure A-8. Brake-Specific Fuel Consumption vs. Engine Torque for Unadjusted (a) and Adjusted (b) Injection Timing.

Table A-15. Brake-Specific Fuel Consumption (g/kW-hr) vs. Engine Torque for Unadjusted Injection Timing.

Torque (N-m)	ULSD	Palm Biodiesel	Jatropha Biodiesel	Soybean Biodiesel	Beef Tallow Biodiesel
0.5	2796.0±0.1	2151.3±0.1	3156.3±0.2	1575.6±0.2	2812.5±0.2
4.5	413.12±0.15	437.41±0.06	443.32±0.14	425.02±0.05	431.66±0.09
9.0	277.60±0.02	315.11±0.04	308.53±0.07	319.99±0.07	308.40±0.07
13.5	252.86±0.01	283.30±0.03	275.71±0.05	279.89±0.03	282.26±0.05
18.0	243.33±0.01	270.24±0.01	269.51±0.03	274.16±0.05	270.86±0.02

Table A-16. Brake-Specific Fuel Consumption (g/kW-hr) vs. Engine Torque for Adjusted Injection Timing.

Torque (N-m)	ULSD	Palm Biodiesel	Jatropha Biodiesel	Soybean Biodiesel	Beef Tallow Biodiesel
0.5	2796.0±0.1	2045.0±0.1	3637.8±0.2	3576.4±0.2	3362.8±0.2
4.5	413.12±0.15	446.87±0.08	421.56±0.14	419.21±0.06	430.57±0.07
9.0	277.60±0.02	316.96±0.03	310.71±0.06	312.99±0.05	309.91±0.03
13.5	252.86±0.01	287.01±0.04	278.36±0.04	284.23±0.03	286.77±0.05
18.0	243.33±0.01	274.44±0.01	273.59±0.04	269.50±0.01	273.71±0.01

Table A-17. Pearson Correlation Coefficients for Brake-Specific CO₂ Emissions (g/kW-hr) as a Function of Fuel Property.

Fuel Property	0.5 N-m		4.5 N-m		9.0 N-m		13.5 N-m		18.0 N-m	
	Unadjusted	Adjusted	Unadjusted	Adjusted	Unadjusted	Adjusted	Unadjusted	Adjusted	Unadjusted	Adjusted
Cetane Number	0.545	-0.639	-0.259	-0.142	-0.783	-0.832	-0.619	-0.610	-0.505	-0.315
Unsat. Degree	-0.604	0.540	0.375	0.219	0.835	0.880	0.701	0.694	0.600	0.417
Unsaturation%	-0.446	0.499	0.396	0.056	0.730	0.787	0.627	0.625	0.538	0.343
Poly-Unsat. %	-0.637	0.551	0.360	0.255	0.852	0.893	0.709	0.701	0.605	0.427
Mono-Unsat. %	0.784	-0.498	-0.360	-0.450	-0.917	-0.938	-0.766	-0.754	-0.664	-0.521
Density	-0.599	0.564	0.348	0.210	0.829	0.874	0.687	0.679	0.582	0.399
Viscosity	0.769	-0.352	-0.551	-0.442	-0.942	-0.968	-0.851	-0.845	-0.771	-0.622
Energy Content	0.575	0.610	-0.992	-0.601	-0.601	-0.583	-0.800	-0.814	-0.867	-0.873

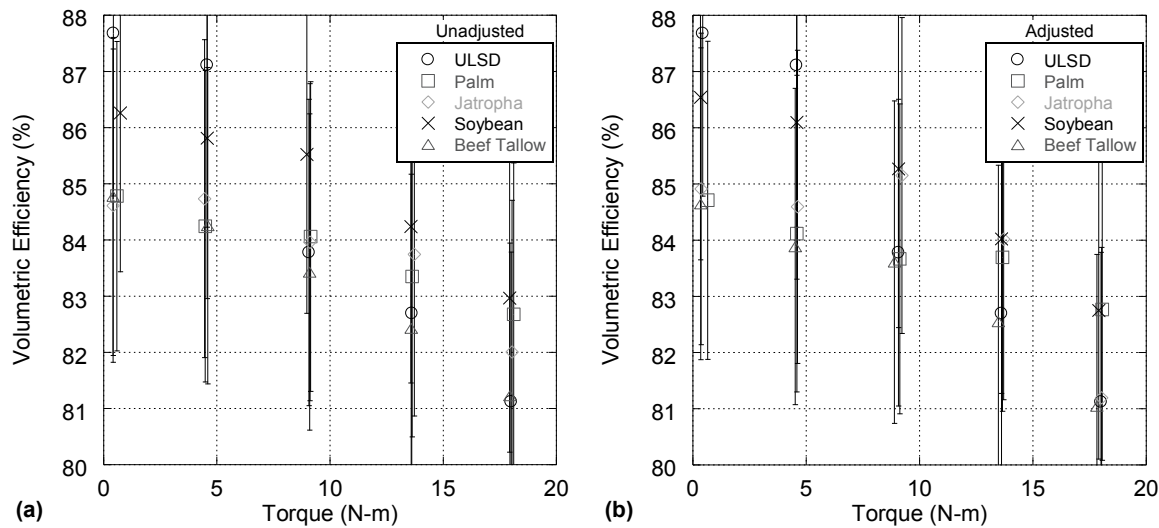


Figure A-9. Volumetric Efficiency vs. Engine Torque for Unadjusted (a) and Adjusted (b) Injection Timing.

Table A-18. Volumetric Efficiency (%) vs. Engine Torque for Unadjusted Injection Timing.

Torque (N-m)	ULSD	Palm Biodiesel	Jatropha Biodiesel	Soybean Biodiesel	Beef Tallow Biodiesel
0.5	87.7±2.9	84.8±2.8	84.6±2.8	86.3±2.8	84.8±2.8
4.5	87.1±2.9	84.2±2.8	84.7±2.8	85.8±2.9	84.3±2.8
9.0	83.8±2.7	84.1±2.8	84.0±2.8	85.5±2.8	83.4±2.8
13.5	82.7±2.7	83.4±2.9	83.7±2.9	84.2±2.8	82.4±2.7
18.0	81.1±2.7	82.7±2.7	82.0±2.7	83.0±2.7	81.2±2.7

Table A-19. Volumetric Efficiency (%) vs. Engine Torque for Adjusted Injection Timing.

Torque (N-m)	ULSD	Palm Biodiesel	Jatropha Biodiesel	Soybean Biodiesel	Beef Tallow Biodiesel
0.5	87.7±2.9	84.7±2.8	84.9±2.8	86.5±2.9	84.6±2.8
4.5	87.1±2.9	84.1±2.8	84.6±2.8	86.1±2.8	83.9±2.8
9.0	83.8±2.7	83.7±2.8	85.2±2.8	85.3±2.8	83.6±2.9
13.5	82.7±2.7	83.7±2.7	84.0±2.9	84.0±2.8	82.6±2.8
18.0	81.1±2.7	82.8±2.7	81.2±2.7	82.8±2.6	81.0±2.7

Table A-20. Combustion Efficiency (%) vs. Engine Torque for Unadjusted Injection Timing.

Torque (N-m)	ULSD	Palm Biodiesel	Jatropha Biodiesel	Soybean Biodiesel	Beef Tallow Biodiesel
0.5	93.4±6.5	97.8+2.2-9.0	96.9+3.1-20.2	96.3+3.70-15.8	97.9+2.1-14.1
4.5	97.6+2.4-12.6	99.0+1.0-6.0	98.7+1.3-13.0	98.4+1.59-4.7	99.1+0.9-7.9
9.0	98.9+1.1-2.2	99.5+0.5-4.1	99.3+0.7-8.0	99.2+0.79-6.5	99.5+0.5-6.0
13.5	99.3+0.7-2.2	99.6+0.4-3.0	99.6+0.4-7.3	99.5+0.46-6.6	99.7+0.3-4.6
18.0	99.4+0.6-2.1	99.6+0.4-2.8	99.6+0.4-6.9	99.6+0.42-7.3	99.7+0.3-3.1

Table A-21. Combustion Efficiency (%) vs. Engine Torque for Adjusted Injection Timing.

Torque (N-m)	ULSD	Palm Biodiesel	Jatropha Biodiesel	Soybean Biodiesel	Beef Tallow Biodiesel
0.5	93.4±6.5	97.3+2.7-9.6	96.1+3.9-20.2	95.3+4.7-17.2	97.4+2.6-15.4
4.5	97.6+2.4-12.6	98.8+1.2-7.0	98.4+1.6-12.8	98.2+1.8-5.8	98.9+1.1-6.0
9.0	98.9+1.1-2.2	99.4+0.6-3.4	99.2+0.8-5.0	99.2+0.8-4.7	99.4+0.6-3.0
13.5	99.3+0.7-2.2	99.6+0.4-3.5	99.5+0.5-6.5	99.5+0.5-3.3	99.6+0.4-4.7
18.0	99.4+0.64-2.1	99.6+0.4-2.2	99.6+0.4-3.9	99.6+0.4-6.1	99.7+0.3-3.2

Table A-22. Fuel Conversion Efficiency (%) vs. Engine Torque for Unadjusted Injection Timing.

Torque (N-m)	ULSD	Palm Biodiesel	Jatropha Biodiesel	Soybean Biodiesel	Beef Tallow Biodiesel
0.5	3.0±0.5	3.9±0.6	2.6±0.9	5.3±1.5	3.0±0.7
4.5	20.1±4.4	19.0±1.6	18.8±3.9	19.6±1.5	19.3±2.6
9.0	30.0±0.8	26.4±1.6	27.0±2.8	26.0±2.7	27.0±2.7
13.5	32.9±0.4	29.3±1.1	30.2±2.2	29.7±1.4	29.5±2.1
18.0	34.2±0.3	30.8±0.3	30.8±1.3	30.3±2.0	30.7±0.9

Table A-23. Fuel Conversion Efficiency (%) vs. Engine Torque for Adjusted Injection Timing.

Torque (N-m)	ULSD	Palm Biodiesel	Jatropha Biodiesel	Soybean Biodiesel	Beef Tallow Biodiesel
0.5	3.0±0.5	4.1±0.7	2.3±0.8	2.3±0.9	2.5±0.7
4.5	20.1±4.4	18.6±2.2	19.7±4.0	19.8±1.8	19.3±2.0
9.0	30.0±0.8	26.2±1.3	26.8±2.1	26.6±2.0	26.8±1.2
13.5	32.9±0.4	29.0±1.6	29.9±1.7	29.3±1.2	29.0±2.2
18.0	34.2±0.3	30.3±0.3	30.4±1.7	30.9±0.3	30.4±0.6

Table A-24. Pearson Correlation Coefficients for Fuel Conversion Efficiency as a Function of Fuel Property.

Fuel Property	0.5 N-m		4.5 N-m		9.0 N-m		13.5 N-m		18.0 N-m	
	Unadjusted	Adjusted								
Cetane Number	-0.610	0.552	-0.384	-0.789	0.576	-0.100	-0.583	-0.507	0.675	-0.879
Unsat. Degree	0.645	-0.449	0.348	0.713	-0.634	-0.016	0.554	0.491	-0.656	0.854
Unsaturation%	0.460	-0.447	0.107	0.711	-0.478	0.020	0.715	0.676	-0.449	0.705
Poly-Unsat. %	0.685	-0.450	0.410	0.710	-0.666	-0.019	0.507	0.438	-0.705	0.886
Mono-Unsat. %	-0.845	0.361	-0.623	-0.608	0.806	0.114	-0.266	-0.182	0.861	-0.958
Density	0.647	-0.471	0.368	0.729	-0.629	0.008	0.551	0.484	-0.671	0.867
Viscosity	-0.778	0.235	-0.405	-0.530	0.792	0.247	-0.370	-0.320	0.703	-0.843
Energy Content	-0.396	-0.656	0.240	0.382	0.569	0.874	0.023	-0.064	-0.023	-0.006

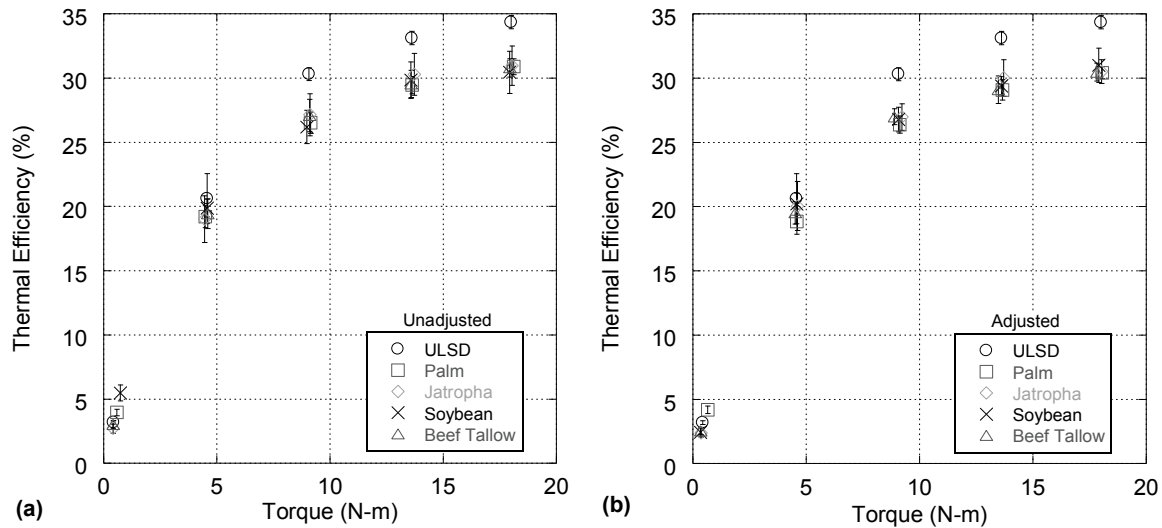


Figure A-10. Thermal Efficiency vs. Engine Torque for Unadjusted (a) and Adjusted (b) Injection Timing.

Table A-25. Thermal Efficiency (%) vs. Engine Torque for Unadjusted Injection Timing.

Torque (N-m)	ULSD	Palm Biodiesel	Jatropha Biodiesel	Soybean Biodiesel	Beef Tallow Biodiesel
0.5	3.2±0.1	4.0±0.3	2.7±0.4	5.5±0.6	3.0±0.3
4.5	20.6±1.9	19.2±0.8	19.0±1.8	19.9±0.7	19.4±1.1
9.0	30.3±0.5	26.5±0.8	27.1±1.6	26.2±1.3	27.1±1.3
13.5	33.1±0.5	29.5±0.7	30.3±1.6	29.8±1.4	29.5±1.1
18.0	34.4±0.5	30.9±0.6	31.0±1.5	30.5±1.6	30.8±0.7

Table A-26. Thermal Efficiency (%) vs. Engine Torque for Adjusted Injection Timing.

Torque (N-m)	ULSD	Palm Biodiesel	Jatropha Biodiesel	Soybean Biodiesel	Beef Tallow Biodiesel
0.5	3.2±0.1	4.2±0.3	2.4±0.3	2.4±0.3	2.5±0.3
4.5	20.6±1.9	18.8±1.0	20.0±1.9	20.2±0.9	19.5±0.9
9.0	30.3±0.5	26.4±0.7	27.0±1.0	26.8±1.0	27.0±0.6
13.5	33.1±0.5	29.1±0.8	30.0±1.4	29.4±0.7	29.0±1.1
18.0	34.4±0.5	30.4±0.5	30.5±0.9	31.0±1.3	30.5±0.7

Table A-27. Pearson Correlation Coefficients for Thermal Efficiency as a Function of Fuel Property.

Fuel Property	0.5 N-m		4.5 N-m		9.0 N-m		13.5 N-m		18.0 N-m	
	Unadjusted	Adjusted								
Cetane Number	-0.625	0.532	-0.527	-0.827	0.516	-0.215	-0.610	-0.531	0.635	-0.893
Unsat. Degree	0.660	-0.428	0.495	0.757	-0.574	0.102	0.584	0.516	-0.611	0.871
Unsaturation%	0.477	-0.426	0.267	0.756	-0.410	0.141	0.742	0.698	-0.397	0.727
Poly-Unsat. %	0.699	-0.429	0.552	0.753	-0.609	0.096	0.538	0.464	-0.662	0.902
Mono-Unsat. %	-0.856	0.340	-0.740	-0.651	0.765	0.012	-0.298	-0.211	0.828	-0.968
Density	0.662	-0.450	0.514	0.772	-0.570	0.124	0.581	0.510	-0.627	0.883
Viscosity	-0.790	0.212	-0.542	-0.584	0.743	0.134	-0.406	-0.348	0.655	-0.864
Energy Content	-0.393	-0.672	0.169	0.320	0.561	0.819	-0.007	-0.078	-0.076	-0.042

A.2 Supplemental Figures and Tables from Chapter 2 – Study 2

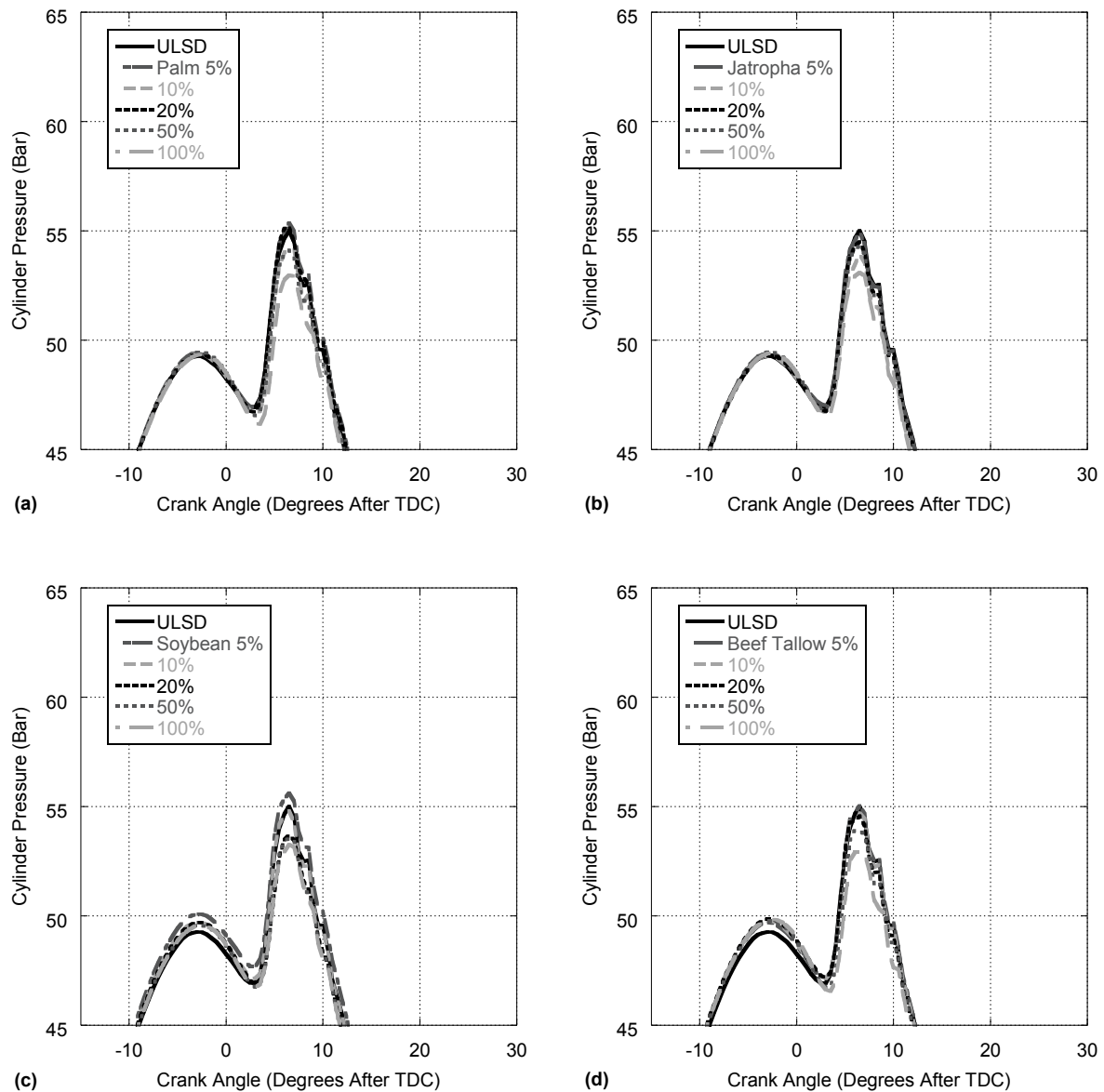


Figure A-11. Cylinder Pressure vs. Engine Crank Angle for Adjusted Palm (a), Jatropha (b), Soybean (c), and Beef Tallow (d) Biodiesel Blends (%-vol.) with ULSD at 0.5 N·m Loading.

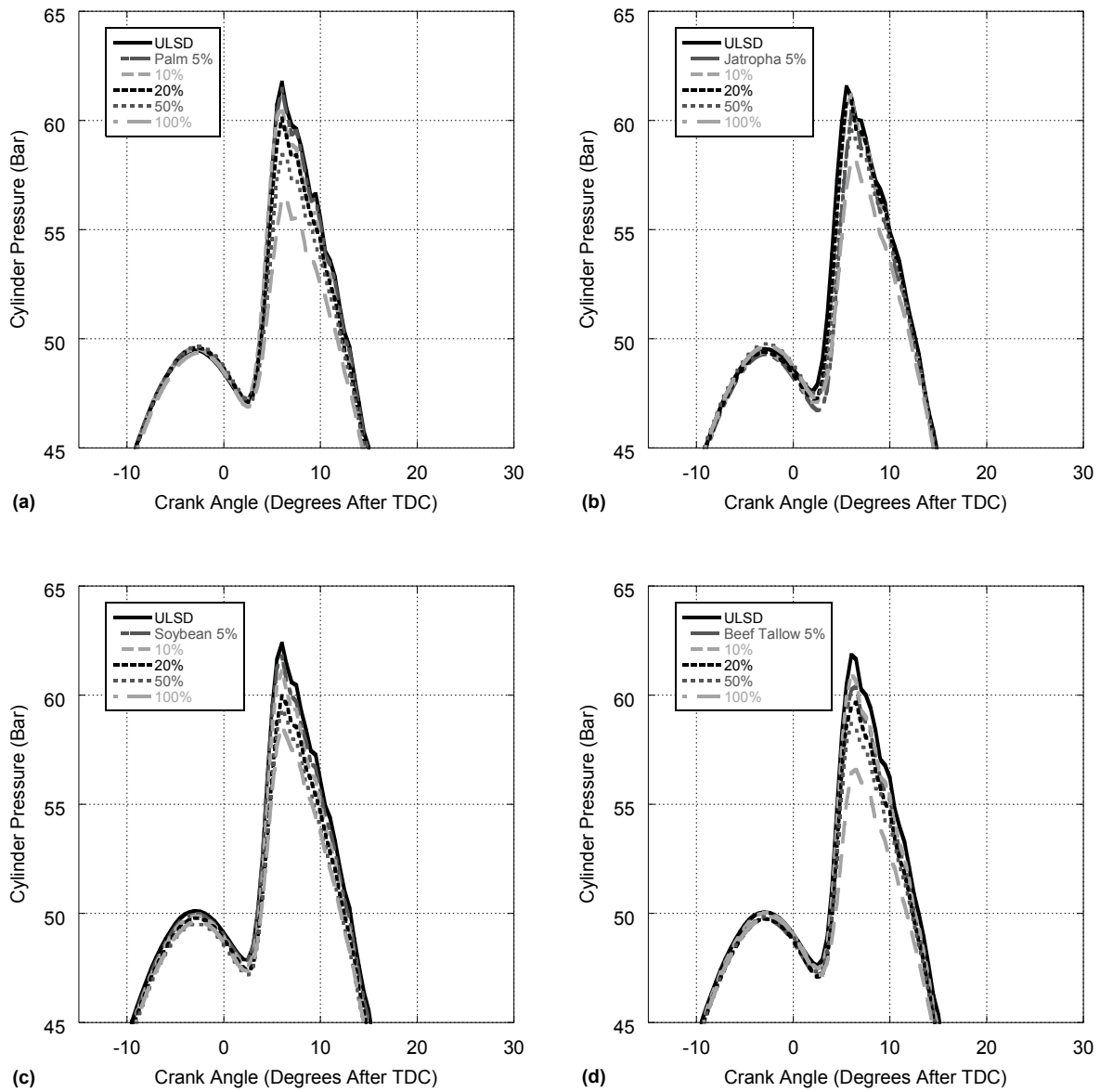


Figure A-12. Cylinder Pressure vs. Engine Crank Angle for Adjusted Palm (a), Jatropha (b), Soybean (c), and Beef Tallow (d) Biodiesel Blends (%-vol.) with ULSD at 4.5 N·m Loading.

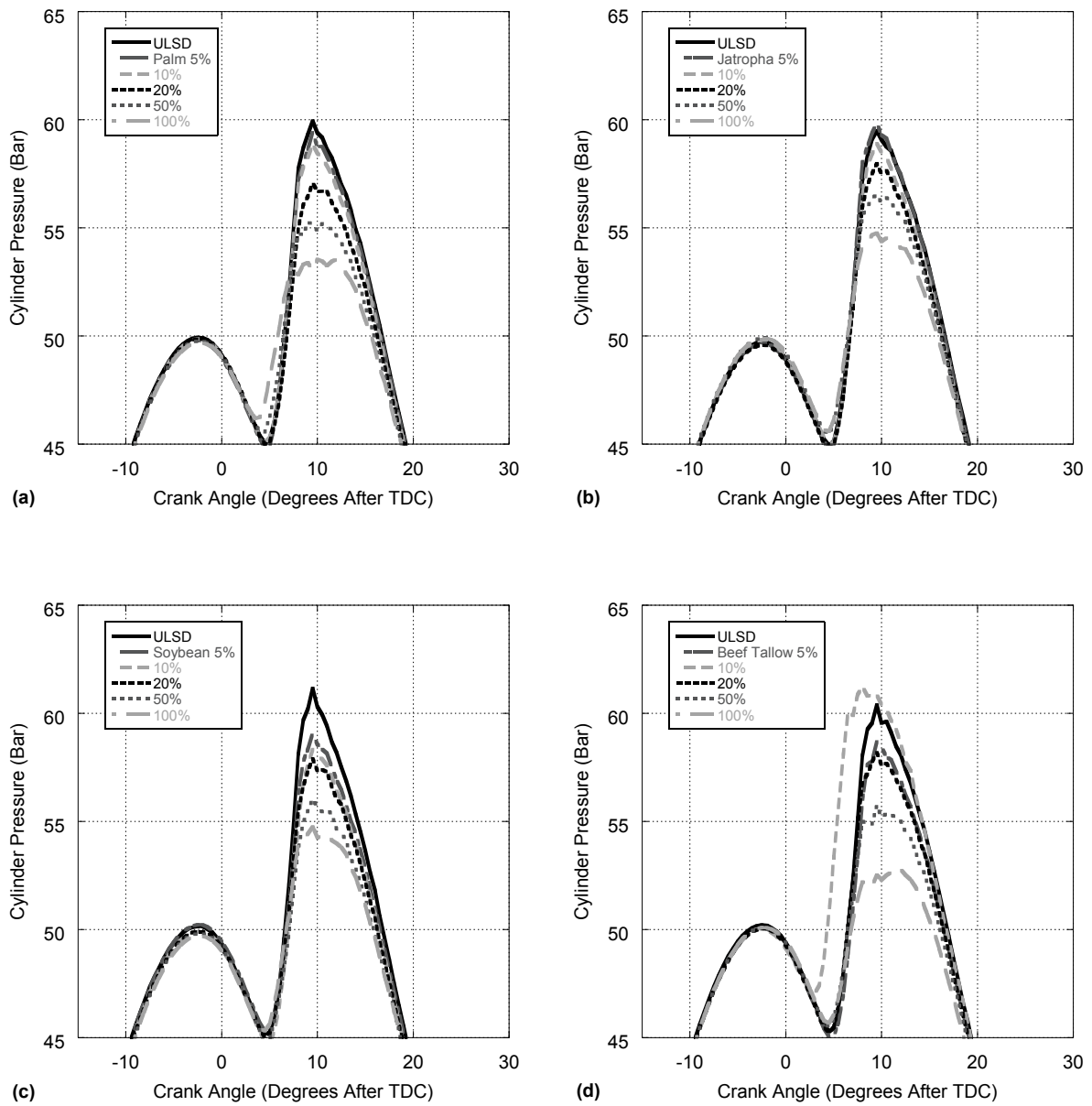


Figure A-13. Cylinder Pressure vs. Engine Crank Angle for Adjusted Palm (a), Jatropha (b), Soybean (c), and Beef Tallow (d) Biodiesel Blends (%-vol.) with ULSD at 13.5 N·m Loading.

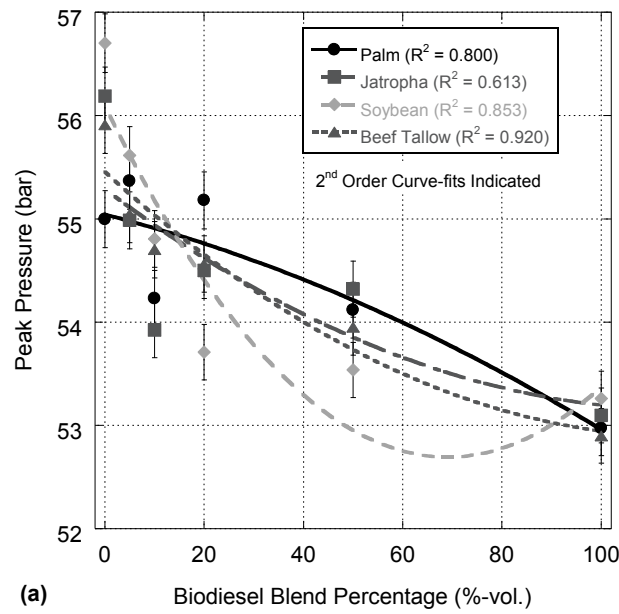


Figure A-14. Peak Cylinder Pressure a Function of Biodiesel Blend Percentage for Blends at 0.5 N·m Loading.

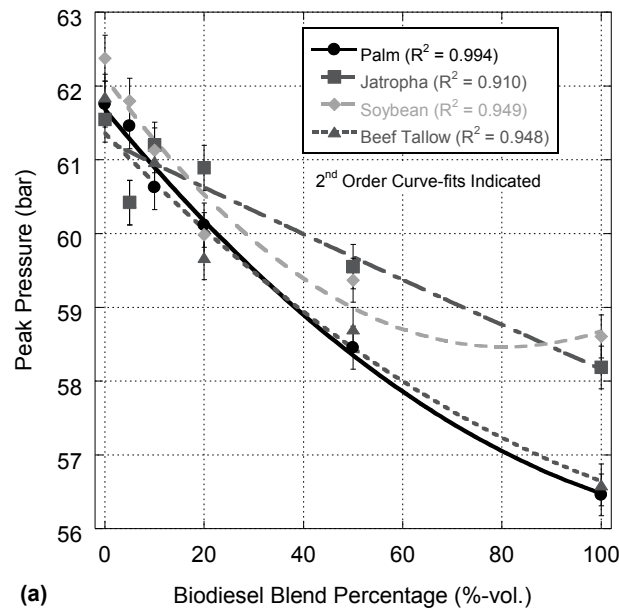


Figure A-15. Peak Cylinder Pressure a Function of Biodiesel Blend Percentage for Blends at 4.5 N·m Loading.

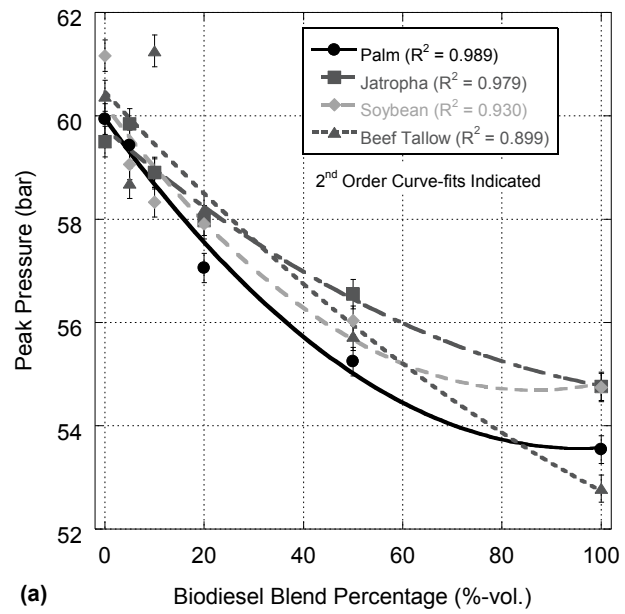


Figure A-16. Peak Cylinder Pressure a Function of Biodiesel Blend Percentage for Blends at 13.5 N·m Loading.

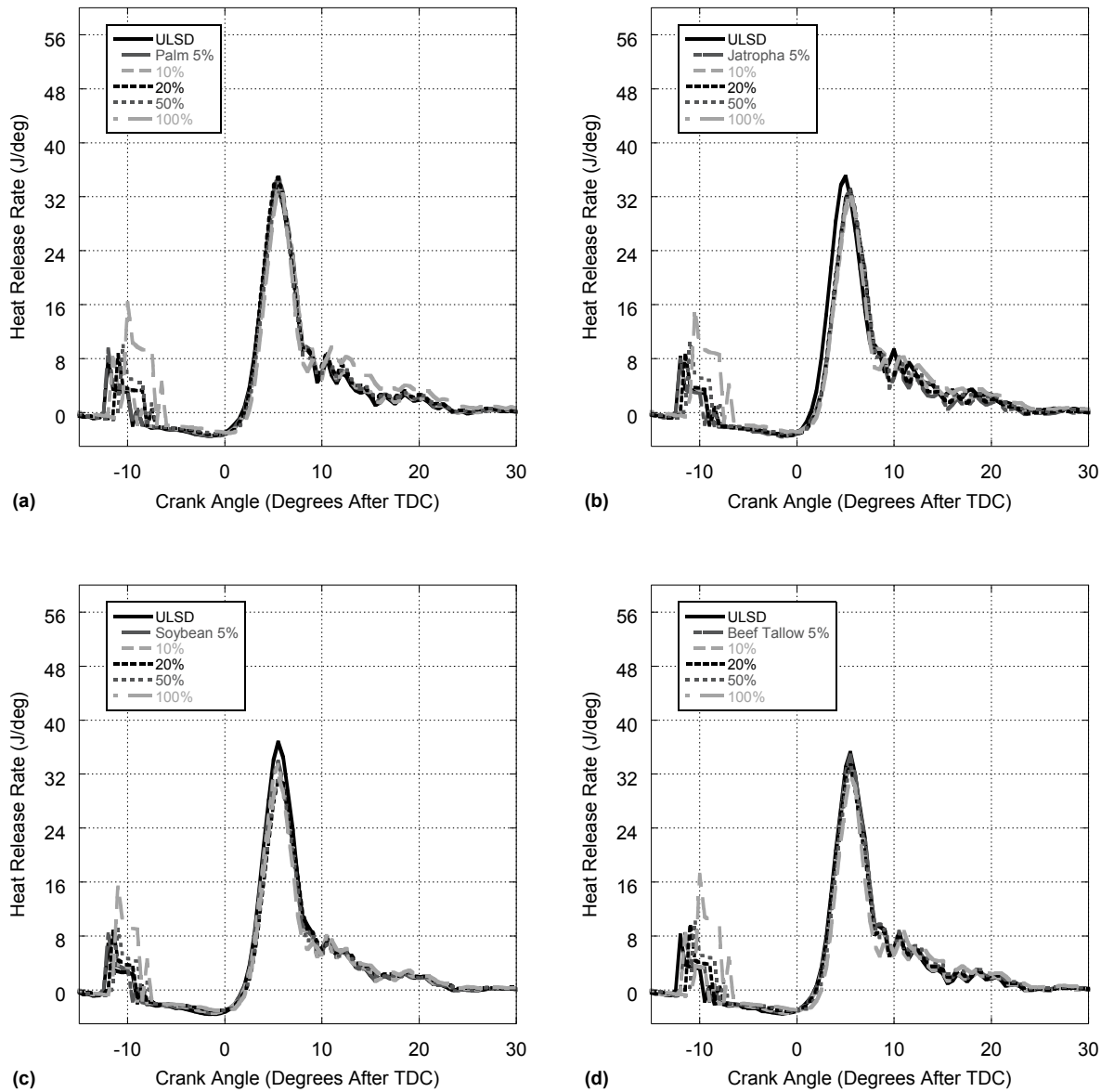


Figure A-17. Heat Release Rate vs. Engine Crank Angle for Adjusted Palm (a), Jatropha (b), Soybean (c), and Beef Tallow (d) Biodiesel Blends (%-vol.) with ULSD at 0.5 N·m Loading.

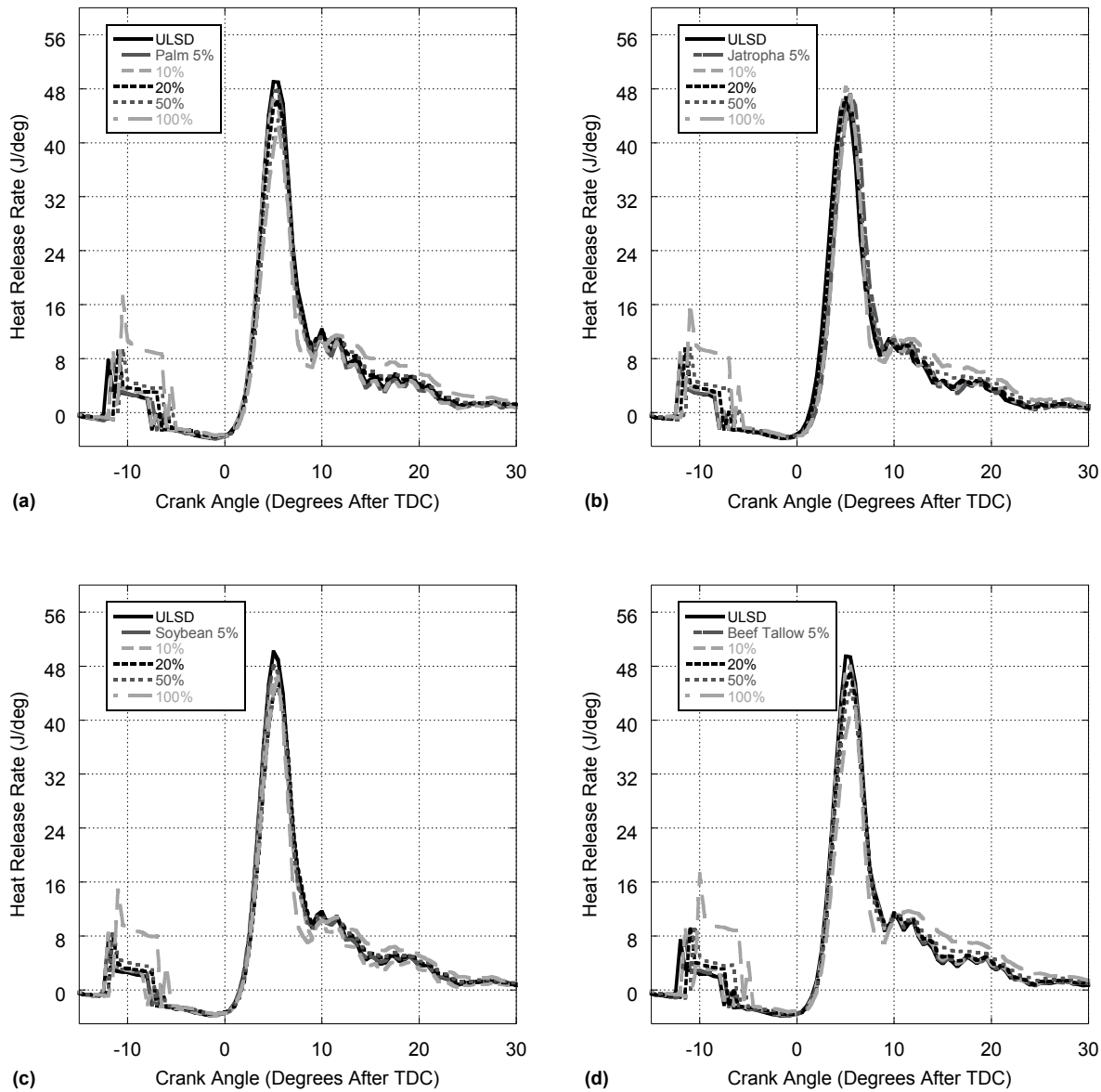


Figure A-18. Heat Release Rate vs. Engine Crank Angle for Adjusted Palm (a), Jatropha (b), Soybean (c), and Beef Tallow (d) Biodiesel Blends (%-vol.) with ULSD at 4.5 N·m Loading.

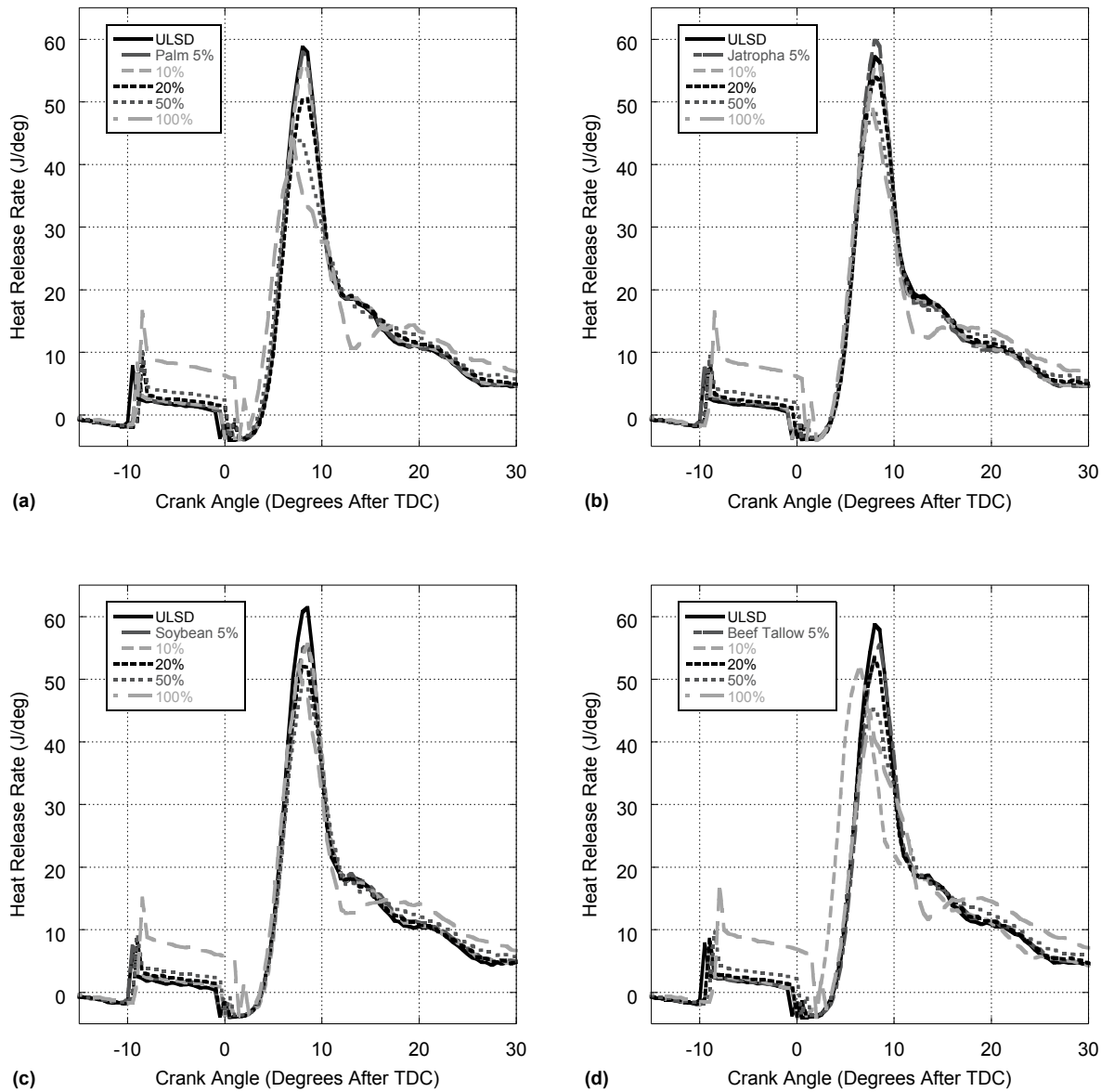


Figure A-19. Heat Release Rate vs. Engine Crank Angle for Adjusted Palm (a), Jatropha (b), Soybean (c), and Beef Tallow (d) Biodiesel Blends (%-vol.) with ULSD at 13.5 N·m Loading.

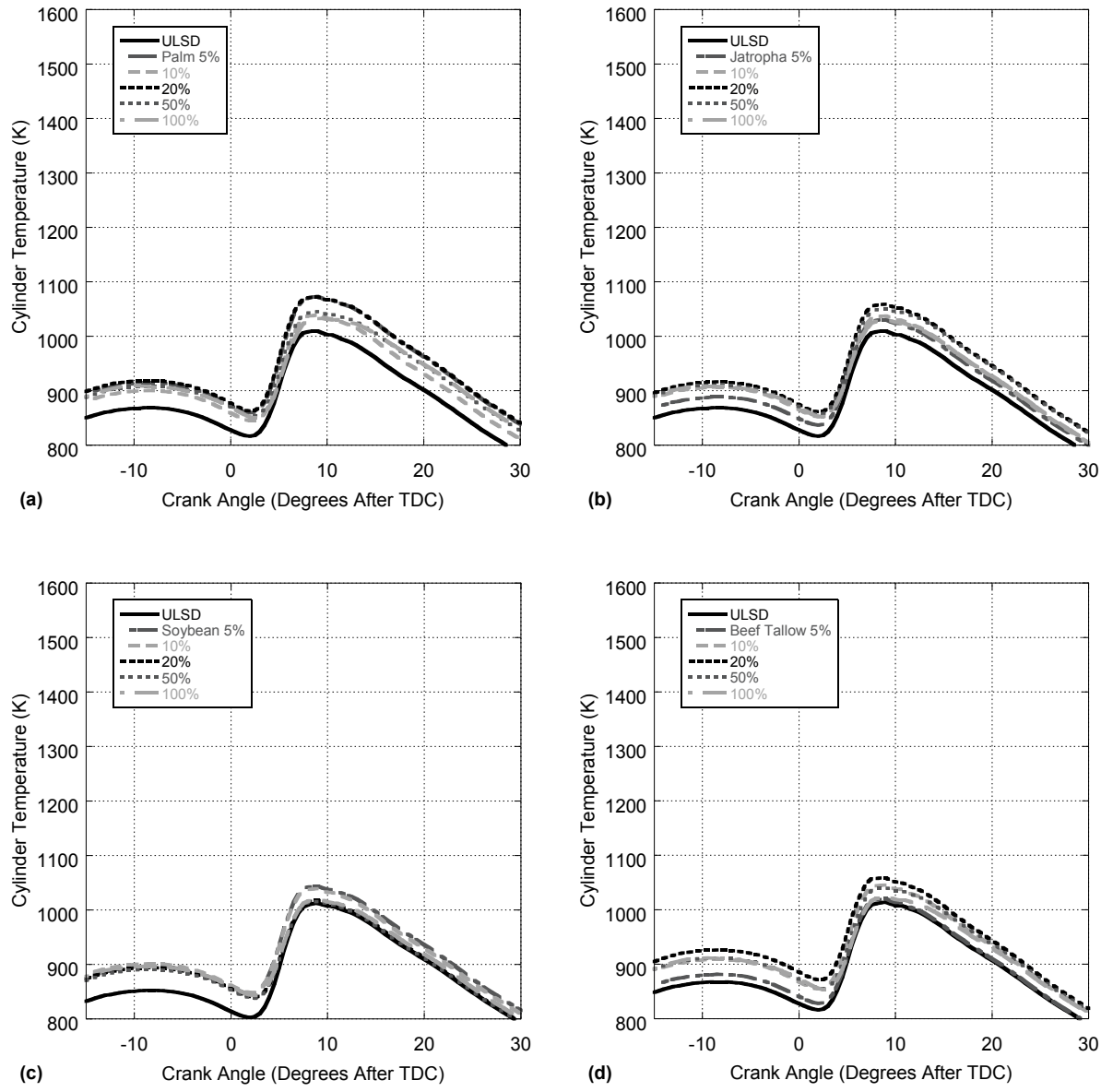


Figure A-20. Average Cylinder Temperature vs. Engine Crank Angle for Adjusted Palm (a), Jatropha (b), Soybean (c), and Beef Tallow (d) Biodiesel Blends (%-vol.) with ULSD at 0.5 N·m Loading.

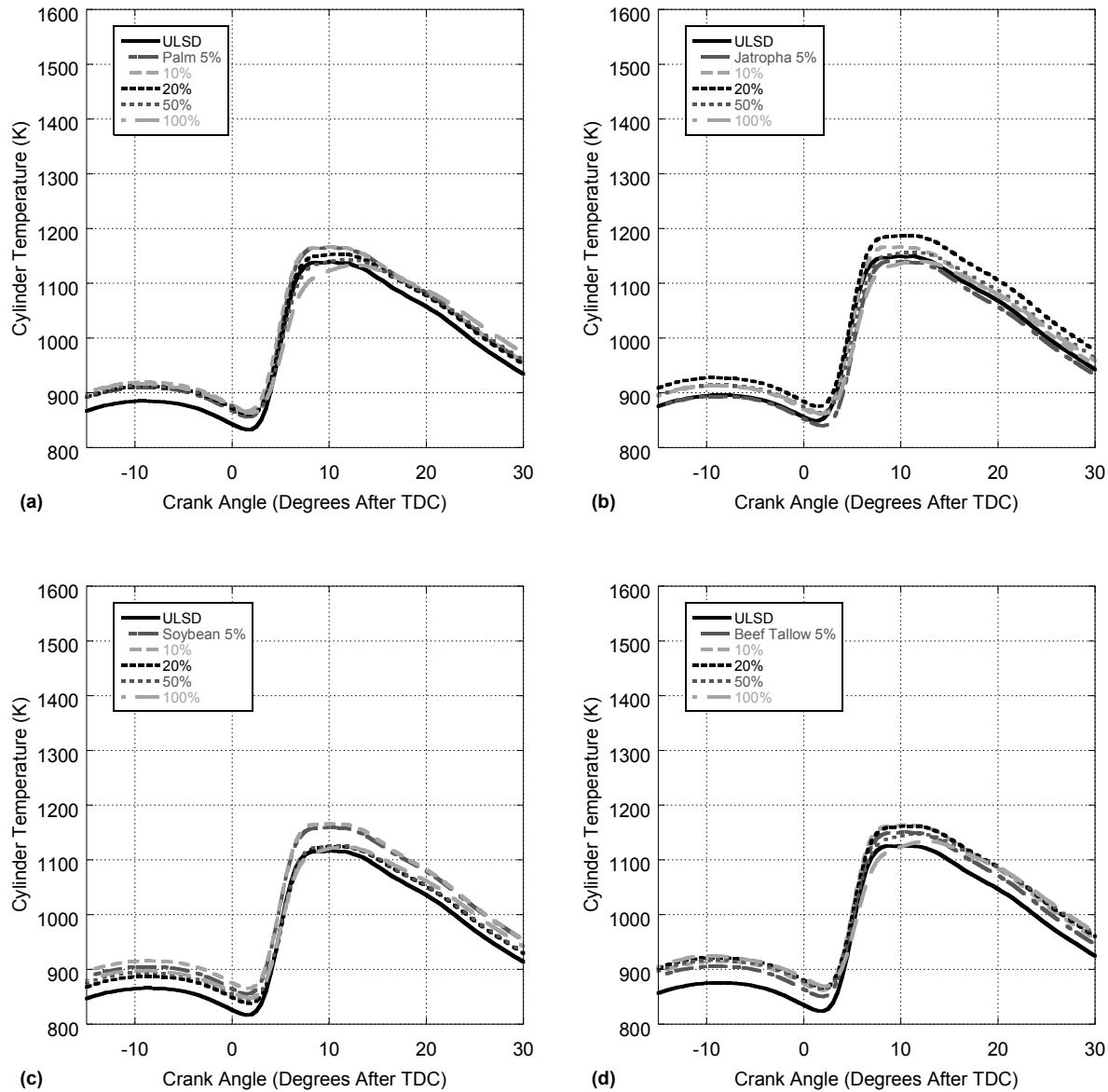


Figure A-21. Average Cylinder Temperature vs. Engine Crank Angle for Adjusted Palm (a), Jatropha (b), Soybean (c), and Beef Tallow (d) Biodiesel Blends (%-vol.) with ULSD at 4.5 N-m Loading.

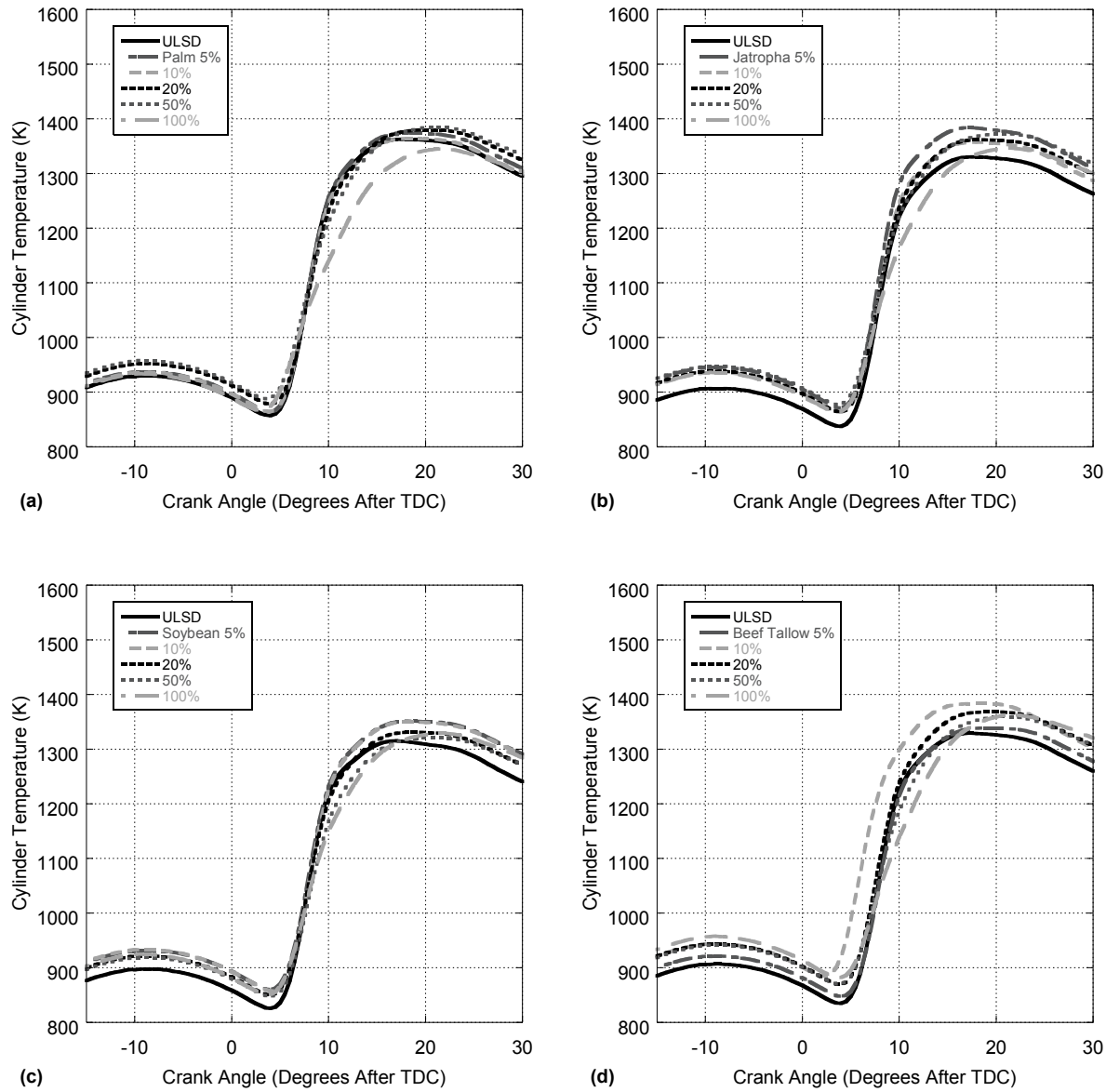


Figure A-22. Average Cylinder Temperature vs. Engine Crank Angle for Adjusted Palm (a), Jatropha (b), Soybean (c), and Beef Tallow (d) Biodiesel Blends (%-vol.) with ULSD at 13.5 N·m Loading.

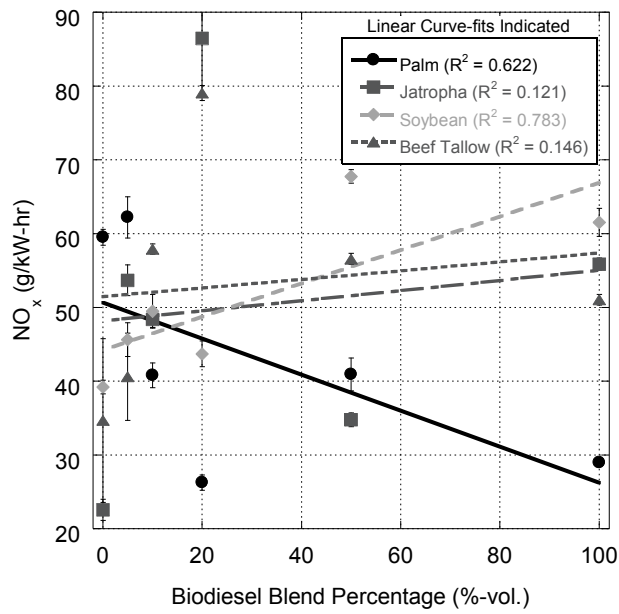


Figure A-23. Brake-Specific NO_x Emissions vs. Blend Percentage for Adjusted Blends at 0.5 N-m Loading. Tier 4 Regulation at 7.5 g/kW-hr (Not Displayed).

Table A-28. Brake-Specific NO_x Emissions vs. Blend Percentage for Adjusted Blends at 0.5 N-m Loading.

Biodiesel Blend %	Palm	Jatropha	Soybean	Beef Tallow
0	59.5 \pm 1.1	22.5 \pm 1.4	39.2 \pm 0.9	34.7 \pm 11.1
5	62.2 \pm 62.8	53.7 \pm 2.1	45.6 \pm 2.3	40. \pm 5.9
10	40.8 \pm 1.7	48.3 \pm 1.1	49.5 \pm 2.3	57.9 \pm 0.7
20	26.2 \pm 1.0	86.5 \pm 7.4	43.7 \pm 1.8	79.0 \pm 1.0
50	40.9 \pm 2.2	34.8 \pm 0.9	67.8 \pm 0.9	56.6 \pm 0.8
100	29.0 \pm 0.4	55.9 \pm 0.8	61.5 \pm 1.9	51.0 \pm 0.7

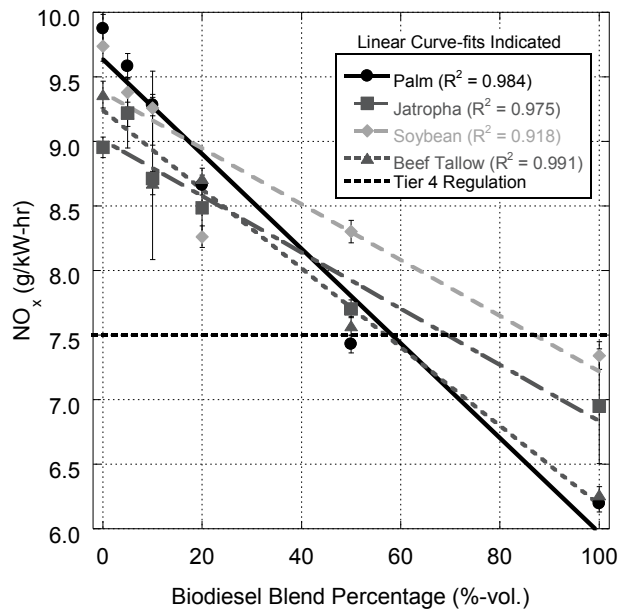


Figure A-24. Brake-Specific NOx Emissions vs. Blend Percentage for Adjusted Blends at 4.5 N·m Loading.

Table A-29. Brake-Specific NOx Emissions vs. Blend Percentage for Adjusted Blends at 4.5 N·m Loading.

Biodiesel Blend %	Palm	Jatropha	Soybean	Beef Tallow
0	9.9 ± 0.1	9.0 ± 0.1	9.7 ± 0.1	9.4 ± 0.1
5	9.6 ± 0.1	9.2 ± 0.3	9.4 ± 0.1	9.2 ± 0.1
10	9.3 ± 0.1	8.7 ± 0.6	9.3 ± 0.3	8.7 ± 0.1
20	8.7 ± 0.1	8.5 ± 0.2	8.3 ± 0.1	8.7 ± 0.1
50	7.4 ± 0.1	7.7 ± 0.1	8.3 ± 0.1	7.6 ± 0.1
100	6.2 ± 0.1	7.0 ± 0.4	7.3 ± 0.1	6.3 ± 0.1

Table A-30. Brake-Specific NOx Emissions vs. Blend Percentage for Adjusted Blends at 9.0 N·m Loading.

Biodiesel Blend %	Palm	Jatropha	Soybean	Beef Tallow
0	6.11 ± 0.06	5.93 ± 0.05	6.37 ± 0.05	6.06 ± 0.06
5	5.98 ± 0.05	6.01 ± 0.05	5.88 ± 0.38	5.77 ± 0.05
10	5.79 ± 0.05	5.74 ± 0.37	5.75 ± 0.38	5.65 ± 0.05
20	5.45 ± 0.05	5.62 ± 0.04	5.47 ± 0.05	5.48 ± 0.05
50	4.81 ± 0.04	5.11 ± 0.33	5.23 ± 0.33	4.78 ± 0.05
100	4.14 ± 0.04	4.53 ± 0.08	4.77 ± 0.04	4.03 ± 0.04

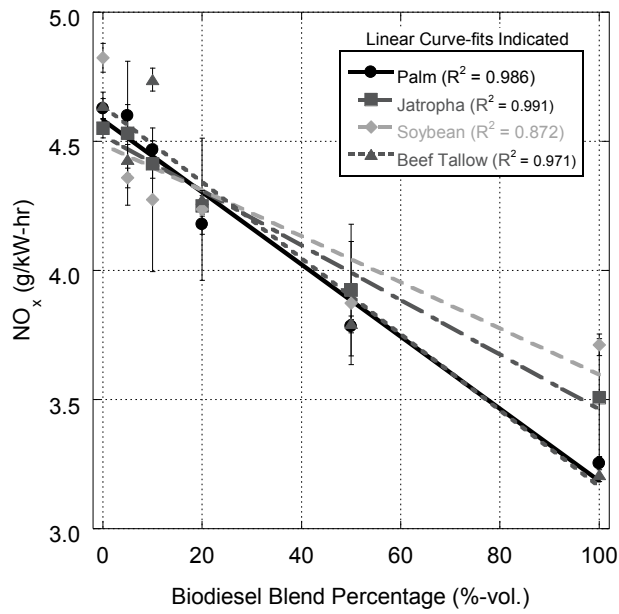


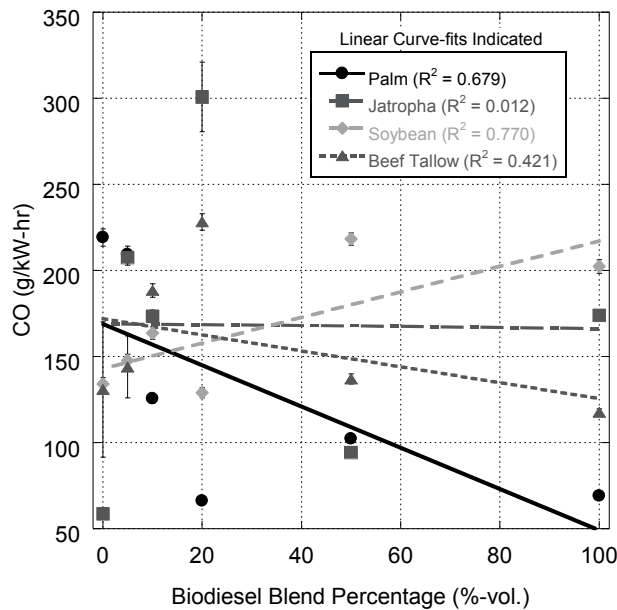
Figure A-25. Brake-Specific NOx Emissions vs. Blend Percentage for Adjusted Blends at 13.5 N-m Loading. Tier 4 Regulation at 7.5 g/kW-hr (Not Displayed).

Table A-31. Brake-Specific NOx Emissions vs. Blend Percentage for Adjusted Blends at 13.5 N-m Loading.

Biodiesel Blend %	Palm	Jatropha	Soybean	Beef Tallow
0	4.63 ± 0.04	4.55 ± 0.04	4.82 ± 0.06	4.64 ± 0.05
5	4.60 ± 0.04	4.53 ± 0.28	4.36 ± 0.04	4.43 ± 0.06
10	4.47 ± 0.04	4.41 ± 0.06	4.27 ± 0.28	4.74 ± 0.04
20	4.18 ± 0.04	4.25 ± 0.04	4.24 ± 0.28	4.27 ± 0.04
50	3.78 ± 0.03	3.92 ± 0.26	3.87 ± 0.24	3.80 ± 0.03
100	3.25 ± 0.02	3.51 ± 0.23	3.71 ± 0.04	3.21 ± 0.03

Table A-32. Brake-Specific NOx Emissions vs. Blend Percentage for Adjusted Blends at 18.0 N-m Loading.

Biodiesel Blend %	Palm	Jatropha	Soybean	Beef Tallow
0	4.00 ± 0.04	3.84 ± 0.03	4.01 ± 0.04	4.11 ± 0.04
5	3.97 ± 0.03	3.92 ± 0.04	3.92 ± 0.04	3.90 ± 0.04
10	3.92 ± 0.03	3.94 ± 0.03	3.95 ± 0.26	3.97 ± 0.03
20	3.74 ± 0.03	3.78 ± 0.03	3.72 ± 0.24	3.80 ± 0.03
50	3.54 ± 0.04	3.59 ± 0.03	3.58 ± 0.23	3.53 ± 0.03
100	3.11 ± 0.02	3.27 ± 0.03	3.43 ± 0.22	3.13 ± 0.03



**Figure A-26. Brake-Specific CO Emissions vs. Blend Percentage for Adjusted Blends at 0.5 N-m Loading.
Tier 4 Regulation at 8.0 g/kW-hr (Not Displayed).**

Table A-33. Brake-Specific CO Emissions vs. Blend Percentage for Adjusted Blends at 0.5 N-m Loading.

Biodiesel Blend %	Palm	Jatropha	Soybean	Beef Tallow
0	219.2 \pm 5.0	58.6 \pm 1.3	134.1 \pm 3.5	130.9 \pm 39.3
5	209.3 \pm 4.9	207.6 \pm 4.5	147.6 \pm 3.6	143.9 \pm 18.0
10	125.6 \pm 2.6	173.3 \pm 3.7	163.6 \pm 3.6	188.4 \pm 3.9
20	66.3 \pm 2.1	300.8 \pm 20.2	129.0 \pm 3.1	228.2 \pm 4.7
50	102.2 \pm 2.4	94.3 \pm 2.2	218.3 \pm 3.6	137.0 \pm 2.9
100	69.1 \pm 1.2	174.0 \pm 3.2	202.3 \pm 3.9	117.7 \pm 2.0

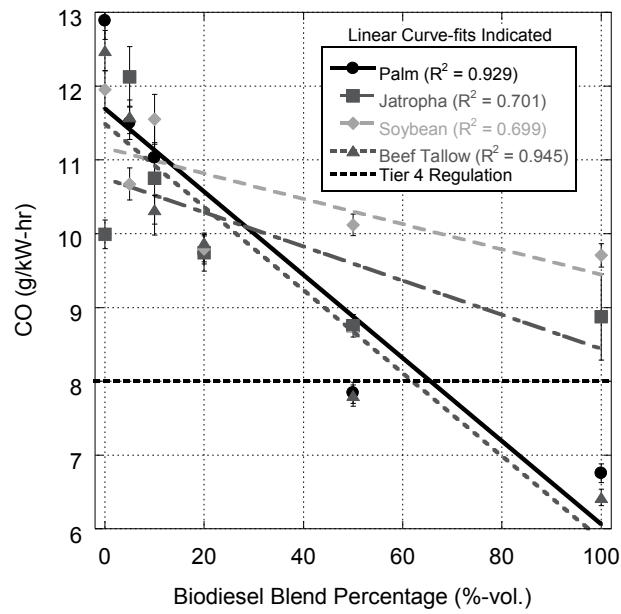
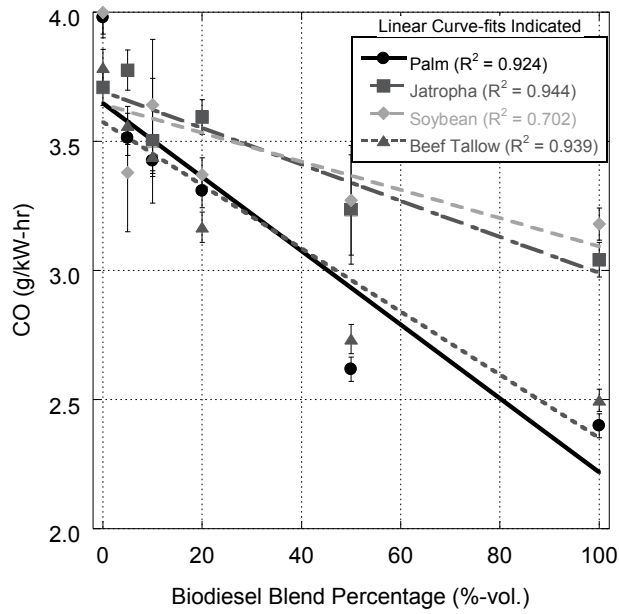


Figure A-27. Brake-Specific CO Emissions vs. Blend Percentage for Adjusted Blends at 4.5 N·m Loading.

Table A-34. Brake-Specific CO Emissions vs. Blend Percentage for Adjusted Blends at 4.5 N·m Loading.

Biodiesel Blend %	Palm	Jatropha	Soybean	Beef Tallow
0	12.9 ± 0.3	10.0 ± 0.2	12.0 ± 0.3	12.5 ± 0.3
5	11.5 ± 0.2	12.1 ± 0.4	10.7 ± 0.2	11.6 ± 0.2
10	11.0 ± 0.2	10.8 ± 0.8	11.6 ± 0.3	10.3 ± 0.2
20	9.7 ± 0.1	9.7 ± 0.2	9.8 ± 0.2	9.9 ± 0.1
50	7.8 ± 0.1	8.8 ± 0.2	10.1 ± 0.1	7.8 ± 0.1
100	6.8 ± 0.1	8.9 ± 0.6	9.7 ± 0.2	6.4 ± 0.1



**Figure A-28. Brake-Specific CO Emissions vs. Blend Percentage for Adjusted Blends at 9.0 N-m Loading.
Tier 4 Regulation at 8.0 g/kW-hr (Not Displayed).**

Table A-35. Brake-Specific CO Emissions vs. Blend Percentage for Adjusted Blends at 9.0 N-m Loading.

Biobiodiesel Blend %	Palm	Jatropha	Soybean	Beef Tallow
0	3.98 ± 0.08	3.71 ± 0.07	4.00 ± 0.08	3.79 ± 0.07
5	3.51 ± 0.07	3.78 ± 0.08	3.38 ± 0.23	3.56 ± 0.07
10	3.43 ± 0.06	3.50 ± 0.24	3.64 ± 0.25	3.44 ± 0.07
20	3.31 ± 0.07	3.59 ± 0.07	3.37 ± 0.07	3.17 ± 0.06
50	2.62 ± 0.05	3.24 ± 0.21	3.27 ± 0.21	2.73 ± 0.06
100	2.40 ± 0.05	3.04 ± 0.07	3.18 ± 0.06	2.50 ± 0.04

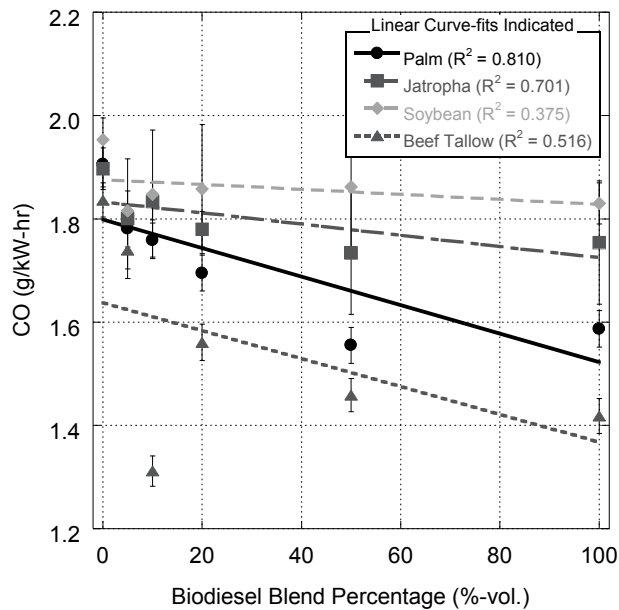


Figure A-29. Brake-Specific CO Emissions vs. Blend Percentage for Adjusted Blends at 13.5 N·m Loading. Tier 4 Regulation at 8.0 g/kW-hr (Not Displayed).

Table A-36. Brake-Specific CO Emissions vs. Blend Percentage for Adjusted Blends at 13.5 N·m Loading.

Biodiesel Blend %	Palm	Jatropha	Soybean	Beef Tallow
0	1.91 ± 0.04	1.90 ± 0.04	1.95 ± 0.04	1.84 ± 0.03
5	1.78 ± 0.04	1.80 ± 0.12	1.82 ± 0.04	1.74 ± 0.04
10	1.76 ± 0.03	1.83 ± 0.04	1.85 ± 0.12	1.31 ± 0.03
20	1.69 ± 0.03	1.78 ± 0.03	1.86 ± 0.12	1.56 ± 0.04
50	1.56 ± 0.03	1.73 ± 0.12	1.86 ± 0.12	1.46 ± 0.03
100	1.59 ± 0.04	1.75 ± 0.12	1.83 ± 0.04	1.42 ± 0.03

Table A-37. Brake-Specific CO Emissions vs. Blend Percentage for Adjusted Blends at 18.0 N·m Loading.

Biodiesel Blend %	Palm	Jatropha	Soybean	Beef Tallow
0	1.35 ± 0.04	1.41 ± 0.06	1.29 ± 0.05	1.25 ± 0.05
5	1.28 ± 0.05	1.31 ± 0.04	1.27 ± 0.05	1.21 ± 0.04
10	1.26 ± 0.05	1.19 ± 0.05	1.20 ± 0.09	1.10 ± 0.04
20	1.28 ± 0.04	1.26 ± 0.05	1.29 ± 0.10	1.09 ± 0.04
50	1.27 ± 0.05	1.31 ± 0.04	1.36 ± 0.10	1.12 ± 0.04
100	1.34 ± 0.04	1.31 ± 0.04	1.39 ± 0.10	1.10 ± 0.04

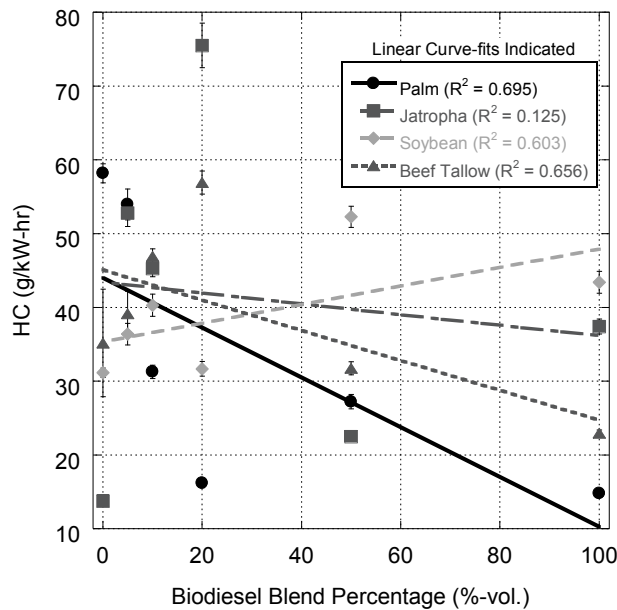


Figure A-30. Brake-Specific HC Emissions vs. Blend Percentage for Adjusted Blends at 0.5 N-m Loading.

Table A-38. Brake-Specific HC Emissions vs. Blend Percentage for Adjusted Blends at 0.5 N-m Loading.

Biodiesel Blend %	Palm	Jatropha	Soybean	Beef Tallow
0	58.2 ± 1.3	13.7 ± 0.4	31.2 ± 0.6	35.2 ± 7.3
5	53.9 ± 2.1	52.8 ± 1.8	36.4 ± 1.5	39.1 ± 3.1
10	31.2 ± 0.9	45.3 ± 1.1	40.3 ± 1.5	46.9 ± 1.0
20	16.2 ± 0.7	75.5 ± 3.0	31.7 ± 1.0	56.9 ± 1.5
50	27.2 ± 1.0	22.5 ± 0.5	52.3 ± 1.4	31.7 ± 0.9
100	14.8 ± 0.4	37.4 ± 1.0	43.4 ± 1.5	23.0 ± 0.4

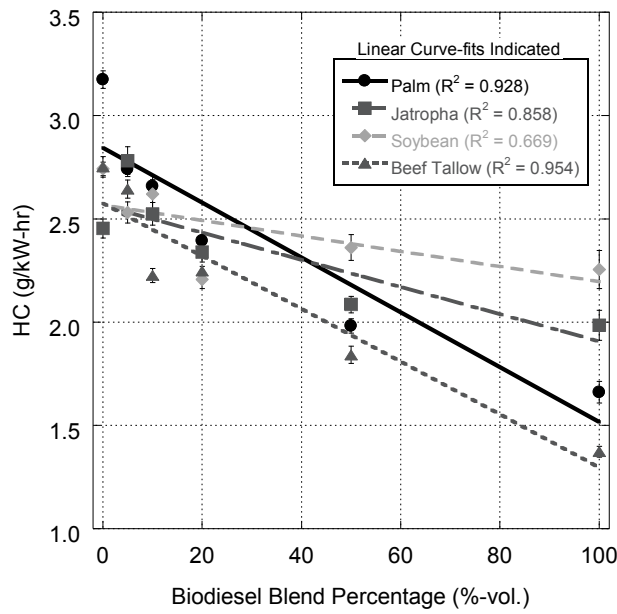


Figure A-31. Brake-Specific HC Emissions vs. Blend Percentage for Adjusted Blends at 4.5 N-m Loading.

Table A-39. Brake-Specific HC Emissions vs. Blend Percentage for Adjusted Blends at 4.5 N-m Loading.

Biodiesel Blend %	Palm	Jatropha	Soybean	Beef Tallow
0	3.175 ± 0.042	2.453 ± 0.046	2.742 ± 0.032	2.751 ± 0.050
5	2.741 ± 0.035	2.782 ± 0.068	2.531 ± 0.052	2.644 ± 0.044
10	2.658 ± 0.031	2.524 ± 0.055	2.620 ± 0.089	2.226 ± 0.034
20	2.393 ± 0.030	2.339 ± 0.048	2.207 ± 0.043	2.247 ± 0.024
50	1.982 ± 0.035	2.086 ± 0.040	2.361 ± 0.063	1.842 ± 0.042
100	1.660 ± 0.052	1.985 ± 0.072	2.255 ± 0.092	1.372 ± 0.027

Table A-40. Brake-Specific HC Emissions vs. Blend Percentage for Adjusted Blends at 9.0 N-m Loading.

Biodiesel Blend %	Palm	Jatropha	Soybean	Beef Tallow
0	1.232 ± 0.018	1.234 ± 0.023	1.203 ± 0.021	1.092 ± 0.029
5	1.022 ± 0.016	1.169 ± 0.021	1.075 ± 0.027	1.018 ± 0.014
10	1.077 ± 0.015	1.088 ± 0.034	1.059 ± 0.034	0.925 ± 0.010
20	1.103 ± 0.017	1.201 ± 0.021	1.133 ± 0.022	0.917 ± 0.011
50	0.794 ± 0.018	1.102 ± 0.024	1.137 ± 0.055	0.748 ± 0.008
100	0.658 ± 0.019	0.970 ± 0.034	0.987 ± 0.027	0.610 ± 0.007

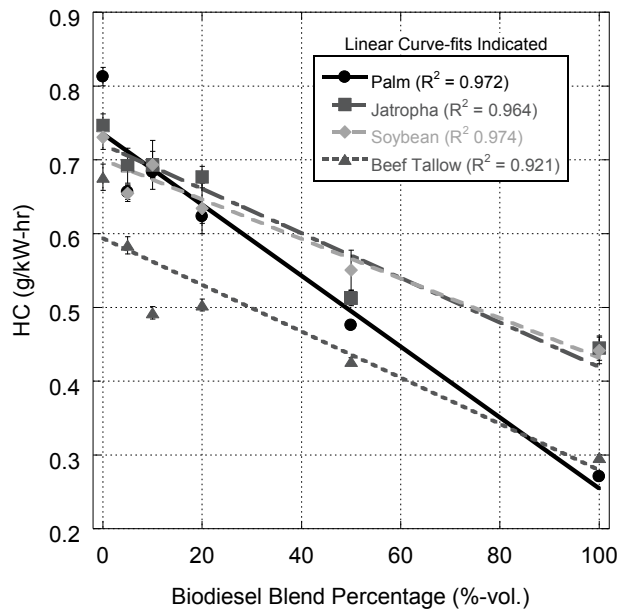


Figure A-32. Brake-Specific HC Emissions vs. Blend Percentage for Adjusted Blends at 13.5 N-m Loading.

Table A-41. Brake-Specific HC Emissions vs. Blend Percentage for Adjusted Blends at 13.5 N-m Loading.

Biodiesel Blend %	Palm	Jatropha	Soybean	Beef Tallow
0	0.813 ± 0.012	0.747 ± 0.016	0.730 ± 0.016	0.677 ± 0.018
5	0.656 ± 0.010	0.692 ± 0.024	0.655 ± 0.011	0.584 ± 0.012
10	0.684 ± 0.007	0.693 ± 0.019	0.693 ± 0.033	0.493 ± 0.009
20	0.623 ± 0.009	0.677 ± 0.015	0.634 ± 0.034	0.503 ± 0.008
50	0.476 ± 0.005	0.513 ± 0.010	0.551 ± 0.027	0.427 ± 0.005
100	0.271 ± 0.004	0.445 ± 0.016	0.442 ± 0.018	0.296 ± 0.004

Table A-42. Brake-Specific HC Emissions vs. Blend Percentage for Adjusted Blends at 18.0 N-m Loading.

Biodiesel Blend %	Palm	Jatropha	Soybean	Beef Tallow
0	0.393 ± 0.008	0.388 ± 0.009	0.423 ± 0.010	0.388 ± 0.007
5	0.330 ± 0.010	0.406 ± 0.013	0.418 ± 0.015	0.348 ± 0.006
10	0.368 ± 0.011	0.413 ± 0.009	0.424 ± 0.028	0.361 ± 0.008
20	0.341 ± 0.010	0.384 ± 0.007	0.380 ± 0.022	0.333 ± 0.007
50	0.294 ± 0.006	0.342 ± 0.008	0.383 ± 0.018	0.303 ± 0.006
100	0.210 ± 0.006	0.274 ± 0.008	0.297 ± 0.015	0.235 ± 0.005

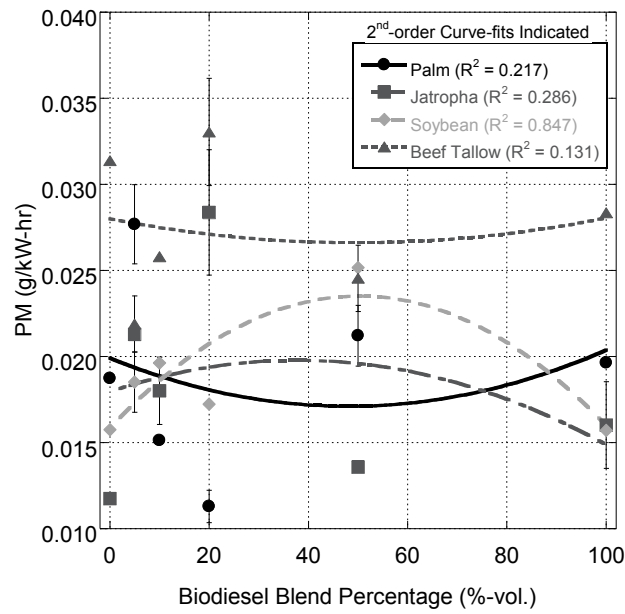


Figure A-33. Brake-Specific PM Emissions vs. Blend Percentage for Adjusted Blends at 0.5 N-m Loading. Tier 4 Regulation at 0.4 g/kW-hr (Not Displayed).

Table A-43. Brake-Specific PM Emissions vs. Blend Percentage for Adjusted Blends at 0.5 N-m Loading.

Biodiesel Blend %	Palm	Jatropha	Soybean	Beef Tallow
0	0.019 ± 0.000	0.012 ± 0.000	0.016 ± 0.000	0.031 ± 0.000
5	0.028 ± 0.002	0.021 ± 0.000	0.019 ± 0.002	0.022 ± 0.002
10	0.015 ± 0.000	0.018 ± 0.002	0.020 ± 0.000	0.026 ± 0.000
20	0.011 ± 0.001	0.028 ± 0.004	0.017 ± 0.000	0.033 ± 0.003
50	0.021 ± 0.002	0.014 ± 0.000	0.025 ± 0.000	0.025 ± 0.002
100	0.020 ± 0.000	0.016 ± 0.003	0.016 ± 0.000	0.028 ± 0.000

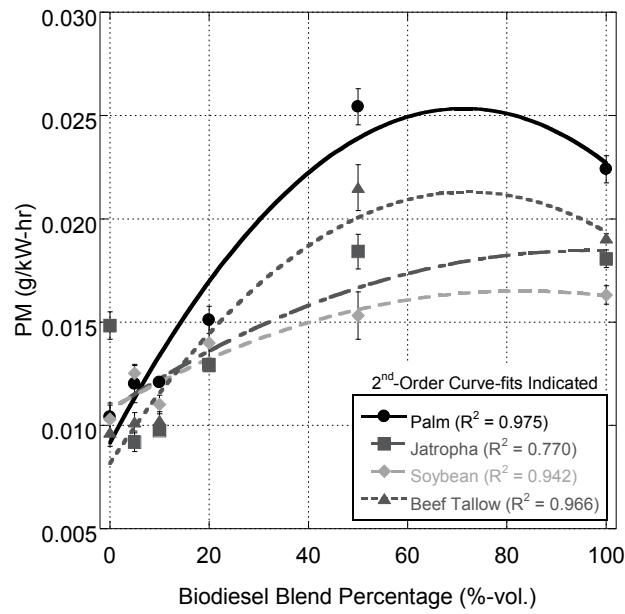


Figure A-34. Brake-Specific PM Emissions vs. Blend Percentage for Adjusted Blends at 4.5 N-m Loading. Tier 4 Regulation at 0.4 g/kW-hr (Not Displayed).

Table A-44. Brake-Specific PM Emissions vs. Blend Percentage for Adjusted Blends at 4.5 N-m Loading.

Biodiesel Blend %	Palm	Jatropha	Soybean	Beef Tallow
0	0.010 ± 0.001	0.015 ± 0.001	0.010 ± 0.001	0.010 ± 0.001
5	0.012 ± 0.001	0.009 ± 0.000	0.013 ± 0.000	0.010 ± 0.000
10	0.012 ± 0.000	0.010 ± 0.000	0.011 ± 0.000	0.010 ± 0.000
20	0.015 ± 0.001	0.013 ± 0.000	0.014 ± 0.001	0.013 ± 0.000
50	0.025 ± 0.001	0.018 ± 0.001	0.015 ± 0.001	0.022 ± 0.001
100	0.022 ± 0.001	0.018 ± 0.000	0.016 ± 0.000	0.019 ± 0.000

Table A-45. Brake-Specific PM Emissions vs. Blend Percentage for Adjusted Blends at 9.0 N-m Loading.

Biodiesel Blend %	Palm	Jatropha	Soybean	Beef Tallow
0	0.021 ± 0.000	0.027 ± 0.000	0.020 ± 0.001	0.020 ± 0.001
5	0.025 ± 0.001	0.023 ± 0.001	0.028 ± 0.000	0.021 ± 0.000
10	0.025 ± 0.000	0.026 ± 0.001	0.023 ± 0.002	0.019 ± 0.000
20	0.030 ± 0.000	0.026 ± 0.001	0.034 ± 0.000	0.024 ± 0.001
50	0.040 ± 0.000	0.033 ± 0.000	0.034 ± 0.002	0.029 ± 0.000
100	0.031 ± 0.000	0.027 ± 0.000	0.029 ± 0.000	0.022 ± 0.001

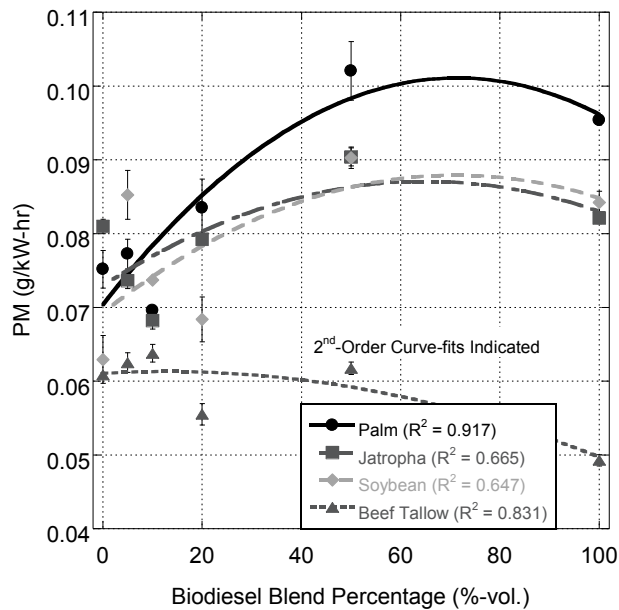


Figure A-35. Brake-Specific PM Emissions vs. Blend Percentage for Adjusted Blends at 13.5 N·m Loading. Tier 4 Regulation at 0.4 g/kW-hr (Not Displayed).

Table A-46. Brake-Specific PM Emissions vs. Blend Percentage for Adjusted Blends at 13.5 N·m Loading.

Biodiesel Blend %	Palm	Jatropha	Soybean	Beef Tallow
0	0.075 ± 0.003	0.081 ± 0.001	0.063 ± 0.003	0.061 ± 0.000
5	0.077 ± 0.002	0.074 ± 0.001	0.085 ± 0.003	0.063 ± 0.001
10	0.070 ± 0.000	0.068 ± 0.001	0.074 ± 0.000	0.064 ± 0.001
20	0.084 ± 0.004	0.079 ± 0.001	0.068 ± 0.003	0.056 ± 0.001
50	0.102 ± 0.004	0.090 ± 0.001	0.090 ± 0.001	0.062 ± 0.001
100	0.095 ± 0.001	0.082 ± 0.001	0.084 ± 0.002	0.049 ± 0.001

Table A-47. Brake-Specific PM Emissions vs. Blend Percentage for Adjusted Blends at 18.0 N·m Loading.

Biodiesel Blend %	Palm	Jatropha	Soybean	Beef Tallow
0	0.455 ± 0.006	0.568 ± 0.020	0.336 ± 0.026	0.351 ± 0.015
5	0.490 ± 0.011	0.462 ± 0.004	0.430 ± 0.003	0.339 ± 0.008
10	0.439 ± 0.006	0.387 ± 0.001	0.356 ± 0.003	0.317 ± 0.001
20	0.428 ± 0.008	0.441 ± 0.017	0.405 ± 0.012	0.319 ± 0.000
50	0.426 ± 0.004	0.400 ± 0.007	0.404 ± 0.011	0.290 ± 0.009
100	0.275 ± 0.001	0.252 ± 0.005	0.309 ± 0.012	0.176 ± 0.009

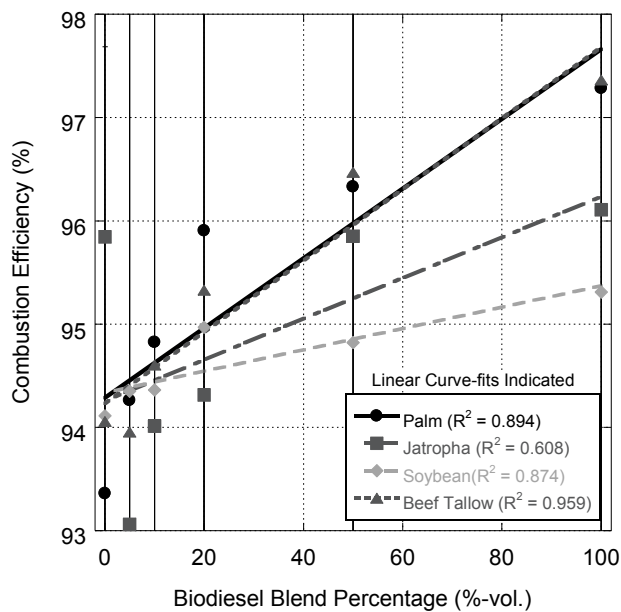


Figure A-36. Combustion Efficiency vs. Blend Percentage for Adjusted Blends at 0.5 N·m Loading.

Table A-48. Combustion Efficiency vs. Blend Percentage for Adjusted Blends at 0.5 N·m Loading.

Biodiesel Blend %	Palm	Jatropha	Soybean	Beef Tallow
0	93 + 6 - 6	96 + 4 - 5	94 + 4 - 4	94 + 6 - 23
5	94 + 6 - 19	93 + 7 - 37	94 + 6 - 10	94 + 6 - 11
10	95 + 5 - 12	94 + 6 - 10	94 + 6 - 27	95 + 5 - 6
20	96 + 4 - 18	94 + 6 - 30	95 + 5 - 9	95 + 5 - 10
50	96 + 4 - 15	96 + 4 - 5	95 + 5 - 12	96 + 4 - 7
100	97 + 3 - 10	96 + 4 - 20	95 + 5 - 17	97 + 3 - 15

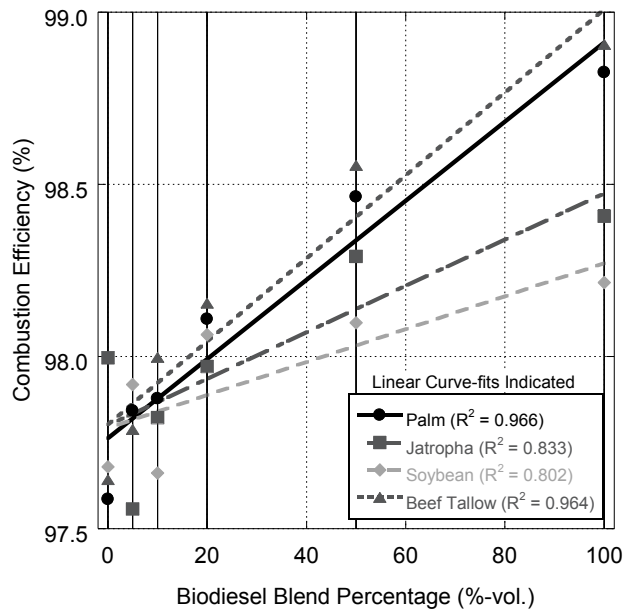


Figure A-37. Combustion Efficiency vs. Blend Percentage for Adjusted Blends at 4.5 N·m Loading.

Table A-49. Combustion Efficiency vs. Blend Percentage for Adjusted Blends at 4.5 N·m Loading.

Biodiesel Blend %	Palm	Jatropha	Soybean	Beef Tallow
0	98 + 2 - 13	98 + 2 - 3	98 + 2 - 3	98 + 2 - 3
5	98 + 2 - 4	98 + 2 - 4	98 + 2 - 10	98 + 2 - 3
10	98 + 2 - 2	98 + 2 - 23	98 + 2 - 12	98 + 2 - 3
20	98 + 2 - 3	98 + 2 - 4	98 + 2 - 3	98 + 2 - 2
50	98 + 2 - 3	98 + 2 - 3	98 + 2 - 4	99 + 1 - 3
100	99 + 1 - 7	98 + 2 - 13	98 + 2 - 6	99 + 1 - 6

Table A-50. Combustion Efficiency vs. Blend Percentage for Adjusted Blends at 9.0 N·m Loading.

Biodiesel Blend %	Palm	Jatropha	Soybean	Beef Tallow
0	99 + 1 - 2	99 + 1 - 2	99 + 1 - 2	99 + 1 - 3
5	99 + 1 - 2	99 + 1 - 2	99 + 1 - 6	99 + 1 - 2
10	99 + 1 - 2	99 + 1 - 10	99 + 1 - 9	99 + 1 - 2
20	99 + 1 - 2	99 + 1 - 2	99 + 1 - 2	99 + 1 - 2
50	99 + 1 - 10	99 + 1 - 10	99 + 1 - 6	99 + 1 - 2
100	99 + 1 - 3	99 + 1 - 5	99 + 1 - 5	99 + 1 - 3

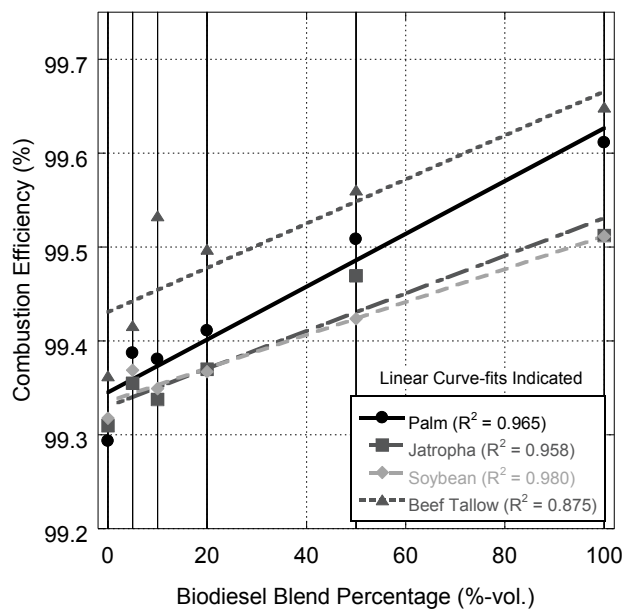


Figure A-38. Combustion Efficiency vs. Blend Percentage for Adjusted Blends at 13.5 N·m Loading.

Table A-51. Combustion Efficiency vs. Blend Percentage for Adjusted Blends at 13.5 N·m Loading.

Biodiesel Blend %	Palm	Jatropha	Soybean	Beef Tallow
0	99 + 1 - 2	99 + 1 - 2	99 + 1 - 3	99 + 1 - 2
5	99 + 1 - 2	99 + 1 - 5	99 + 1 - 2	99 + 1 - 2
10	99 + 1 - 3	99 + 1 - 2	99 + 1 - 6	100 + 0 - 2
20	99 + 1 - 2	99 + 1 - 2	99 + 1 - 9	99 + 1 - 2
50	100 + 0 - 2	99 + 1 - 10	99 + 1 - 6	100 + 0 - 2
100	100 + 0 - 4	100 + 0 - 7	100 + 0 - 3	100 + 0 - 5

Table A-52. Combustion Efficiency vs. Blend Percentage for Adjusted Blends at 18.0 N·m Loading.

Biodiesel Blend %	Palm	Jatropha	Soybean	Beef Tallow
0	99 + 1 - 2	99 + 1 - 3	99 + 1 - 4	99 + 1 - 3
5	99 + 1 - 3	99 + 1 - 2	99 + 1 - 3	100 + 0 - 3
10	99 + 1 - 3	99 + 1 - 2	99 + 1 - 6	100 + 0 - 3
20	99 + 1 - 4	99 + 1 - 3	99 + 1 - 6	100 + 0 - 3
50	100 + 0 - 2	100 + 0 - 7	99 + 1 - 6	100 + 0 - 3
100	100 + 0 - 2	100 + 0 - 4	100 + 0 - 6	100 + 0 - 3

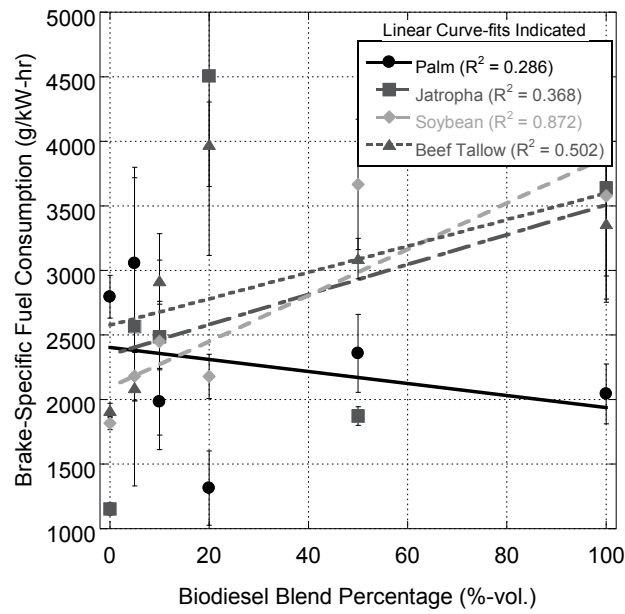


Figure A-39. Brake-Specific Fuel Consumption vs. Blend Percentage for Adjusted Blends at 0.5 N·m Loading.

Table A-53. Brake-Specific Fuel Consumption vs. Blend Percentage for Adjusted Blends at 0.5 N·m Loading.

Biodiesel Blend %	Palm	Jatropha	Soybean	Beef Tallow
0	2796 ± 165	1153 ± 47	1817 ± 52	1915 ± 55
5	3057 ± 660	2565 ± 1234	2181 ± 186	2093 ± 103
10	1984 ± 258	2485 ± 254	2449 ± 837	2921 ± 158
20	1315 ± 288	4507 ± 1390	2179 ± 172	3977 ± 328
50	2358 ± 302	1872 ± 73	3668 ± 506	3092 ± 156
100	2045 ± 232	3638 ± 858	3576 ± 619	3363 ± 608

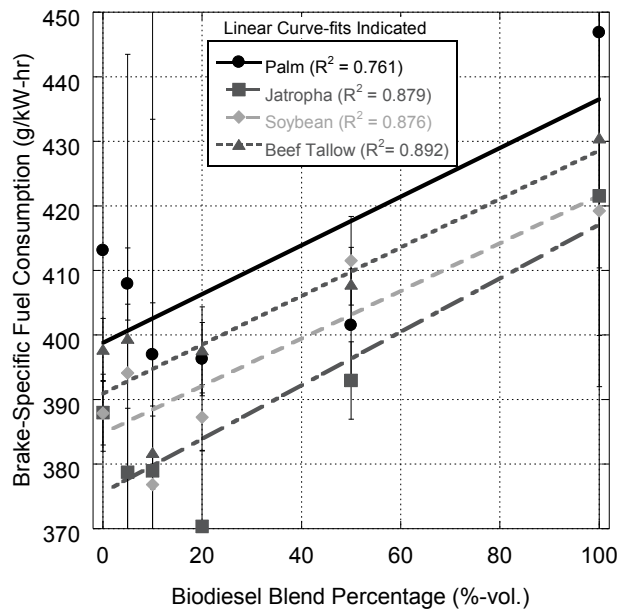


Figure A-40. Brake-Specific Fuel Consumption vs. Blend Percentage for Adjusted Blends at 4.5 N-m Loading.

Table A-54. Brake-Specific Fuel Consumption vs. Blend Percentage for Adjusted Blends at 4.5 N-m Loading.

Biodiesel Blend %	Palm	Jatropha	Soybean	Beef Tallow
0	413 ± 63	388 ± 6	388 ± 5	398 ± 5
5	408 ± 6	379 ± 10	394 ± 49	399 ± 5
10	397 ± 8	379 ± 105	377 ± 57	382 ± 6
20	396 ± 6	370 ± 12	387 ± 5	398 ± 7
50	401 ± 9	393 ± 6	412 ± 7	408 ± 6
100	447 ± 36	422 ± 60	419 ± 27	431 ± 31

Table A-55. Brake-Specific Fuel Consumption vs. Blend Percentage for Adjusted Blends at 9.0 N-m Loading.

Biodiesel Blend %	Palm	Jatropha	Soybean	Beef Tallow
0	278 ± 5	282 ± 3	278 ± 3	285 ± 3
5	286 ± 3	279 ± 3	276 ± 3	280 ± 2
10	282 ± 3	285 ± 28	260 ± 21	283 ± 4
20	283 ± 3	284 ± 3	286 ± 3	281 ± 3
50	291 ± 37	298 ± 31	294 ± 3	296 ± 3
100	317 ± 11	311 ± 17	313 ± 17	310 ± 9

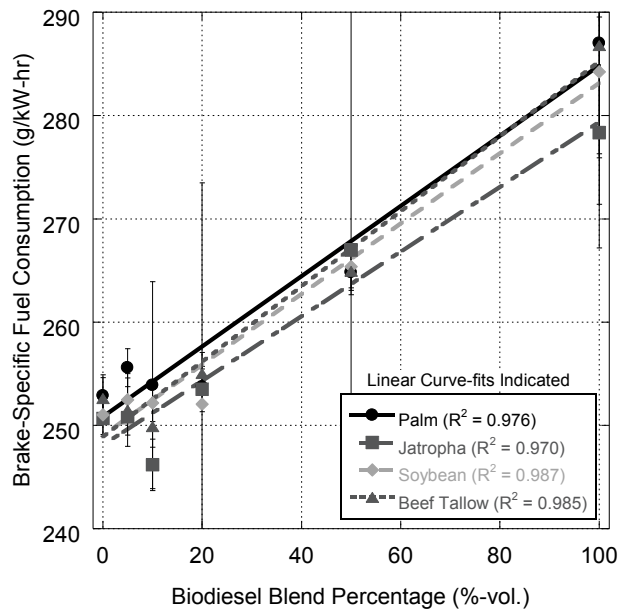


Figure A-41. Brake-Specific Fuel Consumption vs. Blend Percentage for Adjusted Blends at 13.5 N·m Loading.

Table A-56. Brake-Specific Fuel Consumption vs. Blend Percentage for Adjusted Blends at 13.5 N·m Loading.

Biodiesel Blend %	Palm	Jatropha	Soybean	Beef Tallow
0	253 ± 2	251 ± 2	251 ± 2	253 ± 2
5	256 ± 2	251 ± 2	252 ± 2	251 ± 4
10	254 ± 10	246 ± 2	252 ± 2	250 ± 2
20	254 ± 2	254 ± 2	252 ± 21	255 ± 2
50	265 ± 2	267 ± 26	265 ± 2	265 ± 2
100	287 ± 11	278 ± 11	284 ± 8	287 ± 15

Table A-57. Brake-Specific Fuel Consumption vs. Blend Percentage for Adjusted Blends at 18.0 N·m Loading.

Biodiesel Blend %	Palm	Jatropha	Soybean	Beef Tallow
0	243 ± 1	242 ± 2	240 ± 2	243 ± 1
5	246 ± 1	241 ± 1	243 ± 2	241 ± 1
10	244 ± 1	240 ± 1	240 ± 1	241 ± 1
20	250 ± 10	245 ± 1	247 ± 1	244 ± 1
50	257 ± 2	258 ± 20	255 ± 1	256 ± 1
100	274 ± 2	274 ± 11	270 ± 2	274 ± 4

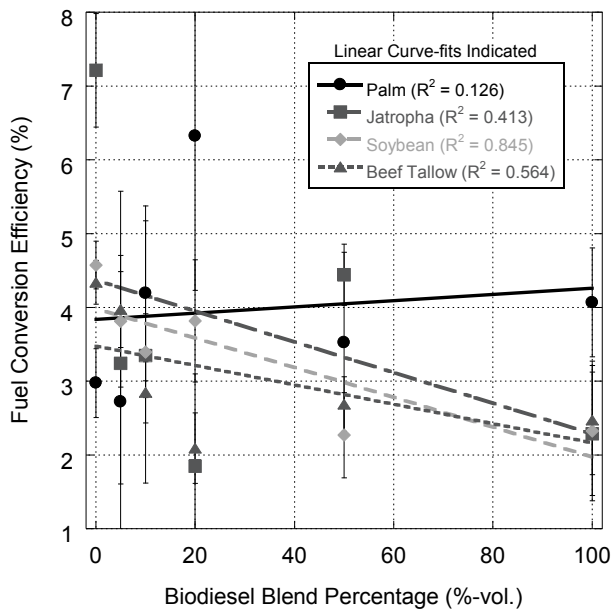


Figure A-42. Fuel Conversion Efficiency vs. Blend Percentage for Adjusted Blends at 0.5 N·m Loading.

Table A-58. Fuel Conversion Efficiency vs. Blend Percentage for Adjusted Blends at 0.5 N·m Loading.

Biodiesel Blend %	Palm	Jatropha	Soybean	Beef Tallow
0	3.0 ± 0.5	7.2 ± 0.8	4.6 ± 0.3	4.3 ± 0.3
5	2.7 ± 1.1	3.2 ± 2.3	3.8 ± 0.9	4.0 ± 0.5
10	4.2 ± 1.2	3.3 ± 0.6	3.4 ± 1.8	2.8 ± 0.4
20	6.3 ± 2.1	1.8 ± 1.3	3.8 ± 0.8	2.1 ± 0.5
50	3.5 ± 1.2	4.4 ± 0.4	2.3 ± 0.6	2.7 ± 0.4
100	4.1 ± 0.7	2.3 ± 0.8	2.3 ± 0.9	2.5 ± 0.7

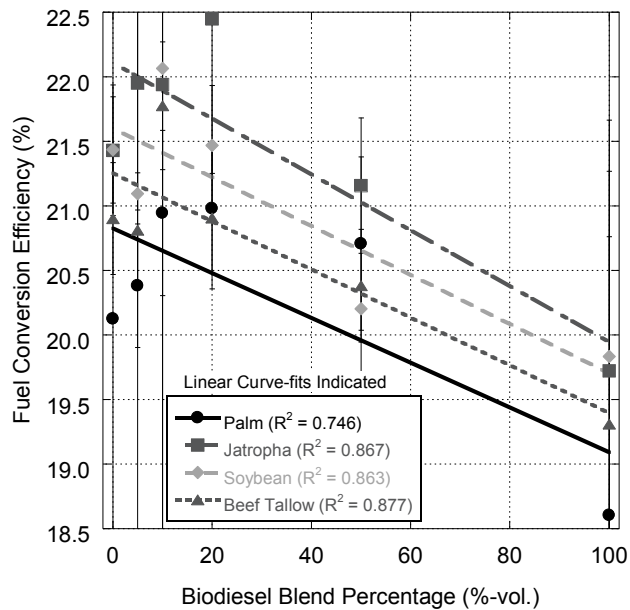


Figure A-43. Fuel Conversion Efficiency vs. Blend Percentage for Adjusted Blends at 4.5 N·m Loading.

Table A-59. Fuel Conversion Efficiency vs. Blend Percentage for Adjusted Blends at 4.5 N·m Loading.

Biodiesel Blend %	Palm	Jatropha	Soybean	Beef Tallow
0	20.1 ± 4.4	21.4 ± 0.5	21.4 ± 0.4	20.9 ± 0.4
5	20.4 ± 0.5	22.0 ± 1.0	21.1 ± 3.7	20.8 ± 0.4
10	20.9 ± 0.6	21.9 ± 8.7	22.1 ± 4.7	21.8 ± 0.5
20	21.0 ± 0.5	22.5 ± 1.2	21.5 ± 0.5	20.9 ± 0.5
50	20.7 ± 0.7	21.2 ± 0.5	20.2 ± 0.5	20.4 ± 0.4
100	18.6 ± 2.2	19.7 ± 4.0	19.8 ± 1.8	19.3 ± 2.0

Table A-60. Conversion Efficiency vs. Blend Percentage for Adjusted Blends at 9.0 N·m Loading.

Biodiesel Blend %	Palm	Jatropha	Soybean	Beef Tallow
0	30.0 ± 0.8	29.5 ± 0.4	29.9 ± 0.5	29.2 ± 0.4
5	29.1 ± 0.4	29.8 ± 0.5	30.1 ± 0.6	29.7 ± 0.4
10	29.5 ± 0.5	29.2 ± 4.1	32.0 ± 3.7	29.4 ± 0.6
20	29.4 ± 0.5	29.3 ± 0.4	29.1 ± 0.5	29.6 ± 0.5
50	28.6 ± 5.1	27.9 ± 4.1	28.3 ± 0.4	28.1 ± 0.4
100	26.2 ± 1.3	26.8 ± 2.1	26.6 ± 2.0	26.8 ± 1.2

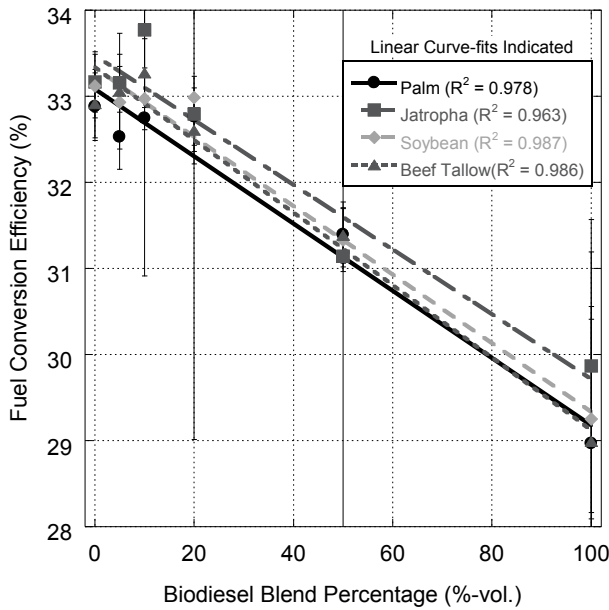


Figure A-44. Fuel Conversion Efficiency vs. Blend Percentage for Adjusted Blends at 13.5 N·m Loading.

Table A-61. Fuel Conversion Efficiency vs. Blend Percentage for Adjusted Blends at 13.5 N·m Loading.

Biodiesel Blend %	Palm	Jatropha	Soybean	Beef Tallow
0	32.9 ± 0.4	33.2 ± 0.4	33.1 ± 0.4	32.9 ± 0.4
5	32.5 ± 0.4	33.2 ± 0.3	32.9 ± 0.4	33.1 ± 0.7
10	32.7 ± 1.8	33.8 ± 0.5	33.0 ± 0.4	33.3 ± 0.4
20	32.8 ± 0.3	32.8 ± 0.4	33.0 ± 4.0	32.6 ± 0.4
50	31.4 ± 0.4	31.1 ± 4.2	31.3 ± 0.4	31.4 ± 0.3
100	29.0 ± 1.6	29.9 ± 1.7	29.3 ± 1.2	29.0 ± 2.2

Table A-62. Fuel Conversion Efficiency vs. Blend Percentage for Adjusted Blends at 18.0 N·m Loading.

Biodiesel Blend %	Palm	Jatropha	Soybean	Beef Tallow
0	34.2 ± 0.3	34.3 ± 0.4	34.6 ± 0.3	34.3 ± 0.3
5	33.8 ± 0.3	34.5 ± 0.3	34.2 ± 0.3	34.4 ± 0.3
10	34.1 ± 0.3	34.7 ± 0.3	34.6 ± 0.2	34.5 ± 0.3
20	33.3 ± 1.8	33.9 ± 0.3	33.7 ± 0.3	34.1 ± 0.3
50	32.3 ± 0.3	32.2 ± 3.6	32.6 ± 0.3	32.4 ± 0.2
100	30.3 ± 0.3	30.4 ± 1.7	30.9 ± 0.3	30.4 ± 0.6

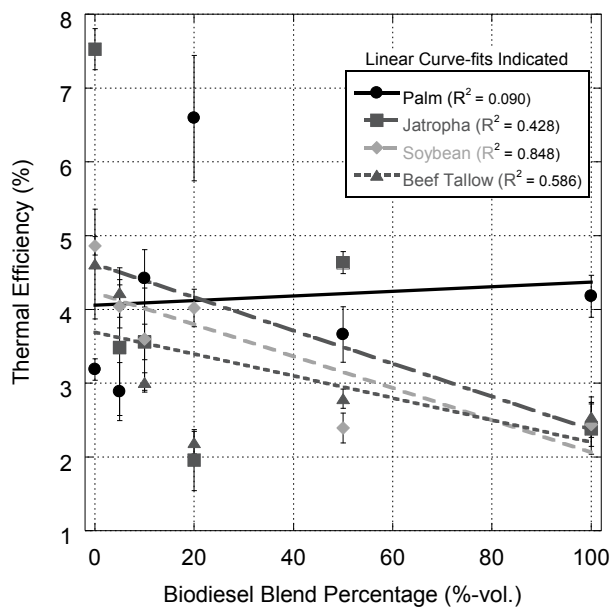


Figure A-45. Thermal Efficiency vs. Blend Percentage for Adjusted Blends at 0.5 N·m Loading.

Table A-63. Thermal Efficiency vs. Blend Percentage for Adjusted Blends at 0.5 N·m Loading.

Biodiesel Blend %	Palm	Jatropha	Soybean	Beef Tallow
0	3.2 ± 0.1	7.5 ± 0.3	4.9 ± 0.1	4.6 ± 0.7
5	2.9 ± 0.4	3.5 ± 0.9	4.0 ± 0.3	4.2 ± 0.3
10	4.4 ± 0.4	3.6 ± 0.2	3.6 ± 0.7	3.0 ± 0.1
20	6.6 ± 0.8	2.0 ± 0.4	4.0 ± 0.3	2.2 ± 0.2
50	3.7 ± 0.4	4.6 ± 0.1	2.4 ± 0.2	2.8 ± 0.1
100	4.2 ± 0.3	2.4 ± 0.3	2.4 ± 0.3	2.5 ± 0.3

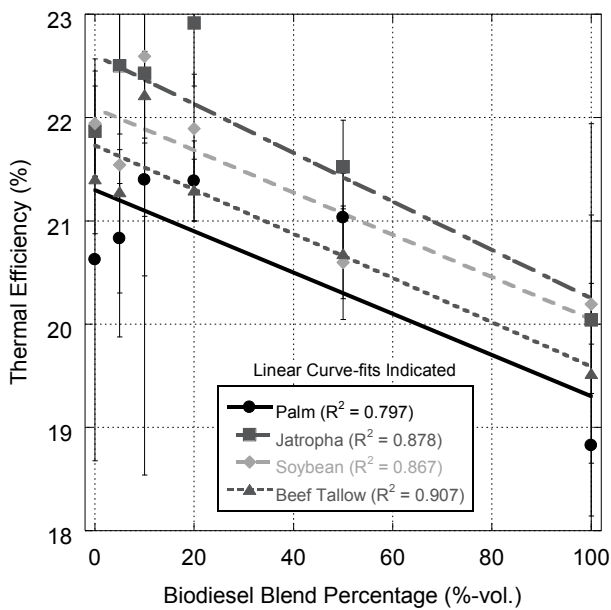


Figure A-46. Thermal Efficiency vs. Blend Percentage for Adjusted Blends at 4.5 N·m Loading.

Table A-64. Thermal Efficiency vs. Blend Percentage for Adjusted Blends at 4.5 N·m Loading.

Biodiesel Blend %	Palm	Jatropha	Soybean	Beef Tallow
0	20.6 ± 1.9	21.9 ± 0.4	21.9 ± 0.5	21.4 ± 0.5
5	20.8 ± 0.5	22.5 ± 0.7	21.5 ± 1.7	21.3 ± 0.4
10	21.4 ± 0.4	22.4 ± 3.9	22.6 ± 2.1	22.2 ± 0.4
20	21.4 ± 0.4	22.9 ± 0.6	21.9 ± 0.5	21.3 ± 0.3
50	21.0 ± 0.4	21.5 ± 0.4	20.6 ± 0.5	20.7 ± 0.4
100	18.8 ± 1.0	20.0 ± 1.9	20.2 ± 0.9	19.5 ± 0.9

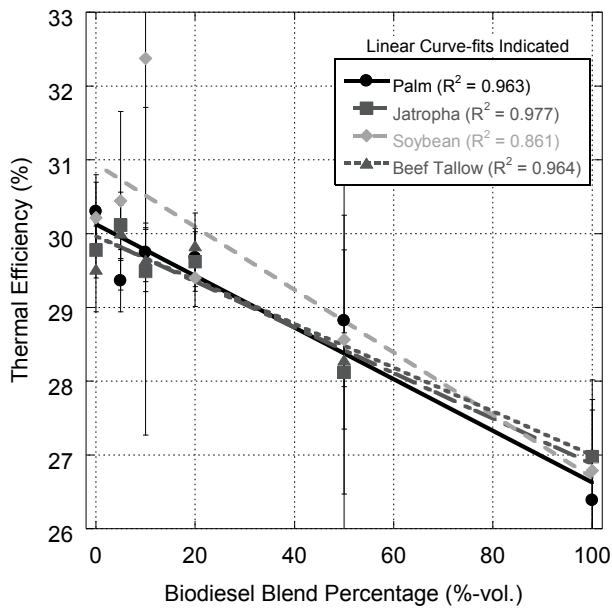


Figure A-47. Thermal Efficiency vs. Blend Percentage for Adjusted Blends at 9.0 N·m Loading.

Table A-65. Thermal Efficiency vs. Blend Percentage for Adjusted Blends at 9.0 N·m Loading.

Biodiesel Blend %	Palm	Jatropha	Soybean	Beef Tallow
0	30.3 ± 0.5	29.8 ± 0.4	30.2 ± 0.5	29.5 ± 0.6
5	29.4 ± 0.4	30.1 ± 0.5	30.4 ± 1.2	30.0 ± 0.4
10	29.7 ± 0.4	29.5 ± 2.2	32.4 ± 2.3	29.6 ± 0.4
20	29.7 ± 0.4	29.6 ± 0.4	29.4 ± 0.4	29.8 ± 0.4
50	28.8 ± 2.4	28.1 ± 2.1	28.6 ± 1.2	28.3 ± 0.4
100	26.4 ± 0.7	27.0 ± 1.0	26.8 ± 1.0	27.0 ± 0.6

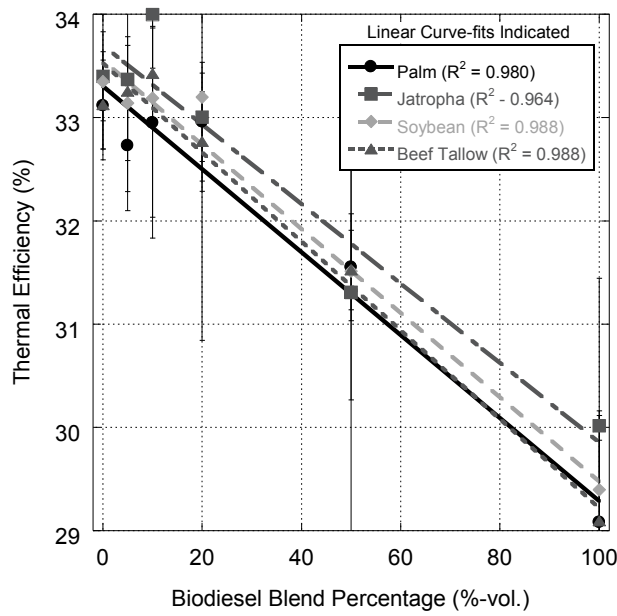


Figure A-48. Thermal Efficiency vs. Blend Percentage for Adjusted Blends at 13.5 N-m Loading.

Table A-66. Thermal Efficiency vs. Blend Percentage for Adjusted Blends at 13.5 N-m Loading.

Biodiesel Blend %	Palm	Jatropha	Soybean	Beef Tallow
0	33.1 ± 0.5	33.4 ± 0.4	33.3 ± 0.7	33.1 ± 0.4
5	32.7 ± 0.4	33.4 ± 1.3	33.1 ± 0.6	33.3 ± 0.5
10	33.0 ± 0.9	34.0 ± 0.5	33.2 ± 1.4	33.4 ± 0.5
20	33.0 ± 0.6	33.0 ± 0.4	33.2 ± 2.4	32.8 ± 0.5
50	31.6 ± 0.5	31.3 ± 2.3	31.5 ± 1.2	31.5 ± 0.4
100	29.1 ± 0.8	30.0 ± 1.4	29.4 ± 0.7	29.1 ± 1.1

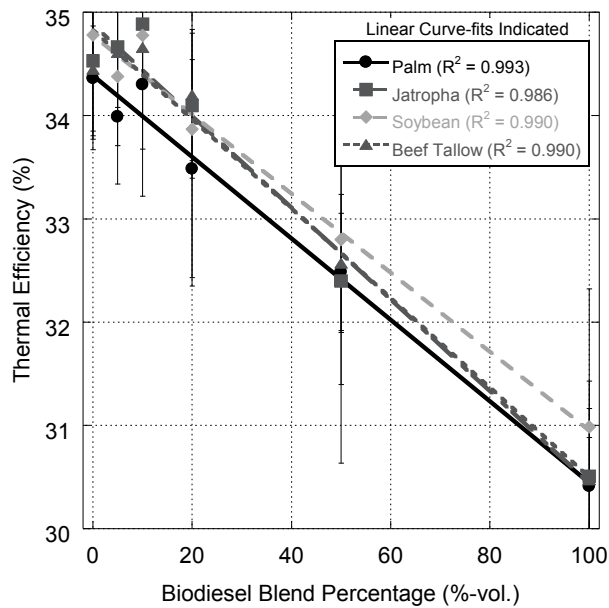


Figure A-49. Thermal Efficiency vs. Blend Percentage for Adjusted Blends at 18.0 N-m Loading.

Table A-67. Thermal Efficiency vs. Blend Percentage for Adjusted Blends at 18.0 N-m Loading.

Biodiesel Blend %	Palm	Jatropha	Soybean	Beef Tallow
0	34.4 \pm 0.5	34.5 \pm 0.7	34.8 \pm 1.0	34.4 \pm 0.8
5	34.0 \pm 0.7	34.7 \pm 0.6	34.4 \pm 0.7	34.6 \pm 0.6
10	34.3 \pm 0.6	34.9 \pm 0.6	34.8 \pm 1.6	34.7 \pm 0.7
20	33.5 \pm 1.1	34.1 \pm 0.7	33.9 \pm 1.5	34.2 \pm 0.6
50	32.5 \pm 0.6	32.4 \pm 1.8	32.8 \pm 1.4	32.6 \pm 0.7
100	30.4 \pm 0.5	30.5 \pm 0.9	31.0 \pm 1.3	30.5 \pm 0.7

A.3 Supplemental Figures and Tables from Chapter 3

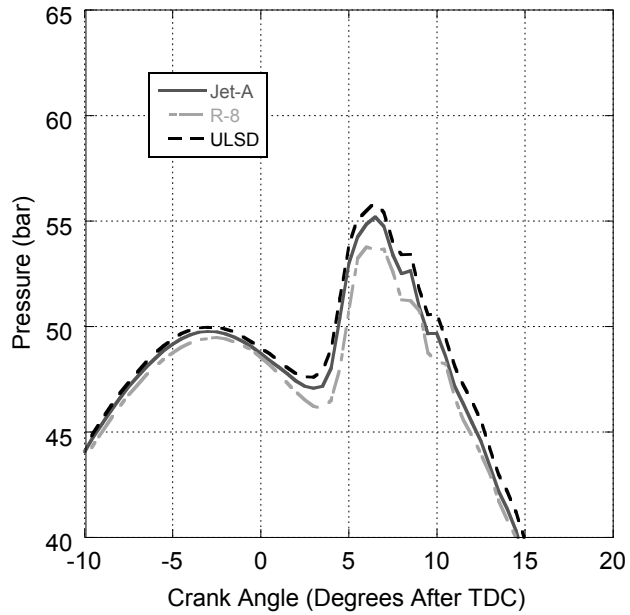


Figure A-50. Cylinder Pressure vs. Engine Crank Angle for Adjusted R-8, Jet-A, and ULSD at 0.5 N-m Loading.

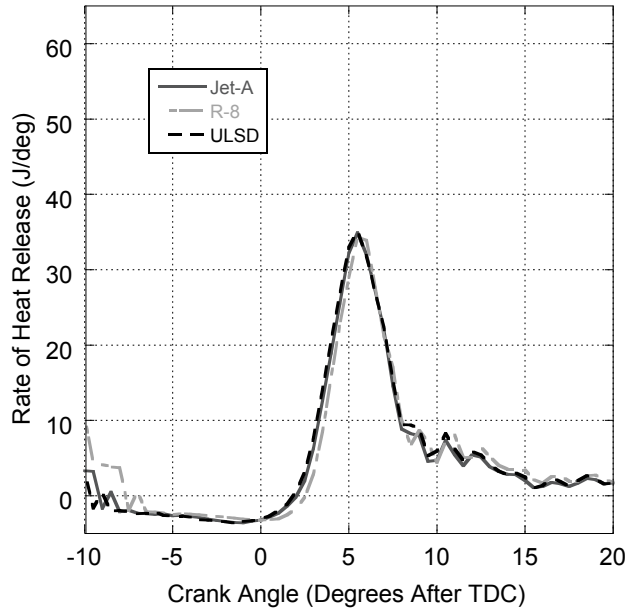


Figure A-51. Heat Release Rate vs. Engine Crank Angle for Adjusted R-8, Jet-A, and ULSD at 0.5 N-m Loading.

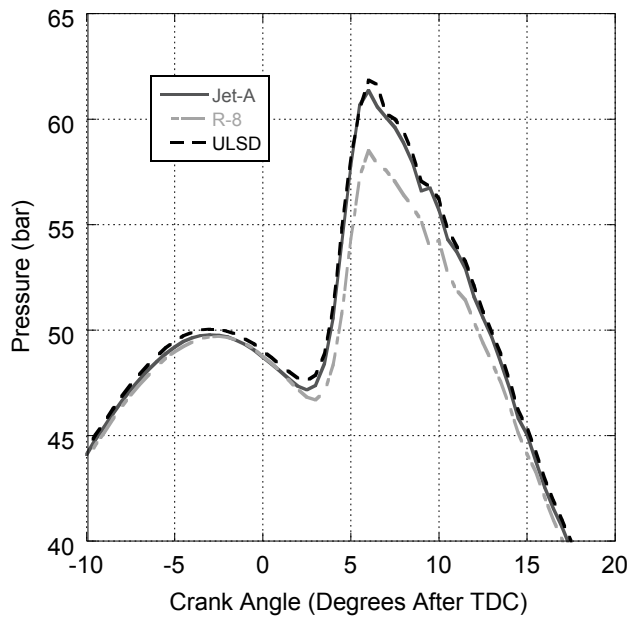


Figure A-52. Cylinder Pressure vs. Engine Crank Angle for Adjusted R-8, Jet-A, and ULSD at 4.5 N-m Loading.

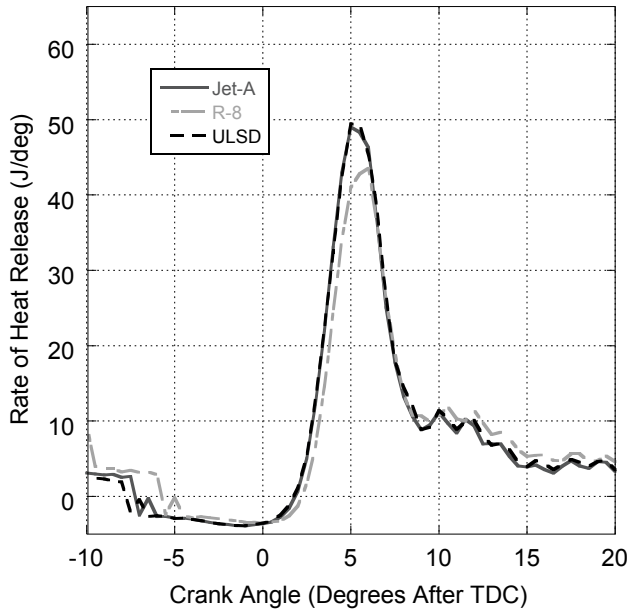


Figure A-53. Heat Release Rate vs. Engine Crank Angle for Adjusted R-8, Jet-A, and ULSD at 4.5 N-m Loading.

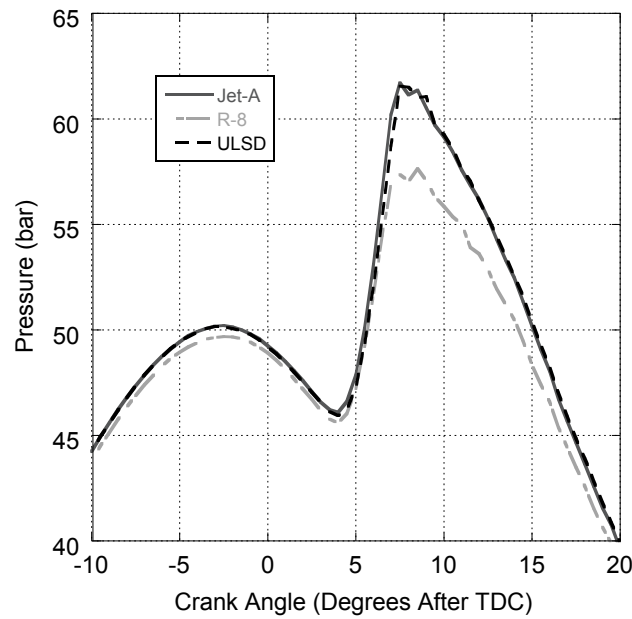


Figure A-54. Cylinder Pressure vs. Engine Crank Angle for Adjusted R-8, Jet-A, and ULSD at 9.0 N-m Loading.

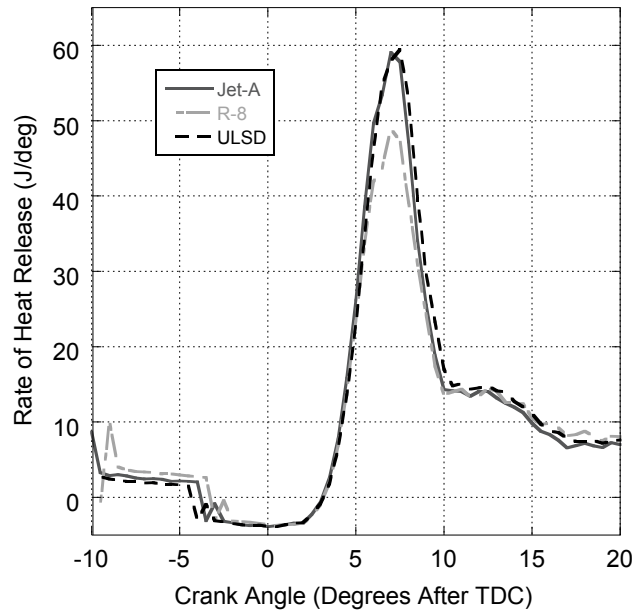


Figure A-55. Heat Release Rate vs. Engine Crank Angle for Adjusted R-8, Jet-A, and ULSD at 9.0 N-m Loading.

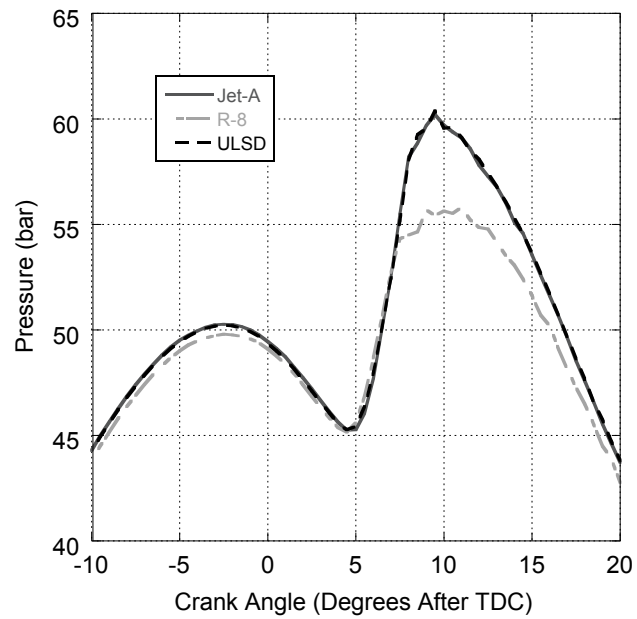


Figure A-56. Cylinder Pressure vs. Engine Crank Angle for Adjusted R-8, Jet-A, and ULSD at 13.5 N·m Loading.

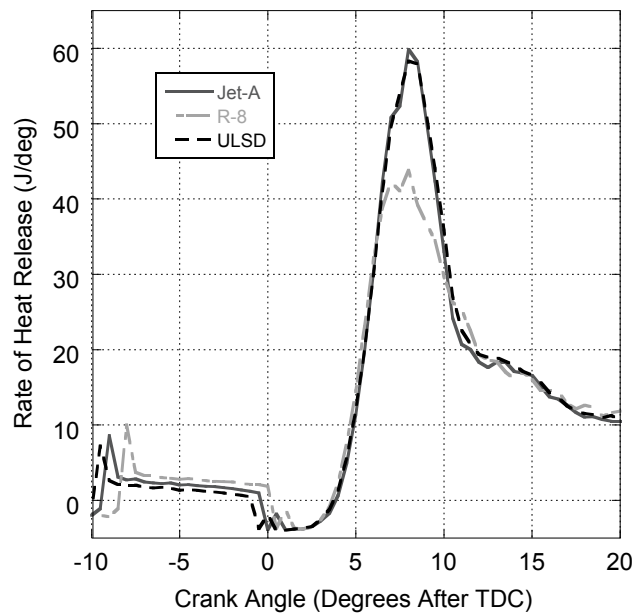


Figure A-57. Heat Release Rate vs. Engine Crank Angle for Adjusted R-8, Jet-A, and ULSD at 13.5 N·m Loading.

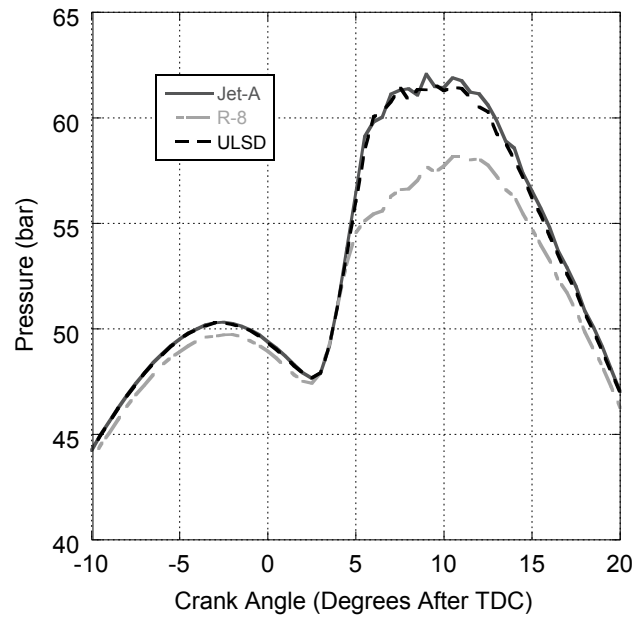


Figure A-58. Cylinder Pressure vs. Engine Crank Angle for Adjusted R-8, Jet-A, and ULSD at 18.0 N·m Loading.

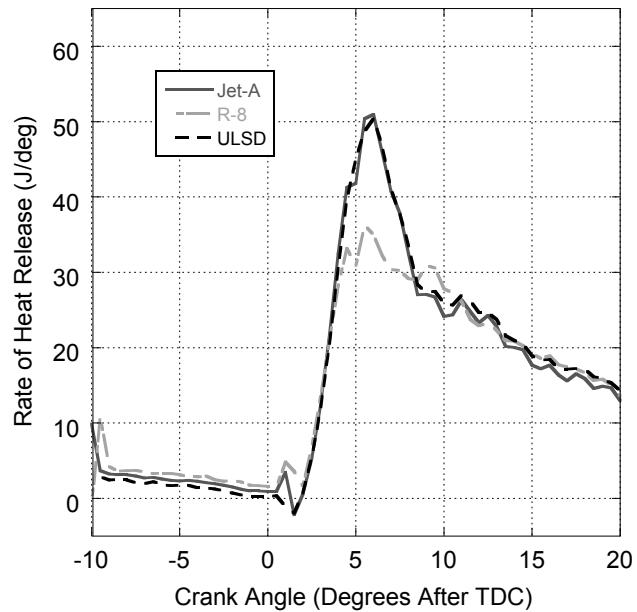


Figure A-59. Heat Release Rate vs. Engine Crank Angle for Adjusted R-8, Jet-A, and ULSD at 18.0 N·m Loading.

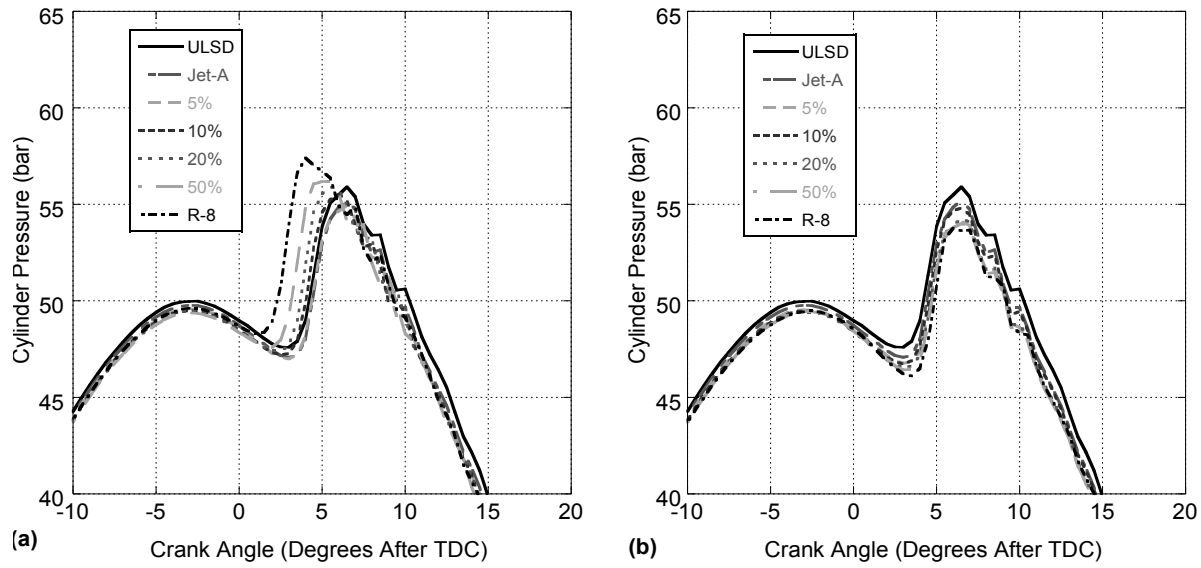


Figure A-60. Cylinder Pressure vs. Engine Crank Angle for Unadjusted (a) and Adjusted (b) Fuel Blends at 0.5 N·m Loading.

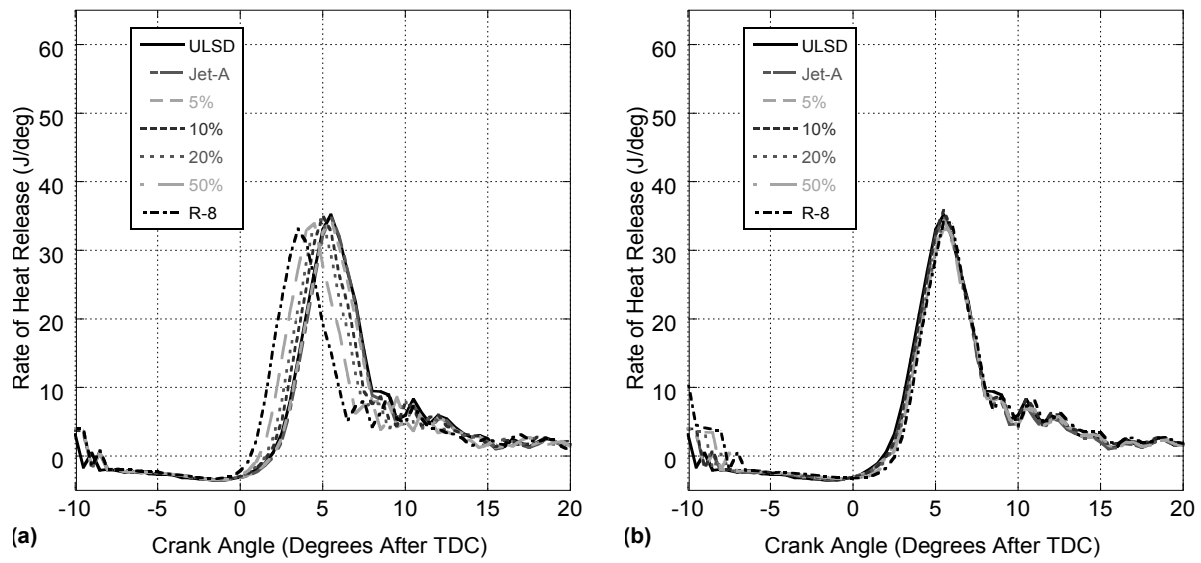


Figure A-61. Heat Release Rate vs. Engine Crank Angle for Unadjusted (a) and Adjusted (b) Fuel Blends at 0.5 N·m Loading.

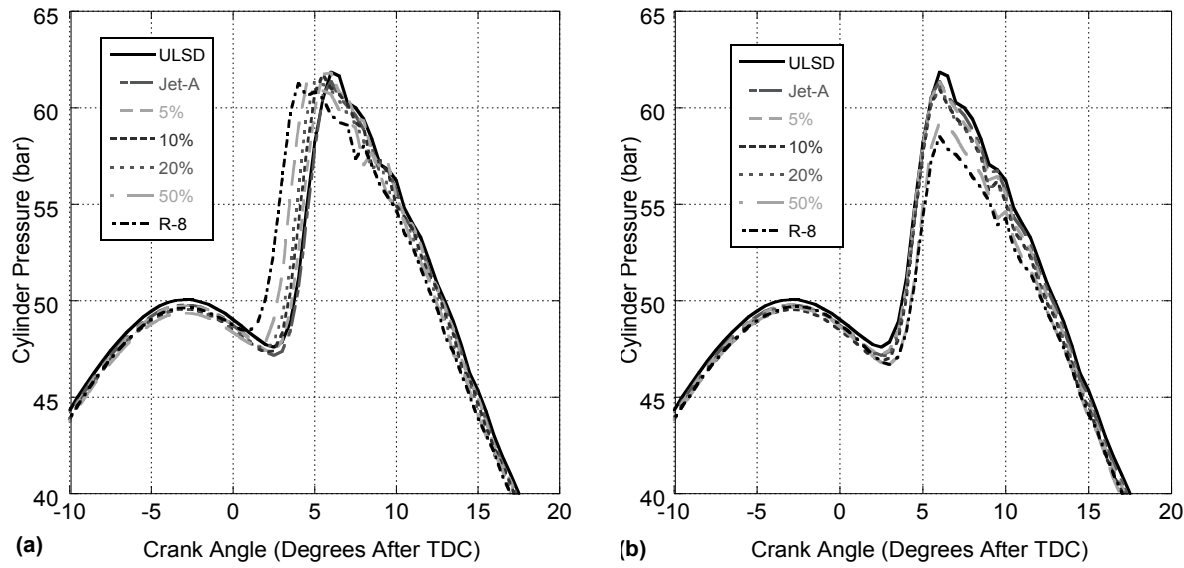


Figure A-62. Cylinder Pressure vs. Engine Crank Angle for Unadjusted (a) and Adjusted (b) Fuel Blends at 4.5 N·m Loading.

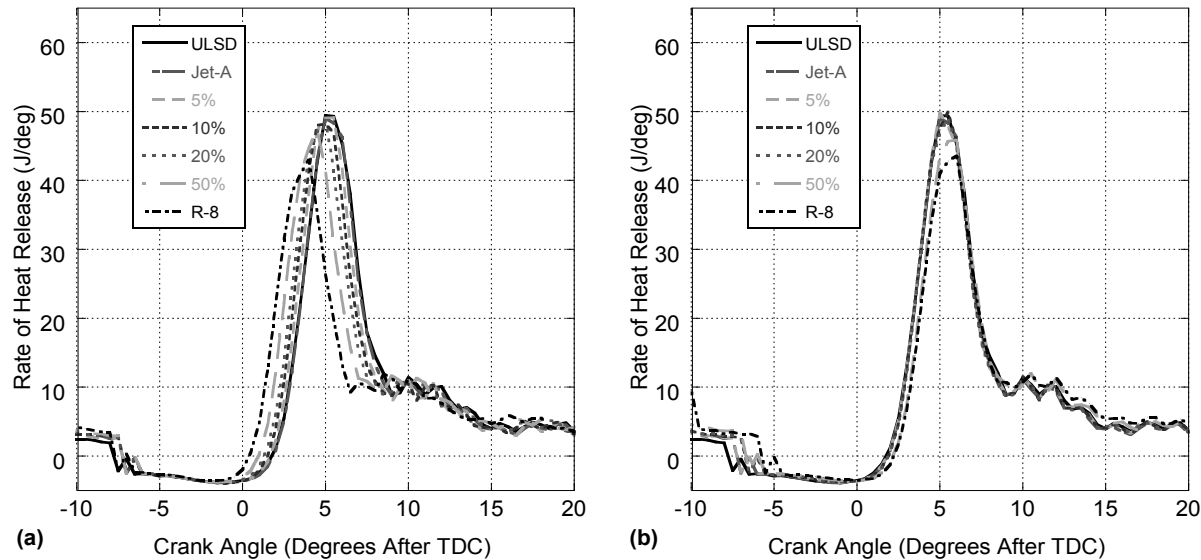


Figure A-63. Heat Release Rate vs. Engine Crank Angle for Unadjusted (a) and Adjusted (b) Fuel Blends at 4.5 N·m Loading.

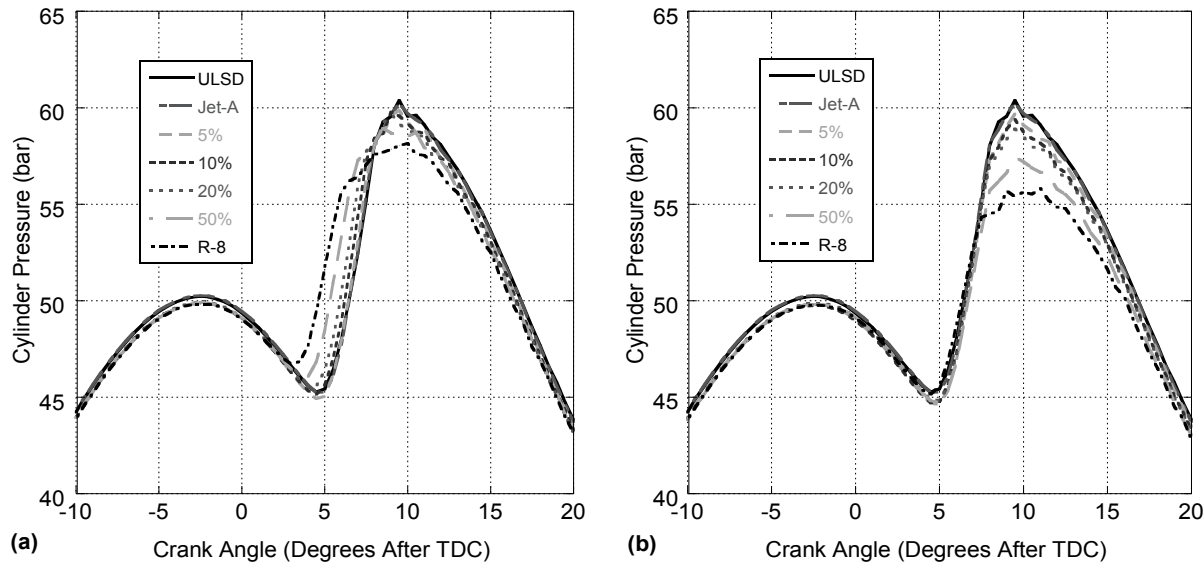


Figure A-64. Cylinder Pressure vs. Engine Crank Angle for Unadjusted (a) and Adjusted (b) Fuel Blends at 13.5 N·m Loading.

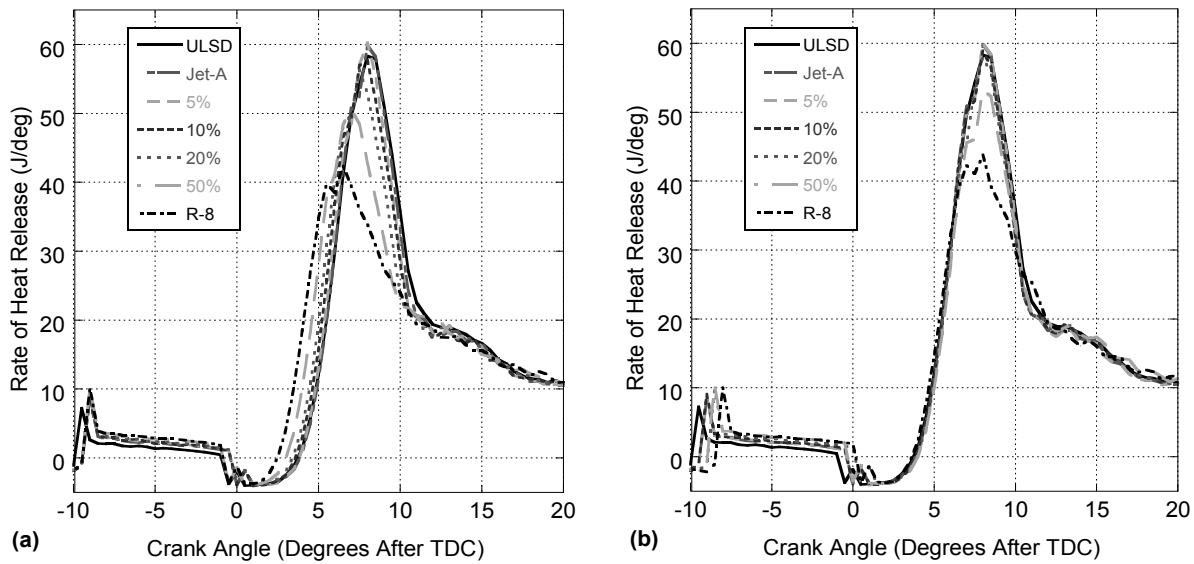


Figure A-65. Heat Release Rate vs. Engine Crank Angle for Unadjusted (a) and Adjusted (b) Fuel Blends at 13.5 N·m Loading.

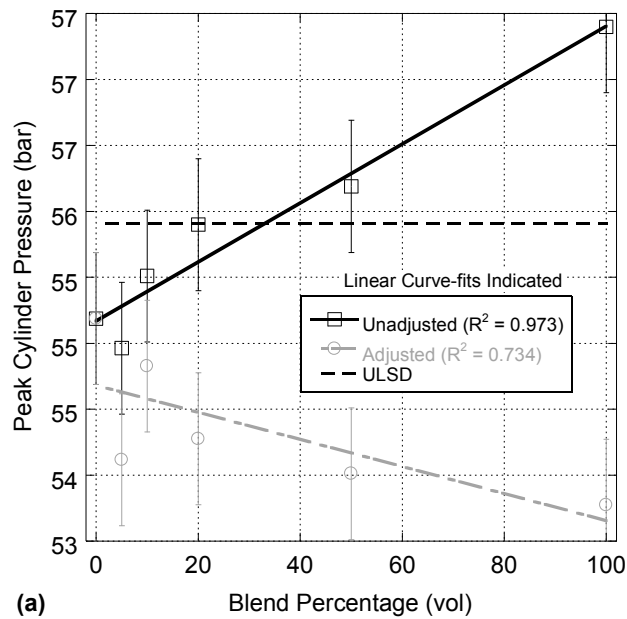


Figure A-66. Peak Cylinder Pressure vs. Blend Percentage for Unadjusted and Adjusted Blends at 0.5 N·m Loading.

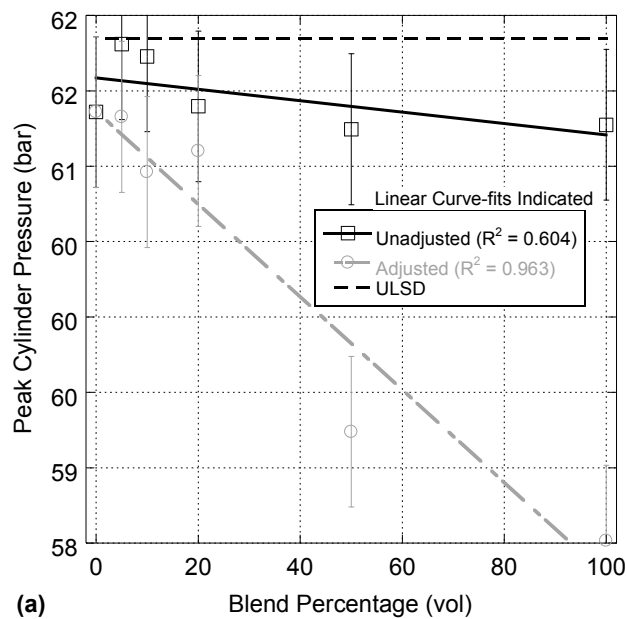


Figure A-67. Peak Cylinder Pressure vs. Blend Percentage for Unadjusted and Adjusted Blends at 4.5 N·m Loading.

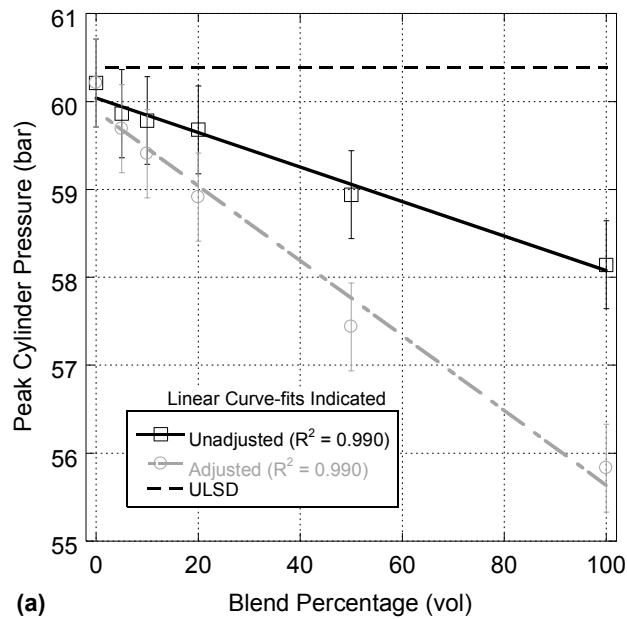


Figure A-68. Peak Cylinder Pressure vs. Blend Percentage for Unadjusted and Adjusted Blends at 13.5 N·m Loading.

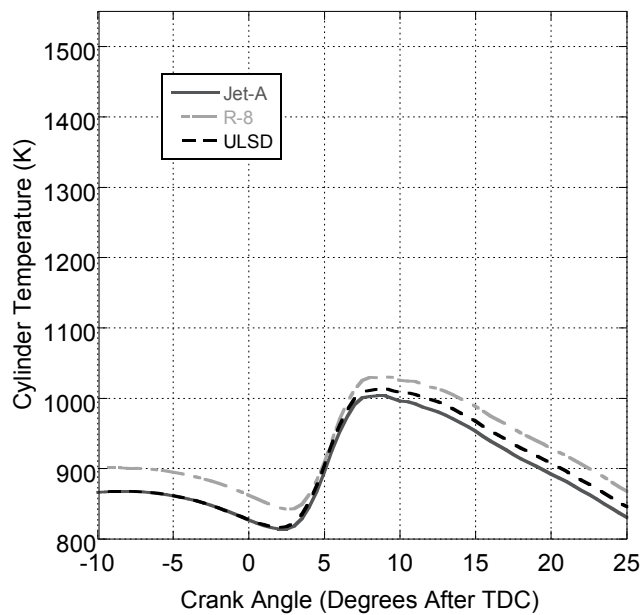


Figure A-69. Cylinder Temperature vs. Engine Crank Angle for Adjusted R-8, Jet-A, and ULSD at 0.5 N·m Loading.

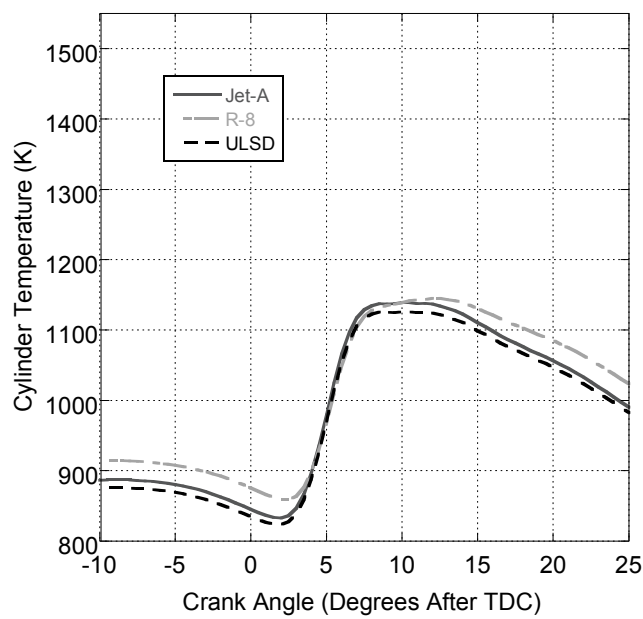


Figure A-70. Cylinder Temperature vs. Engine Crank Angle for Adjusted R-8, Jet-A, and ULSD at 4.5 N·m Loading.

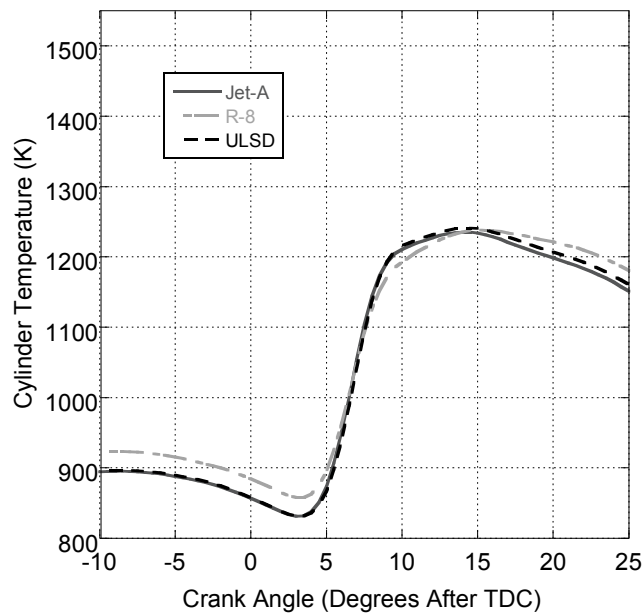


Figure A-71. Cylinder Temperature vs. Engine Crank Angle for Adjusted R-8, Jet-A, and ULSD at 9.0 N·m Loading.

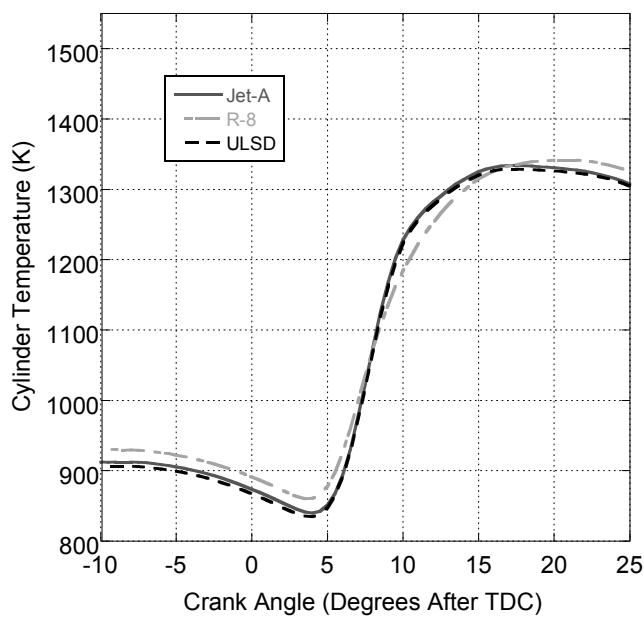


Figure A-72. Cylinder Temperature vs. Engine Crank Angle for Adjusted R-8, Jet-A, and ULSD at 13.5 N-m Loading.

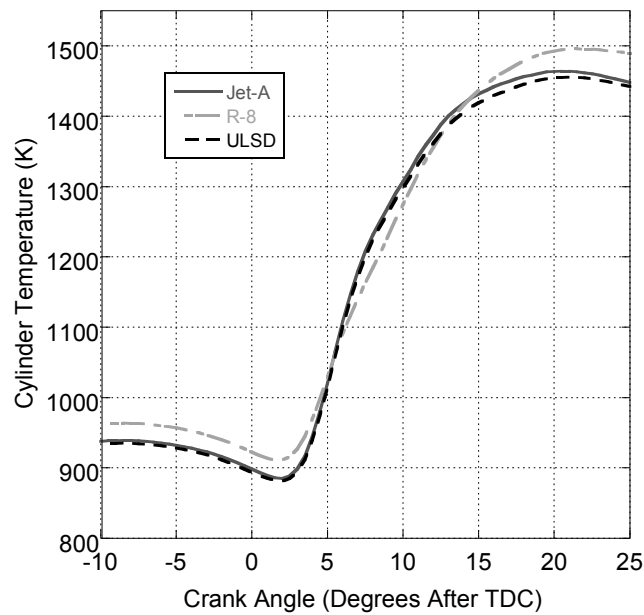


Figure A-73. Cylinder Temperature vs. Engine Crank Angle for Adjusted R-8, Jet-A, and ULSD at 18.0 N-m Loading.

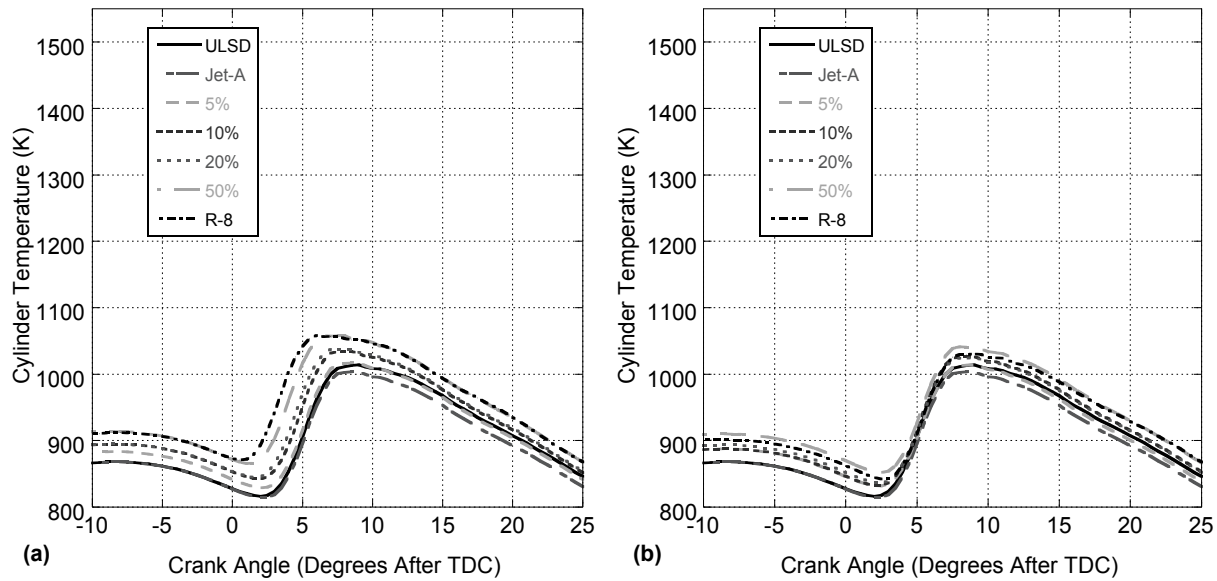


Figure A-74. Cylinder Temperature vs. Engine Crank Angle for Unadjusted (a) and Adjusted (b) Fuel Blends at 0.5 N·m Loading.

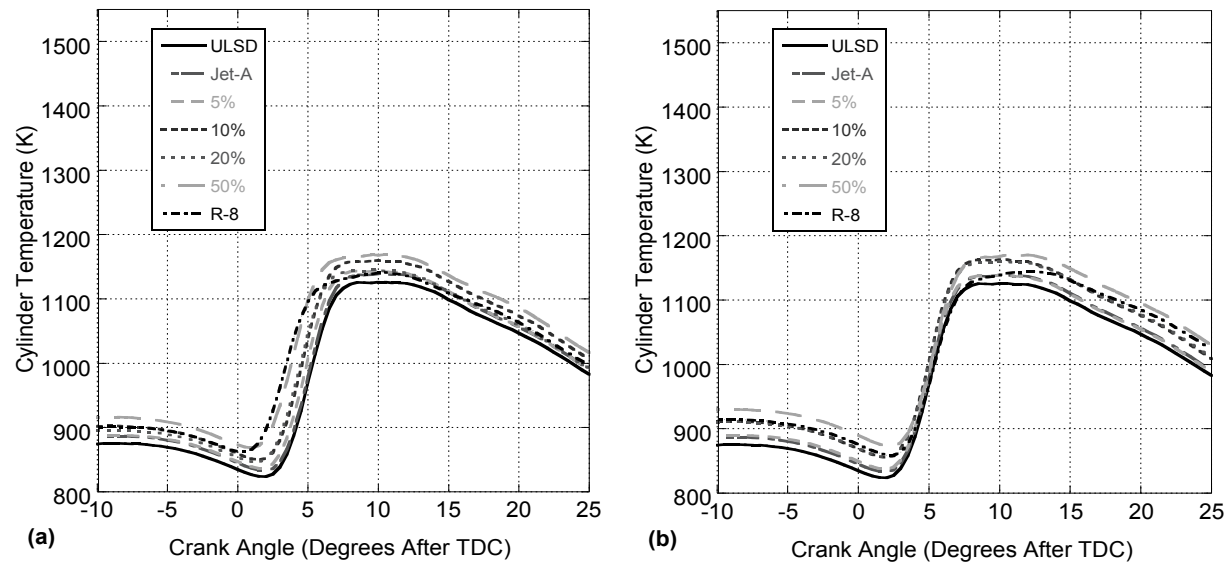


Figure A-75. Cylinder Temperature vs. Engine Crank Angle for Unadjusted (a) and Adjusted (b) Fuel Blends at 4.5 N·m Loading.

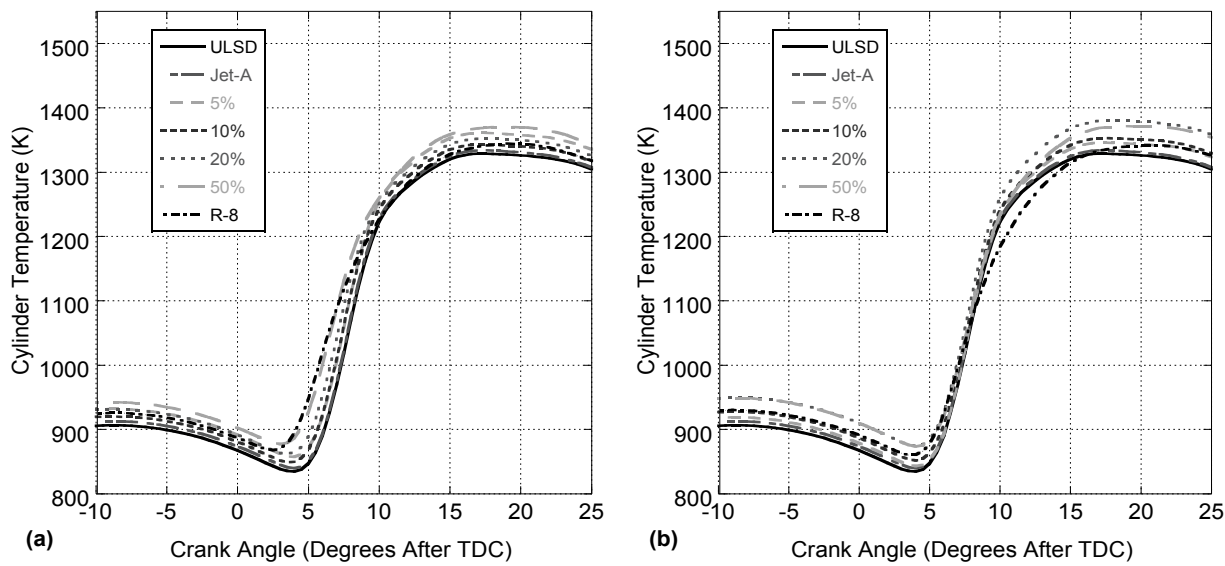


Figure A-76. Cylinder Temperature vs. Engine Crank Angle for Unadjusted (a) and Adjusted (b) Fuel Blends at 13.5 N·m Loading.

Table A-68. Brake-Specific NO_x Emissions (g/kW-hr) vs. Torque for Adjusted R-8, Jet-A, and ULSD.

Torque (N·m)	ULSD	Jet-A	R-8
0.5	34.66 ± 11.11	61.70 ± 1.13	37.26 ± 0.77
4.5	9.36 ± 0.10	9.36 ± 0.15	6.90 ± 0.08
9.0	6.06 ± 0.06	5.86 ± 0.06	4.40 ± 0.04
13.5	4.64 ± 0.05	4.54 ± 0.05	3.48 ± 0.03
18.0	4.11 ± 0.04	4.00 ± 0.04	3.30 ± 0.03

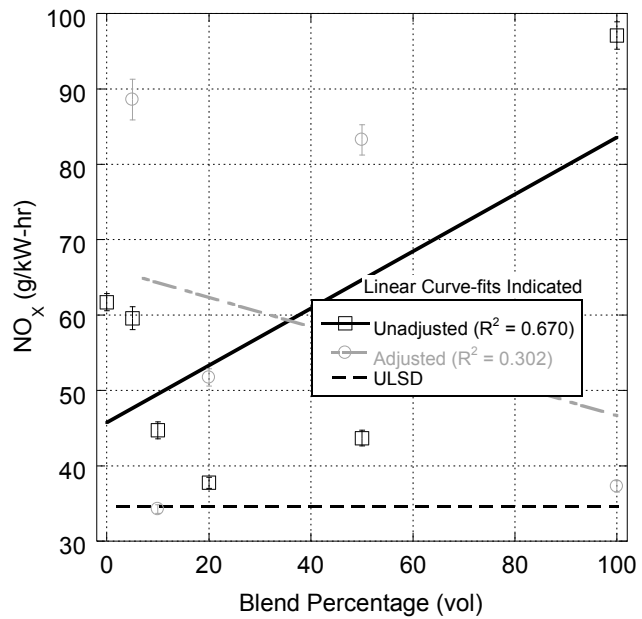


Figure A-6-77. Brake-Specific NO_x Emissions vs. Blend Percentage for Unadjusted and Adjusted Blends at 0.5 N-m Loading. Tier 4 Regulation at 7.5 g/kW-hr (Not Displayed).

Table A-69. Brake-Specific NO_x Emissions (g/kW-hr) vs. Blend Percentage for Unadjusted and Adjusted Blends at 0.5 N-m Loading.

R-8 Blend Percentage	Unadjusted Timing	Adjusted Timing
0	61.7 ± 1.1	61.7 ± 1.1
5	59.6 ± 1.5	88.6 ± 2.7
10	44.7 ± 1.1	34.3 ± 0.6
20	37.7 ± 0.7	51.7 ± 1.1
50	43.7 ± 1.0	83.3 ± 2.0
100	97.1 ± 1.8	37.3 ± 0.8

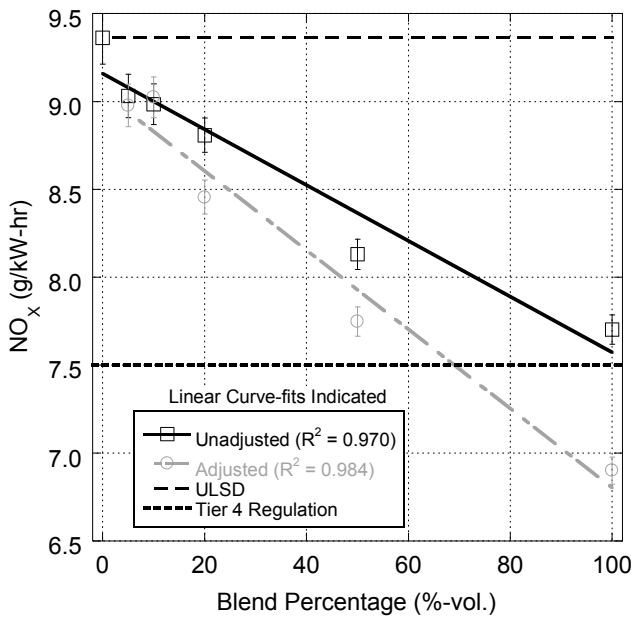


Figure A-78. Brake-Specific NO_x Emissions vs. Blend Percentage for Unadjusted and Adjusted Blends at 4.5 N·m Loading.

Table A-70. Brake-Specific NO_x Emissions (g/kW-hr) vs. Blend Percentage for Unadjusted and Adjusted Blends at 4.5 N·m Loading.

R-8 Blend Percentage	Unadjusted Timing	Adjusted Timing
0	9.4 ± 0.2	9.4 ± 0.2
5	9.0 ± 0.1	9.0 ± 0.1
10	9.0 ± 0.1	9.0 ± 0.1
20	8.8 ± 0.1	8.5 ± 0.1
50	8.1 ± 0.1	7.7 ± 0.1
100	7.7 ± 0.1	6.9 ± 0.1

Table A-71. Brake-Specific NO_x Emissions (g/kW-hr) vs. Blend Percentage for Unadjusted and Adjusted Blends at 9.0 N·m Loading.

R-8 Blend Percentage	Unadjusted Timing	Adjusted Timing
0	5.86 ± 0.06	5.86 ± 0.06
5	5.74 ± 0.06	5.68 ± 0.06
10	5.65 ± 0.05	5.61 ± 0.06
20	5.57 ± 0.05	5.46 ± 0.05
50	5.15 ± 0.05	4.95 ± 0.05
100	4.72 ± 0.04	4.40 ± 0.04

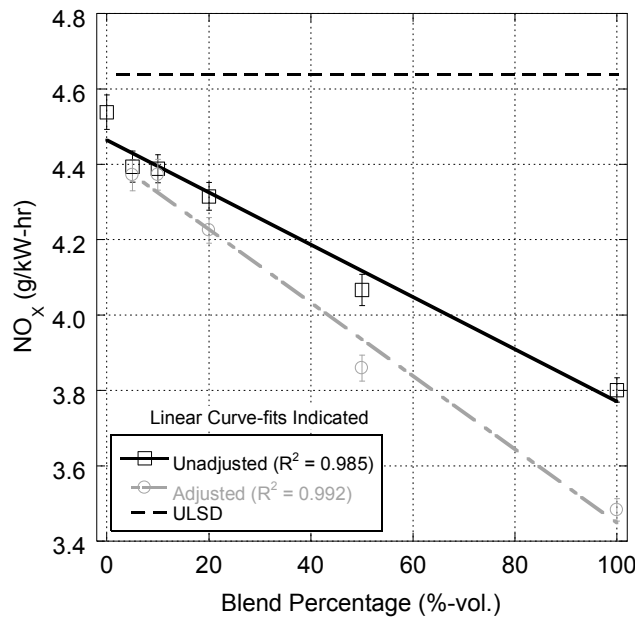


Figure A-79. Brake-Specific NO_x Emissions vs. Blend Percentage for Unadjusted and Adjusted Blends at 13.5 N-m Loading. Tier 4 Regulation at 7.5 g/kW-hr (Not Displayed).

Table A-72. Brake-Specific NO_x Emissions (g/kW-hr) vs. Blend Percentage for Unadjusted and Adjusted Blends at 13.5 N-m Loading.

R-8 Blend Percentage	Unadjusted Timing	Adjusted Timing
0	4.54 ± 0.05	4.54 ± 0.05
5	4.39 ± 0.04	4.37 ± 0.04
10	4.39 ± 0.04	4.37 ± 0.04
20	4.31 ± 0.04	4.22 ± 0.03
50	4.07 ± 0.04	3.86 ± 0.03
100	3.80 ± 0.03	3.48 ± 0.03

Table A-73. Brake-Specific NO_x Emissions (g/kW-hr) vs. Blend Percentage for Unadjusted and Adjusted Blends at 18.0 N-m Loading.

R-8 Blend Percentage	Unadjusted Timing	Adjusted Timing
0	4.00 ± 0.04	4.00 ± 0.04
5	3.92 ± 0.04	3.91 ± 0.04
10	3.92 ± 0.03	3.85 ± 0.04
20	3.85 ± 0.04	3.79 ± 0.03
50	3.78 ± 0.24	3.63 ± 0.03
100	3.53 ± 0.03	3.30 ± 0.03

Table A-74. Brake-Specific CO Emissions (g/kW-hr) vs. Torque for Adjusted R-8, Jet-A, and ULSD.

Torque (N-m)	ULSD	Jet-A	R-8
0.5	130.86 ± 39.32	225.21 ± 4.72	77.72 ± 1.74
4.5	12.48 ± 0.27	11.47 ± 0.27	5.83 ± 0.12
9.0	3.79 ± 0.07	3.61 ± 0.07	2.29 ± 0.06
13.5	1.84 ± 0.03	1.74 ± 0.04	1.24 ± 0.03
18.0	1.25 ± 0.05	1.18 ± 0.05	1.00 ± 0.05

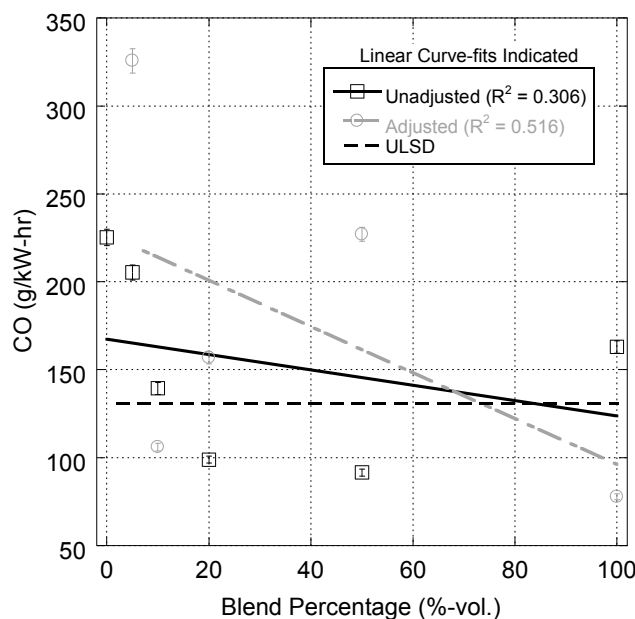


Figure A-80. Brake-Specific CO Emissions vs. Blend Percentage for Unadjusted and Adjusted Blends at 0.5 N-m Loading. Tier 4 Regulation at 8.0 g/kW-hr (Not Displayed).

Table A-75. Brake-Specific CO Emissions (g/kW-hr) vs. Blend Percentage for Unadjusted and Adjusted Blends at 0.5 N-m Loading.

R-8 Blend Percentage	Unadjusted Timing	Adjusted Timing
0	225.2 ± 4.7	225.2 ± 4.7
5	205.3 ± 4.3	325.7 ± 6.9
10	139.4 ± 3.4	105.9 ± 2.3
20	99.0 ± 2.1	156.9 ± 3.6
50	91.6 ± 2.0	227.0 ± 4.0
100	163.0 ± 3.5	77.7 ± 1.7

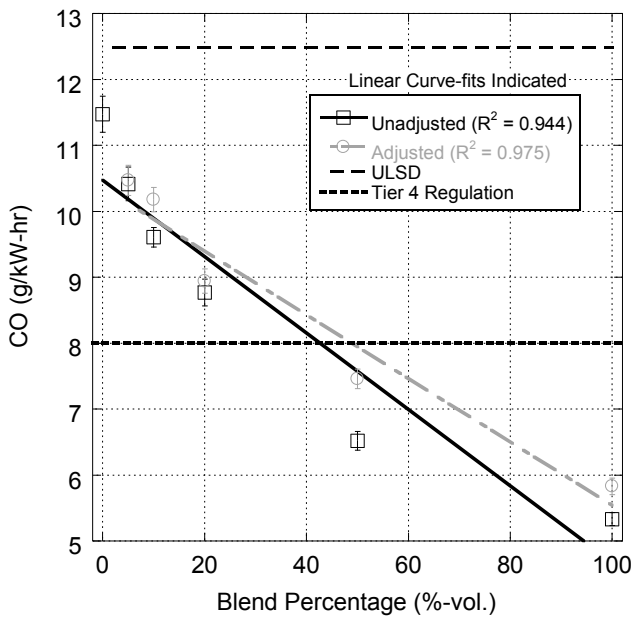


Figure A-81. Brake-Specific CO Emissions vs. Blend Percentage for Unadjusted and Adjusted Blends at 4.5 N·m Loading.

Table A-76. Brake-Specific CO Emissions (g/kW-hr) vs. Blend Percentage for Unadjusted and Adjusted Blends at 4.5 N·m Loading.

R-8 Blend Percentage	Unadjusted Timing	Adjusted Timing
0	11.5 ± 0.3	11.5 ± 0.3
5	10.4 ± 0.3	10.5 ± 0.2
10	9.6 ± 0.1	10.2 ± 0.2
20	8.8 ± 0.2	8.9 ± 0.2
50	6.5 ± 0.1	7.5 ± 0.1
100	5.3 ± 0.1	5.8 ± 0.1

Table A-77. Brake-Specific CO Emissions (g/kW-hr) vs. Blend Percentage for Unadjusted and Adjusted Blends at 9.0 N·m Loading.

R-8 Blend Percentage	Unadjusted Timing	Adjusted Timing
0	3.61 ± 0.07	3.61 ± 0.07
5	3.36 ± 0.07	3.37 ± 0.07
10	3.10 ± 0.06	3.13 ± 0.06
20	2.88 ± 0.06	3.09 ± 0.06
50	2.47 ± 0.05	2.73 ± 0.05
100	2.01 ± 0.05	2.29 ± 0.06

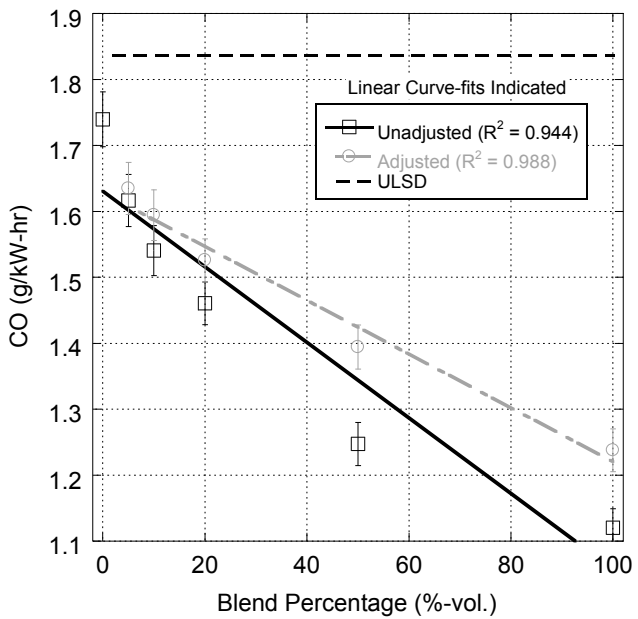


Figure A-82. Brake-Specific CO Emissions vs. Blend Percentage for Unadjusted and Adjusted Blends at 13.5 N-m Loading. Tier 4 Regulation at 8.0 g/kW-hr (Not Displayed).

Table A-78. Brake-Specific CO Emissions (g/kW-hr) vs. Blend Percentage for Unadjusted and Adjusted Blends at 13.5 N-m Loading.

R-8 Blend Percentage	Unadjusted Timing	Adjusted Timing
0	1.74 ± 0.04	1.74 ± 0.04
5	1.62 ± 0.04	1.63 ± 0.04
10	1.54 ± 0.04	1.59 ± 0.04
20	1.46 ± 0.03	1.53 ± 0.03
50	1.25 ± 0.03	1.39 ± 0.03
100	1.12 ± 0.03	1.24 ± 0.03

Table A-79. Brake-Specific CO Emissions (g/kW-hr) vs. Blend Percentage for Unadjusted and Adjusted Blends at 18.0 N-m Loading.

R-8 Blend Percentage	Unadjusted Timing	Adjusted Timing
0	1.18 ± 0.05	1.18 ± 0.05
5	1.11 ± 0.04	1.13 ± 0.04
10	1.12 ± 0.05	1.14 ± 0.05
20	1.05 ± 0.05	1.07 ± 0.04
50	0.98 ± 0.08	1.02 ± 0.04
100	0.98 ± 0.05	1.00 ± 0.05

Table A-80. Brake-Specific HC Emissions (g/kW-hr) vs. Torque for Adjusted R-8, Jet-A, and ULSD.

Torque (N-m)	ULSD	Jet-A	R-8
0.5	35.17 ± 7.30	57.23 ± 1.34	16.15 ± 0.38
4.5	2.75 ± 0.05	2.29 ± 0.08	0.98 ± 0.02
9.0	1.09 ± 0.03	0.84 ± 0.01	0.38 ± 0.01
13.5	0.68 ± 0.02	0.43 ± 0.01	0.24 ± 0.01
18.0	0.39 ± 0.01	0.30 ± 0.02	0.22 ± 0.01

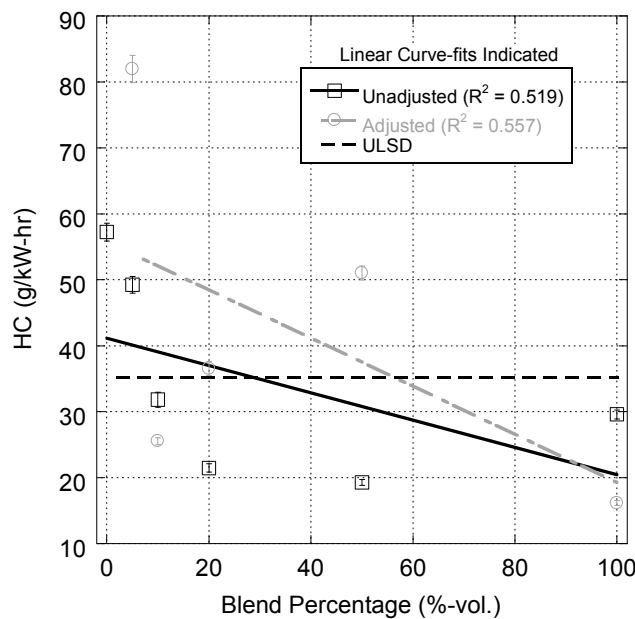


Figure A-83. Brake-Specific HC Emissions vs. Blend Percentage for Unadjusted and Adjusted Blends at 0.5 N-m Loading.

Table A-81. Brake-Specific HC Emissions (g/kW-hr) vs. Blend Percentage for Unadjusted and Adjusted Blends at 0.5 N-m Loading.

R-8 Blend Percentage	Unadjusted Timing	Adjusted Timing
0	57.2 ± 1.3	57.2 ± 1.3
5	49.3 ± 1.3	82.0 ± 2.1
10	31.8 ± 1.1	25.5 ± 0.5
20	21.5 ± 0.6	36.5 ± 1.1
50	19.3 ± 0.5	51.0 ± 1.0
100	29.6 ± 0.7	16.2 ± 0.4

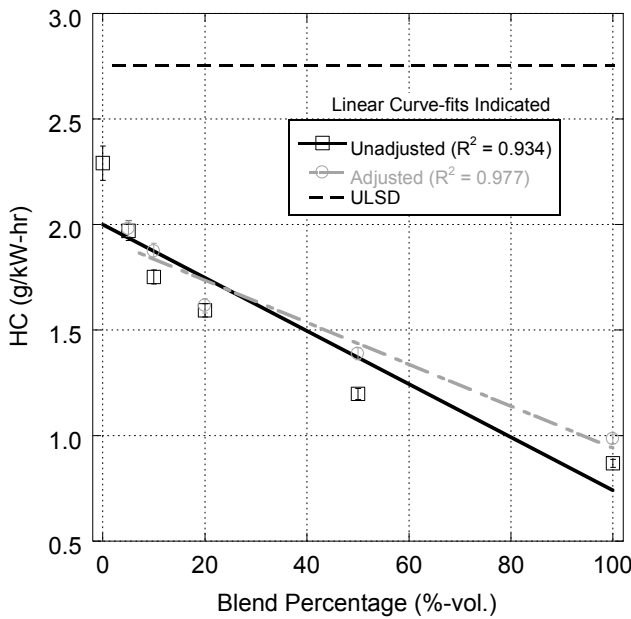


Figure A-84. Brake-Specific HC Emissions vs. Blend Percentage for Unadjusted and Adjusted Blends at 4.5 N-m Loading.

Table A-82. Brake-Specific HC Emissions (g/kW-hr) vs. Blend Percentage for Unadjusted and Adjusted Blends at 4.5 N-m Loading.

R-8 Blend Percentage	Unadjusted Timing	Adjusted Timing
0	2.29 ± 0.08	2.29 ± 0.08
5	1.97 ± 0.05	1.98 ± 0.04
10	1.75 ± 0.03	1.87 ± 0.04
20	1.59 ± 0.03	1.62 ± 0.03
50	1.20 ± 0.03	1.39 ± 0.03
100	0.87 ± 0.02	0.98 ± 0.02

Table A-83. Brake-Specific HC Emissions (g/kW-hr) vs. Blend Percentage for Unadjusted and Adjusted Blends at 9.0 N-m Loading.

R-8 Blend Percentage	Unadjusted Timing	Adjusted Timing
0	0.84 ± 0.01	0.84 ± 0.01
5	0.67 ± 0.02	0.67 ± 0.02
10	0.61 ± 0.01	0.62 ± 0.01
20	0.59 ± 0.01	0.64 ± 0.01
50	0.44 ± 0.01	0.50 ± 0.01
100	0.34 ± 0.01	0.38 ± 0.01

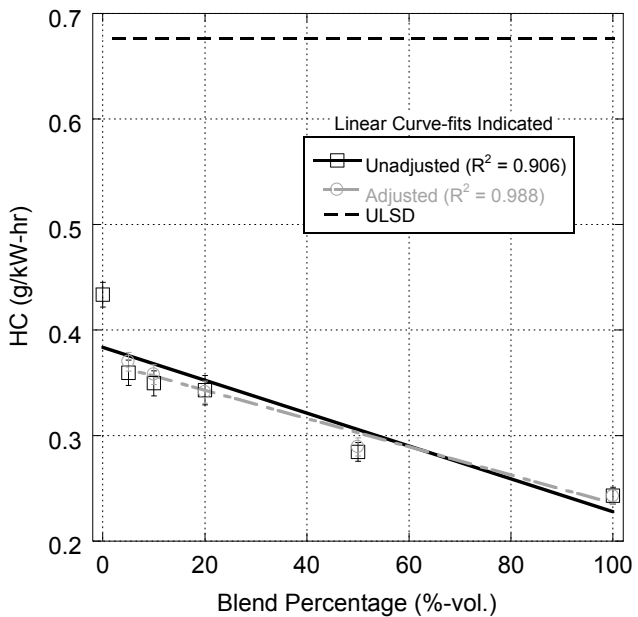


Figure A-85. Brake-Specific HC Emissions vs. Blend Percentage for Unadjusted and Adjusted Blends at 13.5 N·m Loading.

Table A-84. Brake-Specific HC Emissions (g/kW-hr) vs. Blend Percentage for Unadjusted and Adjusted Blends at 13.5 N·m Loading.

R-8 Blend Percentage	Unadjusted Timing	Adjusted Timing
0	0.43 ± 0.01	0.43 ± 0.01
5	0.36 ± 0.01	0.37 ± 0.01
10	0.35 ± 0.01	0.36 ± 0.01
20	0.34 ± 0.01	0.34 ± 0.01
50	0.28 ± 0.01	0.29 ± 0.01
100	0.24 ± 0.01	0.24 ± 0.01

Table A-85. Brake-Specific HC Emissions (g/kW-hr) vs. Blend Percentage for Unadjusted and Adjusted Blends at 18.0 N·m Loading.

R-8 Blend Percentage	Unadjusted Timing	Adjusted Timing
0	0.30 ± 0.02	0.30 ± 0.02
5	0.26 ± 0.01	0.26 ± 0.01
10	0.25 ± 0.01	0.26 ± 0.01
20	0.25 ± 0.01	0.25 ± 0.01
50	0.24 ± 0.01	0.26 ± 0.01
100	0.22 ± 0.01	0.22 ± 0.01

Table A-86. Brake-Specific PM Emissions (g/kW-hr) vs. Torque for Adjusted R-8, Jet-A, and ULSD.

Torque (N-m)	ULSD	Jet-A	R-8
0.5	0.031 ± 0.000	0.014 ± 0.000	0.018 ± 0.002
4.5	0.010 ± 0.001	0.007 ± 0.000	0.014 ± 0.000
9.0	0.020 ± 0.001	0.017 ± 0.000	0.027 ± 0.000
13.5	0.061 ± 0.000	0.051 ± 0.001	0.058 ± 0.000
18.0	0.351 ± 0.015	0.322 ± 0.009	0.240 ± 0.006

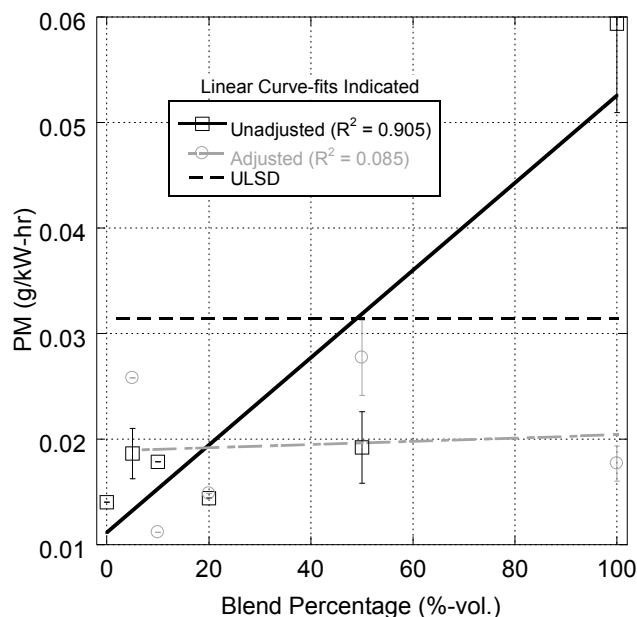


Figure A-86. Brake-Specific PM Emissions vs. Blend Percentage for Unadjusted and Adjusted Blends at 0.5 N-m Loading. Tier 4 Regulation at 0.4 g/kW-hr (Not Displayed).

Table A-87. Brake-Specific PM Emissions (g/kW-hr) vs. Blend Percentage for Unadjusted and Adjusted Blends at 0.5 N-m Loading.

R-8 Blend Percentage	Unadjusted Timing	Adjusted Timing
0	0.014 ± 0.000	0.014 ± 0.000
5	0.019 ± 0.002	0.026 ± 0.000
10	0.018 ± 0.000	0.011 ± 0.000
20	0.014 ± 0.000	0.015 ± 0.000
50	0.019 ± 0.003	0.028 ± 0.004
100	0.059 ± 0.008	0.018 ± 0.002

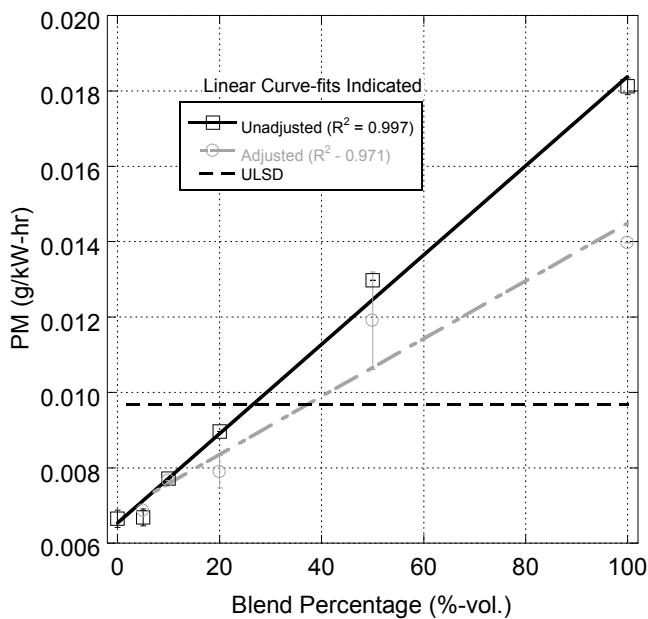


Figure A-87. Brake-Specific PM Emissions vs. Blend Percentage for Unadjusted and Adjusted Blends at 4.5 N·m Loading. Tier 4 Regulation at 0.4 g/kW·hr (Not Displayed).

Table A-88. Brake-Specific PM Emissions (g/kW·hr) vs. Blend Percentage for Unadjusted and Adjusted Blends at 4.5 N·m Loading.

R-8 Blend Percentage	Unadjusted Timing	Adjusted Timing
0	0.0066 ± 0.0002	0.0066 ± 0.0002
5	0.0067 ± 0.0002	0.0069 ± 0.0000
10	0.0077 ± 0.0000	0.0077 ± 0.0000
20	0.0090 ± 0.0000	0.0079 ± 0.0004
50	0.0130 ± 0.0000	0.0119 ± 0.0013
100	0.0181 ± 0.0002	0.0140 ± 0.0000

Table A-89. Brake-Specific PM Emissions (g/kW·hr) vs. Blend Percentage for Unadjusted and Adjusted Blends at 9.0 N·m Loading.

R-8 Blend Percentage	Unadjusted Timing	Adjusted Timing
0	0.0165 ± 0.0001	0.0165 ± 0.0001
5	0.0165 ± 0.0001	0.0165 ± 0.0006
10	0.0198 ± 0.0001	0.0187 ± 0.0001
20	0.0212 ± 0.0004	0.0201 ± 0.0008
50	0.0257 ± 0.0002	0.0242 ± 0.0006
100	0.0309 ± 0.0006	0.0267 ± 0.0000

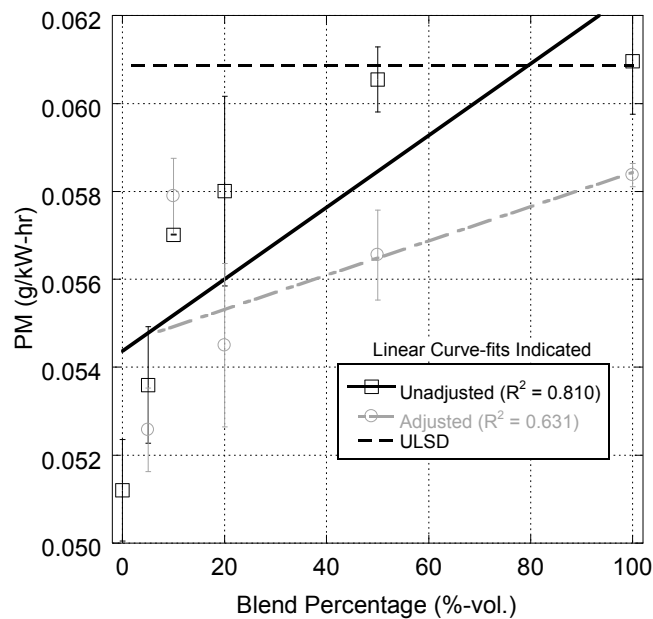


Figure A-88. Brake-Specific PM Emissions vs. Blend Percentage for Unadjusted and Adjusted Blends at 13.5 N·m Loading. Tier 4 Regulation at 0.4 g/kW-hr (Not Displayed).

Table A-90. Brake-Specific PM Emissions (g/kW-hr) vs. Blend Percentage for Unadjusted and Adjusted Blends at 13.5 N·m Loading.

R-8 Blend Percentage	Unadjusted Timing	Adjusted Timing
0	0.051 ± 0.001	0.051 ± 0.001
5	0.054 ± 0.001	0.053 ± 0.001
10	0.057 ± 0.000	0.058 ± 0.001
20	0.058 ± 0.002	0.055 ± 0.002
50	0.061 ± 0.001	0.057 ± 0.001
100	0.061 ± 0.001	0.058 ± 0.000

Table A-91. Brake-Specific PM Emissions (g/kW-hr) vs. Blend Percentage for Unadjusted and Adjusted Blends at 18.0 N·m Loading.

R-8 Blend Percentage	Unadjusted Timing	Adjusted Timing
0	0.322 ± 0.009	0.322 ± 0.009
5	0.299 ± 0.004	0.310 ± 0.006
10	0.320 ± 0.018	0.331 ± 0.007
20	0.278 ± 0.008	0.299 ± 0.001
50	0.247 ± 0.001	0.272 ± 0.013
100	0.232 ± 0.002	0.240 ± 0.006

Table A-92. Combustion Efficiency vs. Torque for Adjusted R-8, Jet-A, and ULSD.

Torque (N-m)	ULSD	Jet-A	R-8
0.5	94.1 + 5.9 - 22.8	93.3 + 6.7 - 7.7	96.8 + 3.2 - 6.7
4.5	97.6 + 2.4 - 3.5	97.8 + 2.2 - 3.0	98.8 + 1.2 - 2.3
9.0	99.0 + 1.0 - 2.8	99.0 + 1.0 - 1.7	99.4 + 0.6 - 2.3
13.5	99.4 + 0.6 - 1.8	99.5 + 0.5 - 2.2	99.6 + 0.4 - 2.3
18.0	99.5 + 0.5 - 3.2	99.5 + 0.5 - 4.0	99.6 + 0.4 - 3.5

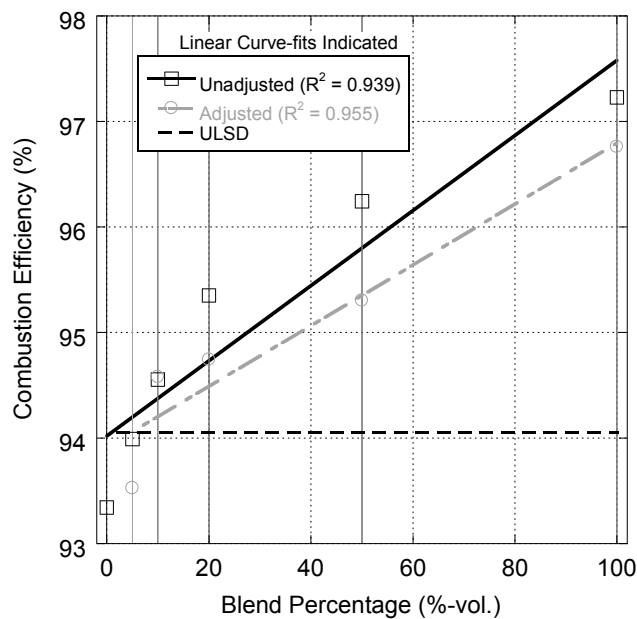


Figure A-89. Combustion Efficiency vs. Blend Percentage for Unadjusted and Adjusted Blends at 0.5 N-loading.

Table A-93. Combustion Efficiency vs. Blend Percentage for Unadjusted and Adjusted Blends at 0.5 N-loading.

R-8 Blend Percentage	Unadjusted Timing	Adjusted Timing
0	93.3 + 6.7 - 7.7	93.3 + 6.7 - 7.7
5	94.0 + 6.0 - 9.0	93.5 + 6.5 - 17.1
10	94.6 + 5.4 - 7.3	94.6 + 4.2 - 4.2
20	95.4 + 4.6 - 4.6	94.7 + 5.3 - 9.1
50	96.2 + 3.8 - 9.4	95.3 + 4.7 - 12.0
100	97.2 + 2.8 - 23.8	96.8 + 3.2 - 6.7

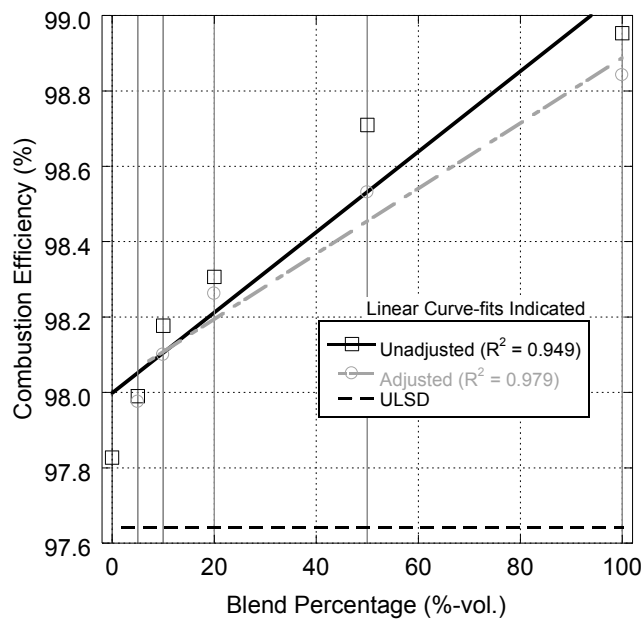


Figure A-90. Combustion Efficiency vs. Blend Percentage for Unadjusted and Adjusted Blends at 4.5 N-Loading.

Table A-94. Combustion Efficiency vs. Blend Percentage for Unadjusted and Adjusted Blends at 4.5 N-Loading.

R-8 Blend Percentage	Unadjusted Timing	Adjusted Timing
0	97.8 + 2.2 - 3.0	97.8 + 2.2 - 3.0
5	98.0 + 2.0 - 2.8	98.0 + 2.0 - 2.3
10	98.2 + 1.8 - 2.1	98.1 + 1.9 - 2.3
20	98.3 + 1.7 - 2.5	98.3 + 1.7 - 3.3
50	98.7 + 1.3 - 2.4	98.5 + 1.5 - 5.0
100	99.0 + 1.0 - 2.2	98.8 + 1.2 - 2.3

Table A-95. Combustion Efficiency vs. Blend Percentage for Unadjusted and Adjusted Blends at 9.0 N-Loading.

R-8 Blend Percentage	Unadjusted Timing	Adjusted Timing
0	99.0 + 1.0 - 1.7	99.0 + 1.0 - 1.7
5	99.1 + 0.9 - 1.9	99.1 + 0.9 - 2.6
10	99.2 + 0.8 - 1.9	99.2 + 0.8 - 1.7
20	99.2 + 0.8 - 2.0	99.2 + 0.8 - 2.4
50	99.4 + 0.6 - 2.0	99.3 + 0.7 - 2.1
100	99.5 + 0.5 - 2.5	99.4 + 0.6 - 2.3

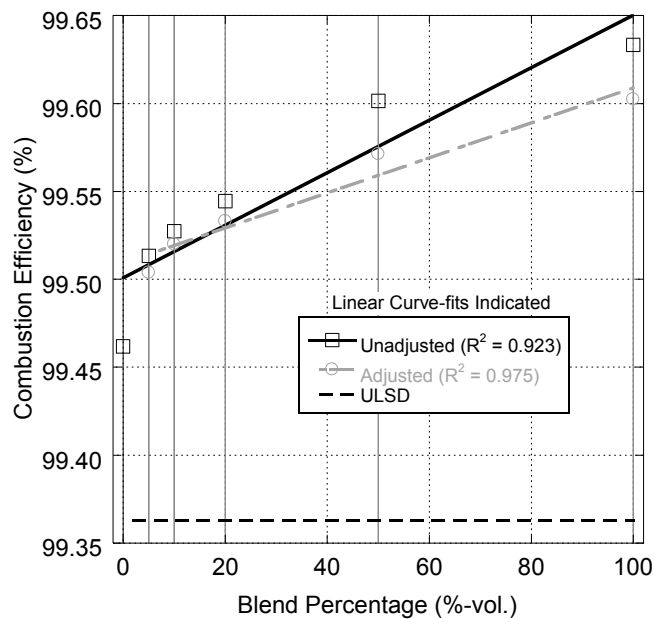


Figure A-91. Combustion Efficiency vs. Blend Percentage for Unadjusted and Adjusted Blends at 13.5 N- Loading.

Table A-96. Combustion Efficiency vs. Blend Percentage for Unadjusted and Adjusted Blends at 13.5 N- Loading.

R-8 Blend Percentage	Unadjusted Timing	Adjusted Timing
0	99.5 + 0.5 - 2.2	99.5 + 0.5 - 2.2
5	99.5 + 0.5 - 2.4	99.5 + 0.5 - 2.0
10	99.5 + 0.5 - 2.2	99.5 + 0.5 - 2.1
20	99.5 + 0.5 - 2.7	99.5 + 0.5 - 2.4
50	99.6 + 0.4 - 2.3	99.6 + 0.4 - 2.2
100	99.6 + 0.4 - 2.4	99.6 + 0.4 - 2.3

Table A-97. Combustion Efficiency vs. Blend Percentage for Unadjusted and Adjusted Blends at 18.0 N- Loading.

R-8 Blend Percentage	Unadjusted Timing	Adjusted Timing
0	99.5 + 0.5 - 4.0	99.5 + 0.5 - 4.0
5	99.6 + 0.4 - 3.0	99.6 + 0.4 - 2.9
10	99.6 + 0.4 - 4.0	99.6 + 0.4 - 2.9
20	99.6 + 0.4 - 3.4	99.6 + 0.4 - 2.9
50	99.6 + 0.4 - 6.3	99.6 + 0.4 - 3.6
100	99.6 + 0.4 - 3.4	99.6 + 0.4 - 3.5

Table A-98. Brake-Specific Fuel Consumption (g/kW-hr) vs. Torque for Adjusted R-8, Jet-A, and ULSD.

Torque (N-m)	ULSD	Jet-A	R-8
0.5	1915.4 ± 55.2	2951.4 ± 207.4	2019.6 ± 98.5
4.5	397.8 ± 4.8	391.0 ± 4.6	365.7 ± 5.1
9.0	284.6 ± 2.7	278.0 ± 2.3	262.0 ± 3.0
13.5	252.6 ± 2.0	247.4 ± 1.6	232.8 ± 2.5
18.0	242.6 ± 1.4	238.1 ± 1.2	230.5 ± 1.4

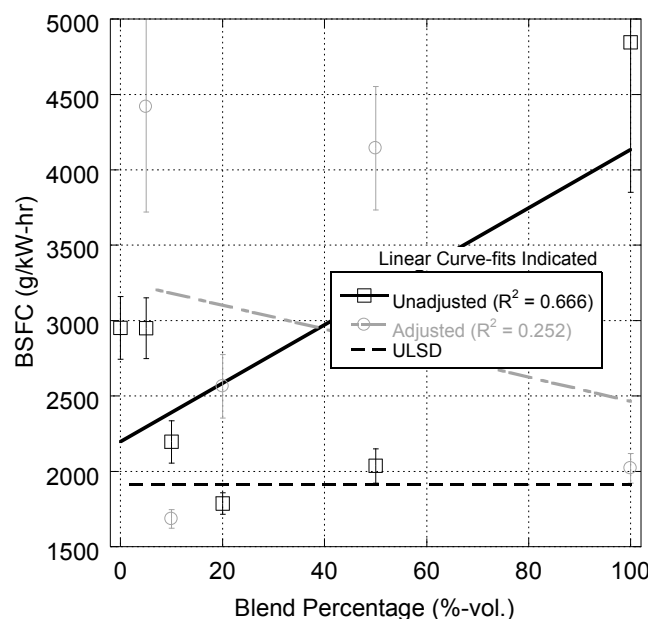


Figure A-92. Brake-Specific Fuel Consumption vs. Blend Percentage for Unadjusted and Adjusted Blends at 0.5N-m Loading.

Table A-99. Brake-Specific Fuel Consumption (g/kW-hr) vs. Blend Percentage for Unadjusted and Adjusted Blends at 0.5N-m Loading.

R-8 Blend Percentage	Unadjusted Timing	Adjusted Timing
0	2951 ± 207	2951 ± 207
5	2950 ± 202	4419 ± 699
10	2196 ± 141	1684 ± 61
20	1785 ± 71	2564 ± 210
50	2036 ± 114	4143 ± 410
100	4846 ± 995	2020 ± 98

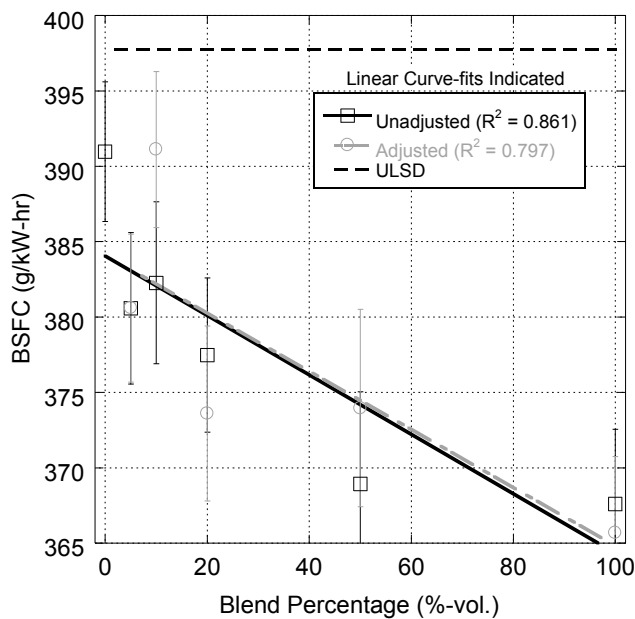


Figure A-93. Brake-Specific Fuel Consumption vs. Blend Percentage for Unadjusted and Adjusted Blends at 4.5 N-m Loading.

Table A-100. Brake-Specific Fuel Consumption (g/kW-hr) vs. Blend Percentage for Unadjusted and Adjusted Blends at 4.5 N-m Loading.

R-8 Blend Percentage	Unadjusted Timing	Adjusted Timing
0	391 ± 5	391 ± 5
5	381 ± 5	381 ± 5
10	382 ± 5	391 ± 5
20	377 ± 5	374 ± 6
50	369 ± 6	374 ± 7
100	368 ± 5	366 ± 5

Table A-101. Brake-Specific Fuel Consumption (g/kW-hr) vs. Blend Percentage for Unadjusted and Adjusted Blends at 9.0 N-m Loading.

R-8 Blend Percentage	Unadjusted Timing	Adjusted Timing
0	278 ± 2	278 ± 2
5	276 ± 3	277 ± 3
10	275 ± 2	276 ± 2
20	273 ± 2	273 ± 3
50	269 ± 2	269 ± 2
100	268 ± 3	262 ± 3

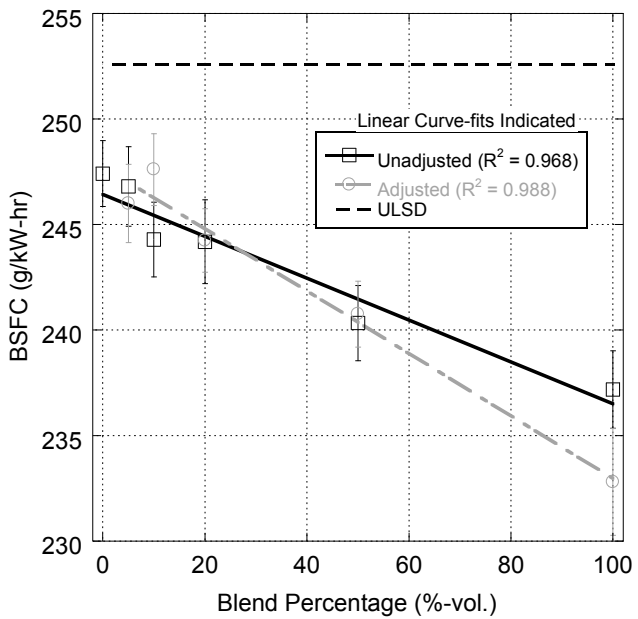


Figure A-94. Brake-Specific Fuel Consumption vs. Blend Percentage for Unadjusted and Adjusted Blends at 13.5 N-m Loading.

Table A-102. Brake-Specific Fuel Consumption (g/kW-hr) vs. Blend Percentage for Unadjusted and Adjusted Blends at 13.5 N-m Loading.

R-8 Blend Percentage	Unadjusted Timing	Adjusted Timing
0	247 \pm 2	247 \pm 2
5	247 \pm 2	246 \pm 2
10	244 \pm 2	248 \pm 2
20	244 \pm 2	244 \pm 2
50	240 \pm 2	241 \pm 2
100	237 \pm 2	233 \pm 3

Table A-103. Brake-Specific Fuel Consumption (g/kW-hr) vs. Blend Percentage for Unadjusted and Adjusted Blends at 18.0 N-m Loading.

R-8 Blend Percentage	Unadjusted Timing	Adjusted Timing
0	238 \pm 1	238 \pm 1
5	238 \pm 1	237 \pm 2
10	237 \pm 1	237 \pm 1
20	236 \pm 1	237 \pm 2
50	232 \pm 1	232 \pm 1
100	230 \pm 1	231 \pm 1

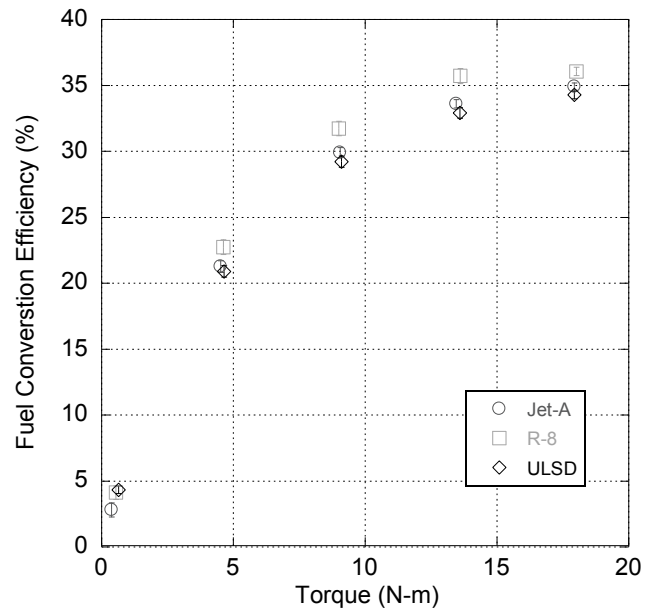


Figure A-95. Fuel Conversion Efficiency vs. Torque for Adjusted R-8, Jet-A, and ULSD.

Table A-104. Fuel Conversion Efficiency vs. Torque for Adjusted R-8, Jet-A, and ULSD.

Torque (N-m)	ULSD	Jet-A	R-8
0.5	4.3 ± 0.3	2.8 ± 0.5	4.1 ± 0.5
4.5	20.9 ± 0.4	21.3 ± 0.4	22.7 ± 0.5
9.0	29.2 ± 0.4	29.9 ± 0.4	31.7 ± 0.5
13.5	32.9 ± 0.4	33.6 ± 0.3	35.7 ± 0.6
18.0	34.3 ± 0.3	34.9 ± 0.3	36.1 ± 0.3

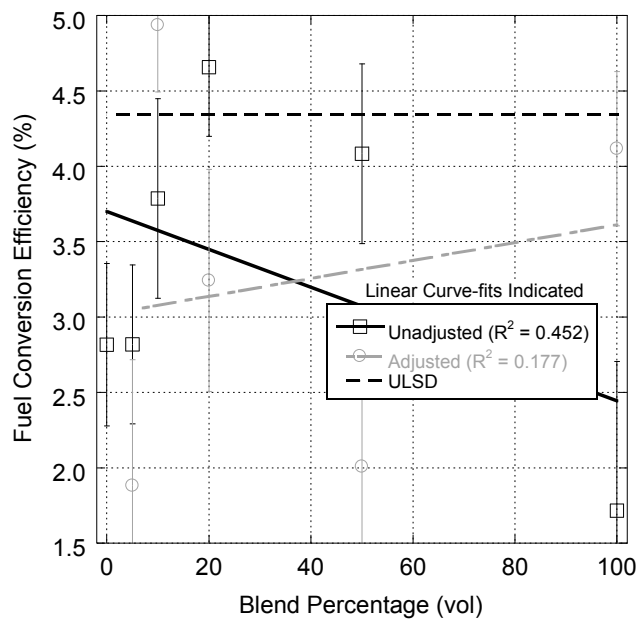


Figure A-96. Fuel Conversion Efficiency vs. Blend Percentage for Unadjusted and Adjusted Blends at 0.5 N·m Loading.

Table A-105. Fuel Conversion Efficiency vs. Blend Percentage for Unadjusted and Adjusted Blends at 0.5 N·m Loading.

R-8 Blend Percentage	Unadjusted Timing	Adjusted Timing
0	2.8 \pm 0.5	2.8 \pm 0.5
5	2.8 \pm 0.5	1.9 \pm 0.8
10	3.8 \pm 0.7	4.9 \pm 0.4
20	4.7 \pm 0.5	3.2 \pm 0.7
50	4.1 \pm 0.6	2.0 \pm 0.6
100	1.7 \pm 1.0	4.1 \pm 0.5

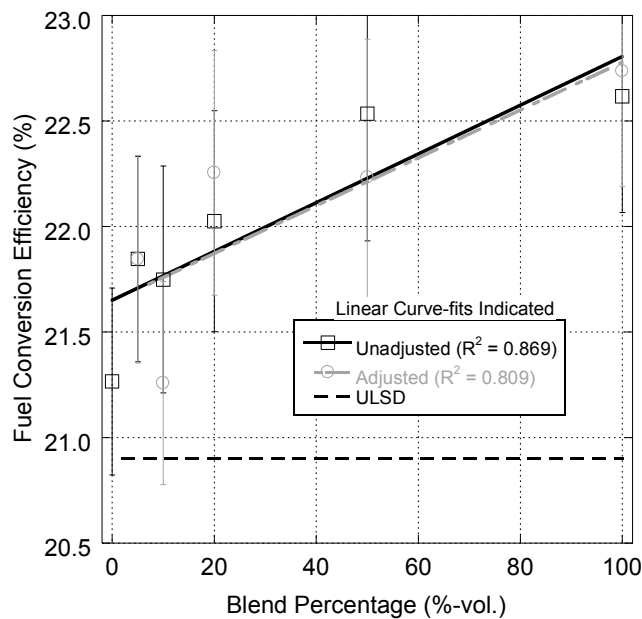


Figure A-97. Fuel Conversion Efficiency vs. Blend Percentage for Unadjusted and Adjusted Blends at 4.5 N·m Loading.

Table A-106. Fuel Conversion Efficiency vs. Blend Percentage for Unadjusted and Adjusted Blends at 4.5 N·m Loading.

R-8 Blend Percentage	Unadjusted Timing	Adjusted Timing
0	21.3 ± 0.4	21.3 ± 0.4
5	21.8 ± 0.5	21.8 ± 0.5
10	21.7 ± 0.5	21.3 ± 0.5
20	22.0 ± 0.5	22.3 ± 0.6
50	22.5 ± 0.6	22.2 ± 0.7
100	22.6 ± 0.6	22.7 ± 0.5

Table A-107. Fuel Conversion Efficiency vs. Blend Percentage for Unadjusted and Adjusted Blends at 9.0 N·m Loading.

R-8 Blend Percentage	Unadjusted Timing	Adjusted Timing
0	29.9 ± 0.4	29.9 ± 0.4
5	30.1 ± 0.4	30.0 ± 0.4
10	30.3 ± 0.4	30.2 ± 0.4
20	30.4 ± 0.4	30.4 ± 0.5
50	30.9 ± 0.4	30.9 ± 0.4
100	31.0 ± 0.5	31.7 ± 0.5

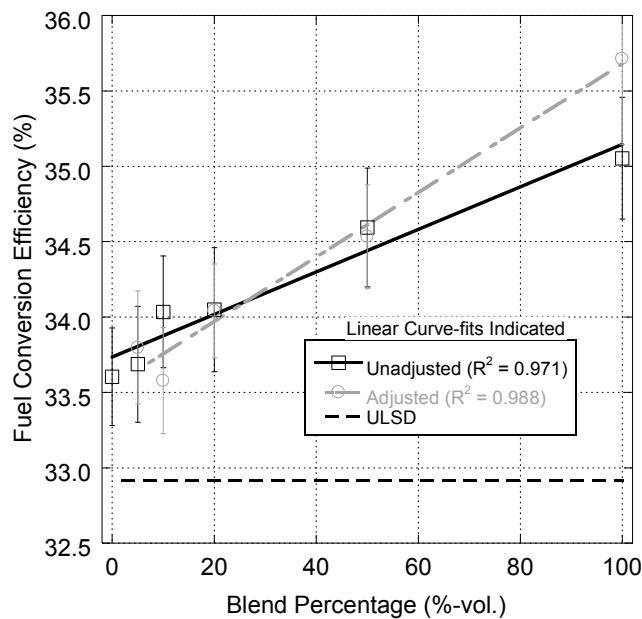


Figure A-98. Fuel Conversion Efficiency vs. Blend Percentage for Unadjusted and Adjusted Blends at 13.5 N·m Loading.

Table A-108. Fuel Conversion Efficiency vs. Blend Percentage for Unadjusted and Adjusted Blends at 13.5 N·m Loading.

R-8 Blend Percentage	Unadjusted Timing	Adjusted Timing
0	33.6 ± 0.3	33.6 ± 0.3
5	33.7 ± 0.4	33.8 ± 0.4
10	34.0 ± 0.4	33.6 ± 0.4
20	34.0 ± 0.4	34.0 ± 0.3
50	34.6 ± 0.4	34.5 ± 0.3
100	35.1 ± 0.4	35.7 ± 0.6

Table A-109. Fuel Conversion Efficiency vs. Blend Percentage for Unadjusted and Adjusted Blends at 18.0 N·m Loading.

R-8 Blend Percentage	Unadjusted Timing	Adjusted Timing
0	34.9 ± 0.3	34.9 ± 0.3
5	35.0 ± 0.3	35.0 ± 0.3
10	35.1 ± 0.3	35.0 ± 0.3
20	35.2 ± 0.3	35.0 ± 0.3
50	35.9 ± 0.3	35.8 ± 0.3
100	36.2 ± 0.3	36.1 ± 0.3

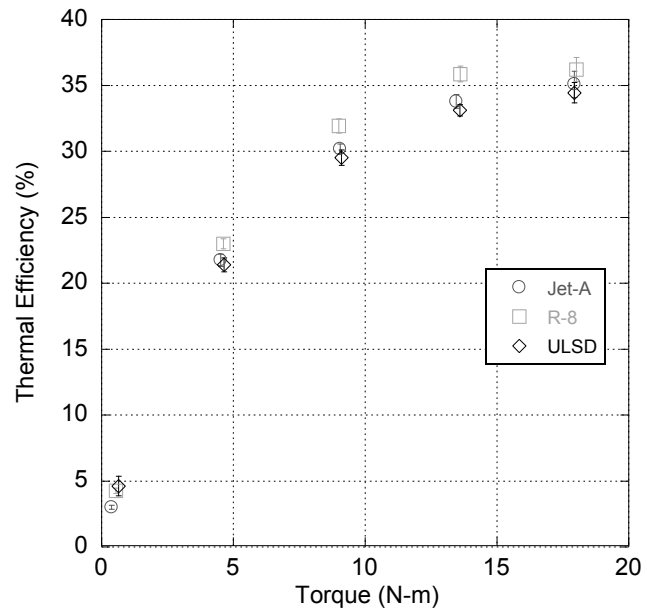


Figure A-99. Thermal Efficiency vs. Torque for Adjusted R-8, Jet-A, and ULSD.

Table A-110. Thermal Efficiency vs. Torque for Adjusted R-8, Jet-A, and ULSD.

Torque (N-m)	ULSD	Jet-A	R-8
0.5	4.6 ± 0.7	3.0 ± 0.2	4.3 ± 0.2
4.5	21.4 ± 0.5	21.7 ± 0.5	23.0 ± 0.4
9.0	29.5 ± 0.6	30.2 ± 0.4	31.9 ± 0.5
13.5	33.1 ± 0.4	33.8 ± 0.5	35.9 ± 0.6
18.0	34.4 ± 0.8	35.1 ± 1.0	36.2 ± 0.9

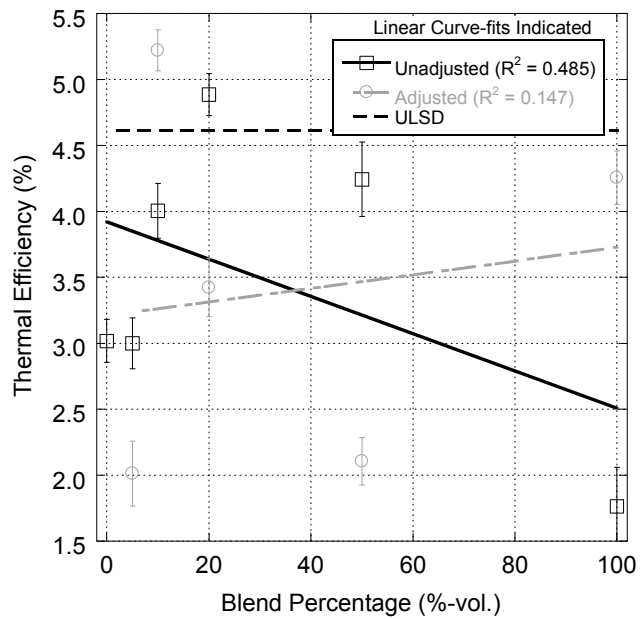


Figure A-100. Thermal Efficiency vs. Blend Percentage for Unadjusted and Adjusted Blends at 0.5 N·m Loading.

Table A-111. Thermal Efficiency vs. Blend Percentage for Unadjusted and Adjusted Blends at 0.5 N·m Loading.

R-8 Blend Percentage	Unadjusted Timing	Adjusted Timing
0	3.0 ± 0.2	3.0 ± 0.2
5	3.0 ± 0.2	2.0 ± 0.2
10	4.0 ± 0.2	5.2 ± 0.2
20	4.9 ± 0.2	3.4 ± 0.2
50	4.2 ± 0.3	2.1 ± 0.2
100	1.8 ± 0.3	4.3 ± 0.2

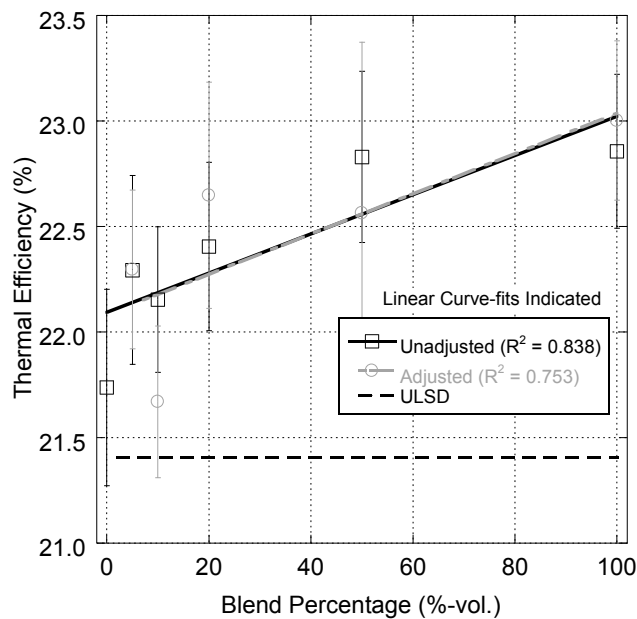


Figure A-101. Thermal Efficiency vs. Blend Percentage for Unadjusted and Adjusted Blends at 4.5 N·m Loading.

Table A-112. Thermal Efficiency vs. Blend Percentage for Unadjusted and Adjusted Blends at 4.5 N·m Loading.

R-8 Blend Percentage	Unadjusted Timing	Adjusted Timing
0	21.7 ± 0.5	21.7 ± 0.5
5	22.3 ± 0.4	22.3 ± 0.4
10	22.2 ± 0.3	21.7 ± 0.4
20	22.4 ± 0.4	22.6 ± 0.5
50	22.8 ± 0.4	22.6 ± 0.8
100	22.9 ± 0.4	23.0 ± 0.4

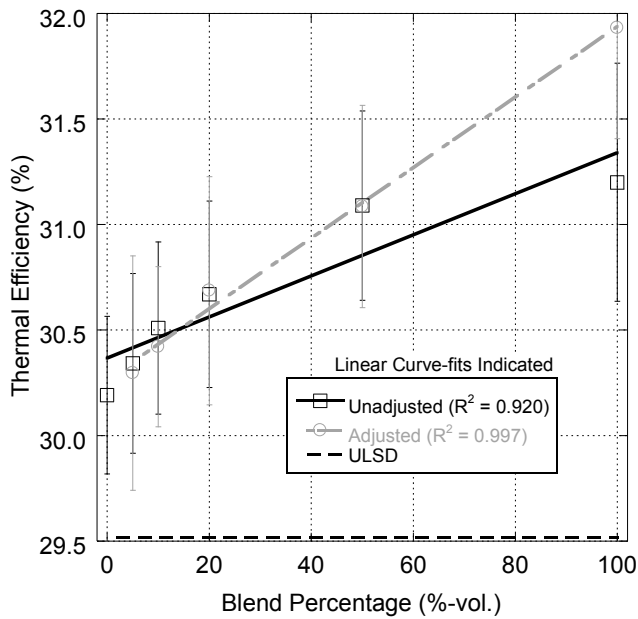


Figure A-102. Thermal Efficiency vs. Blend Percentage for Unadjusted and Adjusted Blends at 9.0 N·m Loading.

Table A-113. Thermal Efficiency vs. Blend Percentage for Unadjusted and Adjusted Blends at 9.0 N·m Loading.

R-8 Blend Percentage	Unadjusted Timing	Adjusted Timing
0	30.2 ± 0.4	30.2 ± 0.4
5	30.3 ± 0.4	30.3 ± 0.6
10	30.5 ± 0.4	30.4 ± 0.4
20	30.7 ± 0.4	30.7 ± 0.5
50	31.1 ± 0.4	31.1 ± 0.5
100	31.2 ± 0.6	31.9 ± 0.5

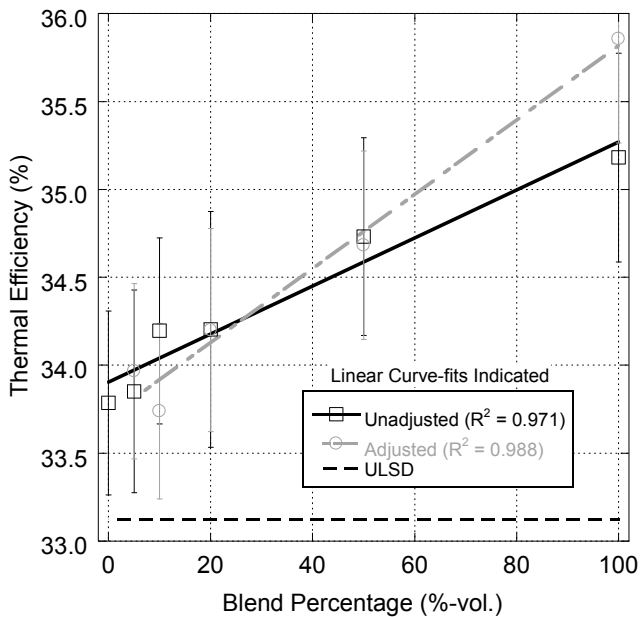


Figure A-103. Thermal Efficiency vs. Blend Percentage for Unadjusted and Adjusted Blends at 13.5 N·m Loading.

Table A-114. Thermal Efficiency vs. Blend Percentage for Unadjusted and Adjusted Blends at 13.5 N·m Loading.

R-8 Blend Percentage	Unadjusted Timing	Adjusted Timing
0	33.8 ± 0.5	33.8 ± 0.5
5	33.9 ± 0.6	34.0 ± 0.5
10	34.2 ± 0.5	33.7 ± 0.5
20	34.2 ± 0.7	34.2 ± 0.6
50	34.7 ± 0.6	34.7 ± 0.5
100	35.2 ± 0.6	35.9 ± 0.6

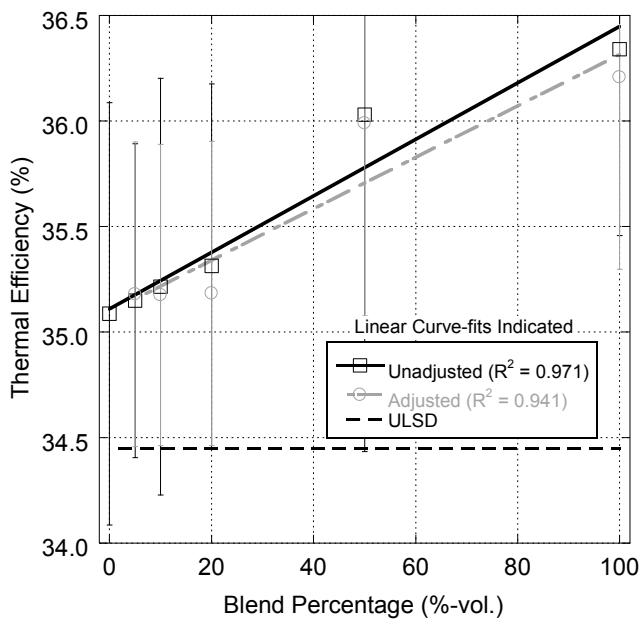


Figure A-104. Thermal Efficiency vs. Blend Percentage for Unadjusted and Adjusted Blends at 18.0 N·m Loading.

Table A-115. Thermal Efficiency vs. Blend Percentage for Unadjusted and Adjusted Blends at 18.0 N·m Loading.

R-8 Blend Percentage	Unadjusted Timing	Adjusted Timing
0	35.1 ± 1.0	35.1 ± 1.0
5	35.1 ± 0.7	35.2 ± 0.7
10	35.2 ± 1.0	35.2 ± 0.7
20	35.3 ± 0.9	35.2 ± 0.7
50	36.0 ± 1.6	36.0 ± 0.9
100	36.3 ± 0.9	36.2 ± 0.9